



**INFLUENCE OF ROUGHNESS ON THE
DYNAMICAL PROPERTIES OF GRANULAR
GASES**

*A thesis submitted in fulfilment of the requirements for the degree of Doctor of
Philosophy*

Author:

Alberto Megías Fernández

Supervisor:

Prof. Dr. Andrés Santos

Creative Commons License

© ⓘ Ⓞ Ⓟ This license allows reusers to distribute, remix, adapt, and build upon the material in any medium or format for noncommercial purposes only, and only so long as attribution is given to the creator. If you remix, adapt, or build upon the material, you must license the modified material under identical terms.

To view a copy of the CC BY-NC-SA code, visit:

<https://creativecommons.org/licenses/by-nc-sa/4.0/>

A mis padres y a mi hermano

A Blanca

There are very, very simple problems that are very hard to understand
Giorgio Parisi, [Nobel Prize in Physics 2021](#)

Resumen

El estudio físico-estadístico de la materia granular es esencial para entender desde un punto de vista fundamental los fenómenos que presentan estos sistemas clásicos de muchas partículas. En condiciones de flujo rápido, los materiales granulares exhiben un comportamiento que recuerda al de un gas y que puede estudiarse desde el punto de vista de la teoría cinética de gases. A diferencia de un gas molecular, un gas granular disipa energía debido a las colisiones entre sus partículas. Por ello, mientras que el modelo más sencillo de un gas molecular consiste en una colección de esferas duras elásticas, para un gas granular, éstas se consideran inelásticas y su extensión más realista consiste en considerar también su rugosidad superficial. Además, un gas granular puede encontrarse tanto en libre evolución, como forzado o sumergido en un fluido intersticial. En este trabajo, se ha tratado de describir la dinámica de gases granulares bajo distintas ligaduras con el objetivo de extraer propiedades específicas del caso rugoso. Para ello, se ha utilizado la ecuación de Boltzmann, añadiendo, en el caso forzado y de suspensiones, términos de tipo Fokker–Planck. Los principales objetivos de la tesis han sido describir teóricamente los estados homogéneos de los gases considerados, el estudio de efectos de memoria en ellos, y la caracterización de las propiedades de transporte e inestabilidades en la descripción hidrodinámica de un gas granular de partículas rugosas. Todo este análisis ha sido complementado con simulaciones por ordenador bajo algoritmos de tipo Monte Carlo y de dinámica molecular.

Abstract

The statistical-physical study of granular matter is essential to understand, from a fundamental point of view, the many different phenomena emerging in these classical many-body systems. Under rapid-flow conditions, granular materials exhibit a gas-like behavior, which can be described from the kinetic theory of gases. However, unlike molecular gases, a granular gas dissipates energy upon particle collisions, thus being completely out of equilibrium. Then, whereas the simplest model for a molecular gas consists in a collection of elastic hard spheres, a granular gas is simply described by inelastic hard spheres, which is usually improved by the consideration of surface roughness in the particles. Moreover, a granular gas can be found in free evolution, externally driven, or even immersed in an interstitial fluid. In this work, the description of the dynamics of granular gases has been carried out with the aim of identifying the specific properties emerging from the model by considering the surface roughness of granular particles. For that end, we have used the Boltzmann equation, adding in the driven and suspension cases a Fokker–Planck-like term. The main objectives of this thesis have been the theoretical description of the homogeneous states of the considered models, as well as the study of memory effects emerging from out-of-equilibrium states, and, finally, the transport properties and the appearance of instabilities in the hydrodynamic description of a granular gas of inelastic and rough particles. All these kinetic-theory analyses have been supplemented with computer simulations from Monte Carlo and molecular dynamics algorithms.

Agradecimientos

Como ya se explicará, uno de los resultados de esta tesis es que muchos “granitos” pueden llevar a resultados muy satisfactorios. La propia consecución de este trabajo es una analogía de ello. Y es que, su realización ha sido posible gracias a la aportación de muchos de estos “granitos” por parte de muchas personas, tanto en el ámbito científico como en el personal.

Como es evidente, en unos simples y cortos párrafos es imposible expresar todo, ni siquiera mencionar a todas esas personas que me han aportado algo durante esta etapa. Sin embargo, me gustaría destacar ciertas personas y momentos que han sido cruciales durante el desarrollo de mi tesis doctoral. Aunque también a usted, lector, debo agradecerle que se haya parado a leer esta memoria y espero que, de alguna forma, aunque no sea en su contenido, algo le resulte interesante o le sea de utilidad, incluso si ha llegado aquí por mera casualidad.

Primero de todo, y como no podría ser de otra forma, quería agradecer todo su tiempo, su trabajo y su ayuda a mi director de tesis, Andrés Santos. Esta historia comenzó con unas clases de Física Cuántica I en inglés, en las que por primera vez disfruté de su labor docente. Ello me llevó a querer (y conseguir) realizar la “Beca de Colaboración” y el TFG con él, que supondría alcanzar mi primer sueño, el de ser graduado en Física. Esa primera época llena de apoyo y consejos conllevó al comienzo y desarrollo de una etapa dura, pero muy bonita: la realización de esta tesis doctoral. Muchas gracias, Andrés, por guiarme, comprenderme, apoyarme y sobre todo, confiar en mí en todo momento, en los mejores y en los de más agobio. Gracias, sobre todo, por querer siempre lo mejor para mí y darme la oportunidad de buscarlo. Llevaré toda mi vida conmigo tus consejos y los conocimientos (en el sentido más amplio de la palabra) que me has transmitido durante estos años.

Quería agradecer también a Antonio Prados su ayuda, su tiempo y su trabajo, del que he podido aprender mucho y conseguir diferentes perspectivas durante el desarrollo de la investigación.

A pesar de que la tesis se ha desarrollado en la Universidad de Extremadura, he podido de disfrutar de estancias de investigación en el extranjero. Primero, me gustaría agradecer a Nikolai V. Brilliantov su gran acogida durante mi estancia en “Skolkovo Institute of Science and Technology” en Moscú, Rusia. Gracias a Nikolai pude asistir a un curso durante mi primer año de doctorado que ha sido fundamental durante mi desarrollo como investigador y, además, me permitió comenzar mi primera experiencia de una colaboración científica en un centro de alto prestigio. Por otro lado, me gustaría agradecer también su gran hospitalidad a Hans J. Herrmann durante mi estancia en

el “Laboratoire de Physique et Mécanique des Milieux Hétérogènes” (PMMH) de la ESPCI en París, Francia. Hans, no solo me acogió con los brazos abiertos, sino que me integró estupendamente desde el primer día en el laboratorio. Le estaré siempre agradecido por lo todo anterior y lo aprendido con él sobre el mundo granular durante esos meses. Finalmente, no podría olvidarme de mis compañeros Ernesto, Fernando, Javier y María de Skoltech y Benjamín, Chloé, Francisco, Juan, Lars, Manon y Samantha de PMMH, entre otros muchos, que me han hecho disfrutar mucho más de estas estancias, me ayudaron y me acogieron con mucho cariño. Así como de Jasmin, Khalil, Mohammed, Matrona, Soheil, Tarik y Tim que me hicieron disfrutar aún más de la escuela MOLSIM-2020 en Ámsterdam, Países Bajos.

Tampoco podría olvidarme de todos los miembros del grupo SPhinX de la Universidad de Extremadura, con los que he trabajado estos cuatro años de tesis doctoral y que muchos de ellos han participado en mi formación y motivación previa como estudiante de Física. Gracias al resto de los investigadores “seniors” Enrique Abad, Antonio Astillero, Santos Bravo, Vicente Garzó, Antonio Gordillo, Juan José Meléndez, Álvaro Rodríguez, Juan Jesús Ruiz y Francisco Vega que me han dado consejo y ayuda siempre, y que han favorecido un ambiente de trabajo muy agradable y cercano. Quería mencionar especialmente a Santos Bravo y Juan Jesús Ruiz por permitirme compartir con ellos labores docentes, así como sus enseñanzas y consejos en este aspecto, que me han hecho crecer mucho más como profesional y sobre todo como persona. También quería destacar a Enrique Abad y Vicente Garzó por sus conversaciones futboleras, pero, sobre todo, por sus labores en la coordinación del grupo, mirando siempre por los más jóvenes y por ayudarnos a alcanzar todos nuestros objetivos. Me siento también orgulloso de haber conocido a mis compañeros de viajes y penurias, con muchas risas y buenos momentos en esos maravillosos “Coffee Breaks”: Ana, Andrés, Beatriz, Costantino, Felipe, Javier, Jesús M., Juan, Juanfran, Lucía, Miguel, Miguel Ángel, Moisés y Rubén. También, debo destacar y valorar la labor de Francisco Naranjo y Nuria María García del Moral como gestores del grupo durante este período. Más aún, quería agradecer lo enriquecedor que ha sido contar con las visitas de Mariano López de Haro y Sławomir Pieprzyk, entre otros.

Además, quería expresar mi profundo agradecimiento a los revisores externos de esta tesis doctoral, Meheboob Alam, Stefan Luding y Satoshi Takada, por su disposición a realizar esta labor, así como por leerla de forma cuidada y, también, por las muy interesantes aportaciones que han contribuido a la mejora de esta memoria.

Mi pasión por el mundo investigador es fruto de muchas personas que me han acompañado en este camino. Primero, gracias a mis profesoras de las asignaturas de Química, Física y Matemáticas: Mari Ángeles, Lola y Fátima. Sin vuestra labor, yo no estaría aquí. Por supuesto, gracias a los amigos que he hecho durante mis estudios de grado y máster, cuya amistad espero preservar toda la vida: Álvaro, Blanca, Celia,

Cristina, David, Germán, Jesús T., Toribio, Virginia y Álex. Además, quería mencionar al personal del Fis & Kids. En especial a Marisa Cancillo por su trabajo, pero aun más, por su cariño al frente de este proyecto tan bonito y darme la oportunidad de haber sido espectador y partícipe de él. Así como a los distintos componentes “seniors” del mismo: Javier Acero, María Cruz Gallego, Agustín García, Antonio Serrano y José Vaquero, entre muchos otros. También a todos mis compañeros del Fis & Kids (muchos), investigadores y alumnos, que me habéis acompañado en esta bonita labor de la difusión científica. Una labor que ha sido complementada estos dos últimos años gracias a Guillermo Mena y Laura Morala, y el resto del equipo de la Real Sociedad Extremeña de Amigos del País de Badajoz, por las charlas del “Café Con”, y a mi amigo, anteriormente mencionado, Álex (García-Quismondo), por pensar siempre en mí para todo esto.

También quería destacar y agradecer a la Asociación de Doctorandos de la Universidad de Extremadura (ADUEX) su labor al frente de la búsqueda del bienestar de los estudiantes de doctorado y ayudar a la creación de vínculos entre nosotros. Me siento afortunado de haber formado parte de la Junta Directiva como secretario y haber compartido trabajo con magníficas personas como Juan, Luz, Marta, Manu, Paula y Sara, así como a las antiguas y futuras Juntas. Quiero añadir también, en este agradecimiento, a la asociación InvestigaEx por su lucha constante por la mejora y dignificación de la labor investigadora en Extremadura, sobre todo, para el personal más precario.

En el ámbito más personal yo no habría conseguido nada sin el apoyo constante de mi familia. En especial, mis padres, Marisa y Francisco. No solo me dieron la vida, también me educaron, cuidaron, aconsejaron, apoyaron en todo momento y me permitieron buscar mis objetivos cuales fueran, siempre desde un amor incondicional, que es mutuo, y del que les estaré eternamente agradecido. Estas líneas son muy pocas con respecto a todo lo que os quiero y os debo. También, a mi hermano mayor, Francisco, por ser mi compañero de vida y quererme, apoyarme y defenderme siempre, te quiero. Gracias también a mi sobrino, Francisco Manuel, por llenar de luz, cariño y alegría nuestras vidas. Así como a las peques, María y Julia, que nos aportan continuamente felicidad. Desearía tener unas palabras de agradecimiento para mis tíos, Dioni, Félix y Paco y para mi prima (y hermana) María por vuestro cariño y apoyo constante, así como el del resto de nuestra gran familia. También, gracias a todos mis amigos, del colegio y fuera de él, por vuestro cariño y apoyo incansable.

Por supuesto, no me olvido de mis abuelos, Francisco y Eugenia, que no han podido disfrutar de la consecución de este trabajo, pero sé, que allá dónde estéis con Adela y Blas, me cuidáis y me mandáis toda la fuerza que necesito día a día. Estoy seguro de que los cuatro estáis muy felices por mí.

Y cómo no hablar de Blanca, con la que he compartido estos años de mi vida y espero que sean muchos más. Gracias por ser mi apoyo incondicional, mi sostén emocional y mi felicidad diaria. Gracias por ser mi teorema. No podría haber hecho nada sin ti y sin

tu cariño constante. Te quiero. También, gracias a Nati y Miguel por su apoyo y ayuda durante todo este tiempo.

Finalmente, agradezco la financiación por parte del Ministerio de Ciencia, Innovación y Universidades por la ayuda FPU18-3503 que ha hecho posible la realización de esta tesis doctoral, y por la ayuda EST22-00145 que me ha permitido realizar la segunda estancia de investigación en el “Laboratoire de Physique et Mécanique des Milieux Hétérogènes” (PMMH) de la ESPCI en París, Francia.

Symbols

The next list describes several symbols that will be later used within the body of the document (not necessary in the publications, whose notation is independent) and the first page of their occurrence. The independence of the publications produces that some symbols could be duplicated. Then, if it is needed, all the possible meanings will be explained below. Notice that, if the symbol is firstly introduced in a publication, the referenced page would correspond to the first page of the section where the publication is inserted.

a_k	k^{th} cumulant of a velocity distribution function (p. 36).
a_{kA}	k^{th} cumulant of a velocity distribution function of a sample A initially further from equilibrium than another sample B (p. 88).
a_{kB}	k^{th} cumulant of a velocity distribution function of a sample B initially closer to equilibrium than another sample A (p. 88).
a_k^0	$\equiv a_k(t_0)$, initial value of a_k (p. 88).
a_{kA}^0	$\equiv a_k(t_0)$, initial value of a_k of a sample A initially closer to the steady-state temperature than another sample B (p. 88).
a_{kB}^0	$\equiv a_k(t_0)$, initial value of a_k of a sample B initially closer to the steady-state temperature than another sample A (p. 88).
$a_{pq}^{(r)}$	Cumulant of order (p, q, r) (p. 44).
a_{pq}	$= a_{pq}^{(0)}$, cumulant of order $(p, q, 0)$ (p. 176).
a_k^{H}	Value of the k^{th} cumulant at the homogeneous cooling state (p. 37).
a_k^{st}	Steady-state value of the k^{th} cumulant (p. 152).
a	Arbitrary vectorial function (p. 305).
A	Arbitrary normalization constant of a velocity distribution function (p. 37).
A	Vectorial function of the velocities coupled with the temperature gradient in the first-order distribution $f^{(1)}$ (p. 242).
b	Arbitrary tensorial function (p. 305).
$B(\cdot, \cdot)$	Differential cross-section (p. 50).
B	Vectorial function of the velocities coupled with the density gradient in the first-order distribution $f^{(1)}$ (p. 242).

$\mathfrak{B}_{ij,\widehat{\sigma}}$	Postcollisional operator for a collision between a pair ij of particles with unit vector $\widehat{\sigma}$ (p. 20).
$\mathfrak{B}_{ij,\widehat{\sigma}}^{\text{put}}$	Postcollisional operator for a collision between a pair ij of particles with unit vector $\widehat{\sigma}$ using putative velocities (p. 80).
$\mathfrak{B}_{ij,\widehat{\sigma}}^{\text{fic}}$	Postcollisional operator for a collision between a pair ij of particles with unit vector $\widehat{\sigma}$ using fictive velocities (p. 80).
c	Modulus of the reduced translational velocity of a particle (p. 28).
c_b	Modulus of the reduced translational velocity of a thermal-bath particle (p. 28).
\mathbf{c}	$= \mathbf{v}/v_{\text{th}}$, reduced translational velocity of a particle (p. 28).
\mathbf{c}_{ij}	$= \mathbf{c}_i - \mathbf{c}_j$, relative reduced translational velocity between particles i and j (p. 35).
\mathbf{c}_b	$= \mathbf{v}/v_{\text{th}}$, reduced translational velocity of a thermal-bath particle (p. 28).
\mathcal{C}_{ij}	Tensorial function of the velocities coupled with $\partial_j u_i$ in the first-order velocity distribution function $f^{(1)}$ (p. 242).
d_t	Translational degrees of freedom (p. 8).
d_r	Rotational degrees of freedom (p. 13).
$d\mathbf{S}$	Cross-section of a differential collisional cylinder (p. 19).
D	Diffusion coefficient (p. 27).
$\mathbf{D}^{(1)}$	Drift vector (p. 306).
$\mathbf{D}^{(2)}$	Diffusion matrix (p. 306).
\mathcal{D}_t	$= \partial_t + \mathbf{u} \cdot \nabla$, material time derivative (p. 54).
$\mathcal{D}_t^{(k)}$	k^{th} -order term of \mathcal{D}_t in a Chapman–Enskog expansion (p. 54).
\mathcal{D}_{KL}	Kullback–Leibler divergence (p. 50).
\mathcal{D}_A	Nonequilibrium entropy of a sample A initially further from the equilibrium (steady) state as compared with another sample B (p. 90).
\mathcal{D}_B	Nonequilibrium entropy of a sample B initially closer to the equilibrium (steady) state as compared with another sample A (p. 90).
\mathcal{D}^0	Initial value of the nonequilibrium entropy of a system (p. 90).
\mathcal{D}_A^0	Initial value of the nonequilibrium entropy of a sample A initially further from the equilibrium (steady) state as compared with another sample B (p. 90).
\mathcal{D}_B^0	Initial value of the nonequilibrium entropy of a sample B initially closer to the equilibrium (steady) state as compared with another sample A (p. 90).
\mathcal{D}^{kin}	Kinetic counterpart of the nonequilibrium entropy (p. 86).
\mathcal{D}^{LE}	Local-equilibrium counterpart of the nonequilibrium entropy (p. 86).
$\mathcal{D}_A^{\text{LE}}$	\mathcal{D}^{LE} curve of a sample A initially further from the equilibrium (steady) state than another sample B (p. 89).
$\mathcal{D}_B^{\text{LE}}$	\mathcal{D}^{LE} curve of a sample B initially closer to the equilibrium (steady) state than another sample B (p. 89).
\mathfrak{D}	Thermal distance (p. 66).
\mathfrak{D}_A	Thermal distance of a sample A initially further from the steady-state temperature as compared with another sample B (p. 215).

\mathfrak{D}_B	Thermal distance of a sample B initially closer to the steady-state temperature as compared with another sample A (p. 215).
E	Kinetic energy of a particle (p. 23).
E^t	Translational kinetic energy of a particle (p. 38).
E^r	Rotational kinetic energy of a particle (p. 38).
E_{12}	Kinetic energy of particles 1 and 2 (p. 23).
E'_{12}	Postcollisional kinetic energy of particles 1 and 2 (p. 23).
\mathcal{E}	Scalar function of the velocities coupled with the divergence of the flow velocity field in the first-order distribution $f^{(1)}$ (p. 242).
f	One-body velocity distribution function (p. 17).
f_b	One-body velocity distribution function for thermal-bath particles (p. 310).
f_H	One-body velocity distribution function at the homogeneous cooling state (p. 34).
f_M	Maxwellian velocity distribution function (p. 32).
f_{ref}	Reference velocity distribution function (p. 50).
f''_i	$\equiv f(\mathbf{\Gamma}''_i)$ with $i = 1, 2$, one-body velocity distribution function of the precollisional velocity variables (p. 20).
f^{LE}	Local-equilibrium velocity distribution function (p. 87).
$f^{(k)}$	k^{th} -order of f in a Chapman–Enskog (or Hilbert) expansion (p. 52).
\mathbf{F}^{ext}	External force applied to a system (p. 17).
\mathbf{F}_{coll}	Effective force due to collisions (p. 29).
\mathbf{F}_{drag}	Drag force (p. 29).
F_X	Rate of change of a macrostate variable of the system X (p. 60).
F_Y	Rate of change of an inner variable of the system Y (p. 60).
\mathfrak{F}	Function that returns the numerical solution of a Langevin-like system of equations (p. 80).
g	Modulus of \mathbf{g} (p. 50).
g_{12}	Modulus of \mathbf{g}_{12} (p. 50).
g''_{12}	Modulus of the precollisional version of \mathbf{g}_{12} (p. 50).
\mathbf{g}	$= \mathbf{v}_b - \mathbf{v}$, relative velocity between thermal-bath and Brownian particles (p. 309).
\mathbf{g}'	Postcollisional version of \mathbf{g} (p. 50).
\mathbf{g}_{12}	Relative velocity of the points at contact in a binary collision between particles 1 and 2 (p. 24).
\mathbf{g}''_{12}	Precollisional version of \mathbf{g}_{12} (p. 24).
\mathbf{G}	$= \{\mathbf{F}^{\text{ext}}/m, \boldsymbol{\tau}^{\text{ext}}/I\}$, generalized force per unit mass (p. 17).
h	Hydrodynamic length scale (p. 53).
H	Boltzmann's H -functional (p. 48).
H_{eq}	Value of H at equilibrium (p. 48).
H^*	Boltzmann's H -functional for the reduced velocity distribution function (p. 120).
I	Moment of inertia of a particle (p. 17).

$I[\cdot]$	Reduced collisional operator (p. 34).
\mathcal{I}	Collisional integral (p. 41).
\mathcal{I}_0	$\equiv 2\pi^{\frac{d_t-1}{2}}/(d_t + 1)$, constant introduced in the computation of the collisional integrals (p. 42).
J	Boltzmann collisional operator (p. 20).
J_G	Gain term of the Boltzmann collisional operator (p. 18).
J_L	Loss term of the Boltzmann collisional operator (p. 18).
$J^{(k)}$	k^{th} -order term of J in a Chapman–Enskog (or Hilbert) expansion (p. 52).
\mathcal{J}	Collisional integral (p. 321).
\mathfrak{J}	Jacobian of the transformation $(\Gamma'_1, \Gamma'_2) \rightarrow (\Gamma_1, \Gamma_2)$ or, equivalently, $(\Gamma_1, \Gamma_2) \rightarrow (\Gamma''_1, \Gamma''_2)$ (p. 20).
ℓ	Mean free path (p. 51).
k_B	Boltzmann constant (p. 27).
k_{\parallel}	Critical wave number associated with the longitudinal modes (p. 243).
k_{\perp}	Critical wave number associated with the transverse modes (p. 243).
L	Characteristic length of a system (p. 51).
L_c	Critical length for instabilities (p. 243).
L^{cell}	Characteristic length of a square cell (p. 73).
$L_{x,y}^{\text{cell}}$	Length of the x or y component of a rectangular cell (p. 73).
$L_k^{(n)}$	Associated Laguerre polynomial (p. 36).
K_d	Constant appearing in the definition of the collisional frequency in d dimensions (p. 31).
Kn	Knudsen number (p. 51).
n	Number density (p. 18).
n_b	Number density of thermal-bath particles (p. 28).
N	Number of particles in a system (p. 15).
$N_{x,y}^{\text{cell}}$	Number of cells in a row (x) or a column (y) of the simulation box (p. 73).
\mathcal{N}_k	Normalization constant of S_k (p. 36).
$\mathcal{N}_{pq}^{(r)}$	Normalization constant of $\Psi_{pq}^{(r)}$ (p. 44).
m	Mass of a particle (p. 17).
m_b	Mass of a thermal-bath particle (p. 28).
P_k	Legendre polynomial of order k (p. 44).
\mathbf{P}, P_{ij}	Pressure tensor (p. 242).
\mathbf{q}	(Total) heat flux (p. 242).
\mathbf{q}_t	Translational counterpart of the heat flux (p. 244).
\mathbf{q}_r	Rotational counterpart of the heat flux (p. 244).
\overline{Q}	Total cross section (p. 309).
\mathbf{Q}_{12}	Impulse exerted by particle 1 on particle 2 in a binary collision (p. 24).
\mathbf{Q}_{12}^-	Impulse acting on the precollisional form of a binary collision (p. 26).
$\mathbf{Q}_{12}^{\parallel}$	Component of \mathbf{Q}_{12} parallel to the unit vector $\hat{\sigma}$ (p. 25).

\mathbf{Q}_{12}^\perp	Component of \mathbf{Q}_{12} perpendicular to the unit vector $\widehat{\sigma}$ (p. 25).
\mathbf{r}	Position of a particle (p. 17).
\mathbf{r}^*	Position of a particle after a small time interval of width δt (p. 17).
\mathbf{r}^{fic}	Fictive positions in an event-driven molecular dynamics algorithm with Langevin-like dynamics (p. 80).
\mathbf{r}^{put}	Putative positions in an event-driven molecular dynamics algorithm with Langevin-like dynamics (p. 80).
r_{ij}	$= \mathbf{r}_i - \mathbf{r}_j $, distance between a pair ij of particles (p. 17).
s	Dimensionless time scale that represents the (local-equilibrium) accumulated average number of collisions per particle up to a certain time (p. 34).
s_0	Accumulated average number of collisions per particle at t_0 (p. 34).
s_w	Waiting number of collisions per particle in the velocity-inversion computational experiment (p. 121).
S	(Nonequilibrium) entropy (p. 47).
S_{eq}	Equilibrium value of the entropy (p. 48).
S_k	k^{th} -order Sonine polynomial (p. 36).
\mathbf{S}_{12}	$= \sigma(\boldsymbol{\omega}_1 + \boldsymbol{\omega}_2)/2$, mean angular velocity vector of particles 1 and 2 in units of their diameter, σ (p. 24).
Sr	Strouhal number (p. 52).
t	Time variable (p. 17).
t_0	Reference initial time value (p. 34).
t_{coll}	Time when a collision event occurs (p. 80).
t_θ	Thermal crossing time (p. 86).
$t_{\mathcal{D}}$	Entropic crossing time (p. 88).
$t_{\mathcal{D}^{\text{LE}}}$	Thermal-distance crossing time (p. 89).
t_O	Overshoot crossing time (p. 89).
t_w	Waiting time (p. 59).
t^*	$= t + \delta t$, time translated by a small time interval δt (from p. 17). $\equiv t\nu_b$ or $\equiv t\nu^{\text{wn}}$, reduced time variable for a system under the action of a thermal bath (introduced in p. 90).
t_K^*	$\equiv \nu_b t_K$, Kovacs waiting time (p. 153).
T	Temperature of a system (p. 32).
T_A	Temperature of a sample A initially further from the equilibrium or steady-state temperature as compared with another sample B (p. 88).
T_b	Temperature associated with a thermal bath (p. 11).
T_B	Temperature of a sample B initially closer to the equilibrium or steady-state temperature as compared with another sample A (p. 88).
T_H	Temperature of a system at the homogeneous cooling state (p. 34).
T_{ref}	Reference bath-temperature (p. 59).
T_t	Translational temperature (p. 38).

T_r	Rotational temperature (p. 38).
T^{wn}	Temperature associated with a thermostat (p. 30).
T^{st}	Steady-state value of the temperature (p. 64).
T^0	$\equiv T(t_0)$, initial temperature (p. 88).
$T_A^0 (T_{0A})$	Initial temperature of a sample A initially further from the equilibrium or steady-state temperature as compared with another sample B (p. 88).
$T_B^0 (T_{0B})$	Initial temperature of a sample B initially closer to the equilibrium or steady-state temperature as compared with another sample A (p. 88).
\mathbf{u}	Flow field of the system (p. 49).
U_{ij}	Potential energy of a pair ij of particles (p. 17).
v	Velocity modulus of a particle (p. 28).
$v_{x,y,z}$	x , y or z velocity component of \mathbf{v} (p. 74).
v_b	Velocity modulus of a thermal-bath particle (p. 28).
v_{th}	Thermal velocity (p. 28).
$v_{\text{th},b}$	Thermal velocity of thermal-bath particles (p. 28).
\mathbf{v}	Translational velocity of a particle (p. 16).
\mathbf{v}'	Postcollisional translational velocity of a particle (p. 21).
\mathbf{v}''	Precollisional translational velocity of a particle (p. 19).
\mathbf{v}^*	Translational velocity of a particle after a small time interval δt (p. 17).
\mathbf{v}_b	Translational velocity of a thermal-bath particle (p. 28).
\mathbf{v}_{ij}	$= \mathbf{v}_i - \mathbf{v}_j$, relative translational velocity of a pair ij of particles (p. 18).
\mathbf{v}'_{ij}	Postcollisional relative translational velocity of a pair ij of particles (p. 21).
\mathbf{v}''_{ij}	Precollisional relative translational velocity of a pair ij of particles (p. 19).
\mathbf{v}^{fic}	Fictive velocities in an event-driven molecular dynamics algorithm with Langevin-like dynamics (p. 80).
\mathbf{v}^{put}	Putative velocities in an event-driven molecular dynamics algorithm with Langevin-like dynamics (p. 80).
V	Modulus of the peculiar velocity (p. 54).
V_{eq}	Volume at equilibrium (p. 59).
\mathbf{V}	$= \mathbf{v} - \mathbf{u}$, peculiar velocity (p. 54).
$\overline{\boldsymbol{\omega}}$	$= \boldsymbol{\omega} / \omega_{\text{th}}$, reduced angular velocity of a particle (p. 39).
\overline{W}	Number of microstates compatible with a given macrostate of the system (p. 47).
W_{12}	$\equiv (\boldsymbol{\omega}_1 + \boldsymbol{\omega}_2) / 2$, mean reduced angular velocity of particles 1 and 2 (p. 42).
W_t	Wiener process (p. 305).
$\mathcal{W}, \bar{\mathcal{W}}$	Random Gaussian variables emerging from the solution of Langevin-like equations (p. 79).
X	Arbitrary macrostate quantity in the context of nonequilibrium processes (p. 59).
\tilde{X}	$\equiv I\bar{\Omega}^2 / d_r T_r$, nondimensional rotational quantity (p. 43).

\tilde{X}^H	Value of $I\bar{\Omega}^2/d_r T_r$ at the homogeneous cooling state (p. 43).
X	Noise-intensity diagonal matrix (p. 308).
Y	Inner arbitrary dynamic quantity of the system in the context of nonequilibrium processes (p. 60).
$\mathcal{Y}, \bar{\mathcal{Y}}$	Random Gaussian variables of unit variance and zero mean appearing in the definition of the variables $\mathcal{W}, \bar{\mathcal{W}}$ (p. 79).
α	Coefficient of normal restitution (p. 8).
$\bar{\alpha}$	Reduced coefficient of normal restitution (p. 25).
β	Coefficient of tangential restitution (p. 8).
$\bar{\beta}$	Reduced coefficient of tangential restitution (p. 25).
γ	Control parameter of the nonlinearity in a drag coefficient (p. 29).
γ_c	Exponent of the high-velocity tail of ϕ_c^H (p. 37). Critical value of the nonlinear parameter γ (p. 152).
γ_c^{IHS}	Value of the exponent γ_c for the inelastic hard-sphere model (p. 37).
γ_c^{IRHS}	Value of the exponent γ_c for the inelastic and rough hard-sphere model (p. 176).
γ_c^{wn}	Value of the exponent γ_c for the externally driven case (p. 46).
γ_{cw}	Exponent of the high-velocity tail of the ϕ_{cw}^H (p. 176).
γ_w	Exponent of the high-velocity tail of ϕ_c^H (p. 176).
$\bar{\gamma}$	Set of noise parameters (p. 80).
$\Gamma(\cdot)$	Gamma function (p. 31).
Γ	Generalized velocity vector of a particle (p. 16).
Γ'	Postcollisional generalized velocity vector of a particle (p. 18).
Γ''	Precollisional generalized velocity vector of a particle (p. 18).
Γ^{put}	Putative generalized velocity vector of a particle (p. 81).
Γ^{fic}	Fictive generalized velocity vector of a particle (p. 81).
$\tilde{\Gamma}$	Generalized reduced-velocity vector of a particle (p. 39).
$\delta(\cdot)$	Dirac delta (p. 27).
δ_{ij}	Kronecker delta (p. 27).
δt	Small perturbative time interval (p. 17).
δQ	Heat transferred in a reversible process (p. 47).
Δt	Time step (or width of a time interval) (p. 69).
Δt_{coll}	$\equiv t_{\text{coll}} - t$, width of a time interval between a time of a collision event and current time (p. 80).
ε	$= \frac{d_r}{d_t} \frac{I}{m} \frac{\chi_r^2}{\chi^2}$, rotational-to-total noise intensity ratio (p. 30).
ε_{cr}	Critical value of ε that controls the emergence of overshoot (p. 214).
ε_{ref}	Reference value of ε in a Mpemba-like effect protocol (p. 214).
ϵ	Bookkeeping parameter (p. 52).
ζ	Cooling rate (p. 33).
ζ^*	Reduced cooling rate (p. 34).
ζ_H	Cooling rate at the homogeneous cooling state (p. 34).

ζ_{H}^*	Reduced cooling rate at the homogeneous cooling state (p. 34).
$\zeta_{\text{H}}^{*\text{MA}}$	Reduced cooling rate at the homogeneous cooling state in the Maxwellian approximation (p. 36).
$\zeta_{\bar{\Omega}}$	Production rate associated with the mean angular velocity evolution (p. 40).
$\zeta_{\bar{\Omega}}^{\text{H}}$	Production rate associated with the mean angular velocity evolution (p. 40).
$\zeta_{\bar{\Omega}}^*$	$\equiv \zeta_{\bar{\Omega}}/\nu$, reduced production rate associated with the mean angular velocity evolution (p. 43).
η	Shear viscosity (p. 242).
η_b	Bulk viscosity (p. 242).
$\boldsymbol{\eta}$	Random Gaussian-distributed force (p. 27).
$\bar{\boldsymbol{\eta}}$	Random Gaussian-distributed force of unit variance (p. 78).
$\bar{\boldsymbol{\eta}}_d$	Random Gaussian-distributed force of unit variance of d dimensions (p. 308).
θ	$= T_r/T_t$, rotational-to-translational temperature ratio (p. 40).
θ^{st}	Steady-state value of θ (p. 214).
θ^{H}	Value of θ at the homogeneous cooling state (p. 43).
$\theta_{\text{M}}^{\text{H}}$	θ^{H} for the Maxwellian approximation (p. 44).
θ^0	Initial condition for θ (p. 214).
θ_{A}^0 ($\theta_{0\text{A}}$)	Initial condition for θ of a sample A initially further from the steady-state temperature as compared with another sample B (p. 215).
θ_{B}^0 ($\theta_{0\text{B}}$)	Initial condition for θ of a sample B initially closer to the steady-state temperature as compared with another sample A (p. 215).
ϑ	Angle formed by \mathbf{v}_{12} and $d\mathbf{S}$ (p. 19). Impact angle in a binary collision (from p. 22).
ϑ''	Precollisional impact angle in a binary collision (p. 22).
$\bar{\vartheta}$	Angle between \mathbf{g}' and \mathbf{g} (p. 309).
Θ	Heaviside step-function (p. 19).
κ	$= 4I/m\sigma^2$, reduced moment of inertia (p. 25).
λ	Thermal conductivity (p. 242).
μ	Dufour-like transport coefficient (p. 242).
μ_k	Collisional moment of order k (p. 34).
μ_k^{H}	Collisional moment of order k at the homogeneous cooling state (p. 35).
$\mu_k^{(p)}$	Coefficient of the k^{th} collisional moment accompanying a_p from a linearization in cumulants of the Sonine approximation (p. 154).
μ_{pq}	$\equiv \mu_{pq}^{(0)}$, collisional moment of order $(p, q, 0)$ (p. 177).
μ_{pq}^{H}	$\equiv \mu_{pq}^{(0)\text{H}}$, collisional moment of order $(p, q, 0)$ at the homogeneous cooling state (p. 177).
$\mu_{pq}^{(r)}$	Collisional moment of order (p, q, r) (p. 41).
$\mu_{pq}^{(r)\text{H}}$	Collisional moment of order (p, q, r) at the homogeneous cooling state (p. 41).
ν	Collision frequency (p. 34).

ν_b	Collision frequency of a system at T_b (p. 86).
ν^{wn}	Collision frequency associated with the thermostat energy injection (p. 31).
ξ	Velocity-divergence transport coefficient (p. 244).
$\xi(v)$	Nonlinear drag coefficient (p. 307).
ξ_0	Constant drag coefficient (p. 27).
ξ_0^*	$\equiv \xi_0/\nu_b$ reduced constant drag coefficient (p. 314).
ξ_{eff}	Effective drag coefficient in a system with Langevin-like dynamics under nonlinear drag (p. 90).
ξ_{QR}	Drag coefficient in the quasi-Rayleigh regime (p. 28).
ξ_t	Translational energy production rate (p. 39).
ξ_r	Rotational energy production rate (p. 39).
$\xi_{t,r}^{\text{H}}$	Energy production rates at the homogeneous cooling state (p. 40).
$\xi_{t,r}^*$	$\equiv \xi_{t,r}/\nu$, reduced energy production rates (p. 43).
$\xi_{t,r}^{\text{H}*}$	Value of $\xi_{t,r}^*$ at the homogeneous cooling state (p. 43).
ω_{ij}	Estimator of the collision rate (p. 69).
ω_{max}	Upper bound estimate of the collision rate (p. 69).
ρ	Mass density (p. 322).
σ	Diameter of a particle (p. 17).
σ_b	Diameter of a thermal-bath particle (p. 28).
σ_{ij}	$= (\sigma_i + \sigma_j)/2$, mean diameter of a pair ij of particles (p. 17).
$\widehat{\sigma}(\widehat{\sigma}_{ij})$	$= (\mathbf{r}_i - \mathbf{r}_j)/r_{ij}$, unit intercenter vector of a pair ij of particles. (p. 19)
$\widehat{\sigma}_{ij}^{\text{fic}}$	Fictive unit intercenter vector in an event-driven molecular dynamics algorithm with Langevin-like dynamics (p. 80).
τ	Mean free time (p. 51).
τ_0	Typical time scale of a problem (p. 51).
τ_b	Mean free time for a dilute gas at T_b (p. 151).
τ_c	Collision duration (p. 53).
τ_h	Hydrodynamic time scale (p. 53).
τ_t	$= T_t/T$, translational temperature ratio (p. 39).
τ_t^{H}	τ_t evaluated at the homogeneous cooling state (p. 39).
τ_r	$= T_r/T$, rotational temperature ratio (p. 39).
τ_r^{H}	τ_r evaluated at the homogeneous cooling state (p. 39).
$\boldsymbol{\tau}^{\text{ext}}$	External torque applied to a system (p. 17).
ϕ	Reduced one-body velocity distribution function (p. 34).
ϕ_i''	$\equiv \phi(\widetilde{\Gamma}_i'')$, precollisional version of the reduced one-body velocity distribution function (p. 35).
ϕ_{H}	Reduced one-body velocity distribution function at the homogeneous cooling state (p. 34).
ϕ_{M}	Maxwellian reduced velocity distribution function (p. 36).
ϕ^{wn}	Reduced one-body steady-state velocity distribution function of an externally

	driven granular gas (p. 46).
ϕ_c	Translational marginal velocity distribution function (p. 43).
ϕ_w	Rotational marginal velocity distribution function (p. 43).
ϕ_{cw}	Marginal velocity distribution function for the variable c^2w^2 (p. 176).
ϕ_c^H	ϕ_c at the homogeneous cooling state (p. 176).
ϕ_w^H	ϕ_w at the homogeneous cooling state (p. 176).
ϕ_{cw}^H	ϕ_{cw} at the homogeneous cooling state (p. 176).
Φ	Slope for the temperature evolution in an homogeneous granular gas of inelastic and rough hard disks under the action of the splitting thermostat (p. 214).
$\Phi_{0,A}$	Initial value of the slope Φ of a sample A initially further from the steady-state temperature as compared with another sample B (p. 215).
$\Phi_{0,B}$	Initial value of the slope Φ of a sample B initially closer to the steady-state temperature as compared with another sample A (p. 215).
χ^2	(Total) noise intensity (p. 27).
χ_t^2	Noise intensity of the translational degrees of freedom (p. 30).
χ_r^2	Noise intensity of the rotational degrees of freedom (p. 30).
ψ	Generic velocity-related quantity (p. 33).
$\Psi_{pq}^{(r)}$	Polynomial of order (p, q, r) forming an orthogonal basis (p. 44).
ω_{th}	Thermal angular velocity (p. 39).
ω	Angular velocity of a particle (p. 16).
ω'	Postcollisional angular velocity of a particle (p. 25).
ω^*	Angular velocity of a particle after a small time interval δt (p. 17).
Ω_d	Solid angle in d dimensions (p. 30).
$\mathbf{\Omega}$	Solid angle vector (p. 19).
$\bar{\mathbf{\Omega}}$	$\equiv \langle \omega \rangle$, mean angular velocity of a system (p. 40).
$\bar{\mathbf{\Omega}}_H$	Value of $\bar{\mathbf{\Omega}}$ at the homogeneous cooling state (p. 40).
$\langle \cdot \rangle_H$	Average at the homogeneous cooling state (p. 35).
$\langle \cdot \rangle_M$	Average under the Maxwellian approximation (p. 37).
$\mathbb{1}_d$	Unit matrix in d dimensions (p. 27).
$\lfloor \cdot \rfloor$	Largest integer smaller than a given real number (p. 69).
$\int_+ d\hat{\sigma}$	$\equiv \int d\hat{\sigma} \Theta(\mathbf{v}_{12} \cdot \hat{\sigma})$, integration in the semiplane $\mathbf{v}_{12} \cdot \hat{\sigma} \geq 0$ (p. 20).

List of Figures

2.1	On the left, we show a sketch of a binary collision between a projectile particle (1) and a target particle (2). The big dashed circle represents the distance at σ from the center of particle 2 where a collision takes place if the center of another sphere is located there. The smaller dashed circle represents the location of particle 1 at the time of collision. On the right part of the figure, there is a scheme of the collision cylinder represented by a reddish cylinder, where ϑ is the angle formed by the vector \mathbf{v}_{12} and $d\mathbf{S}$, which is the differential area at contact shared by the dashed sphere of radius σ centered at particle 2 and the collision cylinder. In addition, the differential solid angle $d\Omega$ is depicted by a yellowish cone.	19
2.2	Sketch of (a) a collision between two hard spheres and (b) the collisional process in the EHS model with the notation of the direct collisional rules for the spatial and velocity quantities. Here, $\vartheta = \arccos(\mathbf{v}_{12} \cdot \widehat{\boldsymbol{\sigma}} /v_{12})$ is the impact angle, which, due to reflective elastic collisions, coincides with its postcollisional version, $\vartheta' = \arccos(\mathbf{v}'_{12} \cdot \widehat{\boldsymbol{\sigma}} /v'_{12})$	22
2.3	Sketch of (a) a collision between two hard inelastic spheres where the reddish glints represent the presence of inelasticity, and (b) the collisional process in the IHS model with the notation of the direct collisional rules for the spatial and velocity quantities. Notice that, as compared with Figure 2.2 , there is no reflection any more due to generally different impact and resulting angles, $\vartheta \neq \vartheta'$	23
2.4	Representation of a collision between (a) two HD and (b) two HS . It can be observed that the evolution of the HD is restricted to the plane and that their associated angular velocities lie along the direction orthogonal to the plane. On the other hand, there is no restriction of this kind for HS , where both translational and angular velocities live in the same three-dimensional vector space.	25
3.1	Sketch of a general Kovacs-like protocol on a macroscopic variable X , with $T_0 > T_{\text{ref}} > T_1$. On the left-hand side of the figure there is a graph of the evolution of X during the Kovacs-like experiment, complemented by a sketch of the protocol for the thermal bath temperature, T_b , on the right-hand side. The blue thick continuous curve corresponds to the real time evolution of the X macroscopic variable. The red dashed curve (--) refers to the relaxation of X from T_0 to T_1 , while the green dashed-dotted (-·-) line depicts the direct evolution of X from T_0 to T_{ref}	59

- 3.2 E. B. Mpemba and D. G. Osborne, Cool?, *Phys. Educ.* **4** pp. 172-175 (1969), DOI: [10.1088/0031-9120/4/3/312](https://doi.org/10.1088/0031-9120/4/3/312). ©IOP Publishing. Reproduced with permission. All rights reserved. Graph of the fitting curve for several experimental points reproducing the time a sample of liquid water started to freeze up in minutes, with respect to the initial temperature of the cooling process. The results come from the original and very first experiments of Mpemba and Osborne. 62
- 4.1 Sketch of initialization cells for (a) squared and (b) cubic, with one particle per cell arrangements. In the three-dimensional cubic case not all cells are displayed to ensure a proper visualization. 75
- 5.1 Sketch of the evolution of the **VDF**, f . The decomposition of the **KLD** into the kinetic and local-equilibrium counterparts is represented. First, the evolution of the **VDF** is involved into a kinetic stage, in which the **VDF** stays completely at a nonequilibrium regime. Then, f enters in local equilibrium (f^{LE}) and the **VDF** is fully described by its instantaneous temperature, $T(t)$, before the relaxation toward equilibrium is completed. 87
- C.1 Steady-state values of (a) the granular temperature, T^{st}/T_b , and (b) the excess kurtosis a_2^{st} , vs. the coefficient of normal restitution α for $\xi_0^* \approx 0.89$ and **HS** ($d_t = 2$). The circles (\circ) stand for **EDMD** simulation results, while the thick black lines (—) refer to the values corresponding to Eqs. (C.1). The values of the coefficient of normal restitution used in the simulations are $\alpha = 0.95, 0.87, 0.6, 0.5, 0.4$ 315
- C.2 Plot T/T_b vs. $t^* \equiv tv_b$ for a system of **HD** ($d_t = 2$), with $\xi_0^* \approx 0.89$, and for (a) $T(0) = T_b/2$ and (b) $T(0) = 2T_b$. The symbols ($\circ, \square, \triangle, +, *$) stand for **EDMD** simulation results, while the lines ($\text{—}, \text{--}, \text{- -}, \cdot, \cdot\cdot, \cdot\cdot\cdot$) refer to the values corresponding to the differential equation, Eq. (C.4), for the different values of the coefficient of normal restitution, $\alpha = 0.95, 0.87, 0.6, 0.5, 0.4$ 315
- C.3 Steady-state values of (a) the granular temperature, $T^{\text{st}}/T^{\text{wn}}$, and (b) the excess kurtosis, a_2^{st} vs. the coefficient of normal restitution α , for **HS** ($d_t = 2$). The circles (\circ) stand for **EDMD** simulation results, while the thick black lines (—) refer to the values corresponding to Eq. (C.12). The values of the coefficient of normal restitution used in the simulations are $\alpha = 0.95, 0.87, 0.6, 0.5, 0.4$. 317

C.4 Plot T/T^{wn} vs. $t^* \equiv tv_b$, for a system of HD ($d_t = 2$), for an initial condition $T(0) \approx 1.46T^{\text{wn}}$ and (a) $\alpha = 0.95, 0.87$ (whose steady value is greater than the initial condition), and (b) $\alpha = 0.6, 0.5, 0.4$ (whose stationary temperature is below its initial value). The symbols ($\circ, \square, \triangle$) stand for EDMD simulation results, while the lines ($—, - -, \cdots$) refer to the values corresponding to the differential equation, Eq. (C.11). 317

List of Tables

1.1	Summary of the models addressed in this thesis and their corresponding occurrences.	14
2.1	Collisional integrals for velocity functions up to quadratic order in terms of two-body averages. Here, $\mathcal{I}_0 \equiv 2\pi^{\frac{d_t-1}{2}}/(d_t + 1)$	42
2.2	Collisional production rates up to second order in velocity moments under the MA in Eq. (2.103).	43
3.1	Classification of sketches for the different scenarios that can be found in a dynamical study of the ME. The figure is divided into the TME and the EME interpretations, the latter being guided by the quantity \mathcal{D}_{KL} [according to its use in Article 1 (Section 5.2)]. The TME is described in the temperature picture, where the effect is studied by means of the nonequilibrium temperature T , and the thermal-distance picture, where \mathfrak{D} is the chosen quantity [according to the notation of the quantity used in Article 6 (Section 9.2), defined such that $\mathfrak{D} = 0$ if and only if $T = T^{\text{st}}$]. Both descriptions are applied to the DME and the IME, in their standard form or via the OME. The red curves refer to the initially hotter system, whereas the blue ones to the initially colder one. In addition, thick continuous lines correspond to the system initially further from the steady state, whereas the dashed (– –) ones represent the initially closest. Notice that in the EME there is neither red nor blue lines because temperature could be meaningless. The green points appearing in the different intersections are crossing points. Finally, notice that the different scenarios are simplified to a single crossing, which is equivalent to find an odd number of them in the EME or in the thermal-distance picture of the TME.	66
5.1	Summary of crossing times t_X (with $X = \theta, \mathcal{D}^{\text{LE}}$) and the necessary conditions derived from LBSA for the emergence of the standard TME and the OME, in the case of a molecular gas of hard d_t -spheres in contact with a background fluid with a nonlinear drag. Here, $R^0 \equiv (T_A^0 - T_B^0)/T_b(a_{2A}^0 - a_{2B}^0)$, $R_+^0 \equiv (T_A^0 + T_B^0 + 2T_b)/T_b(a_{2A}^0 + a_{2B}^0)$, $R_{\text{max}}^0 \equiv A_{12}/A_{11}$, A_{ij} and $\lambda_{+,-}$ are coming from the LBSA developed in Appendix C of Article 1 (Section 5.2). Overlined quantities refer to their values at $T^0 = T_b$	89

Contents

Resumen	vii
Abstract	ix
Agradecimientos	xi
Symbols	xvii
List of Figures	xxvii
List of Tables	xxix
INTRODUCTION	1
1 General introduction	5
1.1 Structure of the thesis	9
2 Kinetic-theoretical description of molecular and granular gaseous flows	15
2.1 Introduction	15
2.2 Derivation of the Boltzmann equation for hard spherical particles	16
2.3 Collisional models	20
2.3.1 Molecular gas of elastic hard spheres	21
2.3.2 Inelastic hard spheres	22
2.3.3 Inelastic and rough hard spheres	23
2.4 Thermostatted states	26
2.4.1 Langevin dynamics with nonlinear drag	28
2.4.2 Splitting thermostat	29
2.5 Homogeneous states	31
2.5.1 Homogeneous molecular gas of hard d_t -spheres	31
2.5.2 Freely evolving homogeneous granular gas: the Homogeneous Cooling State	32
2.5.3 Homogeneous states for driven granular gases	45
2.6 Nonequilibrium entropy and H -theorem	47
2.6.1 H -theorem for molecular gases of hard spheres	48
2.6.2 The problem of the H -theorem in granular gases	50
2.7 The Chapman–Enskog method	51
2.7.1 A brief description of the Hilbert expansion	52

2.7.2	Chapman–Enskog expansion	53
3	Memory effects	57
3.1	Introduction	57
3.2	Kovacs effect	59
3.3	Mpemba effect	61
4	Simulation Methods	67
4.1	Introduction	67
4.2	Direct Simulation Monte Carlo method	68
4.3	Event Driven Molecular Dynamics	70
4.3.1	A general EDMD algorithm	72
4.3.2	Initialization	72
4.3.3	Event detection	73
4.3.4	Event scheduling	75
4.3.5	Last remarks	77
4.3.6	EDMD with Langevin-like dynamics	78
	MOLECULAR GASES	83
5	Thermal and entropic Mpemba effects in molecular gases under nonlinear drag	85
5.1	Summary	85
5.2	Article 1	90
	GRANULAR GASES OF INELASTIC AND SMOOTH PARTICLES	117
6	Nonequilibrium entropy of inelastic hard d_t-spheres	119
6.1	Summary	119
6.2	Article 2	122
6.3	Article 3	145
7	Inelastic hard d_t-spheres under nonlinear drag	151
7.1	Summary	151
7.2	Article 4	154

GRANULAR GASES OF INELASTIC AND ROUGH PARTICLES	173
8 Homogeneous states in the IRHS model	175
8.1 Summary	175
8.2 Article 5	177
9 Mpemba-like effect in the IRHS model	213
9.1 Summary	213
9.2 Article 6	215
10 Nonhomogeneous states in the IRHS model	241
10.1 Summary	241
10.2 Article 7	244
10.3 Article 8	260
RESULTS AND CONCLUSIONS	275
11 Summary of Results and Discussion	277
11.1 Molecular gases	277
11.2 Granular gases of inelastic particles	279
11.2.1 Freely evolving granular gases of inelastic particles	279
11.2.2 Granular gases of inelastic particles under nonlinear drag	281
11.3 Granular gases of inelastic and rough particles	283
11.3.1 Freely evolving granular gases of inelastic and rough particles	283
11.3.2 Driven granular gases of inelastic and rough particles	288
12 Conclusions and Outlook	293
12.1 Conclusions	293
12.1.1 Molecular gases	293
12.1.2 Inelastic granular gases	294
12.1.3 Inelastic and rough granular gases	296
12.2 Outlooks	298
APPENDICES	303
A Fokker–Planck equation associated with a Langevin-like equation	305
A.1 General relations	305
A.2 Langevin dynamics with a nonlinear drag	307
A.3 Splitting thermostat	308

B	Derivation of the nonlinear drag coefficient for a quasi-Rayleigh gas	309
C	Tests and numerical schemes for the thermostatted states	313
C.1	Test results	313
C.1.1	Granular gas of inelastic HD with Langevin dynamics	314
C.1.2	Granular gas of inelastic HD driven by a stochastic thermostat	315
C.2	Numerical scheme for the Langevin dynamics with nonlinear drag	318
C.3	Numerical scheme for the ST	318
D	Balance equations for the IRHS model	321
D.1	Particle (mass) density balance equation	322
D.2	Momentum density balance equation	322
D.3	Energy density balance equation	323
D.3.1	Equation for the translational temperature	323
D.3.2	Equation for the rotational temperature	323
D.3.3	Balance equation for the mean temperature	324
	Bibliography	325
	Index	357

INTRODUCTION

The Granular Gas Poem

*Invisible and swirling,
Particles collide and mix,
A dance of frenzied motion,
In a world of tiny tricks.*

*Granular gases they are called,
A realm beyond our sight,
But their impact is felt,
As they move with all their might.*

*From powders to sand dunes,
These granules have a way,
Of behaving like a fluid,
But they never stay at bay.*

*Their energy is chaotic,
Like a wild and whirling storm,
And yet they find a way,
To maintain their curious form.*

*They flow and bounce and scatter,
In ways we can't explain,
A never-ending story,
Of movement that sustains.*

*So when you next hold sand,
Or pour sugar in a jar,
Remember the granular gases,
That swirl both near and far.*

*For in these tiny particles,
There's a world of mystery,
A hidden universe,
That we can only see through history.*

ChatGPT - OpenAI

General introduction

1

For dust you are, and to dust you shall return
Genesis 3:19

We're All Made of Dust— But It's Star Dust!
William E. Barton, *The Evening News* (Michigan, 1921)

The cosmos is within us.
We are made of star-stuff.
We are a way for the universe to know itself.
Carl Sagan, *Cosmos: A Personal Voyage* (1980)

We are stardust brought to life, then empowered by the universe to figure itself out – and we have only just begun.
Neil deGrasse Tyson, *Astrophysics for People in a Hurry* (2017)

Science and Christianity agree, *we're all made of dust*. This quote must be remembered and highlighted. It is definitively rare that (old) religious writings and (contemporary) science could agree in something so important as the origin of human beings, of course, both under their own words, meanings, and purposes.

Far from the Christian sense, in the early 20th Century, astronomers and astrophysicists began to understand the problem of star and planet formation and so the beginning of living beings' birthplace. Whereas this popular phrase existed before Carl Sagan, it was him (and more recently, Neil deGrasse Tyson, picking up Sagan's baton), in 1980, in a magnificent effort to communicate the mysteries of the Universe in the TV series *Cosmos: A Personal Voyage*, that made this sentence common in literature, cinema, and daily language. Everyone, captured by Sagan's science communication, understood that we were—and still we are—stardust trying to understand the origin of stars. However,

are we trying to comprehend dust itself? The answer to the latter question is “yes,” but certainly the study of dust, sand, powders, in general, “granular materials” is something *modern* in science, and particularly, in physics.

The 20th Century was the “worst” epoch for Newton’s description of Nature. All the classical theories were questioned, and modern concepts and new discoveries arose. In the first decades, most of attention by physicists was paid to quantum, special and general relativity theories, statistical mechanics (actually present since late 1800s), and solid state physical description. However, something apparently simpler, like granular matter, did not become a real hot topic until 1980s, but its importance and presence in physical, chemical, mathematical, and engineering research increased ever since, becoming the study of granular materials not only an essential research branch nowadays, but one of the starting paradigms in the world of complex systems.

But, how do we define granular materials? A widely-spread definition is that granular materials correspond to large collections of discrete and macroscopic particles. Those particles are the *grains* of such conglomerations. The sizes of such grains vary in a huge range of length scales, since orders of magnitude of 1 μm (ultrafine grains), up to hundreds—or even thousands—of kilometers (like asteroids), with very different morphologies [AFP13]. The latter implies that the variety of systems that can be considered a granular material is enormous. In addition, they are involved constantly in a huge diversity of natural processes like geological phenomena, such as avalanches, erosion, dune formation, earthquakes, or landslides, among others [Raj90; SH91; Her95; Her06; Her07; Lob+08; BMB21; ZH21]. But the action of granular materials is not restricted to Earth, but, also, granular matter participates in astrophysical processes in the form of dust, asteroids, or protoplanetary disks [Sán+17; Sch+21], as some examples. Moreover, research in granular materials about the latter systems has reported quite good predictions, like the size distribution of asteroids in Saturn’s rings [Bri+15].

Granular materials are also very present in industrial engineering. In fact, it is estimated that, in the last decades, around 10% of the human energy consumption is due to processes linked to granular matter [Dur12], implying a huge impact in the economy and, more importantly, in global warming. Moreover, granular matter is one of the most used type of material in industry, and it is being situated by some authors to be ranked as the second one, only overcome by water [Bat06; Dur12]. It can be highlighted its implication in industries like pharmaceuticals, agriculture, construction materials, mining, or fossil-fuel treatments, as some examples [Dur12; Ova+14; Sha15; HM16; Che+18; Wil+20]. Therefore, the importance of the understanding about granular processes could solve several natural and industrial issues.

To address the comprehension of granular matter phenomena, one must look at the interactions between grains, which are macroscopically determined by dissipative collisions. In fact, it is important to note that ordinary temperature does not play any role

in their description, since its associated thermal energy scale of the grains is negligible compared to their kinetic energy [JNB96; BP04; Gar19]. The loss of kinetic energy in collisions can be characterized by several causes like friction, internal vibration, or plastic deformation [BP04]. The phenomena underlying granular matter ensembles are plenty and, together with the dissipative character of particles, unveil certain complexity, such that a fully understanding of this topic is a challenge. The dissipative mechanisms and the mechanical properties of the grains, like size, shapes, or masses, as well as possible external interactions, determine important and different effects, consequences of their collective motion, like the Brazil nut effect [Wil76; Her95; HQL01; Gar08], mixing and demixing [Mul02], or aggregation and fragmentation processes [Bri+15; BFP18], among others. In addition, the interest on granular materials does not only reside in their vast applications in different natural and industrial processes, but, also, despite its supposedly simplicity, granular systems have intriguing behaviors differing from those of more usual forms of matter. In fact, whereas some granular flows could recall the classical three states of matter, solid, liquid, and gas [Wee08], granular matter can be consider itself as a different state of matter exhibiting different phase behaviors in between solids and fluids [EP97].

The macroscopic feature of the grains invites to solve simply their single Newton's equations of motion to obtain the real dynamics of the system. However, the number of grains in the composition of a granular material is usually very large. Then, solving this system of coupled second order differential equations is almost impossible from an analytical point of view, and time- and energy-consuming in computational terms. The quite large number of constituents invites to base the theoretical approach essentially on statistical physics, fluid, and continuum mechanics [Gen99; BP04; Gar19], and, of course, simulation methods are the best complement for that [Her99; PS05]. The density and characteristics of a granular flow determine which approach is more appropriate, as well as the expected mechanisms and effects that could be observed *a priori* in the granular system. Roughly speaking, we could classify the granular dynamics into *quasi-static* regimes or *rapid* flows [Gar19]. In the former case, systems are usually dense, and solid- and liquid-like behaviors can be observed, with clogging and jamming [AD06; Ber+16; BC19], crystal-type transitions [KCD22], or frustration [Lee+19] being some examples of underlying phenomena. On the other hand, the rapid flow scheme corresponds to high-speed flows. These fluidized granular systems implies that the grain motions are independent of even its nearest neighbors. Thus, collisions between granular particles are nearly instantaneous—if interactions are noncohesive—as compared with the mean free time, recalling the molecular gas case [Cam90; Gol03; Gar19]. Therefore, these systems are called *granular gases*. This consideration is analogous to the kinetic-theory picture of molecular gases, and, in fact, the mean-square value of their random velocities is commonly known as the *granular temperature* [OUO80]. These fluidized states can be

achieved by strong forcing like shearing, shaking, vibration, or other methods. The way of generating the rapid flow is important to address a proper description of the flow. Mainly, granular gases can be classified into *dry* granular gases or *gas-solid* flows. In the former description, the interaction of the granular gas with the surrounding medium is negligible or absent, and they can be classified into *driven* (externally forced) granular gases, in which there is an external energy injection playing an important role in the dynamics, and *freely evolving* systems, in which there is no external energy sources, and the gas is continuously dissipating energy. Furthermore, when the granular gas is interacting with an interstitial fluid, it is said that we are in conditions of a gas-solid flow or a *suspension*. From a kinetic-theory description, there are similarities between driven granular gases and gas-solid flows, where a Fokker–Planck term into the kinetic equation appears, coming from a stochastic energy injection in the former case, or a Langevin-like interaction in the latter one. Here, these two types are going to be considered as *thermostatted* systems.

Throughout this thesis, we have focused on rapid granular flows in free evolution and thermostatted states. In order to complete the kinetic-theory description of the system, we must infer a model for the dissipative granular interactions. First, for the sake of simplicity, a common description of granular particles, employed in most theoretical models and computer simulations, as well as in many experiments, consists in considering them as hard spheres (**HS**) in three dimensions or hard disks (**HD**) in two-dimensional setups. These hard-core repulsive interactions are, by definition, noncohesive, and the instantaneous approach introduced above is fulfilled. In general, the nature of dissipation is quite complex and usually very dependent on the material of the grain. However, the easiest paradigm, from which one could extract properly the dynamical and statistical features of these rapid flows, consists in considering the hard particles to be inelastic, this feature being accounted for by a coefficient of normal restitution, α , considered to be constant [Cam90; Gol03; Gar19]. Moreover, in this thesis, based on what experimental observations claim [YSS20], we have improved this simple model by considering the effect of surface roughness in particle-particle collisions. Here, it is accounted for by a coefficient of tangential restitution, β , which in the simplest case is considered to be constant as well [BP04; Gar19].

In addition, one expects, as occurs with molecular gases, that rapid granular flows may admit a hydrodynamic description. Then, Navier–Stokes–Fourier (**NSF**) equations could be extended to the granular case. For a usual fluid, $d_t + 2$ conservation or *balance* equations form this description, with d_t being the dimension of the vector space for velocities; one of them corresponds to mass conservation, d_t equations for linear momentum conservation, and another one for energy (temperature) conservation. On the other hand, the dissipation linked to the granular interactions suggests the addition of a sink term in the energy balance equation. Moreover, to complete this

description, usually phenomenological expressions for the constitutive equations are proposed, establishing a form of the fluxes in terms of gradients. For an ordinary fluid, the stress tensor and the heat flux are the fluxes appearing in the NSF scheme, providing, in their phenomenological forms, three main transport coefficients: the shear and bulk viscosities from the former, and the thermal conductivity from the latter. However, in the granular gaseous case, two important modifications are observed. First, dissipation implies that a density gradient contributes to the heat flux, which comes together with a proper transport (Dufour-like) coefficient. Moreover, the sink term in the temperature equation can be affected by transport, complicating in fact the description. Furthermore, a particular feature of granular gases, when one studies its hydrodynamics, is the appearance of instabilities by means of clustering and vortices, which exhibit a time-evolving growth [LH99; PS05] in freely cooling granular gases. Then, in order to infer the proper description arising from the peculiarities of granular interactions, a many-body approach of the problem is needed. Boltzmann or Enskog kinetic theories are applied to granular gaseous flows in order to address those issues [Gar19].

We have tried to describe the latter features with special attention to the effect of the surface roughness of the granular particles on the dynamics. However, in order to answer some questions that will be raised throughout the memoir, we have also studied some properties and effects in molecular gases or inelastic but smooth granular gases. In fact, the nonequilibrium characteristic of the granular gases, in free evolution, externally driven or as a granular suspension with a background fluid, is the perfect scenario to observe memory effects. This approach is good to be understood in simpler models to get a full perspective of the possible phenomenology that one could expect. And not only these effects, but the proper freely evolving granular gas description is not even trivial in the simplest collisional model, where traditional results of Boltzmann equation for molecular gases are completely lost. Then, before entering into the details of the implementation of the surface roughness in the granular interactions, we try to get a more general scope of those topics. This has been crucial in the structure of this thesis which is detailed in the following section.

1.1 Structure of the thesis

The theoretical framework of this thesis is then based on kinetic-theory tools. Moreover, we exclusively work on the dilute regime and, then, the proper kinetic equation for this picture is the so-called Boltzmann equation (BE). In addition, as it will be detailed, we study a certain model of molecular gases, whose knowledge is useful to the description of a certain type of gas-solid flow. We also extract information for certain memory effects arising in granular gases. In fact, we consider three types of particle interaction in our kinetic-theory-based description: elastic, inelastic and smooth, and inelastic and rough

hard particles. Whereas the first one is applied to the mentioned molecular system, the other two models are used for freely evolving and thermostatted granular gaseous models.

The thesis is the result of a compendium of eight scientific publications, which are part of a coherent research line. They are, in order of appearance in the thesis, the following:

- ▶ [MSP22] **Article 1.** A. Megías, A. Santos and A. Prados. ‘Thermal versus entropic Mpemba effect in molecular gases with nonlinear drag’. *Phys. Rev. E* 105 (2022), p. 054140. DOI: [10.1103/PhysRevE.105.054140](https://doi.org/10.1103/PhysRevE.105.054140)
- ▶ [MS20] **Article 2.** A. Megías and A. Santos. ‘Kullback–Leibler divergence of a freely cooling granular gas’. *Entropy* 22 (2020), p. 1308. DOI: [10.3390/e22111308](https://doi.org/10.3390/e22111308)
- ▶ [MS21c] **Article 3.** A. Megías and A. Santos. ‘Relative entropy of freely cooling granular gases. A molecular dynamics study’. *EPJ Web Conf.* 249 (2021), p. 04006. DOI: [10.1051/epjconf/202124904006](https://doi.org/10.1051/epjconf/202124904006)
- ▶ [MS22a] **Article 4.** A. Megías and A. Santos. ‘Kinetic Theory and Memory Effects of Homogeneous Inelastic Granular Gases under Nonlinear Drag’. *Entropy* 24 (2022), p. 1436. DOI: [10.3390/e24101436](https://doi.org/10.3390/e24101436)
- ▶ [MS23] **Article 5.** A. Megías and A. Santos. ‘Translational and rotational non-Gaussianities in homogeneous freely evolving granular gases’. *Phys. Rev. E* (2023). [Accepted paper.](#)
- ▶ [MS22b] **Article 6.** A. Megías and A. Santos. ‘Mpemba-like effect protocol for granular gases of inelastic and rough hard disks’. *Front. Phys.* 10 (2022), p. 971671. DOI: [10.3389/fphy.2022.971671](https://doi.org/10.3389/fphy.2022.971671)
- ▶ [MS21a] **Article 7.** A. Megías and A. Santos. ‘Hydrodynamics of granular gases of inelastic and rough hard disks or spheres. I. Transport coefficients’. *Phys. Rev. E* 104 (2021), p. 034901. DOI: [10.1103/PhysRevE.104.034901](https://doi.org/10.1103/PhysRevE.104.034901)
- ▶ [MS21b] **Article 8.** A. Megías and A. Santos. ‘Hydrodynamics of granular gases of inelastic and rough hard disks or spheres. II. Stability analysis’. *Phys. Rev. E* 104 (2021), p. 034902. DOI: [10.1103/PhysRevE.104.034902](https://doi.org/10.1103/PhysRevE.104.034902)

This thesis is organized in six parts containing different chapters, which are detailed as follows.

First, there is an **Introduction** part, which contains this and other three chapters with the aim of presenting the basic and state-of-the-art knowledge about the investigated topics. After this general introduction, we introduce the necessary features of kinetic theory to understand and put in context all the articles forming part of the thesis in [Chapter 2](#). After that, the main concepts and definitions, related to some memory effects studied in this thesis, are described in [Chapter 3](#), particularly, the Mpemba effect (ME) and the Kovacs effect (KE) are conceptually explained. Moreover, in [Chapter 4](#), we detail the simulation methods implemented to confirm or discard the theoretical

developments of this thesis.

Then, three intermediate parts are classified in order of difficulty of the collisional model used in the kinetic-theory description. The second part of the thesis is dedicated to **Molecular gases**. In this part, we exclusively study a single model of molecular fluid of identical particles, which is developed in [Chapter 5 \(Article 1, reproduced in Section 5.2\)](#). Here, we describe a molecular gas as a collection of elastic hard d_t -spheres in contact with an interstitial fluid. This background fluid is assumed to be in equilibrium at temperature T_b and it is considered to act as a thermal bath on the molecular gas. Therefore, the interactions between the gas molecules and the bath particles are modeled by a coarse-grained Langevin-like description. That is, apart from the collisional-driven evolution of the system, the thermal bath acts on the gas via two forces, a drag force accounting for a viscous action on the molecules and a stochastic force, which models the energy injection due to the thermal action of the bath into the gas particles. In fact, it is imposed that the drag coefficient and the noise intensity of the stochastic force are related via a fluctuation-dissipation relation. Moreover, as a more realistic model than the original Langevin's one [[Lan08](#); [LG97](#)], we set the drag coefficient to be nonlinear, i.e., it is treated as a function of the gas molecule velocity and not as a constant. The system is studied in terms of a Boltzmann–Fokker–Planck equation ([BFPE](#)), in which the collisional contribution comes from the Boltzmann collisional operator, and the Fokker–Planck term describes the action of the bath. This system is known to exhibit the [ME](#) [[SP20](#); [PSP21](#)], which is a memory effect that is also present in granular fluids [[Las+17](#)]. The aim of this work is to study the thermal and entropic descriptions of the memory effect in the particular case of the molecular gas under nonlinear drag. We identify the similarities and differences between those two pictures and elaborate a full description of the phenomenology arising. The theoretical predictions are compared with simulation results to check our approximate theoretical schemes and arguments.

The third part of this thesis, **Granular gases of inelastic and smooth hard particles**, consists in the study of certain aspects related to the simplest collisional model of a granular gas. That is, we model the granular particles by inelastic and smooth hard d_t -spheres. This inelasticity is described by a coefficient of normal restitution, α , such that for $0 \leq \alpha < 1$ particles are inelastic, the molecular gas case being recovered when $\alpha = 1$. This part is divided into two chapters. First, in [Chapter 6](#), we focus on the extension to the granular gaseous realm of a very important feature of Boltzmann kinetic theory of molecular gases, the H -theorem. In this chapter, [Article 2](#) and [Article 3](#) are introduced in [Section 6.2](#) and [Section 6.3](#), respectively. In them, we detail the problems that the original H -theorem exhibits in the inelastic version of the [BE](#) for a monodisperse granular gas in free evolution and provide theoretical arguments in favor of a conjecture about a functional for describing the nonequilibrium granular entropy for this system. Moreover, in [Article 2](#) and [Article 3](#), we show computer simulation

results that reinforce our theoretical schemes. In order to address this problem, we analyze first the homogeneous states of this model of granular gas that, under the BE framework, reaches a state in which the one-particle velocity distribution function (VDF) of the system adopts a scaling form. In this state, the time evolution of the system is completely captured by the temperature continuous cooling. Such a state is called *homogeneous cooling state* (HCS), and it has been widely studied in the literature [Gar19]. We base our theoretical description on the evolution of the system toward the HCS under certain approximations, which are supported by simulation results. Then, we study how the conjecture proposed in Refs. [BPV13; Gar+15] solves the encountered issues in the H -theorem. This proposal consists in considering the *relative entropy*, or *Kullback–Leibler divergence* (KLD) [KL51] of the time-dependent VDF with respect to the HCS VDF, to be the nonequilibrium entropy of the system (up to a minus sign). Under some approximations, we elaborate a toy model for such functional, which turns out to behave as the expected nonequilibrium entropy. Computer simulations support these results and discard other possible candidates. Finally, in **Article 3** (Section 6.3), and for the sake of completeness, we carry out a velocity-inversion computational experiment, based on the original work of Orban and Bellemans [OB67; OB69], in which we show the role of inelasticity when the system is forced to turn back to its initial state.

After this first study about a granular gas of inelastic and smooth granular particles, we consider in **Chapter 7** (**Article 4**, reproduced in Section 7.2) the granular extension to the system studied in **Article 1** (Section 5.2). Here, a monodisperse granular gas of inelastic hard d_t -spheres is surrounded by a background fluid which acts on the granular particles as a thermal bath at temperature T_b and via a drag force, with nonlinear drag coefficient, and a stochastic force, both related by a fluctuation-dissipation relation. The goal of this study is to analyze the effect of the nonlinearities of the drag coefficient into the transient and steady homogeneous states of this gas-solid flow. In order to address this, we introduce similar approaches already elaborated in **Article 1** (Section 5.2) and **Article 2** (Section 6.2). This analysis allows us to study the emergence of some memory effects in this system, which are known to appear in the molecular case. Particularly, we predict the emergence of the ME and the KE. All the theoretical expressions, related to the dynamical description of the system and the appearance of the memory effects, are tested by computer simulation outcomes.

Then, after the study of the molecular and inelastic and smooth case, we investigate the influence of the addition of surface roughness on the collision mechanism of a granular gas in a fourth part of this thesis, called **Granular gases of inelastic and rough particles**. This part splits into three chapters, two of them dedicated to homogeneous states and a last third one focused on the study of the transport properties of a granular gaseous system with inelastic and rough hard particles in free evolution. In **Chapter 8** (**Article 5**, reproduced in Section 8.2), we detail an analysis about the homogeneous

states of a freely evolving granular gas of inelastic and rough **HD** and **HS** from a unified framework in terms of the rotational and translational degrees of freedom, d_t and d_r , respectively, and already introduced in Refs. [**MS19a**; **MS19b**]. Whereas transient states are also introduced, we have focused on the description of the **HCS** features of this system, with the aim of characterizing the non-Gaussian properties of the **VDF** at this particular state. We characterize these non-Gaussianities in terms of the first order nontrivial cumulants from a well-known Sonine expansion, extending previous results of the **HS** case [**VSK14b**], and, also, in terms of the high-velocity tails (**HVT**) of some relevant marginal **VDF** of the system, this being a novel contribution for the rough particle case. All these findings are supported by simulation results too.

Nonetheless, the study of homogeneous states in this model of granular collisions is not only restricted to freely evolving granular particles, but also to another dry and driven setup, in which we assume an injection of energy into inelastic and rough **HD** via their translational and rotational degrees of freedom. A description of this system is introduced in **Article 6** (**Section 9.2**). Contrarily to the freely evolving case, the system reaches a steady state, which is studied together with transient states, describing the evolution of the system toward the stationary. For that, and expecting that the non-Gaussianities for this type of system are less important than in free evolution, we assume that the **VDF** stays close to the Maxwellian at every stage of system evolution and in the steady state. This allows us to solve explicitly the transient and the steady homogeneous states of the system, validating the approximation with computer simulations. Furthermore, in Ref. [**Tor+19**], it was found that the **ME** appears from a single mechanism of injection restricted to the translational degrees of freedom. Then, it is expected that the **ME** is present in these thermostatted states too. Indeed, we apply the theoretical approximate description to satisfactorily infer a theoretical protocol for the preparation of the initial states of the samples involved in a Mpemba-like experiment, in agreement with computer simulation outcomes.

Finally, the last works forming part of this thesis are **Article 7** and **Article 8**, appearing in **Chapter 10**, and reproduced in **Section 10.2** and in **Section 10.3**, respectively. In them, we study the transport properties of a hydrodynamic description of a monodisperse and dilute granular gas of inelastic and rough **HD** or **HS** in free evolution, and using the degrees-of-freedom framework. The main goals of these works are the computation of the **NSF** transport coefficients, in **Article 7** (**Section 10.2**), treating the **HCS** as the base state in the application of the perturbative Chapman–Enskog (**CE**) method, and, in **Article 8**, the determination of the stability of the **HCS** via linear inhomogeneous perturbations of the **HCS** as an application of the results of **Article 7**. For the former problem, we use the simplest approximation to develop the corresponding analysis for the computation of such coefficients. In fact, we recover the results of Ref. [**KSG14**] for **HS** ($d_t = d_r = 3$) and obtain the form of the transport coefficients for certain limiting

cases of interest. All the results derived in **Article 7** are purely theoretical. Afterwards, the knowledge of those outcomes are applied to the mentioned linear stability analysis of the **HCS**, validating previous results for the **HS** reported in Ref. [**GSK18**]. As an important result, we observe a region of the parameter space where the hydrodynamic description of the system seems to break down. However, a discussion from computer simulation results clarifies the situation and shows that a region of permanent unstable systems does not strictly exist.

To clarify the structure of the main part of the memoir, the different models addressed in this thesis and their corresponding chapters and publications are summarized in **Table 1.1**.

Free-streaming model \ Collisional model	Molecular gas	Granular gas of inelastic particles	Granular gas of inelastic and rough particles
Free evolution		Chapter 6 (Articles 2 & 3)	Chapter 8 & Chapter 10 (Articles 5, 7 & 8)
Translational and rotational driving			Chapter 9 (Article 6)
Suspension model with nonlinear drag	Chapter 5 (Article 1)	Chapter 7 (Article 4)	

Table 1.1: Summary of the models addressed in this thesis and their corresponding occurrences.

Once all the publications forming part of this compendium are described and explicitly presented, we discuss, in a fifth part, made of **Chapter 11** and **Chapter 12**, the main **Results and conclusions** of the thesis.

As a colophon, a final part is dedicated to some **Appendices**, in which some computations and additional information are detailed.

Kinetic-theoretical description of molecular and granular gaseous flows

2



©2018 Artists Rights Society (ARS), New York / ADAGE, Paris

Vasily Kandinsky, *Einige Kreise* (1926). [Guggenheim Museum, New York](#).

2.1 Introduction

The kinetic theory of gases became an essential theory in the understanding of nonequilibrium properties of fluids in the late 19th Century, reaching its most powerful results by James C. Maxwell and Ludwig Boltzmann [Bru86a; Bru86b]. The theory was supported by experimental results and afterwards by the development of computer simulation techniques. Whereas it was introduced prior to statistical mechanics, it is nowadays considered to be a branch of it. The idea behind kinetic theory is to fully describe the state of a large physical system—originally a gas—made of N constituents by a time-dependent probability density, where the positions and velocities of the gas particles (or generalized coordinates and their conjugate momenta) are assumed to be random variables of this probability density, which follows integro-differential *kinetic* equations

for its time-evolution.

In 1872, Boltzmann derived its original kinetic equation [Fla73; Cer98], being in more modern terms the very first equation of the well-known Bogoliubov–Born–Green–Kirkwood–Yvon (BBGKY) hierarchy [Yvo35; Bog46; Kir46; BG46; Kir47] after an adequate closure. The closure behind the BE consists in approximating the two-particle VDF in the collisional operator by the product of two one-particle distribution functions. This is based on the hypothesis introduced by J. C. Maxwell [Max67] known as *molecular chaos* or, in the original German word, *Stosszahlansatz* (introduced by Paul Ehrenfest [EE02]), that is, the assumption of statistical uncorrelation of the velocities of the colliding particles. Whereas this might seem quite strong an assumption, it has been widely accepted and justified in the context of dilute systems.

The concepts of kinetic theory have been applied to granular gaseous flows since the late 20th Century. Here, the thermodynamic temperature does not play any significant role in the granular dynamics since it is remarkably smaller than the average kinetic energy in usual experiments at room temperature [BP04; Gar19]. Moreover, experiments have observed evidence of molecular chaos in granular low-density systems [BO07], so that the kinetic-theory approach seems to be applicable.

The aim of this chapter is to introduce, for the sake of self-consistency, the main aspects and results related to kinetic theory of molecular and granular gases that have been used throughout this thesis.

2.2 Derivation of the Boltzmann equation for hard spherical particles

Let us consider an arbitrary dilute monodisperse gas made of a very large number N of identical hard hyperspheres in d_t translational dimensions, such that the dynamics of each individual particle is determined by its general velocities Γ . In the absence of rotations, $\Gamma = \mathbf{v}$ is identical to the translational velocity, while, if rotations are known to be present, one has $\Gamma = \{\mathbf{v}, \boldsymbol{\omega}\}$, $\boldsymbol{\omega}$ being the angular velocity. For the moment, we are not going to specify whether it is a molecular or a granular gas. Each specific collisional model will give us information about how particles modify their velocities in a collision, as will be specified in next Section 2.3.

The aim of this section is to derive the general form of the BE for hard interactions between the particles of the described gas. The derivation will be based on heuristic arguments rather than as the first equation of the BBGKY hierarchy derived from the Liouville equation.

The hard-sphere interaction is defined by the following discontinuous *potential*,

$$U_{ij}(r_{ij}) = \begin{cases} \infty & \text{if } r_{ij} < \sigma_{ij} \\ 0 & \text{if } r_{ij} \geq \sigma_{ij} \end{cases}, \quad (2.1)$$

with $\sigma_{ij} = (\sigma_i + \sigma_j)/2$ the distance of the centers of the spheres at contact, σ_i being the diameter of the i^{th} particle and $r_{ij} = |\mathbf{r}_i - \mathbf{r}_j|$ the distance between their centers. This represents the interaction between impenetrable spheres. All of this can be generalized straightforwardly to hyperspheres with an arbitrary number d_t of translational dimensions. From now on, as we are working with identical particles, it will be considered that $\sigma_i \equiv \sigma, \forall i \in \{1, \dots, N\}$.

Let us consider that all the relevant information about the system is contained in its one-body probability distribution function, $f(\mathbf{r}, \Gamma; t)$, such that $f(\mathbf{r}, \Gamma; t) \text{d}\mathbf{r} \text{d}\Gamma$ is the expected number of particles at time t residing in the differential volume element of the phase space $\text{d}\mathbf{r} \text{d}\Gamma$, that is, the average number of particles localized in the volume element $\text{d}\mathbf{r}$ centered at position \mathbf{r} , and moving with velocities valued between Γ and $\Gamma + \text{d}\Gamma$. The knowledge of this VDF can be employed to obtain macroscopic properties of the gas. Therefore, it is essential to infer its time evolution. The assumption of diluteness allows us to decouple the evolution of the VDF into two terms: a free streaming evolution, where only external forces might apply, and, on the other hand, an interaction-driven evolution, which in the case of HS is equivalent to a collisional-driven change. Hence,

$$\frac{\partial f}{\partial t} = \left(\frac{\partial f}{\partial t} \right)_{\text{str}} + \left(\frac{\partial f}{\partial t} \right)_{\text{coll}}, \quad (2.2)$$

where the first term on the right-hand side corresponds to the free-streaming evolution and the second one to the collisional rate of change. Let us infer these two different contributions.

First of all, to derive the free-streaming term, a collisionless gas will be assumed, namely the Knudsen gas [Cer98]. Thus, in a differential time interval δt , a particle located at \mathbf{r} with velocities $\Gamma = \{\mathbf{v}, \boldsymbol{\omega}\}$ will move to $\mathbf{r}^* = \mathbf{r} + \mathbf{v}\delta t$. Moreover, if external forces and torques are present, then $\mathbf{v}^* = \mathbf{v} + m^{-1}\mathbf{F}^{\text{ext}}\delta t$ and $\boldsymbol{\omega}^* = \boldsymbol{\omega} + I^{-1}\boldsymbol{\tau}^{\text{ext}}\delta t$ for spinning particles. Here, m and I are the mass and moment of inertia of a particle, respectively. The superscript $*$ denotes quantities evaluated at $t^* = t + \delta t$. Hence,

$$f(\mathbf{r}, \Gamma; t) \text{d}\mathbf{r} \text{d}\Gamma = f(\mathbf{r}^*, \Gamma^*; t^*) \text{d}\mathbf{r}^* \text{d}\Gamma^*, \quad (2.3)$$

implying that the Jacobian associated with the transformation $(\mathbf{r}, \Gamma) \rightarrow (\mathbf{r}^*, \Gamma^*)$ is given by,

$$\text{d}\mathbf{r}^* \text{d}\Gamma^* = \left[1 + \frac{\partial}{\partial \Gamma} \cdot \mathbf{G} \delta t + \mathcal{O}(\delta t^2) \right] \text{d}\mathbf{r} \text{d}\Gamma, \quad (2.4)$$

where $\mathbf{G} = \{\mathbf{F}^{\text{ext}}/m, \boldsymbol{\tau}^{\text{ext}}/I\}$ are the *generalized forces per unit mass*. Moreover, the Taylor expansion of $f(\mathbf{r}^*, \boldsymbol{\Gamma}^*; t^*)$ in powers of δt reads, up to first order,

$$f(\mathbf{r}^*, \boldsymbol{\Gamma}^*; t^*) = f(\mathbf{r}, \boldsymbol{\Gamma}; t) + \left[\frac{\partial f(\mathbf{r}, \boldsymbol{\Gamma}; t)}{\partial t} \right]_{\text{str}} \delta t + \mathbf{v} \cdot \nabla f(\mathbf{r}, \boldsymbol{\Gamma}; t) \delta t + \mathbf{G} \cdot \frac{\partial f(\mathbf{r}, \boldsymbol{\Gamma}; t)}{\partial \boldsymbol{\Gamma}} \delta t + \mathcal{O}(\delta t^2), \quad (2.5)$$

with $\nabla \equiv \partial_{\mathbf{r}}$. Using Eqs. (2.3)–(2.5), we finally get

$$\left(\frac{\partial f}{\partial t} \right)_{\text{str}} = -\mathbf{v} \cdot \nabla f - \frac{\partial}{\partial \boldsymbol{\Gamma}} \cdot (f \mathbf{G}). \quad (2.6)$$

In [Section 2.4](#), we will study different types of \mathbf{G} .

In order to complete the time evolution of the one-particle VDF we need to specify its rate of change due to collisions exclusively. Formally, the change due to the interactions would depend on the two-body VDF. However, from the assumption of diluteness, as introduced in [Section 2.1](#), the average distance between particles, n^{-1/d_t} , is much smaller than the interaction range, with n being the particle number density. In our case, due to the hard-core interaction, the average distance is much smaller than the diameter of the (hyper)spheres, σ , that is $n\sigma^{d_t} \ll 1$. Therefore, particles move most of the time due to the free streaming and eventually binary collision occur (collisions involving more than two particles are very improbable and so they are neglected). The latter statement implies that the *mean free path* is much larger than σ , whereas the former establishes that the *mean free time* is much higher than the duration of a collision.

From these considerations, we are going to derive the collisional-driven change of f . That is, we want to consider the change due to collisions of the number of particles $f(\mathbf{r}, \boldsymbol{\Gamma}_1; t) \text{d}\mathbf{r} \text{d}\boldsymbol{\Gamma}_1$ in the differential volume $\text{d}\mathbf{r} \text{d}\boldsymbol{\Gamma}$ of the phase space around the point $(\mathbf{r}, \boldsymbol{\Gamma}_1)$ during a small time interval δt . To that end, we split the collisional mechanism into two processes. In the first one, there are particles in our initial phase space volume that collide during the time interval δt , and, then, they get postcollisional velocities $\boldsymbol{\Gamma}'_1$, such that do not contribute to the number of particles $f(\mathbf{r}, \boldsymbol{\Gamma}_1; t + \delta t) \text{d}\mathbf{r} \text{d}\boldsymbol{\Gamma}_1$. This process defines a loss term, J_L , in the time evolution of f . Second, we must consider those particles with initial precollisional velocities $\boldsymbol{\Gamma}''_1$ involved in a collision such that they are counted in $f(\mathbf{r}, \boldsymbol{\Gamma}_1; t + \delta t) \text{d}\mathbf{r} \text{d}\boldsymbol{\Gamma}_1$. This latter process defines a gain term, J_G , in this collisional-driven change of f . That is,

$$\left(\frac{\partial f}{\partial t} \right)_{\text{coll}} = J_G - J_L. \quad (2.7)$$

We will distinguish between target particles moving with translational velocities \mathbf{v}_2 , and incident particles moving with \mathbf{v}_1 . Working in the frame of reference of particle 2, incident particles move with translational velocities $\mathbf{v}_{12} = \mathbf{v}_1 - \mathbf{v}_2$. Therefore, for each

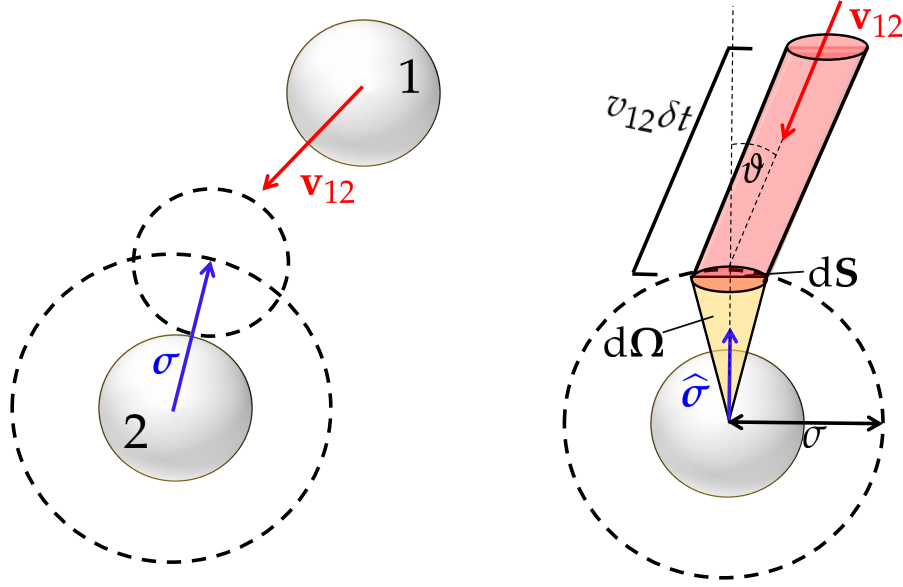


Figure 2.1: On the left, we show a sketch of a binary collision between a projectile particle (1) and a target particle (2). The big dashed circle represents the distance at σ from the center of particle 2 where a collision takes place if the center of another sphere is located there. The smaller dashed circle represents the location of particle 1 at the time of collision. On the right part of the figure, there is a scheme of the collision cylinder represented by a reddish cylinder, where ϑ is the angle formed by the vector \mathbf{v}_{12} and $d\mathbf{S}$, which is the differential area at contact shared by the dashed sphere of radius σ centered at particle 2 and the collision cylinder. In addition, the differential solid angle $d\Omega$ is depicted by a yellowish cone.

target there exists an individual collision cylinder (see Figure 2.1), which accounts for all possible collisions that may occur within the infinitesimal solid angle $d\Omega$ in the direction of the unit vector $\hat{\sigma} = (\mathbf{r}_2 - \mathbf{r}_1)/|\mathbf{r}_2 - \mathbf{r}_1|$. This cylinder has a cross-section $d\mathbf{S} = \sigma^{d_t-1}d\Omega$ and length $v_{12}\delta t$. Therefore, the number of particles scattered per unit time due to collisions of type (Γ_1, Γ_2) into the element of solid angle $d\hat{\sigma}$ around the unit intercenter vector $\hat{\sigma}$ is [GS03; Gar19]

$$\sigma^{d_t-1}|\mathbf{v}_{12} \cdot \hat{\sigma}|f(\Gamma_1)f(\Gamma_2)d\hat{\sigma}d\Gamma_1d\Gamma_2. \quad (2.8)$$

From Figure 2.1, one can deduce that only those velocities with $\mathbf{v}_{12} \cdot \hat{\sigma} \geq 0$ lead to a true impact. Then, the rate of loss per unit time of particles with velocities between Γ_1 and $\Gamma_1 + d\Gamma_1$ is

$$J_L d\Gamma_1 = \sigma^{d_t-1} \int d\Gamma_2 \int d\hat{\sigma} \Theta(\mathbf{v}_{12} \cdot \hat{\sigma})(\mathbf{v}_{12} \cdot \hat{\sigma})f(\Gamma_1)f(\Gamma_2)d\Gamma_1, \quad (2.9)$$

Θ being the Heaviside step-function. Equivalently, for the rate of gain we obtain that

$$J_G d\Gamma_1 = \sigma^{d_t-1} \int d\Gamma_2'' \int d\hat{\sigma} \Theta(\mathbf{v}_{12}'' \cdot \hat{\sigma})(\mathbf{v}_{12}'' \cdot \hat{\sigma})f(\Gamma_1'')f(\Gamma_2'')d\Gamma_1''. \quad (2.10)$$

In this thesis, we will only consider cases in which $(\mathbf{v}_{12}'' \cdot \hat{\sigma}) = -\alpha^{-1}(\mathbf{v}_{12} \cdot \hat{\sigma})$, with

$0 \leq \alpha \leq 1$ a constant coefficient of normal restitution, as it will be specified in [Section 2.3](#). Hence, conveniently changing $\widehat{\sigma} \rightarrow -\widehat{\sigma}$, it is obtained that

$$J_G d\Gamma_1 = \sigma^{d_t-1} \int d\Gamma_2 \int d\widehat{\sigma} \Theta(\mathbf{v}_{12} \cdot \widehat{\sigma})(\mathbf{v}_{12} \cdot \widehat{\sigma})(\alpha \mathfrak{J})^{-1} f(\Gamma_1') f(\Gamma_2'') d\Gamma_1, \quad (2.11)$$

\mathfrak{J} being the Jacobian of the transformation $(\Gamma_1', \Gamma_2') \rightarrow (\Gamma_1, \Gamma_2)$ or, equivalently, $(\Gamma_1, \Gamma_2) \rightarrow (\Gamma_1'', \Gamma_2'')$, that is

$$\mathfrak{J} = \left| \frac{\partial(\Gamma_1', \Gamma_2')}{\partial(\Gamma_1, \Gamma_2)} \right| = \left| \frac{\partial(\Gamma_1, \Gamma_2)}{\partial(\Gamma_1'', \Gamma_2'')} \right|. \quad (2.12)$$

It can be explicitly computed from the chosen collisional model. Thus,

$$\left(\frac{\partial f}{\partial t} \right)_{\text{coll}} \equiv J[\Gamma_1 | f, f] = \sigma^{d_t-1} \int d\Gamma_2 \int_+ d\widehat{\sigma} (\mathbf{v}_{12} \cdot \widehat{\sigma}) [(\alpha \mathfrak{J})^{-1} f_1'' f_2'' - f_1 f_2], \quad (2.13)$$

where the notation $\int_+ d\widehat{\sigma} \equiv \int d\widehat{\sigma} \Theta(\mathbf{v}_{12} \cdot \widehat{\sigma})$ is adopted, J is the integro-differential operator acting on f (usually known as Boltzmann collisional operator), and we defined $f_i \equiv f(\Gamma_i)$ and $f_i'' \equiv f(\Gamma_i'')$ with $i = 1, 2$. Therefore, the [BE](#) for hard d_t -hyperspheres reads

$$\frac{\partial f}{\partial t} + \mathbf{v} \cdot \nabla f + \frac{\partial}{\partial \Gamma} \cdot (f \mathbf{G}) = J[\Gamma | f, f]. \quad (2.14)$$

In next sections, the [BE](#) for different collisional models and external forces will be explicitly written.

2.3 Collisional models

Throughout this thesis, different collisional models for, in general, hard d_t -spheres are considered, d_t being the number of translational degrees of freedom. This will be crucial in the final results of the model. The derivation of the different properties of a specific model has been done under the assumptions of the [BE](#). In fact, from the molecular chaos ansatz, only binary collisions are considered and their binary collisional rules are essential, not only to specify the form of the Boltzmann collisional operator in Eq. (2.13), but also to derive properly the theoretical predictions.

Let us imagine two identical hard d_t -spheres colliding. Then, given two precollisional velocities, the binary direct collisional rules provide the expressions for the postcollisional velocities with respect to the precollisional ones and, the other way around, for the inverse collisional rules. Mathematically, let Γ_1 and Γ_2 be the precollisional velocities of particles 1 and 2, respectively. Therefore, the direct collisional rules establish the form of the postcollisional velocities $\Gamma_i' = \mathfrak{B}_{12, \widehat{\sigma}} \Gamma_i$, with $i \in \{1, 2\}$, where the operator $\mathfrak{B}_{12, \widehat{\sigma}}$ gives the postcollisional version of a certain velocity-related quantity. Moreover, if we now

express $\mathbf{\Gamma}_1$ and $\mathbf{\Gamma}_2$ as the postcollisional velocities of particles 1 and 2, respectively, the binary inverse collisional rules are expressions of the form $\mathbf{\Gamma}_i'' = \mathfrak{B}_{12,\widehat{\sigma}}^{-1}\mathbf{\Gamma}_i$, with double primed quantities denoting their precollisional values.

Three collisional models will be introduced attending to the systems considered. First, elastic collisions for hard d_t -spheres to describe molecular interaction (see [Subsection 2.3.1](#)). Next, granular interactions will be represented by means of two models: first, by introducing inelastic collisions in [Subsection 2.3.2](#) and, then, adding surface roughness to the inelastic collisions in [Subsection 2.3.3](#).

2.3.1 Molecular gas of elastic hard spheres

In this model, it is assumed that a molecular gas is composed by hard d_t -spheres interacting with elastic collisions. In what follows, this representation will be named as elastic hard-sphere (EHS) collisional model. Whereas the tangential component of the relative velocity is preserved in a binary collision, the normal components in a collision between particle 1 and 2 accomplish the following reflection rules for the direct collisions,

$$\mathbf{v}'_{1,2} = \mathfrak{B}_{12,\widehat{\sigma}}\mathbf{v}_{1,2} \equiv \mathbf{v}_{1,2} \mp (\mathbf{v}_{12} \cdot \widehat{\sigma})\widehat{\sigma}, \quad (2.15)$$

where $(\mathbf{v}'_{12} \cdot \widehat{\sigma}) = -(\mathbf{v}_{12} \cdot \widehat{\sigma})$ and, then, $(\mathbf{v}''_{12} \cdot \widehat{\sigma}) = -(\mathbf{v}_{12} \cdot \widehat{\sigma})$. Hence, the inverse or restituting collisional rules become

$$\mathbf{v}''_{1,2} = \mathfrak{B}_{12,\widehat{\sigma}}^{-1}\mathbf{v}_{1,2} \equiv \mathbf{v}_{1,2} \mp (\mathbf{v}_{12} \cdot \widehat{\sigma})\widehat{\sigma}. \quad (2.16)$$

These rules satisfy conservation of linear momentum, i.e.,

$$m\mathbf{v}''_1 + m\mathbf{v}''_2 = m\mathbf{v}_1 + m\mathbf{v}_2 = m\mathbf{v}'_1 + m\mathbf{v}'_2, \quad (2.17)$$

and conservation of energy, that is,

$$\frac{1}{2}m\mathbf{v}''_1{}^2 + \frac{1}{2}m\mathbf{v}''_2{}^2 = \frac{1}{2}m\mathbf{v}_1{}^2 + \frac{1}{2}m\mathbf{v}_2{}^2 = \frac{1}{2}m\mathbf{v}'_1{}^2 + \frac{1}{2}m\mathbf{v}'_2{}^2. \quad (2.18)$$

A sketch of the collisional scheme can be observed in [Figure 2.2](#), where the reflective behavior in the collision is put into manifest.

From the collisional rules in Eq. (2.15), one obtains that the Jacobian of the transformation $(\mathbf{v}'_1, \mathbf{v}'_2) \rightarrow (\mathbf{v}_1, \mathbf{v}_2)$ defined in Eq. (2.12) is $\mathfrak{J} = 1$. Thus, the Boltzmann collisional operator introduced in Eq. (2.13) reads for the EHS model,

$$J[\mathbf{v}_1|f, f] = \sigma^{d_t-1} \int d\mathbf{v}_2 \int_+ d\widehat{\sigma} (\mathbf{v}_{12} \cdot \widehat{\sigma}) (f''_1 f''_2 - f_1 f_2), \quad (2.19)$$

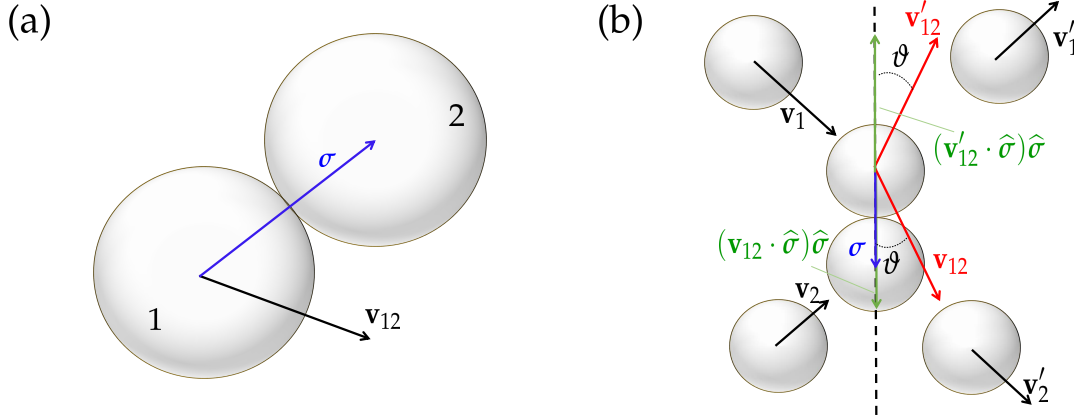


Figure 2.2: Sketch of (a) a collision between two hard spheres and (b) the collisional process in the **EHS** model with the notation of the direct collisional rules for the spatial and velocity quantities. Here, $\vartheta = \arccos(|\mathbf{v}_{12} \cdot \hat{\boldsymbol{\sigma}}|/v_{12})$ is the impact angle, which, due to reflective elastic collisions, coincides with its postcollisional version, $\vartheta' = \arccos(|\mathbf{v}'_{12} \cdot \hat{\boldsymbol{\sigma}}|/v'_{12})$.

where the condition for elastic collisions, $(\mathbf{v}_{12} \cdot \hat{\boldsymbol{\sigma}}) = -(\mathbf{v}'_{12} \cdot \hat{\boldsymbol{\sigma}})$, has been used.

2.3.2 Inelastic hard spheres

The inelastic hard sphere (**IHS**) model is the simplest approximation of a granular interaction of impenetrable grains. It is assumed that the granular particles collide inelastically yielding a loss of energy. The reflective collision characteristic of the molecular case is broken down by a decrement of the normal component of the relative velocity parameterized by the coefficient of normal restitution α ,

$$(\mathbf{v}'_{12} \cdot \hat{\boldsymbol{\sigma}}) = -\alpha(\mathbf{v}_{12} \cdot \hat{\boldsymbol{\sigma}}), \quad (2.20)$$

which is assumed to be constant in this model, and throughout this thesis. There are other models that slightly modify this by the introduction of a dependence of the coefficient of restitution on the impact velocity, such as the viscoelastic model [**Bri+96**; **BP04**; **SP08**]. However, despite the fact that the coefficient of restitution must actually be a function of the impact velocity, its form might not be universal, and the viscoelastic approach is quite specific. The constant coefficient of restitution approximation allows one to extract the properties of granular gases in a simple way. Moreover, recent experiments [**YSS20**] conclude that, in fact, this is a better approach than the viscoelastic model. The coefficient of normal restitution is defined such that $0 \leq \alpha \leq 1$, where $\alpha = 1$ applies for an elastic collision and $\alpha = 0$ describes a completely inelastic collision. As in the molecular case, the tangential component of the relative velocity is preserved in the **IHS** model. Thus, within this collisional model, the direct collisional rules are

$$\mathbf{v}'_{1,2} = \mathfrak{B}_{12,\hat{\boldsymbol{\sigma}}}\mathbf{v}_{1,2} \equiv \mathbf{v}_{1,2} \mp \frac{1+\alpha}{2}(\mathbf{v}_{12} \cdot \hat{\boldsymbol{\sigma}})\hat{\boldsymbol{\sigma}}. \quad (2.21)$$

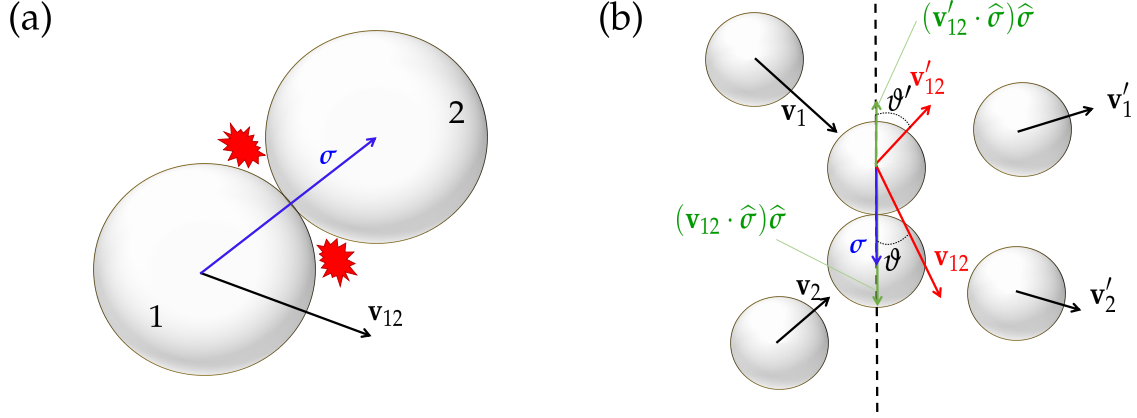


Figure 2.3: Sketch of (a) a collision between two hard inelastic spheres where the reddish glints represent the presence of inelasticity, and (b) the collisional process in the IHS model with the notation of the direct collisional rules for the spatial and velocity quantities. Notice that, as compared with Figure 2.2, there is no reflection any more due to generally different impact and resulting angles, $\vartheta \neq \vartheta'$.

On the other hand, the inverse collisional rules are

$$\mathbf{v}''_{1,2} = \mathfrak{B}_{12,\hat{\sigma}}^{-1} \mathbf{v}_{1,2} \equiv \mathbf{v}_{1,2} \mp \frac{1 + \alpha^{-1}}{2} (\mathbf{v}_{12} \cdot \hat{\sigma}) \hat{\sigma}. \quad (2.22)$$

A sketch of a binary collision for the IHS model is represented in Figure 2.3, in which the lack of the reflective collision behavior is depicted. These collisional rules fulfill conservation of linear momentum [see Eq. (2.17)].

However, due to the inelasticity, conservation of energy does not apply,

$$E'_{12} - E_{12} = \frac{1}{2} m v_1'^2 + \frac{1}{2} m v_2'^2 - \frac{1}{2} m v_1^2 + \frac{1}{2} m v_2^2 = -\frac{m}{4} (1 - \alpha^2) (\mathbf{v}_{12} \cdot \hat{\sigma})^2 \leq 0. \quad (2.23)$$

Notice that for elastic collisions ($\alpha = 1$) one recovers conservation of energy. However, in case of inelasticity ($0 \leq \alpha < 1$) a loss of energy in each binary collision is ensured. Moreover, from the transformation specified in either Eq. (2.21) or Eq. (2.22), one can derive that $\mathfrak{J} = \alpha$ and, therefore, the Boltzmann integro-differential collisional operator reads

$$J[\mathbf{v}_1 | f, f] = \sigma^{d_i-1} \int d\mathbf{v}_2 \int_+ d\hat{\sigma} (\mathbf{v}_{12} \cdot \hat{\sigma}) (\alpha^{-2} f_1'' f_2'' - f_1 f_2). \quad (2.24)$$

It is important to remark that the inversion of the direct collisional rules is not possible in the case of perfectly inelastic particles ($\alpha = 0$).

2.3.3 Inelastic and rough hard spheres

The IHS model is quite an accurate collisional model for describing granular gaseous interactions. In spite of this, its simplicity might skip some other real effects which could be crucial in the phenomenology of granular gases. The first simplest generalization that

can be considered is the assumption of the presence of surface roughness in the hard d_t -spherical grains. Whereas the tangential component of the relative velocity in a binary collision in the **IHS** model stays unaffected, this is not the case in the presence of surface roughness. Moreover, the spinning of hard particles becomes important in the kinetics in the context of this implementation. Therefore, the dynamics of particles can be split up into translational and rotational motion accounted by translational and rotational degrees of freedom, d_t and d_r , respectively. The complexity of considering rotation in high dimensional systems, $d_t \geq 4$, and its lack of verisimilitude in those schemes invite to work just on two- and three-dimensional systems, which can be summarized as **HD** or **HS** systems, respectively. The surface roughness plays a dissipative role into the energy change in a binary collision, in addition to the inelasticity. This effect will be accounted for in the inelastic and rough hard-sphere (**IRHS**) model by the definition of a coefficient of tangential restitution, β , defined by the relation

$$(\widehat{\sigma} \times \mathbf{g}'_{12}) = -\beta(\widehat{\sigma} \times \mathbf{g}_{12}), \quad (2.25)$$

which is assumed to be constant. Here, \mathbf{g}_{12} the relative velocity of the points at contact of particles 1 and 2, defined by

$$\mathbf{g}_{12} = \mathbf{v}_{12} - \widehat{\sigma} \times \mathbf{S}_{12}, \quad (2.26)$$

with $\mathbf{S}_{12} = \sigma(\boldsymbol{\omega}_1 + \boldsymbol{\omega}_2)/2$. From its definition, the range of validity of the coefficient of tangential restitution is $-1 \leq \beta \leq 1$, such that $\beta = -1$ describes perfectly smooth particles and $\beta = 1$ characterizes completely rough particles. Both cases preserve energy if $\alpha = 1$, as we will show later. In fact, the conservative case with $\alpha = \beta = 1$ is known in the literature as Pidduck's gas [Pid22]. Obviously, the description of the **IHS** model developed in **Subsection 2.3.2** is recovered if $\alpha < 1$ and $\beta = -1$.

Thus, we can consider a granular gas of identical **HD** or **HS** of mass m , diameter σ , and moment of inertia I , with positions $\{\mathbf{r}_i\}_{i=1}^N$, and velocities $\{\mathbf{\Gamma}_i\}_{i=1}^N \equiv \{\mathbf{v}_i, \boldsymbol{\omega}_i\}_{i=1}^N$. A sketch of a collision between two **HD** and two **HS** is shown in **Figure 2.4**. In order to derive the direct collisional rules, we impose not only conservation of linear momentum, but, additionally, conservation of angular momentum at the point of contact between the two particles, that is,

$$m\mathbf{v}'_1 + m\mathbf{v}'_2 = m\mathbf{v}_1 + m\mathbf{v}_2, \quad (2.27a)$$

$$I\boldsymbol{\omega}'_1 - \frac{m}{2}\sigma(\widehat{\sigma} \times \mathbf{v}'_1) = I\boldsymbol{\omega}_1 - \frac{m}{2}\sigma(\widehat{\sigma} \times \mathbf{v}_1), \quad (2.27b)$$

$$I\boldsymbol{\omega}'_2 + \frac{m}{2}\sigma(\widehat{\sigma} \times \mathbf{v}'_2) = I\boldsymbol{\omega}_2 + \frac{m}{2}\sigma(\widehat{\sigma} \times \mathbf{v}_2). \quad (2.27c)$$

Let \mathbf{Q}_{12} denote the impulse exerted by particle 1 on particle 2. Then, in general, the

binary collisional rules for spinning spheres 1 and 2 satisfying Eqs. (2.27a) are

$$\mathbf{v}'_{1,2} = \mathbf{v}_{1,2} \mp \frac{\mathbf{Q}_{12}}{m}, \quad \boldsymbol{\omega}'_{1,2} = \boldsymbol{\omega}_{1,2} - \frac{\sigma}{2I} (\widehat{\boldsymbol{\sigma}} \times \mathbf{Q}_{12}). \quad (2.28)$$

If we decompose the impulse into normal and tangential components with respect to $\widehat{\boldsymbol{\sigma}}$,

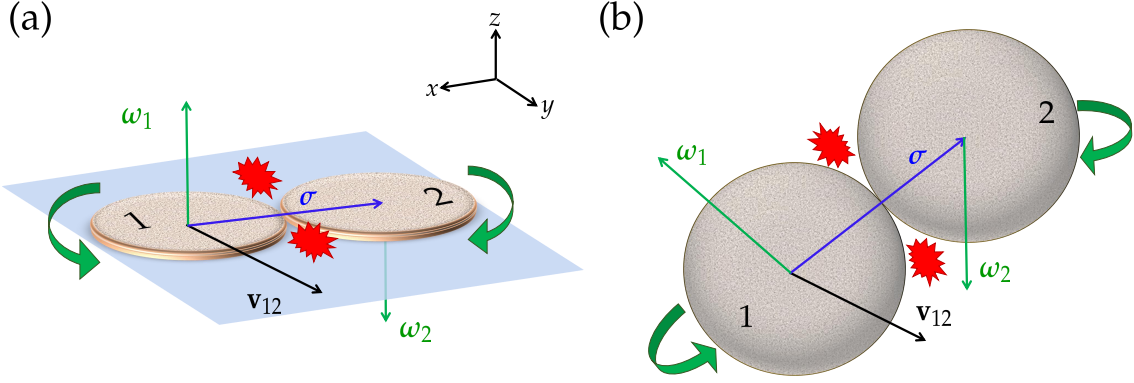


Figure 2.4: Representation of a collision between (a) two HD and (b) two HS. It can be observed that the evolution of the HD is restricted to the plane and that their associated angular velocities lie along the direction orthogonal to the plane. On the other hand, there is no restriction of this kind for HS, where both translational and angular velocities live in the same three-dimensional vector space.

i.e.,

$$\mathbf{Q}_{12} = \mathbf{Q}_{12}^{\parallel} + \mathbf{Q}_{12}^{\perp}, \quad \mathbf{Q}_{12}^{\parallel} = (\widehat{\boldsymbol{\sigma}} \cdot \mathbf{Q}_{12}) \widehat{\boldsymbol{\sigma}}, \quad \mathbf{Q}_{12}^{\perp} = -\widehat{\boldsymbol{\sigma}} \times (\widehat{\boldsymbol{\sigma}} \times \mathbf{Q}_{12}), \quad (2.29)$$

then, from the definitions of the coefficients of restitution in Eqs. (2.20) and (2.25), one obtains

$$(\widehat{\boldsymbol{\sigma}} \cdot \mathbf{Q}_{12}) = m\bar{\alpha}(\widehat{\boldsymbol{\sigma}} \cdot \mathbf{g}_{12}), \quad (\widehat{\boldsymbol{\sigma}} \times \mathbf{Q}_{12}) = m\bar{\beta}(\widehat{\boldsymbol{\sigma}} \times \mathbf{g}_{12}), \quad (2.30)$$

with

$$\bar{\alpha} = \frac{1 + \alpha}{2}, \quad \bar{\beta} = \frac{\kappa}{1 + \kappa} \frac{1 + \beta}{2}, \quad (2.31)$$

κ being the reduced moment of inertia,

$$\kappa = \frac{4I}{m\sigma^2}, \quad (2.32)$$

whose value ranges from $\kappa = 0$ in the case of particles with their masses concentrated at the central point, and $\kappa = 1$ for HD or $\kappa = 2/3$ for HS, in case the mass is concentrated on the surface. Therefore, the impulse is

$$\frac{\mathbf{Q}_{12}}{m} = \bar{\alpha}(\widehat{\boldsymbol{\sigma}} \cdot \mathbf{v}_{12})\widehat{\boldsymbol{\sigma}} + \bar{\beta} [\mathbf{v}_{12} - (\widehat{\boldsymbol{\sigma}} \cdot \mathbf{v}_{12})\widehat{\boldsymbol{\sigma}} - (\widehat{\boldsymbol{\sigma}} \times \mathbf{S}_{12})]. \quad (2.33)$$

This closes the collisional rules in Eqs. (2.28). Following similar steps, the restituting

collisional rules are

$$\mathbf{v}_{1,2}'' = \mathbf{v}_{1,2} \mp \frac{\mathbf{Q}_{12}^-}{m}, \quad \boldsymbol{\omega}_{1,2}'' = \boldsymbol{\omega}_{1,2} - \frac{\sigma}{2I} (\widehat{\boldsymbol{\sigma}} \times \mathbf{Q}_{12}^-), \quad (2.34)$$

with \mathbf{Q}_{12}^- defined as

$$\frac{\mathbf{Q}_{12}^-}{m} = \frac{\bar{\alpha}}{\alpha} (\widehat{\boldsymbol{\sigma}} \cdot \mathbf{v}_{12}) \widehat{\boldsymbol{\sigma}} + \frac{\bar{\beta}}{\beta} [\mathbf{v}_{12} - (\widehat{\boldsymbol{\sigma}} \cdot \mathbf{v}_{12}) \widehat{\boldsymbol{\sigma}} - (\widehat{\boldsymbol{\sigma}} \times \mathbf{S}_{12})]. \quad (2.35)$$

From all these rules, one can prove that energy is dissipated upon collisions. Considering a binary collision between particles 1 and 2, the difference between post and precollisional total kinetic energies is

$$\begin{aligned} E'_{12} - E_{12} &= \frac{m}{2} v_1'^2 + \frac{m}{2} v_2'^2 + \frac{I}{2} \omega_1'^2 + \frac{I}{2} \omega_2'^2 - \frac{m}{2} v_1^2 - \frac{m}{2} v_2^2 - \frac{I}{2} \omega_1^2 - \frac{I}{2} \omega_2^2 \\ &= -m \frac{1 - \alpha^2}{4} (\widehat{\boldsymbol{\sigma}} \cdot \mathbf{v}_{12})^2 - \frac{m\kappa}{1 + \kappa} \frac{1 - \beta^2}{4} [\widehat{\boldsymbol{\sigma}} \times (\widehat{\boldsymbol{\sigma}} \times \mathbf{v}_{12} + 2\mathbf{S}_{12})]^2 \leq 0. \end{aligned} \quad (2.36)$$

Notice that conservation of energy is recovered for elastic particles ($\alpha = 1$) and for either perfectly smooth or completely rough particles ($|\beta| = 1$). In any other case, energy loss is ensured at the collisional level.

Finally, once the binary collisional rules are defined, the Jacobian of the transformation $(\mathbf{v}_1, \mathbf{v}_2, \boldsymbol{\omega}_1, \boldsymbol{\omega}_2) \rightarrow (\mathbf{v}'_1, \mathbf{v}'_2, \boldsymbol{\omega}'_1, \boldsymbol{\omega}'_2)$ is $\mathfrak{J} = \alpha|\beta|$ for **HD**, and $\mathfrak{J} = \alpha|\beta|^2$ for **HS**, i.e.,

$$\mathfrak{J} \equiv \left| \frac{\partial(\mathbf{v}'_1, \mathbf{v}'_2, \boldsymbol{\omega}'_1, \boldsymbol{\omega}'_2)}{\partial(\mathbf{v}_1, \mathbf{v}_2, \boldsymbol{\omega}_1, \boldsymbol{\omega}_2)} \right| = \alpha|\beta|^{2\frac{d_r}{d_t}}, \quad (2.37)$$

which is only valid specifically for **HD** ($d_t = 2, d_r = 1$) and **HS** ($d_t = d_r = 3$) cases. The associated Boltzmann collisional operator [Eq. (2.13)] for this particular model reads

$$J[\Gamma_1[f, f]] = \sigma^{d_t-1} \int d\Gamma_2 \int_+ d\widehat{\boldsymbol{\sigma}} (\mathbf{v}_{12} \cdot \widehat{\boldsymbol{\sigma}}) \left(\frac{f_1'' f_2''}{\alpha^2 |\beta|^{2\frac{d_r}{d_t}}} - f_1 f_2 \right). \quad (2.38)$$

From the **IHS** model, we already knew that the inversion of the direct collisional rules is not possible in the case of perfect inelastic particles ($\alpha = 0$). In addition, this inversion is also not allowed for $\beta = 0$ in the **IRHS** model.

2.4 Thermostatted states

In Section 2.3, we specified the collisional models of the gas, either molecular or granular, which is vital for the explicit form of the Boltzmann collisional operator as defined in

Eq. (2.13). However, attending to the full BE in Eq. (2.14), in order to be completed, we need to specify the generalized external forces per unit mass, \mathbf{G} , defined in Section 2.2 if they act on the system. As we will see in next sections, in this thesis we considered either freely evolving systems, i.e., $\mathbf{G} = \mathbf{0}$, or forced systems. In the latter case, whereas these generalized forces can be fully deterministic, such as gravity—which is widely used to study segregation in granular gases [JY02; BRM05]—along this thesis we have focused on thermostatted systems.

First of all, let us consider Langevin-like systems. That is, we will assume that the particle dynamics of the gas is affected by the action of a thermal bath. In the most basic case, the granular gas is assumed to be immersed in another bath fluid of much smaller particles, so that the effect of the bath on particle i of the granular gas can be modeled by the Langevin equation (LE) [Lan08; LG97; Kam07]

$$\frac{\mathbf{F}_i^{\text{ext}}(\mathbf{r}, t)}{m} \equiv \frac{d\mathbf{v}_i(t)}{dt} = -\xi_0 \mathbf{v}_i(t) + \boldsymbol{\eta}_i(t), \quad (2.39)$$

where ξ_0 is a constant friction or drag coefficient and $\boldsymbol{\eta}_i(t)$ is a random force, usually described as a white noise. That is, this random force is assumed to be Gaussian-distributed and δ -correlated, i.e.,

$$\langle \boldsymbol{\eta}_i(t) \rangle = \mathbf{0}, \quad \langle \boldsymbol{\eta}_i(t) \boldsymbol{\eta}_j(t') \rangle = \chi^2 \delta(t - t') \delta_{ij} \mathbb{1}_{d_t}, \quad (2.40)$$

where $\mathbb{1}_{d_t}$ is the $d_t \times d_t$ unit matrix and χ^2 represents the intensity of the thermostat. In the case of a molecular gas in a thermal bath, from the fluctuation-dissipation theorem (FDT) [CW51; Kub66] one has $\chi^2 = 2\xi_0^2 D$ with $D = T_b/m\xi_0$ being the diffusion coefficient, and T_b the temperature¹ of the bath, here assumed to be constant. Therefore, the counterpart of the BE related to the external force can be deduced from its associated Fokker-Planck equation (see Appendix A), which is

$$\frac{\partial}{\partial \mathbf{v}} \cdot \left(f \frac{\mathbf{F}^{\text{ext}}}{m} \right) \rightarrow -\frac{\partial}{\partial \mathbf{v}} \cdot \left[\left(\xi_0 \mathbf{v} + \frac{\chi^2}{2} \frac{\partial}{\partial \mathbf{v}} \right) f \right] = -\frac{\partial}{\partial \mathbf{v}} \cdot \left[\xi_0 \left(\mathbf{v} + \frac{T_b}{m} \frac{\partial}{\partial \mathbf{v}} \right) f \right]. \quad (2.41)$$

Adding up this term and the Boltzmann collisional operator coming from a specific collisional model to the BE, we obtain the BE for Brownian colliding particles. In general, the BE with a nonzero stochastic external force is usually referred to as BFPE.

The exposed case is widely studied and important in the statistical-physics literature, both historically and conceptually. In this thesis, we use the knowledge from the original LE to derive different BFPE for other stochastic thermostats. Particularly, we have considered the generalization of the LE to a nonlinear velocity-dependent drag

¹Throughout the thesis, temperature has units of energy, except in Chapter 5. Then, we formally take $k_B = 1$, k_B being Boltzmann's constant.

coefficient as a coarse-grained model for interactions with other gaseous particles under some conditions. This generalized thermostat, which is introduced in [Subsection 2.4.1](#), has been applied to [EHS](#) molecular gases and granular gases described by the [IHS](#) model in [Article 1 \(Section 5.2\)](#) and [Article 4 \(Section 7.2\)](#), respectively. In addition, we also considered an energy injection to translational and rotational degrees of freedom applied to a granular gas of [IRHS](#) in the absence of drag forces in [Article 6 \(Section 9.2\)](#), this thermostat being explained in [Subsection 2.4.2](#).

2.4.1 Langevin dynamics with nonlinear drag

Let us consider a *quasi-Rayleigh (QR)* gas, that is, an ensemble of *heavy* Brownian particles (of mass m , diameter σ , number density n and velocities \mathbf{v}) surrounded by a dilute gas of *light* particles (of mass m_b , diameter σ_b , number density n_b , and velocities \mathbf{v}_b) in equilibrium at temperature T_b , acting as a thermal bath on the heavy particles. However, light particle masses, whereas (much) smaller than the heavy ones, are not going to be completely neglected. As derived in Refs. [[Fer00](#); [Fer07](#); [Fer14](#)], under these conditions, a velocity-dependent nonlinear drag coefficient can be obtained as an expansion in powers of the mass ratio m_b/m . This expansion can be derived formally from kinetic theory.

Let us assume for simplicity that both gas and bath particles are hard d_t -spheres such that, whereas gas-gas collisions are given from a certain model which is irrelevant for this derivation, gas-bath interactions are assumed to be elastic. Moreover, we will consider that the Brownian particles are not too far from the thermal equilibrium with the bath. This approach implies that [[Fer00](#); [Fer07](#); [Fer14](#)],

$$\frac{v}{v_b} \simeq \sqrt{\frac{m_b}{m} \frac{c}{c_b}}, \quad (2.42)$$

so that expansions on m_b/m are equivalent to those on v/v_b . Here, \mathbf{c} and \mathbf{c}_b are the reduced velocity variables,

$$\mathbf{c} = \frac{\mathbf{v}}{v_{\text{th}}}, \quad \mathbf{c}_b = \frac{\mathbf{v}_b}{v_{\text{th},b}} \quad (2.43)$$

with $v_{\text{th}} \equiv \sqrt{2T/m}$ and $v_{\text{th},b} \equiv \sqrt{2T_b/m_b}$ the thermal velocities, and, from our assumption, $T \simeq T_b$. The deterministic change of momentum due to the collisions between Brownian and bath particles will be given by the drag force, that is,

$$m \left(\frac{d\mathbf{v}}{dt} \right)_{\text{Brown}} = -m \xi_{\text{QR}}(v) \mathbf{v}, \quad (2.44)$$

where the velocity-dependent drag coefficient $\xi_{\text{QR}}(v)$ can be computed using kinetic-theory arguments. In [Appendix B](#) the drag coefficient is derived using arguments

similar to those followed in [Fer00], but for general d_t dimensions, such that it reads

$$\xi(v) \xrightarrow{\text{QR}} \xi_0 \left(1 + \gamma \frac{mv^2}{T_b} \right), \quad \gamma \equiv \frac{m_b}{2(d_t + 2)m}, \quad (2.45)$$

with ξ_0 being a constant given by the parameters of the problem [see Eq. (B.9)], and γ controls the nonlinear effect, and it is expected to be small. Hence, the first correction from the QR approximation to the drag coefficient corresponds to a quadratic term in the velocity modulus.

In summary, we can consider a gas of hard spheres which, apart from their internal collisions, are in contact with a background fluid acting as a thermal bath within the conditions assumed before. The background fluid, from a coarse-grained description, will act on the gas exerting a force characterized by two components: first, a drag force $\mathbf{F}_{\text{drag}} = -m\xi(v)\mathbf{v}$ with $\xi(v)$ given by Eq. (2.45), and, second, a stochastic force with nonlinear variance $m^2\chi^2(v)$. Then, the equation of motion of i^{th} gas particle is the following one

$$\frac{d\mathbf{v}_i}{dt} = -\xi(v)\mathbf{v}_i + \boldsymbol{\eta}_i + \mathbf{F}_{\text{coll}}, \quad (2.46)$$

where \mathbf{F}_{coll} is the force due to collisions with other particles and $\boldsymbol{\eta}_i$ is a stochastic variable with the white-noise properties given by Eq. (2.40)². Moreover, from FDT, we can impose that

$$\chi^2(v) = \frac{2T_b}{m} \xi(v). \quad (2.47)$$

Therefore, the BFPE for this specific case reads

$$\frac{\partial f}{\partial t} + \mathbf{v} \cdot \nabla f - \frac{\partial}{\partial \mathbf{v}} \cdot \left[\xi(v) \left(\mathbf{v} + \frac{T_b}{m} \frac{\partial}{\partial \mathbf{v}} \right) f \right] = J[\mathbf{v}, f|f]. \quad (2.48)$$

Whereas in a molecular gas the steady temperature would coincide with T_b , this is not so in the granular case. In fact, dissipation of energy due to collisions between granular particles will lead to a smaller temperature. As it will be described in next sections, we have implemented this background fluid interaction with a nonlinear velocity-dependent drag coefficient to both molecular gases of hard spheres and the IHS model for granular gases.

2.4.2 Splitting thermostat

From the IHS and IRHS models of interactions in granular gases, the loss of energy has been discussed at the level of collisions. Experimentally, the process of cooling is

²Note that the noise term in Eq. (2.40) has assumed to be white, this is reasonable due to the *diagonal* and continuous drag coefficient. However, it is not true, in general, if off-diagonal drag matrices or discontinuities appear in the drag force term (see Refs. [Kan17; Jan22]).

usually very fast and it is then convenient to inject energy into the system to observe the properties of the granular fluid in nonequilibrium steady states. Theoretically, this has been commonly modeled via a stochastic volume force acting on the translational degrees of freedom, i.e., a stochastic thermostat, with the properties of a Gaussian white noise. That is, $\mathbf{F}^{\text{ext}}/m$ fulfills the properties in Eq. (2.40), i.e.,

$$\langle \mathbf{F}^{\text{ext}}(t) \rangle = \mathbf{0}, \quad \langle \mathbf{F}_i^{\text{ext}}(t) \mathbf{F}_j^{\text{ext}}(t') \rangle = m^2 \chi_t^2 \delta_{ij} \delta(t - t') \mathbb{1}_{d_t}. \quad (2.49)$$

Nevertheless, in analogy with the generalization in Section 2.2 of the external force per unit mass \mathbf{G} , this thermostat can be generalized as well to act on the rotational degrees of freedom via a stochastic volume torque. That is, we will assume that, apart from the external force defined by Eq. (2.49), there could be an external stochastic torque per unit moment of inertia fulfilling as well the properties of a white noise, i.e.,

$$\langle \boldsymbol{\tau}^{\text{ext}}(t) \rangle = \mathbf{0}, \quad \langle \boldsymbol{\tau}_i^{\text{ext}}(t) \boldsymbol{\tau}_j^{\text{ext}}(t') \rangle = I^2 \chi_r^2 \delta_{ij} \delta(t - t') \mathbb{1}_{d_r}, \quad (2.50)$$

where $\mathbb{1}_{d_r}$ is the $d_r \times d_r$ unit matrix. Then, the associated BFPE is

$$\frac{\partial f}{\partial t} + \mathbf{v} \cdot \nabla f - \frac{\chi_t^2}{2} \left(\frac{\partial}{\partial \mathbf{v}} \right)^2 f - \frac{\chi_r^2}{2} \left(\frac{\partial}{\partial \boldsymbol{\omega}} \right)^2 f = J[\boldsymbol{\Gamma}|f, f]. \quad (2.51)$$

The action of the thermostat over the system can be controlled by the pair of noise intensities (χ_t^2, χ_r^2) . Each value of that pair will describe a specific thermostat belonging to this class. Equivalently, we can define two other quantities to define unequivocally the thermostat, which will be chosen as the *total noise intensity*, χ^2 , and the *rotational-to-total noise intensity ratio*, ε ,

$$\chi^2 = \chi_t^2 + \frac{d_r}{d_t} \frac{I}{m} \chi_r^2, \quad \varepsilon = \frac{d_r}{d_t} \frac{I}{m} \frac{\chi_r^2}{\chi^2}, \quad (2.52)$$

such that each pair (χ^2, ε) defines a unique thermostat, with $0 \leq \varepsilon \leq 1$. Obviously, the freely evolving system is recovered by taking the limit $\chi^2 \rightarrow 0$, regardless of the value of ε . Because the action of this thermostat is divided into translational and rotational energy injections, it will be called *splitting thermostat* (ST) throughout this thesis. In the case $\varepsilon = 0$, we recover a thermostat acting only on the translational degrees of freedom, whereas $\varepsilon = 1$ indicates that the action of the thermostat is concentrated on the rotational ones [CLH02]. In addition, one can define a *noise temperature* from dimensional analysis,

$$T^{\text{wn}} = m \left(\frac{2\sqrt{\pi}}{\Omega_{d_t}} \frac{\chi^2}{n \sigma^{d_t-1}} \right)^{2/3}, \quad (2.53)$$

where the numerical constants have been added for simplification, with Ω_{d_t} being the d_t -dimensional solid angle [see Eq. (B.2)]. Then, it will be equivalent to take either the

pair (χ^2, ε) or the pair $(T^{\text{wn}}, \varepsilon)$ to describe a **ST**. The **BFPE** for this description of the **ST** reads

$$\frac{\partial f}{\partial t} + \mathbf{v} \cdot \nabla f - \frac{\nu^{\text{wn}} T^{\text{wn}}}{4m} \left[(1 - \varepsilon) \left(\frac{\partial}{\partial \mathbf{v}} \right)^2 + \varepsilon \frac{d_t m}{d_r I} \left(\frac{\partial}{\partial \boldsymbol{\omega}} \right)^2 \right] f = J[\Gamma|f, f], \quad (2.54)$$

with

$$\nu^{\text{wn}} \equiv K_{d_t} n \sigma^{d_t-1} \sqrt{\frac{2T^{\text{wn}}}{m}}, \quad K_{d_t} = \frac{\sqrt{2\pi} \frac{d_t-1}{2}}{\Gamma\left(\frac{d_t}{2}\right)}, \quad (2.55)$$

where ν^{wn} is a frequency associated with the thermostat energy injection. Mathematically speaking, one can conclude that there are bijections between the pair of variables (χ_t^2, χ_r^2) , (χ^2, ε) , and $(T^{\text{wn}}, \varepsilon)$. Thus, their descriptions are equivalent and we use any of them as convenient. The main advantage of this **ST** is its two-parameter description, which is used in the work described in Article 6 (Section 9.2).

2.5 Homogeneous states

Once the **BE** is derived [see Eq. (2.14)] and different collisional models and stochastic thermostats used in this thesis are defined in Section 2.3 and Section 2.4, the natural path is to look for solutions of the kinetic equation for each case. As a first step, it seems reasonable to look for solution in homogeneous systems, that is, in the absence of gradients. In that case, Eq. (2.14) becomes

$$\frac{\partial f}{\partial t} + \frac{\partial}{\partial \Gamma} \cdot (f \mathbf{G}) = J[\Gamma|f, f], \quad (2.56)$$

where the forms of the Boltzmann collisional operator and the generalized forces are given once the system model is indicated.

To get a deeper insight into this problem, it is important to distinguish between the molecular and granular cases.

2.5.1 Homogeneous molecular gas of hard d_t -spheres

Let us start from the simplest case of a homogeneous molecular gas of hard d_t -spheres in the absence of external deterministic forces and any other fluid or bath. Then, according to the collisional model for elastic hard d_t -spheres presented in Subsection 2.3.1, and its associated collisional operator defined in Eq. (2.19), the respective form of the **BE** is

$$\frac{\partial f(\mathbf{v}_1; t)}{\partial t} = \sigma^{d_t-1} \int d\mathbf{v}_2 \int_+ d\widehat{\boldsymbol{\sigma}} (\mathbf{v}_{12} \cdot \widehat{\boldsymbol{\sigma}}) [f(\mathbf{v}_1''; t) f(\mathbf{v}_2''; t) - f(\mathbf{v}_1; t) f(\mathbf{v}_2; t)]. \quad (2.57)$$

In addition, for spatially homogeneous and isotropic systems, the **VDF** is expected to depend only on the velocity modulus, v . Moreover, the temperature, which is defined as the mean kinetic energy weighted by the number of degrees of freedom, i.e.,

$$\frac{d_t}{2}T(t) = \frac{1}{2}m\langle v^2 \rangle(t) \equiv \frac{1}{2} \int d\mathbf{v} m v^2 f(\mathbf{v}; t), \quad (2.58)$$

is preserved due to energy conservation upon collisions, i.e., because the second velocity moment, v^2 , is a collisional invariant of the Boltzmann collisional operator. This collisional model possesses three collisional invariants, $\{1, \mathbf{v}, v^2\}$, related to mass, linear momentum, and energy conservation. Hence, it is physically expected that, if the system is initially prepared with an arbitrary **VDF**, it will evolve to equilibrium. The equilibrium **VDF** must coincide with the steady-state solution of Eq. (2.57), which coincides with the Maxwellian **VDF**,

$$f_M(\mathbf{v}) = n v_{\text{th}}^{-d_t} \pi^{-d_t/2} \exp\left(-\frac{mv^2}{2T}\right), \quad (2.59)$$

with T preserved and therefore, coinciding with the initial temperature. This solution can be deduced from the celebrated Boltzmann's H -theorem (see [Subsection 2.6.1](#)), which also shows the property of the Maxwellian **VDF** being an attractor of the **BE**, not only for the homogeneous case.

In case an interaction with a thermal bath is considered in terms of a Langevin-like type equation, as it is the case in [Chapter 5](#) with the nonlinear-drag model introduced in [Subsection 2.4.1](#), the Fokker–Planck-like term of the resulting **BFPE** does not violate the evolution toward equilibrium and the system will reach again the Maxwellian **VDF** with the temperature of the bath, T_b . That is, v^2 is still a collisional invariant, but temperature is not preserved until T_b is reached.

A quite important difference between the original implementation of Langevin dynamics and its extension to a nonlinear drag model is the coupling of the temperature evolution rate with higher moments of the time-dependent **VDF**. This will be further developed in [Article 1 \(Section 5.2\)](#), this fact being responsible for the emergence of memory effects, namely, counterintuitive phenomena due to the memory of the system about previous states or its initial preparation. In [Chapter 3](#), some of these effects studied in this thesis are introduced.

2.5.2 Freely evolving homogeneous granular gas: the Homogeneous Cooling State

The introduction of the granular models associated with a loss of energy, such as the **IHS** or **IRHS** ones described in [Subsection 2.3.2](#) and [Subsection 2.3.3](#), respectively, complicates the analysis of the homogeneous **BE**, in contrast to the apparent simplicity

of the case of elastic collisions.

Let us focus on a monocomponent homogeneous freely evolving granular gas, namely, the evolution is not influenced by any external energy injection or force. A first consequence of the granular dynamics is the energy dissipation, present in both the **IHS** and **IRHS** collisional models, in which the second velocity moments are not collisional invariant any more. In order to present a homogeneous reference state for granular dynamics, usually called *Homogeneous Cooling State (HCS)*, which is governed by this energy dissipation, we will distinguish first between both granular collisional models.

Homogeneous freely evolving states in the IHS model

Let us start from the homogeneous form of the **BE** for the **IHS** model,

$$\frac{\partial f(\mathbf{v}_1; t)}{\partial t} = \sigma^{d_t-1} \int d\mathbf{v}_2 \int_+ d\widehat{\sigma} (\mathbf{v}_{12} \cdot \widehat{\sigma}) [\alpha^{-2} f(\mathbf{v}'_1; t) f(\mathbf{v}'_2; t) - f(\mathbf{v}_1; t) f(\mathbf{v}_2; t)], \quad (2.60)$$

describing the evolution of the one-particle **VDF** of a freely evolving monocomponent homogeneous granular gas of inelastic hard d_t -spheres. It is obvious that the Maxwellian **VDF** is not any more a solution of Eq. (2.60). This fact can be considered as a first indicator of an intrinsically nonequilibrium system.

In analogy with the molecular case, one can define a *granular temperature* as the mean kinetic energy weighted by the degrees of freedom [see Eq. (2.58)]. For this collisional model, we already know that v^2 is not a collisional invariant due to energy dissipation [see Eq. (2.23)]. Then, temperature is not preserved anymore in the system, and it will decay, driving the system asymptotically to a completely frozen (zero-energy) state. To infer the evolution of this temperature dissipation, one can derive the associated differential equation directly from the homogeneous **BE** related to this model. Multiplying v^2 in Eq. (2.60) and integrating over all velocities, we get

$$\frac{\partial T(t)}{\partial t} = -\zeta(t)T(t), \quad (2.61)$$

with $\zeta(t)$ being usually called the *cooling rate*,

$$\zeta(t) \equiv -\frac{mn}{d_t T(t)} \int d\mathbf{v} v^2 J[\mathbf{v}|f, f] = \frac{\pi^{\frac{d_t-1}{2}}}{4d_t \Gamma\left(\frac{d_t+3}{2}\right)} (1 - \alpha^2) \frac{mn \sigma^{d_t-1}}{T(t)} \langle\langle v_{12}^3 \rangle\rangle(t), \quad (2.62)$$

where the notation $\langle\langle \psi(\mathbf{v}_1, \mathbf{v}_2) \rangle\rangle$, with $\psi(\mathbf{v}_1, \mathbf{v}_2)$ being a two-body velocity related quantity, means

$$\langle\langle \psi(\mathbf{v}_1, \mathbf{v}_2) \rangle\rangle(t) = \frac{1}{n^2} \int d\mathbf{v}_1 \int d\mathbf{v}_2 \psi(\mathbf{v}_1, \mathbf{v}_2) f(\mathbf{v}_1; t) f(\mathbf{v}_2; t). \quad (2.63)$$

Notice that for $\alpha < 1$, $\zeta > 0$ because of energy dissipation. Thus, the explicit form of Eq. (2.61) is conditioned to the time dependence of Eq. (2.62), which is hidden in the evolution of the **VDF**. However, it is expected that, after a first *kinetic* evolution of the **VDF**, it will admit a scaling solution of the form,

$$f_{\text{H}}(\mathbf{v}; t) = n v_{\text{th}}^{-d_t}(t) \phi_{\text{H}}(\mathbf{c}), \quad (2.64)$$

with \mathbf{c} the rescaled or reduced velocity defined in Eq. (2.43). When this scaling form is reached, the system evolution is just governed by the temperature continuous decay. In this situation, the system is said to be at the **HCS**, the cooling rate at this state satisfying $\zeta_{\text{H}}(t) \propto \sqrt{T_{\text{H}}(t)}$. In that case, the solution of the evolution equation, Eq. (2.61), is

$$T_{\text{H}}(t) = \frac{T_{\text{H}}(t_0)}{\left[1 + \frac{1}{2}\zeta_{\text{H}}(t_0)(t - t_0)\right]^2}, \quad (2.65)$$

with t_0 being a reference time belonging to the **HCS**. The solution in Eq. (2.65) is the so-called Haff's law of cooling [**Haf83**]. Moreover, it is convenient to measure the evolution of the system not in the *laboratory frame*, but in a *collisional frame*. This alternative description is characterized by the dimensionless time scale

$$s(t) = \frac{1}{2} \int_0^t dt' v(t'), \quad (2.66)$$

$v(t)$ being the inverse of the mean free time, i.e.,

$$v(t) = K_{d_t} n \sigma^{d_t-1} v_{\text{th}}(t), \quad (2.67)$$

with K_{d_t} defined in Eq. (2.55). This $v(t)$ is actually the (local-equilibrium) collision frequency, and then, according to Eq. (2.66), the time scale $s(t)$ represents the (local-equilibrium) accumulated average number of collisions per particle up to time t . In this collisional frame, Haff's cooling law reads

$$T_{\text{H}}(s) = T_{\text{H}}(s_0) \exp[-2\zeta_{\text{H}}^*(s - s_0)], \quad (2.68)$$

with $\zeta_{\text{H}}^* \equiv \zeta_{\text{H}}(t)/v(t)$ the reduced cooling rate at **HCS**, which is a constant due to the **HCS** condition. Comparing Eqs. (2.65) and (2.68), we see that s and t variables are logarithmically related in the **HCS**.

Furthermore, in this collisional frame, the **BE** for an evolving reduced **VDF** $\phi(\mathbf{c}; s) = n^{-1} v_{\text{th}}^{d_t}(t) f(\mathbf{v}; t)$ reads

$$\frac{K_{d_t}}{2} \frac{\partial \phi(\mathbf{c}; s)}{\partial s} + \frac{\mu_2(s)}{d_t} \frac{\partial}{\partial \mathbf{c}} \cdot [\mathbf{c} \phi(\mathbf{c}; s)] = I[\mathbf{c} | \phi, \phi], \quad (2.69)$$

with $I[\mathbf{c}|\phi, \phi]$ being a reduced collisional operator,

$$I[\mathbf{c}_1|\phi, \phi] \equiv \frac{v_{\text{th}}^{d_t-1}}{n\sigma^{d_t-1}} J[\mathbf{v}|f, f] = \int d\mathbf{c}_2 \int_+ d\widehat{\sigma} (\mathbf{c}_{12} \cdot \widehat{\sigma}) [\alpha^{-2} \phi_1'' \phi_2'' - \phi_1 \phi_2], \quad (2.70)$$

and μ_k being the k^{th} collisional moment,

$$\mu_k(s) \equiv - \int d\mathbf{c} c^k I[\mathbf{c}|\phi, \phi], \quad (2.71)$$

or, equivalently,

$$\mu_k(s) = -\frac{1}{2} \int d\mathbf{c}_1 \int d\mathbf{c}_2 \phi(\mathbf{c}_1; s) \phi(\mathbf{c}_2; s) \int_+ d\widehat{\sigma} (\mathbf{c}_{12} \cdot \widehat{\sigma}) (\mathfrak{B}_{12, \widehat{\sigma}} - 1) (c_1^k + c_2^k), \quad (2.72)$$

such that from the definition of cooling rate in Eq. (2.62) one infers that $\zeta = 2\mu_2/d_t$.

Thus, the formal definition of the **HCS VDF** in Eq. (2.64) is equivalent to the steady-state solution of the reduced **BE** in Eq. (2.69),

$$\frac{\mu_2^{\text{H}}}{d_t} \frac{\partial}{\partial \mathbf{c}} \cdot [\mathbf{c} \phi_{\text{H}}(\mathbf{c})] = I[\mathbf{c}|\phi_{\text{H}}, \phi_{\text{H}}]. \quad (2.73)$$

This *steady*³ condition establishes that all the time dependence of the (unscaled) **VDF** f_{H} in the **HCS** occurs through the continuous cooling of the granular temperature, according to Haff's law. From this stationary condition, one can infer some properties of the **HCS VDF**, such as a hierarchy of moment equations,

$$\mu_2^{\text{H}} \langle c^{2k} \rangle_{\text{H}} = \frac{d_t}{2k} \mu_{2k}^{\text{H}}, \quad \langle c^p \rangle_{\text{H}} = \int d\mathbf{c} c^p \phi_{\text{H}}(\mathbf{c}), \quad (2.74)$$

coming from a multiplication of the term c^{2k} in both sides of Eq. (2.72) and integration over the reduced velocity variable \mathbf{c} . This hierarchy of moments equation assumes in its derivation that $c^{2k} \phi_{\text{H}}(\mathbf{c}) \xrightarrow{c \rightarrow \infty} 0$, which is compatible with another known feature of ϕ_{H} , its exponential **HVT**, which will be commented on later.

The exact form of ϕ_{H} is not known up to date, but in the last three decades there have been a vast number of works focused on the study of its properties. Only for $\alpha = 1$ the solution is the Maxwellian **VDF**, but this is the molecular case already studied in **Subsection 2.5.1**, where cooling is eliminated, temperature is preserved, and, then, **HCS** formally does not exist. Without the explicit form of ϕ_{H} , we cannot derive the explicit

³The system is not really in a stationary state because its second velocity moment (granular temperature) monotonically decays due to the energy dissipation. In terms of the **VDF**, f , in the **HCS**, all the time dependence of f_{H} is controlled by the temperature decay, i.e., $\partial_t f_{\text{H}} = (\partial_t T_{\text{H}})(\partial_{T_{\text{H}}} f_{\text{H}}) = -\zeta_{\text{H}} T_{\text{H}} \partial_{T_{\text{H}}} f_{\text{H}} = \frac{1}{2} \zeta_{\text{H}} \partial_{\mathbf{v}} \cdot (\mathbf{v} f_{\text{H}})$, where the last equality comes from the scaling condition of the **HCS VDF** in Eq. (2.64). However, the reduced **VDF** at the **HCS**, ϕ_{H} , is steady, i.e., $\partial_s \phi_{\text{H}} = 0$.

expressions of the collisional moments present in the hierarchy of velocity moments in Eq. (2.74). In order to manage these quantities, we need to make approximations for the **HCS VDF**. For example, let us first focus on the cooling rate, which is proportional to μ_2 . One expects that, at least for $\alpha \lesssim 1$, the **HCS VDF** is close to the Maxwellian one in Eq. (2.59) with a time-dependent granular temperature. In its reduced version, this Maxwellian **VDF** reads

$$\phi_M(\mathbf{c}) = \pi^{-d_t/2} e^{-c^2}. \quad (2.75)$$

Therefore, assuming $\phi_H \approx \phi_M$, the cooling rate can be explicitly computed and, under this approach, one obtains [Gar19]

$$\zeta_H^{*MA} = \frac{1 - \alpha^2}{d_t}. \quad (2.76)$$

This approach is usually known as *Maxwellian approximation (MA)*. However, for not quasi-elastic systems, deviations for this form of the cooling rate, as well as for the **MA** of ϕ_H , are found theoretically and from computer simulations [BRC96; NE98; MS00; HOB00; Cop+03; BP06a; BP06b; SM09]. A way of obtaining information about the **HCS VDF** is from its velocity moments $\langle c^{2k} \rangle_H$ or, equivalently, from the cumulants of the distribution. First of all, due to isotropy, one expects that ϕ_H depends on \mathbf{c} only through its modulus. Thus, a straightforward approach consists in writing ϕ_H as a series expansion of a orthogonal basis of polynomials based on the Gaussian measure. It is quite common in kinetic theory to use Sonine polynomials [CC70; FK72; BP03; Gar19], which are just a special case of associated Laguerre polynomials,

$$S_k(c^2) \equiv L_k^{\left(\frac{d_t}{2}-1\right)}(c^2) = \sum_{j=0}^k \frac{(-1)^j \Gamma\left(\frac{d_t}{2} + k\right)}{\Gamma\left(\frac{d_t}{2} + j\right) (k-j)! j!} c^{2j}, \quad (2.77)$$

fulfilling the orthogonal and normalization condition,

$$\langle S_{k'} | S_k \rangle \equiv \int d\mathbf{c} \phi_M(\mathbf{c}) S_{k'}(c^2) S_k(c^2) = \mathcal{N}_k \delta_{k'k}, \quad \mathcal{N}_k \equiv \frac{\Gamma\left(\frac{d_t}{2} + k\right)}{\Gamma\left(\frac{d_t}{2}\right) k!}. \quad (2.78)$$

Then, an arbitrary isotropic **VDF** $\phi(\mathbf{c})$ is expressed in this expansion as

$$\phi(\mathbf{c}) = \phi_M(\mathbf{c}) \left[1 + \sum_{k \geq 2} a_k S_k(c^2) \right], \quad a_k = \frac{\langle S_k | \phi / \phi_M \rangle}{\mathcal{N}_k}, \quad (2.79)$$

the coefficients a_k being the cumulants of the distribution, where the two leading cumulants are $a_0 = 1$ and $a_1 = 0$, the latter coming from the definition of temperature, Eq. (2.58), using $\langle c^2 \rangle = d_t/2$. Additionally, there is a biunivocal relationship between

the cumulants and the moments of the distribution,

$$\langle c^{2k} \rangle = \langle c^{2k} \rangle_M \left[1 + \sum_{j=2}^k (-1)^j \binom{k}{j} a_j \right], \quad k \geq 2, \quad (2.80)$$

where the subscript M denotes that the quantity is computed using the Maxwellian VDF.

The straightforward extension of the MA for the HCS VDF consists in truncating the series in Eq. (2.79) up to a certain cumulant order. This is the basis of the *Sonine approximation* (SA), widely used in the literature [BRC96; Bre+98; NE98; MS00; HOB00; Bar+02; Cop+03; BP06a; BP06b; SM09; Gar19]. This method consists in the mentioned truncation plus a corresponding linearization of the collisional moments on the cumulants involved in the approximation. This approach is based on the assumption that those cumulants are increasingly small, that is, ϕ_H is not very far from ϕ_M . Under this assumptions, mainly a_2^H and a_3^H have been estimated theoretically by means of different linearizations and successfully compared with simulation results from either direct simulation Monte Carlo (DSMC) or event-driven molecular dynamics (EDMD) techniques. In the work in Article 2 (Section 6.2) this problem is revisited and EDMD is extended to highly inelastic systems.

However, simulation results for a_4^H , a_5^H , and a_6^H reported in Refs. [BP06a; BP06b], as well as the theoretical analysis previously developed in Ref. [HOB00], indicate a growth of their absolute values as their order increases for highly inelastic systems, $\alpha \lesssim 0.6$. Then, those systems may suffer a breakdown of the Sonine expansion, which can be explained [BP06a; BP06b] by the exponential HVT found for the HCS VDF. This tail, predicted by kinetic theory from a standard approach in which the loss term of the collisional operator dominates over the gain term in this high-velocity limit, has the form [NE98; EP97]

$$\phi_H(\mathbf{c}) \sim \mathcal{A} \exp\left(-\gamma_c^{\text{IHS}} c\right), \quad \gamma_c^{\text{IHS}} = \frac{d_t \pi^{\frac{d_t-1}{2}}}{\mu_2^{\text{H}} \Gamma\left(\frac{d_t+1}{2}\right)}, \quad (2.81)$$

for $c \gg 1$. The existence of this non-Maxwellian HVT has been also satisfactorily observed in computer simulations [BCR99; PBF06] and in recent microgravity experiments [YSS20]. In the latter work, the IHS model and the viscoelastic model are compared with the experimental outcomes, concluding a negligible influence of the impact velocity on the coefficient of restitution, thus preferring the constant coefficient of restitution model. Moreover, Haff's cooling law and the exponential form of the HVT were observed. On the other hand, because of some important deviations of the cooling rate observed experimentally with respect to the kinetic-theory predictions, the authors claimed for models that could implement surface roughness.

The HCS is not only important from a descriptive point of view. This state represents the homogeneous base state in the CE method when transport and hydrodynamics of granular gaseous rapid flows are studied. Finally, this HCS is not exclusive of monodisperse systems, but it is also described within the framework of the IHS model in granular mixtures in several works [GD99; MG02; Dah+02; Gar19].

Homogeneous freely evolving states in the IRHS model

Whereas the HCS does not change conceptually with the introduction of the IRHS model, it acquires some implications that may be important, not only from a mathematical point of view, but also phenomenologically, and could solve, for example, the numerical discrepancies observed in Ref. [YSS20].

Let us begin, as before, with the homogeneous BE for the IRHS model for a monodisperse system [MS19a; MS19b],

$$\frac{\partial f(\Gamma_1; t)}{\partial t} = \sigma^{d_t-1} \int d\Gamma_2 \int_+ d\hat{\sigma} (\mathbf{v}_{12} \cdot \hat{\sigma}) \left[\frac{f(\Gamma_1''; t)f(\Gamma_2''; t)}{\alpha^2 |\beta|^{2d_r/d_t}} - f(\Gamma_1; t)f(\Gamma_2; t) \right], \quad (2.82)$$

where rotational degrees of freedom, d_r , are introduced coming from the angular velocity vectors, ω .

In order to start the kinetic description of the system, we need to introduce again the granular temperature. However, in contrast to the simple definition given by Eq. (2.58), we need to take into account that the total kinetic energy for this model is the sum of a translational and a rotational counterparts, as considered in Eq. (2.36), i.e., for the i^{th} particle its total kinetic energy is

$$E_i^{\text{total}} \equiv E_i^t + E_i^r = \frac{1}{2} m v_i^2 + \frac{1}{2} I \omega_i^2. \quad (2.83)$$

Therefore, we can define naturally two *partial* temperatures, one as the average of the translational kinetic energy and the other one as the average of the rotational energy, both of them weighted by their respective degrees of freedom,

$$\frac{d_t}{2} T_t(t) \equiv \frac{1}{2} m \langle v^2 \rangle(t), \quad \frac{d_r}{2} T_r(t) \equiv \frac{1}{2} I \langle \omega^2 \rangle(t), \quad (2.84)$$

where we are explicitly setting $\langle \mathbf{v} \rangle = \mathbf{0}$ without any loss of generality in homogeneous states.

Moreover, from the definition of total kinetic energy, one can define a *mean* granular temperature as the average of the total kinetic energy weighted by the total number of

degrees of freedom,

$$\frac{d_t + d_r}{2} T(t) \equiv \frac{1}{2} m \langle v^2 \rangle(t) + \frac{1}{2} I \langle \omega^2 \rangle(t) = \frac{d_t T_t(t) + d_r T_r(t)}{d_t + d_r}, \quad (2.85)$$

which is identified with a weighted mean of the translational and rotational partial temperatures defined in Eq. (2.84).

Then, from the definitions in Eq. (2.84) and the homogeneous BE for the IRHS model introduced in Eq. (2.82), one can derive the evolution equations for the partial temperatures,

$$\partial_t T_t(t) = -\xi_t(t) T_t(t), \quad \xi_t(t) \equiv -\frac{m}{n d_t T_t(t)} \int d\Gamma v^2 J[\Gamma|f, f], \quad (2.86a)$$

$$\partial_t T_r(t) = -\xi_r(t) T_r(t), \quad \xi_r(t) \equiv -\frac{I}{n d_r T_r(t)} \int d\Gamma \omega^2 J[\Gamma|f, f], \quad (2.86b)$$

with ξ_t and ξ_r being the translational and rotational *energy production rates*, respectively, which do not represent *cooling* rates necessarily. This is because, although the mean temperature decays monotonically, the coefficients ξ_t and ξ_r also take into account a transfer of energy from the translational part to the rotational one, and vice versa. This implies a coupling between both differential equations. However, analogously to what happened with Eq. (2.61), Eqs. (2.86) do not form a closed set of differential equations because the energy production rates depend on the full time-dependent VDF. Moreover, the evolution for the mean granular temperature reads

$$\partial_t T(t) = -\zeta(t) T(t), \quad \zeta(t) \equiv \frac{d_t \xi_t(t) T_t(t) + d_r \xi_r(t) T_r(t)}{(d_t + d_r) T(t)}, \quad (2.87)$$

ζ being the cooling rate for the IRHS model. Again, this equation cannot be solved if the time dependence and the form of the VDF is unknown.

Eqs. (2.84)–(2.87) reflect the dynamics inferred for the partial and mean temperatures from the introduction of the IRHS model into the homogeneous BE. Using the same reasoning as in the case of the IHS model, one expects that, after a first rapid kinetic transient stage, all time dependence of the VDF occurs through the temperature decay equation, Eq. (2.87). In that regime, the HCS is reached and the VDF fulfills the following rescaling,

$$f_H(\Gamma; t) = n \left(\frac{2\tau_t^H}{m} \right)^{-d_t/2} \left(\frac{2\tau_r^H}{I} \right)^{-d_r/2} [T_H(t)]^{-\frac{d_t+d_r}{2}} \phi_H(\tilde{\Gamma}), \quad (2.88)$$

with $\tilde{\Gamma} \equiv \{\mathbf{c}, \mathbf{w}\}$,

$$\mathbf{c} \equiv \frac{\mathbf{v}}{v_{\text{th}}(t)}, \quad \mathbf{w} \equiv \frac{\boldsymbol{\omega}}{\omega_{\text{th}}(t)}; \quad v_{\text{th}} \equiv \sqrt{\frac{2\tau_t T}{m}}, \quad \omega_{\text{th}} \equiv \sqrt{\frac{2\tau_r T}{I}}. \quad (2.89)$$

In Eq. (2.88), the temperature ratios $\tau_t \equiv T_t/T$ and $\tau_r \equiv T_r/T$ acquire necessarily steady values because all time dependence is contained in $T(t)$, and $\phi_H(\tilde{\Gamma})$ does not evolve in time. The condition of τ_t and τ_r reaching a steady form is equivalent to the rotational-to-translational temperature ratio getting a steady value,

$$\theta \equiv \frac{T_r}{T_t} \Rightarrow \tau_t = \frac{d_t + d_r}{d_t + d_r \theta}, \quad \tau_r = \frac{d_t + d_r}{d_t/\theta + d_r}. \quad (2.90)$$

In general, from the differential equations of the partial temperatures in Eqs. (2.86), the evolution of θ is given by

$$\partial_t \theta = -(\xi_r - \xi_t) \theta. \quad (2.91)$$

At the HCS, the rotational-to-translational temperature ratio reaches a constant value and, therefore, $\xi_t^H = \xi_r^H = \zeta_H$, where the last equality comes from the cooling rate definition in Eq. (2.87). Additionally, the unique set of collisional invariants for this collisional model is $\{1, \mathbf{v}\}$ due to conservation of mass and linear momentum. However, ω it is not a collisional invariant. Thus, to complete the description, at least up to second order in velocity moments, we need to derive the evolution equation for the mean angular velocity of the system, $\bar{\Omega} \equiv \langle \omega \rangle$. Then, from the homogeneous BE, Eq. (2.82), one finds

$$\partial_t \bar{\Omega}(t) = -\zeta_{\bar{\Omega}} \bar{\Omega}(t), \quad \zeta_{\bar{\Omega}} \bar{\Omega}(t) \equiv - \int d\Gamma \omega J[\Gamma|f, f]. \quad (2.92)$$

Since the HCS is isotropic and there is no preferred direction, one must have $\bar{\Omega}_H = \mathbf{0}$.

Again, from the HCS condition, $\zeta_H(t)/\sqrt{T_H(t)} \propto \text{const}$ and, therefore, the expression of Haff's law in the laboratory time frame derived from the IHS model, Eq. (2.65), is recovered, except that now the cooling rate is that of the IRHS model. Since in the HCS all the time dependence takes place through temperature, we have,

$$\frac{\partial}{\partial t} \equiv \left(\frac{\partial T_H}{\partial t} \right) \frac{\partial}{\partial T_H} = -\zeta_H(t) T_H(t) \frac{\partial}{\partial T_H}. \quad (2.93)$$

As a consequence, the homogeneous BE for the IRHS can be rewritten, still in the laboratory time frame, as [Gar19]

$$\frac{1}{2} \zeta_H \left(\frac{\partial}{\partial \mathbf{V}} \cdot \mathbf{V} + \frac{\partial}{\partial \omega} \cdot \omega \right) f_H = J[\Gamma|f_H, f_H], \quad (2.94)$$

where we have used the scaling form of f_H and the dependence of the variables in $\tilde{\Gamma}$ with T_H according to their definition in Eq. (2.89), which are dependent on T_H in the HCS.

Following the same steps as in the IHS model, it is also convenient in the IRHS model to define the collisional frame and the s -variable defined in Eqs. (2.66) and (2.67), but taking into account that in this model the thermal velocity is $v_{\text{th}} = \sqrt{2\tau_t T/m}$. Then,

from similar reasoning as in the deduction of Eq. (2.69) and introducing the generalized unsteady scaling $f(\mathbf{v}; t) = n^{-1} v_{\text{th}}^{-d_t}(t) \omega_{\text{th}}^{-d_r}(t) \phi(\mathbf{c}; s)$, the homogeneous BE for a freely evolving granular gas in the IRHS model for the reduced VDF in the collisional frame reads

$$\frac{K_{d_t}}{2} \frac{\partial \phi(\tilde{\Gamma}; s)}{\partial s} + \frac{\mu_{20}^{(0)}(s)}{d_t} \frac{\partial}{\partial \mathbf{c}} \cdot \left[\mathbf{c} \phi(\tilde{\Gamma}; s) \right] + \frac{\mu_{02}^{(0)}(s)}{d_r} \frac{\partial}{\partial \mathbf{w}} \cdot \left[\mathbf{w} \phi(\tilde{\Gamma}; s) \right] = I[\tilde{\Gamma} | \phi, \phi], \quad (2.95)$$

with $I[\tilde{\Gamma} | \phi, \phi]$ being a reduced collisional operator defined analogously to Eq. (2.70) for the IHS case, i.e.,

$$I[\tilde{\Gamma}_1 | \phi, \phi] \equiv \frac{v_{\text{th}}^{d_t-1} \omega_{\text{th}}^{d_r}}{n \sigma^{d_t-1}} J[\mathbf{v} | f, f] = \int d\tilde{\Gamma}_2 \int_+ d\hat{\sigma} (\mathbf{c}_{12} \cdot \hat{\sigma}) \left(\frac{\phi_1'' \phi_2''}{\alpha^2 |\beta|^2 \frac{d_t}{d_r}} - \phi_1 \phi_2 \right). \quad (2.96)$$

In Eq. (2.95), and as a generalization of Eq. (2.72), $\mu_{pq}^{(r)}$ is the collisional moment of order (p, q, r) ,

$$\mu_{pq}^{(r)}(s) \equiv - \int d\tilde{\Gamma} c^p w^q (\mathbf{c} \cdot \mathbf{w})^r I[\tilde{\Gamma} | \phi, \phi] \quad (2.97)$$

or, equivalently,

$$\begin{aligned} \mu_{pq}^{(r)}(s) = & - \frac{1}{2} \int d\tilde{\Gamma}_1 \int d\tilde{\Gamma}_2 \phi(\tilde{\Gamma}_1; s) \phi(\tilde{\Gamma}_2; s) \int_+ d\hat{\sigma} (\mathbf{c}_{12} \cdot \hat{\sigma}) \\ & \times (\mathfrak{B}_{12, \hat{\sigma}} - 1) \left[c_1^p w_1^q (\mathbf{c}_1 \cdot \mathbf{w}_1)^r + c_2^p w_2^q (\mathbf{c}_2 \cdot \mathbf{w}_2)^r \right]. \end{aligned} \quad (2.98)$$

From the definition of the energy production rates in Eqs. (2.86), one infers that $\xi_t = 2\mu_{20}^{(0)}/d_t$ and $\xi_r = 2\mu_{02}^{(0)}/d_r$. From Eq. (2.98), once we know the collisional change of the velocity function $c_1^p w_1^q (\mathbf{c}_1 \cdot \mathbf{w}_1)^r$, we can compute the (p, q, r) -order collisional moment. In general, given an arbitrary one-body velocity dependent function, $\psi(\tilde{\Gamma}_1) \equiv \psi_1$, even if the VDF is unknown, one can formally express its corresponding collisional integral,

$$\begin{aligned} \mathcal{I}[\psi_1 | \phi, \phi] & \equiv \int d\tilde{\Gamma}_1 \psi(\tilde{\Gamma}_1) I[\tilde{\Gamma}_1 | \phi, \phi] \\ & = \int d\tilde{\Gamma}_1 \int d\tilde{\Gamma}_2 \int_+ d\hat{\sigma} (\mathbf{c}_{12} \cdot \hat{\sigma}) \phi(\tilde{\Gamma}_1) \phi(\tilde{\Gamma}_2) (\mathfrak{B}_{12, \hat{\sigma}} - 1) \psi(\tilde{\Gamma}_1), \end{aligned} \quad (2.99)$$

in terms of two-body averages. Then, the HCS condition is equivalent to

$$\frac{\mu_{20}^{(0)\text{H}}}{d_t} \frac{\partial}{\partial \mathbf{c}} \cdot \left[\mathbf{c} \phi_{\text{H}}(\tilde{\Gamma}) \right] + \frac{\mu_{02}^{(0)\text{H}}}{d_r} \frac{\partial}{\partial \mathbf{w}} \cdot \left[\mathbf{w} \phi_{\text{H}}(\tilde{\Gamma}) \right] = I[\tilde{\Gamma} | \phi_{\text{H}}, \phi_{\text{H}}]. \quad (2.100)$$

This is the IRHS counterpart of Eq. (2.73).

In Refs. [MS19a; MS19b], some of the collisional integrals for the velocity moments up to quadratic order are computed in terms of two-body averages, which are associated with conservation of linear momentum, the nonconservation of angular velocity encoded in the quantity $\zeta_{\bar{\Omega}}$, and the energy production rates. In Table 2.1, some of these quantities are summarized in their reduced-velocity version, where the quantity $\mathbf{W}_{12} = (\mathbf{w}_1 + \mathbf{w}_2)/2$ is introduced. Moreover, in the work presented in Article 5 (Section 8.2) of this thesis, an extension to collisional moments of fourth order is carried out.

$\psi(\bar{\Gamma})$	$\mathcal{I}[\psi \phi, \phi]/\mathcal{I}_0$
\mathbf{c}_1	$-\left(\bar{\alpha} + \frac{d_t - 1}{2}\bar{\beta}\right) \langle\langle c_{12} \mathbf{c}_{12} \rangle\rangle + \frac{\sqrt{\pi}\Gamma\left(\frac{3+d_t}{2}\right)}{\Gamma\left(1 + \frac{d_t}{2}\right)} \bar{\beta} \sqrt{\frac{\theta}{\kappa}} \langle\langle \mathbf{c}_{12} \times \mathbf{W}_{12} \rangle\rangle$
\mathbf{w}_1	$-\frac{\bar{\beta}}{\kappa} \left[3\langle\langle c_{12} \mathbf{W}_{12} \rangle\rangle - \langle\langle c_{12}^{-1} \mathbf{c}_{12} (\mathbf{c}_{12} \cdot \mathbf{W}_{12}) \rangle\rangle \right]$
c_1^2	$-2\left(\bar{\alpha} + \frac{d_t - 1}{2}\bar{\beta}\right) \langle\langle c_{12} (\mathbf{c}_1 \cdot \mathbf{c}_{12}) \rangle\rangle + \frac{1}{2}\left(\bar{\alpha}^2 + \frac{d_t - 1}{2}\bar{\beta}^2\right) \langle\langle c_{12}^3 \rangle\rangle + \frac{2\bar{\beta}^2\theta}{\kappa}$ $\times \left[3\langle\langle c_{12} W_{12}^2 \rangle\rangle - \langle\langle c_{12}^{-1} (\mathbf{c}_{12} \cdot \mathbf{W}_{12})^2 \rangle\rangle \right] + \frac{2\sqrt{\pi}\Gamma\left(\frac{3+d_t}{2}\right)}{\Gamma\left(1 + \frac{d_t}{2}\right)} \bar{\beta} \sqrt{\frac{\theta}{\kappa}} \langle\langle (\mathbf{c}_1 \times \mathbf{c}_{12}) \cdot \mathbf{W}_{12} \rangle\rangle$
w_1^2	$-\frac{d_t - 1}{2} \frac{\bar{\beta}^2}{\kappa\theta} \langle\langle c_{12}^3 \rangle\rangle - 2\frac{\bar{\beta}^2}{\kappa^2} \left[3\langle\langle c_{12} W_{12}^2 \rangle\rangle - \langle\langle c_{12}^{-1} (\mathbf{c}_{12} \cdot \mathbf{W}_{12})^2 \rangle\rangle \right]$ $+ 2\frac{\bar{\beta}}{\kappa} \left[3\langle\langle c_{12} (\mathbf{w}_1 \cdot \mathbf{W}_{12}) \rangle\rangle - \langle\langle c_{12}^{-1} (\mathbf{c}_{12} \cdot \mathbf{W}_{12}) (\mathbf{c}_{12} \cdot \mathbf{w}_1) \rangle\rangle \right]$
$\frac{c_1^2 + c_2^2}{2}$	$\left[\bar{\alpha}(1 - \bar{\alpha}) + \frac{d_t - 1}{2}\bar{\beta}(1 - \bar{\beta}) \right] \langle\langle c_{12}^3 \rangle\rangle + \frac{2\bar{\beta}^2\theta}{\kappa} \left[3\langle\langle c_{12} W_{12}^2 \rangle\rangle - \langle\langle c_{12}^{-1} (\mathbf{c}_{12} \cdot \mathbf{W}_{12})^2 \rangle\rangle \right]$
$\frac{w_1^2 + w_2^2}{2}$	$-\frac{d_t - 1}{2} \frac{\bar{\beta}^2}{\kappa\theta} \langle\langle c_{12}^3 \rangle\rangle + 2\frac{\bar{\beta}}{\kappa} \left(1 - \frac{\bar{\beta}}{\kappa} \right) \left[3\langle\langle c_{12} W_{12}^2 \rangle\rangle - \langle\langle c_{12}^{-1} (\mathbf{c}_{12} \cdot \mathbf{W}_{12})^2 \rangle\rangle \right]$

Table 2.1: Collisional integrals for velocity functions up to quadratic order in terms of two-body averages. Here, $\mathcal{I}_0 \equiv 2\pi^{\frac{d_t-1}{2}}/(d_t + 1)$.

Whereas expressions in Table 2.1 are exact in the context of the BE and the IRHS model for HD ($d_t = 2$, $d_r = 1$) and HS ($d_t = d_r = 3$), it is important, from a predictive point of view, to make estimates of the involved two-body averages. In this sense, we need to propose certain forms for the VDF if we want to evaluate explicitly the evolution equations and also to study the HCS. As a first reasonable proposal, we can consider that translational and angular velocities are uncorrelated or that their correlation is negligible⁴. In this approximation, the total VDF can be factorized as a product of its

⁴We will see in Chapter 8 that this is not always true.

marginal translational and rotational **VDF**,

$$\phi(\tilde{\Gamma}) \rightarrow \phi_{\mathbf{c}}(\mathbf{c})\phi_{\mathbf{w}}(\mathbf{w}), \quad (2.101)$$

where $\phi_{\mathbf{c}}$ and $\phi_{\mathbf{w}}$ refer to the translational and rotational marginal **VDF**, respectively, defined as

$$\phi_{\mathbf{c}}(\mathbf{c}) \equiv \int d\mathbf{w} \phi(\tilde{\Gamma}), \quad \phi_{\mathbf{w}}(\mathbf{w}) \equiv \int d\mathbf{c} \phi(\tilde{\Gamma}). \quad (2.102)$$

As explained in Refs. [San18; Gar19; MS19a; MS19b; MS21c], an apparently good approach consists in choosing $\phi_{\mathbf{c}}(\mathbf{c}) \rightarrow \phi_{\mathbf{M}}(\mathbf{c})$ from arguments of maximum-entropy formalism of this translational part, but not to give explicitly any form for the rotational marginal **VDF**. This is because, up to the order of the quantities in Table 2.1, no powers above quadratic are observed for the angular velocity. Thus, we take

$$\phi(\tilde{\Gamma}) \approx \phi_{\mathbf{M}}(\mathbf{c})\phi_{\mathbf{w}}(\mathbf{w}), \quad (2.103)$$

as a sort of **MA**. Thus, within this approximation, the form of the principal production rates appearing in the evolution equations of the system are summarized in Table 2.2. In this table, $\zeta_{\tilde{\Omega}}^* \equiv \zeta_{\tilde{\Omega}}/v$, $\xi_{t,r}^* \equiv \xi_{t,r}/v$, and $\zeta^* \equiv \zeta/v$, with the collisional frequency ν defined in Eq. (2.67), and the quantity $\tilde{X} \equiv I\tilde{\Omega}^2/d_r T_r$ is introduced.

Production rate	Expression in the approximation $\phi(\tilde{\Gamma}) \rightarrow \phi_{\mathbf{M}}(\mathbf{c})\phi_{\mathbf{w}}(\mathbf{w})$
$\zeta_{\tilde{\Omega}}^*$	$\frac{2}{d_t} \frac{1+\beta}{1+\kappa}$
ξ_t^*	$\frac{1-\alpha^2}{d_t} + \frac{2d_r\kappa(1+\beta)}{d_t^2(1+\kappa)^2} \left[\frac{(1-\beta)}{2} (\kappa + \theta + \tilde{X}) + 1 - \theta - \tilde{X} \right]$
ξ_r^*	$\frac{2\kappa(1+\beta)}{d_t(1+\kappa)^2} \left[\frac{1-\beta}{2\kappa} \left(\frac{\kappa}{\theta} + 1 + \tilde{X} \right) + 1 - \frac{1}{\theta} + \tilde{X} \right]$
ζ^*	$\frac{1-\alpha^2}{d_t + d_r\theta} + \frac{1-\beta^2}{d_t(1+\kappa)} \frac{d_r/d_t}{1 + d_r\theta/d_t} (\kappa + \theta + \tilde{X})$

Table 2.2: Collisional production rates up to second order in velocity moments under the **MA** in Eq. (2.103).

In general, the basic evolution equations in the collisional frame read

$$\frac{K_{d_t}}{2} \frac{\partial \ln T}{\partial s} = -\zeta^*, \quad \frac{K_{d_t}}{2} \frac{\partial \ln \theta}{\partial s} = -\xi_r^* + \xi_t^*, \quad \frac{K_{d_t}}{2} \frac{\partial \ln \tilde{X}}{\partial s} = -2\zeta_{\tilde{\Omega}}^* + \xi_r^*. \quad (2.104)$$

As expected, Table 2.2 shows that $\zeta^* \geq 0$, the equality being fulfilled only if $\alpha = |\beta| = 1$. In addition, it can be easily proved that $2\zeta_{\tilde{\Omega}}^* - \xi_r^* \geq 0$ [Gar19; MS19b], implying that \tilde{X} tends to 0 monotonically, so that $\tilde{X}^{\text{H}} = 0$. Finally, the solution for θ^{H} comes from the condition $\xi_t^{*\text{H}} = \xi_r^{*\text{H}}$. Within the **MA**, the **HCS** solution for the rotational-to-translational

temperature ratio is given by

$$\theta_M^H = \sqrt{h_\theta^2 + \frac{d_t}{d_r}} + h_\theta, \quad h_\theta \equiv \frac{d_t(1+\kappa)^2}{2d_r\kappa(1+\beta)^2} \left[1 - \alpha^2 - \frac{1 - \frac{d_r}{d_t}\kappa}{1+\kappa}(1-\beta^2) \right] + \frac{1}{2} \left(1 - \frac{d_t}{d_r} \right). \quad (2.105)$$

This expression clearly signals a nonequipartition between translational and rotational degrees of freedom. In Refs. [VSK14b; Gar19; MS19b], a linear stability analysis of the HCS is done under *homogeneous* perturbations in the context of the MA given by Eq. (2.103).

Whereas this approach is a good reference to study the HCS, correlations between translational and angular velocities are known to be present [Bri+07] and might be relevant. Then, the factorization in Eq. (2.101) for the HCS VDF needs to be corrected in some ranges of parameters. As occurs in the analysis of the IHS model, the HCS VDF in the IRHS model is non-Maxwellian. As an extension of the smooth case, applying a Grad–Sonine methodology in the IRHS consists in the expansion of the VDF $\phi(\tilde{\Gamma})$ around a two-temperature Maxwellian distribution in terms of a proper set of orthogonal basis of polynomials. In this case,

$$\phi(\tilde{\Gamma}) = \phi_M(\tilde{\Gamma}) \sum_{p=0}^{\infty} \sum_{q=0}^{\infty} \sum_{r=0}^{\infty} a_{pq}^{(r)} \Psi_{pq}^{(r)}(\tilde{\Gamma}), \quad \phi_M(\tilde{\Gamma}) = \pi^{-d_t-d_r} e^{-c^2-w^2}, \quad (2.106a)$$

$$\Psi_{pq}^{(r)}(\tilde{\Gamma}) \equiv L_p^{(2r+\frac{d_t}{2}-1)}(c^2) L_q^{(2r+\frac{d_r}{2}-1)}(w^2) (c^2w^2)^r P_{2r} \left(\frac{|\mathbf{c} \cdot \mathbf{w}|}{cw} \right), \quad (2.106b)$$

with $L_j^{(\ell)}(x)$ being the associated Laguerre polynomials and $P_j(x)$ being the Legendre polynomials [AS72]. Then, the orthonormalization condition for the basis $\left\{ \Psi_{pq}^{(r)} \right\}_{p,q,r=1}^{\infty}$ is

$$\langle \Psi_{p'q'}^{(r')} | \Psi_{pq}^{(r)} \rangle = \mathcal{N}_{pq}^{(r)} \delta_{pp'} \delta_{qq'} \delta_{rr'}, \quad \mathcal{N}_{pq}^{(r)} \equiv \frac{\Gamma \left(2r + \frac{d_t}{2} + p \right) \Gamma \left(2r + \frac{d_r}{2} + q \right)}{\Gamma \left(\frac{d_t}{2} \right) \Gamma \left(\frac{d_r}{2} \right) (4r+1)p!q!}. \quad (2.107)$$

The coefficients $a_{pq}^{(r)}$ are the cumulants of the VDF and they are defined as

$$a_{pq}^{(r)} = \frac{\langle \Psi_{pq}^{(r)} \rangle}{\mathcal{N}_{pq}^{(r)}}. \quad (2.108)$$

The expansion in Eq. (2.106a) accounts for the correlations between translational and rotational velocities. In the study of the HCS VDF, before this approach was considered standard (see Refs. [VSK14b; MS23]), original works of Goldshtein and Shapiro [GS95] and Aspelmeier *et al.* [AHZ01] already proposed Sonine expansions for translational and

rotational velocities around $\phi_M(\tilde{\Gamma})$, but correlations between \mathbf{c} and \mathbf{w} were not considered. Again, a truncation of Eq. (2.106a) for the first nontrivial cumulants, together with the proper consistent linearization of the collisional moments in terms of the nonneglected cumulants, has been the approach to study deviations from the Maxwellian in the thermal part of the VDF. First, in Ref. [VSK14b], a SA was performed to study the cumulants in systems of HS, namely, $a_{pq}^{(r)}$ with $p + q + 2r \leq 2$ were considered nonzero, thus improving a previous approach [SKS11] where $a_{00}^{(1)}$ was not considered in the truncation for HS. An extension of this study in terms of the translational and rotational degrees of freedom, valid for both HD and HS, is developed in Article 5 (Section 8.2). Moreover, as will be summarized in Article 5 (Section 8.2), the HVT of the marginal VDF at the HCS were analyzed.

As an important remark, the HCS for both IHS and IRHS is not always a stable state under *inhomogeneous* perturbations. The conditions under which this homogeneous state is unstable have been of interest of the granular gas community. These unstable states come in the form of clustering or vortices and are predicted by linear stability analysis of the HCS under inhomogeneous perturbations. The inhomogeneities have been theoretically studied using the CE method introduced in Section 2.7, from which the transport coefficients to describe the granular hydrodynamics are computed. Therefore, this linear stability analysis is performed on the balance equations of the granular gas taking advantage of the knowledge of the transport coefficients. These instabilities were first predicted for inelastic systems [GZ93; BRM98; BRC99; LH99; Gar05; Mit+11; Mit+12; Mit+14; FH17; Gar19] and, in the last decade, roughness came into play for HS [Mit+13; GSK18]. In Article 7 (Section 10.2) and Article 8 (Section 10.3), the analysis has been extended to HD and generalized the description to be dependent on the number of degrees of freedom, d_t and d_r .

2.5.3 Homogeneous states for driven granular gases

Granular gases in free evolution are very difficult to be studied experimentally. After just a few of collisions per particle, the system is almost frozen. Then, in order to study granular dynamics, usually grains are excited by some external energy injection. In addition, some granular suspensions can be found, where the granular fluid is usually assumed to be interacting with a certain background fluid in terms of Langevin-like models, in analogy to molecular gaseous models. Mathematically, this is translated into a Fokker–Planck-like term in the homogeneous BFPE. In those situations, the continuous decay of the temperature due to inelasticity or roughness mechanisms is counterbalanced by energy injection, either from an external source or from the interaction with a thermal bath. Therefore, the addition of these sources forces the granular gas to reach a steady state. The analysis in these systems takes advantage of quantities already computed from

the purely collisional part for the different collisional models. The steady homogeneous driven states must come from the stationary form of Eq. (2.56),

$$\frac{\partial}{\partial \Gamma} \cdot (f \mathbf{G}) = J[\Gamma|f, f], \quad (2.109)$$

in which we need to specify each collisional model and thermostat.

In the case where the system is in contact with a background fluid, this is usually modeled as a Langevin-like equation for the noncollisional part of the **BFPE** due to a coarse-grained consideration of the interaction. Furthermore, whereas a molecular fluid reaches a Maxwellian **VDF** at the temperature associated with the thermal bath, a granular gas will get a steady temperature lower than T_b , due to the loss of energy upon collisions. Moreover, the stationary **VDF** is expected to be non-Maxwellian, but much closer to it as compared with the **HCS** one. Those are the main conclusions obtained in the application of the **IHS** model with Langevin-like interactions for granular suspensions [**CVG12**; **CVG13**]. In this thesis, in Article 4 (**Section 7.2**) we extended these model to the more realistic case in which the drag coefficient is not constant but velocity-dependent, as described in **Subsection 2.4.1**.

On the other hand, the energy injection may come from an external source without any drag or thermal bath. The aim of this external driving is to compensate for the loss of energy upon collisions and then get a dynamic steady state. This driven system is generally described by a homogeneous stochastic force modeled as a white noise and characterized by a certain noise intensity. In that case, one expects that the final temperature will be proportional to a proper power of the noise intensity and a function of the coefficients of restitution involved in the selected model. Characterization of granular gases within the **IHS** model and driven by a stochastic force of this type has been of interest in the last few decades, were both the steady temperature and the stationary **VDF** have been studied from kinetic theory and computer simulations [**NE98**; **MS00**; **CVG12**]. The way of studying the non-Gaussianities of driven systems comes from the same type of mathematical tools as used in the **HCS**. The first nontrivial cumulants of the steady distribution are in general smaller than in the **HCS** case. Moreover, the **HVT** for the steady-state distribution is not exponential, but a stretched exponential, $\phi^{\text{wn}}(\mathbf{c}) \sim \exp(-\gamma_c^{\text{wn}} c^{3/2})$ for $c \gg 1$, that is, between Maxwellian and **HCS** behavior. Recently, in Ref. [**CZ22**] this 3/2-exponent for the tail of the distribution has been found to be a characteristic, not only for dilute driven systems, but also for dense ones. In fact, it has been observed that, not only the driving makes the **VDF** *more Gaussian*, but also the instabilities observed in the **HCS** vanish [**Noi+97**; **NBE98**; **Noi+99**; **VAZ11**; **GCV13b**; **GCV13a**] and the homogeneous driven states become stable under linear inhomogeneous perturbations.

The homogeneous states for rough **HS** subjected to a stochastic force have been studied

in Refs. [VS15; MS19a], where steady values of temperature, rotational-to-translational temperature ratio, and first cumulants were determined. In this thesis, we generalize the injection of energy using the ST introduced in Subsection 2.4.2. The stationary and transient homogeneous states are controlled in the ST by two parameters, which for convenience have been taken as $\{T^{\text{wn}}, \varepsilon\}$. More details about this work can be found in Article 6 (Section 9.2).

2.6 Nonequilibrium entropy and H -theorem

The term “entropy” comes etymologically from the Greek word “ἐντροπή” meaning “change”. This widely-used physical concept was introduced in the origins of classical equilibrium thermodynamics mainly by Rudolf Clausius to account for the increment of *non-usable energy* or irreversibility in his studies about the power of heat and Carnot’s theory [Cla50]. Then, the second law of thermodynamics was born and the entropy change of a system was defined as a state function whose change is given by $dS = T^{-1}\delta Q$, with δQ referring to the heat transferred as if the process were reversible. Moreover, a postulate was formulated: the entropy of the universe tends to a maximum, i.e., $\dot{S} \geq 0$, where the dot notation stands for the time derivative. Next, a statistical meaning for entropy was given by L. Boltzmann by defining entropy—in the microcanonical ensemble—as $S = \ln \bar{W}$, with \bar{W} the number of microstates compatible with a given macrostate of the system [Bol95]. Later, Boltzmann defined the entropy production in the context of its kinetic equation and demonstrated the existence of a quantity acting as entropy, proving the irreversibility toward the equilibrium state in this context [Bol72; Bol03]. This result was later called the H -theorem and it was under discussion by several scientists of the period, where some thought experiments were fundamental to understand Boltzmann kinetic theory and solve some formulated paradoxes. The implications of this H -theorem have been and still are immense.

From the H -theorem, the concept of nonequilibrium entropy started to arise. Entropy was firstly understood only from the point of view of equilibrium systems, without paying attention to nonequilibrium processes. Proper definitions have been under discussion in the community of nonequilibrium thermodynamics [JCL93] and statistical physics [BS92; MS96]. For example, in Ref. [Guj22] it is proposed that conceptually a nonequilibrium entropy is defined from an extension of the space of equilibrium states by considering nonequilibrium states as well. Then, the function associated with the nonequilibrium entropy is a state function fulfilling the second law of thermodynamics due to the internal evolution of the nonequilibrium variables, exclusively, in isolation. Of course, a nonequilibrium entropy must be connected to equilibrium entropy and it must reduce to the original concept in case of equilibrium. From the original Boltzmann kinetic theory for molecular gases, we will see in Subsection 2.6.1 that nonequilibrium

entropy is related with the already mentioned H -quantity, but this definition represents problems in the granular gas case, as introduced in [Subsection 2.6.2](#), and developed in [Chapter 6](#).

Finally, the physical interpretation of entropy and its statistical interpretation was the seed of the mathematical information theory, C. Shannon being its main forerunner from the definition of Shannon's entropy [[Sha48](#)], which was actually a mathematically founded formulation of the H functional of Boltzmann's theory, with the aim of *measuring missing information*. Information theory has been useful for several processes, not only physical ones, since its birth. Nowadays, there is a continuous feedback between physical and mathematical knowledge of entropy, which has been specially exploited by statistical physicists.

2.6.1 H -theorem for molecular gases of hard spheres

Evolving toward equilibrium is a particular case of dissipation of energy or increment of entropy. Boltzmann derived a transport equation with the purpose of describing how a system out of equilibrium evolves up to it [[Bol72](#); [Bol03](#); [Bru86a](#); [Bru86b](#)]. In this process, Boltzmann obtained a quantity which acts like an entropy, that is, it is compatible with the second law of thermodynamics, implying that the progress toward the equilibrium state is irreversible.

Let us work under the assumptions of [BE](#) for an isolated molecular system, i.e., $\mathbf{F}^{\text{ext}} = 0$. For the sake of simplicity, a monocomponent rarefied molecular gas of elastic hard spheres is considered, that is, the collisional model described in [Section 2.7](#) will be used, so that the [BE](#) reads

$$\frac{\partial}{\partial t} f + \mathbf{v} \cdot \nabla f = \sigma^{d_t-1} \int d\mathbf{v}_2 \int_+ d\widehat{\sigma} (\mathbf{v}_{12} \cdot \widehat{\sigma}) (f_1'' f_2'' - f_1 f_2). \quad (2.110)$$

The irreversibility hidden in the [BE](#) is more general than the described system, but it will be enough to capture its essence, which is contained in the Boltzmann's H -theorem [[Bol195](#); [GS03](#)]. The theorem states that the following functional H —originally called E by Boltzmann [[Bol72](#); [Bol03](#); [Bru86a](#); [Bru86b](#); [Cer98](#)—of the one-particle distribution function f ,

$$H(t) = \int d\mathbf{r} \int d\mathbf{v} f(\mathbf{r}, \mathbf{v}, t) \ln f(\mathbf{r}, \mathbf{v}, t), \quad (2.111)$$

is a Lyapunov functional for the [BE](#) or, equivalently,

$$S(t) = - [H(t) - H_{\text{eq}}] + S_{\text{eq}} \quad (2.112)$$

is the nonequilibrium entropy of the system, with H_{eq} the value of the H functional for the final equilibrium distribution and S_{eq} the value of the entropy at equilibrium. That

is, the theorem ensures that

$$\dot{S}(t) \geq 0 \quad \forall t \geq 0, \quad (2.113)$$

or, equivalently, $\dot{H}(t) \leq 0 \quad \forall t \geq 0$.

In order to prove the statement, we will define the hydrodynamic quantity $\psi(\mathbf{v}) = -\ln f(\mathbf{v})$, which, after its insertion into the BE defined in Eq. (2.110), and integrating over all possible velocities and positions, yields

$$\dot{S}(t) = \frac{1}{4} \int d\mathbf{r} \int d\mathbf{v}_1 \int d\mathbf{v}_2 \int_+ d\widehat{\sigma} (\mathbf{v}_{12} \cdot \widehat{\sigma}) (f_1'' f_2'' - f_1 f_2) \ln \frac{f_1'' f_2''}{f_1 f_2}, \quad (2.114)$$

as the entropy production. The integrand of the entropy production is positive definite because $f \geq 0$, $(\mathbf{v}_{12} \cdot \widehat{\sigma}) \geq 0$, and, for positive real-valued variables x, y , the quantity $(x - y) \ln(x/y) \geq 0$, where the identity is fulfilled if and only if $x = y$. Thus, the time variation of the entropy fulfills condition (2.113) and the equality $\dot{S} = 0$ is only reached if $\ln f$ is a collisional invariant. From Subsection 2.5.1 we know that the set of collisional invariants for the molecular case are $\{1, \mathbf{v}, v^2\}$, and it can be proved that all collisional invariants must be a linear combination of those three, i.e, $A_0 + \mathbf{A}_1 \cdot \mathbf{v} + A_2 v^2$ [GS03], where these coefficients A_0 , \mathbf{A}_1 and A_2 can be expressed in terms of the hydrodynamic fields associated with the collisional invariants, i.e,

$$n(\mathbf{r}, t) = \int d\mathbf{v} f(\mathbf{r}, \mathbf{v}; t), \quad (2.115)$$

being the number density,

$$\mathbf{u}(\mathbf{r}, t) = \frac{1}{n(\mathbf{r}, t)} \int d\mathbf{v} \mathbf{v} f(\mathbf{r}, \mathbf{v}; t), \quad (2.116)$$

the flow field, and $T(\mathbf{r}; t)$, the temperature as defined in Eq. (2.58). Then, it is straightforwardly deduced that the local version of the Maxwellian VDF in Eq. (2.59),

$$f_M(\mathbf{r}, \mathbf{v}; t) = n(\mathbf{r}, t) \left[\frac{m}{2\pi T(\mathbf{r}, t)} \right]^{d_t/2} \exp \left\{ -\frac{m [\mathbf{v} - \mathbf{u}(\mathbf{r}, t)]^2}{2T(\mathbf{r}, t)} \right\}, \quad (2.117)$$

is the local equilibrium solution.

After its formulation, Boltzmann got a lot of criticisms for his H -theorem. Some of them came from well-founded paradoxes, such as Loschmidt's, and Poincaré-Zermelo's ones [Cer98]. Loschmidt observed an apparently contradiction between the H -theorem and the reversibility of collisions in the molecular case, together with the time reversibility of Newton's equations of motion. Some authors proposed solutions based on the fluctuation theorem [Mur21] or the zero-probability measure of second-law-violating

initial conditions [HHP87]. Additionally, Poincaré and Zermelo pointed out that, from the theory formulated by the former, the so-called Poincaré’s recurrence theorem [Poi90] and later extended by Zermelo [Bru66], any mechanical system with a finite number of degrees of freedom will eventually pass arbitrarily close to its initial state. This, apparently, contradicted the statement of Boltzmann’s H -theorem. However, this paradox is solved in the thermodynamic limit and Boltzmann himself inferred a very large time—even larger than the estimated age of the Universe—of recurrence for a gas of 10^{18} particles in a box of 1 cm^3 [Bru66; Cer98]. Despite the residual existence of some retractors, the H -theorem is fundamental in the kinetic theory of gases and has been generalized to plenty of statistical-physical systems.

2.6.2 The problem of the H -theorem in granular gases

The original H -theorem applies for whatever molecular interaction, in which the transformation $(\Gamma''_1, \Gamma''_2) \rightarrow (\Gamma_1, \Gamma_2)$ is unitary, that is, the associated Jacobian $\mathfrak{J} = 1$, and its differential cross section stays invariant, i.e., $B(g''_{12}, \bar{\vartheta}''_1) = B(g_{12}, \bar{\vartheta}_1)$. However, those are not the conditions of either the IHS or the IRHS models, which include already an irreversibility factor in their definition of the collisional rules. In those cases, it is known that the described system is always out of equilibrium and does not reach in the long-time limit an equilibrium state but the HCS in the free-cooling homogeneous case. It is straightforward to show that the Maxwell–Boltzmann VDF is not a solution of the inelastic BE characterized by the collisional operator in Eq. (2.24) or the inelastic and rough version in Eq. (2.38).

Let us now change a few aspects of the paradigm. We consider grains instead of molecules in homogeneous states and replace the word “equilibrium” by HCS. Then, the relevant question is, is there any Lyapunov functional analogue to the H quantity that ensures the evolution of the granular gas toward the HCS? Whereas the arguments of Subsection 2.6.1 are very simple, there is still no answer—either positive or negative—to that question. However, García de Soria *et al.* proposed in Ref. [Gar+15] that the proper nonequilibrium entropy in the case of inelastic granular gases described by the IHS model would not be related with Shannon’s entropy, but with the *relative entropy* or *Kullback–Leibler divergence* (KLD) of the VDF with respect to the HCS. In general, the KLD of a normalized probability distribution, $f(x)$, with respect to a reference one, $f_{\text{ref}}(x)$, is defined by

$$\mathcal{D}_{\text{KL}}(f|f_{\text{ref}}) = \int dx f(x) \ln \frac{f(x)}{f_{\text{ref}}(x)}. \quad (2.118)$$

The arguments in Ref. [Gar+15] were developed at the level of kinetic Kac’s equation, proving the validity only for quasielastic systems. Moreover, they also tested the hypothesis with computer simulations. However, in the works in Article 2 (Section 6.2)

and Article 3 (Section 6.3) appearing in Chapter 6 of this thesis, we extend and focus the discussion at the level of the BE, studying the problem for HD and HS for all values of the coefficient of restitution. Furthermore, some arguments based on a toy model are made.

Moreover, in this thesis the KLD as a nonequilibrium entropy has been used also in Article 1 (Section 5.2) and Article 6 (Section 9.2) to study the ME in molecular and granular gases, respectively. Additionally, we exploit the KLD not only as a nonequilibrium entropy, but also as a functional quantifying how much a given probability distribution diverges from a reference one, taking advantage of its meaning from information theory. Concretely, it is useful in Article 5 (Section 8.2) to measure the goodness of the SA in the HCS for granular gases of inelastic and rough HD and HS, as well as in Article 8 (Section 10.3) to detect the appearance of clustering in EDMD simulations.

2.7 The Chapman–Enskog method

In order to solve the BE for molecular realistic nonequilibrium situations or for granular gaseous nonhomogeneous flows, perturbative methods⁵ become fundamental. For that, we need to define a proper perturbative parameter. In order to infer it, we need to investigate the order of magnitude of typical quantities which can control the evolution of f under different stages. To simplify the scheme, we will ignore external forces without any loss of generalization because the perturbation method will be essentially performed to the Boltzmann collisional operator. Let us denote by τ_0 a typical time scale, by L a typical length scale of the problem, and by v_{th} the typical velocity scale. Then, the orders of magnitude of terms conforming the BE of a monocomponent isolated system are

$$\frac{\partial f}{\partial t} = \mathcal{O}(\tau_0^{-1}f), \quad \mathbf{v} \cdot \nabla f = \mathcal{O}(v_{\text{th}}L^{-1}f), \quad J[\Gamma|f, f] = \mathcal{O}(n\sigma^{d_t-1}v_{\text{th}}f), \quad (2.119)$$

where we can relate $n\sigma^{d_t-1}$ to the mean free path for hard d_t -spheres,

$$\ell = \frac{1}{K_{d_t}n\sigma^{d_t-1}}. \quad (2.120)$$

In addition, one can define the mean free time as $\tau = \ell/v_{\text{th}}$. Then, two dimensionless numbers naturally arise. The first one, related to the length scales, is the Knudsen number, Kn, defined as

$$\text{Kn} = \frac{\ell}{L}. \quad (2.121)$$

⁵In homogeneous states we have also introduced the perturbative method coming from the Grad–Sonine expansions explained in Subsection 2.5.2 for granular gases, where the perturbative parameters were the cumulants of the VDF.

The second one is τ/τ_0 , which can be related to Kn via the Strouhal number Sr, common in the context of continuum theory, as [Cer88]

$$\frac{\tau}{\tau_0} = \text{Sr Kn}, \quad \text{Sr} = \frac{L}{\tau_0 v_{\text{th}}}. \quad (2.122)$$

As a first approximation, one can take $\text{Sr} \simeq 1$, so that time and length scales are comparable, and one could compare the orders of magnitude in both sides of the BE by means of Kn. Then, if $\text{Kn} \ll 1$, the mean free path is much smaller than the characteristic length of the system. We will work under this assumption.

2.7.1 A brief description of the Hilbert expansion

The first attempt to solve the BE through an expansion in terms of a bookkeeping parameter $\epsilon \sim \text{Kn}$, assumed to be small, was described by Hilbert [Cer88; Tar08], who proposed the following series expansion of the VDF

$$f = f^{(0)} + \epsilon f^{(1)} + \epsilon^2 f^{(2)} + \dots. \quad (2.123)$$

In addition, from dimensional and scale analysis, he introduced another ϵ into the left hand-side of the BE, that is,

$$\epsilon \left(\frac{\partial f}{\partial t} + \mathbf{v} \cdot \nabla f \right) = J[\Gamma|f, f]. \quad (2.124)$$

Thus, inserting Eq. (2.123) into the collisional operator, we can expand the latter as follows,

$$J = J^{(0)} + \epsilon J^{(1)} + \epsilon^2 J^{(2)} + \dots, \quad (2.125a)$$

$$J^{(0)} = J[\Gamma|f^{(0)}, f^{(0)}], \quad J^{(n)} = \sum_{k=0}^n J[\Gamma|f^{(k)}, f^{(n-k)}]. \quad (2.125b)$$

This scheme leads to the following recurrence problem by equating powers of ϵ ,

$$J^{(0)} = 0, \quad \frac{\partial f^{(n-1)}}{\partial t} + \mathbf{v} \cdot \nabla f^{(n-1)} = J^{(n)}, \quad (n \geq 1). \quad (2.126)$$

Note that, in the elastic case, the condition $J^{(0)} = 0$ ensures that f_0 is the Maxwellian VDF. However, this expansion faces some mathematical problems as described in [Cer88]. Some of these are solved by using the CE expansion.

2.7.2 Chapman–Enskog expansion

The CE expansion [CC70; Cer88] is based on a perturbative scheme, not only for the VDF (as Hilbert’s), but also on the derivative operators. This is related to the assumption that the spatio-temporal dependence of the one-particle VDF is through a functional dependence on the hydrodynamic fields of the theory. Let us briefly develop this, first for a monocomponent isolated molecular gas, and then extended to granular gases.

In nonhomogeneous flows of a molecular gas, one can define the *hydrodynamic* length scale, h , which is the typical distance along which the VDF changes notably. This hydrodynamic scale is assumed to be of the order of the typical length of the system, L . Apart from the lengths L , ℓ , and h , a fourth length scale is the particle diameter σ , which, in the context of the BE is $\sigma \ll \ell$. Therefore, one can define two other time scales associated with their respective length scales: the duration of a collision $\tau_c = \sigma/v_{\text{th}}$, which is assumed to be instantaneous in the BE framework, i.e., $\tau_c \ll \tau = \ell/v_{\text{th}}$, and the hydrodynamic time $\tau_h = h/v_{\text{th}}$. Then, under the assumption of small Kn, i.e., $\text{Kn} \ll 1$, we have $\tau \ll \tau_h$.

Immersed in this description, one can decompose the evolution of the VDF into two different evolution stages. First, for times of the order of τ , we have the *kinetic regime*, in which the VDF relaxes rapidly toward *local equilibrium*. The latter is achieved for times $\tau \ll t \ll \tau_h$, where, given a small region around a space point \mathbf{r} , the VDF is close to the Maxwellian one with the values of the proper collisional-invariant hydrodynamic fields at that point. Finally, for times of the order of τ_h , the VDF evolves slowly up to *global equilibrium* reached at $t \gg \tau_h$. This last evolution stage is dominated by hydrodynamics and is then called *hydrodynamic regime*.

This two-stage description for the VDF can be extended to granular gaseous flows and has been conveniently adapted to freely evolving inelastic and rough HD and HS in Article 7 (Section 10.2). A granular gas in free evolution does not reach equilibrium any more, either locally or globally. Then, the homogeneous base state for this method in the granular context is the HCS. That is, in the kinetic stage, the VDF is expected to reach the local version of the HCS VDF. In the hydrodynamic stage, the system then relaxes slowly toward the HCS. According to this picture, one should choose properly the hydrodynamic fields that take place in this description. Straightforwardly from the two collisional-invariant quantities $\{1, \mathbf{v}\}$, it is clear that the number density,

$$n(\mathbf{r}, t) = \int d\Gamma f(\Gamma, \mathbf{r}; t), \quad (2.127)$$

and the flow field,

$$\mathbf{u}(\mathbf{r}, t) = \frac{1}{n(\mathbf{r}, t)} \int d\Gamma \mathbf{v} f(\Gamma, \mathbf{r}; t), \quad (2.128)$$

are fundamental fields in the hydrodynamic description of the system⁶. On the other hand, the granular temperature $T(\mathbf{r}; t)$ field is not preserved. It is given by

$$T(\mathbf{r}; t) = \frac{1}{(d_t + d_r)n(\mathbf{r}, t)} \int d\Gamma (mV^2 + I\omega^2) f(\Gamma, \mathbf{r}; t), \quad (2.129)$$

with $\mathbf{V} = \mathbf{v} - \mathbf{u}$ the peculiar velocity⁷. With this definition of the temperature field, Eq. (2.129), we are extending the analysis for the most general case, the IRHS model, in which surface roughness is accounted for. In spite of the cooling, the mean granular temperature is assumed to be a good slow hydrodynamic quantity [DB11; Gar19] for the CE description⁸. Arguments in favor of this hypothesis come from kinetic model and computer simulation results for the IHS model [Bre+98; BC01; BD05; SA05; MSG05; MSG07; GSM07; Gar19]. This reasoning leads to propose the following functional dependence for the VDF in the hydrodynamic regime,

$$f(\Gamma, \mathbf{r}; t) = f[\Gamma, \mathbf{r} | n(t), \mathbf{u}(t), T(t)]. \quad (2.130)$$

That is, in order to know the value of the complete one-particle VDF f at a certain instant t , it is enough to know the value of the hydrodynamic fields n , \mathbf{u} and T at this same time. However, to know the VDF at the point \mathbf{r} , it is not enough to know the hydrodynamic fields at that point but also, at least, within a neighborhood of the point. This is equivalent to know the gradients of the hydrodynamic fields and, assuming they are small, perform an expansion in those gradients. Hence, not only a Hilbert-like expansion is considered for f [see Eq. (2.123)], but also

$$\mathcal{D}_t = \mathcal{D}_t^{(0)} + \epsilon \mathcal{D}_t^{(1)} + \epsilon^2 \mathcal{D}_t^{(2)} + \dots, \quad (2.131a)$$

$$\nabla^k \rightarrow \epsilon^k \nabla^k, \quad (2.131b)$$

where

$$\mathcal{D}_t \equiv \partial_t + \mathbf{u} \cdot \nabla \quad (2.132)$$

is the material time-derivative. The functional dependence of f on the hydrodynamic fields established in Eq. (2.130) induces the following important property,

$$\mathcal{D}_t f^{(k)} = \mathcal{D}_t n \frac{\partial f^{(k)}}{\partial n} + \mathcal{D}_t \mathbf{u} \cdot \frac{\partial f^{(k)}}{\partial \mathbf{u}} + \mathcal{D}_t \frac{\partial f^{(k)}}{\partial T}, \quad (2.133)$$

⁶Notice that Eqs. (2.127) and (2.128) extend Eqs. (2.115) and (2.116), respectively, to the cases where the angular velocities are relevant.

⁷Notice that in Eq. (2.85), being applicable to homogeneous and isotropic states, we took $\mathbf{u} = 0$ without loss of generality.

⁸Alternative expansions around $1 - \alpha$ for nearly elastic HD or HS based on the analysis of molecular gases and not considering the HCS as the base state were done in, e.g., Refs. [Lun+84; JR85; JM89; Jen98; GS95; SG98], but their results did not reproduce satisfactorily well the transport coefficient as reported later for CE method (see, for example, Ref. [Bre+98; Gar19]).

which must be applied to any other hydrodynamic quantity $\psi(\Gamma, \mathbf{r}; t)$,

$$\mathcal{D}_t \psi = \mathcal{D}_t n \frac{\partial \psi}{\partial n} + \mathcal{D}_t \mathbf{u} \cdot \frac{\partial \psi}{\partial \mathbf{u}} + \mathcal{D}_t T \frac{\partial \psi}{\partial T}. \quad (2.134)$$

Here, $\mathcal{D}_t n$, $\mathcal{D}_t \mathbf{u}$, and $\mathcal{D}_t T$ are given by their respective associated balance equations, where the most significant difference with respect to the molecular case is the appearance of the cooling rate due to the temperature dissipation (see [Appendix D](#)). Putting together the expansions in Eqs. (2.123), (2.125), (2.131), (2.133), and (2.134), a hierarchy of equations appear for the different orders of truncation. The zeroth-order equations are compatible with the local version of the [HCS](#), while the first order refers to the [NSF](#) transport equations. Comparing balance equations with the [NSF](#) and using phenomenological forms for the fluxes, one can compute the [NSF](#) transport coefficients. This methodology has been used in Article 7 ([Section 10.2](#)) to compute these coefficients for dilute granular gases of inelastic and rough [HD](#) and [HS](#).

Memory effects | 3



© 2023 Salvador Dalí, Gala-Salvador Dalí Foundation / Artists Rights Society (ARS), New York

Salvador Dalí, *La persistence de la mémoire* (1931). [The Museum of Modern Art, New York](#)

3.1 Introduction

For human beings, the ability to remember facts, experiences, dates, images, events and many concepts is quite an important fact that is certainly present during our lifetime. However, the memory softens over time, as Dalí's limp watches do. The passage of time wrecks havoc not only on our external appearance, but also on our mind. And this aging cannot be avoided either for humans or for everything in the universe. Nevertheless, we do not only store information in our minds to avoid its loss. Since the very early times of humanity, our ancestors transmitted their art and discoveries to future generations in many different ways: old paintings and constructions, lately writings, then photographs and movies, and nowadays, we also sophisticatedly save data in magnetic materials. We are indeed obsessed about saving information with the aim (sometimes) of progressing in knowledge. But this is not something just human. The universe is actually sharing

with us different events of its past, accessible by local and present observations, like recently discovered gravitational waves or the useful cosmic microwave background radiation. Even more, nature is full of these examples. Biologists can study the aging of a tree by just observing the different rings in a transverse section of its trunk. Moreover, the geological history of Earth can be studied by different patterns that are not yet erased. Then, we are surrounded by signs of our natural past, and their identification and interpretation are of huge importance to give an answer to the big question of where we come from. However, as occurs with human minds, the effect of time makes these elements and signs to deteriorate and, at the end, they will completely perish.

We can infer from this argumentation that memory is lost when balance is reached. Therefore, in words of Keim *et al.* in the review paper [Kei+19]: *Memory engages us in a study that targets phenomena related to transient or far-from-equilibrium behavior.* And this is the key of memory, at least, from a statistical physics point of view. A system at equilibrium satisfies a Markovian-process description, which by definition is memoryless, namely, it does not preserve—and then, erases—any sort of remembrance about its past. Roughly speaking, this is because the probability of the next state does only depend on the current state of the system. Then, when a system equilibrates, one cannot infer anything about its past or initial preparation. Hence, a memory effect is a phenomenon which emerges during a nonequilibrium stage of a physical system due to any reminiscence of its previous states. In physics, there is a huge number of memory effects found in different kind of systems. Maybe one of the most studied examples is the hysteresis loops in magnetic materials [RCW76; Ber98]¹. Other examples are echoes [Hah50; Kei+19], which are characterized by a time reversal path or return of some signal, in analogy to the popular echo of sound; associative memory coming from collective behavior in a complex system and used, for example, in network theory [Hop82]; some systems might exhibit memory about the initial conditions in their dynamics, like in air bubble formation [Sch+09]; among others.

Let us come back to the context of the thesis. Kinetic theory of gases, by definition, describes the evolution of a gaseous system toward equilibrium. Then, this stage of relaxation is a nonequilibrium process and memory effects might arise. Furthermore, inelastic (or rough) interactions make granular gases, by definition, to be out of equilibrium. On the other hand, whereas the classical example of freely evolving elastic hard d_t -spheres is too simple and *very Markovian* to show up any sort of phenomenon of this type, the action of thermostats might induce memory at the level of statistical correlations. In this thesis, we have studied two types of memory effects: the KE and the ME, which will be introduced in the next two sections.

¹Whereas it was discovered in magnetic systems, it is not restricted to them. See, for example, Refs. [Dia14; PSF03].

3.2 Kovacs effect

The KE is no more than an echo response due to the inner variables of a system, when it is tried to be suddenly equilibrated, attending just to the macrostate. Then, the system is observed first to recede from this reference state, and then relax toward it, guided by some of its macrostate variables.

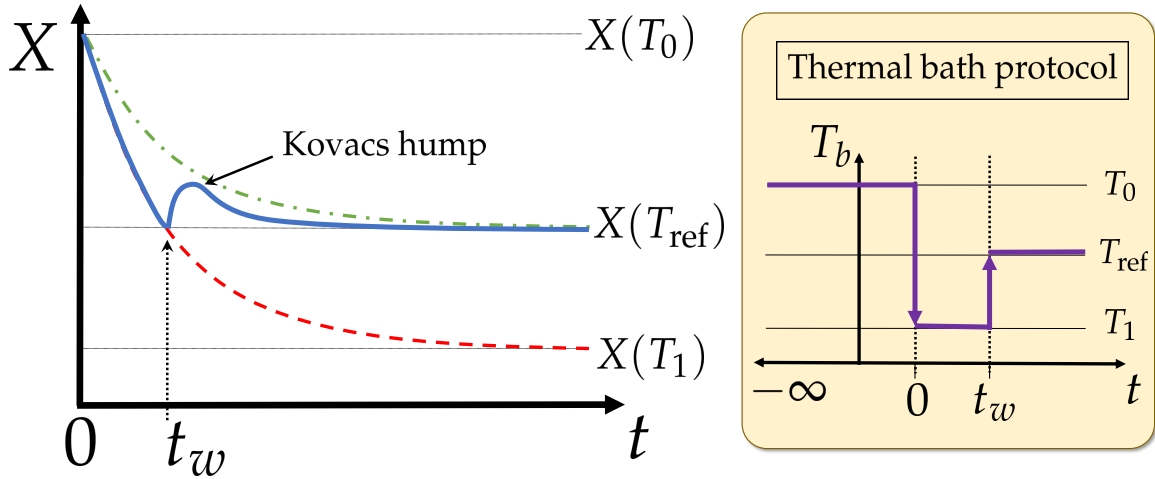


Figure 3.1: Sketch of a general Kovacs-like protocol on a macroscopic variable X , with $T_0 > T_{ref} > T_1$. On the left-hand side of the figure there is a graph of the evolution of X during the Kovacs-like experiment, complemented by a sketch of the protocol for the thermal bath temperature, T_b , on the right-hand side. The blue thick continuous curve corresponds to the real time evolution of the X macroscopic variable. The red dashed curve (– –) refers to the relaxation of X from T_0 to T_1 , while the green dashed-dotted (– · –) line depicts the direct evolution of X from T_0 to T_{ref} .

This effect is called after A. J. Kovacs due to his discovery of the phenomenon in amorphous polymers, as reported in Refs. [Kov63; KSF63]. Kovacs and collaborators first studied the relaxation of a sample of polyvinyl acetate in an isobaric cooling process from an initial temperature, T_0 , to a lower reference one, T_{ref} . Then, the system was let to equilibrate at a certain volume $V_{eq}(T_{ref})$, and this value was annotated. After this first measurement, the original experiment consisted in two main stages. First, the system at the same initial temperature was quenched to a lower temperature compared to the previous reference one, $T_0 > T_{ref} > T_1$, letting the system now to get the equilibrium volume, $V_{eq}(T_{ref})$, at a certain *waiting time*, t_w . At this time, they heated the sample up to T_{ref} immediately, from a sudden change in the thermal bath temperature which was in contact to the sample. The system is, at this instant, characterized by the temperature T_{ref} and the volume value at equilibrium, $V_{eq}(T_{ref})$. Despite the thermodynamic variables being at the equilibrium values, the volume of the sample was observed to first increase and, then, to evolve back to $V_{eq}(T_{ref})$ in an isothermal process. Attending to the evolution of the volume, a hump appeared at $t > t_w$. Kovacs *et al.* explained this anomaly in Ref. [Kov+79] by the action of inner variables of the system in a nonequilibrium process. Therefore, whereas its macrostate corresponded to the equilibrium variables, the system was not at the equilibrium state. The system response showed in fact a reminiscence of

its previous states.

In general, we can define a Kovacs-like protocol for a macroscopic variable X playing the role of the volume in the original experiment for a system in contact with a thermal bath. Again, a reference temperature is fixed, and the value of this variable at equilibrium or steady thermalized system is known, i.e., $X(T_{\text{ref}})$. Then, the system from an initial temperature T_0 is cooled down to T_1 , such that, $T_0 > T_{\text{ref}} > T_1$. At the waiting time t_w , the system is at $X(T_{\text{ref}})$ and, then, the bath temperature is suddenly changed to T_{ref} . If the system is at a nonequilibrium state, it is expected to exhibit a nonmonotonic behavior in terms of a Kovacs hump. A sketch of this protocol is represented in [Figure 3.1](#). This is the direct generalization of the Kovacs experiment. However, one could also consider a heating process rather than the original cooling one. A system exhibiting the [KE](#) is expected to be dynamically described by a system of coupled differential equations,

$$\begin{cases} \dot{X} = F_X(X, Y_1, Y_2, \dots), \\ \dot{Y}_1 = F_{Y_1}(X, Y_1, Y_2, \dots), \\ \dot{Y}_2 = F_{Y_2}(X, Y_1, Y_2, \dots), \\ \vdots \end{cases} \quad (3.1)$$

with $\{Y_n\}$ being the set of inner variables acting on the evolution of X , and F_X and $\{F_{Y_n}\}$ being the corresponding functions for the rates of change of the macrostate guiding variable and inner variables, respectively. Furthermore, it is common to choose X as a nonequilibrium temperature instead of the volume (see, for example, Refs. [[PB10](#); [PT14](#); [PSP21](#); [Mom+21](#)]).

This [KE](#) has been observed in different systems, many of them characterized by slow glassy dynamics [[Hod94](#); [BB02](#); [AS04](#); [CLL04](#); [MS04](#); [ALN06](#); [Mor+20](#); [Lul+21](#)], studied in the context of linear response theory [[PB10](#); [RP14](#)], in active matter [[KSI17](#)], observed theoretically in driven granular gases of hard [[PT14](#)] and viscoelastic particles [[Mom+21](#)], and also in molecular gases under nonlinear drag [[PSP21](#)], among other systems. In the latter three works, the guiding quantity is the temperature—either granular or molecular—and its evolution equation exhibits a coupling with higher moments of the [VDF](#) playing the role of inner variables of the system. In the case of inelastic granular gases, the granular temperature evolution depends explicitly on the whole [VDF](#) throughout the cooling rate expression, i.e., $Y_{n-1} = a_n$ with $n \geq 2$. On the other hand, in the work of molecular gases, the velocity dependence of the drag coefficient (see [Subsection 2.4.1](#)) implies an explicit coupling of the temperature evolution with the fourth cumulant, $Y_1 = a_2$, of the [VDF](#). However, in the latter example, the evolution of a_2 of course depends explicitly on higher-order cumulants.

Furthermore, we study the Kovacs humps mechanism in an inelastic granular gas described by the [IHS](#) model and interacting with a thermal bath with a nonlinear

drag introduced in Article 4 (Section 7.2). As we will see, the granular temperature dependence is more complex due to the combination of the latter two couplings.

3.3 Mpemba effect

The ME is usually formulated as a counterintuitive phenomenon in which, given two samples (generally of a fluid) at different temperatures, the initially hotter one may arrive more quickly to equilibrium than the other colder sample. We will see throughout this section that more interpretations of the ME are possible.

The effect was originally studied in water. In the 1960s, it was observed that hot water may freeze down faster than initially colder samples, as reported by the person that gave it the name to the ME, Erasto B. Mpemba. At that time, E. B. Mpemba (1950 – 2020) was a Tanzanian high-school student, who was helped by D. Osborne (1932 – 2014), publishing the finding in Refs. [MO69; Osb79]. It can be said that the discovery of the effect by Mpemba was a stroke of serendipity. In 1963, Mpemba had to make ice cream with his schoolmates. The method they applied consisted in boiling a mixture of milk and sugar and, after a first cooling at room temperature, the mixture was put inside a refrigerator. However, one day, due to the high demand of the refrigerator usage, Mpemba decided to enter directly the boiling milk inside the refrigerator—skipping the second step of the recipe—at the same time a schoolmate entered his tempered sample. An hour later, Mpemba was astonished to observe that his sample had already frozen down, whereas his schoolmate’s had not. Mpemba asked his physics teacher about that, but the teacher did not contemplate that Mpemba’s observation could be possible, and argued that Mpemba was certainly confused. Mpemba first believed his teacher, but then, ice-cream sellers agreed with him. Young Erasto insisted in his findings, whereas his thoughts were disregarded at the high school until Dr. Denis Osborne appeared. Osborne visited the school to give a talk about “Physics and national development”, and during the question turn Mpemba asked about the effect he observed. Dr. Osborne, instead of ignoring him, was curious about this observation for which he had not an answer, and asked a technician to reproduce it. The results were in favor of Mpemba’s findings and they were later reported in Ref. [MO69], where experimental results of the time a sample of water took to start freezing against the initial temperature were presented. It is reproduced in Figure 3.2. It is curious that, despite his discovery, Mpemba never studied physics but devoted himself to the preservation of the wildlife in a Tanzanian natural reserve.

One can say that the ME is an example of Stigler’s law of eponymy [Sti80], since Mpemba was not actually the first one in observing the effect, but classical authors like Aristotle [Ros31], F. Bacon [Bac20], or R. Descartes [Des37] commented it before.

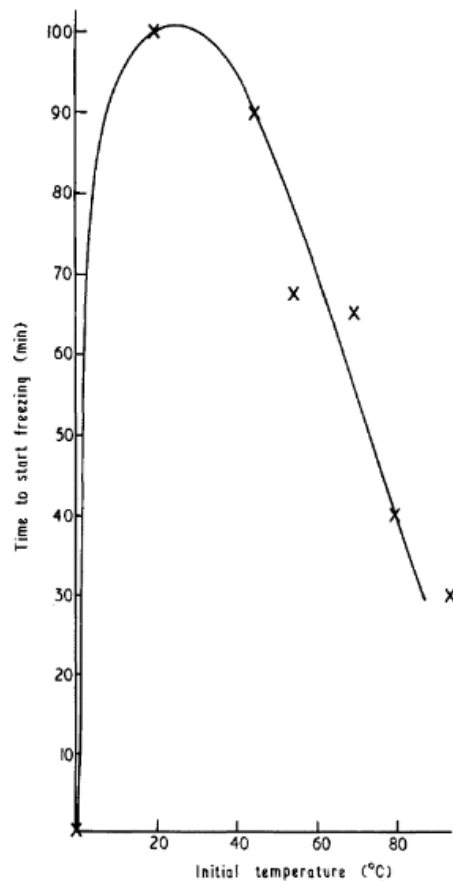


Figure 3.2: E. B. Mpemba and D. G. Osborne, *Cool?*, *Phys. Educ.* 4 pp. 172-175 (1969), DOI: [10.1088/0031-9120/4/3/312](https://doi.org/10.1088/0031-9120/4/3/312). ©IOP Publishing. Reproduced with permission. All rights reserved. Graph of the fitting curve for several experimental points reproducing the time a sample of liquid water started to freeze up in minutes, with respect to the initial temperature of the cooling process. The results come from the original and very first experiments of Mpemba and Osborne.

Moreover, the ME was common in the popular belief of cold countries, whereas scientifically it was hidden under Newton's law of cooling [New01] which, by definition, denies the existence of this phenomenon. Although the ME in water is not a very recent issue in science, it is still unsolved [Elk18]. In fact, the scientific community is divided into supporters, who observe the effect experimentally and propose different explanations [Kel69; Fir71; Dee71; Fra74; Gal74; Wal77; Fre79; Kum80; Han81; WOB88; Aue95; Kni96; Mac96; Jen06; ERS08; Kat09; VM10; Bro11; VM12; BT12; Zha+14; VK15; Sun15; JG15; IC16; GLH19; BKC21; Tan+23] and detractors, who are skeptical and either consider that the experimental methods used were flawed or give negative results [Bal06; BL16; BH20; ES21].

Whereas the discussion in water is still alive, the ME went beyond this substance and has been studied in a vast variety of complex physical systems, like carbon nanotube resonators [Gre+11], clathrate hydrates [Ahn+16], Ising models [Gon+21; TYR23; VD21], spin glasses [Bai+19], non-Markovian mean-field systems [YH20; YH22], active systems [SL22], quantum systems [CLL21; CTH23], ideal gases [Žuk+22], nonequilibrium

systems with Markovian dynamics [LR17; Kli+19; CKB21; BGM21]², models based on Landau’s theory of phase transition [HR22], and colloidal experiments [KB20; KCB22], among others. In 2017, Lasanta *et al.* described the ME in granular gases in Ref. [Las+17] for homogeneous states, both in free evolution and driven by a stochastic thermostat, with the binary collisions being described by the IHS model. Afterwards, it has been observed in other collisional models, like the IRHS one [Tor+19], Maxwell models [Bis+20], or viscoelastic particles [Mom+21]; also in anisotropically driven granular gases [BPR21; BPR22], inertial suspensions [THS21; Tak21]—where the ME has been described also by the viscosity of the system as the guiding macrostate quantity [THS21]—, or binary mixtures [GG21]. Furthermore, Santos and Prados described the conditions for the observation of the ME in a molecular gas in contact with a background fluid [SP20], where the interaction between the gas and the background fluid was described by the coarse-grained model explained in Subsection 2.4.1. Later, in Ref. [PSP21], a glassy behavior and its implication on the ME in the same system was detailed.

Therefore, the ME is observed in several nonequilibrium processes. However, the nature of this effect is not unique and, unlike the KE, it is not described by a given *a priori* protocol. There are mainly two different ways to look for ME in a complex system. The first one is due to an anomalous relaxation of the samples, and the second one consists in considering that the effect is immersed in a phase transition, like occurs in models based on Landau’s theory. In the terminology of water studies, the first methodology corresponds to an anomalous cooling, whereas the second one refers to differences between both samples in the freezing process. In this thesis, following the granular gas methodologies, we considered the anomalous relaxation picture. Then, we could categorize the ME as a memory effect due to a dependence of the dynamics on the initial conditions or initial preparation.

Furthermore, it is worth mentioning that the effect has been originally studied in terms of the temperature associated with the physical system. However, in other situations the definition of temperature is meaningless, and then the relaxation of its probability distribution through a nonequilibrium entropy functional is used as the guiding quantity. We will refer from now on as *thermal ME* (TME) or *entropic ME* (EME) if the description is the former or the latter, respectively. Interestingly, these two descriptions can be equivalent or not, depending on the studied system. On the one hand, the TME states that the temperature of the hotter system arrives earlier to its steady-state value as compared with an initially colder one, according to the definition given at the very beginning of this section. On the other hand, the EME corresponds to the effect associated with the possibility that a sample starting from an initial state

²At the beginning of this chapter it was said that to observe memory effects we cannot have Markovian processes. Whereas the dynamics are Markovian, in these models the systems are initially very far from equilibrium and suffer a first nonequilibrium relaxation in usually very asymmetric potential landscapes, playing the role of the necessary *non-Markovianity*.

further from equilibrium (or steadiness), as compared to other sample of the same system, evolves earlier toward it, as measured by some entropy functional. The latter quantity would play the role of a nonequilibrium entropy, typically with a negative sign to study a monotonic decreasing quantity, instead of an increasing one. Intuitively, if the relaxation times of the higher moments of the distribution are comparable to, or greater than, the typical time corresponding to the hotter sample overpassing the relaxation of the colder sample, then the entropic description may yield results different from the thermal one. By contrast, if the relaxation of those higher moments is much more rapid than the temperature relaxation (so that, the probability distribution is fully described by the instantaneous temperature), both descriptions are then expected to be equivalent. Thus, one must be cautious in the choice of the framework, in order to interpret properly the results.

Another point to highlight is how to predict theoretically the **ME**. Let us focus on the anomalous cooling context and kinetic-theory based systems, where one looks for a dynamical description like Eq. (3.1), with X being either the temperature in a **TME** or the nonequilibrium entropy in an **EME** description. In the context of the **TME**, we will work firstly under the assumption that the temperature curve does not overshoot the steady value, i.e., $T(t) - T^{\text{st}} \geq 0 \forall t \geq t_0$, $T^{\text{st}} = \lim_{t \rightarrow \infty} T(t)$ being the steady-state temperature, and t_0 the initial time. Within this analysis, the appearance of the **TME** is used to be linked with a single crossing of the two temperature curves, usually at short times. Then, a linear analysis of the relaxation with respect to the initial conditions applies, see Refs. [Las+17; SP20; Bis+20; GG21; BPR21; Mom+21; BPR22]. In these works, the authors can predict analytically the crossing time, i.e., the moment when both curves intersect. Nevertheless, the effect is not generally just restricted to short times, as observed in Ref. [Tor+19]. Therefore, in general, the **TME** must be detected if an odd number of crossing times appear, something that can be extrapolated to the **EME**. If there is no crossing, or there are an even number of them, the initially hotter (or further from steadiness) sample will in the end take longer to reach the final state than the initially colder sample.

Although it may seem that those are the only possibilities for observing **ME**, this is not the case for **TME**. The reason resides in the initial assumption $T(t) - T^{\text{st}} \geq 0$ for all finite $t \geq t_0$. If this condition is not fulfilled, even appearing a crossing (or an odd number of them), the initially hotter sample could overshoot the value T^{st} in such a way that it will ultimately arrive the last one to the final steady state. Let us see the problem the other way around. One can face the case of two samples initially at different temperature, whose associated evolution curves do not intersect, but the initially colder system overshoots the T^{st} value and finally reaches the asymptotic value later than the other sample. This is an example of **TME** without any crossing point, and we called it *overshoot ME* (**OME**) in Ref. [MSP22], which recalls the supercooling

mechanism proposed for water [Aue95]. As a matter of fact, this cannot occur in the entropic interpretation because of a positive semidefinite *thermal distance* for the difference $T - T^{\text{st}}$ would constrain us to work just on the number-of-crossing detection framework, capturing the OME to this classical interpretation.

The last but not least remark is that the ME experiment can also be generalized to a heating process in lieu of the cooling one. This is usually referred to as *inverse ME (IME)* and it is only meaningful in the context of TME. If a system admits IME, then one could find an initially colder sample that warms up more quickly than a hotter one. Again, a thermal distance for $T - T^{\text{st}}$ already considers these cases with the same detection mechanism based on the crossing points. On the contrary, the TME appearing in the classical cooling experiment is sometimes called *direct ME (DME)*. See Table 3.1 for a visual characterization of all the explained phenomenology.

In Article 1 (Section 5.2), we study the ME phenomenology in the model proposed in Ref. [SP20] of a molecular gas under nonlinear drag. Differences between TME and EME are described, as well as the introduction of the OME. Moreover, in Article 4 (Section 7.2), the TME is studied for a granular gas also under nonlinear drag. In the kinetic-theory based systems, it is difficult to create a protocol to generate the proper initial states of the dynamics needed for the emergence of the effect. The initialization protocol is something fundamental if the effect is wanted to be replicated in real experiments. Takada *et al.* proposed in Ref. [THS21] a protocol based on sheared states. In Article 6 (Section 9.2), we develop a protocol to generate the proper initial conditions, but in homogeneous states for a granular gas based on the IRHS model with the ST.

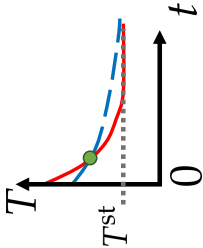
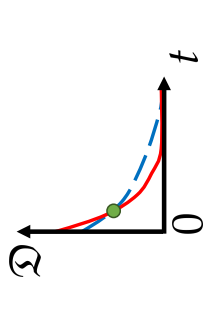
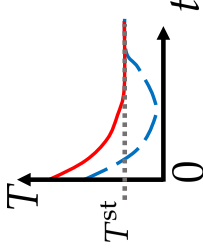
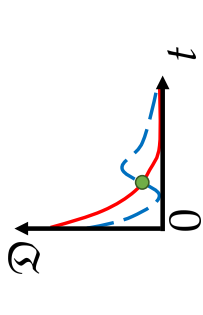
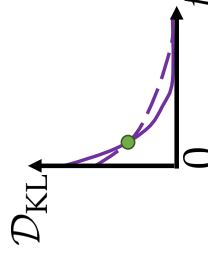
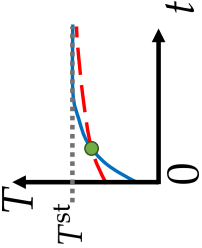
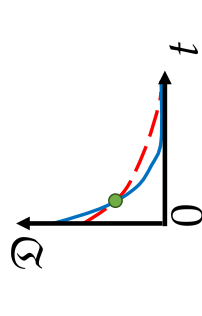
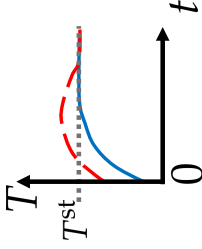
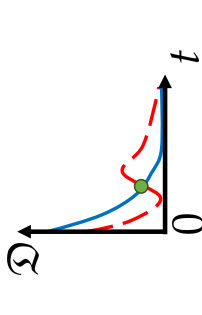
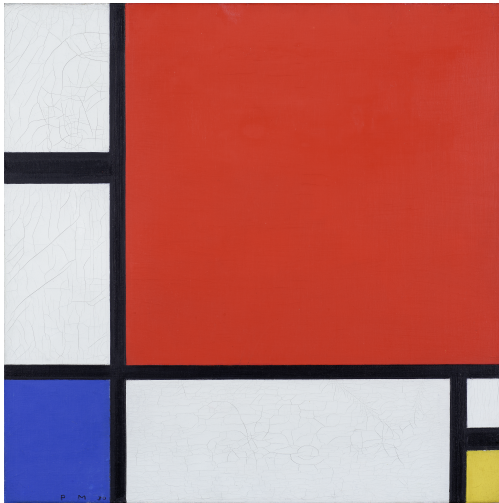
		TME			EME	
		standard TME		OME		EME
		Temperature	Thermal distance	Temperature	Thermal distance	Entropy
DME						
IME						

Table 3.1: Classification of sketches for the different scenarios that can be found in a dynamical study of the ME. The figure is divided into the TME and the EME interpretations, the latter being guided by the quantity \mathcal{D}_{KL} [according to its use in Article 1 (Section 5.2)]. The TME is described in the temperature picture, where the effect is studied by means of the nonequilibrium temperature T , and the thermal-distance picture, where \mathfrak{D} is the chosen quantity [according to the notation of the quantity used in Article 6 (Section 9.2), defined such that $\mathfrak{D} = 0$ if and only if $T = T^{\text{st}}$]. Both descriptions are applied to the DME and the IME, in their standard form or via the OME. The red curves refer to the initially hotter system, whereas the blue ones to the initially colder one. In addition, thick continuous lines correspond to the system initially further from the steady state, whereas the dashed ($- -$) ones represent the initially closest. Notice that in the EME there is neither red nor blue lines because temperature could be meaningless. The green points appearing in the different intersections are crossing points. Finally, notice that the different scenarios are simplified to a single crossing, which is equivalent to find an odd number of them in the EME or in the thermal-distance picture of the TME.



Piet Mondrian, *Komposition mit Rot, Blau und Gelb* (1930). [Kunsthaus Zürich](#).

4.1 Introduction

In order to check the validity of the theoretical results derived in this thesis, it is important to compare them with computer simulations as a first *quasi-experimental* approach. In the granular matter world, different computational schemes have been developed. In this thesis, only methods applicable to low-density states have been considered, with [DSMC](#) and [EDMD](#) methods being the most common ones. Whereas the former is stochastic, the latter is deterministic, and both give us different useful pieces of information to compare with the theoretical predictions and approaches. Although molecular dynamics ([MD](#)) schemes are older than [DSMC](#), the latter is firstly introduced here due to its *simplicity*.

4.2 Direct Simulation Monte Carlo method

The **DSMC** method consists in a probabilistic computational method to simulate a physical rarefied gaseous system. This method was developed sixty years ago by G. A. Bird, who firstly proposed it in Ref. [Bir63] as an alternative to **MD** simulations, which tend to be computationally harder and slower at low densities. Despite its lack of attention during the first few years, it became later a fundamental simulation method in the rarefied gas dynamics community. The original algorithms [Bir94; Bir13] have been extended and continuously improved to an ample variety of systems, being not only important in molecular gases but also in dilute granular gases [PS05], atmospherical systems [AG00], aerospace problems [SC13], astrophysical flows [Wei14], etc.

The method uses Monte Carlo techniques to determine the time-dependent **VDF** from *quasi-particles* or *simulators*, each one being a *probability quantum* in the phase space, and representing a great number of real particles. Formally speaking, each simulator is a representative state of a stochastic variable. From now on, we will abuse the language by terming particles to these simulators. The statistical base of the method is closely related to the **BE**, even though it is formally considered as a numerical resolution of it [Wag92; Ste19]. That is, the particle positions and velocities are random variables following a stochastic process based on the **BE**, where the Monte Carlo-like scheme is immersed in the collisional part of the process using an acceptance-rejection Metropolis-like criterion [Met+53] adapted to a proper scattering process [Bir94; Bir13]. Unless otherwise indicated, only hard d_t -sphere interactions are considered.

Basically, the method assumes that the evolution of the **VDF** can be separated into a collisional and free-streaming part, as considered in the deduction of the **BE** [see Eq. (2.2)]. As every spatio-temporal numerical finite-difference method, time and space are discretized. Space is usually divided into cells of typical length smaller than the mean free path. However, in this thesis only homogeneous schemes for **DSMC** have been considered and, therefore, positions play no role anymore in the method. Moreover, in homogeneous flows, the free streaming part is only characterized by the action of the external forces. In this thesis, external actions on the system have only being considered through thermostats, as explained in Section 2.4.

Let us assume a **DSMC** scheme for a homogeneous gas of hard d_t -spheres simulated by N particles with velocities $\{\Gamma_i(t)\}_{i=1}^N$ at a certain instant t . The discrete **VDF** for the numerical scheme is given by,

$$n^{-1}f(\Gamma; t) = \frac{1}{N} \sum_{i=1}^N \delta(\Gamma_i(t) - \Gamma). \quad (4.1)$$

At the very beginning, it is necessary to initialize the set of velocities in accordance

with a certain probability distribution. According to Eq. (4.1), the time evolution of the discrete VDF is driven through the change of the velocities of the particles. After this first initialization process, velocities are updated from t to $t + \Delta t$, where the time step Δt is much smaller than the mean free time. This is done by splitting the algorithm into the two different stages mentioned before.

In the collisional stage, the method approximates the change of the VDF due to an estimation of collisional encounters. First, a number $\lfloor \frac{1}{2}N\bar{\omega}_{\max}\Delta t \rfloor$ of pairs [Bir94; MS00; PS05; SM09; Bir13] are randomly and equiprobably chosen, with $\bar{\omega}_{\max}$ being an upper bound estimate for the one-particle collision rate, such that the ignored decimals in the before rounding off are saved for the next iterative step. Given a chosen pair ij , a collision is accepted with probability $\bar{\omega}_{ij}/\bar{\omega}_{\max}$, where $\bar{\omega}_{ij} = \Omega_{d_t} n \sigma^{d_t-1} |\mathbf{v}_{ij} \cdot \hat{\sigma}_{ij}|$ is the estimator of the collision rate for the specific pair, $\mathbf{v}_{ij} \equiv \mathbf{v}_i - \mathbf{v}_j$ being the relative velocity of the particles involved in the chosen pair and $\hat{\sigma}_{ij}$ being a random vector drawn from a uniform probability distribution in the unit d_t -sphere. If the collision is accepted for such a pair, the velocities of the particles are updated according to the collisional rules corresponding to the chosen model, $\Gamma_{i,j}(t + \Delta t) = \mathfrak{B}_{ij, \hat{\sigma}_{ij}} \Gamma_{i,j}(t)$.

Whereas $\bar{\omega}_{\max}$ is usually chosen as a constant, this is not the case for freely evolving granular gases [PS05; SM09], where this quantity must be updated due to the continuous cooling of the system. This can be done in two ways: first, since $\bar{\omega}_{\max}$ is usually related to a maximum velocity proportional to $v_{\text{th}}(t)$, one can rescale $\bar{\omega}_{\max}$ according to the instantaneous value of $v_{\text{th}}(t)$, which is related to the temperature; another way is to rescale all velocities periodically¹ to a fixed value of the mean temperature, saving the multiplicative factors to reconstruct the real instantaneous temperatures of the system. Notice that the latter method does not affect the evolution of the *rescaled* VDF, but only the temperature quantities. In order to be more accurate, not only in the freely evolving case, but in every considered system, $\bar{\omega}_{\max}$ should be related to the real maximum velocity of the system. However, this consideration has a computational cost in the algorithm.

Afterwards, in the free-streaming stage, if there is an external force, velocities are updated according to its action. In this thesis, only thermostats have been considered and, therefore, all the velocities at $t + \Delta t$ are modified according to the associated Langevin-like stochastic differential equation (SDE). A general DSMC algorithm for our homogeneous (granular) gas can be read in Algorithm 1.

¹This method used to work better than the first one. This occurs because, if we simply correct $\bar{\omega}_{\max}$, one might get very small values in large runs due to the continuous cooling, not only in the value of the estimated frequency, but, more importantly, in all velocity vectors. Then, numerical errors due to the computational management of float numbers likely appear.

Algorithm 1: General algorithm for [DSMC](#).

- 1: Initialize the N velocity vectors $\{\Gamma_i\}_{i=1}^N$. Set to zero the number of collisions `number_colls` and the cumulative decimals of sampled collisions `dcolls`. Set $t \leftarrow 0$.
 - 2: If the predefined condition for the velocity rescaling is satisfied, rescale the velocities.
 - 3: Get ω_{\max} .
 - 4: Estimate the number of colliding particles: $\text{ncolls} \leftarrow \lfloor \frac{1}{2}N\omega_{\max}\Delta t \rfloor + \text{dcolls}$. Save the decimals not considered in the before estimation:
 $\text{dcolls} \leftarrow \frac{1}{2}N\omega_{\max}\Delta t - \text{ncolls}$.
 - 5: Get the sample of colliding pairs randomly: $i1 \leftarrow \text{int_rand}(N, \text{ncolls})$,
 $i2 \leftarrow (i + \text{int_rand}(N - 1, \text{ncolls}) + 1) \% N$. With $\text{int_rand}(N, \text{ncolls})$ get a vector of `ncolls` components whose elements are integer random number up to N .
 - 6: Set $k \leftarrow 0$.
 - 7: **for** $0 \leq k < \text{ncolls}$ **do**:
 - 8: Set $\{i, j\} \leftarrow \{i1[k], i2[k]\}$.
 - 9: Get the unit intercenter vector $\hat{\sigma}_{ij}$ from a uniform random distribution.
 - 10: Apply the acceptance-rejection algorithm. If the collision is accepted, update the velocities of the colliding pair according to the binary collisional rules:
 $\Gamma_{i,j} \leftarrow \mathfrak{B}_{ij, \hat{\sigma}_{ij}} \Gamma_{i,j}$.
 - 11: **end for**
 - 12: Increase the number of collisions by the number of accepted collisions `icolls`:
`number_colls` \leftarrow `icolls`.
 - 13: If a thermostat is considered, update the velocities by solving numerically the associated Langevin-like [SDE](#) between t and $t + \Delta t$.
 - 14: Update $t \leftarrow t + \Delta t$.
 - 15: If the final condition is reached, this is the end of the program. Otherwise, go back to step 2.
-

4.3 Event Driven Molecular Dynamics

Whereas the [DSMC](#) method is a stochastic algorithm based on the assumptions underlying the [BE](#), the [MD](#) technique solves numerically the equations describing the dynamics of the constituents of a physical system.

If we have a classical, many-body mechanical system, [MD](#) solves Newton's equations of motion for the particles in order to elaborate a computational experiment similar to a real one. In fact, the idea behind a [MD](#) algorithm is very close to the idea of an experiment: we first prepare the system (sample) and we measure numerically certain quantities during the process. The measurements are subdued to statistical errors

that are avoided as much as possible by replicating its realization several times. The observables computed from a MD simulation must be functions of the positions and momenta of the particles.

Newton's equations of motion are numerically solved in this technique, which depends on the interaction potential of the system constituents. This is usually named as *force-based MD* algorithms. For integrating the equation of motion, it is necessary to discretize time in units of a time step, Δt . The system advances in multiples of this time step and the integration is reduced to a discretization algorithm for solving differential equations. Additionally to this scheme, we need to define the proper boundary conditions according to the experiment we want to computationally reproduce.

However, in this thesis only hard interactions are considered, such that the potential is singular and, therefore, no interparticle force is actually considered in this case. Instead, hard particles interact via collisions, so that, if no collision occurs, the particles evolve in uniform rectilinear motion in the absence of external forces or accelerate in case they are moving under a certain force field. Let us assume that we use a *time-driven* molecular dynamics (TDMD) algorithm for simulating N hard d_t -spheres under the absence of external forces. Then, after each time step Δt , we must update positions of the hard particles according to their constant velocity and rectilinear motion and check whether there is any overlap. In case there are overlaps, we need to go back to the time when the collision occurs and update the velocities according to the collision rules and, then, continue with the simulation. The idea of this kind of algorithm is simple and is an extension of a typical force-based MD simulation. Nevertheless, this approach has mainly two disadvantages. First, we need to define a very small—compared with the mean free time— Δt in order not to miss any collision. The other one is the need of performing a $\mathcal{O}(N^2)$ checking of the overlaps for each time step, which is computationally very inefficient, and even more if Δt is restricted to be small.

Hence, a way of solving those drawbacks is to impose the progress of the system by just considering the times where an event occurs, this events commonly being the particle-particle collisions and particle-boundary interactions. This type of algorithms is called *event-driven* molecular dynamics (EDMD), and its challenge is to efficiently list and update the events characterizing the system improving the complexity associated with an ordinary time-driven algorithm. The very first EDMD algorithms were proposed in the pioneering works of Alder and Wainwright [AW57; AW59]. In this thesis, in Article 2 (Section 6.2) and Article 3 (Section 6.3), the EDMD simulations were performed by using the software DynamO [BSL11]. However, in the other works described in Article 1 (Section 5.2), Article 4 (Section 7.2), Article 5 (Section 8.2), Article 6 (Section 9.2), and Article 8 (Section 10.3), a hand-made EDMD Python-based program created from scratch was used [Meg23]. This latter program is sequential, since it was proved to be fast enough acting on the considered problems, but parallel implementations could

speed up the algorithms [ML04]. Depending on the problem, a vast number methods to improve and accelerate the EDMD has been proposed, see for example Refs. [Iso99; Iso16; Iso17; IK15; KE19]. A brief description of a general EDMD program and specific algorithms used in our own are introduced in what follows.

4.3.1 A general EDMD algorithm

In principle, an EDMD algorithm is based on the steps presented in Algorithm 2. Here, it is assumed the absence of external forces.²

Algorithm 2: Basic EDMD loop.

- 1: Initialize the particle positions $\{\mathbf{r}_i\}_{i=1}^N$ and velocities $\{\mathbf{\Gamma}_i\}_{i=1}^N$.
 - 2: Initialize the ordered event list by determining their occurring times.
 - 3: Extract the earliest valid event, occurring at time t^* .
 - 4: Update the positions of the particles according to a free streaming, i.e., $\mathbf{r}_k \leftarrow \mathbf{r}_k + \mathbf{v}_k (t^* - t), \forall k \in \{1, \dots, N\}$.
 - 5: If the earliest event is a particle-particle collision between particles i and j , update the velocities according to the binary collisional rules, $\mathbf{\Gamma}_{i,j} \leftarrow \mathfrak{B}_{ij, \hat{\sigma}_{ij}} \mathbf{\Gamma}_{i,j}$. If not, in case of a particle-boundary interaction, the position and velocity of the involved particle must change according to the boundary conditions.
 - 6: Compute the earliest future events for the particles involved in the previous event and update the list.
 - 7: Update the system time $t \leftarrow t^*$.
 - 8: Check the end-of-program condition. If it is not fulfilled, return to step 3.
-

4.3.2 Initialization

The first part of an EDMD algorithm corresponds to initialize the positions and velocities of the particles. As in the DSMC algorithm we need to determine the initial velocities of the particles according to a certain VDF, managing the discrete VDF as defined in Eq. (4.1).

With respect to the positions, they are described as points in a discrete finite volume (box) of the d_t -dimensional space. In analogy to the velocities, they must be initially organized according to a certain initial distribution. The initial arrangement of the particles depends on the problem to be studied, from ordered states to completely randomized distributions. In the original algorithm used in this thesis, the implemented way of initializing has been hybrid. We divided the simulated box into identical square or cubic cells in two and three dimensional setups, respectively. The idea is to choose a

²If there is any deterministic external force field affecting the particles dynamics, particle positions should be updated according to the equations of motion.

fixed number of particles per cell and to assign random positions inside a cell avoiding overlaps. If the number of particles per cell is *a priori* established, the number of cells is constrained to the number density of the problem, $n\sigma^{d_t}$. The definition of these cells is very useful to speed up the event detection and scheduling, as will be explained later. In [Algorithm 3](#), the algorithm for this hybrid arrangement is presented in a rectangular box, fixing one particle per cell for a monodisperse system of hard disks of diameter σ .

Algorithm 3: Function for the hybrid arrangement of particle positions in rectangular cells of volume $L_x^{\text{cell}} \times L_y^{\text{cell}}$, in a box with $N_x^{\text{cell}} \times N_y^{\text{cell}}$ cells, for one particle per cell.

- 1: **procedure** CELLARRANGEMENT2D($r_x, r_y, \sigma, N_x^{\text{cell}}, N_y^{\text{cell}}, L_x^{\text{cell}}, L_y^{\text{cell}}$) \triangleright ($r_x[i], r_y[i]$) is the position of the i^{th} particle.
 - 2: **for** $0 \leq k < N_x^{\text{cell}}$ **do**:
 - 3: **for** $0 \leq \ell < N_y^{\text{cell}}$ **do**:
 - 4: $r_x[\ell + kN_y^{\text{cell}}] \leftarrow \text{randf}(kL_x^{\text{cell}} + \sigma/2, (k+1)L_x^{\text{cell}} - \sigma/2)$ \triangleright $\text{randf}(a, b)$ gives a uniform random number in (a, b) .
 - 5: $r_y[\ell + kN_y^{\text{cell}}] \leftarrow \text{randf}(\ell L_y^{\text{cell}} + \sigma/2, (\ell+1)L_y^{\text{cell}} - \sigma/2)$
 - 6: **end for**
 - 7: **end for**
 - 8: **return** r_x, r_y
 - 9: **end procedure**
-

4.3.3 Event detection

The event detection refers to the part of the [EDMD](#) program that predicts new events. In fact, in the steps 2 and 6 of [Algorithm 2](#), new events are detected and their associated time is computed. There are, essentially, two types of events, as introduced before: a pairwise particle collision and a boundary interaction.

First, to predict a particle-particle collision, we need to solve, for each particle i , the equation $r_{ij}(t^*) = \sigma_{ij} \forall j \neq i$, with $r_{ij} \equiv |\mathbf{r}_i - \mathbf{r}_j|$ and $\sigma_{ij} \equiv (\sigma_i + \sigma_j)/2$ being the mean diameter. Therefore, given an instant t , the collision condition for a pair of particles with positions $\{\mathbf{r}_i, \mathbf{r}_j\}$ and translational velocities $\{\mathbf{v}_i, \mathbf{v}_j\}$ can be rewritten, in the absence of an external deterministic force field, as

$$|\mathbf{r}_i(t) + \mathbf{v}_i(t)(t^* - t) - \mathbf{r}_j(t) - \mathbf{v}_j(t)(t^* - t)| = \sigma_{ij}. \quad (4.2)$$

After squaring, this condition can be reduced to the following second degree equation,

$$v_{ij}^2(t^* - t)^2 + 2\mathbf{r}_{ij} \cdot \mathbf{v}_{ij}(t^* - t) + r_{ij}^2 - \sigma_{ij}^2 = 0. \quad (4.3)$$

A collision will actually occur if $\mathbf{r}_{ij} \cdot \mathbf{v}_{ij} < 0$ (particles are approaching) and $(\mathbf{r}_{ij} \cdot \mathbf{v}_{ij})^2 -$

$v_{ij}^2 (r_{ij}^2 - \sigma_{ij}^2) > 0$ (physical solution). Assuming there is no overlap between particles, the solution that accounts for a future collision between particles i and j is

$$t^* = t - \frac{\mathbf{r}_{ij} \cdot \mathbf{v}_{ij}}{v_{ij}^2} - \sqrt{\left(\frac{\mathbf{r}_{ij} \cdot \mathbf{v}_{ij}}{v_{ij}^2}\right)^2 - \frac{r_{ij}^2 - \sigma_{ij}^2}{v_{ij}^2}}. \quad (4.4)$$

However, it is discussed in Ref. [PS05] that the latter equation could lead to some numerical errors, which are mostly solved if the implemented (equivalent) equation is the following one,

$$t^* = t + (r_{ij}^2 - \sigma_{ij}^2) \left[-\mathbf{v}_{ij} \cdot \mathbf{r}_{ij} + \sqrt{(\mathbf{v}_{ij} \cdot \mathbf{r}_{ij})^2 - v_{ij}^2 (r_{ij}^2 - \sigma_{ij}^2)} \right]^{-1}. \quad (4.5)$$

Moreover, to avoid forbidden states, the algorithm introduced in Ref. [Ban+14] is executed for particle-particle collision detection. Given the state of particles i and j at time t , this algorithm works as written in Algorithm 4. Notice that in the step 1 of this algorithm we are asking for the necessary condition for a collision to occur, in step 2 we are detecting an overlap, and in step 3 we are checking for the other condition to ensure the collision.

Algorithm 4: Stable algorithm for predicting pairwise particle collisions proposed in Ref. [Ban+14].

- 1: If $\mathbf{r}_{ij} \cdot \mathbf{v}_{ij} \geq 0$ then return ∞ .
 - 2: If $r_{ij}^2 - \sigma_{ij}^2 \leq 0$ (overlapping particles) then return t .
 - 3: If $(\mathbf{r}_{ij} \cdot \mathbf{v}_{ij})^2 - v_{ij}^2 (r_{ij}^2 - \sigma_{ij}^2) \leq 0$ then return ∞ .
 - 4: Else, return t^* as expressed in Eq. (4.5).
-

To detect a boundary event, we need to compute the time the particle takes to arrive to a certain border. Let us imagine a three-dimensional problem, such that the position of particle i is given by the vector $\mathbf{r}_i = (r_x, r_y, r_z)$ inside of the rectangular box $[0, L_x] \times [0, L_y] \times [0, L_z]$, and with translational velocity $\mathbf{v}_i = (v_x, v_y, v_z)$. To compute the time to the closest boundary event, we need to determine first each individual time to arrive to a boundary. For example, the Algorithm 5 summarizes how to predict boundary events in the direction of the x axis.

Algorithm 5: Prediction of a boundary event time at the x axis.

- 1: If $v_x > 0$, then $t_x \leftarrow (L_x - r_x - \sigma_i/2)/v_x$.
 - 2: If $v_x < 0$, then $t_x \leftarrow (-r_x + \sigma_i/2)/v_x$.
 - 3: Else (if $v_x = 0$), then $t_x \leftarrow \infty$.
-

Whereas the procedure for prediction of boundary events has a linear complexity $\mathcal{O}(N)$, the detection of pairwise collisions increases quadratically with respect to the number of particles, $\mathcal{O}(N^2)$. In order to speed up the algorithm for event detection,

we took advantage of the cell division of the simulation box already introduced in [Subsection 4.3.2](#). Then, given a particle in a certain cell, we will only look for events in the closest neighbor cells. Therefore, fixing a particle, their possible collisions are searched inside the proper cell and within its next neighboring ones. Moreover, the transfer of a particle from one cell to another is considered now as a boundary event, whereas boundary conditions are only applied to those cells in contact with the borders of the simulation box. In order to look for efficiency, it is essential to choose an appropriate number of particles per cell. A suitable value is the result of a competence between the number of transferring cell events per particle and the frequency of collision, both being highly dependent on the number density of the system. A very high number of particles per cell might cause an excessively large number of collisions within a cell, approaching the original quadratic complexity. On the other hand, a very small number of particles per cell determines a transfer-dominating algorithm, thus delaying the advance of the program. According to the discussion in Ref. [\[ML04\]](#), a low-density system, which is the case considered throughout this thesis, has an optimal number of particles per cell of order unit, reaching the unity equality in two-dimensional systems. Therefore, in the developed [EDMD](#) program, we have fixed a rate of one particle per cell, which is imposed since initialization (see [Algorithm 3](#)), as depicted in [Fig. 4.1](#). We assumed squared or cubic boxes in the systems studied in this thesis, i.e., $L = L_i \forall i \in \{1, \dots, d_t\}$. However, other more complex arrangements could be considered for specific problems with a certain geometry.

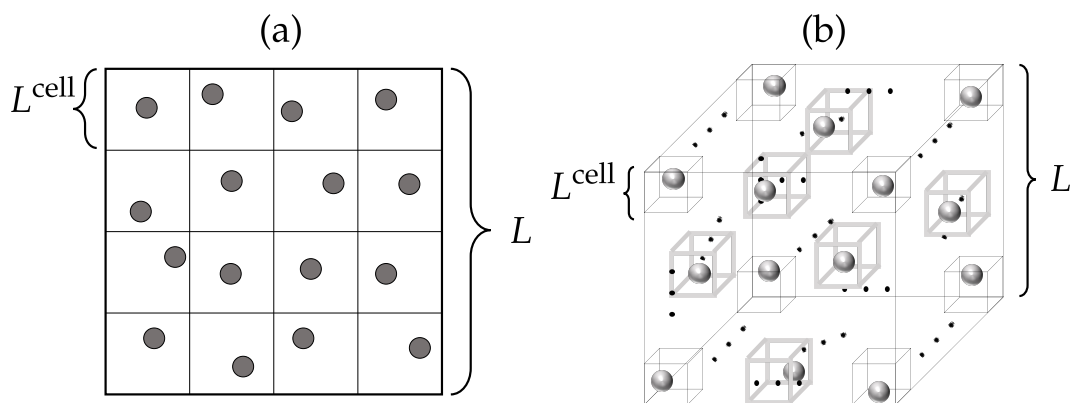


Figure 4.1: Sketch of initialization cells for (a) squared and (b) cubic, with one particle per cell arrangements. In the three-dimensional cubic case not all cells are displayed to ensure a proper visualization.

4.3.4 Event scheduling

One of the challenges of the [EDMD](#) since its beginning was to choose a proper scheduling algorithm, not only for initializing but also for sorting the events.

The initialization of the event list was already discussed in [Subsection 4.3.3](#), where a *cell-list* method, widely accepted in literature [\[ML04; Rap04; BSL11\]](#), was explained.

It improves the initialization of the event list from being quadratically complex in the number of particles to be linear. This method is proved to be very efficient in the case of monodisperse hard d_t -spheres, in contrast to other algorithms as *nearest-neighbor-list* (NNL) methods proposed in case of high polydispersity and nonspherical particles [DTS05; Mic10]. In these NNL methods, instead of considering cells, each particle identifies its closest neighbors in a certain range of action to look for events there. Nevertheless, since polydisperse or nonspherical particles are not cases explored in this thesis, these NNL methods have not been implemented.

The way of sorting the events and maintaining the event list updated represents the core of the computational cost in an EDMD program. An appropriate manner would consist in using a proper data structure for the event list which would allow for an efficient sorting and updating. In the pioneering works of Rapaport [Rap80], binary-tree structures were proposed and, later, complete binary trees found to be optimal [MC95]. Therefore, in our Python-based program, this complete binary tree has been implemented by using a heap queue (priority queue) [SW11], specifically from the Python library `heapq` [Pyt23].

In fact, we proceed by defining a heap queue for each particle and the closest event feeds the main event heap queue. These sublists of events are not saved during all the program since they are only defined during the initialization or updating of the main event priority queue. When the closest future event is extracted from the main list, it is first checked to be valid, that is, we do examine if the particles involved have not suffered any other event since its prediction and if that time is actually referring to a future (and not past) event that could be duplicated. For that, we identify the state of a particle, not only by their positions and velocities, but also by their current cell, the times it has suffered a collision, or the total times it has changed from one box cell to another, as proposed in Ref. [ML04]. Hence, the event array is made of the time of occurrence, the particles taking part in it, its type, and the particle states at its prediction, in order to guarantee a proper event validation. If the event results to be invalid, the event list is updated by searching the closest future events for the particles involved. In case the event extracted is concluded to be valid, the particles are upgraded to their new states and the main event list is again updated by inserting new future closest events of the particles involved. The routine for the event processing during the main loop, taking place after initialization and during the final condition is not reached, is summarized in [Algorithm 6](#).

Algorithm 6: Event processing loop in an [EDMD](#) algorithm.

- 1: Extract the next event from the priority queue.
 - 2: Check whether the event is valid or not. If it is valid, upgrade the time to the event time and the particles states according to the event type.
 - 3: Predict new future closest events for the particles involved in the extracted event.
 - 4: Update the event heap queue by scheduling these new events.
 - 5: Check the stop condition. If it is not fulfilled return to 1.
-

4.3.5 Last remarks

The [EDMD](#) main algorithm is almost finished after the description of the last processes. However, some problems might appear during the running of the program associated with numerical errors. First of all, although we have considered only low-density systems, the probability of an overlap increases for moderately ones. The algorithm introduced in Ref. [[Ban+14](#)] is very efficient to avoid those problems, but in case they were present, it is important to perform periodically two processes: to save the state of the system and to check the presence of overlaps. Whereas the former is memory consuming, the latter, as already discussed, is time consuming. In case an overlap is detected and persistently present, we can turn back the simulation to a previous state again to correct the numerical error. The overlap checking was one of the reasons of choosing [EDMD](#) over [TDMD](#) algorithms. Nevertheless, their detection in [EDMD](#) is not necessary to be as recurrent as it must be in [TDMD](#).

Moreover, the granular gaseous case is quite special if we compare with the [EHS](#) model for molecular gases. In freely evolving granular gaseous systems, their velocities decrease continuously according to the energy loss in the collisional process and reflected in Haff's law of cooling. Therefore, computationally speaking, the managing of these small quantities can lead to strong numerical errors and a deceleration of the program running until an almost stopping of the system. This issue is solved by a periodical rescaling of the particle velocities, as proposed for example in Ref. [[Lut01](#); [FR13](#)], and already considered in the [DSMC](#) algorithm. This rescaling allows for the long time study of a granular gas.

Finally, it is worth mentioning the possibility for a homogeneous granular gas to spontaneously face cluster or vortex instabilities, as already introduced in [Subsection 2.5.2](#). The rescaling permits the long-time observation of this phenomenon. Moreover, an important and exclusive issue in a granular gas [MD](#) simulation is the inelastic collapse associated with clustering formation, in which a chain of stucked-together particles enters in an infinite entangled state that makes the [EDMD](#) algorithm to fall down in an infinite number of collisional events in finite time, thus stopping the progress of the program [[TP19](#)]. This granular phenomenon was first studied in one-dimensional

problems and subsequently in two- and three-dimensional setups for the IHS model. If we want to study large-scale simulations with clustering instability, we must avoid the program to stop at this inelastic collapse. This issue is solved in an EDMD algorithm with some techniques proposed in the literature [MY94; PS05], like the introduction of the TC model [LM98] or a slight modification of the collisional rule [DB97; Gro97]. We chose the first method to be implemented in our program.

4.3.6 EDMD with Langevin-like dynamics

Up to now, we just only considered gaseous systems whose particle evolution is only submitted to a collisional process. However, particles can be subjected to other interactions due to their presence in a certain medium or the application of external force fields. In the latter case, e.g., considering the action of gravity, the modification of the classical program resides only in the free evolution equation of motion, where the associated acceleration due to the action of the force must be properly integrated. However, a nontrivial situation comes in the case of the action of stochastic forces, which transform the deterministic equations of motion into Langevin-type equations for particle velocities. These associated SDE produce erratic Brownian-like motions, i.e., the Langevin-type differential equation for velocity induces as well a SDE for the particle positions. This becomes a problem for the event prediction process because of the random trajectories of the particles. Hence, the implementation of stochastic forces, no matter if they come from possibly external sources or due to the action of a background fluid, is not an easy task.

We address this issue using the *Approximate Green Function* (AGF) algorithm proposed in Refs. [SVM07; Sca12]. To expose the derivation of the crucial equations of the problem, we will start from the original case of the LE with constant friction coefficient. That is, the time evolution of the translational velocities is described by Eq. (2.39). Moreover, taking into account the time evolution of the particle positions, we have the following system of SDE,

$$\frac{d\mathbf{v}_i(t)}{dt} = -\xi_0 \mathbf{v}_i(t) + v_b \xi_0^{1/2} \bar{\boldsymbol{\eta}}_i(t), \quad (4.6a)$$

$$\frac{d\mathbf{r}_i(t)}{dt} = \mathbf{v}_i(t), \quad \forall i \in \{1, \dots, N\}, \quad (4.6b)$$

where we used the FDT, with v_b being the thermal velocity associated with the bath temperature, and each $\bar{\boldsymbol{\eta}}_i$ being a Gaussian random vector representing the effect of a zero-mean and delta-correlated white noise with unit variance,

$$\langle \bar{\boldsymbol{\eta}}_i(t) \rangle = \mathbf{0}, \quad \langle \bar{\boldsymbol{\eta}}_i(t) \bar{\boldsymbol{\eta}}_j(t') \rangle = \mathbb{1}_{d_i} \delta_{ij} \delta(t - t'). \quad (4.7)$$

Let us integrate the system of SDE from t to $t + \Delta t$. Hence [Sca12; AT17],

$$\mathbf{v}_i(t + \Delta t) = \mathbf{v}_i(t)e^{-\xi_0\Delta t} + v_b \xi_0^{1/2} \int_0^{\Delta t} dt' e^{\xi_0(t'-\Delta t)} \bar{\boldsymbol{\eta}}_i(t'), \quad (4.8a)$$

$$\mathbf{r}_i(t + \Delta t) = \mathbf{r}_i(t) + \xi_0^{-1} \mathbf{v}_i(t) \left(1 - e^{-\xi_0\Delta t}\right) + v_b \xi_0^{1/2} \int_0^{\Delta t} dt' \int_0^{t'} dt'' e^{\xi_0(t''-t')} \bar{\boldsymbol{\eta}}_i(t''). \quad (4.8b)$$

In these equations, two random variables appear,

$$\boldsymbol{\mathcal{W}}_i = \int_0^{\Delta t} dt' e^{\xi_0(t'-\Delta t)} \bar{\boldsymbol{\eta}}_i(t'), \quad \bar{\boldsymbol{\mathcal{W}}}_i = \int_0^{\Delta t} dt' \int_0^{t'} dt'' e^{\xi_0(t''-t')} \bar{\boldsymbol{\eta}}_i(t''), \quad (4.9)$$

which are Gaussian random variables with the following properties

$$\boldsymbol{\mathcal{W}} = \sqrt{\langle \mathcal{W}^2 \rangle} \boldsymbol{\mathcal{Y}}, \quad \bar{\boldsymbol{\mathcal{W}}} = \frac{\langle \boldsymbol{\mathcal{W}} \cdot \bar{\boldsymbol{\mathcal{W}}} \rangle}{\sqrt{\langle \mathcal{W}^2 \rangle}} \boldsymbol{\mathcal{Y}} + \sqrt{\langle \bar{\mathcal{W}}^2 \rangle - \frac{\langle \boldsymbol{\mathcal{W}} \cdot \bar{\boldsymbol{\mathcal{W}}} \rangle^2}{\langle \mathcal{W}^2 \rangle}} \bar{\boldsymbol{\mathcal{Y}}}, \quad (4.10)$$

where $\boldsymbol{\mathcal{Y}}, \bar{\boldsymbol{\mathcal{Y}}}$ are drawn from Gaussian probability distributions, i.e.,

$$P(\boldsymbol{\mathcal{Y}}) = (2\pi)^{-d_t/2} e^{-\boldsymbol{\mathcal{Y}}^2/2}, \quad P(\bar{\boldsymbol{\mathcal{Y}}}) = (2\pi)^{-d_t/2} e^{-\bar{\boldsymbol{\mathcal{Y}}}^2/2}, \quad (4.11)$$

and the expected quantities in Eq. (4.10) in the case of the LE read

$$\langle \mathcal{W}^2 \rangle = \frac{1}{2} \xi_0^{-1} \left(1 - e^{-2\xi_0\Delta t}\right), \quad (4.12a)$$

$$\langle \boldsymbol{\mathcal{W}} \cdot \bar{\boldsymbol{\mathcal{W}}} \rangle = \frac{1}{2} \xi_0^{-2} \left(1 - e^{-\xi_0\Delta t}\right)^2, \quad (4.12b)$$

$$\langle \bar{\mathcal{W}}^2 \rangle = \frac{1}{2} \xi_0^{-3} \left(2\xi_0\Delta t - 3 - e^{-2\xi_0\Delta t} + 4e^{-\xi_0\Delta t}\right). \quad (4.12c)$$

Thus, the solutions of the equations of motion during the free-streaming stage at $t + \Delta t$ in Eq. (4.8a)

$$\mathbf{v}_i(t + \Delta t) = \mathbf{v}_i(t)e^{-\xi_0\Delta t} + \frac{v_b}{\sqrt{2}} \sqrt{1 - e^{-2\xi_0\Delta t}} \boldsymbol{\mathcal{Y}}_i, \quad (4.13a)$$

$$\begin{aligned} \mathbf{r}_i(t + \Delta t) = & \mathbf{r}_i(t) + \xi_0^{-1} \mathbf{v}_i(t) \left(1 - e^{-\xi_0\Delta t}\right) + \frac{v_b}{\sqrt{2}} \xi_0^{-1} \left(1 - e^{-\xi_0\Delta t}\right)^{3/2} \left(1 + e^{-\xi_0\Delta t}\right)^{-1/2} \boldsymbol{\mathcal{Y}}_i \\ & + v_b \xi_0^{-1} \sqrt{\xi_0\Delta t - 1 + e^{-2\xi_0\Delta t}} \left(\frac{3 - e^{-\xi_0\Delta t}}{1 + e^{-\xi_0\Delta t}}\right) \bar{\boldsymbol{\mathcal{Y}}}_i, \quad \forall i \in \{1, \dots, N\}. \end{aligned} \quad (4.13b)$$

Equations (4.13) solve the dynamics between t and $t + \Delta t$ in free evolution due to the action of the thermal bath inducing the LE. From them, the AGF algorithm splits up the dynamics in two stages. In the first one, starting from the system at t , $\{\mathbf{r}_i(t), \mathbf{v}_i(t)\}$,

and according to Eqs. (4.13), one computes the *putative* positions and velocities at $t + \Delta t$, $\{\mathbf{r}_i^{\text{put}}, \mathbf{v}_i^{\text{put}}\}$. Thus, one can define *fictive* velocities as $\mathbf{v}_i^{\text{fic}} = [\mathbf{r}_i^{\text{put}} - \mathbf{r}_i(t)]/\Delta t$. In the second stage, we run a classical **EDMD** algorithm for events taking place only in the time interval $(t, t + \Delta t]$. In this latter stage, including the event-list prediction, putative positions and fictive velocities are used as the proper variables, i.e., the states are described by $\{\mathbf{r}_i^{\text{put}}, \mathbf{v}_i^{\text{fic}}\}$. All valid events within this interval are performed. Then, the states of the particles are updated: the states at $t + \Delta t$ for particles that did not suffer any collision in the interval are given by $\{\mathbf{r}_i^{\text{put}}, \mathbf{v}_i^{\text{put}}\}$; otherwise, their states will be updated according to a two-step numerical scheme, where positions are modified using the resulting fictive velocities after the collision rules are applied. The resulting velocities are coming from the application of the collision rules to the putative velocities using the position unit vectors computed in the event prediction. That is, in the case of a collision between particles i and j at $t_{\text{coll}} \in (t, t + \Delta t]$, the latter steps follow,

$$\mathbf{r}_i(t + \Delta t) \approx \mathbf{r}_i(t) + \mathbf{v}_i^{\text{fic}} \Delta t_{\text{coll}} + \mathbf{v}_i^{\text{fic}'} (\Delta t - \Delta t_{\text{coll}}), \quad (4.14a)$$

$$\mathbf{v}_i(t + \Delta t) \approx \mathfrak{B}_{\hat{\sigma}_{ij}^{\text{fic}}}^{ij, \text{put}} \mathbf{v}_i^{\text{put}}, \quad (4.14b)$$

where $\Delta t_{\text{coll}} = t_{\text{coll}} - t$, $\hat{\sigma}_{ij}^{\text{fic}} = [\mathbf{r}_{ij}(t) + \mathbf{v}_{ij}^{\text{fic}} \Delta t_{\text{coll}}] / |\mathbf{r}_{ij}(t) + \mathbf{v}_{ij}^{\text{fic}} \Delta t_{\text{coll}}|$ is a fictive unit intercenter vector at the time of collision, $\mathbf{v}_i^{\text{fic}'} = \mathfrak{B}_{\hat{\sigma}_{ij}^{\text{fic}}}^{ij, \text{fic}} \mathbf{v}_i^{\text{fic}}$ is the postcollisional fictive velocity, and the operators $\mathfrak{B}_{ij, \hat{\sigma}}^{\text{fic}}$ and $\mathfrak{B}_{ij, \hat{\sigma}}^{\text{put}}$ refer to the postcollisional operators for a pair ij with intercenter unit vector $\hat{\sigma}$ and using the fictive and putative velocities in the collisional rules, respectively.

To ensure the convergence of the method, the time step must be chosen such that $v_b \sqrt{\xi_0^{-1} \Delta t} \ll \sigma$, that is, the mean free displacement in Δt is much smaller than the diameter, which is the typical length of the interaction, as explained in Refs. [SVM07; Sca12].

Whereas this is the original algorithm for a gas of hard spheres with Langevin dynamics, it can be generalized to an arbitrary bath interaction. Let us assume that the particle velocities follow a Langevin-like **SDE**, so that their solutions at $t + \Delta t$ can be expressed as functions of their states at t (explicit scheme), the noise parameters (noise intensity, constants related to the drag coefficient, etc.) $\bar{\gamma}$, the time-step Δt , and the corresponding random variables driven from a Gaussian distribution in Eq. (4.11),

$$\Gamma_i(t + \Delta t) \approx \mathfrak{F}_1[\Gamma_i(t), \bar{\gamma}, \Delta t, \mathcal{Y}_i], \quad (4.15a)$$

$$\mathbf{r}_i(t + \Delta t) \approx \mathfrak{F}_2[\mathbf{r}_i(t), \mathbf{v}_i(t), \bar{\gamma}, \Delta t, \mathcal{Y}_i, \bar{\mathcal{W}}_i]. \quad (4.15b)$$

Notice that we are considering the usual and simple case that the rotational degrees of freedom, while possibly present, are not explicitly coupled to the positions $\mathbf{r}_i(t)$.

In case of nonanalytic solutions like Eqs. (4.14), the numerically alternative used is the Euler-Maruyama method for SDE, which can be improved by using Runge-Kutta techniques [KP92]. The concrete schemes for the Langevin dynamics with nonlinear drag (see Subsection 2.4.1) and the ST (see Subsection 2.4.2) are explicitly derived in Appendix C. Hence, for an arbitrary stochastic thermostat or bath interaction, the algorithm for a collision event is given by Algorithm 7 and the whole AGF algorithm loop can be read in Algorithm 8.

Algorithm 7: Collisional routine in an AGF algorithm.

- 1: Get the collisional time interval Δt_{coll} , the total one Δt , the fictive velocities of the colliding particles $\Gamma_{i,j}^{\text{fic}}$ and their positions at current time t , $\mathbf{r}_{i,j}$.
 - 2: Compute the intercenter vector at contact time

$$\widehat{\sigma}_{ij}^{\text{fic}} \leftarrow (\mathbf{r}_{ij} + \mathbf{v}_{ij}^{\text{fic}} \Delta t_{\text{coll}}) / |\mathbf{r}_{ij} + \mathbf{v}_{ij}^{\text{fic}} \Delta t_{\text{coll}}|.$$
 - 3: Determine the postcollisional fictive velocities according to the collisional rules, i.e.,

$$\Gamma_{i,j}^{\text{fic}'} \leftarrow \mathfrak{B}_{ij, \widehat{\sigma}_{ij}^{\text{fic}}}^{\text{fic}} \Gamma_{i,j}^{\text{fic}}.$$
 - 4: Calculate the final positions for the colliding particles according to Eqs. (4.14):

$$\mathbf{r}_{i,j} \leftarrow \mathbf{r}_{i,j} + \mathbf{v}_{i,j}^{\text{fic}} \Delta t_{\text{coll}} + \mathbf{v}_{i,j}^{\text{fic}'} (\Delta t - \Delta t_{\text{coll}}),$$
 taking into account boundary conditions.
 - 5: Compute the resulting velocities of the colliding particles: $\Gamma_{i,j} \leftarrow \mathfrak{B}_{ij, \widehat{\sigma}_{ij}^{\text{fic}}}^{\text{put}} \Gamma_{i,j}^{\text{put}}.$
 - 6: Return $\mathbf{r}_{i,j}$ and $\Gamma_{i,j}$.
-

Algorithm 8: Main AGF loop.

- 1: Get the current state of the particles, $\{\mathbf{r}_i, \Gamma_i\}_{i=1}^N$ and current time t .
 - 2: Compute the putative positions and velocities as the solutions of the associated Langevin-like SDE after a Δt , i.e., $\Gamma_i^{\text{put}} \leftarrow \mathfrak{F}_1[\Gamma_i, \bar{\gamma}, \Delta t, \mathcal{Y}_i]$ and $\mathbf{r}_i^{\text{put}} \leftarrow \mathfrak{F}_2[\mathbf{r}_i, \mathbf{v}_i(t), \bar{\gamma}, \Delta t, \bar{\mathcal{Y}}_i]$.
 - 3: Get the fictive velocities as $\mathbf{v}_i^{\text{fic}} \leftarrow [\mathbf{r}_i - \mathbf{r}_i^{\text{put}}] / \Delta t$. Considering the case that noise is not coupled to angular displacements, fictive angular velocities (if defined) are set to coincide with putative angular velocities.
 - 4: Create the event list with the fictive states, $\{\mathbf{r}_i^{\text{fic}}, \Gamma_i^{\text{fic}}\}_{i=1}^N$.
 - 5: Run the EDMD algorithm (see, for example, Algorithm 2) between t and $t + \Delta t$, using Algorithm 7 in case of collision events, and save the indices of colliding particles in a list, $\{i_1, \dots, i_{n_{\text{cp}}}\}$, with n_{cp} being the total number of colliding particles.
 - 6: For noncolliding particles, update positions and velocities, i.e., $\mathbf{r}_i \leftarrow \mathbf{r}_i^{\text{put}}$ and $\Gamma_i \leftarrow \Gamma_i^{\text{put}}, \forall i \notin \{i_1, \dots, i_{n_{\text{cp}}}\}$.
 - 7: Update time, $t \leftarrow t + \Delta t$.
 - 8: Check the end-of-program condition. If it is not fulfilled, go back to 1.
-

This algorithm is used in the works exposed in Article 1 (Section 5.2), Article 4 (Section 7.2), and Article 6 (Section 9.2) to reproduce the action of the nonlinear drag Langevin-like

dynamics introduced in [Subsection 2.4.1](#), and the ST described in [Subsection 2.4.2](#).

MOLECULAR GASES

Thermal and entropic Mpemba effects in molecular gases under nonlinear drag

5

5.1 Summary

The ME is studied in detail in a dilute and homogeneous molecular gas made of hard d_t -spherical identical particles of mass m and diameter σ , and surrounded by an interstitial fluid at equilibrium, at temperature T_b . The interaction of the background fluid with the molecular gas is assumed to be described by a Langevin-like relation, as described in the thermostatted model presented in Subsection 2.4.1. That is, the interaction is assumed to be split into a drag force, with a coefficient assumed to depend quadratically on the velocity modulus, and a stochastic force, whose noise intensity is related to the drag coefficient via a fluctuation-dissipation relation. The dynamics of the system is studied from a kinetic-theory point of view, whose associated homogeneous BFPE corresponds to Eq. (2.48) in the absence of gradients. Moreover, it was already known that, in this model, the TME is present [SP20; PSP21], also in the collisionless case [PSP21], and had been previously studied in terms of crossing times of the temperature evolution curves for the samples involved in the effect (see Section 3.3). Furthermore, as already introduced in Section 3.3, in previous literature about the ME, both the TME and the EME descriptions have been developed. Usually, the former description has been applied to kinetic-theory-based systems [Las+17; Tor+19; Bis+20; SP20; GG21; BPR21; PSP21; Mom+21; THS21; BPR22], whereas the second one has been employed in stochastic-process descriptions of physical systems [LR17; Kli+19; KB20; CKB21; BGM21; CLL21; Lin+22; SL22; YH22]. However, the emergence of the ME has typically been interpreted with a similar argumentation from both descriptions.

The main goal of this chapter is to stress the conceptual characterization of the ME from the thermal and entropic interpretations and expose their differences and common characteristics in the context of the introduced molecular gaseous system. This discussion is based on the whole phenomenology arising in the ME. For this

objective, we use the **BFPE** to introduce the kinetic-theory description of the system. For the thermal description, the evolution equations of the first three moments of the time-dependent **VDF** are derived as a truncation of a full hierarchy of moment equations from a Sonine expansion of the isotropic **VDF**. To work in dimensionless terms, we define a time and temperature reference scale, v_b^{-1} and T_b , respectively. This hierarchy is truncated in two different ways, that is, two **SA** were implemented. In the first one, termed in Article 1 (**Section 5.2**) as *basic SA (BSA)*, the system of differential equations is just made for the evolution of the temperature, T , and the fourth cumulant, a_2 . The **BSA** is the approach indeed previously considered in Ref. [SP20]. In this **BSA**, higher-order cumulants are neglected, as well as nonlinear terms of a_2 . This is compared with an *extended SA (ESA)*, which considers the evolution equation of the sixth cumulant, a_3 , and neglects $a_n \forall n \geq 4$, as well as the nonlinear terms of a_2 and a_3 . These systems of coupled differential equations are built from Eqs. (17) and (19) of Article 1 (**Section 5.2**). Then, if we compare the dynamic description of the molecular gas with that introduced in Eqs. (3.1) of **Chapter 3**, the inner variables acting on the thermal evolution are the cumulants of the **VDF**, especially a_2 , which appears explicitly in the equation of the slope of the temperature, \dot{T} . In fact, the **ESA** is mainly introduced to improve the theoretical approach, as compared with simulation results, already observed in Ref. [PSP21]. In Ref. [SP20], the explicit coupling of a_2 with the evolution equation of T/T_b was already derived, inferring the emergence of the **TME** from it for short times of the evolution. Under this approach, a linearization of the evolution equations around the initial conditions applies, this being called in Article 1 (**Section 5.2**) as *linearized BSA (LBSA)*. Then, one can even derive algebraically the crossing time, denoted as t_θ and defined in Eq. (26) of Article 1 (**Section 5.2**)¹. This short evolution is guaranteed when the system is not subjected to extreme either quenching or heating [PSP21].

Once the thermal description is introduced, we characterize entropically the system by its associated nonequilibrium entropy. The functional used for that description is the **KLD** with the Maxwellian **VDF** at T_b —the equilibrium **VDF**—as the reference **VDF**. For this case, $\mathcal{D}_{\text{KL}}(\cdot|f_M^{\text{eq}})$ is equivalent, up to a constant, to the H -functional, $H(\cdot)$, which was already introduced as the nonequilibrium entropy for molecular gases in **Subsection 2.6.1**. Then, the discussion about the **EME** is based on the decomposition of the nonequilibrium entropy into a kinetic and a local-equilibrium counterparts, i.e., $\mathcal{D}_{\text{KL}}(f(t)|f_M^{\text{eq}}) = \mathcal{D}^{\text{kin}}(t) + \mathcal{D}^{\text{LE}}(T(t))$ [see Eq. (11) of Article 1 (**Section 5.2**)]. The kinetic part accounts for the *distance*² between the time-dependent **VDF** and the local-equilibrium **VDF**, which coincides with the Maxwellian **VDF** at the instantaneous temperature, $T(t)$ [see Eqs. (10) and (12a) of Article 1 (**Section 5.2**)]. On the other hand, the local-equilibrium counterpart measures how far the local-equilibrium **VDF** is from the equilibrium **VDF**,

¹Note that, in Article 1 (**Section 5.2**), θ denotes the ratio T/T_b .

²Note that the \mathcal{D}_{KL} is not, strictly speaking, a distance function. In general, it is not symmetric and it does not fulfill the triangle inequality [KL51].

which results to be a convex and positive function of $T(t)/T_b$ [see Eq. (12b) of Article 1 (Section 5.2)]. A schematic representation of this two-stage description is sketched in Figure 5.1. Therefore, if the ME arises at large times, that is, in the hydrodynamic stage, when the instantaneous VDF coincides with the local-equilibrium one, then $\mathcal{D}^{\text{kin}} \approx 0$, whereas $\mathcal{D}_{\text{KL}}(t) \approx \mathcal{D}^{\text{LE}}(T(t))$. Hence, TME and EME become approximately equivalent during that stage. However, it was observed that TME tends to arise during the first part of the evolution [SP20], becoming \mathcal{D}^{kin} essential in this discussion and breaking down a general equivalence between the thermal and entropic descriptions. In fact, the VDF at this kinetic regime is in a completely nonequilibrium state and therefore, memory effects, like ME, are expected to occur before the VDF acquires the local-equilibrium form. To simplify the entropic analysis, we derive a *renormalized SA* [based on the toy model derived in Article 2 (Section 6.2)] for $\mathcal{D}^{\text{kin}}(t)$. In this approach, the VDF is assumed to be compatible with a Gamma distribution along the system evolution, resulting that $\mathcal{D}^{\text{kin}}(t) \propto a_2^2(t)$ [see Eq. (24) of Article 1 (Section 5.2)]. This Gamma approximation is introduced because of two facts: first, it is a two-parameter exponential probability distribution than can be made to accommodate any other exponential-like one (for example, it can be reduced straightforwardly to the Maxwellian one); second, the initial state of our computer simulated systems are generated from this distribution.

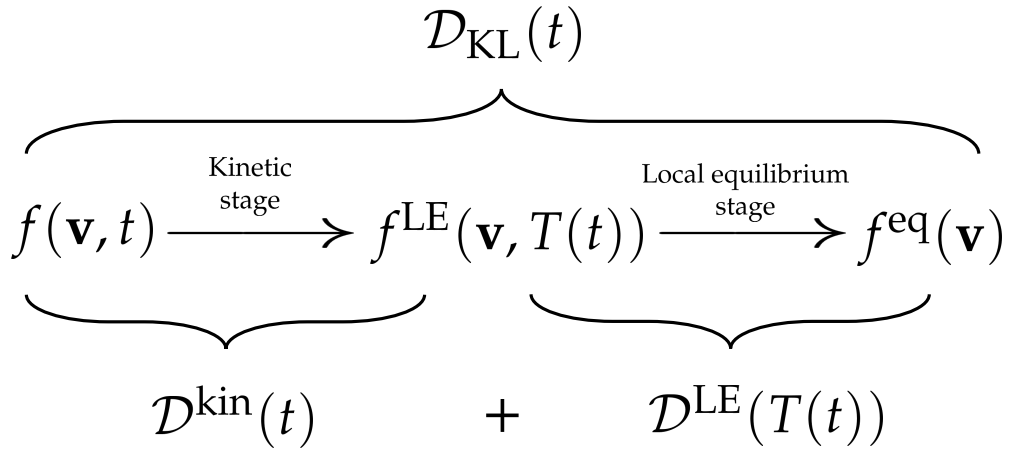


Figure 5.1: Sketch of the evolution of the VDF, f . The decomposition of the KLD into the kinetic and local-equilibrium counterparts is represented. First, the evolution of the VDF is involved into a kinetic stage, in which the VDF stays completely at a nonequilibrium regime. Then, f enters in local equilibrium (f^{LE}) and the VDF is fully described by its instantaneous temperature, $T(t)$, before the relaxation toward equilibrium is completed.

Once the mathematical descriptions of the TME and EME, respectively guided by the nonequilibrium temperature and entropy, are introduced, the possible scenarios in which the ME can arise are discussed. Let us imagine two samples, A and B, the former referring to that sample whose initial temperature is further from the equilibrium value. As a first approach, we assume that $T(t)$ does not cross its steady equilibrium value, T_b , during the evolution. If the temperature curve of system A arrives earlier to equilibrium than B, TME will be present. According to the description in Section 3.3, if the initial

conditions fulfill $T_A^0/T_b > T_B^0/T_b > 1$ (cooling process) then, if a **TME** emerges, it is said to be a **DME**. On the other hand, if $T_A^0/T_b < T_B^0/T_b < 1$, a **TME** is classified as an **IME**. In the former case, we need that $\dot{T}_A(0)/T_b < \dot{T}_B(0)/T_b$, which is found to be equivalent to $a_{2A}^0 > a_{2B}^0$, in the **LBSA**, and the other way around in the latter preparation. Moreover, under the **LBSA** scheme, this necessary condition for the **TME** is completed by imposing $t_\theta > 0$ to its expression, finally resulting in Eqs. (27) and (28) of Article 1 (Section 5.2). On the other hand, if the initially further from equilibrium—as accounted for by the full **VDF** via the **KLD**—relaxes earlier to the equilibrium distribution, the **EME** is said to be present.

Under those considerations, the **ME** is characterized by the appearance of a crossing between the evolution curves at either t_θ or $t_{\mathcal{D}}$, in the **TME** or the **EME** contexts, respectively. As explained in Section 3.3, an even number of crossings indicates the existence of the **ME**, as well. However, as we are working in the rapid kinetic stage, more than one crossing is quite unlikely. The possible phenomenology is then summarized into 8 possible events, they being referred to in Article 1 (Section 5.2) as

- ▶ **ET1**: **EME** and **DME** are present and $t_{\mathcal{D}} < t_\theta$.
- ▶ **TE1**: **EME** and **DME** are present and $t_{\mathcal{D}} > t_\theta$.
- ▶ **ET2**: **EME** and **IME** are present and $t_{\mathcal{D}} < t_\theta$.
- ▶ **TE2**: **EME** and **IME** are present and $t_{\mathcal{D}} > t_\theta$.
- ▶ **T1**: only **DME** (and not **EME**) is present.
- ▶ **T2**: only **IME** (and not **EME**) is present.
- ▶ **E1**: only **EME** (and not **DME**) is present in a cooling process.
- ▶ **E2**: only **EME** (and not **IME**) is present in a heating process.

The comparisons between t_θ and $t_{\mathcal{D}}$ are coming from the result $\mathcal{D}^{\text{kin}}(t) \propto a_2^2(t)$, as derived in the toy model approach [see Eq. (24) of Article 1 (Section 5.2)]. Thus, whereas one could think about the case in which both **EME** and **TME** are present and $t_{\mathcal{D}} \approx t_\theta$, this is concluded to be just present in the hydrodynamic stage and, then, discarded from our kinetic-stage analysis. The conditions under which these events arise are classified in Table I of Article 1 (Section 5.2).

After the identification of the phenomenology in the absence of overshoot, we compute numerically the phase diagrams of the different latter events. This can be observed in Figure 4 of Article 1 (Section 5.2). Some illustrative examples, whose details are exposed in Table II of Article 1 (Section 5.2), are shown from numerical solutions of the **LBSA** in Figures 5–8 of Article 1 (Section 5.2).

Furthermore, we consider the case in which the temperature evolution of (at least) one of the samples overshoots the equilibrium value. Then, we characterize a new event compatible with the **TME**, such that T_A will arrive earlier to T_b as compared with T_B , but in the absence of crossovers (or with an odd number of them). One expects that

	Standard TME	OME
t_X	$t_\theta = \frac{1}{\lambda_+ - \lambda_-} \ln \left(1 + \frac{A_{11}^{-1}}{R_{\max}^0/R^0 - 1} \right)$	$t_{\mathcal{D}^{\text{LE}}} = \frac{1}{\bar{\lambda}_+ - \bar{\lambda}_-} \ln \left(1 + \frac{\bar{A}_{11}^{-1}}{\bar{R}_{\max}^0/R_+^0 - 1} \right)$
If ...	$0 < R^0 < R_{\max}^0$	$(0 < R_+^0 < R_{\max}^0) \wedge (R^0 < 0 \vee R^0 > \bar{R}_{\max}^0)$

Table 5.1: Summary of crossing times t_X (with $X = \theta, \mathcal{D}^{\text{LE}}$) and the necessary conditions derived from **LBSA** for the emergence of the standard **TME** and the **OME**, in the case of a molecular gas of hard d_t -spheres in contact with a background fluid with a nonlinear drag. Here, $R^0 \equiv (T_A^0 - T_B^0)/T_b(a_{2A}^0 - a_{2B}^0)$, $R_+^0 \equiv (T_A^0 + T_B^0 + 2T_b)/T_b(a_{2A}^0 + a_{2B}^0)$, $R_{\max}^0 \equiv A_{12}/A_{11}$, A_{ij} and $\lambda_{+,-}$ are coming from the **LBSA** developed in Appendix C of Article 1 (Section 5.2). Overlined quantities refer to their values at $T^0 = T_b$.

system B overshoots T_b in such a way that T_A can overtake the evolution of T_B toward T_b . This is called the **OME**, already introduced in Section 3.3, and it is expected to occur in states initially close to the equilibrium temperature, T_b , for this system. To analyze the **OME**, a **LBSA** is built from initial conditions at $|T(0) - T_b| \ll 1$ [see Eqs. (30) of Article 1 (Section 5.2)]. Then, the crossover time of $T(t)$ through T_b is computed, t_O , together with the necessary conditions for the overshoot to appear [see Eq. (33) of Article 1 (Section 5.2)]. In contrast to what happened in the standard version of the **TME**, one must look for an initially much faster decay (growth) of system B than A in a cooling (heating) experiment. Moreover, whereas there is no crossing between the thermal curves, we realize that there is, in fact, a crossover between $\mathcal{D}_A^{\text{LE}}(t)$ and $\mathcal{D}_B^{\text{LE}}(t)$ at $t = t_{\mathcal{D}^{\text{LE}}}$. The latter crossing time is predicted from **LBSA**, and the conditions for the initial preparations to observe the **OME** are also derived [see Eqs. (35)–(37) of Article 1 (Section 5.2)]. To derive the latter necessary conditions, we impose that $t_{\mathcal{D}^{\text{LE}}} > 0$ and $t_\theta < 0$ (no crossing between T_A and T_B). A comparison between the standard **TME** and the **OME** in this system is summarized in Table 5.1. We then conclude that \mathcal{D}^{LE} , being a convex and positive function of $T(t)/T_b$, which, in addition, $\mathcal{D}^{\text{LE}} = 0$ if and only if $T(t) = T_b$, describes both the standard **TME** (**DME** and **IME**) and the **OME** in the crossing-time characterization of the **TME**. That is, the \mathcal{D}^{LE} acts as the thermal distance introduced in Section 3.3. Afterwards, some numerical examples from the **LBSA** for the **OME** were given in Figures 9 and 10 of Article 1 (Section 5.2).

Finally, we compare the theoretical predictions with **DSMC** and **EDMD** computer simulations from hand-made computer programs [Meg23]. Here, it is necessary to implement the Langevin dynamics of the system according to the Fokker–Planck term of the **BFPE** in the free-streaming stages of both algorithms, as indicated in Chapter 4. Concretely, we use the **AGF** algorithm reported on Refs. [SVM07; Sca12] adapted to the **LE** of this problem (see Appendix A), which is detailed both in Article 1 (Section 5.2) and in Appendix C. Representative cases for the different predicted events are shown. It is observed that the simulation outcomes reproduce the predictions. Moreover, numerical

solutions coming from BSA and ESA are compared with the simulation data, concluding a quantitatively better agreement with the ESA.

5.2 Article 1

Title: Thermal versus entropic Mpemba effect in molecular gases with nonlinear drag

Authors: Alberto Megías¹, Andrés Santos^{1,2}, and Antonio Prados³

Affiliations:

¹ Departamento de Física, Universidad de Extremadura, E-06006 Badajoz, Spain

² Instituto de Computación Científica Avanzada (ICCAEx), Universidad de Extremadura, E-06006 Badajoz, Spain

³ Física Teórica, Universidad de Sevilla, Apartado de Correos 1065, E-41080 Sevilla, Spain

Journal: Physical Review E

Volume: 105

Pages: 054140

Year: 2022

DOI: [10.1103/PhysRevE.105.054140](https://doi.org/10.1103/PhysRevE.105.054140)



Copy of the preprint of the work: “Alberto Megías, Andrés Santos, and Antonio Prados, ‘Thermal versus entropic Mpemba effect in molecular gases with nonlinear drag’, *Physical Review E* **105**, 054140 (2022) <https://doi.org/10.1103/PhysRevE.105.054140>.”

Thermal versus entropic Mpemba effect in molecular gases with nonlinear drag

Alberto Megías*

Departamento de Física, Universidad de Extremadura, E-06006 Badajoz, Spain

Andrés Santos†

*Departamento de Física, Universidad de Extremadura, E-06006 Badajoz, Spain and
Instituto de Computación Científica Avanzada (ICCAEx),
Universidad de Extremadura, E-06006 Badajoz, Spain*

Antonio Prados‡

*Física Teórica, Universidad de Sevilla, Apartado de Correos 1065, E-41080 Sevilla, Spain
(Dated: May 31, 2022)*

Loosely speaking, the Mpemba effect appears when hotter systems cool sooner or, in a more abstract way, when systems further from equilibrium relax faster. In this paper, we investigate the Mpemba effect in a molecular gas with nonlinear drag, both analytically (by employing the tools of kinetic theory) and numerically (direct simulation Monte Carlo of the kinetic equation and event-driven molecular dynamics). The analysis is carried out via two alternative routes, recently considered in the literature: first, the kinetic or thermal route, in which the Mpemba effect is characterized by the crossing of the evolution curves of the kinetic temperature (average kinetic energy), and, second, the stochastic thermodynamics or entropic route, in which the Mpemba effect is characterized by the crossing of the distance to equilibrium in probability space. In general, a nonmutual correspondence between the thermal and entropic Mpemba effects is found, i.e., there may appear the thermal effect without its entropic counterpart or vice versa. Furthermore, a nontrivial overshoot with respect to equilibrium of the thermal relaxation makes it necessary to revise the usual definition of the thermal Mpemba effect, which is shown to be better described in terms of the relaxation of the local equilibrium distribution. Our theoretical framework, which involves an extended Sonine approximation in which not only the excess kurtosis but also the sixth cumulant is retained, gives an excellent account of the behavior observed in simulations.

I. INTRODUCTION

In recent years, memory effects have become a hot topic in nonequilibrium statistical physics research [1]. Those phenomena usually imply counterintuitive effects that apparently contradict well-established standard physical laws. One of the most interesting is the Mpemba effect (ME): Given two samples of a fluid in a common thermal bath, the initially hotter one may cool more rapidly than that initially cooler. The well-known Newton’s law of cooling, according to which the temperature evolution is predetermined by its initial value, is thus violated in the presence of the ME. Original studies of the ME deal with water [2–32], and even today there is still a lack of consensus about its existence in this very complex system [33–35].

In a more general context, the ME can be recast as “the initially further from equilibrium relaxes faster,” with the separation from equilibrium being defined in a suitable way, see below. With such an interpretation, Mpemba-like effects have been investigated in a large variety of many-body systems: molecular gases [36, 37], mixtures [38], granular gases [39–45], inertial suspen-

sions [46, 47], spin glasses [48], carbon nanotube resonators [49], clathrate hydrates [50], Markovian models [51–55], active systems [56], Ising models [57–59], non-Markovian mean-field systems [60, 61], or quantum systems [62]. Very recently, the ME has been analyzed in the framework of Landau’s theory of phase transitions [63]. Also, it has been experimentally observed in colloids [64, 65].

There have been two main approaches to the ME: the kinetic-theory or “thermal” approach [36–44, 46, 47] and the stochastic-process (or thermodynamics) or “entropic” approach [51–56, 62, 64, 65]. In the thermal approach, kinetic theory makes it possible to define in a natural way an out-of-equilibrium time-dependent temperature $T(t)$ as basically the average kinetic energy, i.e.,

$$T(t) = \frac{m}{dk_B} \langle v^2 \rangle, \quad (1)$$

where d is the dimensionality of the system, m is the mass of a particle, and k_B is the Boltzmann constant. This definition allows for a simple, and close in spirit to the original studies in water, characterization of the separation from equilibrium at temperature T_{eq} : The initially hotter (colder) sample A (B) translates into that having the larger (smaller) initial value of the kinetic temperature, $T_A^0 > T_B^0 > T_{\text{eq}}$. A *thermal* Mpemba effect (TME) is observed if the evolution curves for the temperature cross at a certain time t_θ , $T_A(t_\theta) = T_B(t_\theta)$, and that of the initially hotter remains below the other one for longer

* albertom@unex.es

† andres@unex.es

‡ prados@us.es

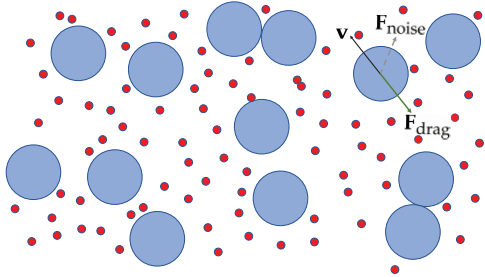


FIG. 1. Illustration of the system considered in this paper. A molecular gas of hard particles (represented by the large blue circles) is coupled to a thermal bath (made of particles represented by the small red circles) via a drag force $\mathbf{F}_{\text{drag}} = -m\zeta(v)\mathbf{v}$, where $\zeta(v)$ is a velocity-dependent drag coefficient, and a stochastic force $\mathbf{F}_{\text{noise}} = m\zeta(v)\boldsymbol{\eta}$, where $\boldsymbol{\eta}$ is a Gaussian white-noise term. In addition, the particles are subjected to binary elastic collisions.

times, $T_{\text{eq}} < T_A(t) < T_B(t)$ for $t > t_\theta$. Additionally, a Mpemba effect may exist in the absence of a temperature crossing if $T_B(t)$ overshoots the equilibrium value at a certain time t_O , i.e., $T_B(t_O) = T_{\text{eq}}$, then reaches a minimum, and finally relaxes to equilibrium later than sample A. This overshoot effect would be the analog of the supercooling phenomenon in water.

In the stochastic-process approach, the starting point is usually a Markov process $\mathbf{x}(t)$. The state of the system at time t is determined by a probability distribution $P(\mathbf{x}, t)$, which typically obeys a master equation, for discrete \mathbf{x} , or a Fokker–Planck equation, for continuous \mathbf{x} . The Kullback–Leibler divergence (KLD) or relative entropy [66] is defined as

$$\mathcal{D}(t) \equiv \left\langle \ln \frac{P}{P^{\text{eq}}} \right\rangle = \int d\mathbf{x} P(\mathbf{x}, t) \ln \frac{P(\mathbf{x}, t)}{P^{\text{eq}}(\mathbf{x})}, \quad (2)$$

where $P^{\text{eq}}(\mathbf{x})$ stands for the equilibrium probability distribution. The H -theorem [67] ensures that $\mathcal{D}(t)$ monotonically decreases to zero over a nonequilibrium process and thus $\mathcal{D}(t)$ can be interpreted as the distance to equilibrium from a physical standpoint [68]. Also, \mathcal{D} can be understood as (the opposite of) the nonequilibrium entropy relative to the equilibrium state. The ME is translated as follows in this context: The further from (closer to) sample A (B) has the larger (smaller) initial value of \mathcal{D} , i.e., $\mathcal{D}_A^0 > \mathcal{D}_B^0 > 0$. The entropic Mpemba effect (EME) emerges when the evolution curves for \mathcal{D} cross at a certain time $t_{\mathcal{D}}$, $\mathcal{D}_A(t_{\mathcal{D}}) = \mathcal{D}_B(t_{\mathcal{D}})$, and $0 < \mathcal{D}_A(t) < \mathcal{D}_B(t)$ for $t > t_{\mathcal{D}}$.

The two effects described above, TME and EME, are equivalent if a biunivocal correspondence between nonequilibrium temperature and (entropic) distance to equilibrium exists. Yet, this is not the case in general, as we will show. In fact, the main aim of this paper is to analyze the correspondence between the TME and

the EME in a prototypical system, where the two approaches can be carried out analytically—at least in an approximate, systematic, way. Specifically, we consider a molecular gas of hard particles that is coupled to a thermal bath, with the resulting drag force being nonlinear in the velocity [36]. In addition, there are binary elastic collisions between the particles. See Fig. 1 for an illustration of the system. The evolution equation of the velocity distribution function (VDF) is given by the Enskog–Fokker–Planck equation (EFPE)—the Enskog term accounts for binary collisions, whereas the Fokker–Planck term models the interaction with the thermal bath, see Sec. II for details. To look into the system dynamics, we employ a hybrid approach that includes both a theoretical and a numerical analysis: kinetic-theory tools—via a Sonine approximation of the EFPE equation—for the former and direct simulation Monte Carlo (DSMC), together with event-driven molecular dynamics (EDMD), simulations for the latter.

Note that it is the nonlinearity of the drag force that the ME stems from. As a consequence, the time evolution of the kinetic temperature is coupled to other moments and the kinetic temperature of the nonlinear fluid shows algebraic nonexponential relaxation and strong memory effects after a quench [37]. Note also that elastic collisions do not change the average kinetic energy: Were the drag absent, the kinetic temperature would remain constant throughout the whole time evolution. Still, an initial nonequilibrium VDF would evolve toward the equilibrium Maxwellian—higher-order velocity cumulants would indeed be affected by collisions and tend to zero in the long-time limit.

The above characterizations of out-of-equilibrium temperature and distance to equilibrium, Eqs. (1) and (2), are quite natural in the molecular fluid. Yet, a different choice may be more adequate in other systems. On the one hand, some kind of nonequilibrium temperature, e.g., in the spirit of the fictive or effective temperature for glassy systems [69–71], may be introduced in systems where the kinetic temperature cannot be defined—for example, Ising models [72]. On the other hand, the L_1 and L_2 norms have been employed in the literature to measure the distance of the VDF to equilibrium [51, 54, 64]. Alternative choices for the observables characterizing the thermal relaxation and the distance to equilibrium may quantitatively affect the values of the crossing times t_θ and $t_{\mathcal{D}}$, and even the own existence of the TME and the EME.

With the above definitions, both the TME and the EME can be investigated. Some basic questions arise, though. Does the TME imply the EME, or vice versa? When both of them are present, how close are the respective crossover times t_θ and $t_{\mathcal{D}}$? Is it possible to observe the ME if the kinetic temperature of at least one of the two samples overshoots its equilibrium value? The theoretical framework developed in this paper, which is supported by computer simulations, answers these key questions.

The paper is organized as follows. Section II puts forward our model system for a fluid with nonlinear drag. Also, the local equilibrium concept is introduced and its implications for the entropic distance are discussed. In Sec. III, we derive the evolution equations for the relevant physical quantities, within the Sonine approximation schemes developed in this paper. From this knowledge, the general phenomenology of TME and EME is predicted and described from heuristic arguments in Sec. IV. Afterwards, in Sec. V a singular case for TME, induced by the appearance of an overshoot effect, is investigated. Thus, Secs. II–V constitute the core of the theoretical framework developed in the paper. In addition, we present simulation results supporting the theoretical predictions in Sec. VI. Finally, conclusions are presented in Sec. VII, including a discussion on the definition of nonequilibrium temperature for a general system. Some technical parts are relegated to appendices.

II. MODEL SYSTEM AND LOCAL EQUILIBRIUM

Let us consider the following model for a fluid with nonlinear drag [36, 37, 73–75]: a d -dimensional fluid of elastic hard spheres of mass m and diameter σ , with number density n , subjected to a stochastic force composed by a white-noise term with nonlinear variance plus a nonlinear drag force. This scheme mimics a system of elastic spheres assumed to be suspended in a background fluid in equilibrium at temperature T_b , as depicted in Fig. 1.

The (spatially uniform) EFPE for the one-body VDF $f(\mathbf{v}, t)$ reads

$$\partial_t f(\mathbf{v}, t) - \frac{\partial}{\partial \mathbf{v}} \cdot \left[\zeta(v) \mathbf{v} + \frac{\xi^2(v)}{2} \frac{\partial}{\partial \mathbf{v}} \right] f(\mathbf{v}, t) = J[\mathbf{v}|f, f], \quad (3)$$

where

$$J[\mathbf{v}_1|f, f] = \sigma^{d-1} g_c \int d\mathbf{v}_2 \int_+ d\hat{\boldsymbol{\sigma}} \mathbf{v}_{12} \cdot \hat{\boldsymbol{\sigma}} \times [f(\mathbf{v}'_1, t) f(\mathbf{v}'_2, t) - f(\mathbf{v}_1, t) f(\mathbf{v}_2, t)] \quad (4)$$

is the usual Boltzmann–Enskog collision operator with $\mathbf{v}_{12} \equiv \mathbf{v}_1 - \mathbf{v}_2$, $g_c = \lim_{r \rightarrow \sigma^+} g(r)$ being the contact value of the pair correlation function, and $\int_+ d\hat{\boldsymbol{\sigma}} \equiv \int d\hat{\boldsymbol{\sigma}} \Theta(\mathbf{v}_{12} \cdot \hat{\boldsymbol{\sigma}})$. In addition, the drag component of the stochastic force is $-m\zeta(v)\mathbf{v}$, while the white-noise counterpart has a nonlinear variance $m^2\xi^2(v)$. The functions $\zeta(v)$ and $\xi^2(v)$ are connected via the fluctuation-dissipation theorem as

$$\xi^2(v) = \frac{2k_B T_b}{m} \zeta(v), \quad (5)$$

where T_b is the temperature of the background fluid. This ensures that the only stationary solution of the EFPE is the equilibrium Maxwellian,

$$f^{\text{eq}}(\mathbf{v}) = n \left(\frac{m}{2\pi k_B T_b} \right)^{d/2} e^{-m v^2 / 2k_B T_b}. \quad (6)$$

A quadratic dependence of the drag coefficient naturally appears when the hard spheres and the background fluid particles have a comparable mass [36, 37, 73–75],

$$\zeta(v) = \zeta_0 \left(1 + \gamma \frac{m v^2}{k_B T_b} \right). \quad (7)$$

The coefficients ζ_0 and γ are both positive and measure the zero-velocity value of the drag coefficient and the degree of nonlinearity of the drag force, respectively. Note that, due to the nonlinearity of the drag force, the implementation of the Langevin equation associated with the free streaming of particles between collisions is far from trivial. This issue is discussed in Appendix A.

The two approaches to the ME can be implemented in the nonlinear fluid introduced above. Translating Eqs. (1) and (2) to our model system, we have that the nonequilibrium temperature $T(t)$ is given by

$$T(t) = \frac{m}{dk_B} \langle v^2 \rangle = \frac{m}{ndk_B} \int d\mathbf{v} v^2 f(\mathbf{v}, t), \quad (8)$$

and the relative entropy is

$$\mathcal{D}(t) = \left\langle \ln \frac{f}{f^{\text{eq}}} \right\rangle = \frac{1}{n} \int d\mathbf{v} f(\mathbf{v}, t) \ln \frac{f(\mathbf{v}, t)}{f^{\text{eq}}(\mathbf{v})}, \quad (9)$$

where $n \equiv \int d\mathbf{v} f(\mathbf{v}, t)$ is the number density.

On physical grounds, it is expected that the evolution of the gas toward equilibrium takes place along two stages [76]. First, a rapid “kinetic” stage where the VDF approaches the so-called local equilibrium (LE) form,

$$f^{\text{LE}}(\mathbf{v}; T(t)) = n \left[\frac{m}{2\pi k_B T(t)} \right]^{d/2} e^{-m v^2 / 2k_B T(t)}, \quad (10)$$

i.e., f^{LE} has the Maxwellian shape but with the time-dependent temperature. Second, a slower “hydrodynamic” stage, where the VDF is close to f^{LE} and the evolution of the VDF takes place via the temperature.

The above discussion suggests the following decomposition for the relative entropy,

$$\mathcal{D}(t) = \mathcal{D}^{\text{kin}}(t) + \mathcal{D}^{\text{LE}}(T(t)), \quad (11)$$

where

$$\mathcal{D}^{\text{kin}}(t) = \frac{1}{n} \int d\mathbf{v} f(\mathbf{v}, t) \ln \frac{f(\mathbf{v}, t)}{f^{\text{LE}}(\mathbf{v}; T(t))} \quad (12a)$$

and

$$\begin{aligned} \mathcal{D}^{\text{LE}}(T(t)) &= \frac{1}{n} \int d\mathbf{v} f^{\text{LE}}(\mathbf{v}; T(t)) \ln \frac{f^{\text{LE}}(\mathbf{v}; T(t))}{f^{\text{eq}}(\mathbf{v})} \\ &= \frac{d}{2} [\theta(t) - 1 - \ln \theta(t)], \quad \theta(t) \equiv \frac{T(t)}{T_b}. \end{aligned} \quad (12b)$$

Both \mathcal{D}^{kin} and \mathcal{D}^{LE} are positive definite [77]. To split \mathcal{D} into the sum of \mathcal{D}^{kin} and \mathcal{D}^{LE} , we have employed that the average of the kinetic energy with $f(\mathbf{v}, t)$ is the same

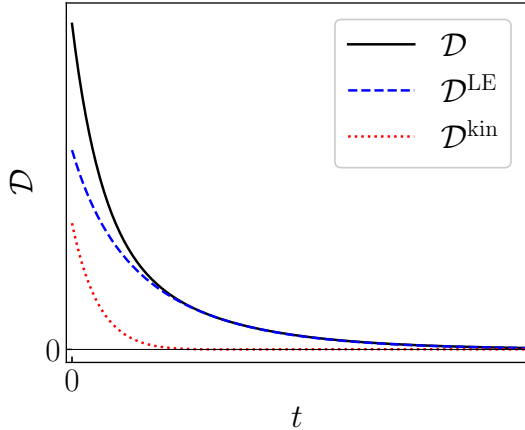


FIG. 2. Sketch showing a typical evolution of the total KLD (solid line), its LE contribution (dashed line), and its kinetic contribution (dotted line).

as with $f^{\text{LE}}(\mathbf{v}; T(t))$. A generalization of this idea makes it possible to define a nonequilibrium temperature and an analogous splitting of \mathcal{D} in quite a general class of systems, see Sec. VII for further details.

The first contribution to the total \mathcal{D} , \mathcal{D}^{kin} , is a measure of the departure of the true VDF from the LE one, and depends explicitly on time through the whole VDF $f(\mathbf{v}, t)$. In contrast, the second contribution \mathcal{D}^{LE} measures the deviation of the LE state from the asymptotic equilibrium state and only depends on time through the nonequilibrium temperature $T(t)$, namely on the temperature ratio $\theta(t)$. More specifically, \mathcal{D}^{LE} monotonically increases as $|\theta - 1|$ increases in the domains $\theta > 1$ and $\theta < 1$ separately. Figure 2 presents a sketch of the temporal evolution of \mathcal{D} and its two contributions, \mathcal{D}^{LE} and \mathcal{D}^{kin} [78].

The TME and EME can be directly related if the crossing comes about in the hydrodynamic regime, since therein $\mathcal{D}^{\text{kin}} \approx 0$ and $\mathcal{D}(t) \approx \mathcal{D}^{\text{LE}}(\theta(t))$ —which is a function of temperature only, as explicitly stated by our notation. Therefore, the TME and EME become equivalent during the hydrodynamic stage, and $t_\theta \simeq t_{\mathcal{D}}$. However, we will show that in most situations the ME occurs during the kinetic stage, the contribution \mathcal{D}^{kin} is then relevant, and the physical picture is much more complex. In fact, the two-stage relaxation picture may even break down under certain conditions, as discussed in Ref. [79].

III. EVOLUTION EQUATIONS

Multiplying both sides of Eq. (3) by v^2 and integrating over velocity one readily obtains the evolution equation

4

for the time-dependent temperature,

$$\frac{\dot{T}}{\zeta_0} = -2(T - T_b) \left[1 + (d+2)\gamma \frac{T}{T_b} \right] - 2(d+2)\gamma \frac{T^2}{T_b} a_2, \quad (13)$$

where

$$a_2(t) \equiv \frac{d}{d+2} \frac{\langle v^4 \rangle}{\langle v^2 \rangle^2} - 1 \quad (14)$$

is the excess kurtosis.

Using as unit of time the mean free time—average time between collisions—at equilibrium,

$$\tau_b = \frac{K_d}{g_c n \sigma^{d-1} \sqrt{2k_B T_b/m}}, \quad K_d \equiv \frac{\sqrt{2}\Gamma(d/2)}{\pi^{\frac{d-1}{2}}}, \quad (15)$$

the dimensionless time t^* and zero-velocity drag coefficient ζ_0^* can be defined as

$$t^* = t/\tau_b, \quad \zeta_0^* = \zeta_0 \tau_b. \quad (16)$$

The parameter ζ_0^* measures the relative relevance of the drag force (i.e., the interactions between the particles and the background fluid) and hard-sphere binary collisions. The limit $\zeta_0^* \rightarrow 0$ corresponds to negligible drag force, where the EFPE reduces to the Enskog equation. The limit $\zeta_0^* \rightarrow \infty$ corresponds to negligible collisions, where the EFPE reduces to the Fokker–Planck equation [80]. In this work, we typically consider the value $\zeta_0^* = 1$, for which the drag force and binary collisions are comparable and act over the same timescale. Note that both the drag force and binary collisions drive by themselves the system to equilibrium, independently of the magnitude of the other interaction, with the entropic distance monotonically decreasing to zero [81].

In the remainder of the paper we employ dimensionless quantities. Dimensionless temperature is identified with the temperature ratio θ defined in Eq. (12b). For simplicity, henceforth the stars on t^* and ζ_0^* are dropped. The evolution equation for the temperature, Eq. (13), thus reads

$$\frac{\dot{\theta}}{\zeta_0} = -2(\theta - 1) [1 + (d+2)\gamma\theta] - 2(d+2)\gamma\theta^2 a_2. \quad (17)$$

Notice that one gets Newton's cooling law $\dot{\theta} = -2\zeta_0(\theta - 1)$ in the linear case $\gamma = 0$. However, if $\gamma \neq 0$, then the evolution of temperature is coupled to that of the fourth-degree moment $\langle v^4 \rangle$ through a_2 . Next, the evolution equation for $\langle v^4 \rangle$ stemming from the EFPE, Eq. (3), is coupled to the sixth-degree moment $\langle v^6 \rangle$ due to the nonlinear drag term and to all the moments $\langle v^\ell \rangle$ due to the collision term, and so on. Thus, the full evolution of $\theta(t)$ is coupled to the infinite hierarchy of moment equations, which are derived in Appendix B by introducing a Sonine expansion of the VDF. By retaining only the first two terms in the expansion, which involve the excess kurtosis (or fourth-order cumulant) a_2 and the sixth-order

cumulant a_3 ,

$$a_3(t) = 1 + 3a_2 - \frac{d^2}{(d+2)(d+4)} \frac{\langle v^6 \rangle}{\langle v^2 \rangle^3}, \quad (18)$$

and neglecting nonlinear terms in the cumulants one gets

$$\begin{aligned} \frac{\dot{a}_2}{\zeta_0} = & -8\gamma(\theta - 1) + 4 \left[2\gamma - (d+8)\gamma\theta - \frac{1}{\theta} \right] a_2 \\ & + 4(d+4)\gamma\theta a_3 - \frac{8(d-1)\sqrt{\theta}}{d(d+2)\zeta_0} \left(a_2 - \frac{a_3}{4} \right), \end{aligned} \quad (19a)$$

$$\begin{aligned} \frac{\dot{a}_3}{\zeta_0} = & -24\gamma(2-3\theta)a_2 + 6 \left[4\gamma - (d+14)\gamma\theta - \frac{1}{\theta} \right] a_3 \\ & + \frac{\sqrt{\theta}}{\zeta_0} \frac{3(d-1)}{d(d+2)(d+4)} [4a_2 - (4d+19)a_3]. \end{aligned} \quad (19b)$$

Equations (17) and (19) make a closed set of three coupled differential equations, nonlinear in the temperature but linear in the cumulants.

In this paper, we consider two Sonine approximations. The roughest approximation consists of neglecting a_3 , setting $a_3 = 0$ in Eq. (19a), and dealing then with Eqs. (17) and (19a) for the pair (θ, a_2) . Here, we term this approach the basic Sonine approximation (BSA) [82]. A more sophisticated theory is obtained by keeping a_3 and dealing then with Eqs. (17) and (19). We term this approach the extended Sonine approximation (ESA) [83].

IV. THERMAL VERSUS ENTROPIC MPEMBA EFFECTS

A. Heuristic arguments

Now we proceed to study the ME in the theoretical framework of the Sonine approximations we have just introduced. To start with, let us consider two samples (A and B) at the *same* initial temperatures $\theta_A(0) \equiv \theta_A^0$ and $\theta_B(0) \equiv \theta_B^0$, above the equilibrium value, i.e., $\theta_A^0 = \theta_B^0 > 1$. According to Eq. (17), the initial slopes $\dot{\theta}_A(0)$ and $\dot{\theta}_B(0)$ satisfy the inequality $\dot{\theta}_A(0) < \dot{\theta}_B(0)$ if $a_{2A}(0) \equiv a_{2A}^0 > a_{2B}(0) \equiv a_{2B}^0$, in which case sample A is expected to reach equilibrium before sample B. It must be brought to bear that the latter statement is true if $\theta(t) - 1$ keeps its initial sign along the whole relaxation to equilibrium, a condition that is assumed throughout this section. Exceptions to this fact, due to the overshoot of θ with respect to its equilibrium value, are discussed in Sec. V.

In order to analyze the TME described in Sec. I, let us take now $\theta_A^0 > \theta_B^0 > 1$. As discussed above, $\dot{\theta}_A(0) < \dot{\theta}_B(0)$ if $a_{2A}^0 > a_{2B}^0$. In that way, it can be expected that, by a convenient choice of the initial-condition values (θ_A^0, a_{2A}^0) and (θ_B^0, a_{2B}^0) , the evolution curves $\theta_A(t)$ and $\theta_B(t)$ intersect at a certain crossover time t_θ . That

is, $\theta_A(t_\theta) = \theta_B(t_\theta)$ and $\dot{\theta}_A(t_\theta) < \dot{\theta}_B(t_\theta)$, which entails $a_{2A}(t_\theta) > a_{2B}(t_\theta)$ and $1 < \theta_A(t) < \theta_B(t)$ for $t > t_\theta$. This is the typical framework for the emergence of the (direct) TME in the kinetic description [36, 37, 39].

The inverse TME is analogous, except that, instead of $\theta_A^0 > \theta_B^0 > 1$, one now has $\theta_A^0 < \theta_B^0 < 1$. If now $a_{2B}^0 > a_{2A}^0$, then $\dot{\theta}_B(0) < \dot{\theta}_A(0)$, so that it is in principle possible that the evolution curve $\theta_A(t)$ intersects $\theta_B(t)$ at a certain crossover time t_θ .

Note that, without loss of generality, we denote by A the sample with an initial temperature farther from the equilibrium one, both in the direct and inverse TME. Thus, the necessary (but, of course, not sufficient) conditions for the direct and inverse TME are $a_{2A}^0 > a_{2B}^0$ and $a_{2B}^0 > a_{2A}^0$, respectively.

In this work, we analyze both the TME and the EME. In the latter, it is the evolution curves of the relative entropy \mathcal{D} that intersect at a certain time $t_{\mathcal{D}}$, as described in Sec. I [84]. In particular, we want to understand whether the TME implies the EME or not. Also, when both the TME and the EME are present, we would like to investigate the relation between the crossing times t_θ and $t_{\mathcal{D}}$.

Let us address the questions above by simple heuristic arguments. First, we consider the case in which the further from equilibrium sample in the kinetic approach (A) is also the further from equilibrium in the entropic approach, i.e., $\mathcal{D}_A^0 > \mathcal{D}_B^0$. Therein, the existence of the TME implies that of the EME, and vice versa, as shown below. Note that $\mathcal{D}_A^0 > \mathcal{D}_B^0$ if \mathcal{D}^0 increases with $|\theta^0 - 1|$. This is indeed true for the LE contribution \mathcal{D}^{LE} , but not necessarily so for the total KLD \mathcal{D} if the kinetic contribution \mathcal{D}^{kin} plays a relevant role.

For the direct TME, we have $\theta_A^0 > \theta_B^0 > 1$ and $\mathcal{D}_A^0 > \mathcal{D}_B^0$. If the TME exists, then one has $\theta_B(t) > \theta_A(t) > 1$ after the crossover. In particular, this holds for sufficiently long times belonging to the hydrodynamic stage, where both $\mathcal{D}_A^{\text{kin}}$ and $\mathcal{D}_B^{\text{kin}}$ are negligible, and thus one has $\mathcal{D}_B(t) > \mathcal{D}_A(t)$ (EME) in the same stage. Reciprocally, if the EME exists, then $\mathcal{D}_B(t) > \mathcal{D}_A(t)$ in the hydrodynamic stage after the crossover, implying $\theta_B(t) > \theta_A(t) > 1$ (TME) in the same regime. An analogous reasoning applies to the inverse TME, i.e., $1 > \theta_B^0 > \theta_A^0$ and $\mathcal{D}_A^0 > \mathcal{D}_B^0$.

Provided that the TME and EME are present, the argument above does not tell us the relative positioning of the crossover times t_θ and $t_{\mathcal{D}}$, i.e., whether $t_\theta > t_{\mathcal{D}}$ or $t_\theta < t_{\mathcal{D}}$. Let us start by considering that the direct TME takes place at t_θ . Therefore, we have that $\mathcal{D}_A^{\text{LE}}(t_\theta) = \mathcal{D}_B^{\text{LE}}(t_\theta)$ and only the kinetic part contributes to the KLD difference at t_θ , $\mathcal{D}_A(t_\theta) - \mathcal{D}_B(t_\theta) = \mathcal{D}_A^{\text{kin}}(t_\theta) - \mathcal{D}_B^{\text{kin}}(t_\theta)$. This implies that $\mathcal{D}_A(t_\theta) < \mathcal{D}_B(t_\theta)$ (and hence $t_{\mathcal{D}} < t_\theta$) if $\mathcal{D}_A^{\text{kin}}(t_\theta) < \mathcal{D}_B^{\text{kin}}(t_\theta)$, while $\mathcal{D}_A(t_\theta) > \mathcal{D}_B(t_\theta)$ (and hence $t_{\mathcal{D}} > t_\theta$) otherwise.

For the sake of simplicity, and to go beyond the generic analysis of the previous paragraph, let us assume that the values of the excess kurtoses at the crossover time t_θ are small enough as to approximate $\mathcal{D}^{\text{kin}} \propto a_2^2$. The

TABLE I. Summary of possible cases regarding the occurrence of the TME and the EME.

Case	Type of ME	Initial condition	If ...	then ...
ET1	Direct TME & EME	$\theta_A^0 > \theta_B^0 > 1$, $a_{2A}^0 > a_{2B}^0$, $\mathcal{D}_A^0 > \mathcal{D}_B^0$	$ a_{2A}(t_\theta) < a_{2B}(t_\theta) $	$t_D < t_\theta$
TE1	Direct TME & EME	$\theta_A^0 > \theta_B^0 > 1$, $a_{2A}^0 > a_{2B}^0$, $\mathcal{D}_A^0 > \mathcal{D}_B^0$	$ a_{2A}(t_\theta) > a_{2B}(t_\theta) $	$t_D > t_\theta$
ET2	Inverse TME & EME	$\theta_A^0 < \theta_B^0 < 1$, $a_{2A}^0 < a_{2B}^0$, $\mathcal{D}_A^0 > \mathcal{D}_B^0$	$ a_{2A}(t_\theta) < a_{2B}(t_\theta) $	$t_D < t_\theta$
TE2	Inverse TME & EME	$\theta_A^0 < \theta_B^0 < 1$, $a_{2A}^0 < a_{2B}^0$, $\mathcal{D}_A^0 > \mathcal{D}_B^0$	$ a_{2A}(t_\theta) > a_{2B}(t_\theta) $	$t_D > t_\theta$
T1	Direct TME	$\theta_A^0 > \theta_B^0 > 1$, $a_{2A}^0 > a_{2B}^0$	$\mathcal{D}_B^0 > \mathcal{D}_A^0$	No EME
T2	Inverse TME	$\theta_A^0 < \theta_B^0 < 1$, $a_{2A}^0 < a_{2B}^0$	$\mathcal{D}_B^0 > \mathcal{D}_A^0$	No EME
E1	EME	$\mathcal{D}_B^0 > \mathcal{D}_A^0$	$\theta_A^0 > \theta_B^0 > 1$	No Direct TME
E2	EME	$\mathcal{D}_B^0 > \mathcal{D}_A^0$	$\theta_A^0 < \theta_B^0 < 1$	No Inverse TME

proportionality constant may depend on the details of the VDF—see Eq. (24) below for the specific example of a gamma distribution. Within this approximation, the first case, $t_D < t_\theta$, is expected if $|a_{2A}(t_\theta)| < |a_{2B}(t_\theta)|$, while the second case, $t_D > t_\theta$, is expected if $|a_{2A}(t_\theta)| > |a_{2B}(t_\theta)|$. Both scenarios are possible, even recalling that $a_{2A}(t_\theta) > a_{2B}(t_\theta)$ is a necessary condition to have the TME, because the sign of the excess kurtoses of samples A and B may be different. For the case of the inverse TME, the sign of $t_D - t_\theta$ coincides again with that of $|a_{2A}(t_\theta)| - |a_{2B}(t_\theta)|$.

The different possibilities analyzed above for the case $\mathcal{D}_A^0 > \mathcal{D}_B^0$ are summarized in Table I, specifically as cases labeled ET1, TE1 (for the direct ME) and ET2, TE2 (for the inverse ME).

Now we move onto the situation in which the further from equilibrium sample in the kinetic approach (A) is, however, the closer to equilibrium in the entropic approach, $\mathcal{D}_A^0 < \mathcal{D}_B^0$. On account of Eq. (12b), the condition $\mathcal{D}_B^0 > \mathcal{D}_A^0$ requires

$$\mathcal{D}_B^{\text{kin},0} - \mathcal{D}_A^{\text{kin},0} > \frac{d}{2} \left(\theta_A^0 - \theta_B^0 - \ln \frac{\theta_A^0}{\theta_B^0} \right) > 0. \quad (20)$$

Additional cases are possible, which are labeled as T1, T2, E1, and E2 in Table I. The TME and the EME are no longer biunivocally related. For example, in the T1 case, the direct TME is present but no genuine EME takes place: $\theta_A^0 > \theta_B^0 > 1$ and $\theta_B(t) > \theta_A(t) > 1$ for $t > t_\theta$, but $\mathcal{D}_B > \mathcal{D}_A$ both initially and for asymptotically long times. Note, however, that this does not prevent the difference $\mathcal{D}_B(t) - \mathcal{D}_A(t)$ from changing its sign an even number of times during the transient relaxation.

To fix ideas and for further use, let us take the VDF corresponding to a gamma distribution [85] for the probability density of the variable $x = c^2$. Using the condition $\langle c^2 \rangle = \frac{d}{2}$, the reduced VDF associated with the gamma distribution reads

$$\phi(\mathbf{c}) = \pi^{-d/2} \frac{\Gamma(\frac{d}{2}) z^{d/2}}{\Gamma(\frac{dz}{2})} c^{d(z-1)} e^{-zc^2}, \quad z \equiv \frac{1}{1 + \frac{d+2}{2} a_2}. \quad (21)$$

Note that this includes the LE distribution, Eq. (B10), as the special case $a_2 = 0$. Thus, the deviations of the distribution (21) from LE are monitored by the excess

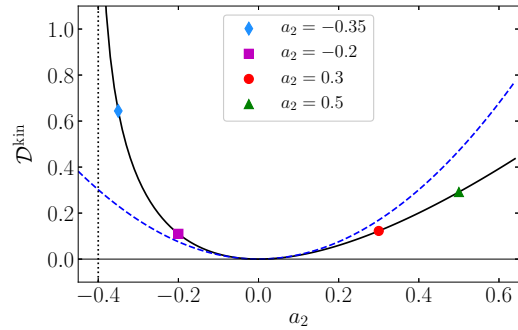


FIG. 3. Dependence of \mathcal{D}^{kin} with a_2 for a gamma distribution. Specifically, we plot the exact expression (solid line), given by Eq. (23), and the small $|a_2|$ approximation (dotted line), given by Eq. (24), for $d = 3$. Symbols correspond to the particular values at $a_2 = -0.35, -0.20, 0.30$, and 0.50 considered in Table II.

kurtosis a_2 only. In particular, the sixth cumulant is given by

$$a_3 = \frac{4}{d+4} a_2 \left(1 - \frac{d+2}{2} a_2 \right). \quad (22)$$

The KLD of the gamma distribution with respect to the LE one is [86]

$$\mathcal{D}^{\text{kin}} = \frac{d}{2} \left\{ \ln z + (z-1) \left[\psi \left(\frac{dz}{2} \right) - 1 \right] \right\} + \ln \frac{\Gamma(\frac{d}{2})}{\Gamma(\frac{dz}{2})}, \quad (23)$$

in which $\psi(x) = d \ln \Gamma(x) / dx$ is the digamma function [87]. For small $|a_2|$, one has

$$\mathcal{D}^{\text{kin}} \approx \frac{d(d+2)^2}{16} \left[\frac{d}{2} \psi' \left(\frac{d}{2} \right) - 1 \right] a_2^2, \quad (24)$$

where $\psi'(x) \equiv d\psi(x)/dx$.

The dependence of \mathcal{D}^{kin} , as given by Eq. (23), as a function of a_2 in the three-dimensional case ($d = 3$) is shown in Fig. 3. We observe that \mathcal{D}^{kin} grows more rapidly for negative than for positive values of a_2 , exhibiting a vertical asymptote at $a_2 = -2/(d+2)$, which corresponds to $z \rightarrow \infty$.

B. Linearized analysis

To provide a simple, but yet more quantitative, study, in the remainder of this section (and also in Sec. V) we adopt the linearization scheme put forward in Ref. [36]. The starting point is the BSA described by Eqs. (17) and (19a), setting $a_3 \rightarrow 0$ in the latter. Furthermore, the temperature ratio θ is linearized around a reference value θ_r close to $\theta^0 \equiv \theta(0)$. The solution of the resulting set of two differential equations is [36]

$$\begin{aligned} \theta(t) = & B_1 + [A_{11}(\theta^0 - B_1) - A_{12}(a_2^0 - B_2)] e^{-\lambda_- t} \\ & - [(A_{11} - 1)(\theta^0 - B_1) - A_{12}(a_2^0 - B_2)] e^{-\lambda_+ t}, \end{aligned} \quad (25a)$$

$$\begin{aligned} a_2(t) = & B_2 + [A_{22}(a_2^0 - B_2) - A_{21}(\theta^0 - B_1)] e^{-\lambda_- t} \\ & - [(A_{22} - 1)(a_2^0 - B_2) - A_{21}(\theta^0 - B_1)] e^{-\lambda_+ t}, \end{aligned} \quad (25b)$$

in which $a_2^0 \equiv a_2(0)$, and the expressions of the parameters λ_{\pm} , B_i , and A_{ij} can be found in Appendix C. We refer to Eqs. (25) as the linearized basic Sonine approximation (LBSA). When using the LBSA to investigate the ME, we are assuming that $\theta(t)$ is close to θ_r , which in turn is close to θ^0 . This entails that the LBSA is expected to be applicable to the kinetic stage only—i.e., when the ME comes about for short times.

The LBSA can be applied to the evolution of the two samples A and B with the convenient choice $\theta_r = \theta_B^0$ [36]. It is then straightforward to find the crossover time t_{θ} as

$$t_{\theta} = \frac{1}{\lambda_+ - \lambda_-} \ln \left(1 + \frac{A_{11}^{-1}}{R_{\max}^0/R^0 - 1} \right), \quad (26)$$

where

$$R^0 \equiv \frac{\theta_A^0 - \theta_B^0}{a_{2A}^0 - a_{2B}^0}, \quad R_{\max}^0 \equiv \frac{A_{12}}{A_{11}}. \quad (27)$$

Therefore, in the LBSA, the crossover time t_{θ} depends on the set of four initial values θ_A^0 , a_{2A}^0 , θ_B^0 , and a_{2B}^0 only through the ratio R^0 . Moreover, Eq. (26) is meaningful only if

$$0 < R^0 < R_{\max}^0. \quad (28)$$

Otherwise, no TME—either direct or inverse—exists.

The determination of the crossover time $t_{\mathcal{D}}$ is much more involved, even in the simple LBSA. It is obtained as the solution of a transcendental equation and the solution depends on θ_A^0 , a_{2A}^0 , θ_B^0 , and a_{2B}^0 . The locus separating the region where $t_{\mathcal{D}} < t_{\theta}$ from the region where $t_{\mathcal{D}} > t_{\theta}$ is approximately given by the condition $|a_{2A}(t_{\theta})| = |a_{2B}(t_{\theta})|$; the sign of $t_{\mathcal{D}} - t_{\theta}$ is the same as that of $|a_{2A}(t_{\theta})| - |a_{2B}(t_{\theta})|$ —as discussed in the previous section. See cases ET1, TE1, ET2, and TE2 in Table I. Furthermore, cases T1, T2, E1, and E2 are possible if the initial values of the KLD cross the locus $\mathcal{D}_A^0 = \mathcal{D}_B^0$, as

TABLE II. Four representative choices for the initial values a_{2A}^0 and a_{2B}^0 ($d = 3$). The numerical values of \mathcal{D}^{kin} , as given by Eq. (23) with $d = 3$, are also included. The sixth column gives the cases (see Table I) that, in principle, are associated with each pair (a_{2A}^0, a_{2B}^0) . However, some of them (enclosed in parentheses) are not actually observed (see Fig. 4).

Label	a_{2A}^0	a_{2B}^0	$\mathcal{D}_A^{\text{kin},0}$	$\mathcal{D}_B^{\text{kin},0}$	Cases
I	0.50	-0.35	0.292	0.644	ET1, (TE1), T1, E1, E2
II	0.50	-0.20	0.292	0.110	ET1, TE1
III	-0.35	0.30	0.644	0.122	ET2, TE2
IV	-0.20	0.50	0.110	0.292	(ET2), (TE2), T2, E1, E2

summarized in Table I and described in Sec. IV A. If the locus $\mathcal{D}_A^0 = \mathcal{D}_B^0$ happens to separate regions ET1 and T1 (or ET2 and T2), then one has $t_{\mathcal{D}} \rightarrow 0$ on the locus, so that $0 < t_{\mathcal{D}} < t_{\theta}$ in region ET1 (or ET2) and formally $t_{\mathcal{D}} < 0 < t_{\theta}$ in region T1 (or T2).

C. Illustrative examples

Let us choose the four representative pairs (a_{2A}^0, a_{2B}^0) presented in Table II. Since the scenarios ET1 and TE1 described in Table I require $a_{2A}^0 > a_{2B}^0$, they are *in principle* feasible for the pairs I and II. Analogously, the scenarios ET2 and TE2 might be possible for the pairs III and IV. Next, by assuming the initial VDF has the gamma form, Eq. (21), we have $\mathcal{D}_B^{\text{kin},0} > \mathcal{D}_A^{\text{kin},0}$ for the pairs I and IV, but not for the pairs II and III; in view of Eq. (20), we conclude that, *in principle*, cases T1, E1, and E2 are possible for pair I and cases T2, E1, and E2 for pair IV.

The phase diagrams predicted by the LBSA are shown in Fig. 4 for $\zeta_0 = 1$, $\gamma = 0.1$, and $d = 3$. We observe that, at least for that choice of the parameters, case TE1 is absent for the class of initial conditions I, while cases ET2 and TE2 are absent for the class of initial conditions IV. This confirms that the initial conditions shown in the third column of Table I for the cases ET1, TE1, ET2, and TE2 represent necessary—but not sufficient—conditions for their occurrence, the actual realization of those scenarios depending on the evolution of $a_{2A}(t)$ and $a_{2B}(t)$.

The time evolution of the differences

$$\Delta \mathcal{D} \equiv \mathcal{D}_A - \mathcal{D}_B, \quad \Delta \mathcal{D}^{\text{LE}} \equiv \mathcal{D}_A^{\text{LE}} - \mathcal{D}_B^{\text{LE}} \quad (29)$$

for the representative points indicated in Fig. 4 are displayed in Figs. 5–8, where the difference $\Delta \mathcal{D}^{\text{kin}} = \mathcal{D}_A^{\text{kin}} - \mathcal{D}_B^{\text{kin}} = \Delta \mathcal{D} - \Delta \mathcal{D}^{\text{LE}}$ is also included. The change of sign of $\mathcal{D}_A^{\text{LE}} - \mathcal{D}_B^{\text{LE}}$ and $\mathcal{D}_A - \mathcal{D}_B$ during their evolution signals the presence of the TME and EME, respectively. Here, we made an extra ansatz to evaluate $\mathcal{D}^{\text{kin}}(t)$. As we are working with an initial gamma distribution and the final equilibrium state is a particular case of such a distribution—with $a_2 = 0$, we have assumed that the VDF during its time evolution is sufficiently close to a

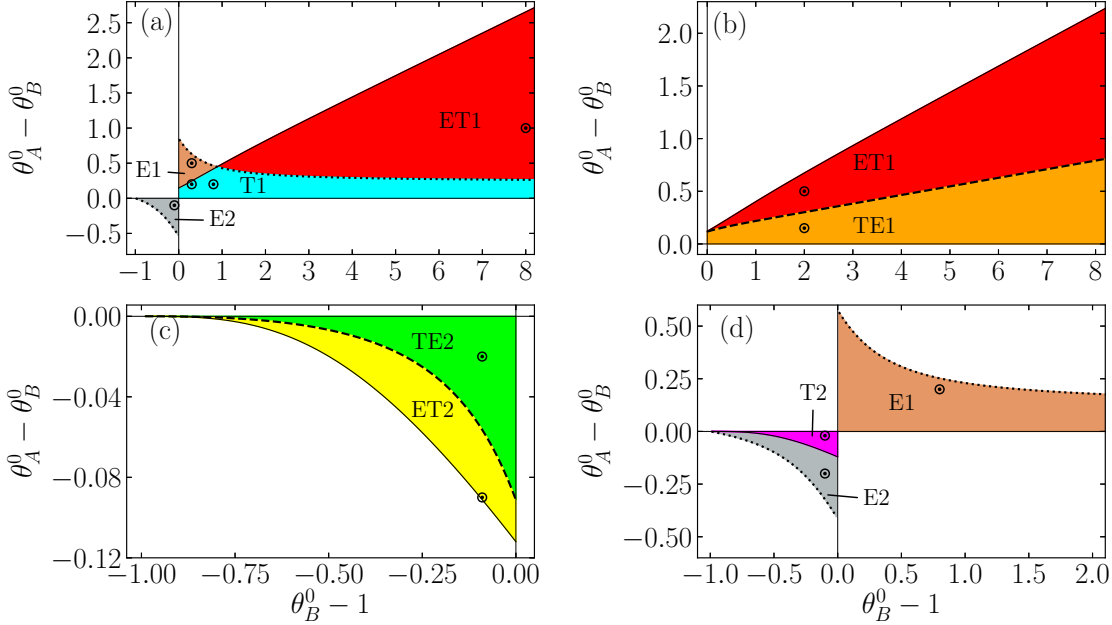


FIG. 4. Phase diagrams in the representation $\theta_A^0 - \theta_B^0$ vs $\theta_B^0 - 1$. Specifically, they are plotted for $\zeta_0 = 1$, $\gamma = 0.1$, $d = 3$, and the four representative choices of (a_{2A}^0, a_{2B}^0) displayed in Table II: (a) I, (b) II, (c) III, and (d) IV. The solid, dashed, and dotted lines represent the loci $R^0 = R_{\max}^0$, $t_\theta = t_D$, and $\mathcal{D}_A^0 = \mathcal{D}_B^0$, respectively. The labels in each region correspond to the cases described in Table I and the circles represent the specific examples considered in Figs. 5–8. Note that $\theta_A^0 > \theta_B^0 > 1$ and $\theta_A^0 < \theta_B^0 < 1$ refer to the direct TME and inverse TME, respectively.

gamma distribution so as to estimate $\mathcal{D}^{\text{kin}}(t)$ by Eq. (23) with an excess kurtosis $a_2(t)$ given by Eq. (25b).

Figures 5(b) and 5(c) are both examples of the scenario T1 for the class of initial conditions I. In Fig. 5(b), where $(\theta_B^0 - 1, \theta_A^0 - \theta_B^0) = (0.8, 0.2)$ [see Fig. 4(a)], the difference $\mathcal{D}_A^0 - \mathcal{D}_B^0$ presents a negative local maximum. When moving horizontally in Fig. 4(a) to the point $(\theta_B^0 - 1, \theta_A^0 - \theta_B^0) = (0.3, 0.2)$, however, Fig. 5(c) shows that the local maximum of $\mathcal{D}_A^0 - \mathcal{D}_B^0$ becomes positive and $\mathcal{D}_A^0 - \mathcal{D}_B^0$ vanishes twice during the time evolution. While interesting, this does not qualify as an EME because, as already said above Eq. (20), $\mathcal{D}_B > \mathcal{D}_A$ both initially and for asymptotically long times. Next, moving vertically in Fig. 4(a) to the point $(\theta_B^0 - 1, \theta_A^0 - \theta_B^0) = (0.3, 0.5)$, the local maximum observed in Fig. 5(d) is again positive but there is a single crossing $\mathcal{D}_A^0 - \mathcal{D}_B^0 = 0$, which results in the E1 scenario.

V. OVERSHOOT MPEMBA EFFECT

In Sec. IV, we have assumed that, even though the evolution of $\theta(t)$ may not be monotonic, $\theta(t) - 1$ does not change sign, i.e., the temperature does not overshoot the equilibrium value. However, such an overshoot $\theta(t_O) = 1$

at a finite time t_O is possible. In general, $a_2(t_O) \neq 0$, and Eq. (17) shows that $\dot{\theta}(t_O)/\zeta_0\gamma = -2(d+2)a_2(t_O) \neq 0$. As a consequence, starting from $\theta^0 > 1$, $\theta(t) - 1$ develops a hump with a negative minimum if $a_2(t_O) > 0$; analogously, starting from $\theta^0 < 1$ and if $a_2(t_O) < 0$, $\theta(t) - 1$ develops a hump with a positive maximum, reminiscent of the Kovacs effect [37, 88–94]. We will refer to this crossover $\theta(t_O) = 1$ and subsequent hump, either positive or negative, as an overshoot phenomenon.

Given the fact that the relaxation of $a_2(t)$ is generally much faster than that of $\theta(t)$, at least if $\theta^0 = O(1)$ [37], it is reasonable to expect that the overshoot effect requires initial values $|\theta^0 - 1| \ll 1$, unless $|a_2^0|$ is unphysically large. This suggests a theoretical treatment based on the LBSA (25) with $\theta_r \rightarrow 1$, i.e.,

$$\theta(t) = 1 + [\bar{A}_{11}(\theta^0 - 1) - \bar{A}_{12}a_2^0]e^{-\bar{\lambda}t} - [(\bar{A}_{11} - 1)(\theta^0 - 1) - \bar{A}_{12}a_2^0]e^{-\bar{\lambda}_+t}, \quad (30a)$$

$$a_2(t) = [\bar{A}_{22}a_2^0 - \bar{A}_{21}(\theta^0 - 1)]e^{-\bar{\lambda}t} - [(\bar{A}_{22} - 1)a_2^0 - \bar{A}_{21}(\theta^0 - 1)]e^{-\bar{\lambda}_+t}, \quad (30b)$$

where overlined quantities refer to their values at $\theta_r = 1$. Following the same methodology as in Eqs. (26) and (27),

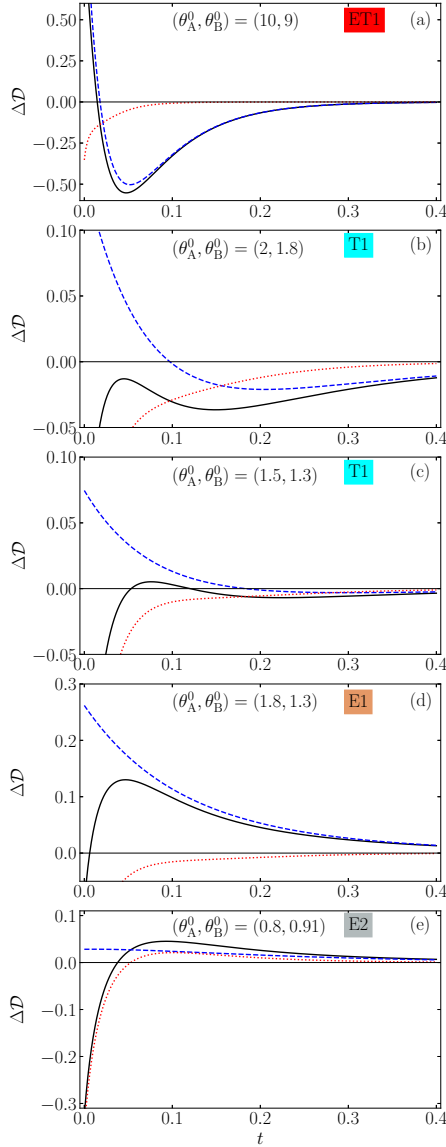


FIG. 5. Time evolution of the difference of the relative entropies for the representative initial condition I in Table II, $(a_{2A}^0, a_{2B}^0) = (0.50, -0.35)$. Parameter values are $\zeta_0 = 1$, $\gamma = 0.1$, $d = 3$. Specifically, we represent $\mathcal{D}_A^{\text{kin}} - \mathcal{D}_B^{\text{kin}}$ (dotted lines), $\mathcal{D}_A^{\text{LE}} - \mathcal{D}_B^{\text{LE}}$ (dashed lines), and $\mathcal{D}_A - \mathcal{D}_B$ (solid lines) for different pairs of initial temperatures, namely: (a) $(\theta_B^0 - 1, \theta_A^0 - \theta_B^0) = (8, 1)$, (b) $(\theta_B^0 - 1, \theta_A^0 - \theta_B^0) = (0.8, 0.2)$, (c) $(\theta_B^0 - 1, \theta_A^0 - \theta_B^0) = (0.3, 0.2)$, (d) $(\theta_B^0 - 1, \theta_A^0 - \theta_B^0) = (0.3, 0.5)$, and (e) $(\theta_B^0 - 1, \theta_A^0 - \theta_B^0) = (-0.09, -0.11)$. Panels (a), (b), (c), (d) and (e) represent examples of cases ET1, T1, T1, E1, and E2, respectively [see Fig. 4(a)].

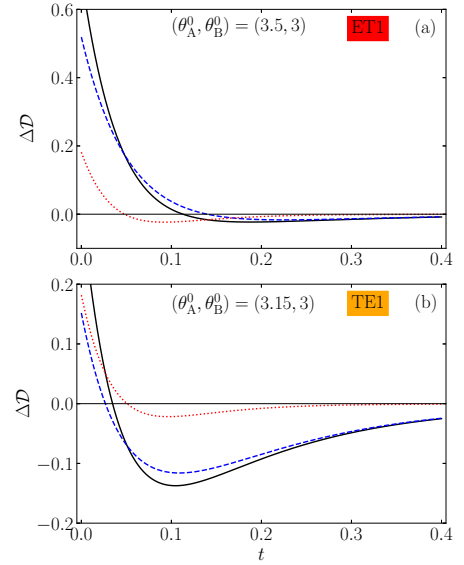


FIG. 6. Same as in Fig. 5, but now for the representative initial condition II in Table II, $(a_{2A}^0, a_{2B}^0) = (0.50, -0.20)$. Here, initial conditions for the temperatures are: (a) $(\theta_B^0 - 1, \theta_A^0 - \theta_B^0) = (2.0, 0.5)$ and (b) $(\theta_B^0 - 1, \theta_A^0 - \theta_B^0) = (2.00, 0.15)$. Panels (a) and (b) represent examples of cases ET1 and TE1, respectively [see Fig. 4(b)].

we find

$$t_O = \frac{1}{\lambda_+ - \lambda_-} \ln \left[1 + \frac{\bar{A}_{11}^{-1}}{R_{\max}^0 a_2^0 / (\theta^0 - 1) - 1} \right], \quad (31)$$

where

$$\bar{R}_{\max}^0 \equiv \frac{\bar{A}_{12}}{\bar{A}_{11}}. \quad (32)$$

Therefore, according to the LBSA, the overshoot effect appears if

$$0 < \frac{\theta^0 - 1}{a_2^0} < \bar{R}_{\max}^0. \quad (33)$$

It is interesting to look into the possible change of the ME phenomenology brought about by the overshoot-induced humps. As we show below, the existence of humps may make it necessary to change the preception of considering the TME present only when the evolution curves of the temperature of the two samples intersect. To be more specific, we consider, as before, samples A and B with A being the initially hotter, i.e., $\theta_A^0 > \theta_B^0 > 1$. Let us assume that the colder sample B fulfills condition (33) but the hotter sample does not. In that case, $\theta_B(t)$ might not be crossed by the curve $\theta_A(t)$, which remains always above the equilibrium temperature, and yet relax more slowly to equilibrium than A

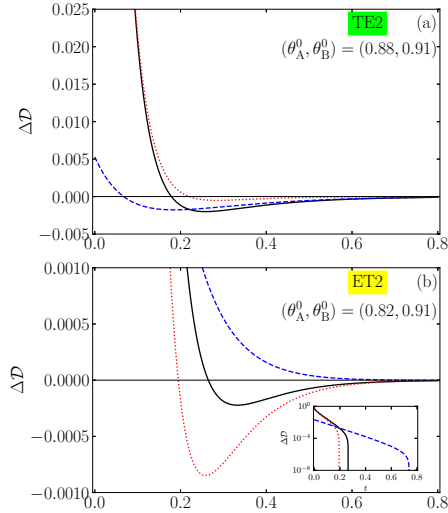


FIG. 7. Same as in Fig. 5, but now for the representative initial condition III in Table II, $(a_{2A}^0, a_{2B}^0) = (-0.35, 0.30)$. In this case, the initial conditions for the temperatures chosen are: (a) $(\theta_B^0 - 1, \theta_A^0 - \theta_B^0) = (-0.09, -0.03)$ and (b) $(\theta_B^0 - 1, \theta_A^0 - \theta_B^0) = (-0.09, -0.09)$. Panels (a) and (b) represent examples of cases TE2 and ET2, respectively [see Fig. 4(c)]. Note that $\Delta\mathcal{D}$ is plotted in logarithmic scale in the inset of panel (b) to favor the perception of the crossover times, at which $\Delta\mathcal{D}$ vanishes.

but from below. We could then say that a (direct) TME is present without the existence of a standard crossover time t_θ , provided that a crossover between the LE KLD curves $\mathcal{D}_A^{\text{LE}}(t)$ and $\mathcal{D}_B^{\text{LE}}(t)$ occurs at a certain time $t_{\mathcal{D}^{\text{LE}}}$. A completely analogous situation is possible for the inverse ME, i.e., when $\theta_A^0 < \theta_B^0 < 1$. We will refer to this phenomenon, where $\mathcal{D}_A^{\text{LE}}$ and $\mathcal{D}_B^{\text{LE}}$ intersect but $\theta_A(t)$ and $\theta_B(t)$ do not, as the overshoot ME (OME). This phenomenon is reminiscent of the ME observed in Ref. [21] in supercooled water.

The different scenarios where overshoot-induced humps appear are illustrated in Fig. 9 for direct preparations, i.e., $\theta_A^0 > \theta_B^0 > 1$. In Fig. 9(a), $\theta_A(t)$ and $\theta_B(t)$ do not cross each other, but they both exhibit humps, the one in system B being stronger than in system A. This makes the latter system relax to equilibrium earlier than the former, which physically qualifies as a direct TME. While in the thermal scheme there is no crossing, the positiveness of \mathcal{D}^{LE} forces an intersection between A and B curves, as observed in Fig. 9(b). This is the essence of the OME.

On the other hand, the existence of humps or of a finite crossover time t_θ does not ensure the existence of TME. In fact, in Fig. 9(c) there is a crossing between the thermal curves, but the overshoot-induced humps make the initially hotter system relax later to the equilibrium state, thus frustrating the TME. This is signaled by a

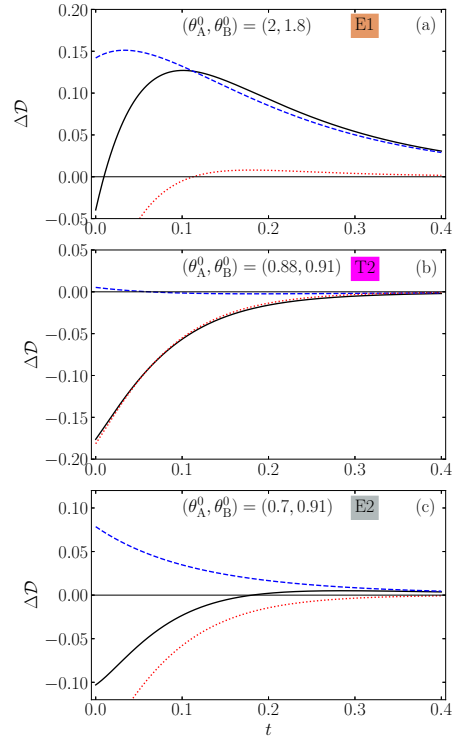


FIG. 8. Same as in Fig. 5, but now for the representative initial condition IV in Table II, $(a_{2A}^0, a_{2B}^0) = (-0.20, 0.50)$. Here, initial temperatures are: (a) $(\theta_B^0 - 1, \theta_A^0 - \theta_B^0) = (0.8, 0.2)$, (b) $(\theta_B^0 - 1, \theta_A^0 - \theta_B^0) = (-0.09, -0.03)$, and (c) $(\theta_B^0 - 1, \theta_A^0 - \theta_B^0) = (-0.09, -0.21)$. Panels (a), (b), and (c) represent examples of cases E1, T2, and E2, respectively [see Fig. 4(d)].

pair of intersections in the \mathcal{D}^{LE} curves of Fig. 9(d), so the OME is absent. The third different scenario is reflected in Figs. 9(e) and 9(f), where there is no crossover either in the thermal evolution or in \mathcal{D}^{LE} , even though sample B exhibits a thermal hump.

The analogous cases for inverse preparations $\theta_A^0 < \theta_B^0 < 1$ are illustrated in Fig. 10.

To summarize, the OME is characterized by a single crossing $\mathcal{D}_A^{\text{LE}} = \mathcal{D}_B^{\text{LE}}$ at a certain time $t_{\mathcal{D}^{\text{LE}}}$, without any crossing between θ_A and θ_B . In order to establish the conditions under which this may happen, let us assume again $|\theta - 1| \ll 1$ and approximate $\ln \theta \approx \theta - 1 - \frac{1}{2}(\theta - 1)^2$ in Eq. (12b). Therefore, the condition $\mathcal{D}_A^{\text{LE}}(t_{\mathcal{D}^{\text{LE}}}) = \mathcal{D}_B^{\text{LE}}(t_{\mathcal{D}^{\text{LE}}})$ with $\theta_A(t_{\mathcal{D}^{\text{LE}}}) \neq \theta_B(t_{\mathcal{D}^{\text{LE}}})$ translates into

$$\theta_A(t_{\mathcal{D}^{\text{LE}}}) - 1 = 1 - \theta_B(t_{\mathcal{D}^{\text{LE}}}). \quad (34)$$

Making use of Eq. (30a) entails

$$t_{\mathcal{D}^{\text{LE}}} = \frac{1}{\lambda_+ - \lambda_-} \ln \left(1 + \frac{\bar{A}_{11}^{-1}}{R_{\text{max}}^0 / R_+^0 - 1} \right), \quad (35)$$

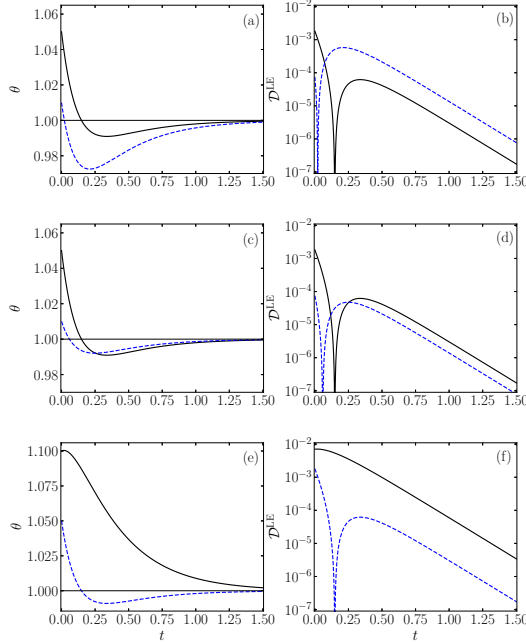


FIG. 9. Time evolution of the temperature and LE relative entropy of samples A and B for the direct case, $\theta_A^0 > \theta_B^0 > 1$. Specifically, we show $\{\theta_A, \mathcal{D}_A^{\text{LE}}\}$ (solid lines) and $\{\theta_B, \mathcal{D}_B^{\text{LE}}\}$ (dashed lines), as obtained from Eq. (30a). Initial conditions are [(a) and (b)] $(\theta_A^0, \theta_B^0) = (1.05, 1.01)$ and $(a_{2A}^0, a_{2B}^0) = (0.5, 0.5)$, [(c) and (d)] $(\theta_A^0, \theta_B^0) = (1.05, 1.01)$ and $(a_{2A}^0, a_{2B}^0) = (0.5, 0.2)$, and [(e) and (f)] $(\theta_A^0, \theta_B^0) = (1.1, 1.05)$ and $(a_{2A}^0, a_{2B}^0) = (-0.35, 0.5)$. In all cases, $\zeta_0 = 1$, $\gamma = 0.1$, and $d = 3$.

where \bar{R}_{max}^0 is defined in Eq. (32) and

$$R_+^0 \equiv \frac{\theta_A^0 + \theta_B^0 - 2}{a_{2A}^0 + a_{2B}^0}. \quad (36)$$

Note the difference between this parameter R_+^0 and the parameter R^0 defined before in Eq. (27). Since $t_{\mathcal{D}^{\text{LE}}}$ must be finite in the OME, the corresponding condition on the initial preparation is

$$0 < R_+^0 < \bar{R}_{\text{max}}^0, \quad (37a)$$

$$R^0 < 0 \text{ or } R^0 > \bar{R}_{\text{max}}^0. \quad (37b)$$

The supplementary condition (37b) represents the violation of Eq. (28) (with $\theta_r \rightarrow 1$) and is needed to exclude any thermal crossing.

According to Eq. (33), if both systems A and B exhibit overshoot-induced humps, the condition given by Eq. (37a) is ensured. As a test, note that $\bar{R}_{\text{max}}^0 = 0.172$ for all the cases considered in Figs. 9 and 10. The

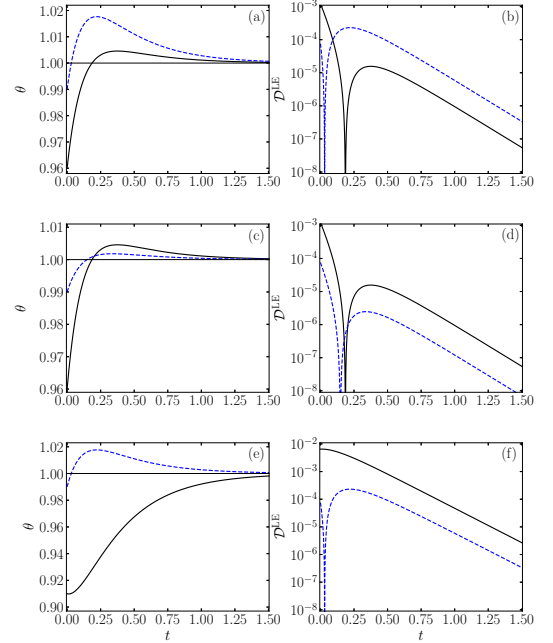


FIG. 10. Same as in Fig. 9, but now for the inverse case $\theta_A^0 < \theta_B^0 < 1$. Initial conditions are [(a) and (b)] $(\theta_A^0, \theta_B^0) = (0.96, 0.99)$ and $(a_{2A}^0, a_{2B}^0) = (-0.35, -0.35)$, [(c) and (d)] $(\theta_A^0, \theta_B^0) = (0.96, 0.99)$ and $(a_{2A}^0, a_{2B}^0) = (-0.35, -0.1)$, and [(e) and (f)] $(\theta_A^0, \theta_B^0) = (0.91, 0.99)$ and $(a_{2A}^0, a_{2B}^0) = (0.3, -0.35)$.

values of (R_+^0, R^0) are $(0.060, \infty)$, $(0.086, 0.133)$, and $(1, -0.059)$ in the cases represented in Figs. 9(a) and 9(b), Figs. 9(c) and 9(d), and Figs. 9(e) and 9(f), respectively. Analogously, (R_+^0, R^0) are $(0.071, \infty)$, $(0.111, 0.120)$, and $(2, -0.123)$ in the cases represented in Figs. 10(a) and 10(b), Figs. 10(c) and 10(d), and Figs. 10(e) and 10(f), respectively. Thus, the OME double condition (37) is fulfilled only in the cases (a) and (b) of Figs. 9 and 10.

VI. SIMULATION RESULTS

In this section, our simulation results are used to test the theoretical predictions stemming from the numerical solutions of: (i) the (nonlinear) BSA, Eqs. (17) and (19a) with $a_3 \rightarrow 0$, and ESA, Eqs. (17) and (19). The theoretical results for the KLD $\mathcal{D}(t)$ and $\mathcal{D}^{\text{LE}}(t)$ are constructed by introducing the theoretical $\theta(t)$ and $a_2(t)$ in Eqs. (12b) and (23), respectively.

The employed computer simulation schemes, DSMC and EDMD, to build the simulation curves are presented in Appendix D. In all cases, the (reduced) initial VDF has been taken as the gamma distribution given by Eq. (21) with the chosen value of the initial excess kurtosis a_2^0 ,

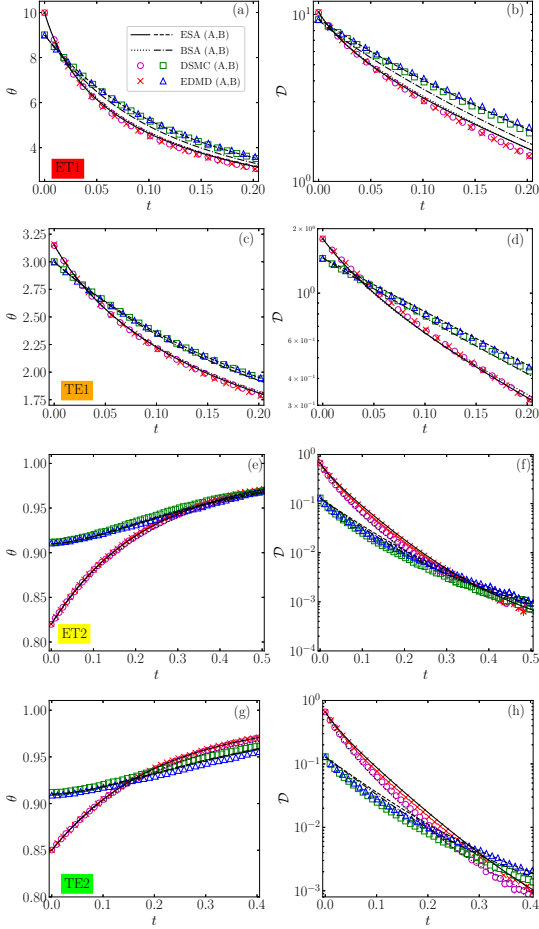


FIG. 11. ME for cases when $\theta - 1$ does not change its sign. Specifically, we plot the time evolution of the temperature and relative entropy for samples A and B: $\{\theta_A, \mathcal{D}_A\}$ (solid and dotted lines, circles, and crosses) and $\{\theta_B, \mathcal{D}_B\}$ (dashed and dash-dotted lines, squares, and triangles). Initial conditions are [(a) and (b)] $(\theta_A^0, \theta_B^0) = (10, 9)$ and $(a_{2A}^0, a_{2B}^0) = (0.5, -0.35)$, [(c) and (d)] $(\theta_A^0, \theta_B^0) = (3.15, 3)$ and $(a_{2A}^0, a_{2B}^0) = (0.5, -0.2)$, [(e) and (f)] $(\theta_A^0, \theta_B^0) = (0.82, 0.91)$ and $(a_{2A}^0, a_{2B}^0) = (-0.35, 0.3)$, and [(g) and (h)] $(\theta_A^0, \theta_B^0) = (0.85, 0.91)$ and $(a_{2A}^0, a_{2B}^0) = (-0.35, 0.3)$. Other parameter values are $\zeta_0 = 1$, $\gamma = 0.1$, and $d = 3$.

as previously done in Refs. [39, 95, 96]. The KLD from simulations is computed as described in Refs. [95, 96].

Figures 11 and 12 contain the theoretical and simulation results of the time evolution of the temperature ratio θ and the KLD \mathcal{D} . The graphs for the cumulants a_2 and a_3 are presented in Appendix E. Samples A and B are prepared with the representative values of the cumulants in Table II, namely pairs I and II (III and IV) for

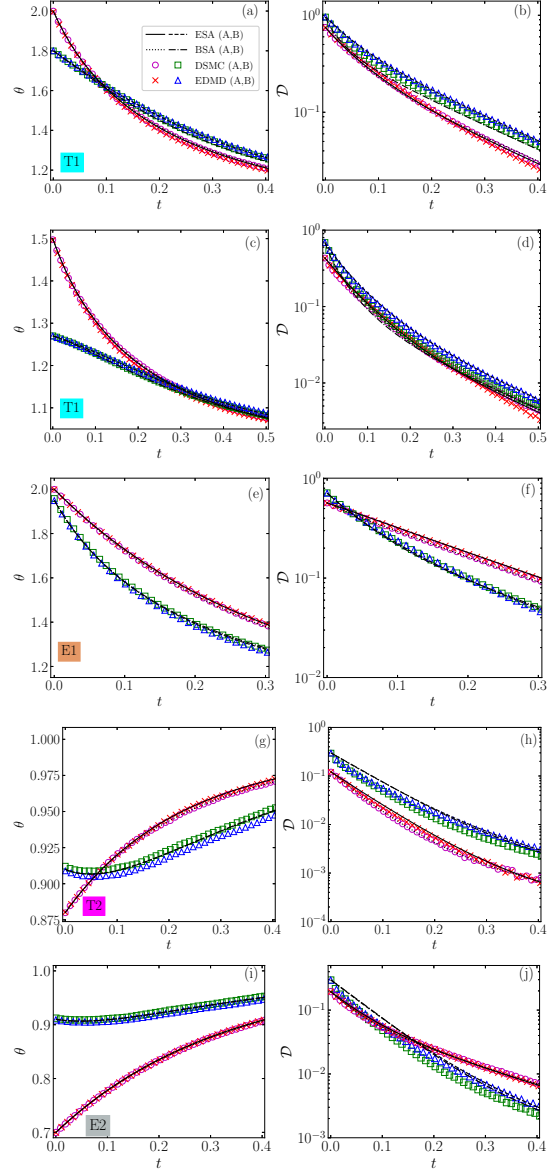


FIG. 12. Same as in Fig. 11, except that the initial conditions are [(a) and (b)] $(\theta_A^0, \theta_B^0) = (2, 1.8)$ and $(a_{2A}^0, a_{2B}^0) = (0.5, -0.35)$, [(c) and (d)] $(\theta_A^0, \theta_B^0) = (1.5, 1.27)$ and $(a_{2A}^0, a_{2B}^0) = (0.5, -0.35)$, [(e) and (f)] $(\theta_A^0, \theta_B^0) = (2, 1.95)$ and $(a_{2A}^0, a_{2B}^0) = (-0.2, 0.5)$, [(g) and (h)] $(\theta_A^0, \theta_B^0) = (0.88, 0.91)$ and $(a_{2A}^0, a_{2B}^0) = (-0.2, 0.5)$, and [(i) and (j)] $(\theta_A^0, \theta_B^0) = (0.7, 0.91)$ and $(a_{2A}^0, a_{2B}^0) = (-0.2, 0.5)$.

the direct (inverse) ME, and different values of the initial temperatures θ_A^0 and θ_B^0 . Pairs (θ_A^0, θ_B^0) are chosen

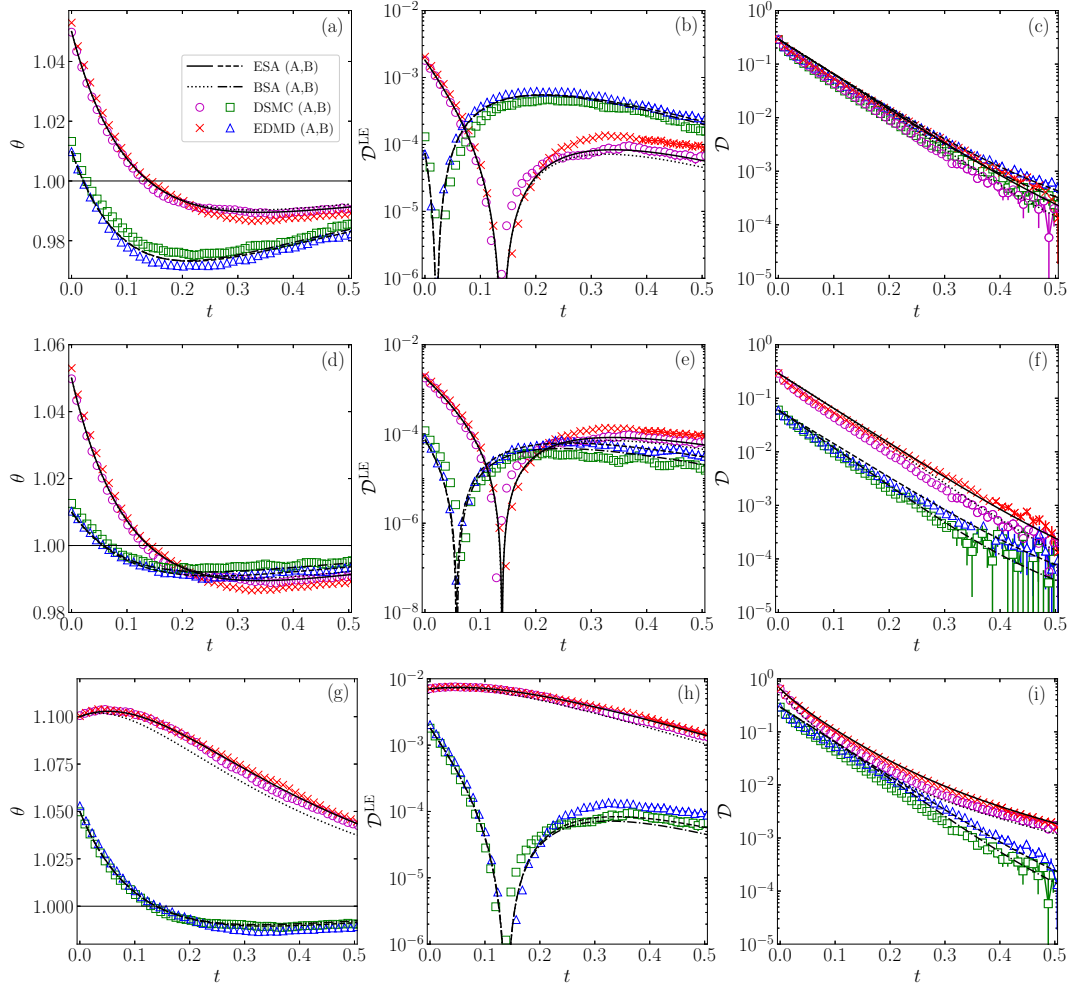


FIG. 13. ME for cases case in which $\theta - 1$ changes sign, i.e., the OME. In this case, we show the time evolution of: $\{\theta_A, \mathcal{D}_A^{\text{LE}}, \mathcal{D}_A\}$ (solid and dotted lines, circles, and crosses) and $\{\theta_B, \mathcal{D}_B^{\text{LE}}, \mathcal{D}_B\}$ (dashed and dash-dotted lines, squares, and triangles). Parameter values and initial conditions correspond to those in Fig. 9.

to illustrate the different cases summarized in Table I. Specifically, we present the cases ET1 in Figs. 11(a) and 11(b), TE1 in Figs. 11(c) and 11(d), ET2 in Figs. 11(e) and 11(f), TE2 in Figs. 11(g) and 11(h), T1 in Figs. 12(a) and 12(b), T1 with a double crossing in \mathcal{D} in Figs. 12(c) and 12(d), E1 in Figs. 12(e) and 12(f), T2 in Figs. 12(g) and 12(h), and E2 in Figs. 12(i) and 12(j). Note that the cases in Figs. 11(a) and 11(b), 11(c) and 11(d), 11(e) and (f), 12(a) and 12(b), 12(g) and 12(h), and 12(i) 12(j) are the same as in Figs. 5(a), 6(b), 7(b), 5(b), 8(b), and 8(c), respectively. Moreover, the case in Figs. 12(c) and 12(d) is close to the case in Fig. 5(c).

It must be remarked that the classification of the case

in Figs. 11(e) and 11(f) as ET2 is less clear than expected. The LBSA theory predicts the ET2 behavior with a wide difference between t_θ and $t_{\mathcal{D}}$, as observed in the inset of Fig. 7(b). Still, nonlinearities reduce the time difference $t_\theta - t_{\mathcal{D}}$. Moreover, the double crossing in \mathcal{D} predicted by the LBSA for the case of Figs. 12(c) and 12(c)(d) is not actually observed in the simulations. The shallow positive maximum of $\mathcal{D}_A - \mathcal{D}_B$ predicted by the LBSA, as seen in Fig. 5(c), is washed out by nonlinear contributions—at least in the case represented in Figs. 12(c) and 12(d).

Let us now turn to the OME predicted by the LBSA, which we have discussed in Sec. V. Figures 13 and 14

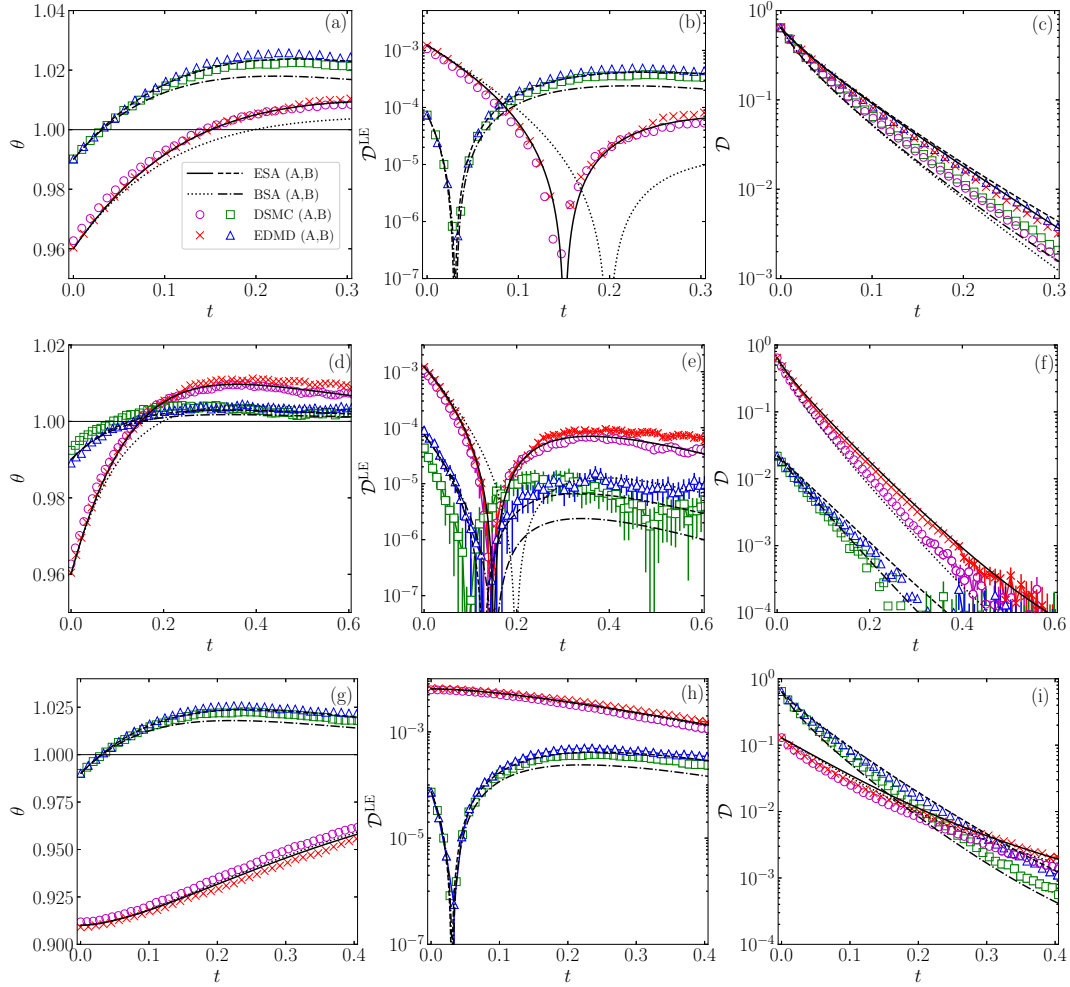


FIG. 14. Same as in Fig. 13, but now for the initial conditions in Fig. 10.

show the time evolution of θ , \mathcal{D}^{LE} , and \mathcal{D} for the same cases as considered in Figs. 9 and 10, respectively. Again, the graphs for a_2 and a_3 can be found in Appendix E. We see that the overshoot behavior and the OME phenomenology are indeed present. The crossover characterizing the TME is accounted for by the intersection of the \mathcal{D}^{LE} curves in Figs. 13(a)–13(c) and 14(a)–14(c), though the corresponding temperature curves never cross.

The figures in this section show that our theoretical predictions for both $\theta(t)$ and $\mathcal{D}(t)$ are generally in very good agreement with DSMC and EDMD simulation results. This is especially true for the ESA, which still gives a good account of the behavior of the fourth cumulant $a_2(t)$ and a fair account of the behavior of the sixth cumulant $a_3(t)$ (see Figs. 17–20), consistently with the results

reported in Ref. [37]. The improvement of the ESA over the BSA can be understood by noticing that the values of the cumulant a_3 are typically of the same magnitude as those of a_2 . It is also worth highlighting the generally good agreement between the simulation results for the relative entropy \mathcal{D} and those obtained from Eqs. (12b) and (23) when θ and a_2 are given by either the BSA or the ESA. This means that the gamma distribution in Eq. (21) represents a convenient proxy of the unknown time-dependent VDF. This ansatz is further confirmed by the generally fair agreement (not shown) between the simulation data for a_3 and the right-hand side of Eq. (22) when plugging the simulation data of a_2 , especially in the cases with $a_2 < 0$.

Finally, we note that small deviations between EDMD

and DSMC simulation are observed (especially for the subtler quantities \mathcal{D} and a_3), despite the low density of the systems. This might be a consequence of the approximations carried out in the numerical implementation of the Langevin dynamics in the *approximate Green function* (AGF) algorithm explained in Appendix D2. Nevertheless, there is a good agreement for the collisional scheme, as tested in Appendix D3.

VII. CONCLUSIONS

In this paper, we have analyzed in depth the relaxation to equilibrium of a dilute gas of elastic hard spheres subjected to a nonlinear drag and the associated stochastic force. We have particularly focused on two versions of the ME, namely, the TME and the EME. Our analysis combines theory and simulation. The theoretical approach is based on a Sonine expansion of the solution of the EFPE, Eq. (3). The simulation approach comprises both DSMC results, which integrate numerically Eq. (3), and EDMD results.

We have employed the Kullback–Leibler divergence (or relative entropy) \mathcal{D} , defined in Eq. (9), to measure the distance to equilibrium and monitor the possible emergence of the EME. It must be remarked that other distances to equilibrium have been employed in the literature, as long as they share some common properties of monotonicity, convexity, etc. However, the choice of the distance function does not impinge on the existence of the EME—for a thorough discussion of this issue, see Ref. [51]. The KLD choice for the distance function is quite natural due, to its connection to the nonequilibrium entropy, and especially convenient for comparing the TME and EME, since \mathcal{D} can be decomposed into two summands, see Eqs. (11) and (12). First, the hydrodynamic LE contribution \mathcal{D}^{LE} , which only depends on the temperature and, second, the kinetic-stage correction \mathcal{D}^{kin} , which depends on the whole VDF. To obtain an approximate expression for the latter within the Sonine approximation, we have employed the gamma distribution function, Eq. (23).

For given values of the drag force, i.e., given values of (ζ_0, γ) , the emergence of ME—either direct or inverse—depends on the initial preparations of the two samples (A, whose initial temperature is farther from equilibrium, and B, whose initial temperature is closer to equilibrium). The simplest approach, based on heuristic arguments, is the LBSA given by Eqs. (25). Therein, both the temperature ratio $\theta(t)$ and the excess kurtosis $a_2(t)$ are a linear superposition of two exponentials.

When the difference $\theta - 1$ keeps its initial sign during the relaxation process—i.e., when the temperature does not cross its equilibrium value at a finite time, we have the most usual, standard situation. Bringing to bear that the kinetic-stage contribution \mathcal{D}^{kin} is expected to decay to zero over a shorter timescale than that of the local equilibrium contribution \mathcal{D}^{LE} , we have argued that the

existence of TME implies that of EME (and vice versa) if $\mathcal{D}_A^0 > \mathcal{D}_B^0$. There are two possibilities: either the thermal crossover occurs earlier than the entropic one (scenarios TE1 and TE2 for direct and inverse effects, respectively) or it occurs later than the entropic crossover (scenarios ET1 and ET2 for direct and inverse effects, respectively).

Interestingly, even though θ_A^0 departs from the equilibrium value 1 more than θ_B^0 , one may have $\mathcal{D}_A^0 < \mathcal{D}_B^0$ due to the kinetic contribution \mathcal{D}^{kin} to the entropic distance. This gives rise to the existence of TME without entropy crossover (scenarios T1 and T2 for direct and inverse effects, respectively) or, reciprocally, the existence of EME without thermal crossover (scenarios E1 and E2 for direct and inverse effects, respectively).

A summary of all the possible scenarios above (assuming a constant sign of $\theta - 1$) is provided by Table I. The corresponding phase diagrams in the plane $\theta_A^0 - \theta_B^0$ vs $\theta_B^0 - 1$ are depicted in Fig. 4 for a few representative choices of the initial excess kurtoses a_{2A}^0 and a_{2B}^0 , given in Table II. Those scenarios are modified when the condition of constant sign of $\theta(t) - 1$ is violated, as explained below.

Nonmonotonic evolutions of θ with a crossing of the equilibrium line $\theta = 1$ induce the appearance of overshoot-induced humps. Sample B may relax to equilibrium later than sample A when the temperature of the former overshoots the equilibrium value, a fact that sample A can take advantage of. Even though $\theta_A(t)$ and $\theta_B(t)$ do not intersect, the corresponding curves of \mathcal{D}^{LE} do intersect. We have termed this class of ME as OME. Simple conditions for its existence, Eqs. (37), have been derived by adapting the LBSA to this situation.

The different scenarios for the ME outlined above for the nonlinear fluid, emerging in the extremely simplistic LBSA, have been tested and confirmed by computer simulations (both DSMC and EDMD). These numerical results have also been compared with the more complex nonlinear BSA and ESA. The inclusion of the additional cumulant a_3 in the set of coupled evolution equations allows the ESA to improve over the BSA. Moreover, DSMC and EDMD results are practically indistinguishable, with small discrepancies that can be traced back to the approximations in the EDMD scheme during the free streaming stage, see Appendix D2. On the other hand, the collisional schemes are tested in Appendix D3, with good results.

The ME effect is brought about by the nonlinearity in the drag force, which makes the time-evolution of the kinetic temperature be coupled to that of higher cumulants—specifically, to that of the excess kurtosis a_2 for the quadratic dependence of the drag coefficient in Eq. (7). The nonlinear drag force is also responsible for the algebraic nonexponential relaxation after a temperature quench and for the emergence of Kovacs-like response [37]. It is important to remark that these behaviors, and also the ME, survive in the limit $\zeta_0^* \rightarrow \infty$, in which the EFPE reduces to the Fokker–Planck equation—which, interestingly, successfully models mix-

tures of ultracold atoms [75].

The nonmonotonic relaxation of the kinetic temperature observed in the OME entails the necessity of revisiting the conventional definition of TME. Provided that both initial temperatures are either above (direct case) or below (inverse case) equilibrium, the TME is not necessarily characterized by the crossover of the nonequilibrium temperature but by the crossover of the associated positive-definite quantity \mathcal{D}^{LE} . Within this generalized scheme and for a general complex system, we propose the following, more dependable, definition of the TME based on the idea of local equilibrium: The TME exists in a pair of different initially prepared setups if there are an odd number of crossings between their LE relative entropy \mathcal{D}^{LE} curves. On another note, the definition of the EME is not affected, due to the monotonic decay of the whole relative entropy \mathcal{D} to equilibrium. The EME exists in a pair of samples if their relaxation curves for \mathcal{D} present an odd number of crossings.

It is relevant to stress that the splitting of \mathcal{D} into “kinetic” and “local-equilibrium” contributions can be done on quite a general basis, not only for the molecular fluid we are analyzing in this paper. Moreover, this allows for defining a nonequilibrium temperature $T(t)$, even in systems for which the kinetic temperature makes no sense. Let us consider a general system with Hamiltonian $H(\mathbf{x})$, in which $\mathcal{D}(t)$ is given by Eq. (2). The system is initially prepared in a certain state with average energy $\langle H \rangle^0$ and is put in contact with a thermal bath at temperature T_b . Thus the probability distribution function $P(\mathbf{x}, t)$ relaxes toward the equilibrium distribution $P^{\text{eq}}(\mathbf{x}) = \exp[-H(\mathbf{x})/k_B T_b]/Z(T_b)$, where $Z(T_b)$ is the partition function. One can always introduce a LE distribution with the canonical form $P^{\text{LE}}(\mathbf{x}, T(t)) \equiv \exp[-H(\mathbf{x})/k_B T(t)]/Z(T(t))$, with $T(t)$ being determined self-consistently by the condition

$$\langle H \rangle(t) = \int d\mathbf{x} H(\mathbf{x}) P(\mathbf{x}, t) = \int d\mathbf{x} H(\mathbf{x}) P^{\text{LE}}(\mathbf{x}, T(t)). \quad (38)$$

In this way, $T(t)$ corresponds to the temperature that a system would have at equilibrium if it had an average energy equal to the instantaneous value $\langle H \rangle(t)$. With such a definition of the nonequilibrium temperature $T(t)$, is it easily shown that

$$\mathcal{D}(t) = \mathcal{D}^{\text{kin}}(t) + \mathcal{D}^{\text{LE}}(T(t)), \quad (39)$$

where \mathcal{D}^{kin} and \mathcal{D}^{LE} are given by

$$\mathcal{D}^{\text{kin}}(t) = \int d\mathbf{x} P(\mathbf{x}, t) \ln \frac{P(\mathbf{x}, t)}{P^{\text{LE}}(\mathbf{x}, T(t))}, \quad (40a)$$

$$\mathcal{D}^{\text{LE}}(T(t)) = \int d\mathbf{x} P^{\text{LE}}(\mathbf{x}, T(t)) \ln \frac{P^{\text{LE}}(\mathbf{x}, T(t))}{P^{\text{eq}}(\mathbf{x})}. \quad (40b)$$

Note that $T(t)$ may in general overshoot its equilibrium value T_b , leading to an OME, but \mathcal{D}^{LE} is positive definite and makes it possible to introduce the more reliable definition of the TME explained in the previous paragraph [97].

We expect this work can motivate the experimental investigation, making use of a suitable aging protocol to prepare the initial samples, of the whole variety of ME phenomenology described in this work. Specifically, our predicting and observing the OME—as a novel unexpected behavior—in this molecular gas driven by a nonlinear drag opens the door to its finding in other complex systems. Also, we plan to employ the theoretical and computational framework developed here to study the relaxation times of pairs of temperature quenches thermodynamically equidistant from equilibrium [98, 99], one above and the other one below.

ACKNOWLEDGMENTS

A.M. and A.S. acknowledge financial support from Grant No. PID2020-112936GB-I00 funded by MCIN/AEI/10.13039/501100011033, and from Grants No. IB20079 and No. GR21014 funded by Junta de Extremadura (Spain) and by ERDF “A way of making Europe.” A.P. acknowledges financial support from Grant No. PGC2018-093998-B-I00 funded by MCIN/AEI/10.13039/501100011033/ and by ERDF “A way of making Europe.” A.M. is grateful to the Spanish Ministerio de Ciencia, Innovación y Universidades for a predoctoral fellowship FPU2018-3503. We are grateful to the computing facilities of the Instituto de Computación Científica Avanzada of the University of Extremadura (ICCAEx), where our simulations were run.

Appendix A: Langevin Equation under Nonlinear Drag

In this Appendix, we discuss the Langevin equation associated with the left-hand side of Eq. (3), since the effect of interparticle collisions represented by the right-hand side is well known.

Let us start writing the Langevin equation as

$$\dot{\mathbf{v}}(t) = -\zeta(v(t))\mathbf{v}_i(t) + \xi(v(t))\boldsymbol{\eta}(t), \quad (A1)$$

where $\boldsymbol{\eta}(t)$ is a Gaussian white-noise stochastic term with the statistical properties

$$\langle \boldsymbol{\eta}(t) \rangle_{\text{noise}} = 0, \quad \langle \boldsymbol{\eta}(t)\boldsymbol{\eta}(t') \rangle_{\text{noise}} = \mathbf{l}\delta(t-t'), \quad (A2)$$

where \mathbf{l} is the $d \times d$ unit tensor and $\langle \cdot \rangle_{\text{noise}}$ reads for an average over different realizations. Let us define a Wiener process $W(t)$ with elemental increment $dW(t) = \xi(v(t))\boldsymbol{\eta}(t)dt$. This is the case of a multiplicative noise and, therefore, there is no a unique way of interpreting the proper time within a given interval $[t, t+h]$ at which the process $W(t)$ must be evaluated [100]. In general, one can choose a time $t+\epsilon h$ parameterized by $0 \leq \epsilon \leq 1$.

Hence, the associated Fokker–Planck equation is [100]

$$\partial_t f(\mathbf{v}) - \frac{\partial}{\partial \mathbf{v}} \cdot \left[\zeta(v) \mathbf{v} + \frac{\xi^{2\epsilon}(v)}{2} \frac{\partial}{\partial \mathbf{v}} \xi^{2(1-\epsilon)}(v) \right] f(\mathbf{v}) = 0. \quad (\text{A3})$$

The specific choices $\epsilon = 0$, $\frac{1}{2}$, and 1 correspond to the Itô [67], Stratonovich [67], and Klimontovich [101] interpretations, respectively.

The (differential) fluctuation-dissipation relation stemming from Eq. (A3) turns out to be

$$\zeta(v) = \frac{m\xi^2(v)}{2k_B T_b} - \frac{1-\epsilon}{2v} \frac{\partial \xi^2(v)}{\partial v}. \quad (\text{A4})$$

Only in the Klimontovich interpretation ($\epsilon = 1$) does one recover the conventional fluctuation-dissipation relation, Eq. (5), holding for constant drag coefficient and additive noise. In that case, the left-hand sides of Eqs. (3) and (A3) coincide.

On the other hand, from a simulation point of view, the Itô interpretation ($\epsilon = 0$) is the simplest one to implement. Fortunately, even if $\epsilon \neq 0$ (as happens in the Stratonovich and Klimontovich interpretations), one can always apply the Itô interpretation to the Langevin equation, provided that the original drag coefficient $\zeta(v)$ is replaced by an effective one ζ_{eff} (“spurious drift”). Note first the mathematical identity

$$\xi^{2\epsilon}(v) \frac{\partial}{\partial \mathbf{v}} \xi^{2(1-\epsilon)}(v) f(\mathbf{v}) = \frac{\partial}{\partial \mathbf{v}} \xi^2(v) f(\mathbf{v}) - \epsilon \frac{\partial \xi^2(v)}{\partial v} f(\mathbf{v}). \quad (\text{A5})$$

Inserting this into Eq. (A3), one gets

$$\partial_t f(\mathbf{v}) - \frac{\partial}{\partial \mathbf{v}} \cdot \left[\zeta_{\text{eff}}(v) \mathbf{v} + \frac{\partial \xi^2(v)}{\partial \mathbf{v}} \frac{1}{2} \right] f(\mathbf{v}) = 0, \quad (\text{A6})$$

where

$$\begin{aligned} \zeta_{\text{eff}}(v) &\equiv \zeta(v) - \frac{\epsilon}{2v} \frac{\partial \xi^2(v)}{\partial v} \\ &= \frac{m\xi^2(v)}{2k_B T_b} - \frac{1-\epsilon}{2v} \frac{\partial \xi^2(v)}{\partial v}. \end{aligned} \quad (\text{A7})$$

In the particular case of Eq. (7) and $\epsilon = 1$, the effective drag coefficient becomes

$$\zeta_{\text{eff}}(v) = \zeta(v) - 2\zeta_0\gamma. \quad (\text{A8})$$

Thus, the original Langevin equation, Eq. (A1), in the Klimontovich interpretation is equivalent to the Langevin equation

$$\dot{\mathbf{v}}(t) = -\zeta_{\text{eff}}(v(t))\mathbf{v}(t) + \xi(v(t))\boldsymbol{\eta}(t) \quad (\text{A9})$$

in the Itô interpretation.

Appendix B: Derivation of the evolution equations

To write the hierarchy of moment equations, it is convenient to introduce dimensionless quantities [36]. First,

we define a rescaled velocity \mathbf{c} as

$$\mathbf{c} \equiv \frac{\mathbf{v}}{v_{\text{th}}(t)}, \quad v_{\text{th}}(t) \equiv \sqrt{\frac{2k_B T(t)}{m}}, \quad (\text{B1})$$

in which $v_{\text{th}}(t)$ is the thermal velocity at time t . Analogously, the dimensionless VDF is introduced as

$$\phi(\mathbf{c}, t) \equiv \frac{v_{\text{th}}^d(t)}{n} f(\mathbf{v}, t). \quad (\text{B2})$$

In terms of these reduced quantities, the EFPE, Eq. (3), can be rewritten as

$$\begin{aligned} \partial_t \phi(\mathbf{c}, t) &= \frac{1}{2\theta} \partial_{\mathbf{c}} \cdot \left[\dot{\theta} \mathbf{c} + \zeta_0 (1 + \gamma\theta c^2) (2\theta \mathbf{c} + \partial_{\mathbf{c}}) \right] \phi(\mathbf{c}, t) \\ &\quad + K_d \sqrt{\theta} I[\mathbf{c}|\phi, \phi], \end{aligned} \quad (\text{B3})$$

where θ is the temperature ratio—as defined in Eq. (12b)—and

$$\begin{aligned} I[\mathbf{c}_1|\phi, \phi] &= \int d\mathbf{c}_2 \int_+ d\hat{\boldsymbol{\sigma}} \mathbf{c}_{12} \cdot \hat{\boldsymbol{\sigma}} \\ &\quad \times [\phi(\mathbf{c}'_1, t)\phi(\mathbf{c}'_2, t) - \phi(\mathbf{c}_1, t)\phi(\mathbf{c}_2, t)] \end{aligned} \quad (\text{B4})$$

is the reduced collision operator with $\mathbf{c}_{12} \equiv \mathbf{c}_1 - \mathbf{c}_2$. In Eq. (B3), and consistently with the main text, dimensionless variables are used—recall that the stars on the dimensionless time t^* and the zero-velocity drag coefficient ζ_0^* are dropped.

Multiplying both sides of Eq. (B3) by c^ℓ and defining the reduced moments

$$M_\ell(t) \equiv \langle c^\ell \rangle = \int d\mathbf{c} c^\ell \phi(\mathbf{c}, t), \quad (\text{B5})$$

one obtains the hierarchy of equations [36]

$$\begin{aligned} \frac{\dot{M}_\ell}{\zeta_0} &= \ell \left\{ \left[(\ell-2)\gamma + (d+2)\gamma\theta(1+a_2) - \frac{1}{\theta} \right] M_\ell \right. \\ &\quad \left. - 2\gamma\theta M_{\ell+2} + \frac{d+\ell-2}{2} \frac{M_{\ell-2}}{\theta} \right\} - \frac{K_d}{\zeta_0} \sqrt{\theta} \mu_\ell, \end{aligned} \quad (\text{B6})$$

where we have introduced the collisional moments μ_ℓ as

$$\mu_\ell \equiv - \int d\mathbf{c} c^\ell I[\mathbf{c}|\phi, \phi]. \quad (\text{B7})$$

Note that $M_0 = 1$, $M_2 = \frac{d}{2}$, and $M_4 = \frac{d(d+2)}{4}(1+a_2)$ [see Eq. (14)]. Conservation of mass and energy imply that $\mu_0 = \mu_2 = 0$, so that Eq. (B6) is obviously consistent with $\dot{M}_0 = \dot{M}_2 = 0$.

Making use of the explicit form of the collision operator, it is possible to express the collisional moments as two-particle averages of the form

$$\mu_\ell = \int d\mathbf{c}_1 \int d\mathbf{c}_2 \phi(\mathbf{c}_1)\phi(\mathbf{c}_2)\Phi_\ell(\mathbf{c}_1, \mathbf{c}_2). \quad (\text{B8})$$

In particular, $\Phi_2 = 0$ and, after some algebra, one gets

$$\Phi_4(\mathbf{c}_1, \mathbf{c}_2) = \frac{2\pi^{\frac{d-1}{2}}}{\Gamma(\frac{d+5}{2})} c_{12} [d(\mathbf{C} \cdot \mathbf{c}_{12})^2 - c_{12}^2 C^2], \quad (\text{B9a})$$

$$\Phi_6(\mathbf{c}_1, \mathbf{c}_2) = 3\Phi_4(\mathbf{c}_1, \mathbf{c}_2) \left(C^2 + \frac{c_{12}^2}{4} \right), \quad (\text{B9b})$$

where $\mathbf{C} \equiv \frac{1}{2}(\mathbf{c}_1 + \mathbf{c}_2)$ is the center-of-mass reduced velocity.

1. Sonine approximation

Let us first consider the case of linear drag force, i.e., $\gamma = 0$. In that case, the LE state defined in Eq. (10) is an exact solution of the EFPE, Eq. (3). Equivalently, in reduced variables,

$$\phi^{\text{LE}}(\mathbf{c}) = \pi^{-d/2} e^{-c^2} \implies M_{2k}^{\text{LE}} = \frac{[d + 2(k-1)]!!}{2^k}, \quad (\text{B10})$$

becomes an exact stationary solution to Eqs. (B3) and (B6), because of the properties $I[\mathbf{c}|\phi^{\text{LE}}, \phi^{\text{LE}}] = 0$, $\mu_\ell^{\text{LE}} = 0$. Moreover, the solution to Eq. (17) is simply $\theta(t) = 1 + [\theta(0) - 1]e^{-2\zeta_0 t}$, as stated in the main text. Thus, if $\gamma = 0$ and the system is initially prepared in an equilibrium state with a temperature $T(0)$, its coupling to a bath at temperature T_b makes the temperature evolve toward T_b but otherwise the system remains always in local equilibrium, i.e., the VDF is Maxwellian with the time-dependent temperature.

Going back to the nonlinear case $\gamma \neq 0$, the VDF can be represented by the Sonine expansion

$$\phi(\mathbf{c}; t) = \phi^{\text{LE}}(\mathbf{c}) \left[1 + \sum_{j=2}^{\infty} a_j(t) L_j^{(\frac{d-2}{2})}(c^2) \right], \quad (\text{B11})$$

where $L_j^{(\frac{d-2}{2})}(c^2)$ are generalized Laguerre (or Sonine) polynomials and the coefficients $a_j = [j! \Gamma(\frac{d}{2}) / \Gamma(j + \frac{d}{2})] \langle L_j^{(\frac{d-2}{2})}(c^2) \rangle$ are the cumulants of the nonequilibrium VDF. The associated velocity moments are

$$M_{2k} = M_{2k}^{\text{LE}} \left[1 + \sum_{j=2}^k (-1)^j \binom{k}{j} a_j \right], \quad k \geq 2. \quad (\text{B12})$$

In particular,

$$M_6 = \frac{d(d+2)(d+4)}{8} (1 + 3a_2 - a_3), \quad (\text{B13a})$$

$$M_8 = \frac{d(d+2)(d+4)(d+6)}{16} (1 + 6a_2 - 4a_3 + a_4). \quad (\text{B13b})$$

The infinite moment hierarchy, Eq. (B6), cannot be solved in an exact way in general. This is even the case for linear drag, $\gamma = 0$, when the initial state is not a Maxwellian. As a consequence, the exact evolution of the temperature ratio $\theta(t)$ cannot be obtained from Eq. (17) if $\gamma \neq 0$.

Let us suppose, however, that the initial condition and subsequent evolution are sufficiently close to the LE state as to assume both the cumulants in Eq. (B11) beyond a_3 and the quadratic terms in a_2, a_3 (i.e., those proportional to a_2^2, a_3^2 , and $a_2 a_3$) being negligible. In that case, the two first nontrivial collisional moments become [102]

$$\mu_4 \approx \frac{2(d-1)}{K_d} \left(a_2 - \frac{a_3}{4} \right), \quad (\text{B14a})$$

$$\mu_6 \approx \frac{3(d-1)(2d+9)}{2K_d} \left(a_2 - \frac{3a_3}{4} \right). \quad (\text{B14b})$$

Within this scheme, Eq. (B6) with $\ell = 4$ and $\ell = 6$ yields Eq. (19) in the main text.

Appendix C: Parameters in Eqs. (25)

The parameters λ_{\pm} , B_i , and A_{ij} are given by

$$\lambda_{\pm} = \frac{\Lambda_{11} + \Lambda_{22} \pm \sqrt{(\Lambda_{11} - \Lambda_{22})^2 + 4\Lambda_{12}\Lambda_{21}}}{2}, \quad (\text{C1a})$$

$$B_1 = \theta_r + \frac{\Lambda_{22}C_1 - \Lambda_{12}C_2}{\Lambda_{11}\Lambda_{22} - \Lambda_{12}\Lambda_{21}}, \quad B_2 = \frac{\Lambda_{11}C_2 - \Lambda_{21}C_1}{\Lambda_{11}\Lambda_{22} - \Lambda_{12}\Lambda_{21}}, \quad (\text{C1b})$$

$$A_{11} = \frac{\lambda_+ - \Lambda_{11}}{\lambda_+ - \lambda_-}, \quad A_{22} = \frac{\lambda_+ - \Lambda_{22}}{\lambda_+ - \lambda_-}, \quad (\text{C1c})$$

$$A_{12} = \frac{\Lambda_{12}}{\lambda_+ - \lambda_-}, \quad A_{21} = \frac{\Lambda_{21}}{\lambda_+ - \lambda_-}, \quad (\text{C1d})$$

where

$$\Lambda_{11} = 2\zeta_0 [1 + (d+2)\gamma(2\theta_r - 1)], \quad (\text{C2a})$$

$$\Lambda_{22} = \zeta_0 \left[\frac{4}{\theta_r} - 8\gamma + 4(d+8)\gamma\theta_r \right] + \frac{8(d-1)}{d(d+2)} \sqrt{\theta_r}, \quad (\text{C2b})$$

$$\Lambda_{12} = 2\zeta_0(d+2)\gamma\theta_r^2, \quad \Lambda_{21} = 8\zeta_0\gamma, \quad (\text{C2c})$$

$$C_1 = 2\zeta_0(1 - \theta_r) [1 + (d+2)\gamma\theta_r], \quad C_2 = 8\zeta_0\gamma(1 - \theta_r). \quad (\text{C2d})$$

Appendix D: Computer Simulation Schemes

We have performed DSMC and EDMD simulations of the model to test the theoretical predictions. In both schemes, the nonlinear drag is implemented at the level of stochastic equations of motion by using Eq. (A9) and applying the associated Wiener process at time t within the interval $[t, t+h]$.

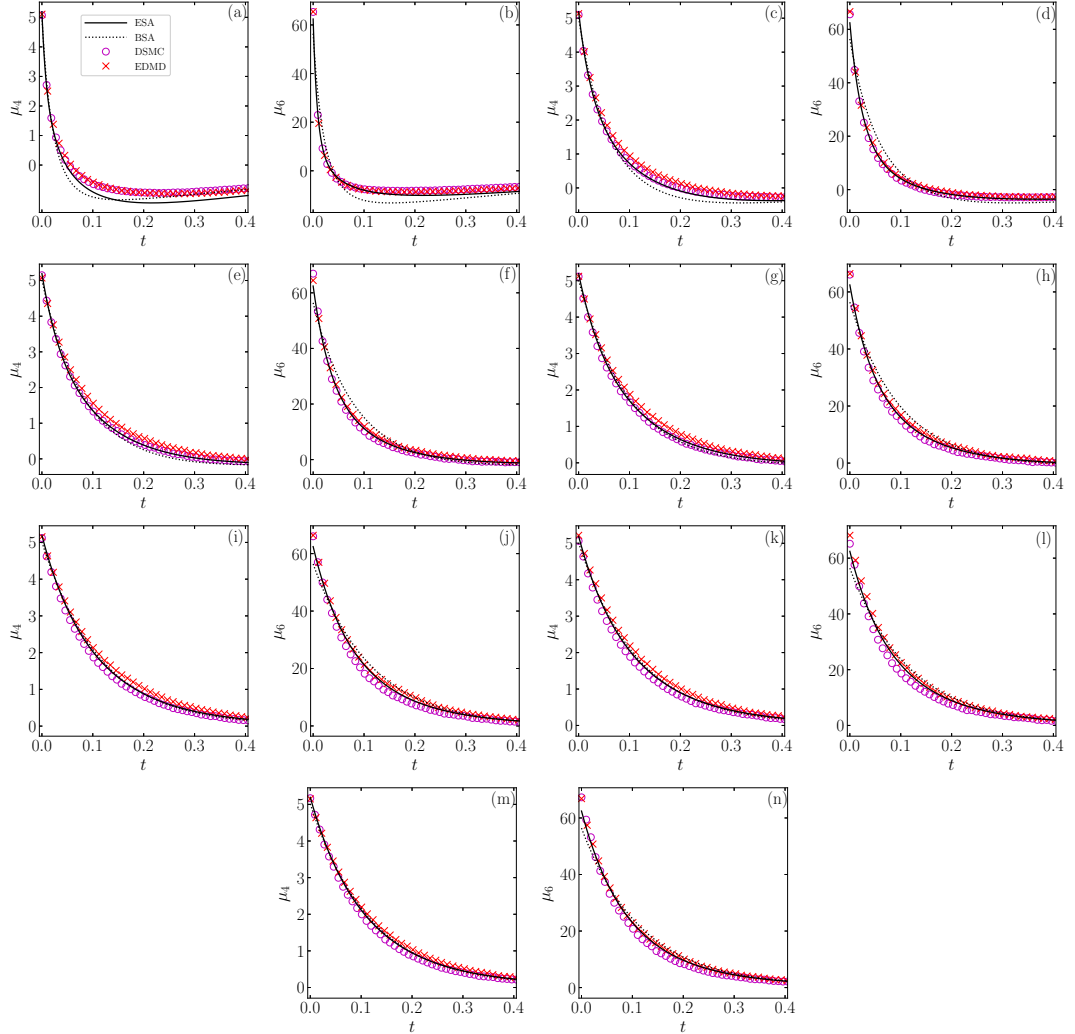


FIG. 15. Evolution of the collisional moments μ_4 and μ_6 for $\zeta_0 = 1$, $\gamma = 0.1$, $d = 3$, and initial conditions $a_2^0 = 0.5$ and [(a) and (b)] $\theta^0 = 10$, [(c) and (d)] $\theta^0 = 3.15$, [(e) and (f)] $\theta^0 = 2$, [(g) and (h)] $\theta^0 = 1.5$, [(i) and (j)] $\theta^0 = 1.05$, [(k) and (l)] $\theta^0 = 1.01$, and [(m) and (n)] $\theta^0 = 0.91$. Symbols correspond to simulation data for DSMC (o) and EDMD (x) schemes, while lines represent the theoretical predictions for ESA (—) and BSA (···).

1. Direct simulation Monte Carlo

The implementation of DSMC for this system is based on the pioneering work by Bird [103, 104], except for our taking into account of both the nonlinear drag and white-noise forces during the free-streaming stage of the algorithm [105].

Let us assume a homogeneous system of N particles, where their dynamics is just controlled by their velocities $\{\mathbf{v}_i\}$ with $i = 1, \dots, N$, and positions are obviated. The

discrete VDF of such a system of particles is given by

$$n^{-1}f(\mathbf{v}, t) = \frac{1}{N} \sum_{i=1}^N \delta(\mathbf{v}_i(t) - \mathbf{v}). \quad (\text{D1})$$

At the initialization of the system, the squared moduli of the particles velocities $\{v_i^2(0)\}$ are drawn from a gamma distribution parameterized by $\langle v^2(0) \rangle = dk_B T^0/m$ and $\langle v^4(0) \rangle = d(d+2)(k_B T^0/m)^2(1+a_2^0)$. Next, the velocity vectors $\{\mathbf{v}_i(0)\}$ are constructed from these moduli, with random directions. To enforce a vanishing initial total

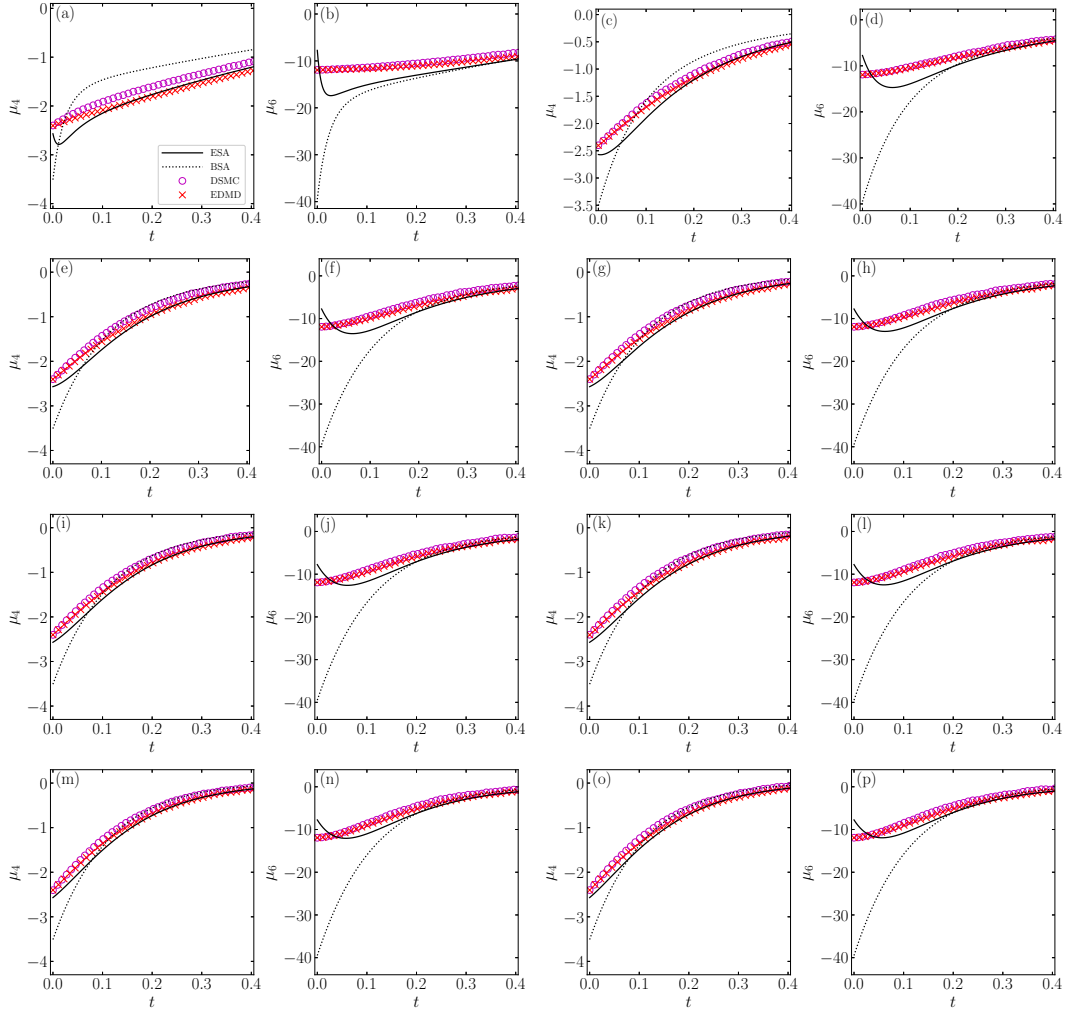


FIG. 16. Evolution of the collisional moments μ_4 and μ_6 for $\zeta_0 = 1$, $\gamma = 0.1$, $d = 3$, and initial conditions $a_2^0 = -0.35$ and [(a) and (b)] $\theta^0 = 9$, [(c) and (d)] $\theta^0 = 1.8$, [(e) and (f)] $\theta^0 = 1.27$, [(g) and (h)] $\theta^0 = 1.1$, and [(i) and (j)] $\theta^0 = 0.99$, [(k) and (l)] $\theta^0 = 0.96$, [(m) and (n)] $\theta^0 = 0.85$, and [(o) and (p)] $\theta^0 = 0.82$. Symbols correspond to simulation data for DSMC (o) and EDMD (x) schemes, while lines represent the theoretical predictions for ESA (—) and BSA (···).

momentum, the velocity of every particle is subsequently subtracted by the amount $N^{-1} \sum_i \mathbf{v}_i(0)$.

After initialization, velocities are updated from t to $t+h$ (where the time step h is much smaller than the mean free time) by splitting the algorithm into two different stages: collisions and free streaming.

During the collision stage, a number $\frac{1}{2}N\omega_{\max}h$ of pairs are randomly chosen with uniform probability, where ω_{\max} is an upper bound estimate for the collision rate of one particle. Then, given a pair ij , the collision is accepted (acceptance-rejection Metropolis criterion) with

probability $\Theta(\mathbf{v}_{ij} \cdot \hat{\boldsymbol{\sigma}}_{ij})\omega_{ij}/\omega_{\max}$, where $\hat{\boldsymbol{\sigma}}_{ij}$ a random vector in the unit d -sphere and $\omega_{ij} = \Omega_d \sigma^{d-1} n g_c |\mathbf{v}_{ij} \cdot \hat{\boldsymbol{\sigma}}_{ij}|$ with $\Omega_d = 2\pi^{d/2}/\Gamma(d/2)$ being the d -dimensional solid angle. If the collision is accepted for the given pair, then postcollisional velocities are assigned following the collisional rules for elastic hard spheres, namely $\mathbf{v}_{i,j} \rightarrow \mathbf{v}_{i,j} \mp (\mathbf{v}_{ij} \cdot \hat{\boldsymbol{\sigma}}_{ij})\hat{\boldsymbol{\sigma}}_{ij}$. If $\omega_{ij} > \omega_{\max}$ in one of the sampled pairs, then the collision is accepted and the estimate is updated as $\omega_{\max} = \omega_{ij}$.

During free streaming, velocities are updated accord-

ing to the scheme given by (A9), namely

$$\begin{aligned} \mathbf{v}_i(t) \rightarrow \mathbf{v}_i(t+h) \approx & \mathbf{v}_i(t) - \zeta_{\text{eff}}(v_i(t))\mathbf{v}_i(t)h \\ & + \xi(v_i(t))\sqrt{h}\mathbf{Y}_i + \mathcal{O}(h^{3/2}), \end{aligned} \quad (\text{D2})$$

where \mathbf{Y}_i is a random vector drawn from the Gaussian probability distribution

$$P(\mathbf{Y}) = (2\pi)^{-d/2} e^{-Y^2/2}. \quad (\text{D3})$$

In our DSMC algorithm we took $N = 10^4$ three-dimensional particles ($d = 3$) and chose a time step $h = 10^{-2}\lambda/\sqrt{2k_B T_b/m}$, where $\lambda = (\sqrt{2\pi}n\sigma^2)^{-1}$ is the mean free path.

2. Event-driven molecular dynamics

EDMD algorithms are based on the evolution driven by events which can be particle-particle collisions, boundary effects, or other more complex interactions. Between two consecutive events, there is a free streaming of particles. Again, the stochastic and drag forces directly influence the particle dynamics. Whereas in DSMC positions were not required, in EDMD they are essential and are affected by the nonlinear noise, as explained below.

In order to implement the effect of the Langevin dynamics in our EDMD simulations, we have followed the AGF algorithm proposed in Ref. [106]. Since $\mathbf{r}_i(t) = \mathbf{v}(t)$, Eq. (D2) must be supplemented by [106]

$$\begin{aligned} \mathbf{r}_i(t) \rightarrow \mathbf{r}_i(t+h) \approx & \mathbf{r}_i(t) + \mathbf{v}_i(t)h \left[1 - \frac{\zeta_{\text{eff}}(v_i(t))}{2}h \right] \\ & + \frac{1}{2}\xi(v_i(t))h^{3/2}\mathbf{W}_i + \mathcal{O}(h^{5/2}), \end{aligned} \quad (\text{D4})$$

with

$$\mathbf{W}_i = \mathbf{Y}_i + \sqrt{\frac{5}{3}}\bar{\mathbf{Y}}_i, \quad (\text{D5})$$

where we have particularized the algorithm to the three-dimensional geometry, \mathbf{Y}_i is the random vector appearing in Eq. (D2), and $\bar{\mathbf{Y}}_i$ is an independent random vector, also drawn from the Gaussian distribution (D3). Notice that, since the equation for $\mathbf{v}_i(t)$ is expanded up to $\mathcal{O}(h^{3/2})$ and $\mathbf{r}_i(t+h) - \mathbf{r}_i(t) \sim \mathbf{v}_i(t)h$, then the equation for $\mathbf{r}_i(t)$ needs to be expanded up to $\mathcal{O}(h^{5/2})$.

In our EDMD simulations, we deal with a system of $N = 1.065 \times 10^4$ spheres and reduced number density $n\sigma^3 = 10^{-3}$. The time step is $h = 10^{-3}\lambda/\sqrt{2k_B T_b/m}$, and periodic boundary conditions are used.

3. Test of the time evolution of the collisional moments μ_4 and μ_6

Let us present now a comparison between the collisional moments μ_4 and μ_6 measured in simulations and

those provided by the ESA and the BSA. In the ESA, those collisional moments are given by Eqs. (B14), complemented with the numerical solution of Eqs. (17) and (19). Analogously, in the BSA, the collisional moments are given by Eqs. (B14) with $a_3 \rightarrow 0$, complemented with the numerical solution of Eqs. (17) and (19a), again with $a_3 \rightarrow 0$.

In the simulations (both DSMC and EDMD), the following numerical scheme has been used to address the computation of the collisional moments [105, 107]. We randomly choose $N' = 10^6$ pairs of particles out of the total number $N(N-1)/2 = 5 \times 10^7$ and approximate the collisional moments as

$$\mu_\ell = \frac{1}{N'} \sum_{ij}^{N'} \Phi_\ell(\mathbf{c}_i, \mathbf{c}_j), \quad (\text{D6})$$

where Φ_4 and Φ_6 are given by Eqs. (B9).

Figures 15 and 16 show the time evolution of μ_4 and μ_6 , as measured in our DSMC and EDMD simulations and as predicted by the BSA and ESA, for a number of representative initial conditions. A very good agreement between DSMC and EDMD is found; the small differences between them could explain the deviations observed in Figs. 10–12. There is also a general good agreement with the ESA results, while the BSA predictions exhibit important deviations in the initial stage, especially in the case of μ_6 . The deviations of the BSA and ESA are due to the nonnegligible role played by nonlinear terms of the form a_2^2 , a_3^2 , and $a_2 a_3$, as well as by higher-order cumulants. Interestingly, those deviations are more relevant for negative a_2^0 than for positive a_2^0 and tend to increase as the initial temperature θ^0 grows—in accordance with the results in Ref. [37] for a quench to low temperatures.

Appendix E: Evolution of the cumulants a_2 and a_3

In this Appendix we present a comparison between the simulation results for the cumulants a_2 and a_3 , and the theoretical predictions BSA (for a_2 only) and ESA. The results are displayed in Figs. 17–20.

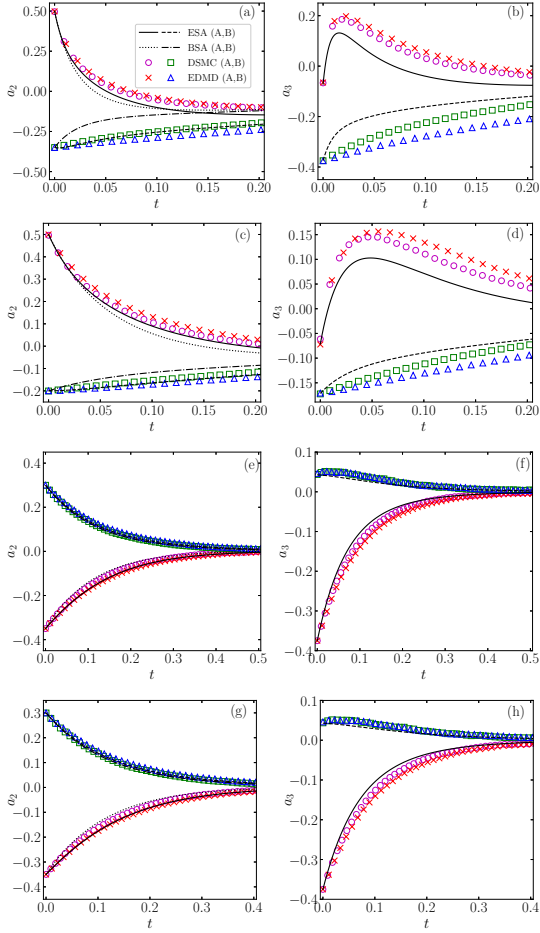


FIG. 17. Same as in Fig. 11, except that the quantities plotted are a_2 and a_3 .

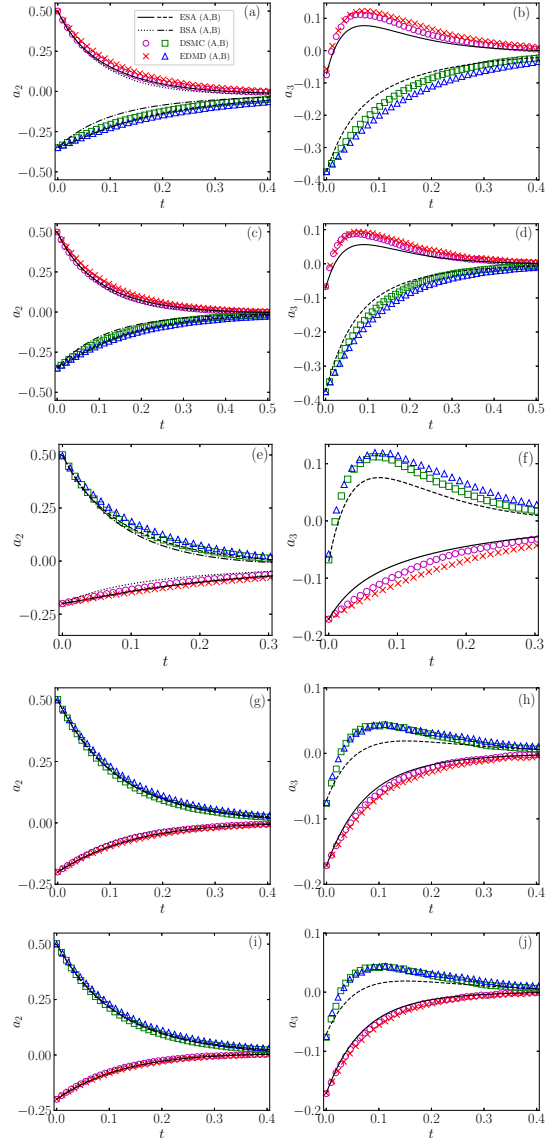


FIG. 18. Same as in Fig. 12, except that the quantities plotted are a_2 and a_3 .

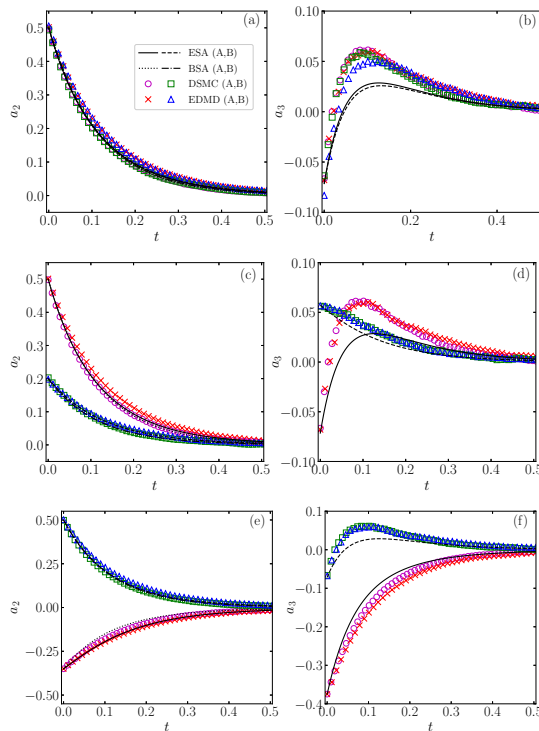


FIG. 19. Same as in Fig. 13, except that the quantities plotted are a_2 and a_3 .

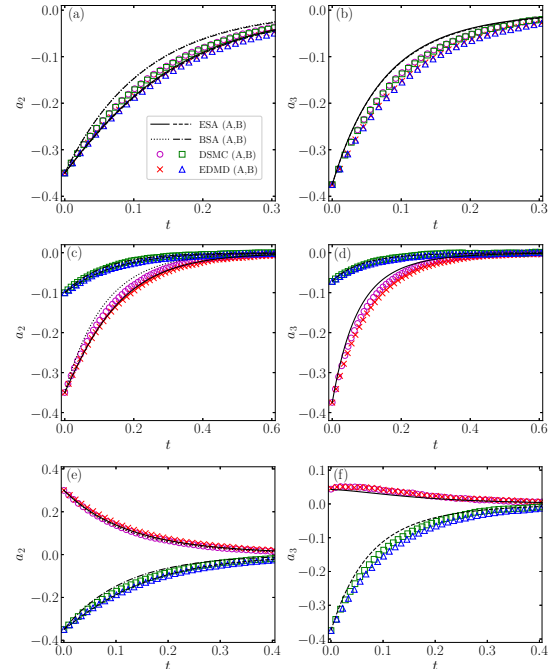


FIG. 20. Same as in Fig. 14, except that the quantities plotted are a_2 and a_3 .

- [1] N. C. Keim, J. D. Paulsen, Z. Zeravcic, S. Sastri, and S. R. Nagel, Memory formation in matter, *Rev. Mod. Phys.* **91**, 035002 (2019).
- [2] E. B. Mpemba and D. G. Osborne, Cooler?, *Phys. Educ.* **4**, 172 (1969).
- [3] G. S. Kell, The freezing of hot and cold water, *Am. J. Phys.* **37**, 564 (1969).
- [4] I. Firth, Cooler?, *Phys. Educ.* **6**, 32 (1971).
- [5] E. Deeson, Cooler-lower down, *Phys. Educ.* **6**, 42 (1971).
- [6] F. C. Frank, The Descartes-Mpemba phenomenon, *Phys. Educ.* **9**, 284 (1974).
- [7] R. Gallea, The Bacon-Descartes-Mpemba phenomenon, *Phys. Educ.* **9**, 490 (1974).
- [8] J. Walker, Hot water freezes faster than cold water. Why does it do so?, *Sci. Am.* **237**, 246 (1977).
- [9] D. G. Osborne, Mind on ice, *Phys. Educ.* **14**, 414 (1979).
- [10] M. Freeman, Cooler still—an answer?, *Phys. Educ.* **14**, 417 (1979).
- [11] K. Kumar, Mpemba effect and 18th century ice-cream, *Phys. Educ.* **15**, 268 (1980).
- [12] J. W. Hanneken, Mpemba effect and cooling by radiation to the sky, *Phys. Educ.* **16**, 7 (1981).
- [13] B. Wojciechowski, I. Owczarek, and G. Bednarz, Freezing of aqueous solutions containing gases, *Cryst. Res. Technol.* **23**, 843 (1988).
- [14] D. Auerbach, Supercooling and the Mpemba effect: When hot water freezes quicker than cold, *Am. J. Phys.* **63**, 882 (1995).
- [15] C. A. Knight, The Mpemba effect: The freezing times of cold and hot water, *Am. J. Phys.* **64**, 524 (1996).
- [16] P. K. Maciejewski, Evidence of a convective instability allowing warm water to freeze in less time than cold water, *J. Heat Transf.* **118**, 65 (1996).
- [17] M. Jeng, The Mpemba effect: When can hot water freeze faster than cold?, *Am. J. Phys.* **74**, 514 (2006).
- [18] S. Esposito, R. De Risi, and L. Somma, Mpemba effect and phase transitions in the adiabatic cooling of water before freezing, *Physica A* **387**, 757 (2008).
- [19] J. I. Katz, When hot water freezes before cold, *Am. J. Phys.* **77**, 27 (2009).
- [20] M. Vynnycky and S. L. Mitchell, Evaporative cooling and the Mpemba effect, *Heat Mass Transf.* **46**, 881 (2010).
- [21] J. D. Brownridge, When does hot water freeze faster than cold water? A search for the Mpemba effect, *Am. J. Phys.* **79**, 78 (2011).

- [22] M. Vynnycky and N. Maeno, Axisymmetric natural convection-driven evaporation of hot water and the Mpemba effect, *Int. J. Heat Mass Transf.* **55**, 7297 (2012).
- [23] M. Balázovič and B. Tomášik, The Mpemba effect, Shechtman's quasicrystals and student exploration activities, *Phys. Educ.* **47**, 568 (2012).
- [24] X. Zhang, Y. Huang, Z. Ma, Y. Zhou, J. Zhou, W. Zheng, Q. Jiang, and C. Q. Sun, Hydrogen-bond memory and water-skin supersolidity resolving the Mpemba paradox, *Phys. Chem. Chem. Phys.* **16**, 22995 (2014).
- [25] M. Vynnycky and S. Kimura, Can natural convection alone explain the Mpemba effect?, *Int. J. Heat Mass Transf.* **80**, 243 (2015).
- [26] C. Q. Sun, Behind the Mpemba paradox, *Temperature* **2**, 38 (2015).
- [27] M. Balázovič and B. Tomášik, Paradox of temperature decreasing without unique explanation, *Temperature* **2**, 61 (2015).
- [28] A. A. Romanovsky, Which is the correct answer to the Mpemba puzzle?, *Temperature* **2**, 63 (2015).
- [29] J. Jin and W. A. Goddard, Mechanisms underlying the Mpemba effect in water from molecular dynamics simulations, *J. Phys. Chem. C* **119**, 2622 (2015).
- [30] R. T. Ibekwe and J. P. Cullerne, Investigating the Mpemba effect: when hot water freezes faster than cold water, *Phys. Educ.* **51**, 025011 (2016).
- [31] A. Gijón, A. Lasanta, and E. R. Hernández, Paths towards equilibrium in molecular systems: The case of water, *Phys. Rev. E* **100**, 032103 (2019).
- [32] J. Bechhoefer, A. Kumar, and R. Chétrite, A fresh understanding of the Mpemba effect, *Nat. Rev. Phys.* **3**, 534 (2021).
- [33] H. C. Burridge and P. F. Linden, Questioning the Mpemba effect: hot water does not cool more quickly than cold, *Sci. Rep.* **6**, 37665 (2016).
- [34] H. C. Burridge and O. Hallstadius, Observing the Mpemba effect with minimal bias and the value of the Mpemba effect to scientific outreach and engagement, *Proc. R. Soc. A* **476**, 20190829 (2020).
- [35] D. C. Elton and P. D. Spencer, Pathological Water Science — Four Examples and What They Have in Common, in *Biomechanical and Related Systems*, Biologically-Inspired Systems, Vol. 17, edited by A. Gadomski (Springer, Cham., 2021) pp. 155–169.
- [36] A. Santos and A. Prados, Mpemba effect in molecular gases under nonlinear drag, *Phys. Fluids* **32**, 072010 (2020).
- [37] A. Patrón, B. Sánchez-Rey, and A. Prados, Strong non-exponential relaxation and memory effects in a fluid with nonlinear drag, *Phys. Rev. E* **104**, 064127 (2021).
- [38] R. Gómez González, N. Khalil, and V. Garzó, Mpemba-like effect in driven binary mixtures, *Phys. Fluids* **33**, 053301 (2021).
- [39] A. Lasanta, F. Vega Reyes, A. Prados, and A. Santos, When the hotter cools more quickly: Mpemba effect in granular fluids, *Phys. Rev. Lett.* **119**, 148001 (2017).
- [40] A. Torrente, M. A. López-Castaño, A. Lasanta, F. Vega Reyes, A. Prados, and A. Santos, Large Mpemba-like effect in a gas of inelastic rough hard spheres, *Phys. Rev. E* **99**, 060901(R) (2019).
- [41] A. Biswas, V. V. Prasad, O. Raz, and R. Rajesh, Mpemba effect in driven granular Maxwell gases, *Phys. Rev. E* **102**, 012906 (2020).
- [42] E. Mompó, M. A. López Castaño, A. Torrente, F. Vega Reyes, and A. Lasanta, Memory effects in a gas of viscoelastic particles, *Phys. Fluids* **33**, 062005 (2021).
- [43] R. Gómez González and V. Garzó, Time-dependent homogeneous states of binary granular suspensions, *Phys. Fluids* **33**, 093315 (2021).
- [44] A. Biswas, V. V. Prasad, and R. Rajesh, Mpemba effect in an anisotropically driven granular gas, *EPL* **136**, 46001 (2021).
- [45] A. Biswas, V. V. Prasad, and R. Rajesh, Mpemba effect in anisotropically driven inelastic Maxwell gases, *J. Stat. Phys.* **186**, 45 (2022).
- [46] S. Takada, H. Hayakawa, and A. Santos, Mpemba effect in inertial suspensions, *Phys. Rev. E* **103**, 032901 (2021).
- [47] S. Takada, Homogeneous cooling and heating states of dilute soft-core gases under nonlinear drag, *EPJ Web Conf.* **249**, 04001 (2021).
- [48] M. Baity-Jesi, E. Calore, A. Cruz, L. A. Fernandez, J. M. Gil-Narvión, A. Gordillo-Guerrero, D. Iñiguez, A. Lasanta, A. Maiorano, E. Marinari, V. Martin-Mayor, J. Moreno-Gordo, A. Muñoz-Sudupe, D. Navarro, G. Parisi, S. Perez-Gavero, F. Ricci-Tersenghi, J. J. Ruiz-Lorenzo, S. F. Schifano, B. Seoane, A. Tarancón, R. Tripiccion, and D. Yllanes, The Mpemba effect in spin glasses is a persistent memory effect, *Proc. Natl. Acad. Sci. U.S.A.* **116**, 15350 (2019).
- [49] P. A. Greaney, G. Lani, G. Cicero, and J. C. Grossman, Mpemba-like behavior in carbon nanotube resonators, *Metall. Mater. Trans. A* **42**, 3907 (2011).
- [50] Y.-H. Ahn, H. Kang, D.-Y. Koh, and H. Lee, Experimental verifications of Mpemba-like behaviors of clathrate hydrates, *Korean J. Chem. Eng.* **33**, 1903 (2016).
- [51] Z. Lu and O. Raz, Nonequilibrium thermodynamics of the Markovian Mpemba effect and its inverse, *Proc. Natl. Acad. Sci. U.S.A.* **114**, 5083 (2017).
- [52] I. Klich, O. Raz, O. Hirschberg, and M. Vucelja, Mpemba index and anomalous relaxation, *Phys. Rev. X* **9**, 021060 (2019).
- [53] R. Chétrite, A. Kumar, and J. Bechhoefer, The metastable Mpemba effect corresponds to a non-monotonic temperature dependence of extractable work, *Front. Phys.* **9**, 654271 (2021).
- [54] D. M. Busiello, D. Gupta, and A. Maritan, Inducing and optimizing Markovian Mpemba effect with stochastic reset, *New J. Phys.* **23**, 103012 (2021).
- [55] J. Lin, K. Li, J. He, J. Ren, and J. Wang, Power statistics of Otto heat engines with the Mpemba effect, *Phys. Rev. E* **105**, 014104 (2022).
- [56] F. J. Schwarzendahl and H. Löwen, Anomalous cooling and overcooling of active systems, arXiv:2111.06109 10.48550/arXiv.2111.06109 (2021).
- [57] I. González-Adalid Pemartín, E. Mompó, A. Lasanta, V. Martín-Mayor, and J. Salas, Slow growth of magnetic domains helps fast evolution routes for out-of-equilibrium dynamics, *Phys. Rev. E* **104**, 044114 (2021).
- [58] G. Teza, R. Yaacoby, and O. Raz, Relaxation shortcuts through boundary coupling, arXiv:2112.10187 10.48550/arXiv.2112.10187 (2021).
- [59] N. Vadakkayila and S. K. Das, Should a hotter paramagnet transform quicker to a ferromag-

- net? Monte Carlo simulation results for Ising model, *Phys. Chem. Chem. Phys.* **23**, 11186 (2021).
- [60] Z.-Y. Yang and J.-X. Hou, Non-Markovian Mpemba effect in mean-field systems, *Phys. Rev. E* **101**, 052106 (2020).
- [61] Z.-Y. Yang and J.-X. Hou, Mpemba effect of a mean-field system: The phase transition time, *Phys. Rev. E* **105**, 014119 (2022).
- [62] F. Carollo, A. Lasanta, and I. Lesanovsky, Exponentially accelerated approach to stationarity in Markovian open quantum systems through the Mpemba effect, *Phys. Rev. Lett.* **127**, 060401 (2021).
- [63] R. Holtzman and O. Raz, Landau theory for the Mpemba effect through phase transitions, arXiv:2204.03995 10.48550/arXiv.2204.03995 (2022).
- [64] A. Kumar and J. Bechhoefer, Exponentially faster cooling in a colloidal system, *Nature (Lond.)* **584**, 64 (2020).
- [65] A. Kumar, R. Chétrite, and J. Bechhoefer, Anomalous heating in a colloidal system, *Proc. Natl. Acad. Sci. U.S.A.* **119**, e2118484119 (2022).
- [66] S. Kullback and R. A. Leibler, On information and sufficiency, *Ann. Math. Statist.* **22**, 79 (1951).
- [67] N. G. V. Kampen, *Stochastic Processes in Physics and Chemistry* (North-Holland, Amsterdam, 2007).
- [68] Strictly speaking, the KLD does not have the properties of a distance; e.g., it does not satisfy the triangle inequality.
- [69] G. W. Scherer, Theories of relaxation, *J. Non-Cryst. Solids* **123**, 75 (1990).
- [70] A. Cavagna, Supercooled liquids for pedestrians, *Phys. Rep.* **476**, 51 (2009).
- [71] L. Berthier and G. Biroli, Theoretical perspective on the glass transition and amorphous materials, *Rev. Mod. Phys.* **83**, 587 (2011).
- [72] J. J. Brey and A. Prados, Dynamical behavior of a one-dimensional Ising model submitted to continuous heating and cooling processes, *Phys. Rev. B* **49**, 984 (1994).
- [73] L. Ferrari, Particles dispersed in a dilute gas: Limits of validity of the Langevin equation, *Chem. Phys.* **336**, 27 (2007).
- [74] L. Ferrari, Particles dispersed in a dilute gas. II. From the Langevin equation to a more general kinetic approach, *Chem. Phys.* **428**, 144 (2014).
- [75] M. Hohmann, F. Kindermann, T. Lausch, D. Mayer, F. Schmidt, E. Lutz, and A. Widera, Individual tracer atoms in an ultracold dilute gas, *Phys. Rev. Lett.* **118**, 263401 (2017).
- [76] J. R. Dorfman and H. van Beijeren, The kinetic theory of gases, in *Statistical Mechanics, Part B*, edited by B. Berne (Plenum, New York, 1977) pp. 65–179.
- [77] Note that, because of the second equality in Eq. (12b), the entropic “distance” \mathcal{D} from f to f^{eq} is exactly given by the distance from f to f^{LE} plus the distance from f^{LE} to f^{eq} . The decomposition (11) can be schematically depicted as
- $$\overbrace{f(\mathbf{v}, t) \longrightarrow f^{\text{LE}}(\mathbf{v}; T(t)) \longrightarrow f^{\text{eq}}(\mathbf{v})}^{\mathcal{D}(t)}$$
- $$\underbrace{\hspace{1.5cm}}_{\mathcal{D}^{\text{kin}}(t)} \quad \underbrace{\hspace{1.5cm}}_{\mathcal{D}^{\text{LE}}(T(t))}$$
- [78] The sketch in Fig. 2 was actually obtained from the solution of the BSA (see Sec. B1) and the application of Eqs. (12b) and (23) for the initial condition $\theta^0 = 2$, $a_2^0 = 0.5$.
- [79] T. R. Kirkpatrick, D. Belitz, and J. R. Dorfman, Non-hydrodynamic initial conditions are not soon forgotten, *Phys. Rev. E* **104**, 024111 (2021).
- [80] In that case, $\tau_b \rightarrow \infty$ and one has to change the definition of dimensionless time to $\zeta_0 t$.
- [81] M. Jauregui, A. L. F. Lucchi, J. H. Y. Passos, and R. S. Mendes, Stationary solution and h theorem for a generalized Fokker-Planck equation, *Phys. Rev. E* **104**, 034130 (2021).
- [82] This was the approach carried out in a previous work to analyze the TME [36].
- [83] This approximation has been employed in Ref. [37] to study the response of the nonlinear fluid to a low-temperature quench.
- [84] For the EME, there is not a clear cut distinction between the direct and inverse EME (since the relative entropy \mathcal{D} is positive definite), unless the initial temperatures are known.
- [85] R. V. Hogg and A. T. Craig, *Introduction to Mathematical Statistics*, 4th ed. (Macmillan Publishing, New York, 1978) pp. 103–108.
- [86] W. D. Penny, KL-Divergences of Normal, Gamma, Dirichlet, and Wishart densities, www.fil.ion.ucl.ac.uk/~wpenny/publications/densities
- [87] M. Abramowitz and I. A. Stegun, eds., *Handbook of Mathematical Functions* (Dover, New York, 1972).
- [88] A. J. Kovacs, Transition vitreuse dans les polymères amorphes. Etude phénoménologique, *Fortschr. Hochpolym.-Forsch.* **3**, 394 (1963).
- [89] A. J. Kovacs, J. J. Aklonis, J. M. Hutchinson, and A. R. Ramos, Isobaric volume and enthalpy recovery of glasses. II. A transparent multiparameter theory, *J. Polym. Sci. Polym. Phys. Ed.* **17**, 1097 (1979).
- [90] A. Prados and J. J. Brey, The Kovacs effect: a master equation analysis, *J. Stat. Mech.*, P02009 (2010).
- [91] E. Bouchbinder and J. S. Langer, Nonequilibrium thermodynamics of the Kovacs effect, *Soft Matter* **6**, 3065 (2010).
- [92] A. Prados and E. Trizac, Kovacs-like memory effect in driven granular gases, *Phys. Rev. Lett.* **112**, 198001 (2014).
- [93] E. Trizac and A. Prados, Memory effect in uniformly heated granular gases, *Phys. Rev. E* **90**, 012204 (2014).
- [94] A. Lasanta, F. Vega Reyes, A. Prados, and A. Santos, On the emergence of large and complex memory effects in nonequilibrium fluids, *New J. Phys.* **21**, 033042 (2019).
- [95] A. Megías and A. Santos, Kullback–Leibler divergence of a freely cooling granular gas, *Entropy* **22**, 1308 (2020).
- [96] A. Megías and A. Santos, Relative entropy of freely cooling granular gases. A molecular dynamics study, *EPJ Web Conf.* **249**, 04006 (2021).
- [97] A similar distance to a local equilibrium distribution has been recently introduced to analyze the relaxation of an Ising ferromagnet in the weak coupling limit [108].
- [98] A. Lapolla and A. Godec, Faster uphill relaxation in thermodynamically equidistant temperature quenches, *Phys. Rev. Lett.* **125**, 110602 (2020).
- [99] T. Van Vu and Y. Hasegawa, Toward relaxation asymmetry: Heating is faster than cooling, *Phys. Rev. Res.* **3**, 043160 (2021).

- [100] R. Mannella and P. V. E. McClintock, Itô versus Stratonovich: 30 years later, *Fluct. Noise Lett.* **11**, 1240010 (2012).
- [101] Y. L. Klimontovich, Nonlinear Brownian motion, *Physics-Uspokhi* **37**, 737 (1994).
- [102] N. Brilliantov and T. Pöschel, Breakdown of the Sonine expansion for the velocity distribution of granular gases, *Europhys. Lett.* **74**, 424 (2006), Erratum: **75**, 188 (2006).
- [103] G. A. Bird, *Molecular Gas Dynamics and the Direct Simulation of Gas Flows* (Clarendon, Oxford, UK, 1994).
- [104] G. A. Bird, *The DSMC Method* (CreateSpace Independent Publishing Platform, Scotts Valley, CA, 2013).
- [105] J. M. Montanero and A. Santos, Computer simulation of uniformly heated granular fluids, *Granul. Matter* **2**, 53 (2000).
- [106] A. Scala, Event-driven Langevin simulations of hard spheres, *Phys. Rev. E* **86**, 026709 (2012).
- [107] A. Santos and J. M. Montanero, The second and third Sonine coefficients of a freely cooling granular gas revisited, *Granul. Matter* **11**, 157 (2009).
- [108] G. Teza, R. Yaacoby, and O. Raz, Far from equilibrium relaxation in the weak coupling limit, arXiv:2203.11644 10.48550/arXiv.2203.11644 (2022).

**GRANULAR GASES OF INELASTIC AND
SMOOTH PARTICLES**

Nonequilibrium entropy of inelastic hard d_t -spheres

6

6.1 Summary

In this chapter, the nonequilibrium entropy of a homogeneous freely evolving dilute granular gas made of hard d_t -spheres, described by the IHS collisional model, is studied. Concretely, the particles are considered to be identical, with diameter σ , mass m , and coefficient of normal restitution α , assumed to be constant. Their evolution is just subjected to their mutual collisions, and neither external force fields nor spatial gradients are considered. The system is then described by the homogeneous BE written in Eq. (2.60).

The aim of this chapter is to address the problem of the existence of an H -theorem associated with the homogeneous and inelastic BE. We recall that an inelastic granular gas reaches, during its time evolution, a scaling solution, as already introduced in Subsection 2.5.2, which corresponds to the HCS. Then, one expects that if the system remains in homogeneous states, the HCS solution might be an attractor of the evolution of the system. Whereas this argument seems to be reasonable, it has not yet been mathematically proven. In fact, inelasticity breaks down the symmetry underlying in the collisional rules, violating the original hypotheses, on which the original proof of the molecular H -theorem is sustained (see Subsection 2.6.2). In this chapter, we try to give arguments in favor of an H -theorem for homogeneous and inelastic granular gases based on the choice of the KLD functional (identifying the reference VDF as the HCS one) as the possible Lyapunov functional that would solve the problem. This conjecture has been previously formulated in Refs. [BPV13; Gar+15; PP17], but it is still not proved or disproved.

In Article 2 (Section 6.2), the homogeneous states of the granular gas of inelastic d_t -spheres is studied from a Sonine expansion of the VDF both in transient states and in the HCS. To develop the evolution equations, we truncate the Sonine expansion

up to the sixth cumulant a_3 , and the considered slopes are linearized with respect to a_2 and a_3 . Then, the system of evolution equations for the granular gas is formed by Haff's law with the cooling rate approximated within this SA, and the differential equations of a_2 and a_3 . Moreover, the proper linearizations of the equations for \dot{a}_2 and \dot{a}_3 are derived in such a way that their steady states coincide with the best approximate HCS values reported on Ref. [SM09]. In fact, this SA allows us to solve explicitly the system of differential equations for \dot{a}_2 and \dot{a}_3 , see Eqs. (25)–(29) of Article 2 (Section 6.2). These theoretical approaches are tested with EDMD simulation results from the DynamO software [BSL11] for a wide range of values of α , covering elastic, quasielastic, intermediately inelastic, and highly inelastic systems. The HCS values for the fourth and sixth cumulants are compared and concluded to be in good agreement with already reported DSMC values in Ref. [SM09]. Moreover, the evolution equations for a_2 and a_3 under this SA are compared for a wide variety of initial conditions, getting quite a good quantitative agreement for the evolution of a_2 and a more qualitative agreement for the evolution of a_3 , which improves for initial conditions not far from a Maxwellian distribution.

Once the homogeneous states of the system are studied, the quest of a proper nonequilibrium entropy is discussed. First of all, the original H functional [see Eq. (2.111)] presents certain problems that preclude its candidature to be the nonequilibrium entropy of the system. First of all, as already mentioned, the proof of the original H -theorem does not fit any more. Moreover, it presents the so-called measure problem, as introduced in Ref. [MT11]. That is, the H -functional is not invariant under nonunitary transformations. In this system, there exists a natural scaling which is not unitary, $\mathbf{v} \rightarrow \mathbf{c}$. In fact, it is proved that Shannon's measure in the \mathbf{v} space coincides with the H functional for the rescaled VDF, $\phi(\mathbf{c})$, called H^* in Article 2 [see Eq. (34) of Article 2 (Section 6.2)], plus an additional term, which increases with time. This H^* , which could be thought as a possibly candidate, still presents the measure problem. This is solved by the KLD. Then, admitting that a relative measure of entropy as the KLD is required, we need to choose the proper reference VDF, f_{ref} . We compare two possible choices. First, if this reference VDF is chosen as the Maxwellian distribution, $f_{\text{ref}} = f_M$, then, the time dependent KLD will coincide with H^* plus a numerical constant [see Eq. (37) of Article 2 (Section 6.2)]. Moreover, the other choice is the well-based conjecture $f_{\text{ref}} = f_H$. These two choices are analyzed via a numerical Sonine-approximated scheme [see Eqs. (39) and (40) of Article 2 (Section 6.2)] and EDMD simulations for a wide variety of initial conditions and both HD ($d_t = 2$) and HS ($d_t = 3$) systems, as can be observed in Figures 6–9 of Article 2 (Section 6.2). Here, we do observe cases that reject the former choice, whereas all of them are in agreement with the conjecture. Finally, we develop a toy model based on a SA of the KLD up to a_2 . That approximate scheme, together with the evolution equation of the fourth cumulant, indicates a monotonic decay of $\mathcal{D}_{\text{KL}}(f|f_H)$. This latter argument is

in favor of the conjecture of $S = -\mathcal{D}_{\text{KL}}(f|f_{\text{H}})$ being a proper nonequilibrium entropy for this system. At the end of Article 2 (Section 6.2), the quantity $\mathcal{D}_{\text{KL}}(f_{\text{H}}|f_{\text{M}})$ is computed numerically and from EDMD simulation results, which indicates how far one VDF is from the other.

In addition, the toy model derived in Article 2 (Section 6.2) has been extended to an arbitrary reference VDF in Article 3 (Section 6.3). Here, in Article 3 (Section 6.3), we find that, under this approach, there are counterexamples for the choice $\mathcal{D}_{\text{KL}}(f|f_{\text{M}})$ as a possible nonequilibrium entropy, in quite good agreement with new EDMD simulation results for HS. Moreover, these additional simulations are still in accordance with the conjecture $S = -\mathcal{D}_{\text{KL}}(f|f_{\text{H}})$ [see Figure 1 of Article 3 (Section 6.3)]. Finally, in Article 3 (Section 6.3), a Maxwell-demon-like experiment in EDMD simulations was carried out, based on Orban and Bellemans' pioneering works [OB67; OB69] for the EHS model, and Aharony's work [Aha71], including a source of irreversibility in the particle dynamics. We let the system evolve up to a certain *waiting* number of collisions per particle, s_w , and, then, all the velocities are inverted. The evolution of the system is guided by $\mathcal{D}_{\text{KL}}(f|f_{\text{M}})$ in the elastic case, and by $\mathcal{D}_{\text{KL}}(f|f_{\text{H}})$ for $\alpha < 1$. In the elastic case ($\alpha = 1$), original results of Refs. [OB67; OB69] were observed, with the system entering in an anti-kinetic stage, trying to restore its initial state, and this stage being symmetric with respect to the previous evolution. After this returning regime, the system again evolves up to equilibrium. Notice that, in the elastic case, H and $\mathcal{D}_{\text{KL}}(f|f_{\text{M}})$ coincide up to a numerical constant. Moreover, for $\alpha < 1$, this anti-kinetic stage is almost completely suppressed. Only a small hump in the evolution of the KLD is observed in the inelastic case. This is a consequence of the irreversibility introduced into the granular dynamics by the IHS model [see Eqs. (8) and (9) of Article 3 (Section 6.3)]. The results are quite similar to Aharony's observations [Aha71]. These humps are indeed observed to decrease as inelasticity increases [see Figure 2 of Article 3 (Section 6.3)].

6.2 Article 2

Title: Kullback–Leibler Divergence of a Freely Cooling Granular Gas

Authors: Alberto Megías¹ and Andrés Santos^{1,2}

Affiliations:

¹ Departamento de Física, Universidad de Extremadura, E-06006 Badajoz, Spain

² Instituto de Computación Científica Avanzada (ICCAEx), Universidad de Extremadura, E-06006 Badajoz, Spain

Journal: Entropy

Volume: 22

Pages: 1308

Year: 2020

DOI: [10.3390/e22111308](https://doi.org/10.3390/e22111308)



Copy of the preprint of the work: “Alberto Megías, and Andrés Santos, ‘Kullback–Leibler Divergence of a Freely Cooling Granular Gas’, *Entropy* **22** 11, 1308 (2020) <https://doi.org/10.3390/e22111308>.”

Article

Kullback–Leibler Divergence of a Freely Cooling Granular Gas

Alberto Megías¹ and Andrés Santos^{2,*}

¹ Departamento de Física, Universidad de Extremadura, E-06006 Badajoz, Spain; albertom@unex.es

² Departamento de Física and Instituto de Computación Científica Avanzada (ICCAEx), Universidad de Extremadura, E-06006 Badajoz, Spain

* Correspondence: andres@unex.es; Tel.: +34-924-289-651

Received: date; Accepted: date; Published: date

Abstract: Finding the proper entropy-like Lyapunov functional associated with the inelastic Boltzmann equation for an isolated freely cooling granular gas is a still unsolved challenge. The original H -theorem hypotheses do not fit here and the H -functional presents some additional measure problems that are solved by the Kullback–Leibler divergence (KLD) of a reference velocity distribution function from the actual distribution. The right choice of the reference distribution in the KLD is crucial for the latter to qualify or not as a Lyapunov functional, the asymptotic “homogeneous cooling state” (HCS) distribution being a potential candidate. Due to the lack of a formal proof far from the quasielastic limit, the aim of this work is to support this conjecture aided by molecular dynamics simulations of inelastic hard disks and spheres in a wide range of values for the coefficient of restitution (α) and for different initial conditions. Our results reject the Maxwellian distribution as a possible reference, whereas they reinforce the HCS one. Moreover, the KLD is used to measure the amount of information lost on using the former rather than the latter, revealing a non-monotonic dependence with α .

Keywords: Kullback–Leibler divergence; granular gases; kinetic theory; molecular dynamics

1. Introduction

Thermodynamics and information theory are clearly connected via the entropy concept. This idea allows physicists to understand plenty of details and consequences in the evolution and intrinsic behavior of physical systems. However, finding the entropy-like Lyapunov functional for a given problem is not an easy task. Thankfully, information theory provides tools that one can use in physics problems, usually proving a rewarding feedback. Along this paper, and as usually done in the context of information theory [1,2] and nonequilibrium statistical mechanics [3,4], we borrow from equilibrium statistical mechanics and thermodynamics the use of the term “entropy” in a broader sense. The same applies to the term “temperature,” introduced in Equation (3) below.

In this work, we address the quest of finding the Lyapunov functional of an isolated freely cooling monodisperse granular gas, modeled by identical inelastic and smooth hard disks ($d = 2$) or hard spheres ($d = 3$) with constant coefficient of restitution (α). The interest of this study does not only reside in the mathematical challenge, but also in the physical consequences for granular matter. Typically, for a classical gas, Boltzmann’s H -theorem provides the desired entropy-like Lyapunov functional [5,6]. Nevertheless, inelasticity plays a fundamental role in the dynamics, and the hypotheses of the latter theorem are not applicable. Previous works have proposed the Kullback–Leibler divergence (KLD) [7,8] as the proper alternative to the H -functional [9–12]. One of the aims of this paper is to explore with molecular dynamics (MD) simulations [13] the validity of the KLD as a Lyapunov functional in the whole range of definition of α and for both disks and spheres.

The freely cooling one-particle velocity distribution function (VDF) of our granular-gas model is expected to asymptotically reach a scaled form, the so-called “homogenous cooling state” (HCS), f_{HCS} . Although its explicit form is unknown, there is a vast amount of literature about it [14–22]

and recent experiments have demonstrated some of their properties [23]. While computational and experimental evidence supporting the HCS are overwhelming, a rigorous mathematical proof on its existence and long-time approach has only been achieved for inelastic Maxwell models described by the Boltzmann equation [24–28].

The HCS VDF f_{HCS} is usually expressed as an infinite expansion around the Maxwellian VDF in terms of Sonine polynomials [5,14,15], even though the expansion may break down for large inelasticities [29,30]. Here, in order to provide a detailed description of the problem for both the stationary and transient regimes, we revisit some well-known results and also provide new simulation data and theoretical expressions obtained from a truncation in the Sonine expansion up to the sixth cumulant. In particular, our MD simulation results for the HCS fourth and sixth cumulants are compared with previous “direct simulation Monte Carlo” (DSMC) results [18,19] and a good agreement is found.

The paper is structured as follows. In Section 2, the Sonine expansion formalism is presented and simulation and theoretical results for the fourth and sixth cumulants are provided. The measure problem introduced by the original H -functional is established in Section 3 and the KLD for two different reference VDFs is studied and compared with MD simulation outcomes. Finally, in Section 4, some concluding remarks of this work are presented and discussed.

2. Free Cooling Evolution of Velocity Cumulants

2.1. Boltzmann Equation and HCS

Consider a model of a monodisperse granular gas consisting of an isolated collection of inelastic hard d -spheres of mass m , diameter σ , and a constant coefficient of normal restitution $\alpha < 1$. Under the molecular chaos ansatz (*Stosszahlansatz*), the free cooling of a homogeneous and isotropic gas can be described by the Boltzmann equation [14]

$$\partial_t f(\mathbf{v}_1; t) = n\sigma^{d-1} I[\mathbf{v}_1|f, f] \equiv n\sigma^{d-1} \int d\mathbf{v}_2 \int_+ d\hat{\sigma} (\mathbf{v}_{12} \cdot \hat{\sigma}) [\alpha^{-2} f(\mathbf{v}_1''; t) f(\mathbf{v}_2''; t) - f(\mathbf{v}_1; t) f(\mathbf{v}_2; t)], \quad (1)$$

where n is the number density, $\mathbf{v}_{12} = \mathbf{v}_1 - \mathbf{v}_2$ is the relative velocity of the two colliding particles, $\hat{\sigma}$ is a unit vector along the line of centers from particle 1 to particle 2, the subscript $+$ in the integral over $\hat{\sigma}$ means the constraint $\mathbf{v}_{12} \cdot \hat{\sigma} > 0$, and

$$\mathbf{v}_1'' = \mathbf{v}_1 - \frac{1+\alpha}{2\alpha} (\mathbf{v}_{12} \cdot \hat{\sigma}) \hat{\sigma}, \quad \mathbf{v}_2'' = \mathbf{v}_2 + \frac{1+\alpha}{2\alpha} (\mathbf{v}_{12} \cdot \hat{\sigma}) \hat{\sigma} \quad (2)$$

are precollisional velocities. Note that we have defined the VDF with the normalization condition $\int d\mathbf{v} f(\mathbf{v}; t) = 1$.

An important quantity is the *granular temperature* defined as

$$T(t) = \frac{m}{d} \langle v^2 \rangle, \quad \langle X(\mathbf{v}) \rangle \equiv \int d\mathbf{v} X(\mathbf{v}) f(\mathbf{v}; t). \quad (3)$$

Taking moments in Equation (1), one finds the cooling equation

$$\partial_t T(t) = -\zeta(t) T(t), \quad (4)$$

where the cooling rate is given by

$$\zeta(t) = -\frac{mn\sigma^{d-1}}{T(t)d} \int d\mathbf{v} v^2 I[\mathbf{v}|f, f] = (1-\alpha^2) \frac{mn\sigma^{d-1}}{T(t)} \frac{\pi^{(d-1)/2}}{4d\Gamma(\frac{d+3}{2})} \langle\langle v_{12}^3 \rangle\rangle, \quad (5a)$$

$$\langle\langle X(\mathbf{v}_1, \mathbf{v}_2) \rangle\rangle \equiv \int d\mathbf{v}_1 \int d\mathbf{v}_2 X(\mathbf{v}_1, \mathbf{v}_2) f(\mathbf{v}_1; t) f(\mathbf{v}_2; t). \quad (5b)$$

Let us introduce the *thermal* velocity $v_{\text{th}}(t) \equiv \sqrt{2T(t)/m}$, which allows us to define the rescaled VDF $\phi(\mathbf{c}; s)$ as

$$f(\mathbf{v}; t) = v_{\text{th}}^{-d}(t) \phi(\mathbf{c}; s), \quad \mathbf{c} \equiv \frac{\mathbf{v}}{v_{\text{th}}(t)}, \quad (6)$$

where the variable s in $\phi(\mathbf{c}; s)$ is a scaled time defined by

$$s(t) = \frac{1}{2} \int_0^t dt' \nu(t'), \quad \nu(t) \equiv \kappa n \sigma^{d-1} v_{\text{th}}(t), \quad \kappa \equiv \frac{\sqrt{2}\pi^{(d-1)/2}}{\Gamma(\frac{d}{2})}. \quad (7)$$

Here, ν is the (nominal) collision frequency, so that $s(t)$ represents the (nominal) accumulated average number of collisions per particle up to time t . In terms of these dimensionless quantities, the Boltzmann Equation (1) can be rewritten as

$$\frac{\kappa}{2} \partial_s \phi(\mathbf{c}; s) + \frac{\mu_2(s)}{d} \frac{\partial}{\partial \mathbf{c}} \cdot [c \phi(\mathbf{c}; s)] = I[c|\phi, \phi], \quad \mu_k(s) \equiv - \int d\mathbf{c} c^k I[c|\phi, \phi], \quad (8)$$

where we have taken into account that $\zeta(t)/n\sigma^{d-1}v_{\text{th}}(t) = 2\mu_2(s)/d$. The associated hierarchy of moment equations is

$$\frac{\kappa}{2} \partial_s \langle c^k \rangle = F_k(s) \equiv \frac{k\mu_2(s)}{d} \langle c^k \rangle - \mu_k(s). \quad (9)$$

Note that $F_0 = F_2 = 0$, since $\mu_0 = 0$ and $\langle c^2 \rangle = \frac{d}{2}$.

In the long-time limit, the free cooling is expected to reach an asymptotic regime (the HCS) in which the scaled VCF is stationary, i.e., $\phi(\mathbf{c}; s) \rightarrow \phi_{\text{H}}(\mathbf{c})$, where $\phi_{\text{H}}(\mathbf{c})$ satisfies the integrodifferential equation

$$\frac{\mu_2^{\text{H}}}{d} \frac{\partial}{\partial \mathbf{c}} \cdot [c \phi_{\text{H}}(\mathbf{c})] = I[c|\phi_{\text{H}}, \phi_{\text{H}}]. \quad (10)$$

Henceforth, a subscript or superscript H on a quantity means that the quantity is evaluated in the HCS. Within that regime, Equation (5a) shows that $\zeta_{\text{H}}(t)/\sqrt{T_{\text{H}}(t)} = \text{const}$, so that the solution to Equation (4) gives rise to the well-known cooling Haff's law [14,15,31]

$$T_{\text{H}}(t) = \frac{T_{\text{H}}(t_0)}{\left[1 + \frac{1}{2}\zeta_{\text{H}}(t_0)(t - t_0)\right]^2}, \quad (11)$$

t_0 being an arbitrary time belonging to the HCS regime. Also in the HCS regime, $\mu_2(s) \rightarrow \mu_2^{\text{H}} = \text{const}$ and thus Equation (4) becomes $\partial_s T_{\text{H}}(s) = -(4/\kappa d)\mu_2^{\text{H}} T_{\text{H}}(s)$, whose solution is

$$T_{\text{H}}(s) = T_{\text{H}}(s_0) e^{-4\mu_2^{\text{H}}(s-s_0)/\kappa d}. \quad (12)$$

Therefore, in the HCS, the temperature decays exponentially with the average number of collisions per particle.

2.2. Sonine Expansion Formalism

The Maxwell-Boltzmann VDF $\phi_{\text{M}}(\mathbf{c}) = \pi^{-d/2} e^{-c^2}$ is not a solution of the HCS Boltzmann Equation (10). While its analytic form has not been found, the HCS solution is known to be rather close to ϕ_{M} in the domain of thermal velocities ($c \sim 1$) [20]. Thus, it is convenient to represent the time-dependent VDF in terms of a Sonine polynomial expansion,

$$\phi(\mathbf{c}; s) = \phi_{\text{M}}(\mathbf{c}) \left[1 + \sum_{k=2}^{\infty} a_k(s) S_k(c^2) \right], \quad (13)$$

where

$$S_k(x) = L_k^{(\frac{d}{2}-1)}(x) = \sum_{j=0}^k \frac{(-1)^j \Gamma(\frac{d}{2} + k)}{\Gamma(\frac{d}{2} + j) (k-j)!} x^j \quad (14)$$

are Sonine (or generalized Laguerre) polynomials, which satisfy the orthogonalization condition

$$\langle S_k | S_{k'} \rangle \equiv \int dc \phi_M(c) S_k(c^2) S_{k'}(c^2) = \mathcal{N}_k \delta_{k,k'}, \quad \mathcal{N}_k \equiv \frac{\Gamma(\frac{d}{2} + k)}{\Gamma(\frac{d}{2}) k!}. \quad (15)$$

In Equation (13), the Sonine coefficient $a_k(s)$ is the $2k$ -th cumulant of the VDF at time s . According to Equation (15),

$$a_k(s) = \frac{\langle S_k(c^2) \rangle}{\mathcal{N}_k}. \quad (16)$$

In particular, $a_0(s) = 1$, $a_1(s) = 0$, and

$$a_2(s) = \frac{4}{d(d+2)} \langle c^4 \rangle - 1, \quad a_3(s) = 1 + 3a_2 - \frac{8}{d(d+2)(d+4)} \langle c^6 \rangle. \quad (17)$$

2.3. Truncated Sonine Approximation

Thus far, all the results presented in Sections 2.1 and 2.2 are formally exact within the framework of the homogeneous Boltzmann Equation (1). However, in order to obtain explicit results, we need to resort to approximations.

As usual [15–19,29,32], we will start by neglecting the coefficients a_k with $k \geq 4$ in Equation (13), as well as the nonlinear terms a_2^2 , $a_2 a_3$, and a_3^2 in the bilinear collision operator $I[c|\phi, \phi]$. Given a functional $X[\phi]$ of the scaled VDF $\phi(c)$, we will use the notation $\mathcal{L}_3 \{X\}$ to denote the result of that truncation and linearization procedure. Furthermore, if a_3 is also neglected, the corresponding approximation will be denoted by $\mathcal{L}_2 \{X\}$. In particular, in the case of the collisional moments μ_2 , μ_4 , and μ_6 , one has

$$\mathcal{L}_3 \{\mu_2\} = A_0 + A_2 a_2 + A_3 a_3, \quad \mathcal{L}_3 \{\mu_4\} = B_0 + B_2 a_2 + B_3 a_3, \quad \mathcal{L}_3 \{\mu_6\} = C_0 + C_2 a_2 + C_3 a_3, \quad (18)$$

where the expressions for the coefficients A_i , B_i , and C_i as functions of α and d can be found in Ref. [29] and in Appendix A of Ref. [19]. Obviously, $\mathcal{L}_2 \{\mu_2\}$, $\mathcal{L}_2 \{\mu_4\}$, and $\mathcal{L}_2 \{\mu_6\}$ are obtained by formally setting $A_3 \rightarrow 0$, $B_3 \rightarrow 0$, and $C_3 \rightarrow 0$, respectively.

Let us first use the simple approximation \mathcal{L}_2 to estimate a_2^H . From Equation (9), we have that $F_4^H = 0$. Thus, the obvious approximation [17] consists of

$$\mathcal{L}_2 \left\{ \frac{F_4^H}{\langle c^4 \rangle_H} \right\} = 0 \Rightarrow a_2^{H,a} = \frac{(d+2)A_0 - B_0}{B_2 - (d+2)(A_2 + A_0)} = \frac{16(1-\alpha)(1-2\alpha^2)}{9 + 24d - (41 - 8d)\alpha + 30(1-\alpha)\alpha^2}, \quad (19)$$

where, in the last steps, use has been made of the explicit expressions of A_0 , A_2 , B_0 , and B_2 . However, this is not by any means the only possibility of estimating a_2^H [18,19,33]. In particular, one can start from the logarithmic time derivative of the fourth moment and then take

$$\mathcal{L}_2 \left\{ \frac{F_4^H}{\langle c^4 \rangle_H} \right\} = 0 \Rightarrow a_2^{H,b} = \frac{(d+2)A_0 - B_0}{B_2 - B_0 - (d+2)A_2} = \frac{16(1-\alpha)(1-2\alpha^2)}{25 + 24d - (57 - 8d)\alpha - 2(1-\alpha)\alpha^2}. \quad (20)$$

Note that

$$\frac{a_2^{H,a}}{a_2^{H,b}} = 1 + a_2^{H,a} = \frac{1}{1 - a_2^{H,b}}. \quad (21)$$

Both approximations ($a_2^{H,a}$ and $a_2^{H,b}$) are practically indistinguishable in the region $0.6 \lesssim \alpha < 1$, but $a_2^{H,b}$ is much more accurate than $a_2^{H,a}$ for higher inelasticity [18,19].

Next, to estimate a_3^H , we start from the exact condition $F_6^H = 0$ and carry out either the linearization

$$\mathcal{L}_3 \{F_6^H\} = 0 \Rightarrow a_3^{H,a} = G_a(a_2^H) \equiv \frac{C_0 - \frac{3}{4}(d+2)(d+4)A_0 + [C_2 - \frac{3}{4}(d+2)(d+4)(3A_0 + A_2)]a_2^H}{\frac{3}{4}(d+2)(d+4)(A_3 - A_0) - C_3} \quad (22)$$

or, alternatively,

$$\mathcal{L}_3 \left\{ \frac{F_6^H}{\langle c^6 \rangle_H} \right\} = 0 \Rightarrow a_3^{H,b} = G_b(a_2^H) \equiv \frac{C_0 - \frac{3}{4}(d+2)(d+4)A_0 + [C_2 - 3C_0 - \frac{3}{4}(d+2)(d+4)A_2]a_2^H}{\frac{3}{4}(d+2)(d+4)A_3 - C_3 - C_0}. \quad (23)$$

In Equations (22) and (23), a_3^H is expressed in terms of a_2^H . Using Equations (19) and (20), four possibilities in principle arise, namely

$$a_3^{H,aa} = G_a(a_2^{H,a}), \quad a_3^{H,ab} = G_a(a_2^{H,b}), \quad a_3^{H,ba} = G_b(a_2^{H,a}), \quad a_3^{H,bb} = G_b(a_2^{H,b}). \quad (24)$$

Comparison with DSMC results shows that the best general estimates are provided by $a_3^{H,aa}$ and $a_3^{H,ab}$. In what follows, we choose $a_2^{H,b}$ for the fourth cumulant and, for the sake of consistency with that choice, we adopt $a_3^{H,ab}$ for the sixth cumulant. To simplify the notation, we make $a_2^{H,b} \rightarrow a_2^H$ and $a_3^{H,ab} \rightarrow a_3^H$.

Once the (approximate) HCS values a_2^H and a_3^H have been obtained, we turn our attention to the evolution equations of $a_2(s)$ and $a_3(s)$. Approximating Equation (9) with $k = 4$ as $\frac{\kappa}{2} \partial_s \ln \langle c^4 \rangle = \mathcal{L}_2 \{F_4(s) / \langle c^4 \rangle\}$, one obtains

$$\partial_s a_2(s) = -K_2 [1 + a_2(s)] [a_2(s) - a_2^H], \quad K_2 \equiv \frac{8}{d(d+2)\kappa} [B_2 - B_0 - (d+2)A_2]. \quad (25)$$

Its solution is

$$a_2(s) = a_2^H + \frac{1 + a_2^H}{X_0 e^{\gamma s} - 1}, \quad X_0 \equiv \frac{1 + a_2(0)}{a_2(0) - a_2^H}, \quad \gamma \equiv (1 + a_2^H) K_2. \quad (26)$$

Analogously, if Equation (9) with $k = 6$ is approximated as $\frac{\kappa}{2} \partial_s \langle c^6 \rangle = \mathcal{L}_3 \{F_6(s)\}$, the resulting evolution equation for a_3 is

$$\partial_s a_3(s) = 3\partial_s a_2(s) - K_2' [a_2(s) - a_2^H] - K_3 [a_3(s) - a_3^H], \quad (27)$$

where

$$K_2' \equiv \frac{16}{d(d+2)(d+4)\kappa} \left[\frac{3}{4}(d+2)(d+4)(A_2 + 3A_0) - C_2 \right], \quad (28a)$$

$$K_3 \equiv \frac{16}{d(d+2)(d+4)\kappa} \left[\frac{3}{4}(d+2)(d+4)(A_3 - A_0) - C_3 \right]. \quad (28b)$$

Taking into account Equation (26), the solution to Equation (27) is

$$a_3(s) = a_3^H + Y_0 e^{-K_3 s} + (1 + a_2^H) \left[\frac{3}{X_0 e^{\gamma s} - 1} + \left(\frac{K_2'}{K_3} + 3 \right) {}_2F_1 \left(1, \frac{K_3}{\gamma}; \frac{K_3}{\gamma} + 1; X_0 e^{\gamma s} \right) \right], \quad (29a)$$

$$Y_0 \equiv a_3(0) - a_3^H - (1 + a_2^H) \left[\frac{3}{X_0 - 1} + \left(\frac{K_2'}{K_3} + 3 \right) {}_2F_1 \left(1, \frac{K_3}{\gamma}; \frac{K_3}{\gamma} + 1; X_0 \right) \right], \quad (29b)$$

where ${}_2F_1(a, b; c; z)$ is the hypergeometric function [34].

As far as we know, Equations (26) and (29) had not been obtained before.

2.4. Comparison with MD Simulations

The approximate theoretical predictions for a_2^H and a_3^H were tested against results obtained from the DSMC simulation method in, for instance, Refs. [18–20]. However, since the DSMC method is a stochastic scheme to numerically solve the Boltzmann equation [35], it does not prejudice by construction the hypotheses upon which the Boltzmann equation is derived, in particular the molecular chaos ansatz. Therefore, it seems important to validate the Sonine approximations for a_2^H and a_3^H by event-driven MD simulations as well. In addition, the theory allows us to solve the initial-value problem and predict the evolution of the fourth and sixth cumulants, as shown by Equations (26) and (29), and an assessment of those solutions is in order.

In our MD simulations, we studied systems with densities $n\sigma^d \approx 5 \times 10^{-4}$ and 2×10^{-4} for disks and spheres, respectively. It is known that the HCS exhibits a shearing/clustering instability for sufficiently large systems [14,36]. To prevent this, the side length of the simulation box was chosen as $L/\sigma \approx 5 \times 10^3$ for disks and $L/\sigma \approx 4 \times 10^2$ for spheres (see Appendix A for technical details). These values are about 2 and 30 times smaller, respectively, than the critical values beyond which the HCS becomes unstable in the less favorable case considered ($\alpha = 0.1$). Moreover, we have expressly verified that the systems remain stably homogeneous even for long times.

Figures 1a,b show the α -dependence of a_2^H and a_3^H , respectively, for both hard disks ($d = 2$) and spheres ($d = 3$). An excellent agreement between the MD and DSMC simulation results for the whole range of α is observed. This means that the molecular chaos ansatz does not limit the applicability of the Boltzmann description, even for large inelasticities [14], at least for dilute granular gases. As for the approximate theoretical predictions, it is quite apparent that $a_2^{H,b}$ (see Equation (20)) performs very well, even if the fourth cumulant is not small (e.g., $a_2^H \sim 0.2$ at $\alpha = 0.1$). The approximate sixth cumulant $a_3^{H,ab}$ (see Equations (22) and (24)) is less accurate at a quantitative level, especially in the case of disks, but captures quite well the general influence of inelasticity. While a_2^H changes from negative to positive values at $\alpha \simeq 1/\sqrt{2} \simeq 0.71$, a_3^H is always negative. Note that, for large inelasticity, the cumulants a_2^H and a_3^H are comparable in magnitude. Given that the Sonine expansion (13) is only asymptotic [15,30], it is remarkable that a theoretical approach based on the assumptions $|a_3^H| \ll |a_2^H| \ll 1$ does such a good job for high inelasticity as observed in Figure 1.

Next, we study the evolution from a non-HCS state, as monitored by $a_2(s)$ and $a_3(s)$. We have chosen an initial state very far from the HCS: the particles are arranged in an ordered crystalized configuration and all have a common speed $\sqrt{d/2}v_{th}(0)$ along uniformly randomized directions. Therefore, at $s = 0$, $\langle c^k \rangle = (d/2)^{k/2}$, so that $a_2(0) = -\frac{2}{d+2}$ and $a_3(0) = -\frac{16}{(d+2)(d+4)}$.

Figures 2 and 3 compare our MD results with the theoretical predictions (26) and (29), respectively. Four representative values of the coefficient of restitution have been considered, namely $\alpha = 0.1$ (very high inelasticity), 0.4 (high inelasticity), 0.87 (moderately small inelasticity), and 1 (elastic collisions); $\alpha = 0.87$ has been included because it is practically at this value where a_2^H presents a local minimum, both for disks and spheres [see Figure 1a]. Note that, in the case of simulations, the quantity s represents the *actual* average number of collisions per particle and, consequently, is not strictly defined by Equation (7), in contrast to the case of theory. From Figure 2 we observe that, despite the large magnitude of the initial fourth cumulant ($a_2(0) = -\frac{1}{2}$ and $-\frac{2}{5}$ for $d = 2$ and 3, respectively), the simple relaxation law (26) describes very well the full evolution of the cumulant. Discrepancies with the simulation results are visible only in the region ($2 \lesssim s \lesssim 4$) where the curves turn to their stationary values, especially in the case of disks. In what concerns the sixth cumulant, which also has a large initial magnitude ($a_3(0) = -\frac{2}{3}$ and $-\frac{16}{35}$ for $d = 2$ and 3, respectively), the theoretical expression (29) is able to capture, at least, the main qualitative features, including the change from a non-monotonic ($\alpha = 0.1$ and 0.4) to a monotonic ($\alpha = 0.87$ and 1) evolution. Again, the agreement is better for spheres than for disks. Note also that the evolution curves for $\alpha = 0.87$ and 1 are hardly distinguishable from each other.

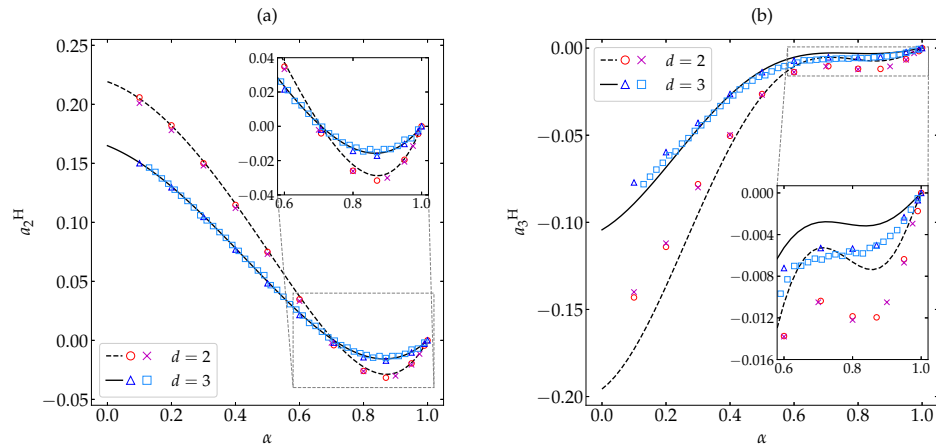


Figure 1. Plot of (a) the HCS fourth cumulant a_2^H and (b) the HCS sixth cumulant a_3^H versus the coefficient of restitution α . Symbols represent simulation results: MD (this work) for disks (\circ) and spheres (\triangle), and DSMC [18,19,29] for disks (\times) and spheres (\square). The lines are the theoretical predictions $a_2^{H,b}$ (see Equation (20)) and $a_3^{H,ab}$ (see Equations (22) and (24)). The insets magnify the region $0.6 \leq \alpha \leq 1.0$. The error bars in the simulation data are smaller than the size of the symbols.

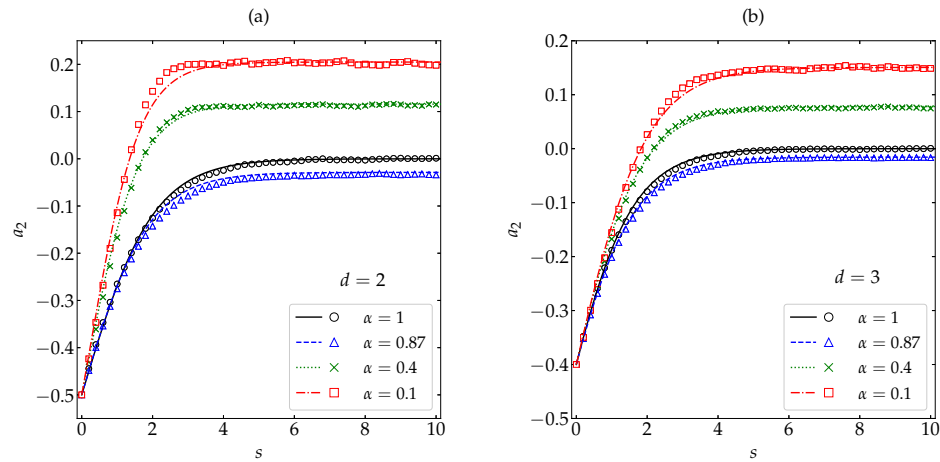


Figure 2. Evolution of the fourth cumulant $a_2(s)$ as a function of the average number of collisions per particle for (a) disks and (b) spheres. Symbols represent MD simulation results, while the lines correspond to the theoretical prediction (26). The values of the coefficient of restitution are (from top to bottom) $\alpha = 0.1$ (\square), 0.4 (\times), 1 (\circ), and 0.87 (\triangle). The error bars in the simulation data are smaller than the size of the symbols.

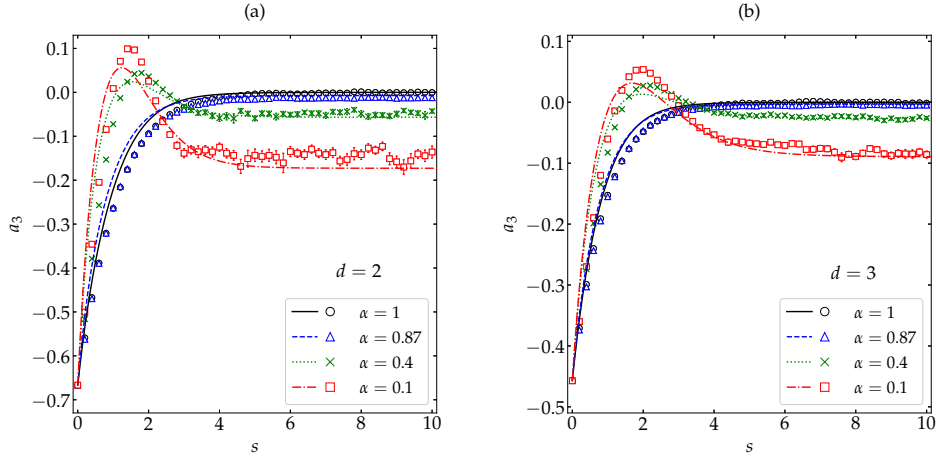


Figure 3. Evolution of the sixth cumulant $a_3(s)$ as a function of the average number of collisions per particle for (a) disks and (b) spheres. Symbols represent MD simulation results, while the lines correspond to the theoretical prediction (29). The values of the coefficient of restitution are (from bottom to top on the right side) $\alpha = 0.1$ (\square), 0.4 (\times), 0.87 (\triangle), and 1 (\circ). The error bars in the simulation data are smaller than the size of the symbols, except in the stationary regime for $\alpha = 0.1$.

In Figures 2 and 3, the initial values $a_2(0)$ and $a_3(0)$ are common to all the coefficients of restitution considered. In order to have a more complete picture, let us now fix the most inelastic systems ($\alpha = 0.1$) and take five different initial conditions. The HCS values of the fourth and sixth cumulants at $\alpha = 0.1$ are $\{a_2^H, a_3^H\} = \{0.206, -0.143\}$ and $\{0.150, -0.077\}$ for $d = 2$ and $d = 3$, respectively. Thus, we have chosen the same initial distribution (hereafter labeled as δ) as in Figures 2 and 3 as a representative example of $a_2(0) < 0$, the Maxwellian distribution (labeled as M) with $a_2(0) = 0$, another one (labeled as I) with $0 < a_2(0) < a_2^H$, and two more (labeled as Γ and S) with $a_2(0) > a_2^H$. The details of those five distributions can be found in Appendix B and the corresponding values of $a_2(0)$ and $a_3(0)$ are shown in Table A1. In the case of $a_2(s)$, Figure 4 shows again an excellent agreement between theory and simulation, except for the initial condition Γ and near the turning point already observed in Figure 2 for the initial condition δ . In what concerns $a_3(s)$, one can observe from Figure 5 that the performance of the approximation (29) is generally fair, especially for the initial conditions M and I. The limitations of Equation (26) for the initial condition Γ and of Equation (29) for the initial conditions Γ , S, and δ are due to the role played by higher-order cumulants in those cases.

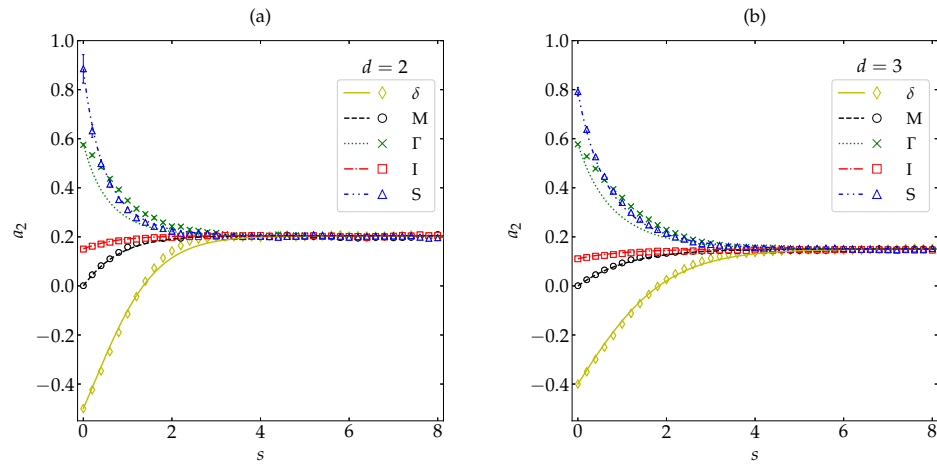


Figure 4. Evolution of the fourth cumulant $a_2(s)$ for a coefficient of restitution $\alpha = 0.1$ as a function of the average number of collisions per particle for (a) disks and (b) spheres. Symbols represent MD simulation results, while the lines correspond to the theoretical prediction (26). Five different initial conditions are considered (see Appendix B): δ (\diamond), M (\circ), Γ (\times), I (\square), and S (\triangle). The error bars in the simulation data are smaller than the size of the symbols, except in the early stage for the initial condition S.

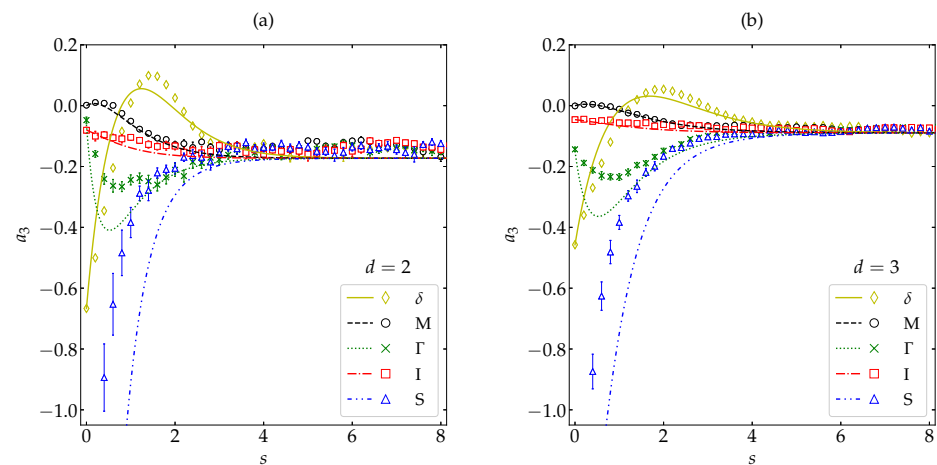


Figure 5. Evolution of the sixth cumulant $a_3(s)$ for a coefficient of restitution $\alpha = 0.1$ as a function of the average number of collisions per particle for (a) disks and (b) spheres. Symbols represent MD simulation results, while the lines correspond to the theoretical prediction (29). Five different initial conditions are considered (see Appendix B): δ (\diamond), M (\circ), Γ (\times), I (\square), and S (\triangle). The error bars in the simulation data are smaller than the size of the symbols, except in the early stage for the initial condition S.

3. KLD as a Lyapunov Functional

In this section, we restrict ourselves to spatially homogeneous states.

3.1. Boltzmann's H-Functional

The introduction of the H -theorem by Ludwig Boltzmann [37] was a revolution in physics and became an inspiration for new mathematical and physical concepts. This theorem is a direct

consequence of the Boltzmann kinetic equation for classical rarefied gases, derived under its molecular chaos assumption [5,6]. Beneath this hypothesis for a classical gas which evolves via *elastic* collisions, the H -functional defined as

$$H(t) = \int d\mathbf{v} f(\mathbf{v}; t) \ln f(\mathbf{v}; t) \quad (30)$$

is proved to be a non-increasing quantity; in other words, $S = -H$, up to a constant, is a non-decreasing entropy-like Lyapunov functional for the assumed gaseous system. After almost a century, once Information Theory was developed, Boltzmann's H -functional was interpreted as Shannon's measure [1] for the one-particle VDF of a rarefied gas.

Nonetheless, the model considered in this paper for a rarefied monocomponent granular gas (inelastic and smooth hard d -spheres with a constant coefficient of restitution) violates Boltzmann's hypothesis of elastic collisions. In fact, a key role in the demonstration of the H -theorem for elastic collisions is played by the condition of collisional symmetry [37]. Consider two colliding particles with precollision velocities $\{v'_1, v'_2\}$ and a relative orientation characterized by the unit vector $-\hat{\sigma}$ (with $v'_{12} \cdot \hat{\sigma} < 0$). After collision, the velocities are, in agreement with Equation (2), given by

$$\mathfrak{C}_{-\hat{\sigma}}\{v'_1, v'_2\} = \{v_1, v_2\}, \quad v_{1,2} = v'_{1,2} \mp \frac{1+\alpha}{2}(v'_{12} \cdot \hat{\sigma})\hat{\sigma}. \quad (31)$$

Next, suppose two colliding particles with precollision velocities $\{v_1, v_2\}$ and a relative orientation characterized by the unit vector $\hat{\sigma}$ (with $v_{12} \cdot \hat{\sigma} > 0$). In that case,

$$\mathfrak{C}_{\hat{\sigma}}\{v_1, v_2\} = \mathfrak{C}_{-\hat{\sigma}}\{v'_1, v'_2\} = \{v'_1, v'_2\}, \quad v'_{1,2} = v_{1,2} \mp \frac{1+\alpha}{2}(v_{12} \cdot \hat{\sigma})\hat{\sigma}. \quad (32)$$

Comparison with Equation (2) shows that

$$v'_{1,2} = v_{1,2} \pm \frac{1-\alpha^2}{2\alpha}(v_{12} \cdot \hat{\sigma})\hat{\sigma}, \quad v'_{12} \cdot \hat{\sigma} = \alpha^2 v_{12} \cdot \hat{\sigma}. \quad (33)$$

Thus, $\mathfrak{C}_{\hat{\sigma}}\mathfrak{C}_{-\hat{\sigma}}\{v'_1, v'_2\} \neq \{v'_1, v'_2\}$ unless $\alpha = 1$ and, therefore, the H -functional, as defined by Equation (30), is not ensured to be non-increasing anymore if $\alpha < 1$.

Furthermore, Boltzmann's H -functional for the model of inelastic particles presents the so-called measure problem [38]. Shannon's measure is invariant under unitary transformations, but not for rescaling. In fact, under the transformation (6),

$$H(s) = \int d\mathbf{v} f(\mathbf{v}, t) \ln f(\mathbf{v}, t) = H^*(s) - \frac{d}{2} \ln \frac{2T(s)}{m}, \quad H^*(s) \equiv \int d\mathbf{c} \phi(\mathbf{c}, s) \ln \phi(\mathbf{c}, s). \quad (34)$$

From Haff's law, Equation (12), it turns out that (in the HCS) H_{H}^* is stationary but $H_{\text{H}}(s)$ grows linearly with the average number of collisions s . Then, one could naively think that a possible candidate to the Lyapunov functional would be $H^*(s)$, but the latter is still non-invariant under a change of variables $\mathbf{c} \rightarrow \tilde{\mathbf{c}} = \mathbf{w}(\mathbf{c})$, $\phi(\mathbf{c}, s) \rightarrow \tilde{\phi}(\tilde{\mathbf{c}}, s) = J^{-1}\phi(\mathbf{c}, s)$, where $J \equiv |\partial\tilde{\mathbf{c}}/\partial\mathbf{c}|$ is the Jacobian of the invertible transformation $\tilde{\mathbf{c}} = \mathbf{w}(\mathbf{c})$. As will be seen below, whereas Shannon's measure presents a problematic weighting of the phase space, the KLD solves this non-invariance issue.

3.2. KLD

In general, given two distribution functions $f(\mathbf{x})$ and $g(\mathbf{x})$, one defines the KLD from g to f (or *relative entropy* of f with respect to g) as [7,8], as

$$\mathcal{D}_{\text{KL}}(f||g) = \int_X d\mathbf{x} f(\mathbf{x}) \ln \frac{f(\mathbf{x})}{g(\mathbf{x})}, \quad (35)$$

where x is a random vector variable defined on the set X . The quantity $\mathcal{D}_{\text{KL}}(f\|g)$ is convex and non-negative, being identically zero if and only if $f = g$. While it is not a distance or metric function (it does not obey either symmetry or triangle inequality properties), $\mathcal{D}_{\text{KL}}(f\|g)$ somehow measures how much a *reference* distribution g *diverges* from the actual distribution f or, equivalently, the amount of information lost when g is used to approximate f .

Therefore, it seems convenient to define the KLD

$$\mathcal{D}_{\text{KL}}(f\|f_{\text{ref}}) = \mathcal{D}_{\text{KL}}(\phi\|\phi_{\text{ref}}) = \int \mathrm{d}\mathbf{c} \phi(\mathbf{c};s) \ln \frac{\phi(\mathbf{c};s)}{\phi_{\text{ref}}(\mathbf{c})} \quad (36)$$

as the entropy-like Lyapunov functional for our problem, where the (stationary) reference function ϕ_{ref} must be an *attractor* to ensure the Lyapunov-functional condition. Thus, if we choose $\phi_{\text{ref}}(\mathbf{c}) = \lim_{s \rightarrow \infty} \phi(\mathbf{c};s)$, assuming that this limit exists, it will minimize the KLD for asymptotically long times. In addition, the definition (36) solves the measure problem posed above, i.e., $\mathcal{D}_{\text{KL}}(\phi\|\phi_{\text{ref}}) = \mathcal{D}_{\text{KL}}(\tilde{\phi}\|\tilde{\phi}_{\text{ref}})$ for any invertible transformation $\mathbf{c} \rightarrow \tilde{\mathbf{c}} = \mathbf{w}(\mathbf{c})$.

If $\mathcal{D}_{\text{KL}}(\phi\|\phi_{\text{ref}})$ is indeed the Lyapunov functional of our problem, the natural conjecture is that $\phi_{\text{ref}}(\mathbf{c}) = \phi_{\text{H}}(\mathbf{c})$ [11]. As a consequence, the challenge is to prove that $\partial_s \mathcal{D}_{\text{KL}}(\phi\|\phi_{\text{H}}) \leq 0$ (see Appendix C for a formal expression of $\partial_s \mathcal{D}_{\text{KL}}(\phi\|\phi_{\text{ref}})$ in the context of the inelastic Boltzmann equation). While in this paper we do not intend to address such a proof from a mathematical point of view, we will provide support by means of MD simulations (see Appendix A for technical details). Before doing that, and in order to put the problem in a proper context, we consider the alternative choice $\phi_{\text{ref}} = \phi_{\text{M}}$.

3.3. MD Simulations

3.3.1. Maxwellian Distribution as a Reference ($\phi_{\text{ref}} = \phi_{\text{M}}$)

If $\phi_{\text{ref}} = \phi_{\text{M}}$ is chosen in Equation (36), one simply has

$$\mathcal{D}_{\text{KL}}(\phi\|\phi_{\text{M}}) = H^*(s) + \frac{d}{2} (1 + \ln \pi), \quad (37)$$

where $H^*(s)$ is defined in Equation (34). Thus, $\mathcal{D}_{\text{KL}}(\phi\|\phi_{\text{M}})$ differs from $H^*(s)$ by a constant, so that $\partial_s \mathcal{D}_{\text{KL}}(\phi\|\phi_{\text{M}}) = \partial_s H^*(s)$.

Note that $\partial_s \mathcal{D}_{\text{KL}}(\phi\|\phi_{\text{M}})$ cannot be semi-definite negative for *arbitrary* initial conditions. For instance, if the initial condition is a Maxwellian, i.e., $\phi(\mathbf{c};0) = \phi_{\text{M}}(\mathbf{c})$, then it is obvious that $\mathcal{D}_{\text{KL}}(\phi\|\phi_{\text{M}})|_{s=0} = 0$ and, given that $\lim_{s \rightarrow \infty} \mathcal{D}_{\text{KL}}(\phi\|\phi_{\text{M}}) = \mathcal{D}_{\text{KL}}(\phi_{\text{H}}\|\phi_{\text{M}}) > 0$, it is impossible that $\partial_s \mathcal{D}_{\text{KL}}(\phi\|\phi_{\text{M}}) \leq 0$ for all s . Nevertheless, in principle, it might happen that $\partial_s \mathcal{D}_{\text{KL}}(\phi\|\phi_{\text{M}}) \leq 0$ for the class of initial conditions such that $\mathcal{D}_{\text{KL}}(\phi\|\phi_{\text{M}})|_{s=0} \geq \mathcal{D}_{\text{KL}}(\phi_{\text{H}}\|\phi_{\text{M}})$, while $\partial_s \mathcal{D}_{\text{KL}}(\phi\|\phi_{\text{M}}) \geq 0$ for the complementary class of initial conditions such that $\mathcal{D}_{\text{KL}}(\phi\|\phi_{\text{M}})|_{s=0} \leq \mathcal{D}_{\text{KL}}(\phi_{\text{H}}\|\phi_{\text{M}})$. If that were the case, one could say that the quantity $[\mathcal{D}_{\text{KL}}(\phi\|\phi_{\text{M}}) - \mathcal{D}_{\text{KL}}(\phi_{\text{H}}\|\phi_{\text{M}})]^2$ would always decrease for every initial condition, thus qualifying as a Lyapunov functional. As will be seen below, this expectation is frustrated by our simulation results.

From the formal Sonine expansion (13), one has

$$\mathcal{D}_{\text{KL}}(\phi\|\phi_{\text{M}}) = \int \mathrm{d}\mathbf{c} \phi_{\text{M}}(\mathbf{c}) \left[1 + \sum_{k=2}^{\infty} a_k(s) S_k(c^2) \right] \ln \left[1 + \sum_{k=2}^{\infty} a_k(s) S_k(c^2) \right]. \quad (38)$$

Now, in the spirit of the truncation approximation of Section 2.3, we can write the approximate expression

$$\mathcal{D}_{\text{KL}}(\phi\|\phi_{\text{M}}) \approx \int \mathrm{d}\mathbf{c} \phi_{\text{M}}(\mathbf{c}) \left[1 + a_2(s) S_2(c^2) + a_3(s) S_3(c^2) \right] \ln \left[1 + a_2(s) S_2(c^2) + a_3(s) S_3(c^2) \right], \quad (39)$$

where $a_2(s)$ and $a_3(s)$ are given by Equations (26) and (29), respectively. Since the truncated Sonine approximation is not positive definite, we will take the real part of the right-hand side of Equation (39) for times such that $1 + a_2(s)S_2(c^2) + a_3(s)S_3(c^2) < 0$ for a certain range of velocities.

Figure 6 shows the evolution of $\mathcal{D}_{\text{KL}}(\phi\|\phi_M)$ for the same initial conditions and the same values of α as in Figures 2 and 3, as obtained from our MD simulations (for details, see Appendix A) and from the crude approximation (39). For that initial condition, one clearly has $\mathcal{D}_{\text{KL}}(\phi\|\phi_M)|_{s=0} > \mathcal{D}_{\text{KL}}(\phi_H\|\phi_M)$. A monotonic behavior $\partial_s \mathcal{D}_{\text{KL}}(\phi\|\phi_M) \leq 0$ is observed only in the cases of small or vanishing inelasticity. For $\alpha = 0.1$ and 0.4 , however, $\mathcal{D}_{\text{KL}}(\phi\|\phi_M)$ does not present a monotonic decay but tends to its asymptotic value $\mathcal{D}_{\text{KL}}(\phi_H\|\phi_M)$ from below, there existing a time ($s \sim 2$) at which $\mathcal{D}_{\text{KL}}(\phi\|\phi_M)$ exhibits a local minimum. This non-monotonic behavior is certainly exaggerated by the truncated Sonine approximation (39), but it is clearly confirmed by our MD simulations, especially in the case of spheres. Therefore, it is quite obvious that, not unexpectedly, both $\mathcal{D}_{\text{KL}}(\phi\|\phi_M)$ and $[\mathcal{D}_{\text{KL}}(\phi\|\phi_M) - \mathcal{D}_{\text{KL}}(\phi_H\|\phi_M)]^2$ must be discarded as a Lyapunov functional for the free cooling of granular gases.

In order to examine how generic the non-monotonic behavior of $\mathcal{D}_{\text{KL}}(\phi\|\phi_M)$ is for high inelasticity, we have taken the case $\alpha = 0.1$ and considered the same five different initial conditions as in Figures 4 and 5 (see Appendix B). The results are displayed in Figure 7, where we can observe that only the initial condition δ exhibits a non-monotonic behavior, whereas $\mathcal{D}_{\text{KL}}(\phi\|\phi_M)$ decays (grows) monotonically in the cases of the initial conditions Γ and S (M and I). This shows that the nonmonotonicity in the time evolution of $\mathcal{D}_{\text{KL}}(\phi\|\phi_M)$ is a rather subtle effect requiring high inelasticity and special initial conditions.

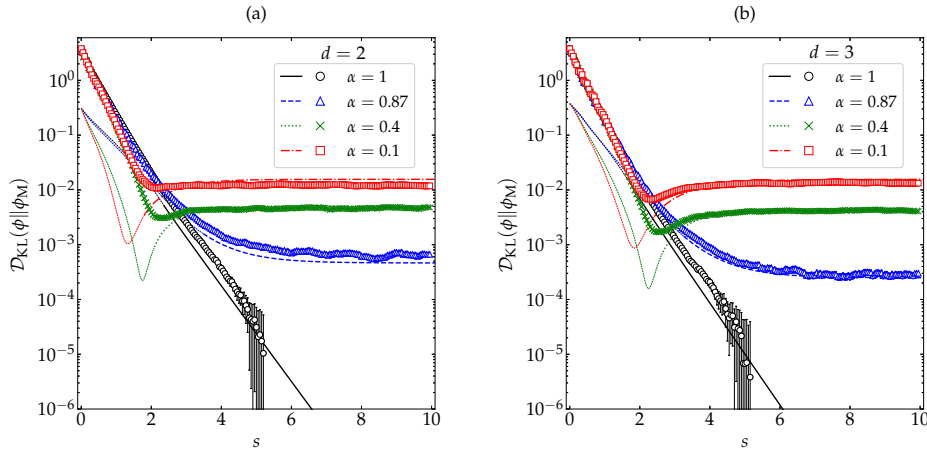


Figure 6. Evolution of $\mathcal{D}_{\text{KL}}(\phi\|\phi_M)$ (in logarithmic scale) as a function of the average number of collisions per particle for (a) disks and (b) spheres. Symbols represent MD simulation results, while the lines correspond to the theoretical approximation (39) (the thin dashed lines for the first stage of the evolution mean that it was necessary to take the real part). The values of the coefficient of restitution are (from top to bottom on the right side) $\alpha = 0.1$ (\square), 0.4 (\times), 0.87 (\triangle), and 1 (\circ). The error bars in the simulation data are smaller than the size of the symbols, except when $\mathcal{D}_{\text{KL}}(\phi\|\phi_M) \lesssim 10^{-4}$ for $\alpha = 1$.

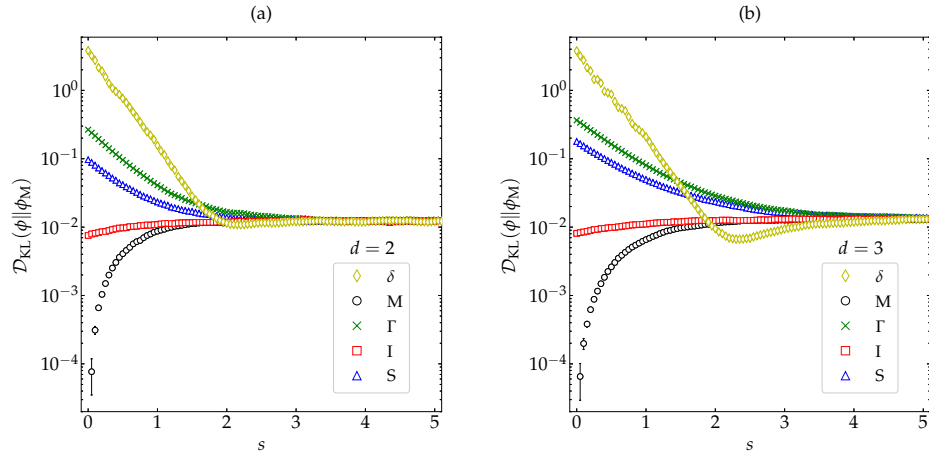


Figure 7. Evolution of $\mathcal{D}_{\text{KL}}(\phi\|\phi_{\text{M}})$ (in logarithmic scale) for a coefficient of restitution $\alpha = 0.1$ as a function of the average number of collisions per particle for hard (a) disks and (b) spheres. Symbols represent MD simulation results. Five different initial conditions are considered (see Appendix B): δ (\diamond), M (\circ), Γ (\times), I (\square), and S (\triangle). The error bars are smaller than the size of the symbols, except when $\mathcal{D}_{\text{KL}}(\phi\|\phi_{\text{M}}) \lesssim 10^{-4}$ for the initial condition M.

3.3.2. HCS Distribution as a Reference ($\phi_{\text{ref}} = \phi_{\text{H}}$)

By using formal arguments from Refs. [39–41], García de Soria et al. [11] proved by means of a perturbation analysis around $\alpha = 1$ that ϕ_{H} is a unique local minimizer of the entropy production, implying that $\partial_s \mathcal{D}_{\text{KL}}(\phi\|\phi_{\text{H}}) \leq 0$, in the *quasielastic* limit. Those authors also conjectured that this result keeps being valid in the whole inelasticity regime, this conjecture being supported by simulations for $\alpha \geq 0.8$ in the freely cooling case.

By performing MD simulations for a wide range of inelasticities ($\alpha = 0.1, 0.2, 0.3, 0.4, 0.5, 0.6, 1/\sqrt{2}, 0.8, 0.87, 0.95$, and 0.99), we have found further support for the inequality $\partial_s \mathcal{D}_{\text{KL}}(\phi\|\phi_{\text{H}}) \leq 0$. As an illustration, Figure 8 shows the evolution of $\mathcal{D}_{\text{KL}}(\phi\|\phi_{\text{H}})$ for $\alpha = 0.1, 0.4, 0.87$, and 1 , starting from the same initial states as in Figures 2, 3, and 6. In the evaluation of $\mathcal{D}_{\text{KL}}(\phi\|\phi_{\text{H}})$, we have used the simulation results for both the transient distribution $\phi(c; s)$ and the asymptotic HCS distribution $\phi_{\text{H}}(c)$ (see Appendix A). Our MD results are compared with a theoretical approximation similar to that of Equation (39), i.e.,

$$\mathcal{D}_{\text{KL}}(\phi\|\phi_{\text{H}}) \approx \int dc \phi_{\text{M}}(c) \left[1 + a_2(s)S_2(c^2) + a_3(s)S_3(c^2) \right] \ln \frac{1 + a_2(s)S_2(c^2) + a_3(s)S_3(c^2)}{1 + a_2^{\text{H}}S_2(c^2) + a_3^{\text{H}}S_3(c^2)}, \quad (40)$$

where again the real part of the right-hand side is taken if $1 + a_2(s)S_2(c^2) + a_3(s)S_3(c^2) < 0$ for a certain range of velocities. The results (both from MD and from the approximate theory) displayed in Figure 8 show that $\mathcal{D}_{\text{KL}}(\phi\|\phi_{\text{H}})$ indeed decays monotonically to 0, even for very strong inelasticity, thus supporting its status as a very sound candidate of Lyapunov functional. It is also interesting to note that the characteristic relaxation time is generally shorter for disks than for spheres and tends to decrease with increasing inelasticity.

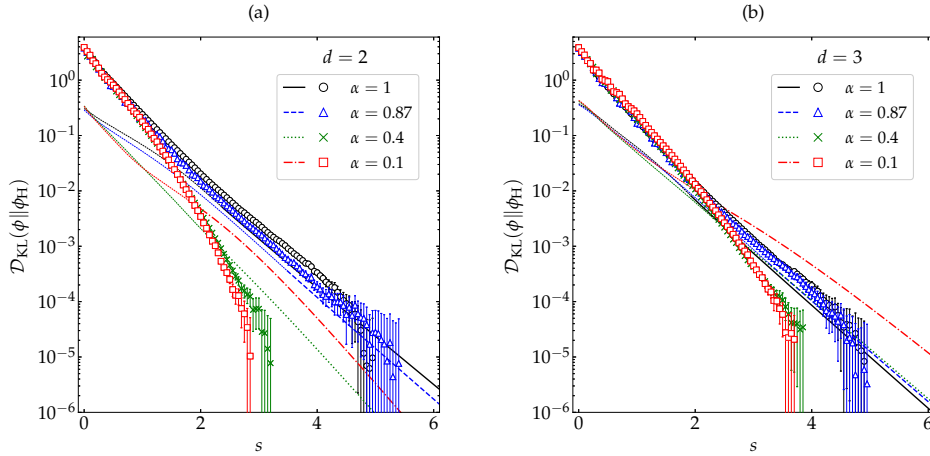


Figure 8. Evolution of $\mathcal{D}_{\text{KL}}(\phi||\phi_{\text{H}})$ (in logarithmic scale) as a function of the average number of collisions per particle for (a) disks and (b) spheres. Symbols represent MD simulation results, while the lines correspond to the theoretical prediction (40) (the thin dashed lines for the first stage of the evolution meaning that it was necessary to take the real part). The values of the coefficient of restitution are $\alpha = 0.1$ (\square), 0.4 (\times), 0.87 (\triangle), and 1 (\circ). The error bars in the simulation data are smaller than the size of the symbols, except when $\mathcal{D}_{\text{KL}}(\phi||\phi_{\text{M}}) \lesssim 10^{-4}$.

In order to reinforce the monotonic decay of $\mathcal{D}_{\text{KL}}(\phi||\phi_{\text{H}})$ observed in Figure 8 for several representative values of the coefficient of restitution, let us now take the most demanding case ($\alpha = 0.1$) and choose the five initial conditions already considered in Figures 4, 5, and 7 (see Appendix B). Figure 9 shows that the evolution of $\mathcal{D}_{\text{KL}}(\phi||\phi_{\text{H}})$ keeps being monotonic for this wide spectrum of representative initial conditions, the relaxation to the HCS being again faster for disks than for spheres. It is also interesting to comment that, although the largest initial divergence corresponds to the initial distribution δ , this divergence decays more rapidly than the other four ones, and even seems to overtake the divergence associated with the initial condition Γ .

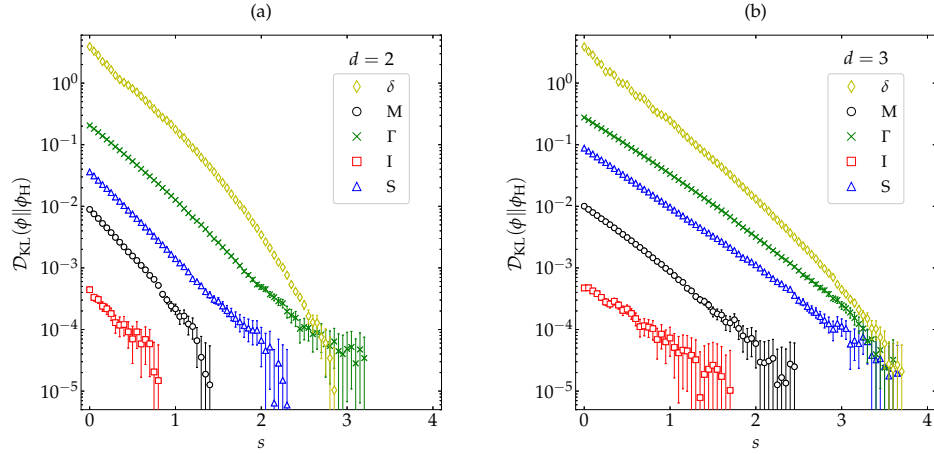


Figure 9. Evolution of $\mathcal{D}_{\text{KL}}(\phi \parallel \phi_{\text{H}})$ (in logarithmic scale) for a coefficient of restitution $\alpha = 0.1$ as a function of the average number of collisions per particle for hard (a) disks and (b) spheres. Symbols represent MD simulation results. Five different initial conditions are considered (see Appendix B): δ (\diamond), M (\circ), Γ (\times), I (\square), and S (\triangle). The error bars are smaller than the size of the symbols, except when $\mathcal{D}_{\text{KL}}(\phi \parallel \phi_{\text{M}}) \lesssim 10^{-4}$.

While a rigorous mathematical proof of $\partial_s \mathcal{D}_{\text{KL}}(\phi \parallel \phi_{\text{H}}) \leq 0$ is still lacking (see, however, Ref. [42] for the sketch of a proof in the context of the linear Boltzmann equation), we will now prove this inequality by using a simplified *toy model*. We start from the infinite series expansion (13) and imagine a formal bookkeeping parameter ϵ in front of the Sonine summation. Then, to the second order in ϵ ,

$$\frac{\phi(c; s)}{\phi_{\text{M}}(c)} \ln \frac{\phi(c; s)}{\phi_{\text{H}}(c)} = \epsilon \sum_{k=2}^{\infty} [a_k(s) - a_k^{\text{H}}] S_k(c^2) + \frac{\epsilon^2}{2} \sum_{k, k'=2}^{\infty} [a_k(s) - a_k^{\text{H}}] [a_{k'}(s) - a_{k'}^{\text{H}}] S_k(c^2) S_{k'}(c^2) + \mathcal{O}(\epsilon^3). \quad (41)$$

Next, taking into account the orthogonality condition (15), we get

$$\mathcal{D}_{\text{KL}}(\phi \parallel \phi_{\text{H}}) = \frac{\epsilon^2}{2} \sum_k \mathcal{N}_k [a_k(s) - a_k^{\text{H}}]^2 + \mathcal{O}(\epsilon^3), \quad (42a)$$

$$\partial_s \mathcal{D}_{\text{KL}}(\phi \parallel \phi_{\text{H}}) = \epsilon^2 \sum_k \mathcal{N}_k [a_k(s) - a_k^{\text{H}}] \partial_s a_k(s) + \mathcal{O}(\epsilon^3). \quad (42b)$$

Interestingly, this approximation preserves the positive-definiteness of the KLD. Note also that, to order ϵ^2 , $\mathcal{D}_{\text{KL}}(\phi \parallel \phi_{\text{H}})$ is symmetric under the exchange $\phi \leftrightarrow \phi_{\text{H}}$, i.e., $\mathcal{D}_{\text{KL}}(\phi \parallel \phi_{\text{H}}) - \mathcal{D}_{\text{KL}}(\phi_{\text{H}} \parallel \phi) = \mathcal{O}(\epsilon^3)$. Finally, consistent with the derivation of Equations (20) and (25), we neglect the cumulants a_k with $k \geq 3$ and apply Equation (25) to obtain

$$\mathcal{D}_{\text{KL}}(\phi \parallel \phi_{\text{H}}) \approx \frac{d(d+2)}{16} [a_2(s) - a_2^{\text{H}}]^2, \quad (43a)$$

$$\partial_s \mathcal{D}_{\text{KL}}(\phi \parallel \phi_{\text{H}}) \approx -\frac{d(d+2)}{8} K_2 [1 + a_2(s)] [a_2(s) - a_2^{\text{H}}]^2 \leq 0, \quad (43b)$$

where we have formally set $\epsilon = 1$. Although a certain number of approximations have been done to derive the toy model (43), it undoubtedly provides further support to the conjecture $\partial_s \mathcal{D}_{\text{KL}}(\phi \parallel \phi_{\text{H}}) \leq 0$.

3.3.3. Relative Entropy of ϕ_{H} with Respect to ϕ_{M}

It is well known that, in a freely cooling granular gas, the HCS VDF is generally close (at least within the range of thermal velocities) to a Maxwellian. In particular, the cumulants a_k^{H} are rather small in magnitude,

except at large inelasticity (see Figure 1). On the other hand, the HCS VDF exhibits an exponential high-velocity tail, $\ln \phi_H(c) \sim -c$, with respect to the Maxwellian behavior, $\ln \phi_M(c) \sim -c^2$ [17,23,43].

Here, we have one more tool to measure how far $\phi_M(c)$ is from $\phi_H(c)$, namely the KLD from ϕ_M to ϕ_H (or relative entropy of ϕ_H with respect to ϕ_M), i.e., $\mathcal{D}_{\text{KL}}(\phi_H \parallel \phi_M)$. Note, however, that, as said at the beginning of this section, the KLD is not a real metric since it does not fulfill either symmetry or triangle inequality properties of a distance.

Figure 10 displays the α -dependence of $\mathcal{D}_{\text{KL}}(\phi_H \parallel \phi_M)$ for both disks and spheres, as obtained from our MD simulations (see again Appendix A) and from the simple estimate (39) with $a_2(s) \rightarrow a_2^{\text{H}}$ and $a_3(s) \rightarrow a_3^{\text{H}}$. We can observe that the theoretical truncated approach successfully captures (i) a weak influence of dimensionality (in contrast to the fourth and sixth cumulants plotted in Figure 1), (ii) a crossover from $\mathcal{D}_{\text{KL}}(\phi_H \parallel \phi_M)|_{d=2} < \mathcal{D}_{\text{KL}}(\phi_H \parallel \phi_M)|_{d=3}$ for very large inelasticity to $\mathcal{D}_{\text{KL}}(\phi_H \parallel \phi_M)|_{d=2} > \mathcal{D}_{\text{KL}}(\phi_H \parallel \phi_M)|_{d=3}$ for smaller inelasticity, and (iii) a non-monotonic dependence on α , with a (small but nonzero) local minimum at about $\alpha = 1/\sqrt{2} \simeq 0.71$ and a local maximum at about $\alpha = 0.87$. The latter property implies that, in the region $0.6 \lesssim \alpha < 1$, three systems differing in the value of α may share the same divergence of ϕ_M from ϕ_H . The qualitative shape of $\mathcal{D}_{\text{KL}}(\phi_H \parallel \phi_M)$ as a function of α agrees with a toy model analogous to that of Equation (43a), namely $\mathcal{D}_{\text{KL}}(\phi_H \parallel \phi_M) \approx \frac{d(d+2)}{16} a_2^{\text{H}^2}$.

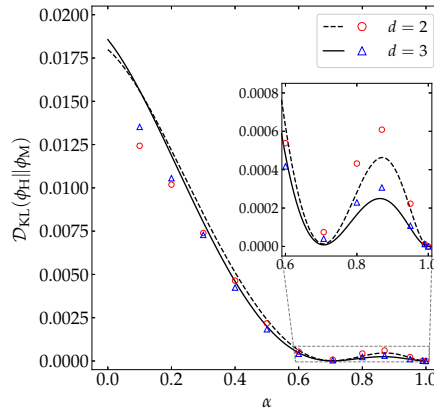


Figure 10. Plot of $\mathcal{D}_{\text{KL}}(\phi_H \parallel \phi_M)$ as a function of the coefficient of restitution α for disks ($- \circ -$) and spheres ($- \triangle -$). Symbols represent MD simulation results, while the lines correspond to the theoretical prediction provided by Equation (39) with $a_2(s) \rightarrow a_2^{\text{H}}$ and $a_3(s) \rightarrow a_3^{\text{H}}$. The inset magnifies the region $0.6 \leq \alpha \leq 1$. The error bars in the simulation data are smaller than the size of the symbols.

4. Summary and Conclusions

In this work, we have mainly focused on the role as a potential entropy-like Lyapunov functional played by the KLD of a reference VDF (ϕ_{ref}) with respect to the *spatially homogeneous* time-dependent VDF (ϕ), i.e., $\mathcal{D}_{\text{KL}}(\phi \parallel \phi_{\text{ref}})$, as supported by MD simulations in a freely cooling granular-gas model.

First, we have revisited the problem of obtaining, by kinetic theory methods, simple approximations for the HCS fourth (a_2^{H}) and sixth (a_3^{H}) cumulants, and have derived explicit time-dependent solutions, $a_2(s)$ and $a_3(s)$, for arbitrary (homogeneous) initial conditions. Comparison with our MD results shows an excellent general performance of a_2^{H} and $a_2(s)$ for values of the coefficient of restitution as low as $\alpha = 0.1$ and for a variety of initial conditions. In the case of the sixth cumulant, however, the agreement is mainly semi-quantitative. In any case, our MD data for a_2^{H} and a_3^{H} agree very well with previous simulations of the inelastic Boltzmann equation [18–20,29], thus validating the applicability of kinetic theory (including the Stosszahlansatz) even for high inelasticity. We emphasize that, to the best of our knowledge, such a comprehensive MD analysis of the fourth and sixth cumulants had not been carried out before. We are not aware either of a previous (approximate) theoretical derivation of the time-dependent quantities $a_2(s)$ and $a_3(s)$.

As a first candidate to a Lyapunov functional, we have considered the KLD with a Maxwellian reference VDF ($\phi_{\text{ref}} = \phi_M$). However, this possibility is clearly discarded as both simulation and a simple theoretical

approach show that $\mathcal{D}_{\text{KL}}(\phi\|\phi_{\text{M}})$ does not relax monotonically for highly inelastic systems and certain initial conditions. On the other hand, when the asymptotic HCS VDF is chosen as a reference ($\phi_{\text{ref}} = \phi_{\text{H}}$), the results show that the relaxation of $\mathcal{D}_{\text{KL}}(\phi\|\phi_{\text{H}})$ is monotonic for a wide spectrum of inelasticities and initial conditions. This is further supported by a simplified toy model, according to which $\partial_s \mathcal{D}_{\text{KL}}(\phi\|\phi_{\text{H}}) \sim -[a_2(s) - a_2^{\text{H}}]^2 \leq 0$. While simulation results supporting the conjecture $\partial_s \mathcal{D}_{\text{KL}}(\phi\|\phi_{\text{H}}) \leq 0$ had been presented before [11], it is subjected here to more stringent tests by considering highly dissipative collisions ($\alpha = 0.1$ and 0.4) and a repertoire of different initial conditions. In fact, it is only under those more extreme conditions when one can reject the Maxwellian as a proper candidate for the reference VDF.

We have also used $\mathcal{D}_{\text{KL}}(\phi_{\text{H}}\|\phi_{\text{M}})$ to characterize the departure of the Maxwellian distribution as an approximation to the actual HCS distribution. Interestingly, we found a non-monotonic influence of the coefficient of restitution on $\mathcal{D}_{\text{KL}}(\phi_{\text{H}}\|\phi_{\text{M}})$, with a (nonzero) local minimum at $\alpha \simeq 1/\sqrt{2} \simeq 0.71$ and a (small) local maximum at $\alpha \simeq 0.87$. This non-monotonicity implies a *degeneracy* of $\mathcal{D}_{\text{KL}}(\phi_{\text{H}}\|\phi_{\text{M}})$ in the sense that three different coefficients of restitution (within the region $0.6 \lesssim \alpha < 1$) may share a common value of the KLD from ϕ_{M} to ϕ_{H} . The analysis of $\mathcal{D}_{\text{KL}}(\phi_{\text{H}}\|\phi_{\text{M}})$ is an additional asset of our work.

We expect that the results presented in this paper may stimulate further studies on the quest of proving (or disproving, if a counterexample is found) the extension of Boltzmann's celebrated *H*-theorem to the realm of dissipative inelastic collisions in homogeneous states. In this respect, it must be remarked that, since the simulation results we have presented are obtained from the MD technique (which numerically solves Newton's equations of motion) and not from the DSMC method (which numerically solves the Boltzmann equation), it is not obvious from a strict mathematical point of view that the obtained results imply the decay of the KLD in the context of the Boltzmann equation. On the other hand, on physical grounds, it is expected that such an implication holds.

As a final remark, it is worth emphasizing that, even if some kind of generalized *H*-theorem could be proved for homogeneous states, its extension to inhomogeneous situations would be far from trivial since the HCS is unstable under long-wavelength perturbations.

Author Contributions: A.S. proposed the idea and A.M. carried out the simulations. Both authors participated in the analysis and discussion of the results and worked on the revision and writing of the final manuscript. All authors have read and agreed to the published version of the manuscript.

Funding: The authors acknowledge financial support from the Spanish Agencia Estatal de Investigación through Grant No. FIS2016-76359-P and the Junta de Extremadura (Spain) through Grant No. GR18079, both partially financed by Fondo Europeo de Desarrollo Regional funds. A.M. is grateful to the Spanish Ministerio de Ciencia, Innovación y Universidades for a predoctoral fellowship FPU2018-3503.

Conflicts of Interest: The authors declare no conflict of interest.

Abbreviations

The following abbreviations are used in this manuscript:

DSMC	Direct simulation Monte Carlo
HCS	Homogenous cooling state
KLD	Kullback–Leibler divergence
MD	Molecular dynamics
VDF	Velocity distribution function

Appendix A. Simulation and Numerical Details

Event-driven MD simulations were carried out using the DynamO software [13] on N particles in a d -dimensional cubic box of side L with periodic boundary conditions. We chose $(N, L/\sigma) = (10^4, 4.641.58)$ and $(1.35 \times 10^4, 407.16)$ for disks and spheres, respectively. Thus, the associated number densities were $n\sigma^2 = 4.64 \times 10^{-4}$ (disks) and $n\sigma^3 = 2.00 \times 10^{-4}$ (spheres). The critical lengths for the development of instabilities at those densities [14] are estimated to be $L_c/\sigma \approx 8.3 \times 10^3$ (disks) and 1.3×10^4 (spheres) for the most demanding case ($\alpha = 0.1$). This represents ratios $L_c/L \approx 1.8$ (disks) $L_c/L \approx 32.8$ (spheres). Those ratios generally increase with decreasing inelasticity. For instance, at $\alpha = 0.87$, one finds $L_c/L \approx 3.4$ (disks) and 62.5 (spheres). Therefore, the simulations are performed in the region of parameters where the systems are stable.

Since the DynamO code is designed for three-dimensional setups, we used it for the two-dimensional case by imposing a coordinate $z = 0$ to every particle and carefully avoiding any overlap in the initial ordered

arrangement. The system melted very quickly and no inhomogeneities were observed thereafter. A velocity rescaling was done periodically in order to avoid numerical errors due to the cooling process and extremely small numbers.

To represent the VDF and the KLD in simulations, let us first introduce the probability distribution function of the velocity modulus,

$$\Phi(c; s) = c^{d-1} \int d\hat{c} \phi(c; s) = \Omega_d c^{d-1} \phi(c; s), \quad \Omega_d \equiv \frac{2\pi^{d/2}}{\Gamma(d/2)}, \quad (\text{A1})$$

where in the second step we have assumed that the VDF $\phi(c; s)$ is isotropic and Ω_d is the d -dimensional solid angle. Thus, Equation (36) can be rewritten as

$$\mathcal{D}_{\text{KL}}(\phi \| \phi_{\text{ref}}) = \int_0^\infty dc \Phi(c; s) \ln \frac{\Phi(c; s)}{\Phi_{\text{ref}}(c)}. \quad (\text{A2})$$

The functions $\Phi(c; s)$ and $\Phi_{\text{H}}(c)$ are numerically approximated by a discrete histogram, with a certain constant bin width Δc , i.e.,

$$\Phi(c; s) \approx \frac{N_i(s)}{N\Delta c}, \quad \Phi_{\text{H}}(c_i) \approx \frac{N_i^{\text{H}}}{N\Delta c}, \quad c_i = \left(i - \frac{1}{2}\right) \Delta c, \quad i = 1, 2, \dots, M. \quad (\text{A3})$$

Here, $N_i(s)$ is the number of particles with a speed c inside the interval $c_i - \Delta c/2 \leq c < c_i + \Delta c/2$, N_i^{H} is evaluated by averaging $N_i(s)$ between $s = 10$ to $s = 40$ with a timestep $\delta s = 0.2$, and M is the total number of bins considered. In consistency with Equation (A3), the Maxwellian VDF is also discretized as

$$\begin{aligned} \Phi_{\text{M}}(c_i) &\approx \frac{\pi^{-d/2} \Omega_d}{\Delta c} \int_{c_i - \Delta c/2}^{c_i + \Delta c/2} dc c^{d-1} e^{-c^2} \\ &= \begin{cases} \frac{e^{-(c_i - \frac{\Delta c}{2})^2} - e^{-(c_i + \frac{\Delta c}{2})^2}}{\Delta c}, & (d = 2), \\ \frac{\text{erf}(c_i + \frac{\Delta c}{2}) - \text{erf}(c_i - \frac{\Delta c}{2})}{\Delta c} + \frac{2}{\sqrt{\pi}} \frac{(c_i - \frac{\Delta c}{2}) e^{-(c_i - \frac{\Delta c}{2})^2} - (c_i + \frac{\Delta c}{2}) e^{-(c_i + \frac{\Delta c}{2})^2}}{\Delta c}, & (d = 3), \end{cases} \end{aligned} \quad (\text{A4})$$

where $\text{erf}(x) = \frac{2}{\sqrt{\pi}} \int_0^x dt e^{-t^2}$ is the error function.

Next, the KLD (A2) with $\phi_{\text{ref}}(c) = \phi_{\text{M}}(c)$ and with $\phi_{\text{ref}}(c) = \phi_{\text{H}}(c)$ are approximated in the simulations by

$$\mathcal{D}_{\text{KL}}(\phi \| \phi_{\text{M}}) \approx \sum_{i=1}^M \frac{N_i(s)}{N} \ln \frac{N_i(s)/N\Delta c}{\Phi_{\text{M}}(c_i)}, \quad \mathcal{D}_{\text{KL}}(\phi \| \phi_{\text{H}}) \approx \sum_{i=1}^M \frac{N_i(s)}{N} \ln \frac{N_i(s)}{N_i^{\text{H}}}, \quad (\text{A5})$$

where $\Phi_{\text{M}}(c_i)$ is given by Equation (A4). Analogously,

$$\mathcal{D}_{\text{KL}}(\phi_{\text{H}} \| \phi_{\text{M}}) \approx \sum_{i=1}^M \frac{N_i^{\text{H}}}{N} \ln \frac{N_i^{\text{H}}/N\Delta c}{\Phi_{\text{M}}(c_i)}. \quad (\text{A6})$$

A comment is now in order. In the case of elastic collisions ($\alpha = 1$), one obviously should have $\Phi_{\text{H}}(c_i) = \Phi_{\text{M}}(c_i)$ and hence $\mathcal{D}_{\text{KL}}(\phi_{\text{H}} \| \phi_{\text{M}})|_{\alpha=1} = 0$. However, since $\Phi_{\text{H}}(c_i)$ is evaluated in simulations by Equation (A3) for any α , the equality $\Phi_{\text{H}}(c_i) = \Phi_{\text{M}}(c_i)$ for $\alpha = 1$ is not identically verified bin to bin due to fluctuations. As a consequence, in the simulations, $\mathcal{D}_{\text{KL}}(\phi_{\text{H}} \| \phi_{\text{M}})|_{\alpha=1} \sim 10^{-5} \neq 0$. This is an unavoidable background noise that was subtracted from the KLD obtained by simulations, i.e., $\mathcal{D}_{\text{KL}}(\phi \| \phi_{\text{ref}}) \rightarrow \mathcal{D}_{\text{KL}}(\phi \| \phi_{\text{ref}}) - \mathcal{D}_{\text{KL}}(\phi_{\text{H}} \| \phi_{\text{M}})|_{\alpha=1}$.

We have chosen the values $\Delta c = 0.03$ and $M = 200$. The results presented in the main text for any given quantity are obtained by averaging over 50 independent realizations.

Appendix B. Initial Conditions

For the analysis of the evolution of $a_2(s)$, $a_3(s)$, $\mathcal{D}_{\text{KL}}(\phi \| \phi_{\text{M}})$, and $\mathcal{D}_{\text{KL}}(\phi \| \phi_{\text{H}})$ with $\alpha = 0.1$, we have chosen five different initial conditions. The first one is the same as considered in Figures 2, 3, 6, and 8, i.e., an ordered

crystallized configuration with isotropic velocities of a common magnitude. In terms of the distribution defined by Equation (A1), this initial condition reads

$$\Phi_\delta(c) = \delta \left(c - \sqrt{d/2} \right), \quad (\text{A7})$$

which will be labeled with the Greek letter δ . The second initial distribution is just a Maxwellian (label M), i.e.,

$$\Phi_M(c) = \frac{2}{\Gamma(\frac{d}{2})} c^{d-1} e^{-c^2}. \quad (\text{A8})$$

Next, we choose the gamma distribution (label Γ) normalized to $\langle c^2 \rangle = \frac{d}{2}$, namely

$$\Phi_\Gamma(c) = \frac{2}{\theta^{\frac{d}{2\theta}} \Gamma(\frac{d}{2\theta})} c^{d/\theta-1} e^{-c^2/\theta}, \quad (\text{A9})$$

where $\theta > 0$ can be freely chosen. The fourth- and sixth-order moments are $\langle c^4 \rangle = \frac{d(d+2\theta)}{4}$ and $\langle c^6 \rangle = \frac{d(d+2\theta)(d+4\theta)}{8}$, so that $a_2 = \frac{2(\theta-1)}{d+2}$ and $a_3 = -\frac{8(\theta-1)(\theta-2)}{(d+2)(d+4)}$. Here, we have taken $\theta = 2.16$ and 2.45 for $d = 2$ and 3 , respectively.

The remaining two initial conditions are prepared by applying a coefficient of normal restitution α_0 and allowing the system to reach the corresponding steady state (in the scaled quantities). Then, at $s = 0$, the coefficient of restitution is abruptly changed to $\alpha = 0.1$ and the evolution toward the corresponding HCS is monitored. We have taken two classes of values of α_0 : (a) $\alpha_0 < 1$, corresponding to dissipative inelastic collisions (label I), and (b) $\alpha_0 > 1$ [44], corresponding to “super-elastic” collisions (label S). More specifically, for the preparation of the initial state I, we have chosen $\alpha_0 = 0.29$ and 0.27 for $d = 2$ and 3 , respectively; the state S has been prepared with $\alpha_0 = 1.29$ and 1.47 for $d = 2$ and 3 , respectively.

Table A1 displays the values of a_2 and a_3 corresponding to, in order of increasing a_2 , the initial states δ , M, I, Γ , and S.

Table A1. Values of the fourth and sixth cumulants for the initial distributions δ , M, I, Γ , and S (see text).

	δ	M	I	Γ	S
$a_2(0)$	-0.500 ($d = 2$)	0	0.151 ($d = 2$)	0.580 ($d = 2$)	0.885 ($d = 2$)
	-0.400 ($d = 3$)		0.111 ($d = 3$)	0.580 ($d = 3$)	0.792 ($d = 3$)
$a_3(0)$	-0.667 ($d = 2$)	0	-0.080 ($d = 2$)	-0.062 ($d = 2$)	-4.733 ($d = 2$)
	-0.457 ($d = 3$)		-0.046 ($d = 3$)	-0.149 ($d = 3$)	-2.219 ($d = 3$)

Appendix C. Formal Expression for $\partial_s \mathcal{D}_{\text{KL}}(\phi \| \phi_{\text{ref}})$

The aim of this appendix is to derive a formal expression for $\partial_s \mathcal{D}_{\text{KL}}(\phi \| \phi_{\text{ref}})$ by following the same steps as in the proof of the conventional H -theorem [6].

Let us consider a generic test function $\psi(c)$. By standard steps, one can easily obtain [14]

$$\begin{aligned} \mathcal{J}[\psi] &\equiv \int \mathrm{d}\mathbf{c} \psi(c) I[c_1 | \phi, \phi] \\ &= \frac{1}{2} \int \mathrm{d}\mathbf{c}_1 \int \mathrm{d}\mathbf{c}_2 \int_+ \mathrm{d}\hat{\sigma} (c_{12} \cdot \hat{\sigma}) \phi(c_1) \phi(c_2) [\psi(c'_1) + \psi(c'_2) - \psi(c_1) - \psi(c_2)]. \end{aligned} \quad (\text{A10})$$

Next, we perform the change of variables $\{c_1, c_2, \hat{\sigma}\} \rightarrow \{c'_1, c'_2, -\hat{\sigma}\}$ and take into account that $\mathrm{d}c'_1 \mathrm{d}c'_2 = \alpha \mathrm{d}c_1 \mathrm{d}c_2$ and $c'_{12} \cdot \hat{\sigma} = -\alpha c_{12} \cdot \hat{\sigma}$ to obtain

$$\begin{aligned} \mathcal{J}[\psi] &= \frac{\alpha^{-2}}{2} \int \mathrm{d}c'_1 \int \mathrm{d}c'_2 \int_+ \mathrm{d}\hat{\sigma} (c'_{12} \cdot \hat{\sigma}) \phi(c_1) \phi(c_2) [\psi(c'_1) + \psi(c'_2) - \psi(c_1) - \psi(c_2)] \\ &= \frac{\alpha^{-2}}{2} \int \mathrm{d}c_1 \int \mathrm{d}c_2 \int_+ \mathrm{d}\hat{\sigma} (c_{12} \cdot \hat{\sigma}) \phi(c'_1) \phi(c'_2) [\psi(c_1) + \psi(c_2) - \psi(c'_1) - \psi(c'_2)], \end{aligned} \quad (\text{A11})$$

where in the second equality we have just renamed $\{c'_1, c'_2, c_1, c_2\} \rightarrow \{c_1, c_2, c'_1, c'_2\}$. Taking the average between Equations (A10) and (A11), we arrive at

$$\begin{aligned} \mathcal{J}[\psi] = & \frac{1}{4} \int d\mathbf{c}_1 \int d\mathbf{c}_2 \int_+ d\hat{\sigma}(\mathbf{c}_{12} \cdot \hat{\sigma}) \left\{ \phi(c_1)\phi(c_2) [\psi(c'_1) + \psi(c'_2) - \psi(c_1) - \psi(c_2)] \right. \\ & \left. - \frac{\phi(c'_1)\phi(c'_2)}{\alpha^2} [\psi(c'_1) + \psi(c'_2) - \psi(c_1) - \psi(c_2)] \right\}. \end{aligned} \quad (\text{A12})$$

Now, we start from the KLD defined by Equation (36) and use the Boltzmann equation (8) to get

$$\frac{\kappa}{2} \partial_s \mathcal{D}_{\text{KL}}(\phi \| \phi_{\text{ref}}) = \mathcal{J} \left[\ln \frac{\phi}{\phi_{\text{ref}}} \right] - \frac{\mu_2}{d} \int d\mathbf{c} \ln \frac{\phi(\mathbf{c})}{\phi_{\text{ref}}(\mathbf{c})} \frac{\partial}{\partial \mathbf{c}} \cdot \mathbf{c} \phi(\mathbf{c}). \quad (\text{A13})$$

where we have taken into account that $\phi_{\text{ref}}(\mathbf{c})$ and $\int d\mathbf{c} \phi(\mathbf{c}) = 1$ are independent of time. Integration by parts of the second term on the right-hand side of Equation (A13) yields

$$\frac{\kappa}{2} \partial_s \mathcal{D}_{\text{KL}}(\phi \| \phi_{\text{ref}}) = \mathcal{J} \left[\ln \frac{\phi}{\phi_{\text{ref}}} \right] - \mu_2 \left[1 + \frac{1}{d} \int d\mathbf{c} \phi(\mathbf{c}) \mathbf{c} \cdot \frac{\partial}{\partial \mathbf{c}} \ln \phi_{\text{ref}}(\mathbf{c}) \right]. \quad (\text{A14})$$

Finally, making use of Equation (A12) with $\psi(\mathbf{c}) = \ln[\phi(\mathbf{c})/\phi_{\text{ref}}(\mathbf{c})]$, we obtain

$$\begin{aligned} \frac{\kappa}{2} \partial_s \mathcal{D}_{\text{KL}}(\phi \| \phi_{\text{ref}}) = & \frac{1}{4} \int d\mathbf{c}_1 \int d\mathbf{c}_2 \int_+ d\hat{\sigma}(\mathbf{c}_{12} \cdot \hat{\sigma}) \left[\phi(c_1)\phi(c_2) \ln \frac{\phi(c'_1)\phi(c'_2)\phi_{\text{ref}}(c_1)\phi_{\text{ref}}(c_2)}{\phi(c_1)\phi(c_2)\phi_{\text{ref}}(c'_1)\phi_{\text{ref}}(c'_2)} \right. \\ & \left. - \frac{\phi(c'_1)\phi(c'_2)}{\alpha^2} \ln \frac{\phi(c'_1)\phi(c'_2)\phi_{\text{ref}}(c_1)\phi_{\text{ref}}(c_2)}{\phi(c_1)\phi(c_2)\phi_{\text{ref}}(c'_1)\phi_{\text{ref}}(c'_2)} \right] - \frac{\mu_2}{d} \int d\mathbf{c} \phi(\mathbf{c}) \mathbf{c} \cdot \frac{\partial}{\partial \mathbf{c}} \ln \frac{\phi_{\text{ref}}(\mathbf{c})}{\phi_{\text{M}}(\mathbf{c})}, \end{aligned} \quad (\text{A15})$$

where we have taken into account that $-\int d\mathbf{c} \phi(\mathbf{c}) \mathbf{c} \cdot \frac{\partial}{\partial \mathbf{c}} \ln \phi_{\text{M}}(\mathbf{c}) = 2 \int d\mathbf{c} c^2 \phi(\mathbf{c}) = d$.

Equation (A15) does not particularly simplify if $\phi_{\text{ref}} = \phi_{\text{H}}$. However, in the case $\phi_{\text{ref}} = \phi_{\text{M}}$, a somewhat simpler expression can be found. First, the last term on the right-hand side of Equation (A15) vanishes if $\phi_{\text{ref}} = \phi_{\text{M}}$. Second, we can use the decomposition $\mathcal{J}[\ln(\phi/\phi_{\text{M}})] = \mathcal{J}[\ln \phi] - \mathcal{J}[\ln \phi_{\text{M}}]$ and take into account that $\ln \phi_{\text{M}}(\mathbf{c}) = -c^2 + \text{const}$ and, therefore, $\mathcal{J}[\ln \phi_{\text{M}}] = \mu_2$ [see Equation (8)]. As a consequence,

$$\begin{aligned} \frac{\kappa}{2} \partial_s \mathcal{D}_{\text{KL}}(\phi \| \phi_{\text{M}}) = & \frac{1}{4} \int d\mathbf{c}_1 \int d\mathbf{c}_2 \int_+ d\hat{\sigma}(\mathbf{c}_{12} \cdot \hat{\sigma}) \left[\phi(c_1)\phi(c_2) \ln \frac{\phi(c'_1)\phi(c'_2)}{\phi(c_1)\phi(c_2)} \right. \\ & \left. - \frac{\phi(c'_1)\phi(c'_2)}{\alpha^2} \ln \frac{\phi(c'_1)\phi(c'_2)}{\phi(c_1)\phi(c_2)} \right] - \mu_2. \end{aligned} \quad (\text{A16})$$

In the special case of elastic collisions ($\alpha = 1$), one has $\mu_2 = 0$ and $c'_i = c_i$, so that the standard H -theorem is recovered, namely

$$\frac{\kappa}{2} \partial_s \mathcal{D}_{\text{KL}}(\phi \| \phi_{\text{M}}) \Big|_{\alpha=1} = -\frac{1}{4} \int d\mathbf{c}_1 \int d\mathbf{c}_2 \int_+ d\hat{\sigma}(\mathbf{c}_{12} \cdot \hat{\sigma}) [\phi(c'_1)\phi(c'_2) - \phi(c_1)\phi(c_2)] \ln \frac{\phi(c'_1)\phi(c'_2)}{\phi(c_1)\phi(c_2)} \leq 0. \quad (\text{A17})$$

References

1. Shannon, C.E. A mathematical theory of communication. *Bell Syst. Tech. J.* **1948**, *27*, 379–423, doi:10.1002/j.1538-7305.1948.tb01338.x.
2. Gray, R.M. *Entropy and Information Theory*, 2nd ed.; Springer: New York, NY, USA, 2011.
3. Brey, J.J.; Santos, A. Nonequilibrium entropy of a gas. *Phys. Rev. A* **1992**, *45*, 8566–8572, doi:10.1103/PhysRevA.45.8566.
4. Kremer, G.M. Thermodynamics and kinetic theory of granular materials. In *Perspectives and Challenges in Statistical Physics and Complex Systems for the Next Decade*; Viswanathan, G.M., Raposo, E.P., da Luz, M.G.E., Eds.; World Scientific: Singapore, 2014; pp. 287–299, doi:10.1142/9789814590143_0016.
5. Chapman, S.; Cowling, T.G. *The Mathematical Theory of Non-Uniform Gases*, 3rd ed.; Cambridge University Press: Cambridge, UK, 1970.
6. Garzó, V.; Santos, A. *Kinetic Theory of Gases in Shear Flows: Nonlinear Transport*; Fundamental Theories of Physics; Springer: Dordrecht, The Netherlands, 2003.

7. Kullback, S.; Leibler, R.A. On Information and Sufficiency. *Ann. Math. Statist.* **1951**, *22*, 79–86, doi:10.1214/aoms/1177729694.
8. Kullback, S. *Information Theory and Statistics*; Dover: New York, NY, USA, 1978.
9. Santos, A.; Kremer, G.M. Relative Entropy of a Freely Cooling Granular Gas. *AIP Conf. Proc.* **2012**, *1501*, 1044–1050, doi:10.1063/1.4769657.
10. Bettolo Marconi, U.M.; Puglisi, A.; Vulpiani, A. About an H-theorem for systems with non-conservative interactions. *J. Stat. Mech.* **2013**, P08003, doi:10.1088/1742-5468/2013/08/P08003.
11. García de Soria, M.I.; Maynar, P.; Mischler, S.; Mouhot, C.; Rey, T.; Trizac, E. Towards an H-theorem for granular gases. *J. Stat. Mech.* **2015**, P11009, doi:10.1088/1742-5468/2015/11/p11009.
12. Plata, C.A.; Prados, A. Global stability and H theorem in lattice models with nonconservative interactions. *Phys. Rev. E* **2017**, *95*, 052121, doi:10.1103/PhysRevE.95.052121.
13. Bannerman, M.N.; Sargant, R.; Lue, L. DynamO: A Free $\mathcal{O}(N)$ General Event-Driven Molecular Dynamics Simulator. *J. Comput. Chem.* **2011**, *32*, 3329–3338, doi:10.1002/jcc.21915.
14. Garzó, V. *Granular Gaseous Flows. A Kinetic Theory Approach to Granular Gaseous Flows*; Springer Nature: Cham, Switzerland, 2019.
15. Brilliantov, N.V.; Pöschel, T. *Kinetic Theory of Granular Gases*; Oxford University Press: Oxford, UK, 2004.
16. Brilliantov, N.; Pöschel, T. Deviation from Maxwell distribution in granular gases with constant restitution coefficient. *Phys. Rev. E* **2000**, *61*, 2809–2812, doi:10.1103/PhysRevE.61.2809.
17. van Noije, T.P.C.; Ernst, M.H. Velocity distributions in homogeneous granular fluids: The free and the heated case. *Granul. Matter* **1998**, *1*, 57–64, doi:10.1007/s100350050009.
18. Montanero, J.M.; Santos, A. Computer simulation of uniformly heated granular fluids. *Granul. Matter* **2000**, *2*, 53–64, doi:10.1007/s100350050035.
19. Santos, A.; Montanero, J.M. The second and third Sonine coefficients of a freely cooling granular gas revisited. *Granul. Matter* **2009**, *11*, 157–168, doi:10.1007/s10035-009-0132-8.
20. Brey, J.J.; Ruiz-Montero, M.J.; Cubero, D. Homogeneous cooling state of a low-density granular flow. *Phys. Rev. E* **1996**, *54*, 3664, doi:10.1103/PhysRevE.54.3664.
21. Ahmad, S.R.; Puri, S. Velocity distributions in a freely evolving granular gas. *Europhys. Lett.* **2006**, *75*, 56–62, doi:10.1209/epl/i2006-10071-3.
22. Ahmad, S.R.; Puri, S. Velocity distributions and aging in a cooling granular gas. *Phys. Rev. E* **2007**, *75*, 031302, doi:10.1103/PhysRevE.75.031302.
23. Yu, P.; Schröter, M.; Sperl, M. Velocity Distribution of a Homogeneously Cooling Granular Gas. *Phys. Rev. Lett.* **2020**, *124*, 208007, doi:10.1103/PhysRevLett.124.208007.
24. Bobylev, A.V.; Cercignani, C.; Toscani, G. Proof of an asymptotic property of self-similar solutions of the Boltzmann equation for granular materials. *J. Stat. Phys.* **2003**, *111*, 403–417, doi:10.1023/A:1022273528296.
25. Bisi, M.; Carrillo, J.A.; Toscani, G. Decay Rates in Probability Metrics Towards Homogeneous Cooling States for the Inelastic Maxwell Model. *J. Stat. Phys.* **2006**, *124*, 625–653, doi:10.1007/s10955-006-9035-9.
26. Bolley, F.; Carrillo, J.A. Tanaka Theorem for Inelastic Maxwell Models. *Commun. Math. Phys.* **2007**, *276*, 287–314, doi:10.1007/s00220-007-0336-x.
27. Carrillo, J.A.; Toscani, G. Contractive probability metrics and asymptotic behavior of dissipative kinetic equations. *Riv. Mat. Univ. Parma* **2007**, *6*, 75–198.
28. Carlen, E.A.; Carrillo, J.A.; Carvalho, M.C. Strong Convergence towards homogeneous cooling states for dissipative Maxwell models. *Ann. I. H. Poincaré* **2009**, *26*, 167–1700, doi:10.1016/j.anihpc.2008.10.005.
29. Brilliantov, N.; Pöschel, T. Breakdown of the Sonine expansion for the velocity distribution of granular gases. *Europhys. Lett.* **2006**, *74*, 424–430, doi:10.1209/epl/i2005-10555-6; Erratum: **2006**, *75*, 188–188, doi:10.1209/epl/i2006-10099-3.
30. Noskowicz, S.H.; Bar-Lev, O.; Serero, D.; Goldhirsch, I. Computer-aided kinetic theory and granular gases. *EPL* **2007**, *79*, 60001, doi:10.1209/0295-5075/79/60001.
31. Brito, R.; Ernst, M.H. Extension of Haff’s cooling law in granular flows. *Europhys. Lett.* **1998**, *43*, 497–502, doi:10.1209/epl/i1998-00388-9.
32. Goldshtein, A.; Shapiro, M. Mechanics of collisional motion of granular materials. Part 1. General hydrodynamic equations. *J. Fluid Mech.* **1995**, *282*, 75–114, doi:10.1017/S0022112095000048.
33. Coppex, F.; Droz, M.; Piasecki, J.; Trizac, E. On the first Sonine correction for granular gases. *Physical A* **2003**, *329*, 114–126, doi:10.1016/S0378-4371(03)00593-4.

34. Abramowitz, M.; Stegun, I.A. (Eds.) *Handbook of Mathematical Functions*; Dover: New York, NY, USA, 1972.
35. Bird, G.A. *Molecular Gas Dynamics and the Direct Simulation of Gas Flows*; Clarendon: Oxford, UK, 1994.
36. Brey, J.J.; Dufty, J.W.; Kim, C.S.; Santos, A. Hydrodynamics for granular flow at low density. *Phys. Rev. E* **1998**, *58*, 4638–4653, doi:10.1103/PhysRevE.58.4638.
37. Boltzmann, L. *Lectures on Gas Theory*; Dover: New York, NY, USA, 1995.
38. Maynar, P.; Trizac, E. Entropy of Continuous Mixtures and the Measure Problem. *Phys. Rev. Lett.* **2011**, *106*, 160603, doi:10.1103/PhysRevLett.106.160603.
39. Mischler, S.; Mouhot, C.; Rodriguez Ricard, M. Cooling Process for Inelastic Boltzmann Equations for Hard Spheres, Part I: The Cauchy Problem. *J. Stat. Phys.* **2006**, *124*, 655–702, doi:10.1007/s10955-006-9096-9.
40. Mischler, S.; Mouhot, C. Cooling Process for Inelastic Boltzmann Equations for Hard Spheres, Part II: Self-Similar Solutions and Tail Behavior. *J. Stat. Phys.* **2006**, *124*, 703–746, doi:10.1007/s10955-006-9097-8.
41. Mischler, S.; Mouhot, C. Stability, Convergence to Self-Similarity and Elastic Limit for the Boltzmann Equation for Inelastic Hard Spheres. *Commun. Math. Phys.* **2009**, *288*, 431–502, doi:10.1007/s00220-009-0773-9.
42. Pettersson, R. On Solutions to the Linear Boltzmann Equation for Granular Gases. *Transp. Theory Stat. Phys.* **2004**, *33*, 527–543, doi:10.1081/TT-200053937.
43. Esipov, S.E.; Pöschel, T. The granular phase diagram. *J. Stat. Phys.* **1997**, *86*, 1385–1395, doi:10.1007/BF02183630.
44. Kuninaka, H.; Hayakawa, H. Anomalous Behavior of the Coefficient of Normal Restitution in Oblique Impact. *Phys. Rev. Lett.* **2004**, *93*, 154301, doi:10.1103/PhysRevLett.93.154301.

6.3 Article 3

Title: Relative entropy of freely cooling granular gases. A molecular dynamics study

Authors: Alberto Megías¹ and Andrés Santos^{1,2}

Affiliations:

¹ Departamento de Física, Universidad de Extremadura, E-06006 Badajoz, Spain

² Instituto de Computación Científica Avanzada (ICCAEx), Universidad de Extremadura, E-06006 Badajoz, Spain

Journal: EPJ Web of Conferences

Volume: 246

Pages: 04006

Year: 2021

DOI: [10.1051/epjconf/202124904006](https://doi.org/10.1051/epjconf/202124904006)



Copy of the preprint of the work: “Alberto Megías, and Andrés Santos, ‘Relative entropy of freely cooling granular gases. A molecular dynamics study’, *EPJ Web of Conferences* 249, 04006 (2021) <https://doi.org/10.1051/epjconf/202124904006>.”

Relative entropy of freely cooling granular gases. A molecular dynamics study

Alberto Megías^{1,*} and Andrés Santos^{1,2,**}

¹Departamento de Física, Universidad de Extremadura, E-06006 Badajoz, Spain

²Instituto de Computación Científica Avanzada (ICCAEx), Universidad de Extremadura, E-06006 Badajoz, Spain

Abstract. Whereas the original Boltzmann's H -theorem applies to elastic collisions, its rigorous generalization to the inelastic case is still lacking. Nonetheless, it has been conjectured in the literature that the relative entropy of the velocity distribution function with respect to the homogeneous cooling state (HCS) represents an adequate nonequilibrium entropy-like functional for an isolated freely cooling granular gas. In this work, we present molecular dynamics results reinforcing this conjecture and rejecting the choice of the Maxwellian over the HCS as a reference distribution. These results are qualitatively predicted by a simplified theoretical toy model. Additionally, a Maxwell-demon-like velocity-inversion simulation experiment highlights the microscopic irreversibility of the granular gas dynamics, monitored by the relative entropy, where a short "anti-kinetic" transient regime appears for nearly elastic collisions only.

1 Introduction

Granular gases are modeled in their simplest form as inelastic hard spheres with a constant coefficient of restitution, α [1–4]. It is well known that granular gases are intrinsically out of equilibrium and that a description by means of kinetic theory is meaningful. In a kinetic-theoretical description of a granular gas, one defines the *granular* temperature as the mean kinetic energy per particle, as an analogue to its definition for molecular gases. Even though this temperature is not a *thermodynamic* temperature, one can look for the nonequilibrium entropy-like functional of this system, i.e., a Lyapunov functional, in analogy with Boltzmann's H -functional and the celebrated H -theorem for elastic collisions

The problem introduced and solved by Boltzmann in 1872 [5] is not easy to extend in the context of granular gases and the associated inelastic form of the renowned Boltzmann equation. The original H -functional is precisely the Shannon measure [6] of the one-particle velocity distribution function [7, 8]. However, it is known that, in its continuous description, Shannon's entropy presents the so-called *measure* problem [9], i.e., it does not weigh properly the phase space. In the elastic case, this problem is easily solved by considering the relative entropy (or Kullback–Leibler divergence [10]) of the one-particle velocity distribution function with respect to the Maxwellian distribution, which becomes the original H -functional up to a constant in that case. Moreover, some relevant properties of the elastic-particle system, like collisional symmetry and reversibility, do not hold anymore in the inelas-

tic scheme. Then, the proper entropy-like functional must solve these issues.

The quest of such a quantity in the homogeneous case has been addressed mathematically in Refs. [11–13] in the context of the inelastic Boltzmann equation, and in Ref. [14] from a stochastic point of view. Both approaches converge into a single functional, which is proved in the *quasielastic* limit, i.e., $1 - \alpha \ll 1$, to be the entropy-like functional associated with this system. In the case of free cooling, the conjectured quantity is the relative entropy of the reduced velocity distribution function, ϕ , with respect to the homogeneous cooling state (HCS), ϕ_H , chosen as the proper reference distribution. This conjecture was recently reinforced with computer simulations in the whole range of inelasticity [15].

In this work, we complement the study carried out in Ref. [15] with new simulations. First, we study the problem by means of a simplified *toy model* [15] and investigate how it highlights the possible Lyapunov character of the proposed functional for two different reference distributions, namely the Maxwellian and the HCS distributions. Next, molecular dynamics (MD) results are presented and compared with the predicted theoretical behavior, including three systems not considered in Ref. [15]. Finally, as a fully original contribution of this work, we report MD results for a sort of Maxwell-demon experiment where the irreversibility of the collisional process and the possibility of an anti-kinetic stage are discussed.

2 A toy model

Let us consider a granular-gas model of inelastic and smooth hard spheres with collisional rules

*e-mail: albertom@unex.es

**e-mail: andres@unex.es

$$\mathbf{v}'_{1,2} = \mathbf{v}_{1,2} \mp \frac{1+\alpha}{2\alpha} (\mathbf{v}_{12} \cdot \widehat{\boldsymbol{\sigma}}) \widehat{\boldsymbol{\sigma}}, \quad \mathbf{v}''_{12} \cdot \widehat{\boldsymbol{\sigma}} = -\frac{1}{\alpha} \mathbf{v}_{12} \cdot \widehat{\boldsymbol{\sigma}}, \quad (1)$$

for the precollisional velocities, where \mathbf{v}_{12} is the relative velocity, and $\widehat{\boldsymbol{\sigma}}$ the unit intercenter vector. We will assume that the system satisfies the inelastic Boltzmann equation, which in reduced units reads

$$\frac{\kappa}{2} \partial_s \phi(\mathbf{c}; s) + \frac{\mu_2(s)}{3} \frac{\partial}{\partial \mathbf{c}} \cdot [\mathbf{c} \phi(\mathbf{c}; s)] = I[\mathbf{c}|\phi, \phi]. \quad (2)$$

Here, $\kappa \equiv 2\sqrt{2\pi}$ is a constant, $\mathbf{c} = \mathbf{v}/v_{\text{th}}$ is the reduced velocity, $v_{\text{th}}(t) = \sqrt{2T(t)/m}$ is the thermal velocity, m is the mass of a particle, $T = m\langle v^2 \rangle/3$ is the granular temperature, which decreases monotonically following Haff's law [3, 4, 16, 17], $s = \frac{1}{2} \int_0^t dt' \nu(t')$ is the (nominal) average number of collisions per particle up to time t , where $\nu(t) = \kappa n \sigma^2 v_{\text{th}}(t)$ is the collision frequency, $I[\mathbf{c}|\phi, \phi]$ is the collisional operator in reduced units, and $\mu_2 = -\int d\mathbf{c} c^2 I[\mathbf{c}|\phi, \phi]$ is the reduced cooling rate.

The relative entropy, or Kullback–Leibler divergence, of a velocity distribution, ϕ , with respect to a reference distribution, ϕ_R , is defined as

$$\mathcal{D}_{\text{KL}}(\phi|\phi_R) = \int d\mathbf{c} \phi(\mathbf{c}) \ln \frac{\phi(\mathbf{c})}{\phi_R(\mathbf{c})}. \quad (3)$$

This functional is convex, non-negative, and identically zero if and only if $\phi = \phi_R$ [10].

We assume that both ϕ and ϕ_R are isotropic and can be expanded around the Maxwellian $\phi_M(\mathbf{c}) = \pi^{-3/2} e^{-c^2}$ in terms of Sonine polynomials,

$$\phi(\mathbf{c}; s) = \phi_M(\mathbf{c}) \left[1 + \sum_{k=2}^{\infty} a_k(s) S_k(c^2) \right], \quad (4)$$

where S_k is the k -th Sonine polynomial and a_k is the $2k$ -th cumulant of the distribution, defined as $a_k = \langle S_k \rangle / N_k$ with $N_k = (2k+1)!!/2^k k!$. By definition, $a_0 = 1$ and $a_1 = 0$, so that the first nontrivial coefficient is the fourth cumulant $a_2 = \frac{4}{15} \langle c^2 \rangle - 1$.

Let us now construct a toy model of $\mathcal{D}_{\text{KL}}(\phi|\phi_R)$ [15] for an arbitrary reference distribution. Imagine a *perturbative* parameter ε in front of the Sonine summation in Eq. (4). Expanding in powers of ε and keeping terms up to second order, we have

$$\begin{aligned} \frac{\phi(\mathbf{c}; s)}{\phi_M(\mathbf{c})} \ln \frac{\phi(\mathbf{c}; s)}{\phi_R(\mathbf{c})} &= \varepsilon \sum_{k=2}^{\infty} \Delta_R a_k(s) S_k(c^2) \\ &+ \frac{\varepsilon^2}{2} \sum_{k=2}^{\infty} \sum_{k'=2}^{\infty} \Delta_R a_k(s) \Delta_R a_{k'}(s) \\ &\times S_k(c^2) S_{k'}(c^2) + \mathcal{O}(\varepsilon^3), \end{aligned} \quad (5)$$

where $\Delta_R a_k(s) \equiv a_k(s) - a_k^R$, a_k^R being the Sonine coefficients for the reference distribution function $\phi_R(\mathbf{c})$. Inserting this expression into Eq. (3) and using the orthogonality condition of the Sonine polynomials, one obtains

$$\mathcal{D}_{\text{KL}}(\phi|\phi_R) = \frac{\varepsilon^2}{2} \sum_{k=2}^{\infty} N_k [\Delta_R a_k(s)]^2 + \mathcal{O}(\varepsilon^3), \quad (6a)$$

$$\partial_s \mathcal{D}_{\text{KL}}(\phi|\phi_R) = \varepsilon^2 \sum_{k=2}^{\infty} N_k \Delta_R a_k(s) \partial_s a_k(s) + \mathcal{O}(\varepsilon^3). \quad (6b)$$

The r.h.s of Eq. (6a) is non-negative, and it is zero if and only if $a_k = a_k^R \forall k \geq 2$, that is, $\phi = \phi_R$, in accordance with the properties of the relative entropy. Next, we neglect terms of $\mathcal{O}(\varepsilon^3)$, formally take $\varepsilon = 1$, and, as usually done in the literature [3, 4, 18–24], discard terms with $k \geq 3$. The result is

$$\mathcal{D}_{\text{KL}}(\phi|\phi_R) \approx \frac{15}{16} [\Delta_R a_2(s)]^2, \quad (7a)$$

$$\partial_s \mathcal{D}_{\text{KL}}(\phi|\phi_R) \approx -\frac{15}{8} K [1 + a_2(s)] \Delta_R a_2(s) \Delta_H a_2(s). \quad (7b)$$

Here, in consistency with the neglect of $a_k(s)$ for $k \geq 3$, we have used the evolution equation $\partial_s a_2(s) = -K[1 + a_2(s)] \Delta_H a_2(s)$ for the fourth cumulant [15], where $\Delta_H a_2(s) \equiv a_2(s) - a_2^H$ and K is a positive constant. Whereas the r.h.s of Eq. (7a) is non-negative, the sign of the r.h.s of Eq. (7b) is determined by the relative signs of $\Delta_R a_2(s)$ and $\Delta_H a_2(s)$.

Let us consider two different reference distributions: the Maxwellian velocity distribution function, ϕ_M , and the HCS velocity distribution function, ϕ_H . In the first case ($R = M$), one has $\Delta_M a_2(s) = a_2(s)$, and, therefore, $\partial_s \mathcal{D}_{\text{KL}}(\phi|\phi_M) \leq 0$ only if either $a_2(s) \geq \max\{a_2^H, 0\}$ or $a_2(s) \leq \min\{a_2^H, 0\}$; conversely, $\partial_s \mathcal{D}_{\text{KL}}(\phi|\phi_M) \geq 0$ only if either $0 \leq a_2(s) \leq a_2^H$ or $a_2^H \leq a_2(s) \leq 0$. Thus, our toy model shows that a monotonic relaxation of $\mathcal{D}_{\text{KL}}(\phi|\phi_M)$ is not guaranteed. Let us assume, for instance, that the initial value $a_2(0)$ is negative and $\alpha \leq 0.71$, so that the steady-value a_2^H is positive [15, 19, 21–24]; due to Bolzano's theorem, during its evolution $a_2(s)$ must cross the zero value, so that $\mathcal{D}_{\text{KL}}(\phi|\phi_M)$ would present a local minimum. Analogously, a local minimum of $\mathcal{D}_{\text{KL}}(\phi|\phi_M)$ is predicted by the toy model if $a_2(0) > 0$ and $\alpha \geq 0.71$, i.e., $a_2^H < 0$. In the case $R = H$, however, $-\partial_s \mathcal{D}_{\text{KL}}(\phi|\phi_H) \propto [\Delta_H a_2(s)]^2$ and the Lyapunov condition $\partial_s \mathcal{D}_{\text{KL}}(\phi|\phi_H) \leq 0$ is fulfilled.

3 Molecular dynamics simulations

In order to check the predictions of the toy model for the two considered reference distributions, we have performed MD simulations using the DynamO software [25] for this model of granular gases. It is well known that the free cooling of granular gases presents long-wavelength instabilities [4, 26]. In order to avoid them, we have simulated systems formed by $N = 1.35 \times 10^4$ particles in a cubic box of side length $L/\sigma = 407.16$, which is at least 30 times smaller than the critical length for the development of instabilities, which are not observed.

Initially, all particles are arranged in an ordered crystallized configuration from which the system melts. The initial velocities are oriented along randomized directions with either a common magnitude (initial distribution δ) or with a magnitude drawn from a Gamma (Γ) distribution. The respective initial values of the fourth cumulant are $a_2(0) = -0.4$ (δ distribution) and $a_2(0) = 0.4$ (Γ distribution). Thus, according to the toy model, a nonmonotonic relaxation of $\mathcal{D}_{\text{KL}}(\phi|\phi_M)$ is expected for the initial distribution δ if $\alpha \leq 0.71$ and for the initial distribution Γ if $\alpha \geq 0.71$.

In Fig. 1 one can observe that, as predicted by the toy model, a local minimum is actually observed during the evolution of $\mathcal{D}_{\text{KL}}(\phi||\phi_M)$ for $\alpha = 0.1$ and 0.4 when starting from the initial condition δ , and for $\alpha = 0.87$ when starting from the initial condition Γ . In the other three cases, however, the evolution of $\mathcal{D}_{\text{KL}}(\phi||\phi_M)$ is monotonic. In contrast, the relative entropy $\mathcal{D}_{\text{KL}}(\phi||\phi_H)$ decays monotonically for the six cases, in qualitative agreement with the toy model.

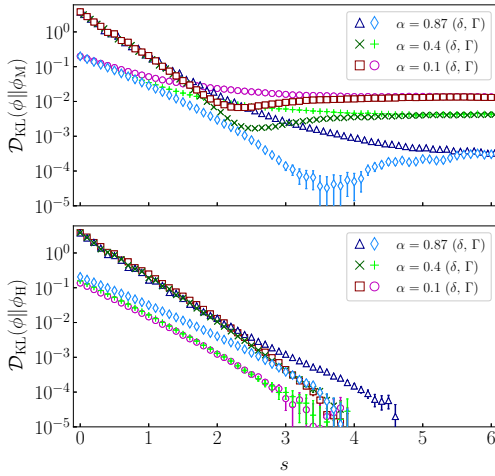


Figure 1. Evolution of $\mathcal{D}_{\text{KL}}(\phi||\phi_R)$ (in logarithmic scale) for $R = M$ (top panel) and $R = H$ (bottom panel). Symbols represent MD simulation results for coefficients of restitution $\alpha = 0.1, 0.4,$ and 0.87 , starting from the initial conditions δ and Γ . The error bars are smaller than the size of the symbols, except when $\mathcal{D}_{\text{KL}}(\phi||\phi_R) \leq 10^{-4}$. Symbols for $s \geq 5$ are discarded in the bottom panel because they appear as purely noise, representing values that are out of the precision of the numerical scheme.

4 Velocity-inversion experiment

A discussion about entropy is not complete if the issue of irreversibility is not included. In the case of *elastic* hard disks, a simulated velocity-inversion experiment (produced by a sort of Maxwell’s demon) was proposed more than forty years ago [27–29], where schemes with “anti-kinetic” parts in the evolution were tested [30] and Loschmidt’s paradox was discussed. In Orban and Bellemans’ pioneering works [27, 28], during the evolution toward equilibrium the velocities of all elastic disks (simulated by MD) were inverted at a given waiting time t_w and Boltzmann’s H -functional was analyzed and seen to revert its decay by retracing its past values (anti-kinetic stage), in agreement with the underlying reversibility of the equations of motion. However, the H -functional resumed its decay after time $t = 2t_w$ and, moreover, due to unavoidable error propagation [31], the initial value of H was not exactly recovered if the velocity inversion took place after a sufficiently long waiting time. In a study involving irreversible particle dynamics, Aharony [29] observed that the

anti-kinetic stage was not symmetric, the system rapidly forgetting the correlations it had at t_w , and thereafter continuing to approach equilibrium.

In this section we revisit the velocity-inversion experiment in a freely cooling granular gas, modeled as inelastic hard spheres, where the collisional rules are given by (1). In this system, collisional symmetry is broken down by the inelasticity of collisions, closely related to a violation of microscopic reversibility. Consider two colliding particles with precollision velocities $\{v_1, v_2\}$ and a relative orientation characterized by the unit vector $\hat{\sigma}$ (with $v_{12} \cdot \hat{\sigma} > 0$). In that case, the postcollisional velocities are $\mathcal{C}_{\hat{\sigma}}\{v_1, v_2\} = \mathcal{C}_{\hat{\sigma}}\mathcal{C}_{-\hat{\sigma}}\{v'_1, v'_2\} = \{v'_1, v'_2\}$, where

$$v'_{1,2} = v_{1,2} \mp \frac{1+\alpha}{2}(v_{12} \cdot \hat{\sigma})\hat{\sigma}, \quad v'_{12} \cdot \hat{\sigma} = -\alpha v_{12} \cdot \hat{\sigma}. \quad (8)$$

Now, we invert the velocities $\{v'_1, v'_2\}$ and obtain the subsequent postcollision velocities, $\mathcal{C}_{\hat{\sigma}}\{-v'_1, -v'_2\} = \{-v_1^\dagger, -v_2^\dagger\}$, where

$$v_{1,2}^\dagger = v_{1,2} \mp \frac{1-\alpha^2}{2}(v_{12} \cdot \hat{\sigma})\hat{\sigma}, \quad v_{12}^\dagger \cdot \hat{\sigma} = \alpha^2 v_{12} \cdot \hat{\sigma}. \quad (9)$$

Therefore, $\mathfrak{I}\mathcal{C}_{\hat{\sigma}}\mathfrak{I}\mathcal{C}_{\hat{\sigma}}\{v_1, v_2\} \neq \{v_1, v_2\}$ (where \mathfrak{I} is the inversion-velocity operator) unless $\alpha = 1$. We studied this effect from MD simulations in a computer experiment similar to those of the works discussed above [27–29]. A waiting time $s_w = 0.5$ was chosen, several values of α were considered, and the evolution was monitored by $\mathcal{D}_{\text{KL}}(\phi||\phi_H)$, which plays the role of H in the elastic case.

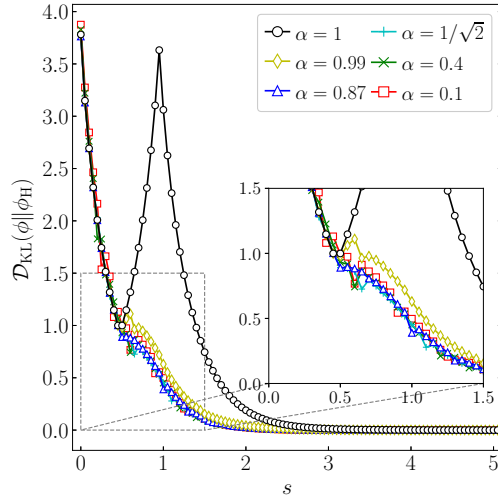


Figure 2. Evolution of $\mathcal{D}_{\text{KL}}(\phi||\phi_H)$ in the velocity-inversion experiment (with a waiting time $s_w = 0.5$). Symbols represent MD simulation results (joined with straight lines as a guide to the eye). The values of the coefficient of restitution are $\alpha = 0.1, 0.4, 1/\sqrt{2}, 0.87, 0.99,$ and 1 . The inset magnifies the behavior around $s = 0.5$. The error bars are smaller than the size of the symbols.

Figure 2 shows the time evolution of $\mathcal{D}_{\text{KL}}(\phi||\phi_H)$ when starting from the δ initial condition and then applying the

velocity inversion. The coefficients of restitution considered are $\alpha = 0.1, 0.4, 1/\sqrt{2}, 0.87, 0.99$, and 1. In the elastic case ($\alpha = 1$), one recovers the results of Ref. [27], i.e., the system almost reaches the original configuration at $s = 1$ but afterwards it evolves toward equilibrium again. Whereas one expects that inelastic collisions erase completely the possibility of a reversible period, in the quasielastic case $\alpha = 0.99$, although it is short, an anti-kinetic transient stage exists after the velocity inversion; this effect is translated into a small growth of $\mathcal{D}_{\text{KL}}(\phi||\phi_{\text{H}})$. Of course, the duration of the anti-kinetic regime becomes longer as α comes closer to 1. On the other hand, as inelasticity increases ($\alpha \leq 0.87$), the influence of the velocity inversion is noticeable by a change of curvature only, and this short effect shrinks with increasing inelasticity, as expected. The effect of inelasticity on the microscopic irreversibility reflected by the behavior of $\mathcal{D}_{\text{KL}}(\phi||\phi_{\text{H}})$ is analogous to that observed by Aharony [29] for the conventional H -functional in the evolution toward equilibrium.

5 Concluding remarks

In this paper we have provided further evidence from MD simulations on the conjecture that the Kullback–Leibler divergence $\mathcal{D}_{\text{KL}}(\phi||\phi_{\text{H}})$ is a possible entropy-like functional for the case of isolated freely cooling granular gases [14, 15], even for strongly inelastic systems. Furthermore, this conjecture is supported by a simple toy model, which, on the other hand, predicts a nonmonotonic behavior of $\mathcal{D}_{\text{KL}}(\phi||\phi_{\text{M}})$ if $a_2(0)$ and a_2^{H} have opposite signs. This theoretical expectation has been nicely confirmed by our simulations.

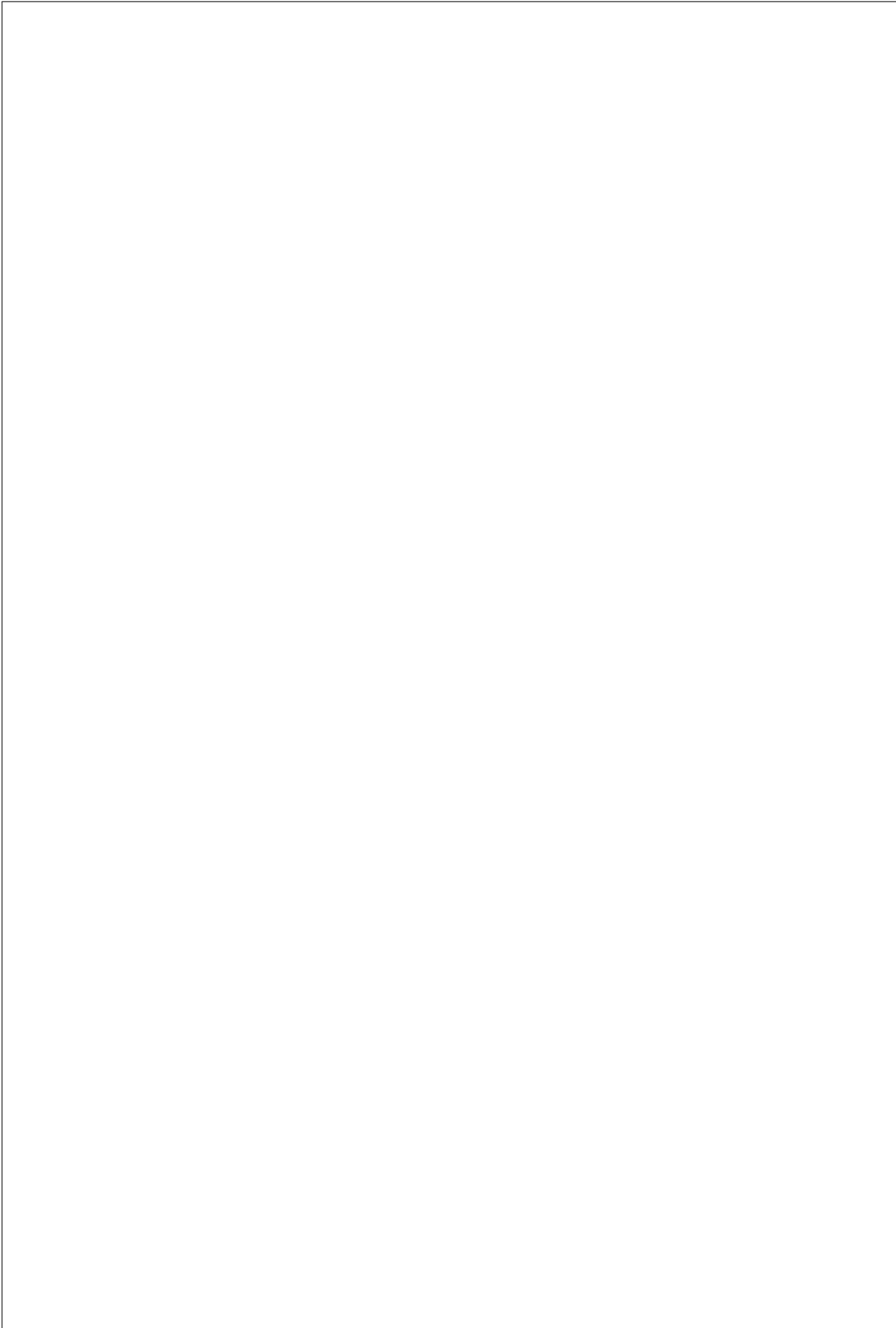
Finally, the classical velocity-inversion experiment [27–30], originally devised for systems relaxing to equilibrium, has been applied on granular gases relaxing to the HCS and monitored via $\mathcal{D}_{\text{KL}}(\phi||\phi_{\text{H}})$. While, as expected, the initial configuration is almost perfectly recovered if the collisions are elastic ($\alpha = 1$), microscopic reversibility is frustrated by inelasticity, no matter how small. In fact, a (short) anti-kinetic stage, where $\partial_s \mathcal{D}_{\text{KL}}(\phi||\phi_{\text{H}}) > 0$, is only possible in the quasielastic regime (e.g., $\alpha = 0.99$) and disappears for sufficiently high inelasticity ($\alpha \lesssim 0.9$).

Acknowledgements

The authors acknowledge financial support from the Grant FIS2016-76359-P/AEI/10.13039/501100011033 and the Junta de Extremadura (Spain) through Grant No. GR18079, both partially financed by Fondo Europeo de Desarrollo Regional funds. A.M. is grateful to the Spanish Ministerio de Ciencia, Innovación y Universidades for a predoctoral fellowship FPU2018-3503.

References

- [1] J.W. Dufty, *J. Phys.: Condens. Matter* **12**, A47 (2000)
- [2] I. Goldhirsch, *Annu. Rev. Fluid Mech.* **35**, 267 (2003)
- [3] N.V. Brilliantov, T. Pöschel, *Kinetic Theory of Granular Gases* (Oxford University Press, Oxford, 2004)
- [4] V. Garzó, *Granular Gaseous Flows. A Kinetic Theory Approach to Granular Gaseous Flows* (Springer Nature, Switzerland, 2019)
- [5] L. Boltzmann, *Lectures on Gas Theory* (Dover, New York, 1995)
- [6] C.E. Shannon, *Bell Syst. Tech. J.* **27**, 379 (1948)
- [7] S. Chapman, T.G. Cowling, *The Mathematical Theory of Non-Uniform Gases*, 3rd edn. (Cambridge University Press, Cambridge, UK, 1970)
- [8] V. Garzó, A. Santos, *Kinetic Theory of Gases in Shear Flows: Nonlinear Transport*, Fundamental Theories of Physics (Springer, Dordrecht, 2003), ISBN 9781402014369
- [9] P. Maynar, E. Trizac, *Phys. Rev. Lett.* **106**, 160603 (2011)
- [10] S. Kullback, R.A. Leibler, *Ann. Math. Statist.* **22**, 79 (1951)
- [11] S. Mischler, C. Mouhot, M. Rodriguez Ricard, *J. Stat. Phys.* **124**, 655 (2006)
- [12] S. Mischler, C. Mouhot, *J. Stat. Phys.* **124**, 703 (2006)
- [13] S. Mischler, C. Mouhot, *Commun. Math. Phys.* **288**, 431 (2009)
- [14] M.I. García de Soria, P. Maynar, S. Mischler, C. Mouhot, T. Rey, E. Trizac, *J. Stat. Mech.* p. P11009 (2015)
- [15] A. Megías, A. Santos, *Entropy* **22**, 1308 (2020)
- [16] P.K. Haff, *J. Fluid Mech.* **134**, 401 (1983)
- [17] R. Brito, M.H. Ernst, *Europhys. Lett.* **43**, 497 (1998)
- [18] A. Goldshtein, M. Shapiro, *J. Fluid Mech.* **282**, 75 (1995)
- [19] J.J. Brey, M.J. Ruiz-Montero, D. Cubero, *Phys. Rev. E* **54**, 3664 (1996)
- [20] T.P.C. van Noije, M.H. Ernst, *Granul. Matter* **1**, 57 (1998)
- [21] N. Brilliantov, T. Pöschel, *Europhys. Lett.* **74**, 424 (2006)
- [22] N. Brilliantov, T. Pöschel, *Europhys. Lett.* **75**, 188 (2006)
- [23] J.M. Montanero, A. Santos, *Granul. Matter* **2**, 53 (2000)
- [24] A. Santos, J.M. Montanero, *Granul. Matter* **11**, 157 (2009)
- [25] M.N. Bannerman, R. Sargant, L. Lue, *J. Comput. Chem.* **32**, 3329 (2011)
- [26] J.J. Brey, J.W. Dufty, C.S. Kim, A. Santos, *Phys. Rev. E* **58**, 4638 (1998)
- [27] J. Orban, A. Bellemans, *Phys. Lett. A* **24**, 620 (1967)
- [28] J. Orban, A. Bellemans, *J. Stat. Phys.* **1**, 467 (1967)
- [29] A. Aharony, *Phys. Lett. A* **37**, 45 (1971)
- [30] R. Balescu, *Physica* **36**, 433 (1967)
- [31] N. Komatsu, T. Abe, *Physica D* **195**, 391 (2004)



Inelastic hard d_t -spheres under nonlinear drag

7

7.1 Summary

The homogeneous states of a dilute granular gas made of inelastic and smooth identical d_t -spheres of diameter σ , mass m , and coefficient of normal restitution α (assumed to be constant), and surrounded by a background fluid, equilibrated at temperature T_b , are studied. The binary collisions between the granular particles are described by the **IHS** model, whereas the interaction between the gas and its surrounding fluid is approximated via the coarse-grain model described in **Subsection 2.4.1**. Granular particles are subjected to drag and stochastic forces, and assumed to follow, in free flow, the **LE** written in Eq. (2.46). Then, the evolution of its one-body **VDF** is described by the **BFPE** written in Eq. (2.48), particularized to the context of the **IHS** collisional model.

The main objective of this chapter is to provide a detailed description of the evolution and steady-state properties of this homogeneous system. For that, we first formally derive, from the **BFPE**, the evolution equation of the granular temperature [see Eq. (8) of Article 4 (**Section 7.2**)]. The granular temperature slope is explicitly coupled to the fourth cumulant of the **VDF**, a_2 , as occurs in Article 1 (**Section 5.2**) in the case of molecular gases. Additionally to the latter term, the cooling rate appears, which is a function of the full **VDF**. Hence, the cooling term breaks down the molecular equilibrium solution, but the system still admits a steady state. To work in dimensionless terms, we define the same time and temperature reference scales as in Article 1 (**Section 5.2**), τ_b and T_b , respectively. In order to complete the evolution description of the granular temperature, we introduce a Sonine expansion for both the time-dependent and the steady **VDF**. Therefore, from the **BFPE**, an infinite hierarchy of moment equations arise [see Eq. (15) of Article 4 (**Section 7.2**)], quite similar to that of Article 1 (**Section 5.2**), but with the additional cooling term coupling.

Since the derived infinite set of coupled nonlinear differential equations is impossible

to be solved, either analytically or numerically, we introduce two approximate schemes for both evolution and steady states. First, we consider a **MA** to approximate the **VDF**, neglecting the differential equations of all the nontrivial cumulants of the **VDF**, as well as their role in the granular temperature evolution. Therefore, the temperature evolves with a self-consistent closed differential equation, from which we infer the **MA** of the steady-state value of the temperature, T^{st}/T_b , this being the physical root of a fourth-degree polynomial [see Eq. (18) of Article 4 (Section 7.2)]. Whereas this is the simplest approach, the already known evolution schemes in the molecular case [SP20; PSP21; MSP22] [see Article 1 (Section 5.2)] indicates that the evolution of the cumulants is essential to infer a good relaxation of the temperature. Moreover, the breakdown of the equilibrium solution due to the cooling is a signature that the steady-state **VDF** deviates from the Maxwellian distribution. Therefore, the second approximation that we introduce consists in a **SA** characterized by a truncation and linearization up to the fourth cumulant, a_2 [see Eqs. (19)–(21) of Article 4 (Section 7.2)], referred to as *first SA* (**FSA**) throughout Article 4 (Section 7.2). From the latter scheme, we also obtain an approximation for the stationary values of the granular temperature, as well as an expression for the steady-state values of the fourth cumulant, a_2^{st} [see Eqs. (22)–(24) of Article 4 (Section 7.2)].

After the derivation of the theoretical predictions, we compare the values of T^{st}/T_b from the **MA** and the **FSA**. The results, from both approaches, are quite similar, but they present small discrepancies. These differences increase with the value of the nonlinear parameter γ [see Eq. (2.45)], which controls the nonlinear part of the drag coefficient [see Figure 2 of Article 4 (Section 7.2)]. All the stationary values of the granular temperature are below the bath temperature, i.e., $T^{\text{st}}/T_b < 1$, for every value of the parameters in the inelastic case, $\alpha < 1$. This is a consequence of the influence of the granular cooling. Moreover, it is predicted that the excess kurtosis is positive in most cases and, only in a small region of the parameter space, a_2^{st} is negative for **HD** and **HS** [see Figure 3 of Article 4 (Section 7.2)]. In fact, there exists a critical value of the nonlinear parameter, $\gamma_c = 1/3(d_t + 2)$, such that for $\gamma > \gamma_c$, a_2^{st} is always positive for whatever inelastic value of the coefficient of normal restitution ($\alpha < 1$).

To complete the theoretical prediction, we compare the **FSA** steady-state predictions with several well-known limiting cases. First, in the absence of drag (but in the presence of the stochastic force), the granular gas would be driven by just a stochastic thermostat, and the corresponding steady conditions are recovered. Then, if no interstitial fluid is contemplated, the **HCS** conditions are retaken (see Subsection 2.5.2). Moreover, in the case of the presence of a interstitial fluid, but with a linear drag coefficient, i.e., $\gamma \rightarrow 0$, results of Refs. [CVG12; CVG13] are recovered. Also, in the limit where the collision frequency ν_b is negligible as compared with the linear part of the drag coefficient (i.e., the gas is assumed to be collisionless), equilibrium is restored because inelasticity does

not play any role.

As a test for the theoretical predictions, we show **DSMC** and **EDMD** outcomes from hand-made computer programs [**Meg23**]. In the **EDMD** algorithm, the **AGF** algorithm is used to reproduce the Langevin-like dynamics in the free-streaming stage of the evolution. We test the steady and evolution states for different values of the coefficient of normal restitution, α , and the nonlinear parameter, γ . The **FSA** is quantitatively better than the **MA**, with the a_2^{st} predictions underestimating the simulation values for very inelastic particles and for $\gamma \sim 0.1$, which is the limiting regime of the **QR** approximation [see Eq. (2.45)].

The second aim of the chapter is to study the emergence of some memory effects in this system. The **FSA** indicates that the evolution of $T(t)/T_b$ is coupled to the excess kurtosis, recalling the scheme presented in Eqs. (3.1). Thus, we expect that, as occurs with the molecular case and other driven granular systems, memory effects, such as **ME** and **KE**, must be present in this gaseous system. First, we show a pair of examples where the **TME** appears. One of them corresponds to the **DME** and another to the **IME** [see Figure 6 of Article 4 (Section 7.2)]. In these cases, **FSA** theoretical curves and simulation results, from **DSMC** and **EDMD** algorithms, are in good agreement. Afterwards, the appearance of Kovacs-like humps is discussed. Foremost, we consider the system to be immersed in a Kovacs-like protocol, as introduced in Section 3.2, with the granular temperature playing the role of the guiding macrostate variable. Then, in the **FSA**, Eq. (29) of Article 4 (Section 7.2) establishes the form of the temperature slope at the waiting time, t_K^* , whose sign is determined by the difference $a_2^{\text{st}} - a_2(t_K^*)$. Thus, one observes an upward hump if $a_2^{\text{st}} > a_2(t_K^*)$ and a downward hump if $a_2^{\text{st}} < a_2(t_K^*)$. This is confirmed by means of **DSMC** and **EDMD** simulation outcomes, as reproduced in Figure 7 of Article 4 (Section 7.2).

7.2 Article 4

Title: Kinetic Theory and Memory Effects of Homogeneous Inelastic Granular Gases under Nonlinear Drag

Authors: Alberto Megías¹ and Andrés Santos^{1,2}

Affiliations:

¹ Departamento de Física, Universidad de Extremadura, E-06006 Badajoz, Spain

² Instituto de Computación Científica Avanzada (ICCAEx), Universidad de Extremadura, E-06006 Badajoz, Spain

Journal: Entropy

Volume: 24

Pages: 1436

Year: 2022

DOI: [10.3390/e24101436](https://doi.org/10.3390/e24101436)



Copy of the preprint of the work: “Alberto Megías, and Andrés Santos. ‘Kinetic Theory and Memory Effects of Homogeneous Inelastic Granular Gases under Nonlinear Drag’, *Entropy* **24** 10, 1436 (2022) <https://doi.org/10.3390/e24101436>.”

Article

Kinetic Theory and Memory Effects of Homogeneous Inelastic Granular Gases under Nonlinear Drag

Alberto Megías¹  Andrés Santos^{2*} 

¹ Departamento de Física, Universidad de Extremadura, E-06006 Badajoz, Spain; albertom@unex.es

² Departamento de Física and Instituto de Computación Científica Avanzada (ICCAEx), Universidad de Extremadura, E-06006 Badajoz, Spain; andres@unex.es

* Correspondence: andres@unex.es

Received: date; Accepted: date; Published: date

Abstract: We study a dilute granular gas immersed in a thermal bath made of smaller particles with masses not much smaller than the granular ones in this work. Granular particles are assumed to have inelastic and hard interactions, losing energy in collisions as accounted by a constant coefficient of normal restitution. The interaction with the thermal bath is modeled by a nonlinear drag force plus a white-noise stochastic force. The kinetic theory for this system is described by an Enskog–Fokker–Planck equation for the one-particle velocity distribution function. To get explicit results of the temperature aging and steady states, Maxwellian and first Sonine approximations are developed. The latter takes into account the coupling of the excess kurtosis with the temperature. Theoretical predictions are compared with direct simulation Monte Carlo and event-driven molecular dynamics simulations. While good results for the granular temperature are obtained from the Maxwellian approximation, a much better agreement, especially as inelasticity and drag nonlinearity increase, is found when using the first Sonine approximation. The latter approximation is, additionally, crucial to account for memory effects such as Mpemba and Kovacs-like ones.

Keywords: granular gases; kinetic theory; Enskog–Fokker–Planck equation; direct simulation Monte Carlo; event-driven molecular dynamics

1. Introduction

Since the late 20th century, the study of granular materials has become of great importance in different branches of science, such as physics, engineering, chemistry, and mathematics, motivated by either fundamental or industrial reasons. It is well known that rapid flows in granular gases in the dilute regime are well described by a modified version of the classical Boltzmann’s kinetic theory for hard particles. The most widely used model for the granular particles is the inelastic hard-sphere (IHS) one, in which particles are assumed to be hard spheres (or, generally, hard d -spheres) that lose energy due to inelasticity, as parameterized by a constant coefficient of normal restitution.

Theoretical predictions have been tested by different experimental setups in the freely evolving case [1,2]. However, it is rather difficult to experimentally replicate the latter granular gaseous systems due to the fast freezing implied by the dissipative interactions. Then, energy injection is very common in granular experiments [3–10]. In addition, granular systems are never found in a vacuum on Earth. From a quick but attentive glance at our close environment, grains might be found, for example, in the form of dust or pollen suspended in the air, sand, or dirtiness, diving down or browsing through a river, or even forming part of more complex systems such as soils. Therefore, fundamental knowledge about driven granular flows contributes to the understanding of a great variety of phenomena in nature. This is one of the reasons why the study of driven granular flows has become quite important, besides its intrinsic interest at physical and mathematical levels. Consequently, modeling driven granular flows constitutes a solid part of granular matter research,

arXiv:2209.06876v2 [cond-mat.soft] 11 Oct 2022

with theorists combining different collisional models and distinct interactions with the surroundings [11–20].

Recent works [21–23] introduced a model for a molecular gas in which the interaction of the particles with a background fluid is described by a stochastic force and a drag force whose associated drag coefficient has a quadratic dependence on the velocity modulus. This latter dependence is motivated by situations where the particle masses in the gas and the background fluid are not disparate [24–26]. The nonlinearity of the drag force implies an explicit coupling of the temperature with higher-order moments of the velocity distribution function (VDF) of the gas, implying the existence of interesting memory effects, such as Mpemba or Kovacs-like ones, as well as nonexponential relaxations [21–23]. On the other hand, the elastic property of the molecular particles implies that the system ends in an equilibrium state described by the common Maxwell–Boltzmann VDF, unlike granular gases, both driven and freely evolving [11,12,14,17,18,27–30], where a coupling of the hydrodynamic quantities with the cumulants of the VDF is always present. To imagine a real situation, one might possibly consider, for example, a microgravity experiment of pollen grains in a dust cloud.

Throughout this work, we study the properties of homogeneous states of a dilute inelastic granular gas immersed in a background fluid made of smaller particles, the influence of the latter on the former being accounted for at a coarse-grained level by the sum of a deterministic nonlinear drag force and a stochastic force. This gives rise to a competition between the pure effects of the bath and the granular energy dissipation. In fact, we look into expected nonGaussianities from a Sonine approximation of the VDF, commonly used in granular gases. The theoretical results are tested against computer simulations, with special attention on the steady-state properties and memory effects.

The paper is organized as follows. We introduce the model for this system and the associated kinetic-theory evolution equations in Section 2. In Section 3, the Maxwellian and first Sonine approximations are constructed, and the steady-state values are theoretically evaluated. Then, Section 4 collects simulation results from the direct simulation Monte Carlo (DSMC) method and the event-driven molecular dynamics (EDMD) algorithm, which are compared to the theoretical predictions for steady and transient states, including memory effects. Finally, some conclusions of this work are exposed in Section 5.

2. The Model

We consider a homogeneous, monodisperse, and dilute granular gas of identical inelastic hard d -spheres of mass m and diameter σ , immersed in a background fluid made of smaller particles. In a coarse-grained description, the interactions between the grains and the fluid particles can be effectively modeled by a drag force plus a stochastic force acting on the grains. If the mass ratio between the fluid and granular particles is not very small, the drag force becomes a nonlinear function of the velocity [24–26]. The model, as said in Section 1, has previously been studied in the case of elastic collisions [21–23] but not, to our knowledge, in the context of the IHS model. Figure 1 shows an illustration of the system and its modeling.

2.1. Enskog–Fokker–Planck Equation

The full dynamics of the system can be studied from the inelastic homogeneous Enskog–Fokker–Planck equation (EFPE),

$$\partial_t f(\mathbf{v}; t) - \partial_{\mathbf{v}} \left[\zeta(v) \mathbf{v} + \frac{\chi^2(v)}{2} \partial_{\mathbf{v}} \right] f(\mathbf{v}; t) = J[\mathbf{v}|f, f], \quad (1)$$

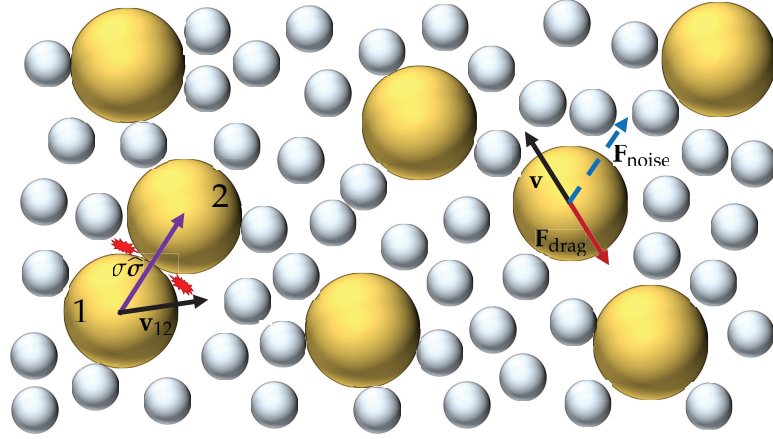


Figure 1. Illustration of the system considered in this paper. A granular gas of hard particles (represented by large yellowish spheres) is coupled to a thermal bath (made of particles represented by the small grayish spheres) via a drag force $\mathbf{F}_{\text{drag}} = -m\zeta(v)\mathbf{v}$, where $\zeta(v)$ is a velocity-dependent drag coefficient, and a stochastic force $\mathbf{F}_{\text{noise}} = m\chi(v)\boldsymbol{\eta}$, where $\boldsymbol{\eta}$ is a Gaussian white-noise term. In addition, the granular particles are subjected to binary inelastic collisions, represented by the red gleam-like lines.

where f is the one-particle VDF, so that $n = \int d\mathbf{v}f(\mathbf{v};t)$ is the number density, and $J[\mathbf{v}|f, f]$ is the usual Enskog–Boltzmann collision operator defined by

$$J[\mathbf{v}_1|f, f] \equiv \sigma^{d-1}g_c \int d\mathbf{v}_2 \int_+ d\hat{\sigma} (\mathbf{v}_{12} \cdot \hat{\sigma}) \left[\alpha^{-2}f(\mathbf{v}'_1)f(\mathbf{v}'_2) - f(\mathbf{v}_1)f(\mathbf{v}_2) \right]. \quad (2)$$

Here, α is the coefficient of normal restitution (see below), $\mathbf{v}_{12} = \mathbf{v}_1 - \mathbf{v}_2$ is the relative velocity, $\hat{\sigma} = (\mathbf{r}_1 - \mathbf{r}_2)/\sigma$ is the intercenter unit vector at contact, $g_c = \lim_{r \rightarrow \sigma^+} g(r)$ is the contact value of the pair correlation function $g(r)$, $\int_+ d\hat{\sigma} \equiv \int d\hat{\sigma} \Theta(\mathbf{v}_{12} \cdot \hat{\sigma})$, Θ being the Heaviside step-function and \mathbf{v}'_i refers to the precollisional velocity of the particle i . Within the IHS model, the collisional rules are expressed by [18,30]

$$\mathbf{v}'_{1/2} = \mathbf{v}_{1/2} \mp \frac{1 + \alpha^{-1}}{2} (\mathbf{v}_{12} \cdot \hat{\sigma}) \hat{\sigma}. \quad (3)$$

From Equation (3), one gets $(\mathbf{v}_{12} \cdot \hat{\sigma}) = -\alpha(\mathbf{v}'_{12} \cdot \hat{\sigma})$; this relation defines the coefficient of normal restitution, which is assumed to be constant.

The second term on the left-hand side of Equation (1) represents the action of a net force $\mathbf{F} = \mathbf{F}_{\text{drag}} + \mathbf{F}_{\text{noise}}$ describing the interaction with the particles of the background fluid. The deterministic nonlinear drag force is $\mathbf{F}_{\text{drag}} = -m\zeta(v)\mathbf{v}$, where the drag coefficient $\zeta(v)$ depends on the velocity. In turn, $\mathbf{F}_{\text{noise}} = m\chi^2(v)\boldsymbol{\eta}$ is a stochastic force, where $\chi^2(v)$ measures its intensity, and $\boldsymbol{\eta}$ is a stochastic vector with the properties of a zero-mean Gaussian white noise with a unit covariance matrix, i.e.,

$$\langle \boldsymbol{\eta}_i(t) \rangle = 0, \quad \langle \boldsymbol{\eta}_i(t)\boldsymbol{\eta}_j(t') \rangle = \mathbb{I} \delta_{ij} \delta(t - t'), \quad (4)$$

where i and j are particle indices, and \mathbb{I} is the $d \times d$ unit matrix so that different Cartesian components of $\boldsymbol{\eta}_i(t)$ are uncorrelated. The functions $\zeta(v)$ and $\chi^2(v)$ are constrained to follow the fluctuation-dissipation theorem as

$$\chi^2(v) = v_b^2 \zeta(v), \quad (5)$$

$v_b = \sqrt{2T_b/m}$ being the thermal velocity associated with the background temperature T_b .

The drag coefficient ζ is commonly assumed to be independent of the velocity. However, a dependence on v cannot be ignored if the mass of a fluid particle is not much smaller than that of grain [24–26]. The first correction to $\zeta = \text{const}$ is a quadratic term [21–23], namely

$$\zeta(v) = \zeta_0 \left(1 + 2\gamma \frac{v^2}{v_b^2} \right), \quad (6)$$

where ζ_0 is the drag coefficient in the zero-velocity limit and γ controls the degree of nonlinearity of the drag force.

2.2. Dynamics

It is well known that, in the case of driven granular gases [11,12,14,17–19,31,32], there exists a competition between the loss and gain of energy due to inelasticity and the action of the thermal bath, respectively. This eventually leads the granular gas to a steady state, in contrast to the freely cooling case [18].

The basic macroscopic quantity characterizing the time evolution of the system is the granular temperature, defined analogously to the standard temperature in kinetic theory as

$$T(t) = \frac{m}{dn} \int d\mathbf{v} v^2 f(\mathbf{v}; t). \quad (7)$$

While in the case of elastic collisions, the asymptotic steady state is that of equilibrium at temperature T_b , i.e., $\lim_{t \rightarrow \infty} T(t) = T_b$, in the IHS model, the steady state is a nonequilibrium one and, moreover, $\lim_{t \rightarrow \infty} T(t) = T^{\text{st}} < T_b$. From the EFPE, one can derive the evolution equation of the granular temperature, which is given by

$$\frac{\partial_t T}{\zeta_0} = 2(T_b - T) \left[1 + (d+2)\gamma \frac{T}{T_b} \right] - 2(d+2)\gamma \frac{T^2}{T_b} a_2 - \frac{\zeta}{\zeta_0} T, \quad (8)$$

where

$$\zeta(t) \equiv -\frac{m}{dT(t)n} \int d\mathbf{v} v^2 J[\mathbf{v}, f, f] \quad (9)$$

is the cooling rate and

$$a_2(t) \equiv \frac{d}{d+2} \frac{n \int d\mathbf{v} v^4 f(\mathbf{v}; t)}{\left[\int d\mathbf{v} v^2 f(\mathbf{v}; t) \right]^2} - 1 \quad (10)$$

is the excess kurtosis (or fourth cumulant) of the time-dependent VDF. The coupling of $T(t)$ to $a_2(t)$ is a direct consequence of the quadratic term in the drag coefficient. As for the cooling rate $\zeta(t)$, it is a consequence of inelasticity and, therefore, vanishes in the elastic case (conservation of energy). Insertion of Equation (2) into Equation (9) yields [18]

$$\zeta(t) = (1 - \alpha^2) \frac{v(t)}{\sqrt{2dn^2}} \frac{\Gamma\left(\frac{d}{2}\right)}{\Gamma\left(\frac{d+3}{2}\right)} \int d\mathbf{v}_1 \int d\mathbf{v}_2 \left[\frac{v_{12}}{v_{\text{th}}(t)} \right]^3 f(\mathbf{v}_1; t) f(\mathbf{v}_2; t). \quad (11)$$

Here, $v_{\text{th}}(t) = \sqrt{2T(t)/m}$ is the time-dependent thermal velocity and

$$v(t) = g_c K_d n \sigma^{d-1} v_{\text{th}}(t), \quad K_d \equiv \frac{\pi^{d-1}}{\sqrt{2}\Gamma(d/2)}, \quad (12)$$

is the time-dependent collision frequency.

Let us rewrite Equation (8) in dimensionless form. First, we introduce the reduced quantities

$$t^* \equiv v_b t, \quad \theta(t^*) \equiv \frac{T(t)}{T_b}, \quad \zeta_0^* \equiv \frac{\zeta_0}{v_b}, \quad \mu_\ell(t^*) \equiv -\frac{1}{nv(t)} \int d\mathbf{v} \left[\frac{v}{v_{\text{th}}(t)} \right]^\ell J[\mathbf{v}|f, f], \quad (13)$$

where $v_b = g_c K_d n \sigma^{d-1} v_b$ is the collision frequency associated with the background temperature T_b . Note that the control parameter ζ_0^* measures the ratio between the characteristic times associated with collisions and drag. In the molecular case, ζ_0^* depends on the bath-to-grain density, size, and mass ratios, but otherwise, it is independent of T_b [21,26]. In terms of the quantities defined in Equation (13), Equation (8) becomes

$$\frac{\dot{\theta}}{\zeta_0^*} = 2(1 - \theta) [1 + (d + 2)\gamma\theta] - 2(d + 2)\gamma\theta^2 a_2 - \frac{2\mu_2 \theta^{3/2}}{d \zeta_0^*}, \quad (14)$$

where henceforth, a dot over a quantity denotes a derivative with respect to t^* , and we have taken into account that $\zeta(t)/v(t) = 2\mu_2(t^*)/d$ and $v(t)/v_b = \theta^{1/2}(t^*)$.

Equation (14) is not a closed equation since it is coupled to the full VDF through a_2 and μ_2 . More generally, taking velocity moments on the EFPE, an infinite hierarchy of moment equations can be derived. In dimensionless form, it reads

$$\frac{\dot{M}_\ell}{\zeta_0^*} = \ell \left\{ \left[(\ell - 2)\gamma + \frac{\mu_2 \sqrt{\theta}}{d \zeta_0^*} + (d + 2)\gamma\theta(1 + a_2) - \frac{1}{\theta} \right] M_\ell - 2\gamma\theta M_{\ell+2} + \frac{d + \ell - 2}{2} \frac{M_{\ell-2}}{\theta} \right\} - \mu_\ell \frac{\sqrt{\theta}}{\zeta_0^*}, \quad (15)$$

where $M_\ell(t^*) \equiv n^{-1} \int d\mathbf{v} [v/v_{\text{th}}(t)]^\ell f(\mathbf{v}; t)$. In particular, $M_0 = 1$, $M_2 = \frac{d}{2}$, $M_4 = \frac{d(d+2)}{4}(1 + a_2)$, and $M_6 = \frac{d(d+2)(d+4)}{8}(1 + 3a_2 - a_3)$, a_3 being the sixth cumulant.

Equation (15) is trivial for $\ell = 0$ and $\ell = 2$. The choice $\ell = 4$ yields

$$\frac{\dot{a}_2}{\zeta_0^*} = 4\gamma\theta \left[\frac{2(1 + a_2)}{\theta} + (d + 2)(1 + a_2)^2 - (d + 4)(1 + 3a_2 - a_3) \right] - 4\frac{a_2}{\theta} + \frac{4}{d} \left[\mu_2(1 + a_2) - \frac{\mu_4}{d + 2} \right] \frac{\sqrt{\theta}}{\zeta_0^*}. \quad (16)$$

Equations (14)–(16) are formally exact in the context of the EFPE, Equation (1). Nevertheless, they cannot be solved because of the infinite nature of the hierarchy (15) and the highly nonlinear dependence of the collisional moments μ_ℓ on the velocity moments of the VDF. This forces us to devise tractable approximations in order to extract information about the dynamics and steady state of the system.

3. Approximate Schemes

3.1. Maxwellian Approximation

The simplest approximation consists of assuming that the VDF remains very close to a Maxwellian during its time evolution so that the excess kurtosis a_2 can be neglected in Equation (14), and the reduced cooling rate μ_2 can be approximated by [11,12,17,18,28,33,34]

$$\mu_2 \approx \mu_2^{(0)} = 1 - \alpha^2. \quad (17)$$

In this Maxwellian approximation (MA), Equation (14) becomes

$$\frac{\dot{\theta}}{\xi_0^*} \approx 2(1-\theta) [1 + (d+2)\gamma\theta] - \frac{2(1-\alpha^2)}{d} \frac{\theta^{3/2}}{\xi_0^*}. \quad (18)$$

This is a closed equation for the temperature ratio $\theta(t^*)$ that can be solved numerically for any initial temperature. The steady-state value θ^{st} in the MA is obtained by equating to zero the right-hand side of Equation (18), which results in a fourth-degree algebraic equation.

3.2. First Sonine Approximation

As we will see later, the MA given by Equation (18) provides a simple and, in general, rather accurate estimate of $\theta(t^*)$ and θ^{st} . However, since the evolution of temperature is governed by its initial value only, the MA is unable to capture memory phenomena, such as Mpemba- or Kovacs-like effects, which are observed even in the case of elastic particles [21–23]. This is a consequence of the absence of any coupling of θ with some other dynamical variable(s).

The next simplest approximation beyond the MA consists of incorporating a_2 into the description but assuming it is small enough as to neglect nonlinear terms involving this quantity, as well as higher-order cumulants, i.e., $a_2^k \rightarrow 0$ for $k \geq 2$ and $a_\ell \rightarrow 0$ for $\ell \geq 3$. This represents the so-called first Sonine approximation (FSA), according to which Equations (14) and (16) become

$$\frac{\dot{\theta}}{\xi_0^*} \approx 2(1-\theta) [1 + (d+2)\gamma\theta] - 2(d+2)\gamma\theta^2 a_2 - \frac{2[\mu_2^{(0)} + \mu_2^{(1)} a_2]}{d} \frac{\theta^{3/2}}{\xi_0^*}, \quad (19a)$$

$$\begin{aligned} \frac{\dot{a}_2}{\xi_0^*} \approx & 4\gamma\theta \left[2\frac{1+a_2}{\theta} + (d+2)(1+2a_2) - (d+4)(1+3a_2) \right] - 4\frac{a_2}{\theta} \\ & + \frac{4}{d} \left\{ \mu_2^{(0)} - \frac{\mu_4^{(0)}}{d+2} + \left[\mu_2^{(0)} + \mu_2^{(1)} - \frac{\mu_4^{(1)}}{d+2} \right] a_2 \right\} \frac{\sqrt{\theta}}{\xi_0^*}, \end{aligned} \quad (19b)$$

where we have used [11,12,17,18,28,33,34]

$$\mu_2 \approx \mu_2^{(0)} + \mu_2^{(1)} a_2, \quad \mu_4 \approx \mu_4^{(0)} + \mu_4^{(1)} a_2, \quad (20)$$

with

$$\mu_2^{(1)} = \frac{3}{16} \mu_2^{(0)}, \quad \mu_4^{(0)} = \left(d + \frac{3}{2} + \alpha^2 \right) \mu_2^{(0)}, \quad (21a)$$

$$\mu_4^{(1)} = \frac{3}{32} (10d + 39 + 10\alpha^2) \mu_2^{(0)} + (d-1)(1+\alpha). \quad (21b)$$

Equations (19) make a set of two coupled differential equations. In contrast to the MA, now the evolution of $\theta(t^*)$ is governed by the initial values of both θ and a_2 . This latter fact implies that the evolution of temperature depends on the initial preparation of the whole VDF, this being a determinant condition for the emergence of memory effects, which will be explored later in Section 4.1.

3.2.1. Steady-State Values

The steady-state values θ^{st} and a_2^{st} in the FSA are obtained by equating to zero the right-hand sides of Equations (19), i.e.,

$$\dot{\theta} = 0 \Rightarrow F_0(\theta^{\text{st}}) + F_1(\theta^{\text{st}})a_2^{\text{st}} = \left[\mu_2^{(0)} + \mu_2^{(1)}a_2^{\text{st}} \right] \frac{(\theta^{\text{st}})^{3/2}}{\zeta_0^*}, \quad (22a)$$

$$a_2 = 0 \Rightarrow G_0(\theta^{\text{st}}) + G_1(\theta^{\text{st}})a_2^{\text{st}} = \left\{ \frac{\mu_4^{(0)}}{d+2} - \mu_2^{(0)} + \left[\frac{\mu_4^{(1)}}{d+2} - \mu_2^{(0)} - \mu_2^{(1)} \right] a_2^{\text{st}} \right\} \frac{(\theta^{\text{st}})^{3/2}}{\zeta_0^*}, \quad (22b)$$

where

$$F_0(\theta) = d(1 - \theta) [1 + (d + 2)\gamma\theta], \quad F_1(\theta) = -d(d + 2)\gamma\theta^2, \quad (23a)$$

$$G_0(\theta) = 2d\gamma\theta(1 - \theta), \quad G_1(\theta) = d\gamma\theta [2 - \theta(d + 8)] - d. \quad (23b)$$

Eliminating a_2^{st} in Equation (22), one gets a closed nonlinear equation for θ^{st} in our FSA. Once numerically solved, a_2^{st} is simply given by either Equation (22a) or Equation (22b). For instance, Equation (22a) gives

$$a_2^{\text{st}} = - \frac{F_0(\theta^{\text{st}}) - \mu_2^{(0)}(\theta^{\text{st}})^{3/2}/\zeta_0^*}{F_1(\theta^{\text{st}}) - \mu_2^{(1)}(\theta^{\text{st}})^{3/2}/\zeta_0^*}. \quad (24)$$

Figure 2 compares the MA and FSA predictions of θ^{st} for three- and two-dimensional granular gases with $\zeta_0^* = 1$. We observe that the breakdown of equipartition (as measured by $1 - \theta^{\text{st}}$) is stronger in 2D than 3D and increases with increasing inelasticity but decreases as the nonlinearity of the drag force grows. Apart from that, the deviations of the MA values with respect to the FSA ones increase with increasing nonlinearity and inelasticity, the MA values tending to be larger (i.e., closer to equipartition) than the FSA ones.

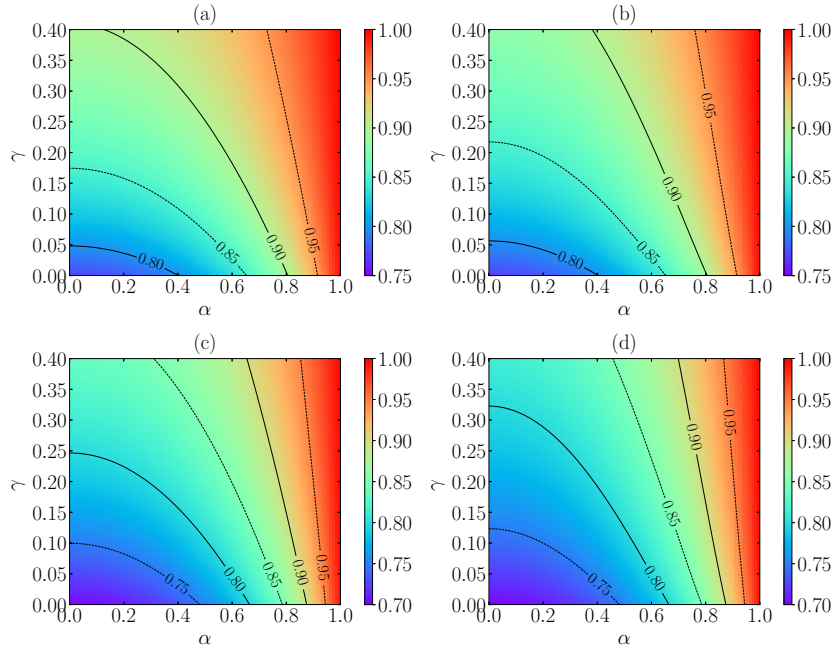


Figure 2. Theoretical predictions for the steady-state value of the reduced temperature θ^{st} as a function of the coefficient of normal restitution α and of the nonlinearity control parameter γ with $\xi_0^* = 1$. Panels (a,c) correspond to the MA, while panels (b,d) correspond to the FSA. The dimensionality of the system is $d = 3$ in panels (a,b) and $d = 2$ in panels (c,d). The contour lines are separated by an amount of $\Delta\theta^{\text{st}} = 0.05$.

The FSA predictions of a_2^{st} are displayed in Figure 3. First, it is quite apparent that the departure from the Maxwellian VDF (as measured by the magnitude of a_2^{st}) is higher in 2D than 3D. It is also noteworthy that a_2^{st} starts growing with increasing γ , reaches a maximum at a certain value $\gamma = \gamma_{\text{max}}(\alpha, \xi_0^*)$, and then it decreases as γ increases beyond $\gamma_{\text{max}}(\alpha, \xi_0^*)$; this effect is more pronounced for small α .

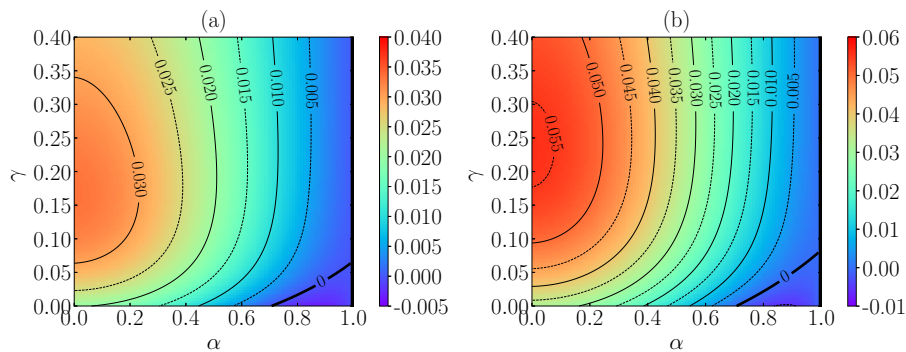


Figure 3. FSA predictions for the steady-state value of the excess kurtosis a_2^{st} as a function of the coefficient of normal restitution α and of the nonlinearity control parameter γ with $\xi_0^* = 1$. The dimensionality of the system is $d = 3$ in panel (a) and $d = 2$ in panel (b). The contour lines are separated by an amount of $\Delta a_2^{\text{st}} = 0.005$. The thickest black line corresponds to the contour $a_2^{\text{st}} = 0$.

Another interesting feature is that a_2^{st} takes negative values (in the domain of small inelasticity) only if γ is smaller than a certain value γ_c . Of course, $a_2^{\text{st}}(\alpha, \gamma)|_{\alpha=1} = 0$ for any γ (since the steady state with $\alpha = 1$ is that of equilibrium), but $\partial_\alpha a_2^{\text{st}}(\alpha, \gamma)|_{\alpha=1} < 0$ if $\gamma < \gamma_c$ and $\partial_\alpha a_2^{\text{st}}(\alpha, \gamma)|_{\alpha=1} > 0$ if $\gamma > \gamma_c$. Thus, the critical value γ_c is determined by the condition $\partial_\alpha a_2^{\text{st}}(\alpha, \gamma_c)|_{\alpha=1} = 0$. Interestingly, the result obtained from the FSA, Equation (24), is quite simple, namely

$$\gamma_c = \frac{1}{3(d+2)}, \quad (25)$$

which is independent of ζ_0^* .

3.2.2. Special Limits

Absence of Drag

Let us first define a *noise temperature* T_n as $T_n = T_b \zeta_0^{*2/3} \propto (\zeta_0 T_b)^{2/3}$, so that $\theta^{3/2}/\zeta_0^* = (T/T_n)^{3/2}$. Now we take the limit of zero drag, $\zeta_0 \rightarrow 0$, with finite noise temperature T_n . This implies $T_b \rightarrow \infty$, and thus, the natural temperature scale of the problem is no longer T_b but T_n , i.e., $\theta^{\text{st}} \rightarrow 0$ but $T^{\text{st}}/T_n = \text{finite}$. From Equations (23) we see that $F_0(0) = d$, $F_1(0) = 0$, $G_0(0) = 0$, and $G_1(0) = -d$. Therefore, Equations (22) reduce to

$$\dot{\theta} = 0 \Rightarrow d \left(\frac{T_n}{T^{\text{st}}} \right)^{3/2} = \mu_2^{\text{st}}, \quad (26a)$$

$$a_2 = 0 \Rightarrow -d \left(\frac{T_n}{T^{\text{st}}} \right)^{3/2} a_2^{\text{st}} = \frac{\mu_4^{\text{st}}}{d+2} - \mu_2^{\text{st}}(1 + a_2^{\text{st}}), \quad (26b)$$

where, for the sake of generality, we have undone the linearizations with respect to a_2^{st} . By the elimination of $(T_n/T^{\text{st}})^{3/2}$, one simply gets $(d+2)\mu_2^{\text{st}} = \mu_4^{\text{st}}$, from which one can then obtain a_2^{st} upon linearization [11,12]. The steady-state temperature is given by $T^{\text{st}}/T_n = (d/\mu_2^{\text{st}})^{2/3}$.

Homogeneous Cooling State

If, in addition to $\zeta_0 \rightarrow 0$, we take the limit $T_n \rightarrow 0$, the asymptotic state becomes the homogeneous cooling state. In that case, T does not reach a true stationary value, but a_2 does. As a consequence, Equation (26a) is not applicable, but Equation (26b), with $T_n = 0$, can still be used to get $(d+2)\mu_2^{\text{st}}(1 + a_2^{\text{st}}) = \mu_4^{\text{st}}$, as expected [11,12,17].

Linear Drag Force

If the drag force is linear in velocity (i.e., $\gamma = 0$), we have $F_0(\theta) = d(1 - \theta)$, $F_1(\theta) = 0$, $G_0(\theta) = 0$, and $G_1(\theta) = -d$. Using Equation (22b), a_2^{st} is given by

$$a_2^{\text{st}} = - \frac{\mu_4^{(0)} - (d+2)\mu_2^{(0)}}{\mu_4^{(0)} - (d+2) \left[\mu_2^{(0)} + \mu_2^{(1)} - d\zeta_0^*/(\theta^{\text{st}})^{3/2} \right]}, \quad (27)$$

thus recovering previous results [31,32].

Collisionless Gas

If the collision frequency ν_b is much smaller than the zero-velocity drag coefficient ζ_0 , the granular dynamics is dominated by the interaction with the background fluid and the grain-grain collisions can be neglected; therefore, the grains behave as Brownian particles. In that case, the relevant dimensionless time is no longer $t^* = \nu_b t$ but $\tau = \zeta_0 t = \zeta_0^* t^*$ and the evolution equations (19) become

$$\frac{d\theta}{d\tau} \approx 2(1-\theta) [1 + (d+2)\gamma\theta] - 2(d+2)\gamma\theta^2 a_2, \quad (28a)$$

$$\frac{da_2}{d\tau} \approx 4\gamma\theta \left[2\frac{1+a_2}{\theta} + (d+2)(1+2a_2) - (d+4)(1+3a_2) \right] - 4\frac{a_2}{\theta}, \quad (28b)$$

It is straightforward to check that the steady-state solution is $\theta^{\text{st}} = 1$ and $a_2^{\text{st}} = 0$, regardless of the value of γ , as expected.

4. Comparison with Computer Simulations

We have carried out DSMC and EDMD computer simulations to validate the theoretical predictions. The DSMC method is based on the acceptance-rejection Monte Carlo Metropolis decision method [35] but adapted to solve the Enskog–Boltzmann equation [36,37], and the algorithm is, consequently, adjusted to agree with the inelastic collisional model [12,17] and reflect the interaction with the bath [23]. On the other hand, the EDMD algorithm is based on the one exposed in Ref. [23], but is adequated to the IHS collisional model. The main difference between DSMC and EDMD is that the latter does not follow any statistical rule to solve the Boltzmann equation but solves the equations of motion of the hard particles. Simulation details about the characteristics of the schemes and numerical particularities can be found in Appendix A.

In Figure 4, results from simulations are compared with the theoretical predictions of θ^{st} (from MA and FSA) and of a_2^{st} (from FSA) in a three-dimensional ($d = 3$) IHS system with $\zeta_0^* = 1$. It can be observed that both the DSMC and EDMD results agree with each other. From Figure 4a, one can conclude that, as expected, FSA works in the prediction of θ^{st} much better than MA for values of γ close to $\gamma_{\text{max}}(\alpha, \zeta_0^*)$ (which corresponds to the maximum magnitude of a_2^{st}). Moreover, FSA gives reasonably good estimates for the values of a_2^{st} , although they get worse for increasing inelasticity, i.e., decreasing α . One might also think that the increase in γ produces a poorer approach; however, according to the theory, the performance of FSA improves if $\gamma > \gamma_{\text{max}}(\alpha, \zeta_0^*)$, which corresponds to a decrease in $|a_2^{\text{st}}|$. Of course, nonlinear terms or higher-order cumulants might play a role that is not accounted for within FSA.

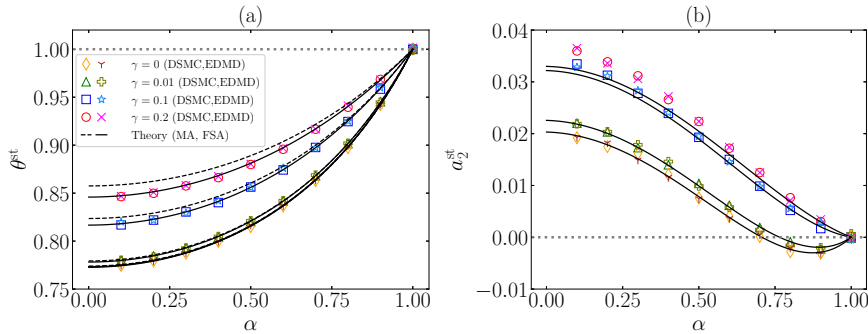


Figure 4. Plots of the steady-state values of (a) the temperature ratio θ^{st} and (b) the excess kurtosis a_2^{st} vs. the coefficient of normal restitution α for $\zeta_0^* = 1$, $d = 3$, and different values of the nonlinear parameter: $\gamma = 0, 0.01, 0.1, 0.2$. The symbols stand for DSMC ($\diamond, \triangle, \square, \circ$) and EDMD ($\nabla, +, *, \times$) simulation results, respectively. Dashed (---) and solid (—) lines refer to MA (only in panel (a)) and FSA predictions, respectively. The horizontal gray dotted lines (\cdots) correspond to the steady-state values in the elastic limit. As representative values, note that, at $\zeta_0^* = 1$, one has $\gamma_{\text{max}} = 0.25, 0.19, 0.17$ for $\alpha = 0.8, 0.5, 0.2$, respectively.

Apart from the steady-state values, we have studied the temporal evolution of θ and a_2 , starting from a Maxwellian VDF at temperature T_b , i.e., $\theta(0) \equiv \theta^0 = 1$ and $a_2(0) \equiv a_2^0 = 0$. Note that this state

is that of equilibrium in the case of elastic collisions ($\alpha = 1$), regardless of the value of the nonlinearity parameter γ . The theoretical and simulation results are displayed in Figure 5 for $d = 3$, $\zeta_0^* = 1$, and some characteristic values of α and γ .

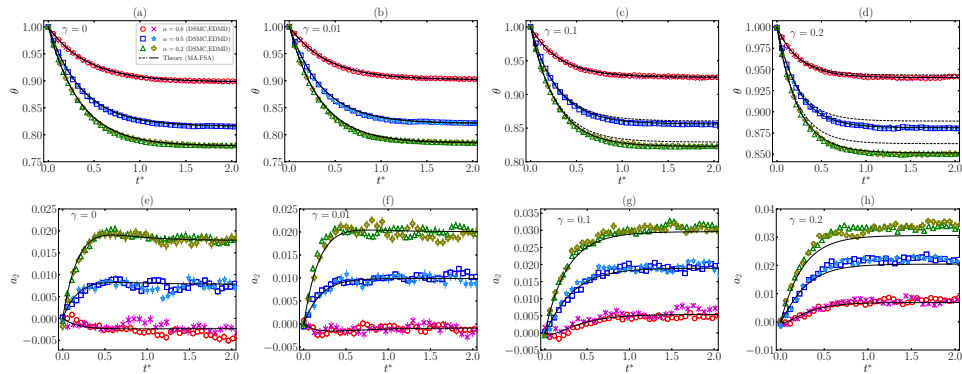


Figure 5. Plots of the time evolution of (a–d) the temperature ratio $\theta(t^*)$ and (e–h) the excess kurtosis $a_2(t^*)$ for $\zeta_0^* = 1$, $d = 3$, and different values of the coefficient of normal restitution ($\alpha = 0.8, 0.5, 0.2$) and the nonlinearity parameter: (a,e) $\gamma = 0$, (b,f) $\gamma = 0.01$, (c,g) $\gamma = 0.1$, and (d,h) $\gamma = 0.2$. The symbols stand for DSMC ($\circ, \square, \triangle$) and EDMD ($\times, *, +$) simulation results, respectively. Dashed (–) and solid (—) lines refer to MA (only in panels (a–d)) and FSA predictions, respectively. All states are initially prepared with a Maxwellian VDF at the bath temperature, i.e., $\theta^0 = 1$ and $a_2^0 = 0$.

We observe that the relaxation of θ is accurately predicted by MA, except for the later stage with small α and/or large γ , in accordance with the discussion of Figure 4. This is remedied by FSA, which exhibits an excellent agreement with simulation results in the case of θ and a fair agreement in the case of a_2 , again in accordance with the discussion of Figure 4. It is also worth mentioning the good mutual agreement between DSMC and EDMD data, even though fluctuations are much higher in a_2 than in θ because of the rather small values of $|a_2|$.

4.1. Memory Effects

Whereas the temperature relaxation from Maxwellian initial states is generally accurate from MA, it misses the explicit dependence of the temperature evolution on the fourth cumulant (see Equation (14)), which, however, is captured by FSA (see Equation (19a)). This coupling of θ to a_2 is a signal of preparation dependence of the system, hence, a signal of memory effects, as occurs in the elastic case reported in Refs. [21–23].

4.1.1. Mpemba Effect

We start the study of memory effects with the Mpemba effect [38–42]. This counterintuitive phenomenon refers to situations in which an initially hotter sample (A) of a fluid—or, more generally, a statistical-mechanical system—cools down sooner than an initially colder one (B) in a cooling experiment. We will refer to this as the direct Mpemba effect (DME). Analogously, the inverse Mpemba effect (IME) occurs in heating experiments if the initially colder sample (B) heats up more rapidly than the initially hotter one (A) [21,23,40,41,43]. In the special case of a molecular gas (i.e., $\alpha = 1$), an extensive study of both DME and IME has recently been carried out [21,23].

Figure 6a,b present an example of DME and IME, respectively. As expected, FSA describes the evolution and crossing for temperatures of samples A and B very well. On the contrary, MA does not predict this memory effect. In addition, from Figure 6c,d we can conclude that FSA captures the relaxation of a_2 toward $a_2^{\text{st}} \neq 0$ quite well.

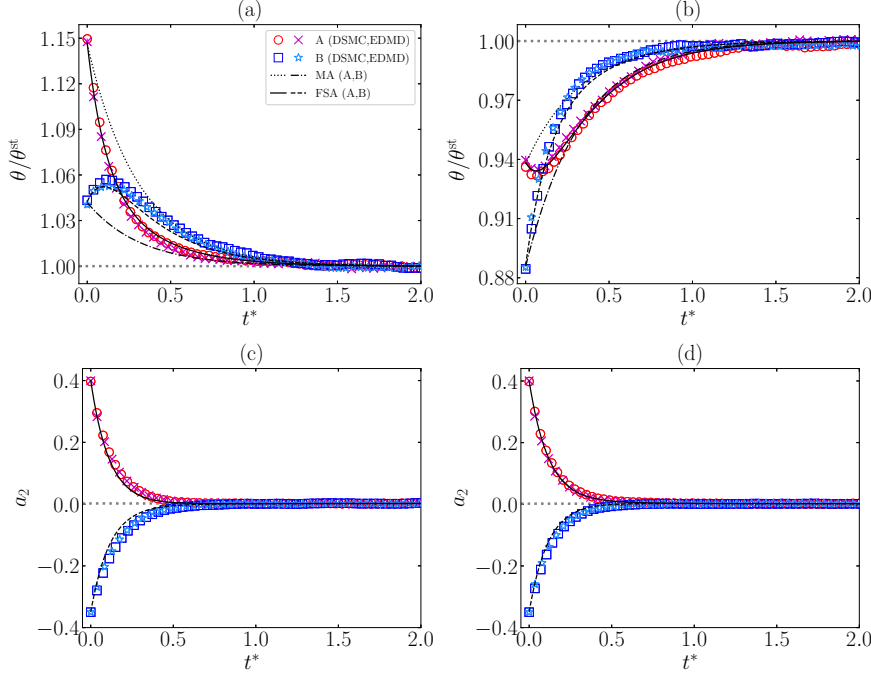


Figure 6. Time evolution of (a,b) $\theta(t^*)/\theta^{\text{st}}$ and (c,d) $a_2(t^*)$ for two samples (A and B) with $\alpha = 0.9$, $\xi_0^* = 1$, $d = 3$, and $\gamma = 0.1$. Panels (a, c) illustrate the DME with initial conditions $\theta_A^0 = 1.1 \simeq 1.15\theta^{\text{st}}$, $a_{2A}^0 = 0.4$, $\theta_B^0 = 1 \simeq 1.04\theta^{\text{st}}$, $a_{2B}^0 = -0.35$, while panels (b, d) illustrate the IME with initial conditions $\theta_A^0 = 0.9 \simeq 0.94\theta^{\text{st}}$, $a_{2A}^0 = 0.4$, $\theta_B^0 = 0.85 \simeq 0.89\theta^{\text{st}}$, $a_{2B}^0 = -0.35$. The symbols stand for DSMC (\circ , \square) and EDMD (\times , $*$) simulation results, respectively. Solid (—) and dashed (---) lines correspond to FSA predictions for samples A and B, respectively, whereas black dotted (\cdots) and dash-dotted (— · —) lines in panels (a,b) refer to MA predictions for samples A and B, respectively. The gray thin horizontal lines correspond to the steady-state values. Note that $a_2^{\text{st}} \neq 0$, despite what panels (c,d) seem to indicate because of the vertical scale.

4.1.2. Kovacs Effect

Next, we turn to another interesting memory effect: the Kovacs effect [44,45]. In contrast to the Mpemba effect, the Kovacs effect has a well-defined two-stage protocol and does not involve a comparison between two samples. In the context of our system, the protocol proceeds as follows. First, the granular gas is put in contact with a bath at temperature T_{b1} and initialized at a temperature $T^0 > T_1^{\text{st}}$, $T_1^{\text{st}} = \theta^{\text{st}}T_{b1}$ being the corresponding steady-state temperature (note that θ^{st} is independent of T_{b1} at fixed ξ_0^*). The system is allowed to relax to the steady state during a time window $0 < t < t_K$, but then, at $t = t_K$, the bath temperature is suddenly modified to a new value T_b , such that $T(t_K) = T^{\text{st}}$, $T^{\text{st}} = \theta^{\text{st}}T_b$ being the new steady-state value. If the system did not retain a memory of its previous history, one would have $T(t) = T^{\text{st}}$ for $t > t_K$, and this is, in fact, the result given by the MA. However, the temperature exhibits a hump for $t > t_K$, before relaxing to T^{st} . This hump is a consequence of the dependence of $\partial_t T$ on the additional variables of the system. According to Equation (14), and maintained in the FSA, Equation (19a), the first relevant quantity to be responsible

for a possible hump is the excess kurtosis of the VDF, as occurs in the elastic limit [22]. In fact, at time $t^* = t_K^*$, such that $\theta(t_K^*) = \theta^{\text{st}}$, the slope of the temperature according to FSA, Equation (19a), reads

$$\dot{\theta}(t_K^*) \approx 2\theta^{\text{st}} \left[(d+2)\zeta_0^* \gamma \theta^{\text{st}} + \frac{\mu_2^{(1)}}{d} \sqrt{\theta^{\text{st}}} \right] [a_2^{\text{st}} - a_2(t_K^*)]. \quad (29)$$

Thus, a nonzero difference $a_2^{\text{st}} - a_2(t_K^*)$ implies the existence of a Kovacs-like hump, its sign being determined by that of this difference; that is, we will obtain an upward hump if $a_2(t_K^*) < a_2^{\text{st}}$ or a downward hump if $a_2(t_K^*) > a_2^{\text{st}}$.

For simplicity, in our study of the Kovacs-like effect, we replace the first stage of the protocol ($0 < t^* < t_K^*$) by just generating the state at $t^* = t_K^*$ with $\theta(t_K^*) = \theta^{\text{st}}$ and $a_2(t_K^*) \neq a_2^{\text{st}}$ (see Appendix A). The effect is illustrated in Figure 7 for the same system as in Figure 6 with the choices $a_2(t_K^*) = -0.35 < a_2^{\text{st}}$ and $a_2(t_K^*) = 0.4 > a_2^{\text{st}}$. Again, the DSMC and EDMD results agree with each other and with the theoretical predictions. However, in the case $a_2(t_K^*) = -0.35$ (upward hump), Figure 7a, we observe that the theoretical curve lies below the simulation results. This might be caused by a nonnegligible value of the sixth cumulant $a_3(t_K^*) = -0.375$, as reported in Ref. [23] in the elastic case. Apart from this small discrepancy, FSA captures the magnitude and sign of the humps, as well as the relaxation of the fourth cumulant, very well.

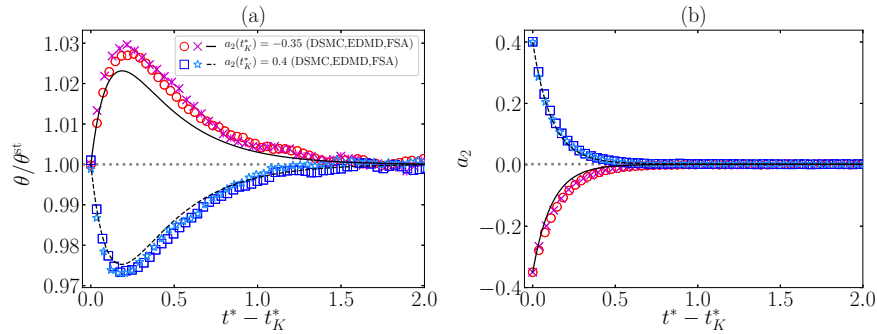


Figure 7. Time evolution for $t^* > t_K^*$ of (a) $\theta(t^*)/\theta^{\text{st}}$ and (b) $a_2(t^*)$ for a system with $\alpha = 0.9$, $\zeta_0^* = 1$, $d = 3$, and $\gamma = 0.1$. The figure illustrates Kovacs-like effects with conditions $\theta(t_K^*) = \theta^{\text{st}}$ and either $a_2(t_K^*) = -0.35$ ($\circ, \square, \text{---}$) or $a_2(t_K^*) = 0.4$ ($\times, *, \text{---}$). The symbols stand for DSMC and EDMD simulation results, while the lines refer to FSA predictions.

5. Conclusions

In this work, we have looked into the dynamics of a dilute granular gas immersed in a thermal bath (at temperature T_b) made of smaller particles but with masses comparable to those of the grains. To mathematically characterize this system, we have worked under the assumptions of Boltzmann's kinetic theory, describing the system by the one-particle VDF, whose evolution is monitored by the EFPE, Equation (1), for the IHS model of hard d -spheres. The action of the bath on the dynamics of the granular gas is modeled by a nonlinear drag force and an associated stochastic force. At a given dimensionality d , the control parameters of the problem are the coefficient of normal restitution (α), the (reduced) drag coefficient at zero velocity (ζ_0^*), and the nonlinearity parameter (γ).

After a general presentation of the kinetic theory description in Section 2, we obtained the evolution equation of the reduced temperature $\theta(t^*) \equiv T(t)/T_b$ (Equation (14)), which is coupled explicitly with the excess kurtosis, a_2 , and depends on every velocity moment through the second collisional moment μ_2 (which is nonzero due to inelasticity). Therefore, the whole dynamics in the context of the EFPE is formally described by Equation (14) and the infinite hierarchy of moment

equations given by Equation (15). In order to give predictions, we proposed two approximations. The first one is MA, which consists of assuming a Maxwellian form for the one-particle VDF, whereas the second one, FSA consists of truncating the Sonine expansion of the VDF up to the first nontrivial cumulant a_2 . Their evolution equations are given by Equations (18) and (19), respectively. The predictions for the steady-state values are exposed in Figures 2 and 3, which show some small discrepancies in θ^{st} between MA and FSA as we increase the inelasticity (decreasing α). Moreover, we observed that, for fixed α and ζ_0^* , a_2^{st} gets its maximum value when the nonlinearity parameter is $\gamma = \gamma_{\text{max}}(\alpha, \zeta_0^*)$. Another interesting feature is the existence of a critical value γ_c , such that for $\gamma > \gamma_c$, the values of a_2^{st} are always positive for every value of α , while for $\gamma < \gamma_c$, we find $a_2^{\text{st}} < 0$ for inelasticities small enough. Interestingly, the value of γ_c given by Equation (25) is found to be independent of ζ_0^* . In addition, some already known limits are recovered in Section 3.2.2.

Furthermore, in order to check the predictions from MA and FSA equations, we carried out DSMC and EDMD simulations for hard spheres ($d = 3$) with fixed $\zeta_0^* = 1$ (which corresponds to comparable time scales associated with drag and collisions). First, from Figure 4a, we can conclude that, whereas MA provides good predictions of θ^{st} , except for large inelasticities and values of γ close to γ_{max} , FSA is much more accurate because it takes into account the influence of a_2^{st} . The latter approach is generally reliable for a_2^{st} , as observed in Figure 4b, although, not unexpectedly, it slightly worsens as $|a_2^{\text{st}}|$ grows. Relaxation curves starting from a Maxwellian initial state in Figure 5 show that FSA agrees very well with both DSMC and EDMD; however, MA exhibits good agreement during the first stage of the evolution but becomes less reliable as the steady state is approached.

A relevant feature of these systems, as already studied in the elastic case [21–23], is the emergence of memory effects, which are not contemplated by MA. FSA predicts the emergence of the Mpemba effect very well for both DME and IME, as can be seen in Figure 6. Analogously, Kovacs-like humps, both upward and downward, are correctly described by FSA, as observed in Figure 7, although the FSA humps are slightly less pronounced (especially the upward one) than the simulation ones. This is presumably due to the role played by a_3 and higher-order cumulants, as occurs in the elastic limit reported in Ref. [23].

To conclude, we expect that this work will motivate research about this type of system and the emergence of memory effects. For instance, one can extend the study to other collisional models (such as that of rough spheres), to nonhomogeneous states, or to a more detailed description of the memory effects observed.

Author Contributions: A.M. worked out the approximations and performed the simulations. A.S. supervised the work. Both authors participated in the analysis and discussion of the results and worked on the revision and writing of the final manuscript. All authors have read and agreed to the published version of the manuscript.

Funding: The authors acknowledge financial support from Grant No. PID2020-112936GB-I00 funded by MCIN/AEI/10.13039/501100011033, and from Grants No. IB20079 and No. GR21014 funded by Junta de Extremadura (Spain) and by ERDF “A way of making Europe.” A.M. is grateful to the Spanish Ministerio de Ciencia, Innovación y Universidades for a predoctoral fellowship FPU2018-3503.

Acknowledgments: The authors are grateful to the computing facilities of the Instituto de Computación Científica Avanzada of the University of Extremadura (ICCAEx), where the simulations were run.

Data Availability: The data presented in this study are available in the online repository <https://github.com/amegiasf/GranularNonlinearDrag>

Conflicts of Interest: The authors declare no conflict of interest.

Abbreviations

The following abbreviations are used in this manuscript:

DME	Direct Mpemba effect
DSMC	Direct simulation Monte Carlo
EDMD	Event-driven molecular dynamics
EFPE	Enskog–Fokker–Planck equation
FSA	First Sonine approximation
IHS	Inelastic hard spheres
IME	Inverse Mpemba effect
MA	Maxwellian approximation
VDF	Velocity distribution function

Appendix A. Simulation Details

Throughout the elaboration of this work, we have used two different algorithms to simulate the considered system: DSMC and EDMD methods. Whereas the former is based on statistical properties and subjected to the assumptions of the Boltzmann equation, such as *Stosszahlansatz*, the latter solves the trajectory of each particle without any extra assumption. On the other hand, the original algorithms are slightly modified for the proper collisional model and the interaction with the thermal bath, as explained below.

In general, the simulation results shown in this work are obtained from averaging over 100 samples in both simulation schemes, and steady-state results come from averaging over 50 points in the mean trajectory once stationary behavior is observed.

Appendix A.1. Direct Simulation Monte Carlo

The DSMC algorithm used in this work is based on the original works of G.A. Bird [36,37], but modified for the IHS collisional model and the implementation of the nonlinear drag. As we considered homogeneous states, only the velocities of the N granular particles, $\{\mathbf{v}_i\}_{i=1}^N$, are used to numerically solve the EFPE. Whereas initial velocities for results in Figures 4 and 5 were drawn from a Maxwellian VDF with $\theta^0 = 1$; in the case of Figures 6 and 7, velocities were initialized from a Gamma VDF (see Refs. [23,30] for additional details). After initialization, particles were updated with a fixed time step, Δt , much smaller than the mean free time. The method is properly divided into two stages: collision and free streaming [12].

In the collision stage, a number $\lfloor \frac{1}{2}N\omega_{\max}\Delta t \rfloor$ of pairs are randomly chosen with equiprobability—the ignored decimals in the rounding are saved for the next iterative step— ω_{\max} being an upper bound estimate for the one-particle collision rate. Then, given a chosen pair ij , a collision is accepted with probability $\Theta(\mathbf{v}_{ij} \cdot \hat{\sigma}_{ij})\omega_{ij}/\omega_{\max}$, where $\hat{\sigma}_{ij}$ is a random vector drawn from a uniform probability distribution in the unit d -sphere, and $\omega_{ij} = \frac{2\pi^{d/2}}{\Gamma(d/2)}g_c n\sigma^{d-1}|\mathbf{v}_{ij} \cdot \hat{\sigma}_{ij}|$. Acceptance implies that the velocities are updated according to the collisional rules in Equation (3), i.e., $\mathbf{v}_{i/j}(t) \rightarrow \mathbf{v}_{i/j}(t + \Delta t) = \mathbf{v}_{i/j} \pm \frac{1 \mp \alpha}{2}(\mathbf{v}_{ij} \cdot \hat{\sigma}_{ij})$.

In the free-streaming stage, each particle velocity is updated according to an Euler numerical algorithm of a Langevin-like equation derived from an Itô interpretation of the Fokker–Planck part of the EFPE (see Ref. [23]),

$$\mathbf{v}_i(t) \rightarrow \mathbf{v}_i(t + \Delta t) = \mathbf{v}_i(t) - [\xi(v_i(t)) - 2\xi_0\gamma] \mathbf{v}_i\Delta t + \chi(v_i(t))\sqrt{\Delta t}\mathbf{Y}_i, \quad (\text{A1})$$

where \mathbf{Y}_i is a random vector drawn from a Gaussian probability distribution with unit variance, $P(\mathbf{Y}) = (2\pi)^{-d/2}e^{-Y^2/2}$.

In the implementations of the DSMC algorithm, we used $N = 10^4$ hard spheres ($d = 3$) and a time step $\Delta t = 10^{-2}\lambda/v_b$, $\lambda = (\sqrt{2\pi}n\sigma^2)^{-1}$ being the mean free path.

Appendix A.2. Event-Driven Molecular Dynamics

EDMD methods compute the evolution of particles driven by events: particle–particle collisions, boundary effects, or other more complex interactions. Analogously to the splitting described in the DSMC algorithm, free streaming of particles occurs between two consecutive events. Here, we need to consider the influence of the stochastic and drag forces not only in the velocities but also in the positions of the N granular particles, $\{\mathbf{r}_i\}_{i=1}^N$. In order to account for this, we followed the *approximate Green Function* algorithm proposed in Ref. [46]. Whereas the velocities are updated according to Equation (A1), the positions follow

$$\mathbf{r}_i(t) \rightarrow \mathbf{r}_i(t + \Delta t) = \mathbf{r}_i(t) + \mathbf{v}_i(t)\Delta t \left[1 - \Delta t \frac{\zeta(v_i(t)) - 2\gamma\zeta_0}{2} \right] + \frac{1}{2}\chi(v_i(t))\Delta t^{3/2}\mathbf{W}_i, \quad (\text{A2})$$

where $\mathbf{W}_i = \mathbf{Y}_i + \sqrt{5/3}\mathbf{Y}'_i$, \mathbf{Y}'_i being another random vector drawn from $P(\mathbf{Y}) = (2\pi)^{-d/2}e^{-Y^2/2}$.

In the EDMD simulations, we defined a set of $N = 8 \times 10^3$ hard spheres ($d = 3$), with a reduced number density $n\sigma^3 = 10^{-3}$, implying a box length $L/\sigma = 2 \times 10^2$, and used a time step $\Delta t \approx 10^{-3}\lambda/v_b$. Periodic boundary conditions were imposed, and no inhomogeneities were observed.

References

1. Tatsumi, S.; Murayama, Y.; Hayakawa, H.; Sano, M. Experimental study on the kinetics of granular gases under microgravity. *J. Fluid Mech.* **2009**, *641*, 521–539. <https://doi.org/10.1017/S002211200999231X>.
2. Yu, P.; Schröter, M.; Sperl, M. Velocity Distribution of a Homogeneously Cooling Granular Gas. *Phys. Rev. Lett.* **2020**, *124*, 208007. <https://doi.org/10.1103/PhysRevLett.124.208007>.
3. Pouliquen, O.; Nicolas, M.; Weidman, P.D. Crystallization of non-Brownian Spheres under Horizontal Shaking. *Phys. Rev. Lett.* **1997**, *79*, 3640–3643. <https://doi.org/10.1103/PhysRevLett.79.3640>.
4. Tennakoon, S.G.K.; Behringer, R.P. Vertical and Horizontal Vibration of Granular Materials: Coulomb Friction and a Novel Switching State. *Phys. Rev. Lett.* **1998**, *81*, 794–797. <https://doi.org/10.1103/PhysRevLett.81.794>.
5. Metcalfe, G.; Tennakoon, S.G.K.; Kondic, L.; Schaeffer, D.G.; Behringer, R.P. Granular friction, Coulomb failure, and the fluid-solid transition for horizontally shaken granular materials. *Phys. Rev. E* **2002**, *65*, 031302. <https://doi.org/10.1103/PhysRevE.65.031302>.
6. Huan, C.; Yang, X.; Candela, D.; Mair, R.W.; Walsworth, R.L. NMR experiments on a three-dimensional vibrofluidized granular medium. *Phys. Rev. E* **2004**, *69*, 041302. <https://doi.org/10.1103/PhysRevE.69.041302>.
7. Schröter, M.; Goldman, D.I.; Swinney, H.L. Stationary state volume fluctuations in a granular medium. *Phys. Rev. E* **2005**, *71*, 030301. <https://doi.org/10.1103/PhysRevE.71.030301>.
8. Abate, A.R.; Durian, D.J. Approach to jamming in an air-fluidized granular bed. *Phys. Rev. E* **2006**, *74*, 031308. <https://doi.org/10.1103/PhysRevE.74.031308>.
9. Eshuis, P.; van der Meer, D.; Alam, M.; van Gerner, H.J.; van der Weele, K.; Lohse, D. Onset of Convection in Strongly Shaken Granular Matter. *Phys. Rev. Lett.* **2010**, *104*, 038001. <https://doi.org/10.1103/PhysRevLett.104.038001>.
10. Michael, B.; Simon, M.; Gustavo, C.; Eric, F. Wave spectroscopy in a driven granular material. *Proc. R. Soc. A* **2022**, *476*, 20220014. <https://doi.org/10.1098/rspa.2022.0014>.
11. van Noije, T.P.C.; Ernst, M.H. Velocity distributions in homogeneous granular fluids: The free and the heated case. *Granul. Matter* **1998**, *1*, 57–64. <https://doi.org/10.1007/s100350050009>.
12. Montanero, J.M.; Santos, A. Computer simulation of uniformly heated granular fluids. *Granul. Matter* **2000**, *2*, 53–64. <https://doi.org/10.1007/s100350050035>.
13. Garzó, V.; Chamorro, M.G.; Vega Reyes, F. Transport properties for driven granular fluids in situations close to homogeneous steady states. *Phys. Rev. E* **2013**, *87*, 032201. <https://doi.org/10.1103/PhysRevE.87.032201>. Erratum in *Phys. Rev. E* **2013**, *87*, 059906. <https://doi.org/10.1103/PhysRevE.87.059906>.
14. Vega Reyes, F.; Santos, A. Steady state in a gas of inelastic rough spheres heated by a uniform stochastic force. *Phys. Fluids* **2015**, *27*, 113301. <https://doi.org/10.1063/1.4934727>.

15. Brey, J.J.; Buzón, V.; Maynar, P.; García de Soria, M.I. Hydrodynamics for a model of a confined quasi-two-dimensional granular gas. *Phys. Rev. E* **2015**, *91*, 052201. <https://doi.org/10.1103/PhysRevE.91.052201>.
16. Garzó, V.; Brito, R.; Soto, R. Enskog kinetic theory for a model of a confined quasi-two-dimensional granular fluid. *Phys. Rev. E* **2018**, *98*, 052904. <https://doi.org/10.1103/PhysRevE.98.052904>.
17. Santos, A.; Montanero, J.M. The second and third Sonine coefficients of a freely cooling granular gas revisited. *Granul. Matter* **2009**, *11*, 157–168. <https://doi.org/10.1007/s10035-009-0132-8>.
18. Garzó, V. *Granular Gaseous Flows. A Kinetic Theory Approach to Granular Gaseous Flows*; Springer Nature: Cham, Switzerland, 2019.
19. Megías, A.; Santos, A. Driven and undriven states of multicomponent granular gases of inelastic and rough hard disks or spheres. *Granul. Matter* **2019**, *21*, 49. <https://doi.org/10.1007/s10035-019-0901-y>.
20. Gómez González, R.; Garzó, V. Kinetic theory of granular particles immersed in a molecular gas. *J. Fluid Mech.* **2022**, *943*, A9. <https://doi.org/10.1017/jfm.2022.410>.
21. Santos, A.; Prados, A. Mpemba effect in molecular gases under nonlinear drag. *Phys. Fluids* **2020**, *32*, 072010. <https://doi.org/10.1063/5.0016243>.
22. Patrón, A.; Sánchez-Rey, B.; Prados, A. Strong nonexponential relaxation and memory effects in a fluid with nonlinear drag. *Phys. Rev. E* **2021**, *104*, 064127. <https://doi.org/10.1103/PhysRevE.104.064127>.
23. Megías, A.; Santos, A.; Prados, A. Thermal versus entropic Mpemba effect in molecular gases with nonlinear drag. *Phys. Rev. E* **2022**, *105*, 054140. <https://doi.org/10.1103/PhysRevE.105.054140>.
24. Ferrari, L. Particles dispersed in a dilute gas: Limits of validity of the Langevin equation. *Chem. Phys.* **2007**, *336*, 27–35. <https://doi.org/10.1016/j.chemphys.2007.05.001>.
25. Ferrari, L. Particles dispersed in a dilute gas. II. From the Langevin equation to a more general kinetic approach. *Chem. Phys.* **2014**, *428*, 144–155. <https://doi.org/10.1016/j.chemphys.2013.10.024>.
26. Hohmann, M.; Kindermann, F.; Lausch, T.; Mayer, D.; Schmidt, F.; Lutz, E.; Widera, A. Individual Tracer Atoms in an Ultracold Dilute Gas. *Phys. Rev. Lett.* **2017**, *118*, 263401. <https://doi.org/10.1103/PhysRevLett.118.263401>.
27. Brilliantov, N.; Pöschel, T. Deviation from Maxwell distribution in granular gases with constant restitution coefficient. *Phys. Rev. E* **2000**, *61*, 2809–2812. <https://doi.org/10.1103/PhysRevE.61.2809>.
28. Brilliantov, N.V.; Pöschel, T. *Kinetic Theory of Granular Gases*; Oxford University Press: Oxford, UK, 2004.
29. Vega Reyes, F.; Santos, A.; Kremer, G.M. Role of roughness on the hydrodynamic homogeneous base state of inelastic spheres. *Phys. Rev. E* **2014**, *89*, 020202(R). <https://doi.org/10.1103/PhysRevE.89.020202>.
30. Megías, A.; Santos, A. Kullback–Leibler divergence of a freely cooling granular gas. *Entropy* **2020**, *22*, 1308. <https://doi.org/10.3390/e22111308>.
31. Chamorro, M.G.; Vega Reyes, F.; Garzó, V. Homogeneous states in granular fluids driven by thermostats. *AIP Conf. Proc.* **2012**, *1501*, 1024–1030. <https://doi.org/10.1063/1.4769654>.
32. Chamorro, M.G.; Vega Reyes, F.; Garzó, V. Homogeneous steady states in a granular fluid driven by a stochastic bath with friction. *J. Stat. Mech.* **2013**, P07013. <https://doi.org/10.1088/1742-5468/2013/07/P07013>.
33. Goldshtein, A.; Shapiro, M. Mechanics of collisional motion of granular materials. Part 1. General hydrodynamic equations. *J. Fluid Mech.* **1995**, *282*, 75–114. <https://doi.org/10.1017/S0022112095000048>.
34. Brilliantov, N.; Pöschel, T. Breakdown of the Sonine expansion for the velocity distribution of granular gases. *Europhys. Lett.* **2006**, *74*, 424–430. <https://doi.org/10.1209/epl/i2005-10555-6>. Erratum in *Europhys. Lett.* **2006**, *75*, 188. <https://doi.org/10.1209/epl/i2006-10099-3>.
35. Metropolis, N.; Rosenbluth, A.W.; Rosenbluth, M.N.; Teller, A.H.; Teller, E. Equation of State Calculations by Fast Computing Machines. *J. Chem. Phys.* **1953**, *21*, 1087–1092. <https://doi.org/10.1063/1.1699114>.
36. Bird, G.A. *Molecular Gas Dynamics and the Direct Simulation of Gas Flows*; Clarendon: Oxford, UK, 1994.
37. Bird, G.A. *The DSMC Method*; CreateSpace Independent Publishing Platform: Scotts Valley, CA, USA, 2013.
38. Mpemba, E.B.; Osborne, D.G. Cool? *Phys. Educ.* **1969**, *4*, 172–175. <https://doi.org/10.1088/0031-9120/4/3/312>.
39. Burrige, H.C.; Linden, P.F. Questioning the Mpemba effect: Hot water does not cool more quickly than cold. *Sci. Rep.* **2016**, *6*, 37665. <https://doi.org/10.1038/srep37665>.
40. Lu, Z.; Raz, O. Nonequilibrium thermodynamics of the Markovian Mpemba effect and its inverse. *Proc. Natl. Acad. Sci. USA* **2017**, *114*, 5083–5088. <https://doi.org/10.1073/pnas.1701264114>.

41. Lasanta, A.; Vega Reyes, F.; Prados, A.; Santos, A. When the Hotter Cools More Quickly: Mpemba Effect in Granular Fluids. *Phys. Rev. Lett.* **2017**, *119*, 148001. <https://doi.org/10.1103/PhysRevE.99.060901>.
42. Bechhoefer, J.; Kumar, A.; Chérite, R. A fresh understanding of the Mpemba effect. *Nat. Rev. Phys.* **2021**, *3*, 534–535. <https://doi.org/10.1038/s42254-021-00349-8>.
43. Gómez González, R.; Khalil, N.; Garzó, V. Mpemba-like effect in driven binary mixtures. *Phys. Fluids* **2021**, *33*, 053301. <https://doi.org/10.1063/5.0050530>.
44. Kovacs, A.J. Transition vitreuse dans les polymères amorphes. Etude phénoménologique. *Fortschr. Hochpolym.-Forsch.* **1963**, *3*, 394–507. <https://doi.org/10.1007/BFb0050366>.
45. Kovacs, A.J.; Aklonis, J.J.; Hutchinson, J.M.; Ramos, A.R. Isobaric volume and enthalpy recovery of glasses. II. A transparent multiparameter theory. *J. Polym. Sci. Polym. Phys. Ed.* **1979**, *17*, 1097–1162. <https://doi.org/10.1002/pol.1979.180170701>.
46. Scala, A. Event-driven Langevin simulations of hard spheres. *Phys. Rev. E* **2012**, *86*, 026709. <https://doi.org/10.1103/PhysRevE.86.026709>.

**GRANULAR GASES OF INELASTIC AND
ROUGH PARTICLES**

Homogeneous states in the IRHS model

8

8.1 Summary

In this chapter, the homogeneous states of a freely evolving dilute and monodisperse granular gas made of inelastic and rough **HD** ($d_t = 2$, $d_r = 1$) or **HS** ($d_t = 3$, $d_r = 3$) are studied. The granular particles are characterized by a common diameter (σ), mass (m), reduced moment of inertia (κ), their binary collisions being described by the **IRHS** model. That is, the inelasticity of the system is parameterized by a coefficient of normal restitution, α , and the effect of the surface roughness in a binary collision is accounted for by a coefficient of tangential restitution, β , both considered to be constant. The evolution of the granular gas one-body **VDF** is characterized by its associated **BE**, written in Eq. (2.82).

It is widely known that the **HCS** solution is not strictly compatible with the Maxwellian **VDF** (see Subsection 2.5.2). Then, the main aim of this chapter is to characterize the non-Gaussianities of the **HCS VDF** by means of its first nontrivial cumulants from a **SA**, and the **HVT** of some marginal **VDF** at the **HCS**, which are studied from an asymptotic analysis of the **BE**. This study is performed in a common framework for **HD** and **HS** systems in terms of the translational and rotational degrees of freedom, d_t and d_r , respectively.

To address this problem, first the homogeneous states are formally introduced and described in the context of the homogeneous **BE** for the **IRHS** model, in Article 5 (Section 8.2). Moreover, we assume, from isotropy arguments, that the instantaneous and **HCS VDF** can be written in terms of a Sonine expansion [see Eqs. (2.107)], and the associated infinite hierarchy of moment equations is derived. In order to obtain explicit results, we introduce certain approximations. First, from a **MA**, we obtain a closed evolution equation for the rotational-to-translational temperature ratio, θ , as well as an approach to its **HCS** values. Afterwards, we construct a **SA** based on the truncation of the full

Sonine expansion up to the first nontrivial cumulants of the **VDF**, that is, those Sonine coefficients $a_{pq}^{(r)}$ such that $p + q + 2r \geq 3$ are neglected. In other words, the nonneglected cumulants are $a_{20} \equiv a_{20}^{(0)}$, $a_{02} \equiv a_{02}^{(0)}$, $a_{11} \equiv a_{11}^{(0)}$, and $a_{00}^{(1)}$, the latter being meaningless in the **HD** case. This **SA** allows us to get a closed set of differential equations for the time-dependent quantities $\{\theta, a_{20}, a_{02}, a_{11}\}$ for the **HD** case and $\{\theta, a_{20}, a_{02}, a_{11}, a_{00}^{(1)}\}$ for the **HS** case, from a proper linearization of the relevant collisional moments with respect to the considered cumulants [see Table I of Article 5 (Section 8.2)]. Therefore, from the steady solutions of the latter differential equations, we obtain the **HCS** values of the involved quantities¹, recovering the already known **HS** results of Ref. [VSK14b]. Even more, the choice of the proper linearized scheme is complemented by a linear stability analysis under homogeneous perturbations of the transient equations, which appears in Appendix A of Article 5 (Section 8.2).

To complete the theoretical description of the **HCS**, we compute the **HVT** for the translational, $\phi_{\mathbf{c}}^{\text{H}}(\mathbf{c})$, rotational, $\phi_{\mathbf{w}}^{\text{H}}(\mathbf{w})$, and the joint marginal **VDF** $\phi_{c^2w^2}^{\text{H}}(c^2w^2)$ [see their definitions in Eq. (2.102) and Eq. (5.1) of Article 5 (Section 8.2)]. The translational marginal **VDF** admits the same exponential form for the **HVT** that the smooth result, $\phi_{\mathbf{c}}^{\text{H}} \sim e^{-\gamma_c c}$, with $\gamma_c \rightarrow \gamma_c^{\text{IRHS}} = d_t \pi^{\frac{d_t-1}{2}} / \mu_{20}^{\text{H}} \Gamma\left(\frac{d_t+1}{2}\right)$, where the expressions of γ_c^{IRHS} [see Eq. (2.81)] and γ_c^{IRHS} are formally the same, except for the generalization $\mu_2^{\text{H}} \rightarrow \mu_{20}^{\text{H}}$. Moreover, the rotational marginal **VDF** adopts an algebraic or scale-free form, $\phi_{\mathbf{w}}^{\text{H}} \sim w^{-\gamma_w}$, implying the divergence of the Sonine coefficients a_{0q}^{H} if $2q \geq \gamma_w - 1$. Finally, we obtain for the **HVT** of the marginal **VDF** of the variable c^2w^2 an algebraic form as well, $\phi_{c^2w^2}^{\text{H}} \sim (c^2w^2)^{-\gamma_{cw}}$. The latter result determines the divergence of the cumulants of the form a_{jj}^{H} if $j \geq \gamma_{cw} - 1$.

Furthermore, we compare the theoretical predictions with **DSMC** and **EDMD** simulation results, coming from custom-built computer programs [Meg23] that mimic homogeneous systems of uniform **HD** ($\kappa = 1/2$) for a wide variety of values of the coefficients of restitution. We obtain the **HCS** results for the rotational-to-translational temperature ratio and the cumulants of the **SA**, i.e., θ^{H} , a_{20}^{H} , a_{02}^{H} and a_{11}^{H} with good agreement, in general. Moreover, the **HVT** are compared with the theoretical predictions, obtaining good accordance between the numerical histograms and the scaling theoretical forms. In fact, there is a good quantitative agreement of the simulation outcomes with the theoretical predicted equation for γ_w , but a more qualitative matching in the case of γ_c and γ_{cw} [see Fig. 9 of Article 5 (Section 8.2)].

¹To localize the regions of the parameter space where the **SA** is expected to work worse, we derive, in the Supplemental Material, a **KLD**-like functional from an approximation similar to the toy model derived in Chapter 6.

8.2 Article 5

Title: Translational and rotational non-Gaussianities in homogeneous freely evolving granular gases

Authors: Alberto Megías¹ and Andrés Santos^{1,2}

Affiliations:

¹ Departamento de Física, Universidad de Extremadura, E-06006 Badajoz, Spain

² Instituto de Computación Científica Avanzada (ICCAEx), Universidad de Extremadura, E-06006 Badajoz, Spain

Journal: Physical Review E

Volume: 108

Pages: 014902

Year: 2023

DOI: [10.1103/PhysRevE.108.014902](https://doi.org/10.1103/PhysRevE.108.014902)



Copy of the preprint of the work: “Alberto Megías, and Andrés Santos. ‘Translational and rotational non-Gaussianities in homogeneous freely evolving granular gases’, *Physical Review E* **108**, 014902 (2023) <https://doi.org/10.1103/PhysRevE.108.014902>.”

Translational and rotational non-Gaussianities in homogeneous freely evolving granular gases

Alberto Megías*

Departamento de Física, Universidad de Extremadura, E-06006 Badajoz, Spain

Andrés Santos†

Departamento de Física, Universidad de Extremadura, E-06006 Badajoz, Spain and

Instituto de Computación Científica Avanzada (ICCAEx),

Universidad de Extremadura, E-06006 Badajoz, Spain

(Dated: July 25, 2023)

The importance of roughness in the modeling of granular gases has been increasingly considered in recent years. In this paper, a freely evolving homogeneous granular gas of inelastic and rough hard disks or spheres is studied under the assumptions of the Boltzmann kinetic equation. The homogeneous cooling state is studied from a theoretical point of view using a Sonine approximation, in contrast to a previous Maxwellian approach. A general theoretical description is done in terms of d_t translational and d_r rotational degrees of freedom, which accounts for the cases of spheres ($d_t = d_r = 3$) and disks ($d_t = 2, d_r = 1$) within a unified framework. The non-Gaussianities of the velocity distribution function of this state are determined by means of the first nontrivial cumulants and by the derivation of non-Maxwellian high-velocity tails. The results are validated by computer simulations using direct simulation Monte Carlo and event-driven molecular dynamics algorithms.

I. INTRODUCTION

Granular systems are themselves worth studying from mechanical, physical, and mathematical points of view. They are very commonly observed in nature, where different geometries can take place. Grains, from a dynamical point of view, move in a three-dimensional space, but constraints make two-dimensional problems become real and of special interest [1–10].

We will focus on the description of granular systems at low-density fluidized states, where the assumptions underlying the Boltzmann equation apply [11–28]. The simplest collisional model for interactions in granular gaseous flows is the inelastic hard-sphere model, where the granular gas is assumed to be composed by inelastic and smooth identical hard disks, spheres, or hyperspheres in d_t translational space dimensions [28–32]. However, this description might be limiting and can be improved by considering rotational degrees of freedom, which may play an important role in the dynamics of granular gases by means of surface roughness. Here, we will use the simplest collisional model that implements roughening, the inelastic and rough hard-sphere model. In the latter model, the inelasticity is parameterized by a constant coefficient of normal restitution, α (in common with the inelastic hard-sphere model), and roughness is introduced by means of a coefficient of tangential restitution, β . Although, in general, the effective coefficient of tangential restitution depends on the impact angle because of friction [33, 34], here we adopt the simplest model with constant β , as frequently done in the literature [12, 28, 32, 35–44].

Whereas in the inelastic hard-sphere model, the d_t -dimensional description of an inelastic gas of smooth and spinless hard (hyper)spheres is straightforward, in the case of rough spheres, where angular velocities come into play, rotational degrees of freedom, d_r , need to be introduced. A description in terms of d_t and d_r becomes highly dependent on the geometry and constraints of the system as antecedently reported [43–46]. As in Ref. [45], we will derive the general description to be valid just for the two relevant cases of hard disks and hard spheres. For hard disks, angular velocities are constrained to the direction orthogonal to the plane of motion, so $d_t = 2$ and $d_r = 1$. For hard spheres, on the other hand, angular and translational velocities are vectors of a Euclidean three-dimensional vector space, i.e., $d_t = d_r = 3$.

It is widely known and studied that the homogeneous Boltzmann equation—for both smooth and rough models—admits a scaling solution, in which the system cools down continuously and the whole evolution is driven by the granular temperature. This state is known as the *homogeneous cooling state* (HCS), and has been of interest for the granular gas community in the last three decades [28, 32, 39, 42, 43, 47–56]. It is worth mentioning that, very recently, the HCS has been experimentally observed in microgravity experiments by Yu *et al.* [57]. In that paper, both Haff’s cooling law and the exponential high-velocity tail of the velocity distribution function (VDF) as predicted by kinetic theory together with the inelastic hard-sphere model are confirmed. In Ref. [57], while the results were compared with the constant and velocity-dependent models for the coefficient of normal restitution, it was concluded that the latter model had a negligible influence on the results, supporting the approximation of constant coefficients of restitution. In fact, the system in Ref. [57] is compatible with a constant $\alpha = 0.66$, highlighting that the latter approximation is

* albertom@unex.es

† andres@unex.es

not subjected only to quasielastic systems. Moreover, the authors proposed a possible influence of surface roughness in the collisional rules due to an overestimate of the relaxation time from the inelastic hard-sphere model as compared with the experimental outcomes. Thus, they claimed that the rotational degrees of freedom could be an answer to these deviations.

Theoretically, some of the early attempts to study the Gaussian deviations of the HCS VDF of a granular gas of rough particles were done in Refs. [12, 35] using a Sonine expansion, that is, an isotropic expansion around a two-temperature—translational and rotational—Maxwellian VDF. However, although velocity correlations were not originally assumed for hard spheres, they were proved to be present [36]. More recently, the first nontrivial velocity cumulants were studied for freely evolving hard spheres [39]. Throughout the present paper, we will expose the results of those cumulants in a common frame for both disks and spheres from the collisional-moment point of view, and we will analyze results for hard disks.

In the case of freely cooling inelastic granular gases, deviations of the HCS VDF from a Maxwellian derived from the inelastic hard-sphere model are not only accounted for by the first nontrivial cumulants, but also an exponential high-velocity tail for this distribution was predicted by kinetic theory and computer simulations [48, 49, 51, 58, 59] and satisfactorily observed experimentally not only for freely evolving granular gases [57] as commented above, but also for uniformly heated systems [60]. Results in Ref. [39] put into manifest a highly populated tail for the marginal VDF of angular velocities in the inelastic and rough hard-sphere model, accompanied by high values of the fourth angular velocity cumulant for some values of the pair (α, β) . However, this marginal distribution was interpreted as being consistent with an exponential form [39], similarly to what occurs in the inelastic hard-sphere model with the total (translational) VDF [48, 49, 58]. In this paper, we study the high-velocity tail for the marginal VDF of the translational and angular velocities, and for their product as well, where theory indicates algebraic tails for the two latter marginal distributions.

The study of the non-Gaussianities of the HCS VDF is also motivated by recent research in nonhomogeneous states [45, 46, 61] from Chapman–Enskog expansions around the HCS solution. Linear stability analyses of the homogeneous state hydrodynamics show that the Maxwellian approximation of the first-order VDF might not work for the hard-disk case [46], and for some very small region of the parameter space for hard spheres, yielding a wrong prediction of a completely unstable region in the parameter space. Therefore, it was conjectured that non-Gaussianities might be crucial in the cited region of parameters, this effect being more important for disks than for spheres [46]. This hypothesis was supported by high values of the first relevant cumulants in hard-sphere systems [39] and by results from the smooth case, where the homogeneous VDF is generally more dis-

parate from a Maxwellian for disks than for spheres [62].

The present paper is structured as follows. In Sec. II, the inelastic and rough hard-sphere model and the binary collisional rules are introduced. Afterwards, the framework of the homogeneous Boltzmann equation is described in Sec. III and the hierarchy of evolution equations, the Sonine expansion of the VDF, and the definitions of cumulants are formally presented. Section IV is devoted to the Sonine approximation, where the infinite expansion is truncated beyond the first few nontrivial coefficients, the associated collisional moments are explicitly written for hard disks, and the HCS cumulants are obtained. Next, we study the forms of the marginal VDF from the Maxwellian and Sonine approximations, as well as their high-velocity tails in Sec. V in the context of the Boltzmann equation. In Sec. VI, we compare the theoretical predictions with direct simulation Monte Carlo (DSMC) and event-driven molecular dynamics (EDMD) computer simulations outcomes. Finally, concluding remarks and main results are summarized in Sec. VII.

II. INELASTIC AND ROUGH HARD PARTICLES

A. System

Let us consider a monodisperse dilute granular gas of hard disks or spheres, which are assumed to be inelastic and rough, their dynamics being described by their translational and angular velocities, \mathbf{v} and $\boldsymbol{\omega}$, respectively. Whereas for spheres ($d_t = d_r = 3$), both \mathbf{v} and $\boldsymbol{\omega}$ are vectors in an Euclidean three-dimensional space, this is not the case for disks ($d_t = 2, d_r = 1$), where $\boldsymbol{\omega}$ is a one-dimensional vector orthogonal to the two-dimensional vector space spanned by \mathbf{v} . In general, however, all vector relations will be written in a three-dimensional Euclidean embedding space.

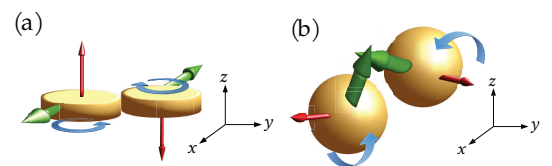


FIG. 1. Illustration of a binary collision of (a) two hard disks and (b) two hard spheres. The (green) thick arrows represent the translational velocity vectors, while the (red) thin arrows depict the angular velocities complemented by the sense of rotation portrayed by the curved (blue) arrows. Notice that in (a) the translational velocities lie on the plane xy , while the angular velocities are constrained to the z direction.

The gas is considered to be formed by a fixed large number of identical hard d_t spheres with mass m , diameter σ , reduced moment of inertia $\kappa = 4I/m\sigma^2$ (I being the moment of inertia), and whose inelasticity and

roughness are characterized by a coefficient of normal restitution, α , and a coefficient of tangential restitution, β , respectively, both assumed to be constant, and defined by

$$(\hat{\boldsymbol{\sigma}} \cdot \mathbf{g}'_{12}) = -\alpha(\hat{\boldsymbol{\sigma}} \cdot \mathbf{g}_{12}), \quad (\hat{\boldsymbol{\sigma}} \times \mathbf{g}'_{12}) = -\beta(\hat{\boldsymbol{\sigma}} \times \mathbf{g}_{12}), \quad (2.1)$$

where $\hat{\boldsymbol{\sigma}}$ is the intercenter unit vector at contact, $\mathbf{g}_{12} = \mathbf{v}_{12} - \frac{\kappa}{2} \hat{\boldsymbol{\sigma}} \times (\boldsymbol{\omega}_1 + \boldsymbol{\omega}_2)$ is the relative velocity of the contact points of particles 1 and 2 (with $\mathbf{v}_{12} = \mathbf{v}_1 - \mathbf{v}_2$), and primed quantities refer to postcollisional values. Note that, while α is nonnegative, β can be either positive or negative. A negative value means that the postcollisional tangential component of the relative velocity maintains the same sign as the precollisional one, implying that the effect of surface friction is not dramatic. On the other hand, if the particles are sufficiently rough, the sign of the tangential component is inverted upon collision. Figure 1 presents a sketch illustrating a collision between (a) two hard disks and (b) two hard spheres.

B. Direct collisional rules

The direct binary collisional rules are obtained from the assumption of conservation of linear and angular momenta at the point of contact in each collision. They can be expressed by [28, 32, 39, 42–46, 63]

$$\mathbf{c}'_{1,2} := \mathcal{B}_{12,\hat{\boldsymbol{\sigma}}} \mathbf{c}_{1,2} = \mathbf{c}_{1,2} \mp \boldsymbol{\Delta}_{12}, \quad (2.2a)$$

$$\mathbf{w}'_{1,2} := \mathcal{B}_{12,\hat{\boldsymbol{\sigma}}} \mathbf{w}_{1,2} = \mathbf{w}_{1,2} - \frac{1}{\sqrt{\kappa\theta}} \hat{\boldsymbol{\sigma}} \times \boldsymbol{\Delta}_{12}, \quad (2.2b)$$

where $\mathcal{B}_{12,\hat{\boldsymbol{\sigma}}}$ is the postcollisional operator acting on a dynamic quantity and giving the result after a collision, θ and $\boldsymbol{\Delta}_{12}$ are defined below, and $\{\mathbf{c}, \mathbf{w}\}$ are the velocities reduced by their thermal value, that is,

$$\mathbf{c} = \frac{\mathbf{v}}{v_{\text{th}}(t)}, \quad \mathbf{w} = \frac{\boldsymbol{\omega}}{\omega_{\text{th}}(t)}. \quad (2.3)$$

Here, $v_{\text{th}}(t) = \sqrt{2T_t(t)/m}$, $\omega_{\text{th}}(t) = \sqrt{2T_r(t)/I}$ are the thermal translational and angular velocities, T_t and T_r being the translational and rotational granular temperatures, respectively, which are defined by [28, 32, 39, 42–46, 63]

$$\frac{d_t}{2} T_t(t) = \frac{m}{2} \langle v^2 \rangle, \quad \frac{d_r}{2} T_r(t) = \frac{I}{2} \langle \omega^2 \rangle, \quad (2.4)$$

where $\langle \dots \rangle = n^{-1} \int d\mathbf{v} \int d\boldsymbol{\omega} (\dots) f(\mathbf{v}, \boldsymbol{\omega}; t)$ represents a one-body average value with respect to the VDF $f(\mathbf{v}, \boldsymbol{\omega}; t)$ normalized as

$$n = \int d\mathbf{v} \int d\boldsymbol{\omega} f(\mathbf{v}, \boldsymbol{\omega}; t), \quad (2.5)$$

n being the particle number density. In Eq. (2.2b), $\theta \equiv T_r/T_t$ is the rotational-to-translational granular temperature ratio. Moreover, the mean granular temperature is

$$T(t) = \frac{d_t T_t(t) + d_r T_r(t)}{d_t + d_r}. \quad (2.6)$$

Finally, the quantity

$$\boldsymbol{\Delta}_{12} = \bar{\alpha}(\mathbf{c}_{12} \cdot \hat{\boldsymbol{\sigma}}) \hat{\boldsymbol{\sigma}} + \bar{\beta} \left[\mathbf{c}_{12} - (\mathbf{c}_{12} \cdot \hat{\boldsymbol{\sigma}}) \hat{\boldsymbol{\sigma}} - 2\sqrt{\frac{\theta}{\kappa}} \hat{\boldsymbol{\sigma}} \times \mathbf{W}_{12} \right] \quad (2.7)$$

is the reduced impulse. In Eq. (2.7), $\mathbf{W}_{12} \equiv \frac{1}{2}(\mathbf{w}_1 + \mathbf{w}_2)$ and

$$\bar{\alpha} = \frac{1 + \alpha}{2}, \quad \bar{\beta} = \frac{\kappa}{1 + \kappa} \frac{1 + \beta}{2} \quad (2.8)$$

are effective coefficients of restitution.

Notice that the sets of vectors $\{\mathbf{c}, \mathbf{w}\}$ and $\{\mathbf{v}, \boldsymbol{\omega}\}$ span the same vector spaces, respectively. Therefore, the use of reduced quantities will be algebraically equivalent to the original velocity description.

C. Inverse collisional rules

The inverse collisional rules relating precollisional velocities $\{\mathbf{c}'_1, \mathbf{w}'_1, \mathbf{c}'_2, \mathbf{w}'_2\}$ to postcollisional velocities $\{\mathbf{c}_1, \mathbf{w}_1, \mathbf{c}_2, \mathbf{w}_2\}$ are [28, 32, 39, 42–46, 63]

$$\mathbf{c}'_{1,2} := \mathcal{B}_{12,\hat{\boldsymbol{\sigma}}}^{-1} \mathbf{c}_{1,2} = \mathbf{c}_{1,2} \mp \boldsymbol{\Delta}_{12}^-, \quad (2.9a)$$

$$\mathbf{w}'_{1,2} := \mathcal{B}_{12,\hat{\boldsymbol{\sigma}}}^{-1} \mathbf{w}_{1,2} = \mathbf{w}_{1,2} - \frac{1}{\sqrt{\kappa\theta}} \hat{\boldsymbol{\sigma}} \times \boldsymbol{\Delta}_{12}^-, \quad (2.9b)$$

with

$$\boldsymbol{\Delta}_{12}^- = \bar{\alpha} \left(\frac{1}{\alpha} - \frac{1}{\beta} \right) (\mathbf{c}_{12} \cdot \hat{\boldsymbol{\sigma}}) \hat{\boldsymbol{\sigma}} + \frac{\boldsymbol{\Delta}_{12}}{\beta}. \quad (2.10)$$

From now on, throughout this paper, we will adopt the notation $\boldsymbol{\Gamma} = \{\mathbf{v}, \boldsymbol{\omega}\}$ and $\tilde{\boldsymbol{\Gamma}} = \{\mathbf{c}, \mathbf{w}\}$.

III. BOLTZMANN EQUATION

A. Basics

We will carry out a description of the system under the assumption of molecular chaos or *Stosszahlansatz* [64], basing the analytical treatment on the homogeneous Boltzmann equation. As said before, we will generally derive the results keeping a dependence on the number of degrees of freedom, d_t and d_r . The homogeneous Boltzmann equation reads

$$\frac{\partial f(\boldsymbol{\Gamma}; t)}{\partial t} = \sigma^{d_t-1} \mathcal{I}_{\boldsymbol{\Gamma}}[f, f], \quad (3.1)$$

where

$$\mathcal{I}_{\boldsymbol{\Gamma}_1}[f, f] = \int d\boldsymbol{\Gamma}_2 \int_+ d\hat{\boldsymbol{\sigma}} (\mathbf{v}_{12} \cdot \hat{\boldsymbol{\sigma}}) \left(\frac{f'_1 f'_2}{\alpha J} - f_1 f_2 \right) \quad (3.2)$$

is the collision operator. Here, $f_{1,2} \equiv f(\boldsymbol{\Gamma}_{1,2})$, $f'_{1,2} \equiv f(\boldsymbol{\Gamma}'_{1,2})$, the subscript $+$ designates the constraint $\mathbf{v}_{12} \cdot$

$\hat{\sigma} > 0$, and J is the Jacobian due to the collisional change of velocities [43], i.e.,

$$J = \left| \frac{\partial(\mathbf{v}'_1, \mathbf{v}'_2, \boldsymbol{\omega}'_1, \boldsymbol{\omega}'_2)}{\partial(\mathbf{v}_1, \mathbf{v}_2, \boldsymbol{\omega}_1, \boldsymbol{\omega}_2)} \right| = \left| \frac{\partial(\mathbf{v}_1, \mathbf{v}_2, \boldsymbol{\omega}_1, \boldsymbol{\omega}_2)}{\partial(\mathbf{v}'_1, \mathbf{v}'_2, \boldsymbol{\omega}'_1, \boldsymbol{\omega}'_2)} \right| = \alpha |\beta|^{2d_r/d_t}. \quad (3.3)$$

Since the temporal change of the VDF is subjected only to collisions, it is convenient to change from laboratory time, t , to *collisional* time, s , as given by

$$s(t) = \frac{1}{2} \int_0^t dt' \nu(t'), \quad (3.4)$$

where $\nu(t)$ is the (nominal) collision frequency, defined by

$$\nu(t) = Kn\sigma^{d_t-1}v_{\text{th}}(t), \quad K \equiv \frac{\sqrt{2}\pi^{\frac{d_t-1}{2}}}{\Gamma\left(\frac{d_t}{2}\right)}. \quad (3.5)$$

This variable $s(t)$ quantifies the accumulated average number of collisions per particle up to time t . Furthermore, the treatment based on the reduced velocities, $\tilde{\Gamma}$, allows us to define the reduced one-body VDF:

$$\phi(\tilde{\Gamma}; s) = n^{-1}v_{\text{th}}^{d_t}(t)\omega_{\text{th}}^{d_r}(t)f(\tilde{\Gamma}; t). \quad (3.6)$$

The homogeneous Boltzmann equation for the reduced VDF then reads

$$\frac{K}{2}\partial_s\phi + \frac{\mu_{20}^{(0)}}{d_t}\frac{\partial}{\partial\mathbf{c}}\cdot(\mathbf{c}\phi) + \frac{\mu_{02}^{(0)}}{d_r}\frac{\partial}{\partial\mathbf{w}}\cdot(\mathbf{w}\phi) = \mathcal{I}_{\tilde{\Gamma}}[\phi, \phi], \quad (3.7)$$

where

$$\begin{aligned} \mu_{pq}^{(r)} &= - \int d\tilde{\Gamma} c^p w^q (\mathbf{c} \cdot \mathbf{w})^r \mathcal{I}_{\tilde{\Gamma}}[\phi, \phi] \\ &= - \frac{1}{2} \int d\tilde{\Gamma}_1 \int d\tilde{\Gamma}_2 \int_+ d\hat{\sigma} (\mathbf{c}_{12} \cdot \hat{\sigma}) \phi(\tilde{\Gamma}_1) \phi(\tilde{\Gamma}_2) \\ &\quad \times (\mathcal{B}_{12, \hat{\sigma}} - 1) [c_1^p w_1^q (\mathbf{c}_1 \cdot \mathbf{w}_1)^r + c_2^p w_2^q (\mathbf{c}_2 \cdot \mathbf{w}_2)^r] \end{aligned} \quad (3.8)$$

are (reduced) collisional moments. Note that, in the particular case of disks on a plane, the index r is meaningless due to the orthogonality between the vector spaces spanned by translational and angular velocities [see Fig. 1(a)]. However, from a general point of view, the three-dimensional vector forms will be maintained.

Upon derivation of Eq. (3.7), use has been made of the evolution equations for the translational and rotational temperatures,

$$\frac{K}{2}\partial_s T_t = -\frac{2}{d_t}\mu_{20}^{(0)}T_t, \quad \frac{K}{2}\partial_s T_r = -\frac{2}{d_r}\mu_{02}^{(0)}T_r, \quad (3.9)$$

which imply

$$\frac{K}{2}\partial_s \ln \theta = 2 \left[\frac{\mu_{20}^{(0)}}{d_t} - \frac{\mu_{02}^{(0)}}{d_r} \right], \quad (3.10a)$$

$$\frac{K}{2}\partial_s T = -\zeta^* T, \quad (3.10b)$$

where $\zeta^* \equiv 2(\mu_{20}^{(0)} + \mu_{02}^{(0)}\theta)/(d_t + d_r\theta)$ is the (reduced) cooling rate, and thus Eq. (3.10b) represents Haff's cooling law [65] for the inelastic and rough hard-sphere model.

From Eq. (3.7), one can directly derive the hierarchy equations for the evolution of the velocity moments $M_{pq}^{(r)} \equiv \langle c^p w^q (\mathbf{c} \cdot \mathbf{w})^r \rangle$:

$$\frac{K}{2}\frac{\partial \ln M_{pq}^{(r)}}{\partial s} - \frac{(p+r)\mu_{20}^{(0)}}{d_t} - \frac{(q+r)\mu_{02}^{(0)}}{d_r} = -\frac{\mu_{pq}^{(r)}}{M_{pq}^{(r)}}. \quad (3.11)$$

B. Collisional moments

The collisional change of a certain velocity function can be obtained by application of the operator $\delta\mathcal{B}_{12, \hat{\sigma}} \equiv \mathcal{B}_{12, \hat{\sigma}} - 1$ on the function. For instance,

$$\begin{aligned} \delta\mathcal{B}_{12, \hat{\sigma}} (c_1^2 + c_2^2) &= 2\bar{\alpha}(\bar{\alpha} - 1)(\mathbf{c}_{12} \cdot \hat{\sigma})^2 + 2\bar{\beta}(\bar{\beta} - 1) \\ &\quad \times (\hat{\sigma} \times \mathbf{c}_{12})^2 + 8\bar{\beta}^2 \frac{\theta}{\kappa} (\hat{\sigma} \times \mathbf{W}_{12})^2 \\ &\quad - 4\bar{\beta}(2\bar{\beta} - 1) \sqrt{\frac{\theta}{\kappa}} \mathbf{c}_{12} \cdot (\hat{\sigma} \times \mathbf{W}_{12}), \end{aligned} \quad (3.12a)$$

$$\begin{aligned} \delta\mathcal{B}_{12, \hat{\sigma}} (w_1^2 + w_2^2) &= \frac{2\bar{\beta}^2}{\kappa\theta} (\hat{\sigma} \times \mathbf{c}_{12})^2 + 8\frac{\bar{\beta}}{\kappa} \left(\frac{\bar{\beta}}{\kappa} - 1 \right) \\ &\quad \times (\hat{\sigma} \times \mathbf{W}_{12})^2 + 4\frac{\bar{\beta}}{\sqrt{\kappa\theta}} \left(2\frac{\bar{\beta}}{\kappa} - 1 \right) \\ &\quad \times \mathbf{W}_{12} \cdot (\hat{\sigma} \times \mathbf{c}_{12}). \end{aligned} \quad (3.12b)$$

The results for $\delta\mathcal{B}_{12, \hat{\sigma}} (c_1^4 + c_2^4)$, $\delta\mathcal{B}_{12, \hat{\sigma}} (w_1^4 + w_2^4)$, $\delta\mathcal{B}_{12, \hat{\sigma}} (c_1^2 w_1^2 + c_2^2 w_2^2)$, and $\delta\mathcal{B}_{12, \hat{\sigma}} [(\mathbf{c}_1 \cdot \mathbf{w}_1)^2 + (\mathbf{c}_2 \cdot \mathbf{w}_2)^2]$ can be found in the Supplemental Material [66].

Inserting the collisional changes into Eq. (3.8), the collisional moments $\mu_{pq}^{(r)}$ can be formally expressed in terms of *two-body* averages of the form

$$\langle\langle \psi \rangle\rangle = \int d\tilde{\Gamma}_1 \int d\tilde{\Gamma}_2 \psi(\tilde{\Gamma}_1, \tilde{\Gamma}_2) \phi(\tilde{\Gamma}_1) \phi(\tilde{\Gamma}_2). \quad (3.13)$$

In particular,

$$\begin{aligned} \mu_{20}^{(0)} &= \frac{B_3}{2} \left\{ \left[\bar{\alpha}(1 - \bar{\alpha}) + \frac{d_t - 1}{2} \bar{\beta}(1 - \bar{\beta}) \right] \langle\langle c_{12}^3 \rangle\rangle \right. \\ &\quad \left. - 2\bar{\beta}^2 \frac{\theta}{\kappa} [3\langle\langle c_{12} W_{12}^2 \rangle\rangle - \langle\langle c_{12}^{-1} (\mathbf{c}_{12} \cdot \mathbf{W}_{12})^2 \rangle\rangle] \right\}, \end{aligned} \quad (3.14a)$$

$$\begin{aligned} \mu_{02}^{(0)} &= \frac{B_3}{2} \frac{\bar{\beta}}{\kappa} \left\{ -\frac{\bar{\beta}}{\theta} \frac{d_t - 1}{2} \langle\langle c_{12}^3 \rangle\rangle + 2 \left(1 - \frac{\bar{\beta}}{\kappa} \right) \right. \\ &\quad \left. \times [3\langle\langle c_{12} W_{12}^2 \rangle\rangle - \langle\langle c_{12}^{-1} (\mathbf{c}_{12} \cdot \mathbf{W}_{12})^2 \rangle\rangle] \right\}, \end{aligned} \quad (3.14b)$$

where the factor $B_3 = \pi^{\frac{d_t-1}{2}}/\Gamma(\frac{d_t+3}{2})$ comes from an angular integral. The formally exact expressions of the collisional moments $\mu_{40}^{(0)}$, $\mu_{04}^{(0)}$, and $\mu_{22}^{(0)}$ in terms of two-body averages are given in the Supplemental Material [66], where also some related tests for the simulation data are included.

C. Sonine expansion

Assuming isotropy, $\phi(\tilde{\Gamma}; s)$ must depend on velocity only through three scalars: c^2 , w^2 , and $(\mathbf{c} \cdot \mathbf{w})^2$. This can be made explicit by the polynomial expansion

$$\phi(\tilde{\Gamma}) = \phi_M(\tilde{\Gamma}) \sum_{j=0}^{\infty} \sum_{k=0}^{\infty} \sum_{\ell=0}^{\infty} a_{jk}^{(\ell)} \Psi_{jk}^{(\ell)}(\tilde{\Gamma}), \quad (3.15)$$

where

$$\phi_M(\tilde{\Gamma}) = \pi^{-(d_t+d_r)/2} e^{-c^2-w^2} \quad (3.16)$$

is the (two-temperature) Maxwellian distribution, $a_{jk}^{(\ell)}$ are Sonine coefficients, and the functions

$$\Psi_{jk}^{(\ell)} = L_j^{(2\ell+\frac{d_t}{2}-1)}(c^2) L_k^{(2\ell+\frac{d_r}{2}-1)}(w^2) (c^2 w^2)^\ell P_{2\ell}(u) \quad (3.17)$$

form a complete set of orthogonal polynomials [39]. Here, $L_j^{(\ell)}(x)$ are associated Laguerre polynomials, $u \equiv (\mathbf{c} \cdot \mathbf{w})/cw$ is the cosine of the angle formed by the vectors \mathbf{c} and \mathbf{w} , and $P_\ell(u)$ are Legendre polynomials [67]. The orthogonality condition is

$$\langle \Psi_{jk}^{(\ell)} | \Psi_{j'k'}^{(\ell')} \rangle = N_{jk}^{(\ell)} \delta_{jj'} \delta_{kk'} \delta_{\ell\ell'}, \quad (3.18a)$$

$$N_{jk}^{(\ell)} = \frac{\Gamma(2\ell + \frac{d_t}{2} + j) \Gamma(2\ell + \frac{d_r}{2} + k)}{\Gamma(\frac{d_t}{2}) \Gamma(\frac{d_r}{2}) (4\ell + 1) j! k!}, \quad (3.18b)$$

where the inner product of two arbitrary real functions $\Phi_1(\tilde{\Gamma})$ and $\Phi_2(\tilde{\Gamma})$ is defined as

$$\langle \Phi_1 | \Phi_2 \rangle = \int d\tilde{\Gamma} \phi_M(\tilde{\Gamma}) \Phi_1(\tilde{\Gamma}) \Phi_2(\tilde{\Gamma}). \quad (3.19)$$

Note that $\langle \Phi \rangle = \langle \Phi | \phi / \phi_M \rangle$. Using Eq. (3.18a) in Eq. (3.15), one can express the Sonine coefficients as

$$a_{jk}^{(\ell)} = \frac{\langle \Psi_{jk}^{(\ell)} \rangle}{N_{jk}^{(\ell)}}. \quad (3.20)$$

In particular, $a_{00}^{(0)} = 1$, $a_{10}^{(0)} = a_{01}^{(0)} = 0$, while

$$a_{20}^{(0)} = \frac{4\langle c^4 \rangle}{d_t(d_t+2)} - 1, \quad a_{02}^{(0)} = \frac{4\langle w^4 \rangle}{d_r(d_r+2)} - 1, \quad (3.21a)$$

$$a_{11}^{(0)} = \frac{4\langle c^2 w^2 \rangle}{d_t d_r} - 1, \quad a_{00}^{(1)} = \frac{8}{15} \left[\langle (\mathbf{c} \cdot \mathbf{w})^2 \rangle - \frac{1}{3} \langle c^2 w^2 \rangle \right] \quad (3.21b)$$

are fourth-order cumulants. Notice that $a_{00}^{(1)}$ is only meaningful in the hard-sphere case and thus it is not expressed in terms of the number of degrees of freedom.

The evolution equations for the cumulants defined by Eqs. (3.21) can be easily obtained from the moment hierarchy, Eq. (3.11), as

$$\frac{K}{2} \partial_s \ln(1 + a_{20}) = \frac{4}{d_t(d_t+2)} \left[(d_t+2)\mu_{20} - \frac{\mu_{40}}{1+a_{20}} \right], \quad (3.22a)$$

$$\frac{K}{2} \partial_s \ln(1 + a_{02}) = \frac{4}{d_r(d_r+2)} \left[(d_r+2)\mu_{02} - \frac{\mu_{04}}{1+a_{02}} \right], \quad (3.22b)$$

$$\frac{K}{2} \partial_s \ln(1 + a_{11}) = \frac{4}{d_r d_t} \left[\frac{d_r}{2} \mu_{20} + \frac{d_t}{2} \mu_{02} - \frac{\mu_{22}}{1+a_{11}} \right], \quad (3.22c)$$

$$\frac{K}{2} \partial_s \ln \left[1 + a_{11} + \frac{5}{2} a_{00}^{(1)} \right] = \frac{4}{3} \left[\frac{1}{2} \mu_{20} + \frac{1}{2} \mu_{02} - \frac{\mu_{00}^{(2)}}{1+a_{11} + \frac{5}{2} a_{00}^{(1)}} \right], \quad (3.22d)$$

where henceforth we simplify the notation as $a_{jk}^{(0)} \rightarrow a_{jk}$ and $\mu_{jk}^{(0)} \rightarrow \mu_{jk}$.

D. Homogeneous cooling state

The scaling method in the description of the kinetic equation suggests that a stationary solution, $\phi = \phi^H$, of Eq. (3.7) applies for long times (hydrodynamic limit). This is the HCS, in which the temperature ratio, θ^H , is constant and the whole time dependence of the unscaled VDF $f^H(\mathbf{\Gamma}; t)$ takes place through the mean temperature $T(t)$ only. On the other hand, this stationary solution $\phi = \phi^H$ is not exactly known.

From Eqs. (3.10a) and (3.22), it follows that, in the HCS,

$$\mu_{20}^H = \frac{d_t}{d_r} \mu_{02}^H, \quad (d_t+2)\mu_{20}^H = \frac{\mu_{40}^H}{1+a_{20}^H}, \quad (3.23a)$$

$$(d_r+2)\mu_{02}^H = \frac{\mu_{04}^H}{1+a_{02}^H}, \quad d_r \mu_{20}^H = \frac{\mu_{22}^H}{1+a_{11}^H}, \quad (3.23b)$$

$$\mu_{20}^H = \frac{\mu_{00}^{(2)H}}{1+a_{11}^H + \frac{5}{2} a_{00}^{(1)H}}. \quad (3.23c)$$

Notice that, as expected, Eq. (3.23c) is only meaningful for spheres ($d_t = d_r = 3$).

IV. APPROXIMATE SCHEMES

All the equations presented in Sec. III are formally exact within the framework of the Boltzmann equation.

TABLE I. Relevant collisional moments from the Sonine approximation in the hard-disk case.

(p, q)	$\mu_{pq}/\sqrt{2\pi}$
(2, 0)	$[2\bar{\alpha}(1-\bar{\alpha}) + \bar{\beta}(1-\bar{\beta})] \left(1 + \frac{3}{16}a_{20}\right) - \theta \frac{\bar{\beta}^2}{\kappa} \left(1 - \frac{a_{20}}{16} + \frac{a_{11}}{4}\right)$
(0, 2)	$\frac{\bar{\beta}}{\kappa} \left(1 - \frac{\bar{\beta}}{\kappa}\right) \left(1 - \frac{a_{20}}{16} + \frac{a_{11}}{4}\right) - \frac{\bar{\beta}^2}{\kappa\theta} \left(1 + \frac{3}{16}a_{20}\right)$
(4, 0)	$8\bar{\alpha}^3(2-\bar{\alpha}) \left(1 + \frac{15}{16}a_{20}\right) + 3\bar{\beta}^3(2-\bar{\beta}) \left(1 + \frac{15}{16}a_{20}\right) + \left(\bar{\alpha} + \frac{\bar{\beta}}{2}\right) \left(9 + \frac{223}{16}a_{20}\right) - \bar{\alpha}^2 \left(17 + \frac{327}{16}a_{20}\right)$ $-\bar{\beta}^2 \left(15 + \frac{281}{16}a_{20}\right) - 4\bar{\alpha}\bar{\beta}(\bar{\alpha}\bar{\beta} - \bar{\alpha} - \bar{\beta}) \left(1 + \frac{15}{16}a_{20}\right) - 4\bar{\alpha}\bar{\beta} \left(1 + \frac{23}{16}a_{20}\right) - \frac{\bar{\beta}^2\theta}{2\kappa} \left\{9 + \frac{35}{16}a_{20} + \frac{27}{4}a_{11}\right.$ $\left. - 4[2\bar{\alpha}(1-\bar{\alpha}) + 3\bar{\beta}(1-\bar{\beta})] \left(1 + \frac{3}{16}a_{20} + \frac{3}{4}a_{11}\right) + 6\frac{\bar{\beta}^2\theta}{\kappa} \left(1 - \frac{1}{16}a_{20} + \frac{1}{2}a_{02} + \frac{1}{2}a_{11}\right)\right\}$
(0, 4)	$\frac{\bar{\beta}}{\kappa} \left[3 \left(1 - \frac{1}{16}a_{20} + a_{02} + \frac{1}{2}a_{11}\right) - 3\frac{\bar{\beta}}{\kappa} \left(2 - 2\frac{\bar{\beta}}{\kappa} + \frac{\bar{\beta}^2}{\kappa^2}\right) \left(1 - \frac{1}{16}a_{20} + \frac{1}{2}a_{02} + \frac{1}{2}a_{11}\right) - \frac{3\bar{\beta}}{2\kappa}a_{02}\right.$ $\left. - 3\frac{\bar{\beta}}{\theta} \left(1 - 2\frac{\bar{\beta}}{\kappa} + 2\frac{\bar{\beta}^2}{\kappa^2}\right) \left(1 + \frac{3}{16}a_{20} + \frac{3}{4}a_{11}\right) - 3\frac{\bar{\beta}^3}{\kappa\theta^2} \left(1 + \frac{15}{16}a_{20}\right)\right]$
(2, 2)	$\left[\bar{\alpha}(1-\bar{\alpha}) + \frac{\bar{\beta}}{2}(1-\bar{\beta})\right] \left(1 + \frac{3}{16}a_{20} + \frac{3}{4}a_{11}\right) + \left(\bar{\alpha} + \frac{\bar{\beta}}{2}\right) \frac{a_{11}}{2} - \frac{\bar{\beta}^2\theta}{\kappa} \left(1 - \frac{1}{16}a_{20} + \frac{1}{2}a_{11} + \frac{3}{4}a_{02}\right)$ $+ \frac{\bar{\beta}}{\kappa} \left\{\frac{5}{4} + \frac{23}{64}a_{20} + \frac{27}{16}a_{11} - 2\left[\bar{\alpha}(1-\bar{\alpha}) + \bar{\beta}\left(1 - \frac{3}{2}\bar{\beta}\right)\right] \left(1 + \frac{3}{16}a_{20} + \frac{3}{4}a_{11}\right) - (\bar{\alpha} + \bar{\beta})a_{11}\right\} + 3\frac{\bar{\beta}^3\theta}{\kappa^2}$ $\times \left(1 - \frac{a_{20}}{16} + \frac{a_{02}}{2} + \frac{a_{11}}{2}\right) - \frac{7\bar{\beta}^2}{4\kappa\theta} \left(1 + \frac{129}{112}a_{20}\right) - \frac{5\bar{\beta}^2}{4\kappa^2} \left(1 + \frac{23}{80}a_{20} + \frac{3}{4}a_{11}\right) + \frac{\bar{\beta}^2}{\kappa\theta} [2\bar{\alpha}(1-\bar{\alpha}) + 3\bar{\beta}(1-\bar{\beta})]$ $\times \left(1 + \frac{15}{16}a_{20}\right) + \frac{\bar{\beta}^2}{\kappa^2} [2\bar{\alpha}(1-\bar{\alpha}) + 3\bar{\beta}(1-2\bar{\beta})] \left(1 + \frac{3}{16}a_{20} + \frac{3}{4}a_{11}\right) + 3\frac{\bar{\beta}^4\theta}{\kappa^3} \left(1 - \frac{a_{20}}{16} + \frac{a_{02}}{2} + \frac{a_{11}}{2}\right)$

However, no explicit results can be obtained unless one makes use of approximations.

A. Maxwellian approximation

The simplest approximation is the Maxwellian one, i.e., $\phi(\tilde{\Gamma}) \rightarrow \phi_M(\tilde{\Gamma})$. In that case [45],

$$\mu_{20} \rightarrow \frac{K}{2} \left\{ 1 - \alpha^2 + \frac{2d_r\kappa(1+\beta)}{d_t(1+\kappa)^2} \left[1 - \theta + \frac{\kappa(1-\beta)}{2} \times \left(1 + \frac{\theta}{\kappa} \right) \right] \right\}, \quad (4.1a)$$

$$\mu_{02} \rightarrow K \frac{d_r\kappa(1+\beta)}{d_t(1+\kappa)^2} \left[1 - \frac{1}{\theta} + \frac{1-\beta}{2} \left(\frac{1}{\theta} + \frac{1}{\kappa} \right) \right], \quad (4.1b)$$

$$\zeta^* \rightarrow \frac{K}{d_t + d_r\theta} \left[1 - \alpha^2 + \frac{d_r}{d_t} \frac{1-\beta^2}{1+\kappa} (\kappa + \theta) \right]. \quad (4.1c)$$

In this Maxwellian approximation, Eqs. (3.9) and (3.10) can be solved to get the evolution of the partial and mean temperatures, as well as the HCS value of the temperature ratio θ^H . However, by construction, the Maxwellian approximation is unable to account for the non-Gaussianities of the VDF, either in the transient evolution to the HCS or in the HCS itself.

B. Sonine approximation

The basic quantities measuring non-Gaussianities are the cumulants defined in Eqs. (3.21). Therefore, as the simplest scheme to capture those cumulants, we introduce the Grad–Sonine methodology [28, 39, 68] and truncate the infinite Sonine expansion, Eq. (3.15), after $j+k+2\ell \geq 3$, i.e.,

$$\phi \rightarrow \phi_S = \phi_M \left[1 + a_{20}\Psi_{20}^{(0)} + a_{02}\Psi_{02}^{(0)} + a_{11}\Psi_{11}^{(0)} + a_{00}^{(1)}\Psi_{00}^{(1)} \right], \quad (4.2)$$

where the term $a_{00}^{(1)}\Psi_{00}^{(1)}$ is not present in the hard-disk case. With the replacement given by Eq. (4.2), the two-body averages appearing in the collisional moments [see, for instance, Eqs. (3.14)] can be explicitly calculated as linear and quadratic functions of the cumulants. Next, our Sonine approximation is constructed by neglecting quadratic terms, so only linear terms are retained.

By particularizing to the hard-sphere case ($d_t = d_r = 3$), previous results are recovered [39]. Moreover, we obtain novel expressions for hard disks ($d_t = 2$, $d_r = 1$), which are displayed in Table I. Further details about some of the computations are available in the Supplemental Material [66].

For consistency with the truncation and linearization steps carried out in the Sonine approximation, the evolution equations in the hard-disk case are obtained by

inserting the expressions in Table I into Eqs. (3.10a) and (3.22a)–(3.22c), and linearizing the bracketed quantities. This gives a closed set of four differential equations, which are linear in the cumulants and nonlinear in the temperature ratio. Likewise, the HCS values are obtained by linearizing Eqs. (3.23a) and (3.23b) with respect to the cumulants. The linear stability of the HCS versus uniform and isotropic perturbations is proved in Appendix A.

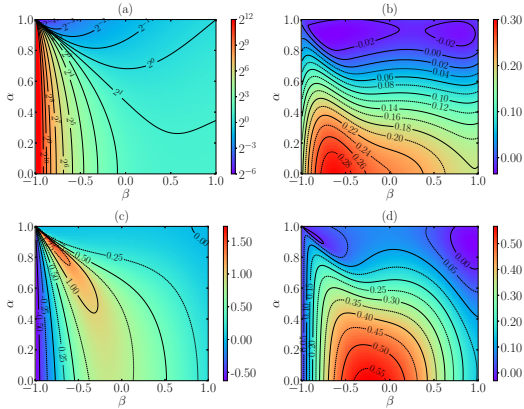


FIG. 2. Theoretical values of (a) θ^H , (b) a_{20}^H , (c) a_{02}^H , and (d) a_{11}^H as functions of the coefficients of restitution, α and β , for uniform disks ($\kappa = \frac{1}{2}$) in the Sonine approximation.

Figures 2 and 3 show the HCS quantities θ^H , a_{20}^H , a_{02}^H , and a_{11}^H , obtained from the Sonine approximation for uniform disks ($\kappa = \frac{1}{2}$) and spheres ($\kappa = \frac{2}{5}$), respectively, as functions of the coefficients of restitution α and β . In the hard-sphere case, the cumulant $a_{00}^{(1)H}$ is also included. It can be observed that, typically, hard-disk systems depart from the Maxwellian state more than hard-sphere systems. Interestingly, both hard-disk and hard-sphere systems present relatively large values of a_{02}^H and a_{11}^H , thus signaling a possible quantitative breakdown of the Sonine approximation, which implicitly assumes small deviations from the Maxwellian VDF.

V. MARGINAL DISTRIBUTION FUNCTIONS AND HIGH-VELOCITY TAILS IN THE HOMOGENEOUS COOLING STATE

A. Marginal distribution functions

As said before, the reduced VDF $\phi(\tilde{\Gamma})$ in isotropic states depend on the three scalars c^2 , w^2 , and c^2w^2 [plus $(\mathbf{c} \cdot \mathbf{w})^2$ only for spheres]. To disentangle those dependencies, it is convenient to define the following *marginal*

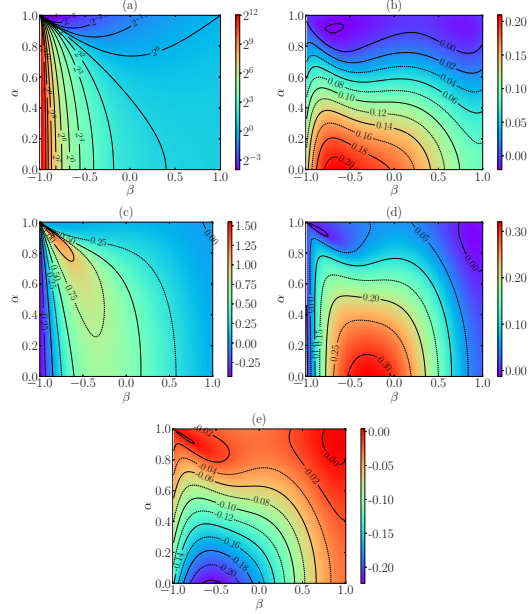


FIG. 3. Theoretical values of (a) θ^H , (b) a_{20}^H , (c) a_{02}^H , (d) a_{11}^H , and (e) $a_{00}^{(1)H}$ as functions of the coefficients of restitution, α and β , for uniform spheres ($\kappa = \frac{2}{5}$) in the Sonine approximation.

distributions [39, 41]:

$$\phi_{\mathbf{c}}(\mathbf{c}) = \int d\mathbf{w} \phi(\tilde{\Gamma}), \quad (5.1a)$$

$$\phi_{\mathbf{w}}(\mathbf{w}) = \int d\mathbf{c} \phi(\tilde{\Gamma}), \quad (5.1b)$$

$$\phi_{c\mathbf{w}}(x) = \int d\tilde{\Gamma} \delta(c^2w^2 - x) \phi(\tilde{\Gamma}), \quad (5.1c)$$

where x represents the product c^2w^2 . Note that, by isotropy, $\phi_{\mathbf{c}}(\mathbf{c})$ and $\phi_{\mathbf{w}}(\mathbf{w})$ depend only on the moduli c and w , respectively. Moreover, the marginal distributions in Eqs. (5.1) are directly related to the cumulants $a_{20}^{(0)}$, $a_{02}^{(0)}$, and $a_{11}^{(0)}$ defined by Eqs. (3.21), namely

$$\int d\mathbf{c} c^4 \phi_{\mathbf{c}}(\mathbf{c}) = \frac{d_t(d_t + 2)}{4} [1 + a_{20}^{(0)}], \quad (5.2a)$$

$$\int d\mathbf{w} w^4 \phi_{\mathbf{w}}(\mathbf{w}) = \frac{d_r(d_r + 2)}{4} [1 + a_{02}^{(0)}], \quad (5.2b)$$

$$\int_0^\infty dx x \phi_{c\mathbf{w}}(x) = \frac{d_t d_r}{4} [1 + a_{11}^{(0)}]. \quad (5.2c)$$

The Maxwellian expressions for these functions are

$$\phi_{\mathbf{c},\text{M}}(\mathbf{c}) = \pi^{-d_t/2} e^{-c^2}, \quad (5.3a)$$

$$\phi_{\mathbf{w},\text{M}}(\mathbf{w}) = \pi^{-d_r/2} e^{-w^2}, \quad (5.3b)$$

$$\phi_{c_w,\text{M}}(x) = \frac{1}{2} \Omega_{d_t} \Omega_{d_r} \pi^{-\frac{d_t+d_r}{2}} x^{\frac{d_t+d_r}{4}-1} K_{\frac{d_t-d_r}{2}}(2\sqrt{x}), \quad (5.3c)$$

where $\Omega_d = 2\pi^{d/2}/\Gamma(\frac{d}{2})$ is the d -dimensional solid angle and $K_d(x)$ is the modified Bessel function of the second kind. In the Sonine approximation defined by Eq. (4.2), one has

$$\frac{\phi_{\mathbf{c},\text{S}}(\mathbf{c})}{\phi_{\mathbf{c},\text{M}}(\mathbf{c})} = 1 + a_{20} \frac{4c^4 - 4(d_t + 2)c^2 + d_t(d_t + 2)}{8}, \quad (5.4a)$$

$$\frac{\phi_{\mathbf{w},\text{S}}(\mathbf{w})}{\phi_{\mathbf{w},\text{M}}(\mathbf{w})} = 1 + a_{02} \frac{4w^4 - 4(d_r + 2)w^2 + d_r(d_r + 2)}{8}, \quad (5.4b)$$

$$\begin{aligned} \frac{\phi_{c_w,\text{S}}(x)}{\phi_{c_w,\text{M}}(x)} = & 1 + \frac{a_{20} + 2a_{11} + a_{02}}{2} x + a_{20} \frac{d_t(d_t + 2)}{8} \\ & + \frac{d_t d_r}{4} a_{11} + a_{02} \frac{d_r(d_r + 2)}{8} \\ & - \sqrt{x} \frac{K_{1-\frac{d_t-d_r}{2}}(2\sqrt{x})}{K_{\frac{d_t-d_r}{2}}(2\sqrt{x})} \left[\frac{a_{20} + a_{02}}{2} \right. \\ & \left. + \frac{d_t + d_r}{4} (a_{20} + 2a_{11} + a_{02}) \right]. \end{aligned} \quad (5.4c)$$

While Eqs. (5.4) may reproduce the correct behavior of the HCS in the *thermal* domain, it is known from the smooth case [48, 49, 58] and from hard-sphere results [39] that they are unable to account for the high-velocity tail.

B. High-velocity tails

Let us now study the high-velocity tail for the marginal VDF in the HCS, in analogy to previous works for the smooth case [48, 58].

To carry out this asymptotic analysis, we start from the homogeneous Boltzmann equation, Eq. (3.7), and split the collisional operator into a loss and a gain term, that is [48, 58],

$$\mathcal{I}_{\tilde{\Gamma}}^L[\phi, \phi] = \mathcal{I}_{\tilde{\Gamma}}^G[\phi, \phi] - \mathcal{I}_{\tilde{\Gamma}}^L[\phi, \phi], \quad (5.5)$$

where the loss term can be written as

$$\mathcal{I}_{\tilde{\Gamma}_1}^L[\phi, \phi] = B_1 \phi(\tilde{\Gamma}_1) \int d\tilde{\Gamma}_2 c_{12} \phi(\tilde{\Gamma}_2), \quad (5.6)$$

with $B_1 = \pi^{\frac{d_t-1}{2}}/\Gamma(\frac{d_t+1}{2})$. The gain term accounts for all the particles that after a collision have velocities $\tilde{\Gamma}_1$. In contrast, the loss term takes into account the amount of particles with $\tilde{\Gamma}_1$ that, after a collision, are not contributing any more to these velocities.

Intuitively, one would expect that escaping from the rapid regime is easier than entering the high-velocity limit, given the low likelihood of encountering rapid particles compared to thermal ones. Thus, the main assumption we will use is that, for high velocities of the HCS, the loss term prevails over the gain term. From Eq. (3.2), and following the case of smooth particles [48], the assumption above can be expressed as

$$\lim_{c_1 \rightarrow \infty \text{ or } w_1 \rightarrow \infty} \frac{\phi^{\text{H}}(\tilde{\Gamma}_1'') \phi^{\text{H}}(\tilde{\Gamma}_2'')}{\phi^{\text{H}}(\tilde{\Gamma}_1) \phi^{\text{H}}(\tilde{\Gamma}_2)} = 0. \quad (5.7)$$

1. Tail of $\phi_{\mathbf{c}}^{\text{H}}(\mathbf{c})$

Integrating over \mathbf{w} on both sides of the stationary version of Eq. (3.7), neglecting the gain term, replacing $c_{12} \rightarrow c_1$ in Eq. (5.6), and taking the limit $c \gg 1$, we get the linear differential equation

$$\frac{\mu_{20}^{\text{H}}}{d_t} \frac{\partial}{\partial c} \phi_{\mathbf{c}}^{\text{H}}(\mathbf{c}) \approx -B_1 \phi_{\mathbf{c}}^{\text{H}}(\mathbf{c}), \quad (5.8)$$

whose solution is

$$\phi_{\mathbf{c}}^{\text{H}}(\mathbf{c}) \approx \mathcal{A}_c e^{-\gamma c}, \quad \gamma_c = \frac{d_t B_1}{\mu_{20}^{\text{H}}}, \quad (5.9)$$

where \mathcal{A}_c is an integration constant. This is equivalent to the result in the smooth case [48, 58], except that now μ_{20}^{H} takes into account the influence of surface roughness. The exponential decay of $\phi_{\mathbf{c}}^{\text{H}}(\mathbf{c})$ implies that all the cumulants of the form $a_{j_0}^{\text{H}}$ are finite.

2. Tail of $\phi_{\mathbf{w}}^{\text{H}}(\mathbf{w})$

Now we integrate over \mathbf{c} on both sides of Eq. (3.7) and neglect again the gain term. This yields

$$\mu_{02}^{\text{H}} \phi_{\mathbf{w}}^{\text{H}}(\mathbf{w}) + \frac{\mu_{02}^{\text{H}}}{d_r} w \frac{\partial}{\partial w} \phi_{\mathbf{w}}^{\text{H}}(\mathbf{w}) \approx -B_1 \overline{c_{12}^{\text{H}}}(\mathbf{w}) \phi_{\mathbf{w}}^{\text{H}}(\mathbf{w}), \quad (5.10)$$

where

$$\overline{c_{12}^{\text{H}}}(\mathbf{w}_1) = \int d\mathbf{c}_1 \int d\tilde{\Gamma}_2 c_{12} \phi_{\mathbf{c}|\mathbf{w}}(\mathbf{c}_1|\mathbf{w}_1) \phi(\tilde{\Gamma}_2). \quad (5.11)$$

Here, $\phi_{\mathbf{c}|\mathbf{w}}(\mathbf{c}|\mathbf{w})$ is a conditional probability distribution function defined as

$$\phi_{\mathbf{c}|\mathbf{w}}(\mathbf{c}|\mathbf{w}) \phi_{\mathbf{w}}(\mathbf{w}) = \phi(\mathbf{c}, \mathbf{w}). \quad (5.12)$$

The quantity $\overline{c_{12}^{\text{H}}}(\mathbf{w})$ represents the average relative translational velocity of those particles with an angular velocity \mathbf{w} . It is a functional of the whole VDF $\phi(\tilde{\Gamma})$, so Eq. (5.10) is not a closed equation for the marginal distribution $\phi_{\mathbf{w}}^{\text{H}}(\mathbf{w})$.

The positive values observed in Figs. 2 and 3 for the cumulant a_{11}^{H} imply that high angular velocities are

positively correlated to high translational velocities, so $\overline{c_{12}^H(\mathbf{w})}$ is expected to increase with w . However, to estimate the tail of $\phi_{\mathbf{w}}^H(\mathbf{w})$, we further assume that the dependence of $\overline{c_{12}^H(\mathbf{w})}$ on w is weak enough as to take $\overline{c_{12}^H(\mathbf{w})} \approx \langle\langle c_{12} \rangle\rangle^H$. With this adiabaticlike approximation, Eq. (5.10) becomes a closed linear equation whose solution is

$$\phi_{\mathbf{w}}^H(\mathbf{w}) \approx \mathcal{A}_w w^{-\gamma_w}, \quad \gamma_w = d_r + \gamma_c \langle\langle c_{12} \rangle\rangle^H, \quad (5.13)$$

where \mathcal{A}_w is the associated integration constant. In the expression of γ_w , we have made use of the HCS condition $\mu_{02}^H/d_r = \mu_{20}^H/d_t$ [see Eqs. (3.23a)].

While, in principle, Eqs. (5.13) are approximate because of the ansatz $\overline{c_{12}^H(\mathbf{w})} \approx \langle\langle c_{12} \rangle\rangle^H$, it accounts for an algebraic decay of $\phi_{\mathbf{w}}^H(\mathbf{w})$ explaining the relatively high values attained by a_{02}^H . In fact, Eqs. (5.13) imply that the coefficients of the form a_{0k}^H diverge if $2k \geq \gamma_w - 1$.

3. Tail of $\phi_{cw}(x)$

Whereas the derivation of the high-velocity tail for ϕ_c is clean, and the one for $\phi_{\mathbf{w}}$, although approximate, is reasonable, in the case of the distribution ϕ_{cw} the reasoning is somewhat more speculative. Let us start by introducing the marginal probability distribution function of the variable w^2 , $\phi_{w^2}(w^2) = (\Omega_{d_r}/2)w^{d_r-2}\phi_{\mathbf{w}}(\mathbf{w})$. According to Eqs. (5.13), the high-velocity tail of $\phi_{w^2}^H(w^2)$ is

$$\phi_{w^2}^H(w^2) \approx \mathcal{A}_w \frac{\Omega_{d_r}}{2} (w^2)^{\frac{d_r-\gamma_w}{2}-1}. \quad (5.14)$$

As can be inferred from Eqs. (5.9) and (5.13), the tail of angular velocities is much more populated than that of translational velocities. Therefore, it is reasonable to expect that the main contribution to $\phi_{cw}(c^2w^2)$ comes essentially from particles with thermal translational velocities ($c \sim 1$) and high angular velocities ($w \gg 1$). Thus, in view of Eq. (5.14), we conjecture that

$$\phi_{cw}^H(x) \approx \mathcal{A}_{cw} x^{-\gamma_{cw}}, \quad \gamma_{cw} = 1 + \frac{\gamma_w - d_r}{2}. \quad (5.15)$$

This algebraic decay would be responsible for the relatively large values of a_{11}^H and implies the divergence of the coefficients of the form a_{jj}^H if $j \geq \gamma_{cw} - 1$. An alternative justification of Eqs. (5.15) is provided in the Supplemental Material [66].

While, according to Eq. (5.9), the asymptotic decay of $\phi_c(\mathbf{c})$ is governed by a velocity scale $c \sim \gamma_c^{-1}$, Eqs. (5.13) and (5.15) show that the decays of $\phi_{\mathbf{w}}(\mathbf{w})$ and $\phi_{cw}(x)$ are scale-free. It can be checked that the exponents γ_c , γ_w , and γ_{cw} are generally smaller for disks than for spheres, meaning that the high-velocity tails are fatter in the former case than in the latter. Apart from that, they exhibit a similar qualitative dependence on the coefficients of restitution.

The consistency of Eq. (5.7) with the tails obtained here is discussed in Appendix B.

VI. SIMULATION RESULTS

To test the theoretical results, we have run two types of computer simulation algorithms for a dilute and homogeneous granular gas of inelastic and rough hard disks ($d_t = 2$, $d_r = 1$) with different values of the coefficients of restitution α and β . In all cases, the disks are assumed to have a uniform mass distribution, so the reduced moment of inertia is $\kappa = \frac{1}{2}$.

First, we used DSMC, as proposed by Bird [69, 70] and conveniently adapted to the granular case [39, 51], to simulate a homogeneous and dilute granular gas of inelastic and rough hard disks, using $N = 10^4$ representative particles. Additionally, we carried out EDMD computer simulations with $N = 1600$ disks in a square box of side length $L/\sigma = 565.7$, which correspond to a number density $n\sigma^2 = 0.005$, thus avoiding spatial instabilities [46]. Whereas the EDMD system has nonzero density, the solid fraction $\varphi = \frac{\pi}{4}n\sigma^2 \simeq 3.9 \times 10^{-3}$ is small enough to expect good agreement with the diluteness assumption. We ran 100 and 50 replicas for DSMC and EDMD, respectively, for each pair (α, β) , not observing instabilities in the EDMD simulations. In addition to averaging over replicas, the stationary HCS values were measured by averaging over instantaneous values at $s = s_{\text{ini}}, s_{\text{ini}} + \delta s, s_{\text{ini}} + 2\delta s, \dots, s_{\text{fin}}$ with $(s_{\text{ini}}, s_{\text{fin}}, \delta s) = (500, 1500, 5)$ and $(150, 200, 1)$ for DSMC and EDMD, except in the case $\alpha = 0.9, \beta = -0.8$, where we took $(450, 500, 1)$ in the EDMD simulations. In the construction of histograms for the marginal distributions, we considered 2^8 bins in the associated velocity variable.

In the Supplemental Material [66], we present a comparison between the Sonine-approximation results [see Eqs. (3.10a) and (3.22)] and simulation data for the temporal evolution toward the HCS of the temperature ratio and the cumulants, starting from an equipartitioned Maxwellian state. A generally good agreement is observed, except for a_{02}^H near the HCS if a_{02}^H reaches relatively high values. Now we present results for the relevant quantities in the HCS.

A. Temperature ratio and cumulants

Figure 4 shows the HCS values of θ^H , a_{20}^H , a_{02}^H , and a_{11}^H versus β for some representative values of α . Figure 5 presents the same quantities versus α for some illustrative values of β . We observe that the Maxwellian approximation provides a good description of θ^H , although it tends to overestimate it if $\alpha \lesssim 0.7$ [see Figs. 5(a)–5(c)]. Those deviations are satisfactorily corrected by the Sonine approximation.

In the case of the cumulants, their qualitative shape as functions of both α and β are well accounted for by the Sonine approximation. The quantitative agreement is good as long as the magnitude of the cumulants is small, thus validating the Sonine approximation in those cases. On the other hand, whenever the Sonine approxi-

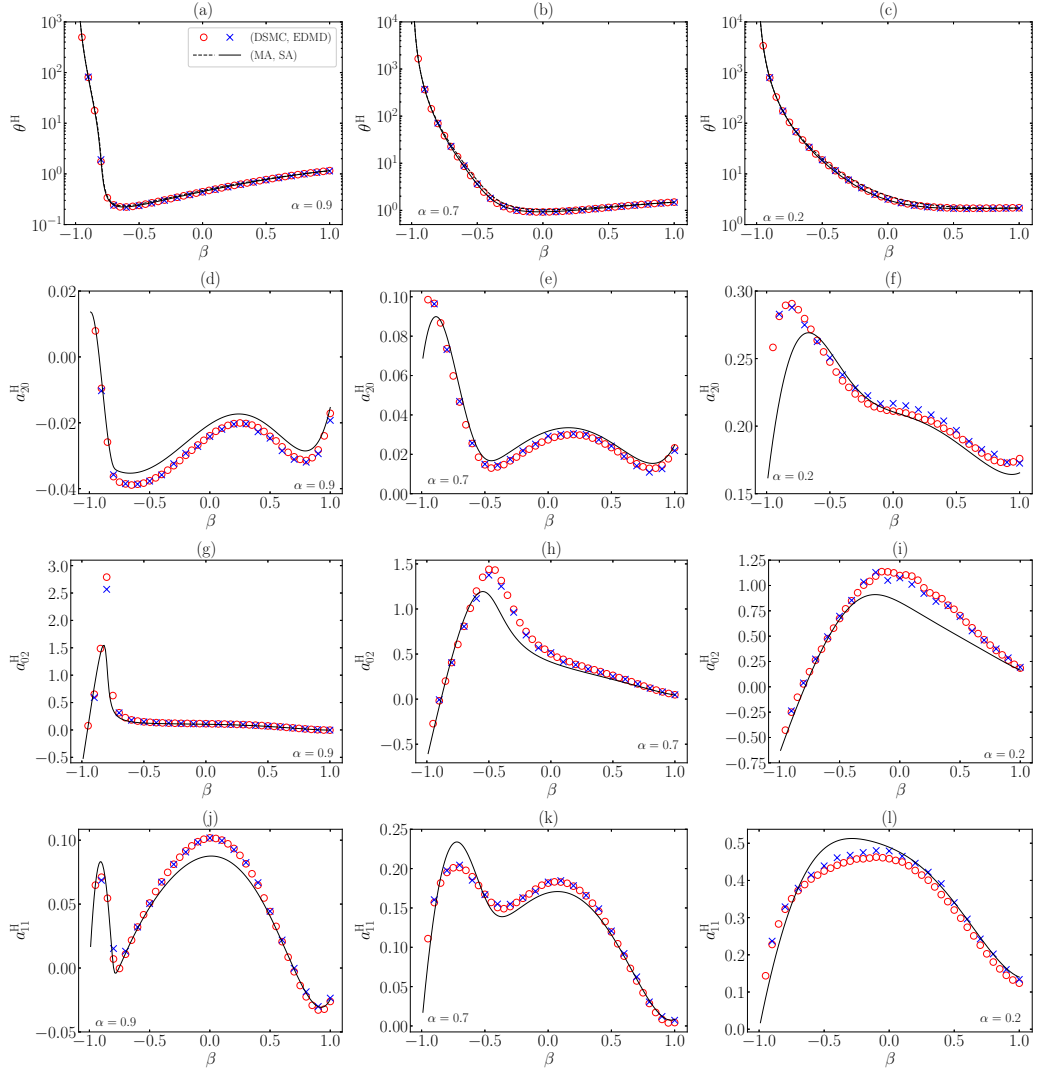


FIG. 4. Plots of (a)–(c) the temperature ratio θ^H , (d)–(f) the cumulant a_{20}^H , (g)–(i) the cumulant a_{02}^H , and (j)–(l) the cumulant a_{11}^H , for uniform disks ($\kappa = \frac{1}{2}$), as functions of the coefficient of tangential restitution β . The left [(a), (d), (g), (j)], middle [(b), (e), (h), (k)], and right [(c), (f), (i), (l)] panels correspond to $\alpha = 0.9, 0.7$, and 0.2 , respectively. Symbols represent DSMC (o) and EDMD (x) results, while the solid lines are theoretical predictions from the Sonine approximation (SA). Additionally, the dashed lines in (a)–(c) represent the Maxwellian approximation (MA) for the temperature ratio. Note that a vertical logarithmic scale is used in (a)–(c).

mation predicts values $a_{ij}^H = O(1)$, the approximation is itself signaling its breakdown. This situation, which is similar to that already reported in the case of HS [39], is especially noteworthy in the cases of a_{02}^H and, to a lesser extent, a_{11}^H , and is clearly indicative of the high-velocity tails discussed in Sec. VB and confirmed below.

B. High-velocity tails

To further observe the non-Gaussianities of the HCS state, Fig. 6 displays the histograms from simulation data of ϕ_c^H , ϕ_w^H , and ϕ_{cw}^H , for nine combinations of coefficients of restitution ($\alpha = 0.9, 0.7, 0.2$, and $\beta = 0.5, 0, -0.5$). Except in the case of ϕ_c^H for $\alpha = 0.9$ (where a_{20}^H is small),

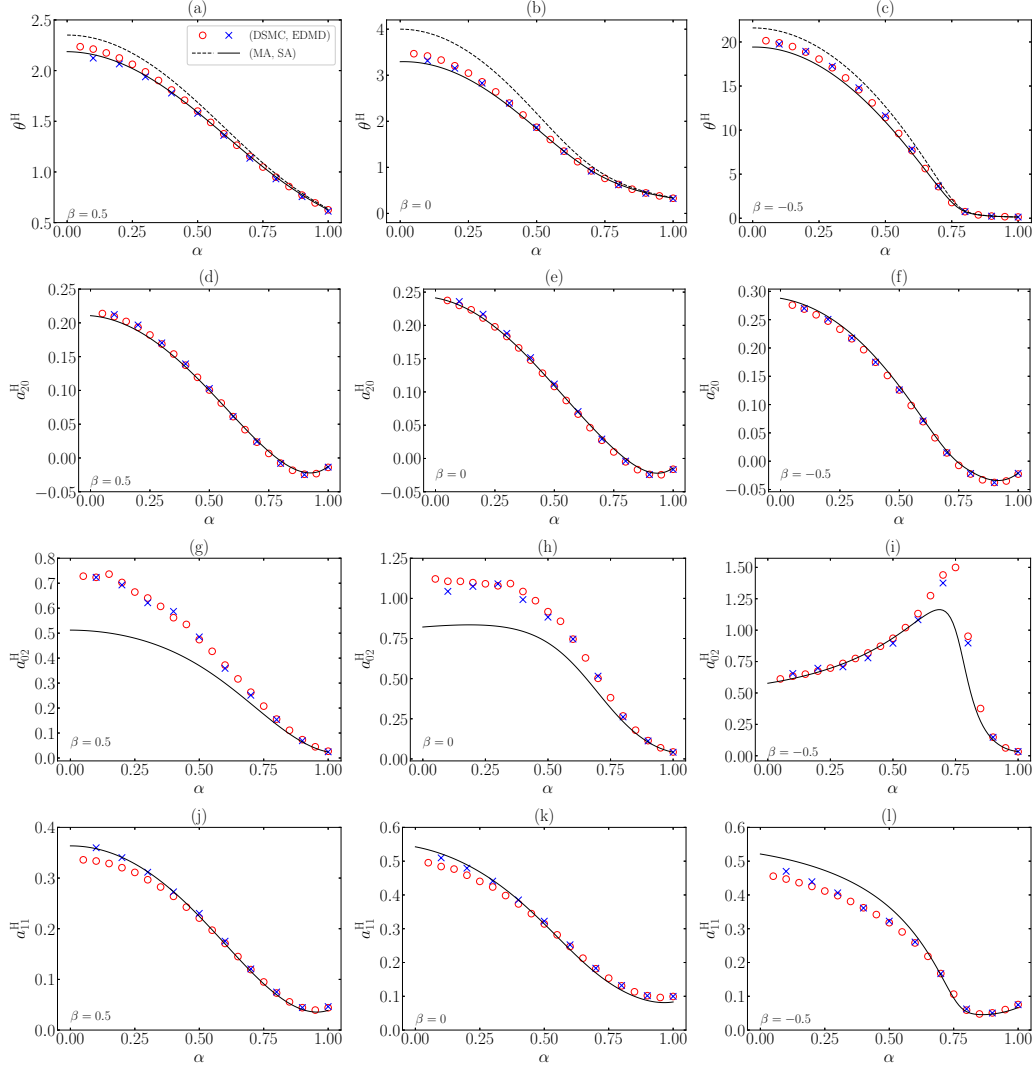


FIG. 5. Same as in Fig. 4, except that the quantities are plotted versus the coefficient of normal restitution α and now the left [(a), (d), (g), (j)], middle [(b), (e), (h), (k)], and right [(c), (f), (i), (l)] panels correspond to $\beta = 0.5, 0$, and -0.5 , respectively.

the deviations from the Maxwellian tail are quite apparent. In fact, the high-velocity tails observed in Fig. 6 are consistent with an exponential tail for ϕ_c^H and power-law tails for ϕ_w^H and ϕ_{cw}^H , in agreement with the analysis in Sec. VB.

A more quantitative test is presented in Fig. 7, where the three cases with $\alpha = 0.7$ have been selected and the straight lines representing the asymptotic tails are included. The theoretical predictions for the exponents derived in Sec. VB (with additional Maxwellian estimates for μ_{20}^H and $\langle c_{12} \rangle^H$) agree reasonably well with the fit-

ted values, except for $\beta = -0.5$, in which case the actual decays are slower than predicted.

Figure 8 shows the exponents γ_c , γ_w , and γ_{cw} as functions of β (for $\alpha = 0.9, 0.7, 0.2$) and α (for $\beta = 0.5, 0, -0.5$). There exists very good agreement between the theoretical estimates and the fitting simulation values in the case of the exponent γ_w , which seems to worsen as β decreases. However, in the case of γ_c and γ_{cw} , the agreement is mainly qualitative. This might be due to the fact that the tails of ϕ_c^H and ϕ_{cw}^H are much less populated than that of ϕ_w^H (see Figs. 6 and 7) and, therefore, it is

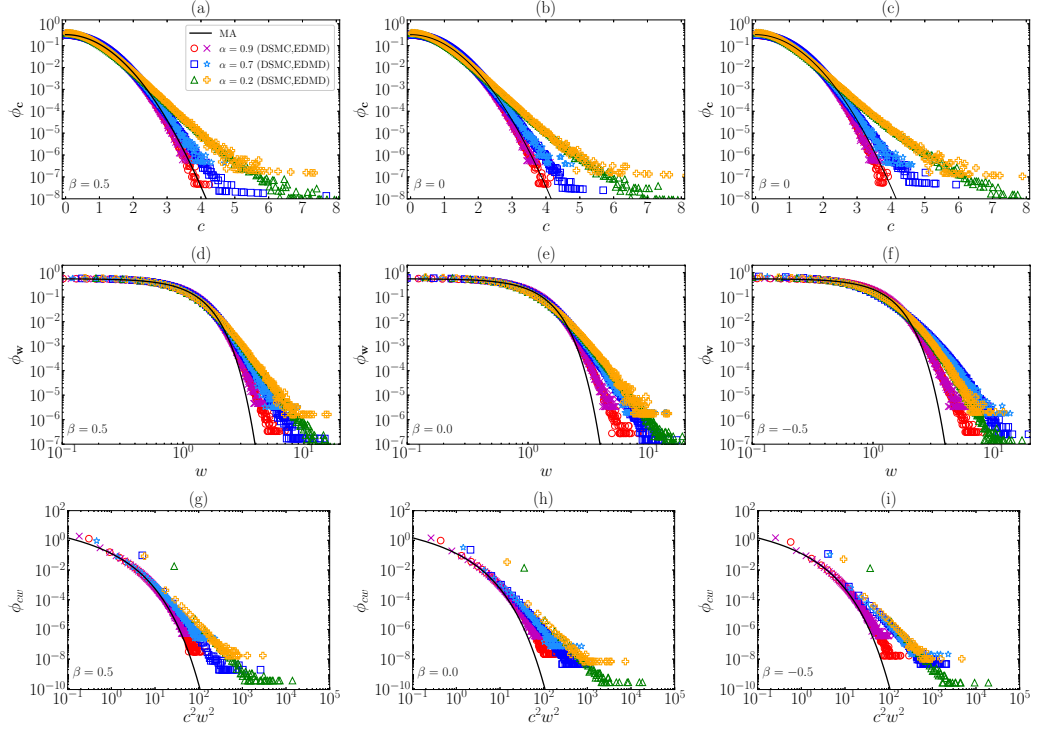


FIG. 6. Simulation histograms for the marginal distributions (a)–(c) ϕ_c , (d)–(f) ϕ_w , and (g)–(i) ϕ_{cw} , for uniform disks ($\kappa = \frac{1}{2}$). The left [(a), (d), (g)], middle [(b), (e), (h)], and right [(c), (f), (i)] panels correspond to $\beta = 0.5, 0$, and -0.5 , respectively. In each panel, three values of α are considered: 0.9 (DSMC: \circ ; EDMD: \times), 0.7 (DSMC: \square ; EDMD: \star), and 0.2 (DSMC: \triangle ; EDMD: $+$). The solid lines represent the marginal distributions in the Maxwellian approximation [see Eqs. (5.3a)]. Note that a log-linear scale is used in (a)–(c) and a log-log scale in (d)–(i).

much more difficult to reach values of c and $c^2 w^2$ high enough to accurately measure the exponents γ_c and γ_{cw} in the simulations. If that were the case, then the values of γ_c and γ_{cw} empirically determined would characterize an intermediate velocity regime previous to the true asymptotic behavior. Of course, one cannot discard that our analysis becomes more limited as β decreases.

Before closing this section, it is worth remarking the excellent mutual agreement between DSMC and EDMD results. There are, however, some small deviations for low values of α , which might be a consequence of the smaller number of disks in the EDMD simulations and also a reflection of possible violations of the molecular chaos ansatz in those highly dissipative systems [71].

VII. CONCLUSIONS

In this paper, we have studied low-density, monodisperse, and homogeneous granular gases of hard disks and hard spheres from a kinetic-theory point of view, using a general framework to express the results in terms of

the number of translational and rotational degrees of freedom, d_t and d_r , respectively. Special attention has been paid to the non-Gaussian features of the HCS, as measured by the fourth-order cumulants and the high-velocity tails of the marginal distributions. The theory has been complemented by DSMC and EDMD computer simulations.

The theoretical approach is based on the Boltzmann equation. First, we have expressed the collisional moments as formally exact functions of the parameters of the system (α , β , and κ) and two-body averages. Next, we have employed a Grad–Sonine expansion of the complete one-body VDF, Eq. (3.15). Then, in analogy to Ref. [39], we have defined the Sonine approximation from the truncation of the Sonine expansion beyond the first nontrivial cumulants defined in Eq. (3.21). This contrasts with the Maxwellian approximation, which is based on approximating the VDF by a two-temperature Maxwellian distribution, i.e., $\phi \approx \phi_M$.

Within the Sonine approximation, and neglecting quadratic terms, the relevant collisional moments have been evaluated, thus recovering previous results for hard

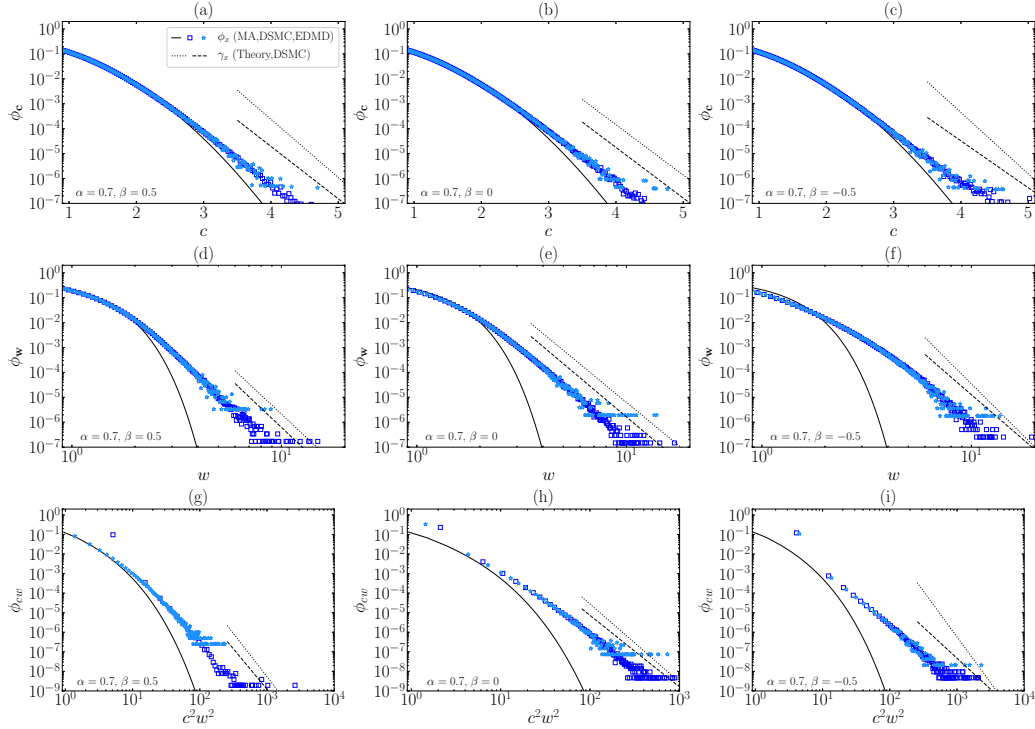


FIG. 7. Same as in Fig. 6, except that only the cases with $\alpha = 0.7$ are shown. The dashed lines represent the exponents γ_c , γ_w , and γ_{cw} obtained by a fit of the DSMC data. The dotted lines represent the theoretical exponents, as given by Eqs. (5.9), (5.13), and (5.15), with the approximations $\mu_{20}^H \approx \mu_{20,M}^H$ [see Eq. (4.1a)] and $\langle\langle c_{12} \rangle\rangle^H \approx \langle\langle c_{12} \rangle\rangle_M = \sqrt{\pi/2}$.

spheres ($d_t = d_r = 3$) [39], and obtaining results for hard disks ($d_t = 2$, $d_r = 1$), as presented in Table I. Cumulant-linearization in Eqs. (3.10a) and (3.22) allows us to deal with a closed set of differential equations for the evolution of the rotational-to-translational temperature ratio (θ) and the fourth-order cumulants. Analogously, the stationary HCS values in the Sonine approximation have been obtained by linearization in Eqs. (3.23). As a consistency test, we have checked in Appendix A that the HCS is linearly stable with respect to homogeneous and isotropic perturbations. The HCS quantities have been shown in Figs. 2 and 3 for uniform disks ($\kappa = \frac{1}{2}$) and uniform spheres ($\kappa = \frac{2}{5}$), respectively. At a qualitative level, their dependence on α and β is very similar for disks and spheres, but the values are generally more extreme in the former system than in the latter. In both cases, the kurtosis for the angular velocity, a_{02}^H , reaches values of $O(1)$ in a lobular region of the parameter space with a vertex at $(\alpha, \beta) = (1, -1)$, thus announcing a breakdown of the Sonine approximation in that region.

Moreover, the non-Gaussianities of the HCS have been studied not only in the context of the first nontrivial cumulants, but also analyzing the tails of the marginal VDF

$\phi_c^H(\mathbf{c})$, $\phi_w^H(\mathbf{w})$, and $\phi_{cw}^H(c^2 w^2)$ defined by Eqs. (5.1). Using previous methods developed for the smooth case [48, 49, 58], which are based on the prevalence of the collisional loss term with respect to the gain term, we have obtained the expected exponential tail $\phi_c^H(\mathbf{c}) \sim e^{-\gamma_c c}$, with formally the same expression for the exponent coefficient γ_c as in the smooth case [see Eq. (5.9)]. On the other hand, we have found much slower scale-free decays $\phi_w^H(\mathbf{w}) \sim w^{-\gamma_w}$ and $\phi_{cw}^H(c^2 w^2) \sim (c^2 w^2)^{-\gamma_{cw}}$, with exponents given by Eqs. (5.13) and (5.15), respectively. These algebraic tails of $\phi_w^H(\mathbf{w})$ and $\phi_{cw}^H(c^2 w^2)$ explain the relatively large values attained by the cumulants a_{02}^H and a_{11}^H , especially in the hard-disk case, and predict divergences in higher-order cumulants which recall the ones already observed in the case of the three-dimensional inelastic and rough Maxwell model [72].

To test the theoretical predictions, we have run DSMC and EDMD computer simulations for hard disks (with $\kappa = \frac{1}{2}$), as described in Sec. VI. First, the quantities θ^H , a_{20}^H , a_{02}^H , and a_{11}^H have been studied for different values of α and β , as depicted in Figs. 4 and 5. The agreement between the Sonine approximation and simulation is rather good, except when the values of the cumulants are not

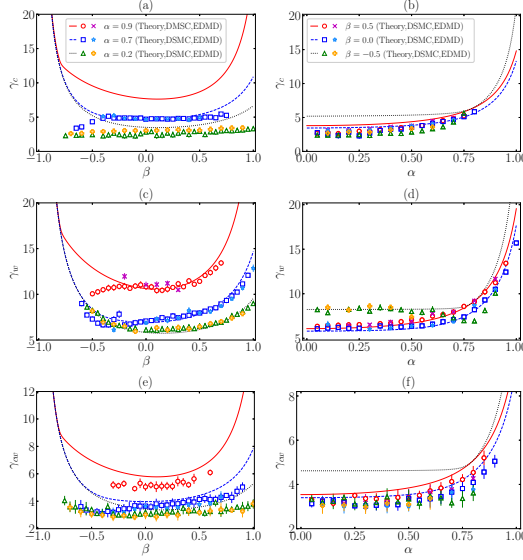


FIG. 8. Plots of (a), (b) γ_c ; (c), (d) γ_w ; and (e), (f) γ_{cw} , for uniform disks ($\kappa = \frac{1}{2}$). The exponents are plotted versus β in the left [(a), (c), (e)] panels and versus α in the right [(b), (d), (f)] panels. Symbols correspond to DSMC (\circ , \square , \triangle) and EDMD (\times , \star , $+$) fitting values, while lines represent the theoretical exponents, as given by Eqs. (5.9), (5.13), and (5.15), with the approximations $\mu_{20}^H \approx \mu_{20,M}^H$ [see Eq. (4.1a)] and $\langle\langle c_{12} \rangle\rangle^H \approx \langle\langle c_{12} \rangle\rangle_M = \sqrt{\pi}/2$.

small. Even in those cases, it is remarkable that the Sonine approximation reproduces qualitatively well the shape of the curves. Second, we have extended the comparison to the three marginal distributions in Figs. 6 and 7, finding that the predicted exponential tail of $\phi_c^H(\mathbf{c})$ and algebraic tails of $\phi_w^H(\mathbf{w})$ and $\phi_{cw}^H(c^2 w^2)$ are supported by simulation data. The theoretical and fitting exponents have been compared in Fig. 8, where a good agreement for γ_w has been observed, while the agreement is more qualitative for γ_c and γ_{cw} . This might be due to a lack of statistically reliable simulation data in the high-velocity regime.

To sum up, the HCS VDF of a monodisperse granular gas of inelastic and rough hard particles is, in general, strongly non-Maxwellian. Moreover, the non-Gaussianities exposed in this paper might solve some inconsistencies reported in the stability analysis of Navier-Stokes hydrodynamics from a Maxwellian approximation in hard-disk systems [46] and improve the predictions of the inelastic hard-sphere model for real experimental systems, such as the one of Ref. [57]. As a follow-up of the study presented in this paper, we plan to extend it to driven hard-disk systems (in analogy to a previous study for hard spheres [41]), whose dynamics has very interesting implications [73, 74]. Finally, we hope this paper

could stimulate further research in all these issues, not only from theoretical and simulation points of view, but also from experimental setups.

The data that support the findings of this study are openly available in Ref. [75].

ACKNOWLEDGMENTS

The authors acknowledge financial support from Grant No. PID2020-112936GB-I00 funded by MCIN/AEI/10.13039/501100011033, and from Grant No. IB20079 funded by Junta de Extremadura (Spain) and by ERDF, “A way of making Europe.” A.M. is grateful to the Spanish Ministerio de Ciencia, Innovación y Universidades for a predoctoral fellowship No. FPU2018-3503. The authors are grateful to the computing facilities of the Instituto de Computación Científica Avanzada of the University of Extremadura (ICCAEx), where the simulations were run.

Appendix A: Linear stability analysis of the homogeneous cooling state

In this Appendix we show that, within the Sonine approximation, the HCS for hard disks is linearly stable under uniform and isotropic perturbations. Let us define the time-dependent set of perturbed quantities:

$$\delta\mathbf{Y}(s) = \begin{pmatrix} \theta(s) - \theta^H \\ a_{20}(s) - a_{20}^H \\ a_{02}(s) - a_{02}^H \\ a_{11}(s) - a_{11}^H \end{pmatrix}. \quad (\text{A1})$$

Insertion into the Sonine approximation versions of Eqs. (3.10a) and (3.22a)–(3.22c), and linearization around the HCS values, yield

$$\partial_s \delta\mathbf{Y}(s) = -\mathbf{L} \cdot \delta\mathbf{Y}(s), \quad (\text{A2})$$

where \mathbf{L} is a constant matrix, its four eigenvalues, $\{\ell_i; i = 1, 2, 3, 4\}$, determining the evolution of $\delta\mathbf{Y}(s)$ from an arbitrary initial perturbation $\delta\mathbf{Y}(0)$.

The dependence of the four eigenvalues on the coefficients of restitution is displayed in Fig. 9 for uniform disks ($\kappa = \frac{1}{2}$). As can be seen, the real parts are always positive, thus signaling the linear stability and attractor character of the HCS under uniform perturbations, as expected on physical grounds. In turn, since the cumulant-linearization scheme within the Sonine approximation is not univocally defined [51, 55], the fact that we get $\text{Re}(\ell_i) > 0$ reinforces the reliability of the linearization criterion applied to the right-hand sides of Eqs. (3.22) and (3.23).

The imaginary parts plotted in Fig. 9(e) show the regions of the parameter space where the decay toward the HCS is oscillatory. In this respect, the plane (α, β) turns out to be split into three disjoint regions: a region where

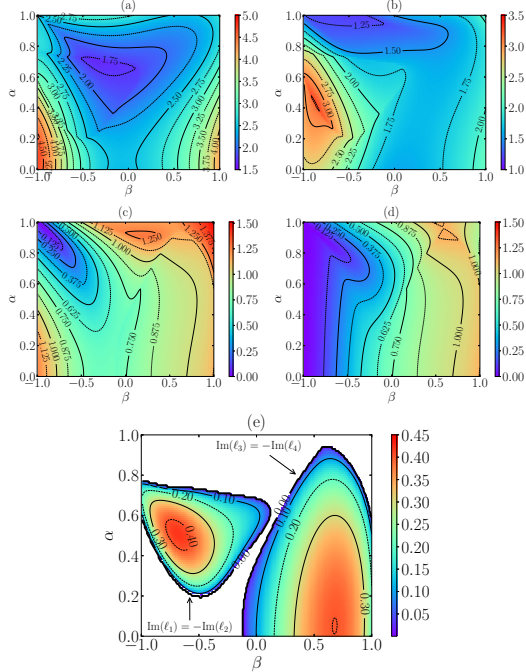


FIG. 9. Plot of the four eigenvalues of the matrix L as functions of α and β for uniform disks ($\kappa = \frac{1}{2}$). (a)–(d) show $\text{Re}(\ell_i)$ for ℓ_1 – ℓ_4 , respectively. The imaginary parts, $\text{Im}(\ell_i)$, are plotted in (e), where all the eigenvalues are real-valued inside the blank region.

(ℓ_1, ℓ_2) make a pair of complex conjugates but (ℓ_3, ℓ_4) are real, a region where (ℓ_3, ℓ_4) make a pair of complex conjugates but (ℓ_1, ℓ_2) are real, and, finally, the blank region in Fig. 9(e), where the four eigenvalues are real.

Appendix B: Consistency of the high-velocity tails

In Sec. VB, the high-velocity tails of the HCS marginal distributions $\phi_c^H(\mathbf{c})$, $\phi_w^H(\mathbf{w})$, and $\phi_{cw}^H(c^2w^2)$ were obtained by assuming Eq. (5.7). Here, we test the self-consistency of that assumption.

1. $\phi_c^H(\mathbf{c})$

Let us insert Eqs. (5.9) into the ratio resulting from the replacement $\phi^H(\tilde{\Gamma}) \rightarrow \phi_c^H(\mathbf{c})$ in Eq. (5.7):

$$\frac{\phi_c^H(\mathbf{c}'_1)\phi_c^H(\mathbf{c}'_2)}{\phi_c^H(\mathbf{c}_1)\phi_c^H(\mathbf{c}_2)} \approx \exp[-\gamma_c(c''_1 + c''_2 - c_1 - c_2)]. \quad (\text{B1})$$

Assuming $c_1 \gg \{1, c_2, w_1, w_2\}$ in the inverse binary collisional rules, Eq. (2.9a), and after some algebra, one gets

15

$$c''_1 \approx c_1 \sqrt{1 + \frac{\bar{\alpha}}{\alpha} \left(\frac{\bar{\alpha}}{\alpha} - 2 \right) \cos^2 \vartheta_c + \frac{\bar{\beta}^2}{\beta^2} \sin^2 \vartheta_c}, \quad (\text{B2a})$$

$$c''_2 \approx c_1 \sqrt{\frac{\bar{\alpha}^2}{\alpha^2} \cos^2 \vartheta_c + \frac{\bar{\beta}^2}{\beta^2} \sin^2 \vartheta_c}, \quad (\text{B2b})$$

where $\vartheta_c = \cos^{-1}|\hat{\mathbf{c}}_1 \cdot \hat{\boldsymbol{\sigma}}|$. Therefore, the exponent in Eq. (B1) is strictly negative, except for smooth particles ($\beta = -1$) and grazing collisions ($\cos \vartheta_c = 0$). Thus, apart from those cases with zero Lebesgue measure, $\lim_{c_1 \rightarrow \infty} \phi_c^H(\mathbf{c}'_1)\phi_c^H(\mathbf{c}'_2)/\phi_c^H(\mathbf{c}_1)\phi_c^H(\mathbf{c}_2) = 0$.

2. $\phi_w^H(\mathbf{w})$

In the rotational case, from Eqs. (5.13) we have

$$\frac{\phi_w^H(\mathbf{w}'_1)\phi_w^H(\mathbf{w}'_2)}{\phi_w^H(\mathbf{w}_1)\phi_w^H(\mathbf{w}_2)} \approx \left(\frac{w'_1 w'_2}{w_1 w_2} \right)^{-\gamma_w}. \quad (\text{B3})$$

Let us take $w_1 \gg \{1, w_2, c_1, c_2\}$. Then,

$$w'_1 \approx w_1 \sqrt{1 + \frac{\bar{\beta}}{\kappa\beta} \left(\frac{\bar{\beta}}{\kappa\beta} - 2 \right) \sin^2 \vartheta_w}, \quad (\text{B4a})$$

$$w'_2 \approx w_1 \frac{\bar{\beta}}{\kappa|\beta|} |\sin \vartheta_w|, \quad (\text{B4b})$$

where $\vartheta_w = \cos^{-1}|\hat{\mathbf{w}}_1 \cdot \hat{\boldsymbol{\sigma}}|$. Therefore, $\lim_{w_1 \rightarrow \infty} \phi_w^H(\mathbf{w}'_1)\phi_w^H(\mathbf{w}'_2)/\phi_w^H(\mathbf{w}_1)\phi_w^H(\mathbf{w}_2) = 0$, except if $\sin \vartheta_w = 0$, which has zero Lebesgue measure in its continuous domain.

3. $\phi_{cw}^H(x)$

From Eqs. (5.15), one has

$$\frac{\phi_{cw}^H(x'_1)\phi_{cw}^H(x'_2)}{\phi_{cw}^H(x_1)\phi_{cw}^H(x_2)} \approx \left(\frac{x'_1 x'_2}{x_1 x_2} \right)^{-\gamma_{cw}}. \quad (\text{B5})$$

If both c_1 and w_1 are much larger than $\{1, c_2, w_2\}$, it is possible to obtain

$$\begin{aligned} x'_1 \approx x_1 & \left[1 + \frac{\bar{\alpha}}{\alpha} \left(\frac{\bar{\alpha}}{\alpha} - 2 \right) \cos^2 \vartheta_c + \frac{\bar{\beta}}{\beta} \left(\frac{\bar{\beta}}{\beta} - 2 \right) \sin^2 \vartheta_c \right. \\ & \left. + \frac{\bar{\beta}^2}{\beta^2} \frac{\theta}{\kappa} \sin^2 \vartheta_w - 2 \frac{\bar{\beta}}{\beta} \left(\frac{\bar{\beta}}{\beta} - 1 \right) \sqrt{\frac{\theta}{\kappa}} \cos \vartheta_{cw} \right] \\ & \times \left[1 + \frac{\bar{\beta}^2}{\beta^2 \kappa \theta} \sin^2 \vartheta_c - \frac{2\bar{\beta}}{\beta \sqrt{\kappa \theta}} \left(\frac{\bar{\beta}}{\beta \kappa} - 1 \right) \cos \theta_{cw} \right. \\ & \left. + \frac{\bar{\beta}}{\beta \kappa} \left(\frac{\bar{\beta}}{\beta \kappa} - 2 \right) \sin^2 \vartheta_w \right], \quad (\text{B6a}) \end{aligned}$$

$$x_2'' \approx \frac{x_1 \bar{\beta}^2}{\kappa \theta \beta^2} \left(\sin^2 \vartheta_c + \frac{\theta}{\kappa} \sin^2 \vartheta_w - 2 \sqrt{\frac{\theta}{\kappa}} \cos \vartheta_{cw} \right) \left[\frac{\bar{\alpha}^2}{\alpha^2} \cos^2 \vartheta_c \right. \\ \left. + \frac{\bar{\beta}^2}{\beta^2} \left(\sin^2 \vartheta_c + \frac{\theta}{\kappa} \sin^2 \vartheta_w - 2 \sqrt{\frac{\theta}{\kappa}} \cos \vartheta_{cw} \right) \right], \quad (\text{B6b})$$

where $\vartheta_{cw} = \cos^{-1}[\hat{\mathbf{c}}_1 \cdot (\hat{\boldsymbol{\sigma}} \times \hat{\mathbf{w}}_1)]$. Thus, $\lim_{x_1 \rightarrow \infty} \frac{\phi_{cw}^H(x_1') \phi_{cw}^H(x_2'')}{\phi_{cw}^H(x_1) \phi_{cw}^H(x_2)} = 0$, except if $\sin \vartheta_c = \sin \vartheta_w = \cos \vartheta_{cw} = 0$, which again have zero Lebesgue measure.

- [1] E. Clement and J. Rajchenbach, Fluidization of a bidimensional powder, *Europhys. Lett.* **16**, 133 (1991).
- [2] K. Feitosa and N. Menon, Breakdown of energy equipartition in a 2D binary vibrated granular gas, *Phys. Rev. Lett.* **88**, 198301 (2002).
- [3] B. Painter, M. Dutt, and R. P. Behringer, Energy dissipation and clustering for a cooling granular material on a substrate, *Physica D* **175**, 43 (2003).
- [4] C. Yanpei, P. Evesque, M. Hou, C. Lecoutre, F. Palencia, and Y. Garrabos, Long range boundary effect of 2D intermediate number density vibro-fluidized granular media in micro-gravity, *J. Phys.: Conf. Ser.* **327**, 012033 (2011).
- [5] R. Bartali, Y. Nahmad-Molinari, and G. M. Rodríguez-Liñán, Low speed granular–granular impact crater opening mechanism in 2D experiments, *Earth Moon Planets* **116**, 115 (2015).
- [6] Y. Grasselli, G. Bossis, and R. Morini, Translational and rotational temperatures of a 2D vibrated granular gas in microgravity, *Eur. Phys. J. E* **38**, 8 (2015).
- [7] C. Scholz and T. Pöschel, Velocity distribution of a homogeneously driven two-dimensional granular gas, *Phys. Rev. Lett.* **118**, 198003 (2017).
- [8] Y. Grasselli, G. Bossis, A. Meunier, and O. Volkova, Dynamics of a 2D vibrated model granular gas in micro-gravity, in *Granular Materials*, edited by M. Sakellariou (IntechOpen, Rijeka, Croatia, 2017) Chap. 4, pp. 71–96.
- [9] M. A. López-Castaño, J. F. González-Saavedra, A. Rodríguez-Rivas, E. Abad, S. B. Yuste, and F. Vega Reyes, Pseudo-two-dimensional dynamics in a system of macroscopic rolling spheres, *Phys. Rev. E* **103**, 042903 (2021).
- [10] M. Ledesma-Motolinía, J. L. Carrillo-Estrada, and F. Donado, Crystallisation in a two-dimensional granular system at constant temperature, *Sci. Rep.* **11**, 16531 (2021).
- [11] S. McNamara, Hydrodynamic modes of a uniform granular medium, *Phys. Fluids A* **5**, 3056 (1993).
- [12] A. Goldshtein and M. Shapiro, Mechanics of collisional motion of granular materials. Part 1. General hydrodynamic equations, *J. Fluid Mech.* **282**, 75 (1995).
- [13] E. L. Grossman, T. Zhou, and E. Ben-Naim, Towards granular hydrodynamics in two dimensions, *Phys. Rev. E* **55**, 4200 (1997).
- [14] N. Sela and I. Goldhirsch, Hydrodynamic equations for rapid flows of smooth inelastic spheres, to Burnett order, *J. Fluid Mech.* **361**, 41 (1998).
- [15] J. W. Dufty, Statistical mechanics, kinetic theory, and hydrodynamics for rapid granular flow, *J. Phys.: Condens. Matter* **12**, A47 (2000).
- [16] J. W. Dufty, Kinetic theory and hydrodynamics for a low density granular gas, *Adv. Complex Syst.* **4**, 397 (2001).
- [17] V. Garzó and J. W. Dufty, Hydrodynamics for a granular mixture at low density, *Phys. Fluids* **14**, 1476 (2002).
- [18] N. Brilliantov and T. Pöschel, Hydrodynamics and transport coefficients for dilute granular gases, *Phys. Rev. E* **67**, 061304 (2003).
- [19] I. Goldhirsch, S. H. Noskowitz, and O. Bar-Lev, Hydrodynamics of nearly smooth granular gases, *J. Phys. Chem. B* **109**, 21449 (2005).
- [20] D. Serero, I. Goldhirsch, S. H. Noskowitz, and M.-L. Tan, Hydrodynamics of granular gases and granular gas mixtures, *J. Fluid Mech.* **554**, 237 (2006).
- [21] F. Vega Reyes and J. S. Urbach, Steady base states for Navier-Stokes granular hydrodynamics with boundary heating and shear, *J. Fluid Mech.* **636**, 279 (2009).
- [22] F. Vega Reyes, A. Santos, and V. Garzó, Non-Newtonian granular hydrodynamics. What do the inelastic simple shear flow and the elastic Fourier flow have in common?, *Phys. Rev. Lett.* **104**, 028001 (2010).
- [23] J. W. Dufty and J. J. Brey, Choosing hydrodynamic fields, *Math. Model. Nat. Phenom.* **6**, 19 (2011).
- [24] V. Garzó and A. Santos, Hydrodynamics of inelastic Maxwell models, *Math. Model. Nat. Phenom.* **6**, 37 (2011).
- [25] G. Gradenigo, A. Sarracino, D. Villamaina, and A. Puglisi, Fluctuating hydrodynamics and correlation lengths in a driven granular fluid, *J. Stat. Mech.* , P08017 (2011).
- [26] G. Gradenigo, A. Sarracino, D. Villamaina, and A. Puglisi, Non-equilibrium length in granular fluids: From experiment to fluctuating hydrodynamics, *EPL* **96**, 14004 (2011).
- [27] M. I. García de Soria, P. Maynar, and E. Trizac, Linear hydrodynamics for driven granular gases, *Phys. Rev. E* **87**, 022201 (2013).
- [28] V. Garzó, *Granular Gaseous Flows. A Kinetic Theory Approach to Granular Gaseous Flows* (Springer Nature, Switzerland, 2019).
- [29] C. S. Campbell, Rapid granular flows, *Annu. Rev. Fluid Mech.* **22**, 57 (1990).
- [30] T. Pöschel and S. Luding, eds., *Granular Gases*, Lecture Notes in Physics, Vol. 564 (Springer, Berlin, 2001).
- [31] I. Goldhirsch, Rapid granular flows, *Annu. Rev. Fluid Mech.* **35**, 267 (2003).
- [32] N. V. Brilliantov and T. Pöschel, *Kinetic Theory of Granular Gases* (Oxford University Press, Oxford, 2004).
- [33] N. Maw, J. R. Barber, and J. N. Fawcett, The oblique impact of elastic spheres, *Wear* **38**, 101 (1976).
- [34] A. Lorenz, C. Tuozzolo, and M. Y. Louge, Measurements of impact properties of small, nearly spherical particles, *Exp. Mech.* **37**, 292 (1997).
- [35] T. Aspelmeier, M. Huthmann, and A. Zippelius, Free cooling of particles with rotational degrees of freedom,

- in *Granular Gases*, Lectures Notes in Physics, Vol. 564, edited by T. Pöschel and S. Luding (Springer, Berlin, 2001) pp. 31–58.
- [36] N. V. Brilliantov, T. Pöschel, W. T. Kranz, and A. Zippelius, Translations and rotations are correlated in granular gases, *Phys. Rev. Lett.* **98**, 128001 (2007).
- [37] A. Santos, G. M. Kremer, and V. Garzó, Energy production rates in fluid mixtures of inelastic rough hard spheres, *Prog. Theor. Phys. Suppl.* **184**, 31 (2010).
- [38] A. Santos, G. M. Kremer, and M. dos Santos, Sonine approximation for collisional moments of granular gases of inelastic rough spheres, *Phys. Fluids* **23**, 030604 (2011).
- [39] F. Vega Reyes, A. Santos, and G. M. Kremer, Role of roughness on the hydrodynamic homogeneous base state of inelastic spheres, *Phys. Rev. E* **89**, 020202(R) (2014).
- [40] F. Vega Reyes, A. Santos, and G. M. Kremer, Properties of the homogeneous cooling state of a gas of inelastic rough particles, *AIP Conf. Proc.* **1628**, 494 (2014).
- [41] F. Vega Reyes and A. Santos, Steady state in a gas of inelastic rough spheres heated by a uniform stochastic force, *Phys. Fluids* **27**, 113301 (2015).
- [42] A. Santos, Interplay between polydispersity, inelasticity, and roughness in the freely cooling regime of hard-disk granular gases, *Phys. Rev. E* **98**, 012904 (2018).
- [43] A. Megías and A. Santos, Driven and undriven states of multicomponent granular gases of inelastic and rough hard disks or spheres, *Granul. Matter* **21**, 49 (2019).
- [44] A. Megías and A. Santos, Energy production rates of multicomponent granular gases of rough particles. A unified view of hard-disk and hard-sphere systems, *AIP Conf. Proc.* **2132**, 080003 (2019).
- [45] A. Megías and A. Santos, Hydrodynamics of granular gases of inelastic and rough hard disks or spheres. I. Transport coefficients, *Phys. Rev. E* **104**, 034901 (2021).
- [46] A. Megías and A. Santos, Hydrodynamics of granular gases of inelastic and rough hard disks or spheres. II. Stability analysis, *Phys. Rev. E* **104**, 034902 (2021).
- [47] J. J. Brey, M. J. Ruiz-Montero, and D. Cubero, Homogeneous cooling state of a low-density granular flow, *Phys. Rev. E* **54**, 3664 (1996).
- [48] T. P. C. van Noije and M. H. Ernst, Velocity distributions in homogeneous granular fluids: the free and the heated case, *Granul. Matter* **1**, 57 (1998).
- [49] J. J. Brey, M. J. Ruiz-Montero, and D. Cubero, On the validity of linear hydrodynamics for low-density granular flows described by the Boltzmann equation, *Europhys. Lett.* **48**, 359 (1999).
- [50] N. Brilliantov and T. Pöschel, Deviation from Maxwell distribution in granular gases with constant restitution coefficient, *Phys. Rev. E* **61**, 2809 (2000).
- [51] J. M. Montanero and A. Santos, Computer simulation of uniformly heated granular fluids, *Granul. Matter* **2**, 53 (2000).
- [52] N. Brilliantov and T. Pöschel, Breakdown of the Sonine expansion for the velocity distribution of granular gases, *Europhys. Lett.* **74**, 424 (2006), **75** 188(E), (2006).
- [53] S. R. Ahmad and S. Puri, Velocity distributions in a freely evolving granular gas, *Europhys. Lett.* **75**, 56 (2006).
- [54] S. R. Ahmad and S. Puri, Velocity distributions and aging in a cooling granular gas, *Phys. Rev. E* **75**, 031302 (2007).
- [55] A. Santos and J. M. Montanero, The second and third Sonine coefficients of a freely cooling granular gas revisited, *Granul. Matter* **11**, 157 (2009).
- [56] N. Khalil, V. Garzó, and A. Santos, Hydrodynamic Burnett equations for inelastic Maxwell models of granular gases, *Phys. Rev. E* **89**, 052201 (2014).
- [57] P. Yu, M. Schröter, and M. Sperl, Velocity distribution of a homogeneously cooling granular gas, *Phys. Rev. Lett.* **124**, 208007 (2020).
- [58] S. E. Esipov and T. Pöschel, The granular phase diagram, *J. Stat. Phys.* **86**, 1385 (1997).
- [59] T. Pöschel, N. V. Brilliantov, and A. Formella, Impact of high-energy tails on granular gas properties, *Phys. Rev. E* **74**, 041302 (2006).
- [60] Y. Chen and J. Zhang, High-energy velocity tails in uniformly heated granular materials, *Phys. Rev. E* **106**, L052903 (2022).
- [61] G. M. Kremer, A. Santos, and V. Garzó, Transport coefficients of a granular gas of inelastic rough hard spheres, *Phys. Rev. E* **90**, 022205 (2014).
- [62] A. Megías and A. Santos, Kullback–Leibler divergence of a freely cooling granular gas, *Entropy* **22**, 1308 (2020).
- [63] V. Garzó, A. Santos, and G. M. Kremer, Impact of roughness on the instability of a free-cooling granular gas, *Phys. Rev. E* **97**, 052901 (2018).
- [64] V. Garzó and A. Santos, *Kinetic Theory of Gases in Shear Flows: Nonlinear Transport*, Fundamental Theories of Physics (Springer, Dordrecht, 2003).
- [65] P. K. Haff, Grain flow as a fluid-mechanical phenomenon, *J. Fluid Mech.* **134**, 401 (1983).
- [66] See Supplemental Material at <http://link.aps.org/supplemental/10.1103/PhysRevE.108.014902> for details on the evaluation of the collisional moments, a Kullback–Leibler divergence-like functional, the high-velocity tail of the marginal distribution $\phi_{cw}(c^2 w^2)$, and further comparisons with computer simulations, which includes Ref. [76].
- [67] M. Abramowitz and I. A. Stegun, eds., *Handbook of Mathematical Functions* (Dover, New York, 1972).
- [68] S. Chapman and T. G. Cowling, *The Mathematical Theory of Non-Uniform Gases*, 3rd ed. (Cambridge University Press, Cambridge, UK, 1970).
- [69] G. A. Bird, *Molecular Gas Dynamics and the Direct Simulation of Gas Flows* (Clarendon, Oxford, UK, 1994).
- [70] G. A. Bird, *The DSMC Method* (CreateSpace Independent Publishing Platform, Scotts Valley, CA, 2013).
- [71] R. Soto and M. Mareschal, Statistical mechanics of fluidized granular media: Short-range velocity correlations, *Phys. Rev. E* **63**, 041303 (2001).
- [72] G. M. Kremer and A. Santos, Granular gas of inelastic and rough Maxwell particles, *J. Stat. Phys.* **189**, 23 (2022).
- [73] A. Torrente, M. A. López-Castaño, A. Lasanta, F. Vega Reyes, A. Prados, and A. Santos, Large Mpemba-like effect in a gas of inelastic rough hard spheres, *Phys. Rev. E* **99**, 060901(R) (2019).
- [74] A. Megías and A. Santos, Mpemba-like effect protocol for granular gases of inelastic and rough hard disks, *Front. Phys.* **10**, 971671 (2022).
- [75] A. Megías, Simulation Results of “Translational and rotational non-Gaussianities in homogenous freely evolving granular gases”, <https://github.com/amegiasf/NonGaussianIRHD>, (2023).
- [76] P. Young, *Everything You Wanted to Know About Data Analysis and Fitting but Were Afraid to Ask*, Springer-Briefs in Physics (Springer, Cham, 2015).

Supplementary Material to “Translational and rotational non-Gaussianities in homogeneous freely evolving granular gases”

Alberto Megías*

Departamento de Física, Universidad de Extremadura, E-06006 Badajoz, Spain

Andrés Santos†

Departamento de Física, Universidad de Extremadura, E-06006 Badajoz, Spain and

Instituto de Computación Científica Avanzada (ICCAEX),

Universidad de Extremadura, E-06006 Badajoz, Spain

(Dated: July 21, 2023)

In this Supplementary Material we give some helpful expressions and integrals used to compute the collisional moments, both as functions of two-body averages, and from the Sonine approximation. We also expose a comparison between the time evolution toward the HCS of the quantities θ , a_{20} , a_{02} and a_{11} , as predicted by the Sonine approximation, and simulation results, as well as for μ_{20}^H , μ_{02}^H , and $\langle\langle c_{12} \rangle\rangle^H$. Finally, some details about the theoretical derivations and fitting of the high-velocity tails are developed.

I. EVALUATION OF THE COLLISIONAL MOMENTS AS FUNCTIONS OF d_t AND d_r

A. Angular integrals

Some angular integrals are used in the computation of collisional moments. Here, we generalize the results for a d -dimensional Euclidean vector space,

$$\int_+ d\hat{\sigma} (\mathbf{c} \cdot \hat{\sigma})^\ell = B_\ell c^\ell, \quad B_\ell \equiv \frac{\pi^{\frac{d_t-1}{2}} \Gamma(\frac{\ell+1}{2})}{\Gamma(\frac{\ell+d_t}{2})} \quad (1.1a)$$

$$\int_+ d\hat{\sigma} (\mathbf{c} \cdot \hat{\sigma})^\ell \hat{\sigma}_i = B_{\ell+1} c^{\ell-1} c_i, \quad (1.1b)$$

$$\int_+ d\hat{\sigma} (\mathbf{c} \cdot \hat{\sigma})^\ell \hat{\sigma}_i \hat{\sigma}_j = B_{\ell+2} c^{\ell-2} c_i c_j + \frac{B_\ell - B_{\ell+2}}{d-1} c^\ell \delta_{ij}^\perp, \quad (1.1c)$$

$$\int_+ d\hat{\sigma} (\mathbf{c} \cdot \hat{\sigma})^\ell \hat{\sigma}_i \hat{\sigma}_j \hat{\sigma}_k = B_{\ell+3} c^{\ell-3} c_i c_j c_k + 3 \frac{B_{\ell+1} - B_{\ell+3}}{d-1} c^{\ell-1} c_{(i} \delta_{jk)}^\perp, \quad (1.1d)$$

$$\int_+ d\hat{\sigma} (\mathbf{c} \cdot \hat{\sigma})^\ell \hat{\sigma}_i \hat{\sigma}_j \hat{\sigma}_k \hat{\sigma}_m = B_{\ell+4} c^{\ell-4} c_i c_j c_k c_m + 6 \frac{B_{\ell+2} - B_{\ell+4}}{d-1} c^{\ell-2} c_{(i} c_j \delta_{km)}^\perp + 3 \frac{B_{\ell+4} - 2B_{\ell+2} + B_\ell}{d^2 - 1} c^\ell \delta_{(ij}^\perp \delta_{km)}^\perp, \quad (1.1e)$$

where $\delta_{ij}^\perp \equiv \delta_{ij} - \hat{c}_i \hat{c}_j$ and the notation with indices enclosed by parentheses means that one is totally symmetrizing the tensors over such indices, i.e.,

$$c_{(i} \delta_{jk)}^\perp = \frac{1}{3} (c_i \delta_{jk}^\perp + c_j \delta_{ik}^\perp + c_k \delta_{ij}^\perp), \quad (1.2a)$$

$$c_{(i} c_j \delta_{km)}^\perp = \frac{1}{6} (c_i c_j \delta_{km}^\perp + c_i c_k \delta_{jm}^\perp + c_i c_m \delta_{jk}^\perp + c_j c_k \delta_{im}^\perp + c_j c_m \delta_{ik}^\perp + c_k c_m \delta_{ij}^\perp), \quad (1.2b)$$

$$\delta_{(ij}^\perp \delta_{km)}^\perp = \frac{1}{3} (\delta_{ij}^\perp \delta_{km}^\perp + \delta_{ik}^\perp \delta_{jm}^\perp + \delta_{im}^\perp \delta_{jk}^\perp). \quad (1.2c)$$

B. Levi-Civita summations for disks and spheres

As introduced in the main text, whereas we worked in a generalized framework, in which expressions are given in terms of the numbers of translational and rotational degrees of freedom of the problem, d_t and d_r , respectively, we

* albertom@unex.es

† andres@unex.es

took into account only two- and three-dimensional setups. In the case of hard disks, translational velocities are vectors of a two-dimensional Euclidean space \mathfrak{C} , whereas the space of the angular velocities is a one-dimensional Euclidean space \mathfrak{W} orthogonal to the previous one, that is, $\mathfrak{W} = \mathfrak{C}^\perp$, such that the total space, $\mathfrak{E}^3 = \mathfrak{C} \oplus \mathfrak{W}$. On the other hand, trivially for hard spheres, $\mathfrak{C} = \mathfrak{W} = \mathfrak{E}^3$. Then, we wrote all relations using general vector notation for elements in the three-dimensional Euclidean space \mathfrak{E}^3 .

Some vector cross products appear in the computation of the collisional moments, involving both translational and angular velocity variables. Then, it is convenient to express formally those vector products in terms of the three-dimensional Levi-Civita tensor in \mathfrak{E}^3 , ε_{ijk} . For example, we face terms of the kind $(\mathbf{c} \times \mathbf{w})_i = \varepsilon_{ijk} c_j w_k$, where we are using Einstein's convention of summation over repeated indices.

Let us denote by $\bar{\delta}_{ij}$ the metric of our translational Euclidean space \mathfrak{C} of dimension $d_t = 2$ and 3 for disks and spheres, respectively. Therefore, if δ_{ij} is the metric of the total embedding space \mathfrak{E}^3 , then $\bar{\delta}_{ij} \delta_{jk} = \bar{\delta}_{ik}$.

During some computations we faced expressions of the kind $\varepsilon_{ijk} \varepsilon_{ilm}$. Thus, using the identity

$$\varepsilon_{ijk} \varepsilon_{lmn} = \delta_{il} (\delta_{jm} \delta_{kn} - \delta_{jn} \delta_{km}) - \delta_{im} \delta_{jl}, \quad (1.3)$$

if the indices i and l are contracted by the metric in \mathfrak{C} , then

$$\bar{\delta}_{il} \varepsilon_{ijk} \varepsilon_{ilm} = d_t (\delta_{jm} \delta_{kn} - \delta_{jn} \delta_{km}) - (\bar{\delta}_{jm} \delta_{kn} - \delta_{jn} \bar{\delta}_{km}) - (\delta_{jm} \bar{\delta}_{kn} - \bar{\delta}_{jn} \delta_{km}), \quad (1.4)$$

where we have used that $\bar{\delta}_{ii} = d_t$.

Let us use this methodology in an example of an angular integral involving translational and rotational variables,

$$\begin{aligned} \int_+ d\hat{\boldsymbol{\sigma}} (\mathbf{c} \cdot \hat{\boldsymbol{\sigma}})^p [\mathbf{c} \cdot (\hat{\boldsymbol{\sigma}} \times \mathbf{w})]^2 &= c_i c_l \left[\int_+ d\hat{\boldsymbol{\sigma}} (\mathbf{c} \cdot \hat{\boldsymbol{\sigma}})^p \hat{\sigma}_j \hat{\sigma}_m \right] \varepsilon_{ijk} \varepsilon_{lmn} w_k w_n \\ &= c_i c_l \left[B_{p+2} c^{p-2} c_j c_m + \frac{B_p - B_{p+2}}{d_t - 1} c^p \bar{\delta}_{jm}^\perp \right] \varepsilon_{ijk} \varepsilon_{lmn} w_k w_n \\ &= c_i c_l \left[B_{p+2} c^{p-2} c_j c_m + \frac{B_p - B_{p+2}}{d_t - 1} c^p (\bar{\delta}_{jm} - \hat{c}_j \hat{c}_m) \right] \varepsilon_{ijk} \varepsilon_{lmn} w_k w_n \\ &= B_{p+2} c^{p-2} [\mathbf{c} \cdot (\mathbf{c} \times \mathbf{w})]^2 + \frac{B_p - B_{p+2}}{d_t - 1} \left\{ c^p [d_t (\delta_{il} \delta_{kn} - \delta_{in} \delta_{kl}) \right. \\ &\quad \left. - (\bar{\delta}_{il} \delta_{kn} - \delta_{in} \bar{\delta}_{kl}) - (\delta_{il} \bar{\delta}_{kn} - \bar{\delta}_{in} \delta_{kl})] c_i c_l w_k w_n - c^{p-2} [\mathbf{c} \cdot (\mathbf{c} \times \mathbf{w})]^2 \right\} \\ &= \frac{B_p - B_{p+2}}{d_t - 1} c^p [d_t (\delta_{il} \delta_{kn} - \delta_{in} \delta_{kl}) - (\bar{\delta}_{il} \delta_{kn} - \delta_{in} \bar{\delta}_{kl}) - (\delta_{il} \bar{\delta}_{kn} - \bar{\delta}_{in} \delta_{kl})] c_i c_l w_k w_n \\ &= \frac{B_p - B_{p+2}}{d_t - 1} [c^{p+2} w^2 - (4 - d_t) c^p (\mathbf{c} \cdot \mathbf{w})^2]. \end{aligned} \quad (1.5)$$

For disks ($d_t = 2$, $d_r = 1$), we have $\mathbf{c} \perp \mathbf{w}$, so that the second term vanishes. Then, one can simply replace $(4 - d_t) c^p (\mathbf{c} \cdot \mathbf{w})^2$ by $\frac{d_r - 1}{2} c^p (\mathbf{c} \cdot \mathbf{w})^2$, which holds both for hard disks and hard spheres. Following the same reasoning, one gets, for instance,

$$\begin{aligned} \int_+ d\hat{\boldsymbol{\sigma}} (\mathbf{c}_{12} \cdot \hat{\boldsymbol{\sigma}})^p [\mathbf{C}_{12} \cdot (\hat{\boldsymbol{\sigma}} \times \mathbf{W}_{12})]^2 &= \left(B_{p+2} - \frac{B_p - B_{p+2}}{d_t - 1} \right) c_{12}^p [\mathbf{C}_{12} \cdot (\mathbf{c}_{12} \times \mathbf{W}_{12})]^2 \\ &\quad + \frac{B_p - B_{p+2}}{d_t - 1} \left[c_{12}^p C_{12}^2 W_{12}^2 - \frac{d_r - 1}{2} c_{12}^p (\mathbf{C}_{12} \cdot \mathbf{W}_{12})^2 \right], \end{aligned} \quad (1.6)$$

where we have called $C_{12} \equiv \frac{1}{2} (\mathbf{c}_1 + \mathbf{c}_2)$.

C. Computations of collisional moments

1. Collisional impulse

In Sec. II B of the main paper we expressed the postcollisional velocities in terms of the (reduced) impulse Δ_{12} . It is then possible to derive the following results:

$$\Delta_{12}^2 = \bar{\alpha}^2 (\mathbf{c}_{12} \cdot \hat{\boldsymbol{\sigma}})^2 + \bar{\beta}^2 [c_{12}^2 - (\mathbf{c}_{12} \cdot \hat{\boldsymbol{\sigma}})^2] + 4 \frac{\theta}{\kappa} (\hat{\boldsymbol{\sigma}} \times \mathbf{W}_{12})^2 - 4 \sqrt{\frac{\theta}{\kappa}} \mathbf{c}_{12} \cdot (\hat{\boldsymbol{\sigma}} \times \mathbf{W}_{12}), \quad (1.7a)$$

$$\hat{\boldsymbol{\sigma}} \cdot \Delta_{12} = \bar{\alpha} (\mathbf{c}_{12} \cdot \hat{\boldsymbol{\sigma}}), \quad (1.7b)$$

$$\begin{aligned} \Delta_{12}^4 = & \bar{\alpha}^4 (\mathbf{c}_{12} \cdot \hat{\boldsymbol{\sigma}})^4 + \bar{\beta}^4 \left\{ c_{12}^4 + (\mathbf{c}_{12} \cdot \hat{\boldsymbol{\sigma}})^4 - 2c_{12}^2 (\mathbf{c}_{12} \cdot \hat{\boldsymbol{\sigma}})^2 + 16 \frac{\theta^2}{\kappa^2} [W_{12}^4 + (\hat{\boldsymbol{\sigma}} \cdot \mathbf{W}_{12})^4 - 2W_{12}^2 (\hat{\boldsymbol{\sigma}} \cdot \mathbf{W}_{12})^2] \right. \\ & + 16 \frac{\theta}{\kappa} [\mathbf{c}_{12} \cdot (\hat{\boldsymbol{\sigma}} \times \mathbf{W}_{12})]^2 - 8 \sqrt{\frac{\theta}{\kappa}} [\mathbf{c}_{12} \cdot (\hat{\boldsymbol{\sigma}} \times \mathbf{W}_{12})] \left[c_{12}^2 - (\mathbf{c}_{12} \cdot \hat{\boldsymbol{\sigma}})^2 + \frac{4\theta}{\kappa} (\hat{\boldsymbol{\sigma}} \times \mathbf{W}_{12})^2 \right] \\ & \left. + 8 \frac{\theta}{\kappa} [W_{12}^2 - (\mathbf{W}_{12} \cdot \hat{\boldsymbol{\sigma}})^2] [c_{12}^2 - (\mathbf{c}_{12} \cdot \hat{\boldsymbol{\sigma}})^2] \right\} + 2\bar{\alpha}^2 \bar{\beta}^2 \left\{ c_{12}^2 (\mathbf{c}_{12} \cdot \hat{\boldsymbol{\sigma}})^2 - (\mathbf{c}_{12} \cdot \hat{\boldsymbol{\sigma}})^4 \right. \\ & \left. + 4 \frac{\theta}{\kappa} [W_{12}^2 - (\hat{\boldsymbol{\sigma}} \cdot \mathbf{W}_{12})^2] (\mathbf{c}_{12} \cdot \hat{\boldsymbol{\sigma}})^2 \right\}, \end{aligned}$$

$$\begin{aligned} \Delta_{12}^2 (\hat{\boldsymbol{\sigma}} \cdot \Delta_{12})^2 = & \bar{\alpha}^4 (\mathbf{c}_{12} \cdot \hat{\boldsymbol{\sigma}})^4 + \bar{\beta}^2 \bar{\alpha}^2 \left\{ c_{12}^2 (\mathbf{c}_{12} \cdot \hat{\boldsymbol{\sigma}})^2 - (\mathbf{c}_{12} \cdot \hat{\boldsymbol{\sigma}})^4 + 4 \frac{\theta}{\kappa} [W_{12}^2 - (\hat{\boldsymbol{\sigma}} \cdot \mathbf{W}_{12})^2] (\mathbf{c}_{12} \cdot \hat{\boldsymbol{\sigma}})^2 \right. \\ & \left. - 4 \sqrt{\frac{\theta}{\kappa}} (\mathbf{c}_{12} \cdot \hat{\boldsymbol{\sigma}}) [\mathbf{c}_{12} \cdot (\hat{\boldsymbol{\sigma}} \times \mathbf{W}_{12})] \right\}, \end{aligned} \quad (1.7c)$$

$$\hat{\boldsymbol{\sigma}} \times \Delta_{12} = \bar{\beta} \left\{ (\hat{\boldsymbol{\sigma}} \times \mathbf{c}_{12}) + 2 \sqrt{\frac{\theta}{\kappa}} [\mathbf{W}_{12} - (\hat{\boldsymbol{\sigma}} \cdot \mathbf{W}_{12}) \hat{\boldsymbol{\sigma}}] \right\}, \quad (1.7d)$$

$$\mathbf{c}_{12} \cdot \Delta_{12} = \bar{\alpha} (\mathbf{c}_{12} \cdot \hat{\boldsymbol{\sigma}})^2 + \bar{\beta} \left[c_{12}^2 - (\mathbf{c}_{12} \cdot \hat{\boldsymbol{\sigma}})^2 - 2 \sqrt{\frac{\theta}{\kappa}} \mathbf{c}_{12} \cdot (\hat{\boldsymbol{\sigma}} \times \mathbf{W}_{12}) \right], \quad (1.7e)$$

$$\mathbf{C}_{12} \cdot \Delta_{12} = \bar{\alpha} (\mathbf{c}_{12} \cdot \hat{\boldsymbol{\sigma}}) (\mathbf{C}_{12} \cdot \hat{\boldsymbol{\sigma}}) + \bar{\beta} \left[\mathbf{c}_{12} \cdot \mathbf{C}_{12} - (\mathbf{c}_{12} \cdot \hat{\boldsymbol{\sigma}}) (\mathbf{C}_{12} \cdot \hat{\boldsymbol{\sigma}}) - 2 \sqrt{\frac{\theta}{\kappa}} \mathbf{C}_{12} \cdot (\hat{\boldsymbol{\sigma}} \times \mathbf{W}_{12}) \right], \quad (1.7f)$$

where use has been made the following vector relations,

$$\hat{\boldsymbol{\sigma}} \times (\hat{\boldsymbol{\sigma}} \times \mathbf{A}) = (\hat{\boldsymbol{\sigma}} \times \mathbf{A}) \hat{\boldsymbol{\sigma}} - \mathbf{A}, \quad (\hat{\boldsymbol{\sigma}} \times \mathbf{A}) \cdot (\hat{\boldsymbol{\sigma}} \times \mathbf{B}) = \mathbf{A} \cdot \mathbf{B} - (\hat{\boldsymbol{\sigma}} \cdot \mathbf{A})(\hat{\boldsymbol{\sigma}} \cdot \mathbf{B}). \quad (1.8)$$

2. Collisional changes

As seen in the main text, the (reduced) collisional moments can be written as

$$\mu_{pq}^{(r)} = -\frac{1}{2} \int d\tilde{\Gamma}_1 \int d\tilde{\Gamma}_2 \int_+ d\hat{\boldsymbol{\sigma}} (\mathbf{c}_{12} \cdot \hat{\boldsymbol{\sigma}}) \phi(\tilde{\Gamma}_1) \phi(\tilde{\Gamma}_2) (\mathcal{B}_{12, \hat{\boldsymbol{\sigma}}} - 1) \left[\psi_{pq}^{(r)}(\tilde{\Gamma}_1) + \psi_{pq}^{(r)}(\tilde{\Gamma}_2) \right], \quad \psi_{pq}^{(r)}(\tilde{\Gamma}) \equiv c^p w^q (\mathbf{c} \cdot \mathbf{w})^r. \quad (1.9)$$

Using Eqs. (1.7a), we have obtained the collisional changes associated with the second- and fourth-order collisional moments. They are displayed in Table I.

3. Collisional moments in terms of two-body averages

Once the collisional changes displayed in Table I are inserted into Eq. (1.9) and the angular integrals are performed (see Sec. IA), the collisional moments can be expressed in terms of two-body averages. The results are listed in Table II, where, as in the main text, we have simplified the notation as $\mu_{pq}^{(0)} \rightarrow \mu_{pq}$. We do not include $\mu_{00}^{(2)}$ because it is meaningful only for hard spheres and is already known.[1]

TABLE I. Collisional changes of the quantities $\psi_{pq}^{(r)}(\tilde{\Gamma})$ with $p + q + 2r = 2$ and 4.

(p, q, r)	$\psi_{pq}^{(r)}(\tilde{\Gamma})$	$(\mathcal{B}_{12, \hat{\sigma}} - 1) [\psi_{pq}^{(r)}(\tilde{\Gamma}_1) + \psi_{pq}^{(r)}(\tilde{\Gamma}_2)]$
(2, 0, 0)	c^2	$2[\Delta_{12}^2 - (\mathbf{c}_{12} \cdot \Delta_{12})]$
(0, 2, 0)	w^2	$\frac{2}{\kappa\theta} [\Delta_{12}^2 - (\hat{\sigma} \cdot \Delta_{12})^2] - \frac{4}{\sqrt{\kappa\theta}} \mathbf{W}_{12} \cdot (\hat{\sigma} \times \Delta_{12})$
(4, 0, 0)	c^4	$2\Delta_{12}^4 + 2[(\mathbf{c}_{12} \cdot \Delta_{12})^2 + 4(\mathbf{C}_{12} \cdot \Delta_{12})^2] + \Delta_{12}^2(c_{12}^2 + 4C_{12}^2) - 4\Delta_{12}^2(\mathbf{c}_{12} \cdot \Delta_{12}) - 8(\mathbf{C}_{12} \cdot \Delta_{12})(\mathbf{c}_{12} \cdot \mathbf{C}_{12}) - (c_{12}^2 + 4C_{12}^2)(\mathbf{c}_{12} \cdot \Delta_{12})$
(0, 4, 0)	w^4	$\frac{2}{\kappa^2\theta^2} [\Delta_{12}^4 + (\hat{\sigma} \cdot \Delta_{12})^4 - 2\Delta_{12}^2(\hat{\sigma} \cdot \Delta_{12})^2] + \frac{2}{\kappa\theta} \left\{ 4[\mathbf{W}_{12} \cdot (\hat{\sigma} \times \Delta_{12})]^2 + [\mathbf{w}_{12} \cdot (\hat{\sigma} \times \Delta_{12})]^2 + \left(2W_{12}^2 + \frac{w_{12}^2}{2} \right) \right.$ $\times [\Delta_{12}^2 - (\hat{\sigma} \cdot \Delta_{12})^2] \left. \right\} - \frac{4}{\sqrt{\kappa\theta}} \left[\left(2W_{12}^2 + \frac{w_{12}^2}{2} \right) \mathbf{W}_{12} \cdot (\hat{\sigma} \times \Delta_{12}) + (\mathbf{W}_{12} \cdot \mathbf{w}_{12}) \mathbf{w}_{12} \cdot (\hat{\sigma} \times \Delta_{12}) \right]$ $- \frac{8}{\kappa\theta\sqrt{\kappa\theta}} [\Delta_{12}^2 - (\hat{\sigma} \cdot \Delta_{12})^2] \mathbf{W}_{12} \cdot (\hat{\sigma} \times \Delta_{12})$
(2, 2, 0)	$c^2 w^2$	$\frac{1}{\kappa\theta} [\Delta_{12}^2 - (\hat{\sigma} \cdot \Delta_{12})^2] \left\{ \frac{1}{2}(4C_{12}^2 + c_{12}^2) + 2[\Delta_{12}^2 - (\mathbf{c}_{12} \cdot \Delta_{12})] \right\} + \frac{2}{\sqrt{\kappa\theta}} \left\{ \mathbf{C}_{12} \cdot (2\Delta_{12} - \mathbf{c}_{12}) [\mathbf{w}_{12} \cdot (\hat{\sigma} \times \Delta_{12})] \right.$ $- \frac{1}{2} [4C_{12}^2 + c_{12}^2 + 4(\Delta_{12}^2 - \mathbf{c}_{12} \cdot \Delta_{12})] [\mathbf{W}_{12} \cdot (\hat{\sigma} \times \Delta_{12})] \left. \right\} + \frac{1}{2} (4W_{12}^2 + w_{12}^2) [\Delta_{12}^2 - (\mathbf{c}_{12} \cdot \Delta_{12})]$ $- 4(\mathbf{W}_{12} \cdot \mathbf{w}_{12})(\mathbf{C}_{12} \cdot \Delta_{12})$
(0, 0, 2)	$(\mathbf{c} \cdot \mathbf{w})^2$	$2(\mathbf{W}_{12} \cdot \Delta_{12})^2 + \frac{1}{2}(\mathbf{w}_{12} \cdot \Delta_{12})^2 + \frac{2}{\kappa\theta} \left\{ [\mathbf{C}_{12} \cdot (\hat{\sigma} \times \Delta_{12})]^2 + \frac{1}{4}[\mathbf{c}_{12} \cdot (\hat{\sigma} \times \Delta_{12})]^2 \right\} - 2(\mathbf{C}_{12} \cdot \mathbf{w}_{12} + \mathbf{W}_{12} \cdot \mathbf{c}_{12})$ $\times (\mathbf{W}_{12} \cdot \Delta_{12}) - 2 \left(\mathbf{C}_{12} \cdot \mathbf{W}_{12} + \frac{1}{4}\mathbf{c}_{12} \cdot \mathbf{w}_{12} \right) (\mathbf{w}_{12} \cdot \Delta_{12}) + \frac{2}{\sqrt{\kappa\theta}} \left\{ (\mathbf{W}_{12} \cdot \Delta_{12}) [\mathbf{c}_{12} \cdot (\hat{\sigma} \times \Delta_{12})] + (\mathbf{w}_{12} \cdot \Delta_{12}) \right.$ $\times [\mathbf{C}_{12} \cdot (\hat{\sigma} \times \Delta_{12})] - \left. \left[2(\mathbf{C}_{12} \cdot \mathbf{W}_{12}) + \frac{1}{2}(\mathbf{c}_{12} \cdot \mathbf{w}_{12}) \right] \mathbf{C}_{12} \cdot (\hat{\sigma} \times \Delta_{12}) - \frac{1}{2} [(\mathbf{C}_{12} \cdot \mathbf{w}_{12}) + (\mathbf{W}_{12} \cdot \mathbf{c}_{12})] \mathbf{c}_{12} \cdot (\hat{\sigma} \times \Delta_{12}) \right.$

Upon derivation of the results of Table II, we have needed to take into account the following relations:

$$\begin{aligned} \frac{\langle\langle \Delta_{12}^4 \rangle\rangle}{2B_5} &= \frac{1}{2} \left(\bar{\alpha}^4 + \bar{\beta}^4 \frac{d_t^2 - 1}{8} + \bar{\alpha}^2 \bar{\beta}^2 \frac{d_t - 1}{2} \right) \langle\langle c_{12}^5 \rangle\rangle + \frac{\theta^2}{\kappa^2} \bar{\beta}^4 [15 \langle\langle c_{12} W_{12}^4 \rangle\rangle - 2d_t \langle\langle c_{12}^{-1} W_{12}^2 (\mathbf{c}_{12} \cdot \mathbf{W}_{12})^2 \rangle\rangle] \\ &- \langle\langle c_{12}^{-3} (\mathbf{c}_{12} \cdot \mathbf{W}_{12})^4 \rangle\rangle + \frac{\theta \bar{\beta}^2}{2\kappa} [\bar{\beta}^2 (d_t + 1) - \bar{\alpha}^2] [5 \langle\langle c_{12}^3 W_{12}^2 \rangle\rangle - 3 \langle\langle c_{12} (\mathbf{c}_{12} \cdot \mathbf{W}_{12})^2 \rangle\rangle], \end{aligned} \quad (1.10a)$$

$$\begin{aligned} \frac{\langle\langle \Delta_{12}^2 (4C_{12}^2 + c_{12}^2) \rangle\rangle}{2B_5} &= \frac{d_t + 3}{8} \left\{ \left(\bar{\alpha}^2 + \bar{\beta}^2 \frac{d_t - 1}{2} \right) \langle\langle c_{12}^3 (c_{12}^2 + 4C_{12}^2) \rangle\rangle + 2\bar{\beta}^2 \frac{\theta}{\kappa} [3 \langle\langle c_{12} W_{12}^2 (c_{12}^2 + 4C_{12}^2) \rangle\rangle] \right. \\ &\left. - \langle\langle c_{12}^{-1} (\mathbf{c}_{12} \cdot \mathbf{W}_{12})^2 (c_{12}^2 + 4C_{12}^2) \rangle\rangle \right\}, \end{aligned} \quad (1.10b)$$

$$\frac{\langle\langle (\mathbf{c}_{12} \cdot \Delta_{12})^2 \rangle\rangle}{2B_5} = \frac{1}{2} \left(\bar{\alpha}^2 + \bar{\beta}^2 \frac{d_t^2 - 1}{8} + \bar{\alpha} \bar{\beta} \frac{d_t - 1}{2} \right) \langle\langle c_{12}^5 \rangle\rangle + \bar{\beta}^2 \frac{\theta}{\kappa} \frac{d_t + 3}{4} [\langle\langle c_{12}^3 W_{12}^2 \rangle\rangle - \langle\langle c_{12} (\mathbf{c}_{12} \cdot \mathbf{W}_{12})^2 \rangle\rangle], \quad (1.10c)$$

$$\begin{aligned} \frac{\langle\langle (\mathbf{C}_{12} \cdot \Delta_{12})(4C_{12}^2 + c_{12}^2) \rangle\rangle}{2B_5} &= \frac{d_t + 3}{8} \left(\bar{\alpha} + \bar{\beta} \frac{d_t - 1}{2} \right) \langle\langle c_{12} (\mathbf{c}_{12} \cdot \mathbf{C}_{12})(4C_{12}^2 + c_{12}^2) \rangle\rangle \\ &- \bar{\beta} \sqrt{\frac{\theta}{\kappa}} \frac{B_2}{B_5} \langle\langle (4C_{12}^2 + c_{12}^2) \mathbf{C}_{12} \cdot (\mathbf{c}_{12} \times \mathbf{W}_{12}) \rangle\rangle, \end{aligned} \quad (1.10d)$$

$$\begin{aligned} \frac{\langle\langle \Delta_{12}^2 (\mathbf{c}_{12} \cdot \Delta_{12}) \rangle\rangle}{2B_5} &= \frac{1}{2} \left[\bar{\alpha}^3 + \frac{d_t - 1}{4} (\bar{\alpha} \bar{\beta}^2 + \bar{\alpha}^2 \bar{\beta}) + \frac{d_t^2 - 1}{8} \bar{\beta}^3 \right] \langle\langle c_{12}^5 \rangle\rangle \\ &+ \frac{1}{2} \frac{\theta}{\kappa} \bar{\beta}^2 \left\{ \left[5\bar{\alpha} + \left(\frac{3d_t - 1}{2} + (d_t + 3) \right) \bar{\beta} \right] \langle\langle c_{12}^3 W_{12}^2 \rangle\rangle - \left[3\bar{\alpha} + \left(\frac{d_t - 3}{2} + (d_t + 3) \right) \bar{\beta} \right] \right. \\ &\left. \times \langle\langle c_{12} (\mathbf{c}_{12} \cdot \mathbf{W}_{12})^2 \rangle\rangle \right\}, \end{aligned} \quad (1.10e)$$

TABLE II. Collisional moments μ_{pq} with $p+q=2$ and 4 in terms of two-body averages.

$$\begin{aligned}
& \frac{d_t+3}{4} \left\{ \frac{-\mu_{pq}/B_5}{\bar{\alpha}(\bar{\alpha}-1) + \frac{d_t-1}{2}\bar{\beta}(\bar{\beta}-1)} \left[\langle c_{12}^3 \rangle + 2\bar{\beta}^2 \frac{\theta}{\kappa} \left[3\langle c_{12} W_{12}^2 \rangle - \langle c_{12}^{-1}(\mathbf{c}_{12} \cdot \mathbf{W}_{12})^2 \rangle \right] \right\} \\
(2.0) & \frac{d_t+3}{4} \left\{ \frac{\bar{\beta}}{\kappa} \left[3\langle c_{12} W_{12}^2 \rangle - \langle c_{12}^{-1}(\mathbf{c}_{12} \cdot \mathbf{W}_{12})^2 \rangle \right] + \frac{\bar{\beta}}{2} \frac{d_t-1}{2} \langle c_{12}^3 \rangle \right\} \\
(0.2) & \left\{ \bar{\alpha}^3(\bar{\alpha}-2) + \frac{d_t^2-1}{8} \bar{\beta}^3(\bar{\beta}-2) + \frac{d_t-1}{2} \bar{\alpha} \bar{\beta}(\bar{\alpha}\bar{\beta}-\bar{\alpha}-\bar{\beta}+1) + \frac{d_t+3}{8} \left[\bar{\alpha}(2\bar{\alpha}-1) + \frac{d_t-1}{2} \bar{\beta}(2\bar{\beta}-1) \right] + \bar{\alpha}^2 + \frac{d_t^2-1-\bar{\beta}^2}{8} \langle c_{12}^5 \rangle \right\} \\
(4.0) & + \left\{ (\bar{\alpha}-\bar{\beta})^2 + \frac{d_t+3}{2} \left[\bar{\alpha}(\bar{\alpha}-1) + \frac{d_t-1}{2} \bar{\beta}(\bar{\beta}-1) \right] \right\} \langle c_{12}^3 C_{12}^2 \rangle + \left\{ 3\bar{\alpha}(\bar{\alpha}-1) + \frac{d_t-1}{2} \bar{\beta} \left[(d_t+3)\bar{\beta}-3 \right] + d_t \left[2\bar{\beta}(\bar{\alpha}-\bar{\beta}) - \bar{\alpha}-\bar{\beta} \frac{d_t-1}{2} \right] \right\} \langle c_{12}(\mathbf{c}_{12} \cdot \mathbf{C}_{12})^2 \rangle + 2 \frac{\theta}{\kappa} \bar{\beta}^2 \\
& \left\{ 3d_t - 1 \right\} \langle c_{12}^3 W_{12}^2 \rangle + \bar{\alpha}(\bar{\alpha}-1) \left(5 \langle c_{12}^3 W_{12}^2 \rangle - 3 \langle c_{12}(\mathbf{c}_{12} \cdot \mathbf{W}_{12})^2 \rangle \right) + (d_t+3) \bar{\beta}(\bar{\beta}-1) \left(\langle c_{12}^3 W_{12}^2 \rangle - \langle c_{12}(\mathbf{c}_{12} \cdot \mathbf{W}_{12})^2 \rangle \right) + (d_t+3) \left[\langle c_{12}^{-1}(\mathbf{C}_{12} \cdot \mathbf{c}_{12} \times \mathbf{W}_{12}) \rangle^2 \right] \\
& + \langle c_{12} C_{12}^2 W_{12}^2 \rangle - \langle c_{12}(\mathbf{C}_{12} \cdot \mathbf{W}_{12})^2 \rangle + 3 \left(\langle c_{12}^3 W_{12}^2 \rangle + 4 \langle c_{12} C_{12}^2 W_{12}^2 \rangle \right) - \left(\langle c_{12}(\mathbf{c}_{12} \cdot \mathbf{W}_{12})^2 \rangle + 4 \langle c_{12}^{-1} C_{12}^2(\mathbf{c}_{12} \cdot \mathbf{W}_{12})^2 \rangle \right) + \frac{\theta}{\kappa} \bar{\beta}^2 \left[15 \langle c_{12} W_{12}^4 \rangle \right] \\
(0.4) & - 2d_t \langle c_{12}^{-1} W_{12}^2(\mathbf{c}_{12} \cdot \mathbf{W}_{12})^2 \rangle - \langle c_{12}^{-3}(\mathbf{c}_{12} \cdot \mathbf{W}_{12})^4 \rangle \left\{ \frac{16 B_4}{3 B_5} \sqrt{\frac{\theta}{\kappa}} \bar{\beta} \left[(d_t-2)\bar{\beta} + 4\bar{\alpha} + (d_t+2) \right] \langle (\mathbf{C}_{12} \cdot \mathbf{c}_{12})[\mathbf{C}_{12} \cdot (\mathbf{c}_{12} \times \mathbf{W}_{12})] \rangle \right\} \\
& \frac{d_t^2-1}{8} \frac{\bar{\beta}^4}{\kappa^2 \theta^2} \langle c_{12}^5 \rangle + \frac{2}{\kappa \theta} \bar{\beta}^2 \left\{ \left[\frac{(d_t+3)(d_t+1)}{4} - \frac{\bar{\beta}}{\kappa} \frac{3d_t-1}{2} + \frac{\bar{\beta}^2}{\kappa^2} \left(\frac{1}{4} + 2 \frac{\bar{\beta}}{\kappa} + \frac{\bar{\beta}^2}{\kappa^2} \right) \right] \langle c_{12}(\mathbf{c}_{12} \cdot \mathbf{W}_{12})^2 \rangle + \frac{(d_t+3)}{32} \right. \\
& \times \left. \left(\langle c_{12}^3 W_{12}^2 \rangle - \langle c_{12}(\mathbf{c}_{12} \cdot \mathbf{w}_{12})^2 \rangle \right) + 2 \frac{\bar{\beta}}{\kappa} \left(\frac{\bar{\beta}}{\kappa} - \frac{1}{2} \right) \left[\frac{3(d_t+3)}{4} \langle c_{12} W_{12}^4 \rangle + \langle c_{12} w_{12}^2 W_{12}^2 \rangle \right] - \frac{d_t+3}{4} \left(4 \langle c_{12}^{-1} W_{12}^2(\mathbf{c}_{12} \cdot \mathbf{W}_{12})^2 \rangle + \langle c_{12}^{-1} w_{12}^2(\mathbf{c}_{12} \cdot \mathbf{W}_{12})^2 \rangle \right) \right. \\
& \left. + \frac{\bar{\beta}}{\kappa} \left[\frac{11-d_t(d_t-4)}{2} \langle c_{12}(\mathbf{w}_{12} \cdot \mathbf{W}_{12})^2 \rangle - (7-d_t) \langle c_{12}(\mathbf{w}_{12} \cdot \mathbf{W}_{12})(\mathbf{c}_{12} \cdot \mathbf{w}_{12}) \rangle - \frac{1}{2} \langle c_{12}^{-2} W_{12}^2(\mathbf{c}_{12} \cdot \mathbf{W}_{12})^2 \rangle + \frac{d_t-2}{2} \left(\langle c_{12}^{-1} w_{12}^2(\mathbf{c}_{12} \cdot \mathbf{W}_{12})^2 \rangle \right) \right. \right. \\
& \left. \left. + \langle c_{12}^{-1} W_{12}^2(\mathbf{c}_{12} \cdot \mathbf{w}_{12})^2 \rangle + \langle c_{12} w_{12}^2 W_{12}^2 \rangle \right] \right\} + \left(\frac{\bar{\beta}}{\kappa} - 4 \frac{\bar{\beta}^2}{\kappa^2} + \frac{\bar{\beta}^3}{\kappa^3} \right) \left(15 \langle c_{12} W_{12}^4 \rangle - 2d_t \langle c_{12}^{-1} W_{12}^2(\mathbf{c}_{12} \cdot \mathbf{W}_{12})^2 \rangle - \langle c_{12}^{-3}(\mathbf{c}_{12} \cdot \mathbf{W}_{12})^4 \rangle \right) \\
(2.2) & \frac{d_t+3}{16} \left[\bar{\alpha}(\bar{\alpha}-1) + \frac{d_t-1}{2} \bar{\beta}(\bar{\beta}-1) \right] \left[4 \langle c_{12}^3 W_{12}^2 \rangle + \langle c_{12}^3 W_{12}^2 \rangle \right] - \frac{d_t+3}{4} \bar{\alpha} + (d_t-1) \bar{\beta} \left[\langle c_{12}(\mathbf{c}_{12} \cdot \mathbf{C}_{12})(\mathbf{w}_{12} \cdot \mathbf{W}_{12}) \rangle + \frac{\bar{\beta}^2}{\kappa \theta} d_t - 1 \right] \left\{ \frac{d_t+3}{8} + \bar{\alpha}(\bar{\alpha}-1) + \frac{d_t+1}{2} \bar{\beta}(\bar{\beta}-1) \right\} \langle c_{12}^5 \rangle \\
& + \frac{d_t+3}{2} \langle c_{12}^3 C_{12}^2 \rangle + \frac{\bar{\beta}^2}{\kappa^2} \left\{ \frac{d_t+3}{2} \langle c_{12} C_{12}^2 W_{12}^2 \rangle - \langle c_{12}^{-1} C_{12}^2(\mathbf{c}_{12} \cdot \mathbf{W}_{12})^2 \rangle + \langle c_{12}^3 W_{12}^2 \rangle \right\} + \frac{3(d_t+3)}{8} + 5\bar{\alpha}(\bar{\alpha}-1) + 5 \frac{d_t+1}{2} \bar{\beta}(\bar{\beta}-1) + (d_t+3) \bar{\beta}^2 - \left[\frac{d_t+3}{8} + 3\bar{\alpha}(\bar{\alpha}-1) \right. \\
& \left. + 2 \frac{d_t+1}{2} \bar{\beta}(\bar{\beta}+1) + (d_t+3) \bar{\beta}^2 \right] \langle c_{12}(\mathbf{c}_{12} \cdot \mathbf{W}_{12})^2 \rangle + 2 \frac{\theta}{\kappa} \bar{\beta} \left\{ \bar{\beta} \left[\frac{\bar{\beta}}{\kappa} - 1 \right] \right\} \left(15 \langle c_{12} W_{12}^4 \rangle - 2d_t \langle c_{12}^{-1} W_{12}^2(\mathbf{c}_{12} \cdot \mathbf{W}_{12})^2 \rangle - \langle c_{12}^{-3}(\mathbf{c}_{12} \cdot \mathbf{W}_{12})^4 \rangle \right) + \frac{d_t+3}{8} \left[4 \langle 3 \langle c_{12} W_{12}^4 \rangle \right. \right. \\
& \left. \left. - \langle c_{12}^{-1} W_{12}^2(\mathbf{c}_{12} \cdot \mathbf{W}_{12})^2 \rangle + 3 \langle c_{12} w_{12}^2 W_{12}^2 \rangle - \langle c_{12}^{-1} w_{12}^2(\mathbf{c}_{12} \cdot \mathbf{W}_{12})^2 \rangle \right\} - \frac{\bar{\beta}}{\kappa} \left\{ \frac{3(d_t+3)}{8} + 5\bar{\alpha}(\bar{\alpha}-1) + \frac{3d_t-1}{2} \bar{\beta}(\bar{\beta}-1) + \frac{d_t+3}{2} \bar{\beta}(2\bar{\beta}-1) \right\} \langle c_{12}^3 W_{12}^2 \rangle \\
& - \left[\frac{d_t+3}{8} + 3\bar{\alpha}(\bar{\alpha}-1) + \frac{d_t+3}{2} \bar{\beta}(2\bar{\beta}-1) \right] \langle c_{12}(\mathbf{c}_{12} \cdot \mathbf{W}_{12})^2 \rangle + \frac{d_t+3}{2} \left[3 \langle c_{12} C_{12}^2(\mathbf{c}_{12} \cdot \mathbf{W}_{12})^2 \rangle - \langle c_{12}^{-1} C_{12}^2(\mathbf{c}_{12} \cdot \mathbf{W}_{12})^2 \rangle \right] + \left[\frac{3(d_t+3)}{4} - 5\bar{\alpha} - (2d_t+1) \bar{\beta} \right] \langle c_{12}(\mathbf{c}_{12} \cdot \mathbf{C}_{12})(\mathbf{w}_{12} \cdot \mathbf{W}_{12}) \rangle \\
& - \left[\frac{d_t+3}{4} - \bar{\alpha} - \frac{d_t+1}{2} \bar{\beta} \right] \langle c_{12}^{-1}(\mathbf{C}_{12} \cdot \mathbf{C}_{12})(\mathbf{c}_{12} \cdot \mathbf{w}_{12}) \rangle + \left(\bar{\alpha} + \frac{d_t+1}{2} \bar{\beta} \right) \langle c_{12}(\mathbf{c}_{12} \cdot \mathbf{W}_{12})(\mathbf{w}_{12} \cdot \mathbf{C}_{12}) \rangle + \left(\bar{\alpha} + \bar{\beta} \right) \langle c_{12}(\mathbf{c}_{12} \cdot \mathbf{w}_{12})(\mathbf{C}_{12} \cdot \mathbf{W}_{12}) \rangle \left\{ - \frac{d_t+3}{4} \left[\bar{\alpha} + \frac{d_t-1}{2} \bar{\beta} \right] \right. \\
& \times \langle c_{12}(\mathbf{c}_{12} \cdot \mathbf{C}_{12})(\mathbf{w}_{12} \cdot \mathbf{W}_{12}) \rangle - \frac{B_4}{3 B_5} \bar{\beta} \sqrt{\frac{\theta}{\kappa}} \left\{ 4(d_t+2) \langle (\mathbf{w}_{12} \cdot \mathbf{W}_{12})(\mathbf{C}_{12} \cdot \mathbf{c}_{12} \times \mathbf{W}_{12}) \rangle - \frac{1}{\theta} \left[(\bar{\alpha} + \bar{\beta}) \langle c_{12}^2 \mathbf{C}_{12} \cdot (\mathbf{c}_{12} \times \mathbf{w}_{12}) \rangle + 8 \frac{\bar{\beta}}{\kappa} (4 \langle (\mathbf{w}_{12} \cdot \mathbf{W}_{12}) \mathbf{c}_{12} \cdot (\mathbf{C}_{12} \times \mathbf{W}_{12}) \rangle \right. \right. \\
& \left. \left. - \langle (\mathbf{c}_{12} \cdot \mathbf{W}_{12}) \mathbf{w}_{12} \cdot (\mathbf{C}_{12} \times \mathbf{W}_{12}) \rangle + 6 \langle c_{12}^2(\mathbf{c}_{12} \cdot \mathbf{W}_{12})(\mathbf{c}_{12} \cdot \mathbf{w}_{12}) \mathbf{c}_{12} \cdot (\mathbf{C}_{12} \times \mathbf{W}_{12}) \rangle \right) \right\} \\
\end{aligned}$$

$$\begin{aligned} \frac{\langle\langle(\mathbf{C}_{12} \cdot \boldsymbol{\Delta}_{12})^2\rangle\rangle}{2B_5} &= \frac{1}{8}(\bar{\alpha} - \bar{\beta})^2 \langle\langle c_{12}^3 C_{12}^2 \rangle\rangle + \frac{1}{8} \left(3\bar{\alpha}^2 + \frac{d_t^2 - 3}{2} \bar{\beta}^2 + 2d_t \bar{\alpha} \bar{\beta} \right) \langle\langle c_{12}(\mathbf{c}_{12} \cdot \mathbf{C}_{12})^2 \rangle\rangle + \frac{\theta}{\kappa} \bar{\beta}^2 \frac{d_t + 3}{4} \\ &\times \left[\langle\langle c_{12}^{-1} [\mathbf{C}_{12} \cdot (\mathbf{c}_{12} \times \mathbf{W}_{12})]^2 \rangle\rangle + \langle\langle c_{12} C_{12}^2 W_{12}^2 \rangle\rangle - \langle\langle c_{12}(\mathbf{C}_{12} \cdot \mathbf{W}_{12})^2 \rangle\rangle \right] + \frac{2B_4}{B_5} \sqrt{\frac{\theta}{\kappa}} \bar{\beta} \\ &\times \left[\left(1 - \frac{B_2}{B_4} + \frac{B_2/B_4 - 1}{d_t - 1} \right) \bar{\beta} - 2\bar{\alpha} \left(1 + \frac{B_2/B_4 - 1}{d_t - 1} \right) \right] \langle\langle (\mathbf{c}_{12} \cdot \mathbf{C}_{12}) \mathbf{C}_{12} \cdot (\mathbf{c}_{12} \times \mathbf{W}_{12}) \rangle\rangle, \quad (1.10f) \end{aligned}$$

$$\frac{\langle\langle (c_{12}^2 + 4C_{12}^2)(\mathbf{c}_{12} \cdot \boldsymbol{\Delta}_{12}) \rangle\rangle}{2B_5} = \frac{d_t + 3}{8} \left(\bar{\alpha} + \bar{\beta} \frac{d_t - 1}{2} \right) \left(\langle\langle c_{12}^5 \rangle\rangle + 4 \langle\langle c_{12}^3 C_{12}^2 \rangle\rangle \right), \quad (1.10g)$$

$$\frac{\langle\langle (\mathbf{C}_{12} \cdot \boldsymbol{\Delta}_{12})(\mathbf{c}_{12} \cdot \mathbf{C}_{12}) \rangle\rangle}{2B_5} = \frac{d_t + 3}{8} \left(\bar{\alpha} + \bar{\beta} \frac{d_t - 1}{2} \right) \langle\langle c_{12}(\mathbf{c}_{12} \cdot \mathbf{C}_{12})^2 \rangle\rangle - 2\sqrt{\frac{\theta}{\kappa}} \frac{B_2}{B_3} \bar{\beta} \langle\langle (\mathbf{c}_{12} \cdot \mathbf{C}_{12}) \mathbf{C}_{12} \cdot (\mathbf{c}_{12} \times \mathbf{W}_{12}) \rangle\rangle, \quad (1.10h)$$

$$\begin{aligned} \frac{\langle\langle (\hat{\boldsymbol{\sigma}} \times \boldsymbol{\Delta}_{12})^2 (4C_{12}^2 + c_{12}^2) \rangle\rangle}{2B_5} &= \bar{\beta}^2 \frac{d_t + 3}{4} \left\{ \frac{d_t - 1}{4} \left(4 \langle\langle c_{12}^3 C_{12}^2 \rangle\rangle + \langle\langle c_{12}^5 \rangle\rangle \right) + \frac{\theta}{\kappa} \left[12 \langle\langle c_{12} W_{12}^2 C_{12}^2 \rangle\rangle + 3 \langle\langle c_{12}^3 W_{12}^2 \rangle\rangle \right. \right. \\ &\quad \left. \left. - 4 \langle\langle C_{12}^2 c_{12}^{-1} (\mathbf{c}_{12} \cdot \mathbf{W}_{12})^2 \rangle\rangle - \langle\langle c_{12}(\mathbf{c}_{12} \cdot \mathbf{W}_{12})^2 \rangle\rangle \right] \right\}, \quad (1.11a) \end{aligned}$$

$$\begin{aligned} \frac{\langle\langle (\hat{\boldsymbol{\sigma}} \times \boldsymbol{\Delta}_{12})^2 [\boldsymbol{\Delta}_{12}^2 - (\mathbf{c}_{12} \cdot \boldsymbol{\Delta}_{12})] \rangle\rangle}{2B_5} &= \frac{\bar{\beta}^2}{2} \left\{ \bar{\alpha}(\bar{\alpha} - 1) \left[\frac{d_t - 1}{4} \langle\langle c_{12}^5 \rangle\rangle + \frac{\theta}{\kappa} \left(5 \langle\langle c_{12}^3 W_{12}^2 \rangle\rangle - 3 \langle\langle c_{12}(\mathbf{c}_{12} \cdot \mathbf{W}_{12})^2 \rangle\rangle \right) \right] \right. \\ &\quad + \bar{\beta}(\bar{\beta} - 1) \left(\frac{d_t^2 - 1}{8} \langle\langle c_{12}^5 \rangle\rangle + \frac{\theta}{\kappa} \frac{3d_t - 1}{2} \langle\langle c_{12}^3 W_{12}^2 \rangle\rangle \right) \\ &\quad + \bar{\beta}(2\bar{\beta} - 1) \frac{\theta}{\kappa} \frac{d_t + 3}{2} \left[\langle\langle c_{12}^3 W_{12}^2 \rangle\rangle - \langle\langle c_{12}(\mathbf{c}_{12} \cdot \mathbf{W}_{12})^2 \rangle\rangle \right] + \bar{\beta}^2 \frac{\theta}{\kappa} \left[\frac{3d_t - 1}{2} \langle\langle c_{12}^3 W_{12}^2 \rangle\rangle \right. \\ &\quad \left. + \frac{2\theta}{\kappa} \left(15 \langle\langle c_{12} W_{12}^4 \rangle\rangle - 2d_t \langle\langle c_{12}^{-1} W_{12}^2 (\mathbf{c}_{12} \cdot \mathbf{W}_{12})^2 \rangle\rangle - \langle\langle c_{12}^{-3} (\mathbf{c}_{12} \cdot \mathbf{W}_{12})^4 \rangle\rangle \right) \right] \right\}, \quad (1.11b) \end{aligned}$$

$$\frac{\langle\langle (\mathbf{C}_{12} \cdot \mathbf{c}_{12}) [\mathbf{w}_{12} \cdot (\hat{\boldsymbol{\sigma}} \times \boldsymbol{\Delta}_{12})] \rangle\rangle}{2B_5} = \bar{\beta} \sqrt{\frac{\theta}{\kappa}} \frac{d_t + 3}{8} \left[3 \langle\langle c_{12}(\mathbf{c}_{12} \cdot \mathbf{C}_{12})(\mathbf{W}_{12} \cdot \mathbf{w}_{12}) \rangle\rangle - \langle\langle c_{12}^{-1} (\mathbf{c}_{12} \cdot \mathbf{C}_{12})(\mathbf{c}_{12} \cdot \mathbf{W}_{12})(\mathbf{c}_{12} \cdot \mathbf{w}_{12}) \rangle\rangle \right], \quad (1.11c)$$

$$\begin{aligned} \frac{\langle\langle (\mathbf{C}_{12} \cdot \boldsymbol{\Delta}_{12}) [\mathbf{w}_{12} \cdot (\hat{\boldsymbol{\sigma}} \times \boldsymbol{\Delta}_{12})] \rangle\rangle}{2B_5} &= \frac{1}{2} \bar{\alpha} \bar{\beta} \left\{ \frac{B_2 - B_4}{B_5(d_t - 1)} \langle\langle c_{12}^2 \mathbf{C}_{12} \cdot (\mathbf{c}_{12} \times \mathbf{w}_{12}) \rangle\rangle + 2\sqrt{\frac{\theta}{\kappa}} \left[\frac{5}{4} \langle\langle c_{12}(\mathbf{C}_{12} \cdot \mathbf{c}_{12})(\mathbf{W}_{12} \cdot \mathbf{w}_{12}) \rangle\rangle \right. \right. \\ &\quad \left. \left. - \frac{1}{4} \left(\langle\langle c_{12}^{-1} (\mathbf{C}_{12} \cdot \mathbf{c}_{12})(\mathbf{W}_{12} \cdot \mathbf{c}_{12})(\mathbf{w}_{12} \cdot \mathbf{c}_{12}) \rangle\rangle + \langle\langle c_{12}(\mathbf{C}_{12} \cdot \mathbf{w}_{12})(\mathbf{W}_{12} \cdot \mathbf{c}_{12}) \rangle\rangle \right) \right] \right. \\ &\quad \left. + \langle\langle c_{12}(\mathbf{c}_{12} \cdot \mathbf{w}_{12})(\mathbf{W}_{12} \cdot \mathbf{C}_{12}) \rangle\rangle \right\} + \frac{1}{2} \bar{\beta}^2 \left\{ \frac{B_4 - B_2}{B_5(d_t - 1)} \langle\langle c_{12}^2 [\mathbf{C}_{12} \cdot (\mathbf{c}_{12} \times \mathbf{w}_{12})] \rangle\rangle \right. \\ &\quad + \sqrt{\frac{\theta}{\kappa}} \left[\frac{2d_t + 1}{2} \langle\langle c_{12}(\mathbf{C}_{12} \cdot \mathbf{c}_{12})(\mathbf{W}_{12} \cdot \mathbf{w}_{12}) \rangle\rangle + \frac{1}{2} \langle\langle c_{12}(\mathbf{C}_{12} \cdot \mathbf{W}_{12})(\mathbf{c}_{12} \cdot \mathbf{w}_{12}) \rangle\rangle \right. \\ &\quad \left. - \frac{d_t + 1}{4} \left(\langle\langle c_{12}^{-1} (\mathbf{c}_{12} \cdot \mathbf{C}_{12})(\mathbf{c}_{12} \cdot \mathbf{W}_{12})(\mathbf{c}_{12} \cdot \mathbf{w}_{12}) \rangle\rangle + \langle\langle c_{12}(\mathbf{C}_{12} \cdot \mathbf{w}_{12})(\mathbf{W}_{12} \cdot \mathbf{c}_{12}) \rangle\rangle \right) \right] \\ &\quad \left. - \frac{4}{3} \frac{B_4}{B_5} \frac{\theta}{\kappa} \left[4 \langle\langle (\mathbf{W}_{12} \cdot \mathbf{w}_{12}) [\mathbf{c}_{12} \cdot (\mathbf{C}_{12} \times \mathbf{W}_{12})] \rangle\rangle - \left(\langle\langle (\mathbf{c}_{12} \cdot \mathbf{W}_{12}) [\mathbf{w}_{12} \cdot (\mathbf{C}_{12} \times \mathbf{W}_{12})] \rangle\rangle \right) \right] \right. \\ &\quad \left. + 2 \langle\langle c_{12}^{-2} (\mathbf{c}_{12} \cdot \mathbf{W}_{12})(\mathbf{c}_{12} \cdot \mathbf{w}_{12}) [\mathbf{c}_{12} \cdot (\mathbf{C}_{12} \times \mathbf{W}_{12})] \rangle\rangle \right\}, \quad (1.11d) \end{aligned}$$

$$\frac{\langle\langle(4C_{12}^2 + \mathbf{c}_{12}^2)\mathbf{W}_{12} \cdot (\hat{\boldsymbol{\sigma}} \times \boldsymbol{\Delta}_{12})\rangle\rangle}{2B_5} = \bar{\beta} \sqrt{\frac{\theta}{\kappa}} \frac{d_t + 3}{8} [3(4\langle\langle c_{12} C_{12}^2 W_{12}^2 \rangle\rangle + \langle\langle c_{12}^3 W_{12}^2 \rangle\rangle) - 4\langle\langle c_{12}^{-1} C_{12}^2 (\mathbf{c}_{12} \cdot \mathbf{W}_{12})^2 \rangle\rangle + \langle\langle c_{12} (\mathbf{c}_{12} \cdot \mathbf{W}_{12})^2 \rangle\rangle] \quad (1.11e)$$

$$\begin{aligned} \frac{\langle\langle(\boldsymbol{\Delta}_{12}^2 - \mathbf{c}_{12} \cdot \boldsymbol{\Delta}_{12})\mathbf{W}_{12} \cdot (\hat{\boldsymbol{\sigma}} \times \boldsymbol{\Delta}_{12})\rangle\rangle}{2B_5} &= \frac{\bar{\beta}}{4} \sqrt{\frac{\theta}{\kappa}} \left\{ \bar{\alpha}(\bar{\alpha} - 1) [5\langle\langle c_{12}^3 W_{12}^2 \rangle\rangle - 3\langle\langle c_{12} (\mathbf{c}_{12} \cdot \mathbf{W}_{12})^2 \rangle\rangle] + \bar{\beta}(\bar{\beta} - 1) \frac{3d_t - 1}{2} \langle\langle c_{12}^3 W_{12}^2 \rangle\rangle \right. \\ &\quad \left. + \bar{\beta}(2\bar{\beta} - 1) \frac{d_t + 3}{2} [\langle\langle c_{12}^3 W_{12}^2 \rangle\rangle - \langle\langle c_{12} (\mathbf{c}_{12} \cdot \mathbf{W}_{12})^2 \rangle\rangle] \right\} \\ &\quad + \frac{1}{2} \bar{\beta}^3 \left(\frac{\theta}{\kappa} \right)^{3/2} [15\langle\langle c_{12} W_{12}^4 \rangle\rangle - 2d_t \langle\langle c_{12}^{-1} W_{12}^2 (\mathbf{c}_{12} \cdot \mathbf{W}_{12})^2 \rangle\rangle - \langle\langle c_{12}^{-3} (\mathbf{c}_{12} \cdot \mathbf{W}_{12})^4 \rangle\rangle], \end{aligned} \quad (1.11f)$$

$$\begin{aligned} \frac{\langle\langle(4W_{12}^2 + w_{12}^2)(\boldsymbol{\Delta}_{12}^2 - \mathbf{c}_{12} \cdot \boldsymbol{\Delta}_{12})\rangle\rangle}{2B_5} &= \frac{d_t + 3}{8} \left\{ \left[\bar{\alpha}(\bar{\alpha} - 1) + \bar{\beta}(\bar{\beta} - 1) \frac{d_t - 1}{2} \right] (\langle\langle c_{12}^3 w_{12}^2 \rangle\rangle + 4\langle\langle c_{12}^3 W_{12}^2 \rangle\rangle) + \right. \\ &\quad \left. + 2\frac{\theta}{\kappa} \bar{\beta}^2 (3\langle\langle c_{12} W_{12}^2 w_{12}^2 \rangle\rangle + 12\langle\langle c_{12} W_{12}^4 \rangle\rangle - 4\langle\langle c_{12}^{-1} W_{12}^2 (\mathbf{c}_{12} \cdot \mathbf{W}_{12})^2 \rangle\rangle) \right. \\ &\quad \left. - \langle\langle c_{12}^{-1} w_{12}^2 (\mathbf{c}_{12} \cdot \mathbf{W}_{12})^2 \rangle\rangle \right\}, \end{aligned} \quad (1.11g)$$

$$\begin{aligned} \frac{\langle\langle(\mathbf{W}_{12} \cdot \mathbf{w}_{12})(\mathbf{C}_{12} \cdot \boldsymbol{\Delta}_{12})\rangle\rangle}{2B_5} &= \bar{\alpha} \frac{d_t + 3}{16} \langle\langle c_{12} (\mathbf{W}_{12} \cdot \mathbf{w}_{12}) (\mathbf{c}_{12} \cdot \mathbf{C}_{12}) \rangle\rangle + \frac{\bar{\beta}}{2} \left[\frac{(d_t - 1)(d_t + 3)}{8} \langle\langle c_{12} (\mathbf{W}_{12} \cdot \mathbf{w}_{12}) (\mathbf{c}_{12} \cdot \mathbf{C}_{12}) \rangle\rangle \right. \\ &\quad \left. - 2\frac{B_2}{B_5} \sqrt{\frac{\theta}{\kappa}} \langle\langle (\mathbf{W}_{12} \cdot \mathbf{w}_{12}) \mathbf{C}_{12} \cdot (\mathbf{c}_{12} \times \mathbf{W}_{12}) \rangle\rangle \right], \end{aligned} \quad (1.11h)$$

$$\begin{aligned} \frac{\langle\langle(\hat{\boldsymbol{\sigma}} \times \boldsymbol{\Delta}_{12})^4\rangle\rangle}{2B_5} &= \bar{\beta}^4 \frac{d_t^2 - 1}{16} \langle\langle c_{12}^5 \rangle\rangle + \frac{\theta^2}{\kappa^2} \bar{\beta}^4 [15\langle\langle c_{12} W_{12}^4 \rangle\rangle - 2d_t \langle\langle c_{12}^{-1} W_{12}^2 (\mathbf{c}_{12} \cdot \mathbf{W}_{12})^2 \rangle\rangle - \langle\langle c_{12}^{-3} (\mathbf{c}_{12} \cdot \mathbf{W}_{12})^4 \rangle\rangle] \\ &\quad + \frac{\theta}{\kappa} \bar{\beta}^4 \frac{d_t + 1}{2} [5\langle\langle c_{12}^3 W_{12}^2 \rangle\rangle - 3\langle\langle c_{12} (\mathbf{c}_{12} \cdot \mathbf{W}_{12})^2 \rangle\rangle], \end{aligned} \quad (1.12a)$$

$$\begin{aligned} \frac{\langle\langle(\mathbf{W}_{12} \cdot (\hat{\boldsymbol{\sigma}} \times \boldsymbol{\Delta}_{12}))^2\rangle\rangle}{2B_5} &= \frac{\bar{\beta}^2}{2} \left\{ \frac{d_t + 3}{8} [\langle\langle c_{12}^3 W_{12}^2 \rangle\rangle - \langle\langle c_{12} (\mathbf{c}_{12} \cdot \mathbf{W}_{12})^2 \rangle\rangle] + \frac{\theta}{2\kappa} [15\langle\langle c_{12} W_{12}^4 \rangle\rangle - 2d_t \langle\langle c_{12}^{-1} W_{12}^2 (\mathbf{c}_{12} \cdot \mathbf{W}_{12})^2 \rangle\rangle] \right. \\ &\quad \left. - \langle\langle c_{12}^{-3} (\mathbf{c}_{12} \cdot \mathbf{W}_{12})^4 \rangle\rangle \right\}, \end{aligned} \quad (1.12b)$$

$$\begin{aligned} \frac{\langle\langle(\mathbf{w}_{12} \cdot (\hat{\boldsymbol{\sigma}} \times \boldsymbol{\Delta}_{12}))^2\rangle\rangle}{2B_5} &= \frac{\bar{\beta}^2}{2} \left\{ \frac{(d_t + 3)}{8} [\langle\langle c_{12}^3 w_{12}^2 \rangle\rangle - \langle\langle c_{12} (\mathbf{c}_{12} \cdot \mathbf{w}_{12})^2 \rangle\rangle] + \frac{\theta}{\kappa} \left[\frac{11 - d_t(d_t - 4)}{2} \langle\langle c_{12} (\mathbf{w}_{12} \cdot \mathbf{W}_{12})^2 \rangle\rangle \right. \right. \\ &\quad \left. - (7 - d_t) \langle\langle c_{12} (\mathbf{w}_{12} \cdot \mathbf{W}_{12}) (\mathbf{c}_{12} \cdot \mathbf{W}_{12}) (\mathbf{c}_{12} \cdot \mathbf{w}_{12}) \rangle\rangle - \frac{1}{2} \langle\langle c_{12}^{-3} (\mathbf{c}_{12} \cdot \mathbf{W}_{12})^2 (\mathbf{c}_{12} \cdot \mathbf{w}_{12})^2 \rangle\rangle \right. \\ &\quad \left. \left. + \frac{d_t - 2}{2} (\langle\langle c_{12}^{-1} w_{12}^2 (\mathbf{c}_{12} \cdot \mathbf{W}_{12})^2 \rangle\rangle + \langle\langle c_{12}^{-1} W_{12}^2 (\mathbf{c}_{12} \cdot \mathbf{w}_{12})^2 \rangle\rangle + \langle\langle c_{12} w_{12}^2 W_{12}^2 \rangle\rangle) \right] \right\}, \end{aligned} \quad (1.12c)$$

$$\begin{aligned} \frac{\langle\langle(4W_{12}^2 + w_{12}^2)(\hat{\boldsymbol{\sigma}} \times \boldsymbol{\Delta}_{12})^2\rangle\rangle}{2B_5} &= \bar{\beta}^2 \frac{d_t + 3}{16} \left\{ (d_t - 1) [4\langle\langle c_{12}^3 W_{12}^2 \rangle\rangle + \langle\langle c_{12}^3 w_{12}^2 \rangle\rangle] + 4\frac{\theta}{\kappa} [12\langle\langle c_{12} W_{12}^4 \rangle\rangle + 3\langle\langle c_{12} w_{12}^2 W_{12}^2 \rangle\rangle] \right. \\ &\quad \left. - 4\langle\langle c_{12}^{-1} W_{12}^2 (\mathbf{c}_{12} \cdot \mathbf{W}_{12})^2 \rangle\rangle - \langle\langle c_{12}^{-1} w_{12}^2 (\mathbf{c}_{12} \cdot \mathbf{W}_{12})^2 \rangle\rangle \right\}, \end{aligned} \quad (1.12d)$$

$$\frac{\langle\langle (4W_{12}^2 + w_{12}^2)[\mathbf{W}_{12} \cdot (\hat{\boldsymbol{\sigma}} \times \boldsymbol{\Delta}_{12})] \rangle\rangle}{2B_5} = \bar{\beta} \sqrt{\frac{\theta}{\kappa}} \frac{d_t + 3}{8} [12\langle\langle c_{12} W_{12}^4 \rangle\rangle + 3\langle\langle c_{12} w_{12}^2 W_{12}^2 \rangle\rangle - 4\langle\langle c_{12}^{-1} W_{12}^2 (\mathbf{c}_{12} \cdot \mathbf{W}_{12})^2 \rangle\rangle - \langle\langle c_{12}^{-1} w_{12}^2 (\mathbf{c}_{12} \cdot \mathbf{W}_{12})^2 \rangle\rangle], \quad (1.12e)$$

$$\frac{\langle\langle (\mathbf{w}_{12} \cdot \mathbf{W}_{12})[\mathbf{w}_{12} \cdot (\hat{\boldsymbol{\sigma}} \times \boldsymbol{\Delta}_{12})] \rangle\rangle}{2B_5} = \bar{\beta} \sqrt{\frac{\theta}{\kappa}} \frac{d_t + 3}{8} [3\langle\langle c_{12} (\mathbf{w}_{12} \cdot \mathbf{W}_{12})^2 \rangle\rangle - \langle\langle c_{12}^{-1} (\mathbf{w}_{12} \cdot \mathbf{W}_{12}) (\mathbf{c}_{12} \cdot \mathbf{W}_{12}) (\mathbf{c}_{12} \cdot \mathbf{w}_{12}) \rangle\rangle], \quad (1.12f)$$

$$\begin{aligned} \frac{\langle\langle (\hat{\boldsymbol{\sigma}} \times \boldsymbol{\Delta}_{12})^2 [\mathbf{W}_{12} \cdot (\hat{\boldsymbol{\sigma}} \times \boldsymbol{\Delta}_{12})] \rangle\rangle}{2B_5} &= \bar{\beta}^3 \sqrt{\frac{\theta}{\kappa}} \left\{ \frac{3d_t - 1}{4} \langle\langle c_{12}^3 W_{12}^2 \rangle\rangle - \frac{d_t - 3}{4} \langle\langle c_{12} (\mathbf{c}_{12} \cdot \mathbf{W}_{12})^2 \rangle\rangle \right. \\ &\quad + \frac{d_t + 3}{2} [\langle\langle c_{12}^3 W_{12}^2 \rangle\rangle - \langle\langle c_{12} (\mathbf{c}_{12} \cdot \mathbf{W}_{12})^2 \rangle\rangle] \\ &\quad \left. + \frac{\theta}{\kappa} [15\langle\langle c_{12} W_{12}^4 \rangle\rangle - 2d_t \langle\langle c_{12}^{-1} W_{12}^2 (\mathbf{c}_{12} \cdot \mathbf{W}_{12})^2 \rangle\rangle - \langle\langle c_{12}^{-3} (\mathbf{c}_{12} \cdot \mathbf{W}_{12})^4 \rangle\rangle] \right\}. \quad (1.12g) \end{aligned}$$

Equations (1.10), (1.11), and (1.12) are related to the evaluation of μ_{40} , μ_{22} , and μ_{04} , respectively.

D. Useful integrals and changes of variable for two-body averages in the Sonine approximation

In this subsection we summarize the most common integral expressions appearing in the two-body averages of the collisional moments appearing in Table II, in the SA.

1. Maxwellian-type integrals I , J_1 , and J_2

Let us start by introducing the integrals[2]

$$I(\epsilon, p, d) \equiv \int d\mathbf{x}_1 \int d\mathbf{x}_2 x_{12}^p e^{-\epsilon x_1^2 - x_2^2}, \quad \epsilon > 0, \quad (1.13)$$

d being the dimension of the vector space where \mathbf{x} resides. It is convenient to transform our general variables \mathbf{x}_1 and \mathbf{x}_2 (in analogy to \mathbf{c}_1 or \mathbf{w}_1 , and \mathbf{c}_2 or \mathbf{w}_2 , respectively) into relative and center-of-mass-like variables of the form

$$\mathbf{x}_{12} = \mathbf{x}_1 - \mathbf{x}_2, \quad \mathbf{X}_{12} = \frac{1}{2}(\epsilon \mathbf{x}_1 + \mathbf{x}_2). \quad (1.14)$$

Therefore,

$$\mathbf{x}_1 = \frac{\mathbf{x}_{12} + 2\mathbf{X}_{12}}{1 + \epsilon}, \quad \mathbf{x}_2 = \frac{2\mathbf{X}_{12} - \epsilon \mathbf{x}_{12}}{1 + \epsilon}, \quad (1.15)$$

with associated Jacobian of the transformation

$$\left| \frac{\partial(\mathbf{x}_1, \mathbf{x}_2)}{\partial(\mathbf{x}_{12}, \mathbf{X}_{12})} \right| = 2^d (1 + \epsilon)^{-d}, \quad (1.16)$$

Note that the original center-of-mass variable is obtained by setting $\epsilon = 1$. Using this change and d -spherical coordinates, Eq. (1.13) reads

$$\begin{aligned} I(\epsilon, p, d) &= (1 + \epsilon)^{-d} \Omega_d^2 \int_0^\infty dx_{12} x_{12}^{d+p-1} e^{-\frac{\epsilon}{1+\epsilon} x_{12}^2} \int_0^\infty dX_{12} X_{12}^{d-1} e^{-\frac{4}{1+\epsilon} X_{12}^2} \\ &= \pi^d \epsilon^{-d/2} \left(\frac{1 + \epsilon}{\epsilon} \right)^{p/2} \frac{\Gamma\left(\frac{d+p}{2}\right)}{\Gamma\left(\frac{d}{2}\right)}, \end{aligned} \quad (1.17)$$

where $\Omega_d = 2\pi^{d/2}/\Gamma\left(\frac{d}{2}\right)$.

Analogously, one can obtain

$$\int d\mathbf{x}_1 \int d\mathbf{x}_2 X_{12}^p e^{-\epsilon x_1^2 - x_2^2} = \frac{1}{2^p} I(\epsilon, p, d). \quad (1.18)$$

Since Eq. (1.17) applies to any $\epsilon > 0$, we can derive with respect to ϵ and then take $\epsilon = 1$ to get

$$\int d\mathbf{x}_1 \int d\mathbf{x}_2 x_{12}^p x_1^{2q} e^{-x_1^2 - x_2^2} = (-1)^q \left[\frac{\partial^q I(\epsilon, p, d)}{\partial \epsilon^q} \right]_{\epsilon=1}, \quad (1.19a)$$

$$\int d\mathbf{x}_1 \int d\mathbf{x}_2 X_{12}^p x_1^{2q} e^{-x_1^2 - x_2^2} = (-1)^q \frac{1}{2^p} \left[\frac{\partial^q I(\epsilon, p, d)}{\partial \epsilon^q} \right]_{\epsilon=1}. \quad (1.19b)$$

Similar steps lead to

$$J_1(p, q, d) \equiv \int d\mathbf{x}_1 \int d\mathbf{x}_2 x_{12}^p X_{12}^q e^{-x_1^2 - x_2^2} = \frac{2^{\frac{p-q}{2}} \pi^d \Gamma\left(\frac{d+p}{2}\right) \Gamma\left(\frac{d+q}{2}\right)}{[\Gamma\left(\frac{d}{2}\right)]^2}, \quad (1.20a)$$

$$\begin{aligned} J_2(p, q, r, d) &\equiv \int d\mathbf{x}_1 \int d\mathbf{x}_2 x_{12}^p X_{12}^q (\mathbf{x}_{12} \cdot \mathbf{X}_{12})^r e^{-x_1^2 - x_2^2} \\ &= \frac{1 + (-1)^r \Gamma\left(\frac{d}{2}\right) \Gamma\left(\frac{1+r}{2}\right)}{2 \sqrt{\pi} \Gamma\left(\frac{d+r}{2}\right)} J_1(p+r, q+r, d). \end{aligned} \quad (1.20b)$$

Note that $J_2(p, q, 0, d) = J_1(p, q, d)$ and $J_2(p, q, r, d) = 0$ if r is odd.

Let us suppose that the vectors $\mathbf{x}_1, \mathbf{x}_2 \in \mathfrak{E}^{d_1}$ and $\mathbf{y}_1, \mathbf{y}_2 \in \mathfrak{E}^{d_2}$ are all embedded in the same d -Euclidean space, \mathfrak{E}^d . Then, the following identity holds,

$$\begin{aligned} \int d\mathbf{x}_1 \int d\mathbf{x}_2 \int d\mathbf{y}_1 \int d\mathbf{y}_2 x_{12}^p X_{12}^q (\mathbf{x}_{12} \cdot \mathbf{X}_{12})^r y_{12}^{p'} Y_{12}^{q'} (\mathbf{y}_{12} \cdot \mathbf{Y}_{12})^{r'} (\mathbf{x}_{12} \cdot \mathbf{Y}_{12})^k e^{-x_1^2 - x_2^2 - y_1^2 - y_2^2} \\ = \frac{1 + (-1)^k \Gamma\left(\frac{d}{2}\right) \Gamma\left(\frac{1+k}{2}\right)}{2 \sqrt{\pi} \Gamma\left(\frac{d+k}{2}\right)} J_2(p+k, q, r, d_1) J_2(p', q'+k, r', d_2), \end{aligned} \quad (1.21)$$

unless $\mathfrak{E}^{d_1} \perp \mathfrak{E}^{d_2}$, in which case the integral with $k > 0$ vanishes because $\mathbf{x}_{12} \cdot \mathbf{Y}_{12} = 0$.

2. Sonine integral I_S

The Sonine approximation of the VDF implies the action of the Sonine polynomials into the integrals involved in the two-body averages. The Sonine polynomial of degree r of a scalar variable x in a d -dimensional problem is given by

$$S_r(x) = \sum_{k=0}^r \frac{(-1)^k \Gamma\left(\frac{d}{2} + r\right)}{\Gamma\left(\frac{d}{2} + k\right) (r-k)! k!} x^k. \quad (1.22)$$

The first three Sonine polynomials are

$$S_0(x) = 1, \quad S_1(x) = -x + \frac{d}{2}, \quad S_2(x) = \frac{1}{2}x^2 - \frac{d+2}{2}x + \frac{d(d+2)}{8}. \quad (1.23)$$

Let us define the following integral where Sonine polynomials are involved,

$$\begin{aligned} I_S(p, q, r, d) &\equiv \int d\mathbf{x}_1 \int d\mathbf{x}_2 x_{12}^p x_1^{2q} e^{-x_1^2 - x_2^2} S_r(x_{12}^2) \\ &= (-1)^q \sum_{k=0}^r \frac{\Gamma\left(\frac{d}{2} + r\right)}{\Gamma\left(\frac{d}{2} + k\right) (r-k)! k!} \left[\frac{\partial^{(q+k)} I(\epsilon, p)}{\partial \epsilon^{q+k}} \right]_{\epsilon=1}, \end{aligned} \quad (1.24)$$

where in the second step we have used Eq. (1.19a).

3. Two-body averages in the Sonine approximation

Within the Sonine approximation described in the main text, we can obtain

$$\begin{aligned} \langle\langle c_{12}^p \rangle\rangle_S &= \pi^{-d_t-d_r} \int d\tilde{\Gamma}_1 \int d\tilde{\Gamma}_2 c_{12}^p e^{-(c_1^2+c_2^2+w_1^2+w_2^2)} [1 + 2a_{20}S_2(c_1^2) + 2a_{02}S_2(w_1^2) + 2a_{11}S_1(c_1^2)S_1(w_1^2) \\ &\quad + 2a_{00}^{(1)}P_2(\hat{\mathbf{c}}_1 \cdot \hat{\mathbf{w}}_1)] \\ &= \pi^{-d_t} [I(1, p, d_t) + 2a_{20}I_S(p, 0, 2, d_t)], \end{aligned} \quad (1.25)$$

where $p = \text{even}$ and in the second step we have taken into account the orthogonality relations of the Sonine polynomials. Analogously,

$$\begin{aligned} \langle\langle c_{12}W_{12}^2 \rangle\rangle_S &= \frac{\pi^{-d_t-d_r}}{4} \int d\tilde{\Gamma}_1 \int d\tilde{\Gamma}_2 c_{12}W_{12}^2 e^{-(c_1^2+c_2^2+w_1^2+w_2^2)} [1 + 2a_{20}S_2(c_1^2) + 2a_{02}S_2(w_1^2) + 2a_{11}S_1(c_1^2)S_1(w_1^2)] \\ &= \frac{\pi^{-d_t-d_r}}{4} [I(1, 1, d_t)I(1, 2, d_r) + 2a_{20}I_S(1, 0, 2, d_t)I(1, 2, d_r) + 2a_{02}I(1, 1, d_t)I_S(2, 0, 2, d_r) \\ &\quad + 2a_{11}I_S(1, 0, 1, d_t)I_S(2, 0, 1, d_r)], \end{aligned} \quad (1.26a)$$

$$\begin{aligned} K_1(p, q, r, s, d_t, d_r) &\equiv \langle\langle c_{12}^p C_{12}^q (\mathbf{c}_{12} \cdot \mathbf{C}_{12})^r W_{12}^s \rangle\rangle_S \\ &= \frac{\pi^{-d_t-d_r}}{2^s} \left\{ I_S(s, 0, 0, d_r) \left[J_2(p, q, r, d_t) + a_{20} \left(J_2(p, q+4, r, d_t) + J_2(p, q, r+2, d_t) \right. \right. \right. \\ &\quad \left. \left. + \frac{1}{16} J_2(p+4, q, r, d_t) + \frac{1}{2} J_2(p+2, q+2, r, d_t) - \frac{d_t+2}{4} (4J_2(p, q+2, r, d_t) + J_2(p+2, q, r, d_t)) \right. \right. \\ &\quad \left. \left. + \frac{d_t(d_t+2)}{4} J_2(p, q, r, d_t) \right) \right] + 2a_{02}J_2(p, q, r, d_t)I_S(s, 0, 2, d_r) + a_{11}I_S(s, 0, 1, d_r) \left[d_t J_2(p, q, r, d_t) \right. \\ &\quad \left. \left. - 2J_2(p, q+2, r, d_t) - \frac{1}{2} J_2(p+2, q, r, d_t) \right) \right] \right\}, \end{aligned} \quad (1.26b)$$

$$\langle\langle c_{12}^p C_{12}^q (\mathbf{c}_{12} \cdot \mathbf{C}_{12})^r W_{12}^s (\mathbf{c}_{12} \cdot \mathbf{W}_{12})^t \rangle\rangle_S = \frac{d_r-1}{2} \left[\frac{(1+(-1)^t)\Gamma(\frac{d_t}{2})\Gamma(\frac{t+1}{2})}{2\sqrt{\pi}\Gamma(\frac{d_t+t}{2})} K_1(p+t, q, r, s+t, d_t, d_r) \right] \quad (1.26c)$$

$$+ 2a_{00}^{(1)}F(p, q, r, s, t, d_t, d_r). \quad (1.26d)$$

In Eq. (1.26c),

$$\begin{aligned} F(p, q, r, s, t, d_t, d_r) &\equiv \pi^{-d_t-d_r} \int d\tilde{\Gamma}_1 \int d\tilde{\Gamma}_2 c_{12}^p C_{12}^q W_{12}^s (\mathbf{c}_{12} \cdot \mathbf{C}_{12})^r (\mathbf{c}_{12} \cdot \mathbf{W}_{12})^t e^{-c_1^2-c_2^2-w_1^2-w_2^2} P_2(\hat{\mathbf{c}}_1 \cdot \hat{\mathbf{w}}_1) \\ &= \pi^{-d_t-d_r} \frac{1+(-1)^t}{2^{s+t+5}} \frac{t}{(1+t)(3+t)} J_2(p+t+2, q, r, 3) I(1, s+t+2, 3), \end{aligned} \quad (1.27)$$

where we have taken into account that the function F is meaningful only for HS.

Furthermore, we have also faced vector products in the averages, for instance,

$$\begin{aligned} \langle\langle c_{12}^{-1} [\mathbf{C}_{12} \cdot (\mathbf{c}_{12} \times \mathbf{W}_{12})]^2 \rangle\rangle &= \langle\langle c_{12} C_{12}^2 W_{12}^2 \rangle\rangle - \langle\langle C_{12}^2 c_{12}^{-1} (\mathbf{c}_{12} \cdot \mathbf{W}_{12})^2 \rangle\rangle - \langle\langle c_{12} (\mathbf{C}_{12} \cdot \mathbf{W}_{12})^2 \rangle\rangle - \langle\langle c_{12}^{-1} W_{12}^2 (\mathbf{c}_{12} \cdot \mathbf{C}_{12})^2 \rangle\rangle \\ &\quad + 2\langle\langle c_{12}^{-1} (\mathbf{c}_{12} \cdot \mathbf{C}_{12}) (\mathbf{C}_{12} \cdot \mathbf{W}_{12}) (\mathbf{c}_{12} \cdot \mathbf{W}_{12}) \rangle\rangle, \end{aligned} \quad (1.28)$$

where we have used the identity $[\mathbf{a} \cdot (\mathbf{b} \times \mathbf{c})]^2 = a^2 b^2 c^2 - a^2 (\mathbf{b} \cdot \mathbf{c})^2 - b^2 (\mathbf{c} \cdot \mathbf{a})^2 - c^2 (\mathbf{a} \cdot \mathbf{b})^2 + 2(\mathbf{a} \cdot \mathbf{b})(\mathbf{b} \cdot \mathbf{c})(\mathbf{c} \cdot \mathbf{a})$. From parity arguments, one can prove that

$$\langle\langle c_{12}^{-1} (\mathbf{c}_{12} \cdot \mathbf{C}_{12}) (\mathbf{C}_{12} \cdot \mathbf{W}_{12}) (\mathbf{c}_{12} \cdot \mathbf{W}_{12}) \rangle\rangle = \langle\langle c_{12}^{-3} (\mathbf{c}_{12} \cdot \mathbf{C}_{12})^2 (\mathbf{c}_{12} \cdot \mathbf{W}_{12})^2 \rangle\rangle, \quad (1.29a)$$

$$\langle\langle c_{12} (\mathbf{C}_{12} \cdot \mathbf{W}_{12})^2 \rangle\rangle = \langle\langle C_{12}^2 c_{12}^{-1} (\mathbf{c}_{12} \cdot \mathbf{W}_{12})^2 \rangle\rangle, \quad (1.29b)$$

$$\langle\langle (\mathbf{c}_{12} \cdot \mathbf{C}_{12}) \mathbf{C}_{12} \cdot (\mathbf{c}_{12} \times \mathbf{W}_{12}) \rangle\rangle = \langle\langle (4C_{12}^2 + c_{12}^2) \mathbf{C}_{12} \cdot (\mathbf{c}_{12} \times \mathbf{W}_{12}) \rangle\rangle = 0. \quad (1.29c)$$

Some of these quantities are similar to those found in the smooth case [3], but here they are more complex due to the introduction of the angular velocities.

In the computation of μ_{22} from the Sonine approximation, one needs to deal with the generalized quantity

$$\begin{aligned} K_2(p, q, r, s, t, u, d_t, d_r) &\equiv \langle\langle c_{12}^p C_{12}^q (\mathbf{c}_{12} \cdot \mathbf{C}_{12})^r w_{12}^s W_{12}^t (\mathbf{w}_{12} \cdot \mathbf{W}_{12})^u \rangle\rangle_S \\ &= \pi^{-d_t - d_r} \left\{ J_2(s, t, u, d_r) \left[J_2(p, q, r, d_t) + a_{20} \left(J_2(p, q + 4, r, d_t) + J_2(p, q, r + 2, d_t) \right. \right. \right. \\ &\quad \left. \left. + \frac{1}{16} J_2(p + 4, q, r, d_t) + \frac{1}{2} J_2(p + 2, q + 2, r, d_t) - \frac{d_t + 2}{4} (4J_2(p, q + 2, r, d_t) + J_2(p + 2, q, r, d_t)) \right. \right. \\ &\quad \left. \left. + \frac{d_t(d_t + 2)}{4} J_2(p, q, r, d_t) \right] + a_{02} J_2(p, q, r, d_t) \left(J_2(s, t + 4, u, d_r) + J_2(s, t, u + 2, d_r) \right) \right. \\ &\quad \left. + \frac{1}{16} J_2(s + 4, t, u, d_r) + \frac{1}{2} J_2(s + 2, t + 2, u, d_r) - \frac{d_t + 2}{4} (4J_2(s, t + 2, u, d_r) + J_2(s + 2, t, u, d_r)) \right. \\ &\quad \left. + \frac{d_t(d_t + 2)}{4} J_2(s, t, u, d_r) \right) + 2a_{11} \left[\left(J_2(p, q + 2, r, d_t) + \frac{1}{4} J_2(p + 2, q, r, d_t) \right. \right. \\ &\quad \left. \left. - \frac{d_t}{2} J_2(p, q, r, d_t) \right) \left(J_2(s, t + 2, u, d_r) + \frac{1}{4} J_2(s + 2, t, u, d_r) - \frac{d_r}{2} J_2(s, t, u, d_r) \right) \right. \\ &\quad \left. \left. + J_2(p, q, r + 1, d_t) J_2(s, t, u + 1, d_r) \right] \right\}. \quad (1.30) \end{aligned}$$

In particular,

$$\langle\langle c_{12} (\mathbf{C}_{12} \cdot \mathbf{c}_{12}) (\mathbf{W}_{12} \cdot \mathbf{w}_{12}) \rangle\rangle_S = K_2(1, 0, 1, 0, 0, 1, d_t, d_r). \quad (1.31)$$

Moreover,

$$\begin{aligned} \langle\langle c_{12} (\mathbf{C}_{12} \cdot \mathbf{W}_{12}) (\mathbf{c}_{12} \cdot \mathbf{w}_{12}) \rangle\rangle_S &= \langle\langle c_{12} (\mathbf{C}_{12} \cdot \mathbf{w}_{12}) (\mathbf{c}_{12} \cdot \mathbf{W}_{12}) \rangle\rangle_S \\ &= \frac{d_r - 1}{54} \pi^{-6} \left[2a_{11} + 5a_{00}^{(1)} \right] J_2(3, 2, 0, 3) J_2(2, 2, 0, 3), \quad (1.32a) \end{aligned}$$

$$\langle\langle c_{12}^{-1} (\mathbf{c}_{12} \cdot \mathbf{C}_{12}) (\mathbf{c}_{12} \cdot \mathbf{W}_{12}) (\mathbf{c}_{12} \cdot \mathbf{w}_{12}) \rangle\rangle_S = \frac{d_r - 1}{27} \pi^{-6} \left[a_{11} + a_{00}^{(1)} \right] J_2(3, 2, 0, 3) J_2(2, 2, 0, 3), \quad (1.32b)$$

$$\langle\langle c_{12}^{-1} w_{12}^2 (\mathbf{c}_{12} \cdot \mathbf{W}_{12})^2 \rangle\rangle_S = \frac{d_r - 1}{2} \left[\frac{1}{3} K_2(1, 0, 0, 2, 2, 0, 3, 3) + a_{00}^{(1)} \frac{\pi^{-6}}{15} J_2(3, 0, 0, 3) J_2(2, 4, 0, 3) \right]. \quad (1.32c)$$

From symmetry arguments, the averages involving a power of $\mathbf{c}_{12} \cdot (\mathbf{C}_{12} \times \mathbf{W}_{12})$, $\mathbf{w}_{12} \cdot (\mathbf{C}_{12} \times \mathbf{W}_{12})$, $\mathbf{C}_{12} \cdot (\mathbf{c}_{12} \times \mathbf{w}_{12})$, or $\mathbf{W}_{12} \cdot (\mathbf{c}_{12} \times \mathbf{w}_{12})$ vanish.

II. KULLBACK–LEIBLER DIVERGENCE-LIKE FUNCTIONAL

In order to characterize the departure of the Sonine approximation for the VDF from the Maxwellian, let us introduce the Kullback–Leibler divergence (or relative entropy) [4], i.e.,

$$\mathcal{D}_{\text{KL}}(\phi \parallel \phi_M) = \int d\tilde{\Gamma} \phi(\tilde{\Gamma}) \ln \frac{\phi(\tilde{\Gamma})}{\phi_M(\tilde{\Gamma})} \approx \frac{1}{2} \int d\tilde{\Gamma} \phi_M(\tilde{\Gamma}) \left[\frac{\phi(\tilde{\Gamma}) - \phi_M(\tilde{\Gamma})}{\phi_M(\tilde{\Gamma})} \right]^2, \quad (2.1)$$

where in the second step we have expanded ϕ around ϕ_M , neglected terms beyond second order, and take into account that $\int d\tilde{\Gamma} [\phi(\tilde{\Gamma}) - \phi_M(\tilde{\Gamma})] = 0$. Inserting the Sonine expansion and using the normalization relation [see Eqs. (3.15)–(3.18) of the main text], one gets

$$\mathcal{D}_{\text{KL}}(\phi \parallel \phi_M) \approx \frac{1}{2} \sum_{j+k+2\ell \geq 2} N_{jk}^{(\ell)} \left| a_{jk}^{(\ell)} \right|^2. \quad (2.2)$$

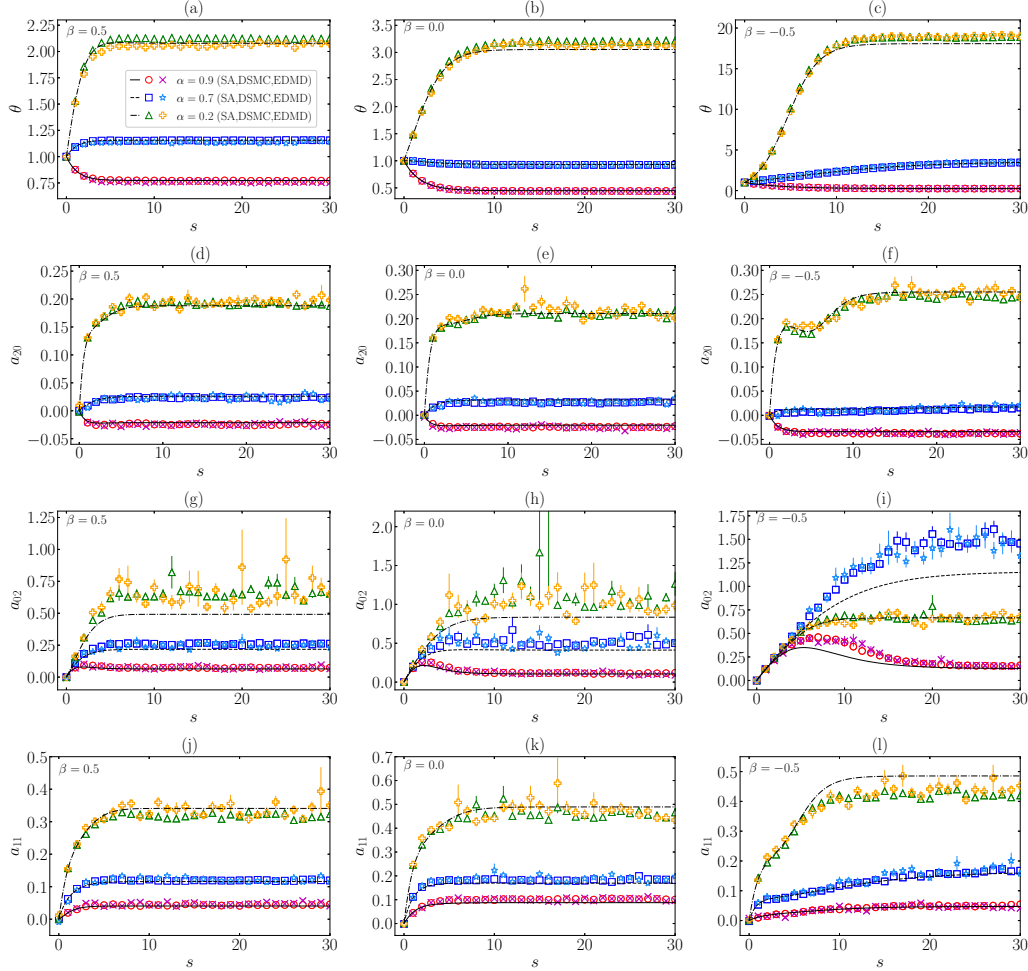


FIG. 1. Plots of (a–c) the temperature ratio $\theta(s)$, (d–f) the cumulant $a_{20}(s)$, (g–i) the cumulant $a_{02}(s)$, and (j)–(l) the cumulant $a_{11}(s)$, for uniform disks ($\kappa = \frac{1}{2}$), as functions of the number of collisions per particle s . The left (a, d, g, j), middle (b, e, h, k), and right (c, f, i, l) panels correspond to $\beta = 0.5, 0$, and -0.5 , respectively. In each panel, three values of α are considered: 0.9 (DSMC: \circ ; EDMD: \times), 0.7 (DSMC: \square ; EDMD: \star), and 0.2 (DSMC: \triangle ; EDMD: $+$). The lines are theoretical predictions from the SA.

This gives $\mathcal{D}_{\text{KL}}(\phi \parallel \phi_{\text{M}})$ as a sum of the squares of the Sonine coefficients, weighted with the normalization constants $N_{jk}^{(\ell)}$. We now divide by the sum of the weights to define a (normalized) average as

$$\mathfrak{D}(\phi \parallel \phi_{\text{M}}) = \frac{\sum_{j+k+2\ell \geq 2} N_{jk}^{(\ell)} |a_{jk}^{(\ell)}|^2}{\sum_{j+k+2\ell \geq 2} N_{jk}^{(\ell)}}. \quad (2.3)$$

In the Sonine approximation, $\mathfrak{D}(\phi \parallel \phi_{\text{M}})$ becomes

$$\mathfrak{D}(\phi \parallel \phi_{\text{M}}) = \frac{1}{N_{\mathfrak{D}}} \left[\frac{d_t(d_t + 2)}{8} |a_{20}|^2 + \frac{d_r(d_r + 2)}{8} |a_{02}|^2 + \frac{d_t d_r}{4} |a_{11}|^2 + (d_r - 1) \frac{45}{32} |a_{00}^{(1)}|^2 \right], \quad (2.4a)$$

$$N_{\mathfrak{D}} \equiv \frac{d_t + d_r}{8} (d_t + d_r + 2) + (d_r - 1) \frac{45}{32}. \quad (2.4b)$$

The Sonine approximation values of $\mathfrak{D}(\phi^H \parallel \phi_M)$ as functions of α and β are plotted in Fig. 2(a) for uniform disks and in Fig. 2(b) for uniform spheres. Comparison with Figs. 2(c) and 3(c) of the main text shows that the general shape of $\mathfrak{D}(\phi^H \parallel \phi_M)$ is dominated by that of a_{02}^H . We observe that the largest deviations of ϕ^H from the Maxwellian distribution occur, paradoxically, in lobes emerging from a vertex at $(\alpha, \beta) = (1, -1)$. This is the region where the Sonine approximation is expected to be less reliable, at least at a quantitative level.

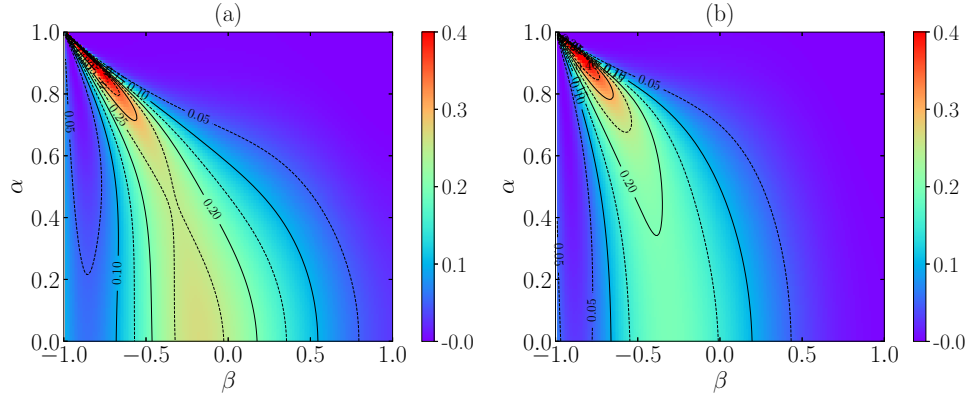


FIG. 2. Quantity $\mathfrak{D}(\phi^H \parallel \phi_M)$ in the Sonine approximation as a function of α and β for (a) uniform disks and (b) uniform spheres.

III. HIGH-VELOCITY TAIL OF THE MARGINAL DISTRIBUTION $\phi_{cw}(c^2 w^2)$

In this section we present an alternative justification for the high-velocity tail of $\phi_{cw}(c^2 w^2)$ given in the main text. Assuming $c \gg 1$ and $w \gg 1$ in the stationary version of the BE for the reduced VDF $\phi(\tilde{\Gamma})$, we get

$$c \frac{\partial \phi^H}{\partial c} + w \frac{\partial \phi^H}{\partial w} \approx -\gamma_c c \phi^H. \quad (3.1)$$

Here, we have (i) neglected the collisional gain term versus the loss term, (ii) taken $c_{12} \rightarrow c_1$, (iii) ignored the dependence on the angle $\cos^{-1}(\hat{\mathbf{c}} \cdot \hat{\mathbf{w}})$ (which only exists for hard spheres), (iv) neglected ϕ^H versus $c\phi^H$, and (v) taken into account that $\mu_{20}^H/d_t = \mu_{02}^H/d_r$ and $\gamma_c = d_t B_1/\mu_{20}^H$. The general solution of this linear first-order partial differential equation can be obtained from the method of characteristics as

$$\phi^H(\tilde{\Gamma}) \approx e^{-\gamma_c c G} \left(\frac{w}{c} \right), \quad (3.2)$$

where $G(y)$ is an unknown function. Now we take the liberty of assuming that the tails of the marginal distributions $\phi_{\mathbf{w}}(\mathbf{w})$ and $\phi_{c^2 w^2}(x)$ can be obtained from Eq. (3.2), i.e.,

$$\phi_{\mathbf{w}}(\mathbf{w}) \approx \Omega_{d_t} \int_0^\infty dc c^{d_t-1} e^{-\gamma_c c G} \left(\frac{w}{c} \right), \quad (3.3a)$$

$$\phi_{c^2 w^2}(x) \approx \frac{\Omega_{d_t} \Omega_{d_r}}{2} x^{\frac{d_r}{2}-1} \int_0^\infty dc c^{d_t-d_r-1} e^{-\gamma_c c G} \left(\frac{\sqrt{x}}{c^2} \right). \quad (3.3b)$$

Consistency of Eq. (3.3a) with the high-velocity tail $\phi_{\mathbf{w}}(\mathbf{w}) \sim w^{-\gamma w}$ implies that $G(y) \sim y^{-\gamma w}$ for large y . Insertion of this asymptotic form of $G(y)$ into Eq. (3.3b) finally yields

$$\phi_{c^2 w^2}^H(x) \sim x^{-\gamma c w}, \quad \gamma c w = 1 + \frac{\gamma w - d_r}{2}, \quad (3.4)$$

in agreement with the result in the main text.

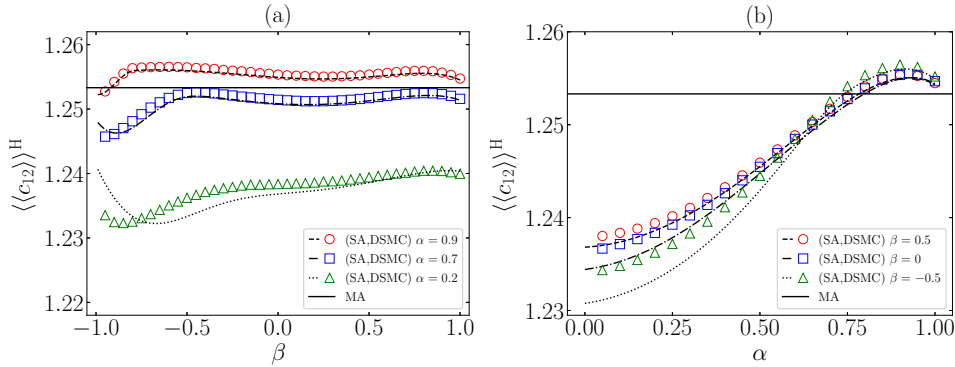


FIG. 3. Two-body average $\langle\langle c_{12} \rangle\rangle^H$ from Maxwellian and Sonine approximations (lines) and DSMC simulation outcomes (symbols) for uniform disks ($\kappa = \frac{1}{2}$) as a function of (a) the coefficient of tangential restitution β (at $\alpha = 0.9, 0.7, \text{ and } 0.2$), (b) the coefficient of normal restitution α (at $\beta = 0.5, 0, \text{ and } -0.5$).

IV. TRANSIENT STATES

In the main text, we focused on the comparison between the theoretical predictions and the simulation data for the HCS. As a complement, here we provide a comparison for the temporal evolution toward the HCS.

Figure 1 shows the evolution of $\theta(s)$, $a_{20}(s)$, $a_{02}(s)$, and $a_{11}(s)$, starting from a Maxwellian and equipartioned initial state, so that $\theta(0) = 1$ and $a_{20}(0) = a_{02}(0) = a_{11}(0) = 0$. We observe that the Sonine-approximation theoretical predictions agree very well with simulations, except close to the HCS values for the cases in which $a_{02}^H, a_{11}^H \sim \mathcal{O}(1)$.

V. COMPUTATION OF $\langle\langle c_{12} \rangle\rangle^H$, μ_{20}^H , AND μ_{02}^H FROM DSMC. COMPARISON WITH THE MAXWELLIAN AND SONINE APPROXIMATIONS

An important point of our work is the exact expression—in the framework of the BE—of the relevant collisional moments in terms of two-body averages, as displayed in Table II. It is then interesting to compute the HCS collisional moments μ_{20}^H and μ_{02}^H from DSMC and compare the results with predictions from the Maxwellian and Sonine approximations.

Before starting with the collisional moments, let us first consider the simple two-body average $\langle\langle c_{12} \rangle\rangle$. It can be computed in simulations as

$$\langle\langle c_{12} \rangle\rangle = \frac{1}{N'} \sum_{ij}^{N'} c_{ij}, \quad (5.1)$$

with, in principle, $N' = N(N-1)/2$ being the total number of pairs. Since we had $N = 10^4$ particles, this would imply $N' \simeq 5 \times 10^7$ pairs. Instead, in order to accelerate the computation, we took a random sample of $N' = 10^5$ pairs, which represent a 2% of the total number of pairs. The results for $\langle\langle c_{12} \rangle\rangle^H$ are displayed in Fig. 3. While the Maxwellian-approximation value, $\langle\langle c_{12} \rangle\rangle_M = \sqrt{\pi/2} \simeq 1.253$, is independent of α and β , the dependence of $\langle\langle c_{12} \rangle\rangle^H$ on both coefficients of restitution is well predicted by the Sonine approximation, at least semi-quantitatively.

Now we turn to the collisional moments μ_{20} and μ_{02} , whose expressions as linear combinations of the three two-body averages $\langle\langle c_{12}^3 \rangle\rangle$, $\langle\langle c_{12} W_{12}^2 \rangle\rangle$, and $\langle\langle c_{12}^{-1} (c_{12} \cdot \mathbf{W}_{12})^2 \rangle\rangle$ are displayed in Table II. Those two-body averages are evaluated by the DSMC method by sums over pairs analogous to Eq. (5.1), again with $N' = 10^5$. From Figs. 4(a–d), we infer that both Maxwellian and, especially, Sonine approximation provide good estimates of the two first collisional moments μ_{20}^H and μ_{02}^H . Moreover, as Figs. 4(e, f) show, the HCS condition $\mu_{20}^H/2\mu_{02}^H = 1$ is very accurately fulfilled by the DSMC data.

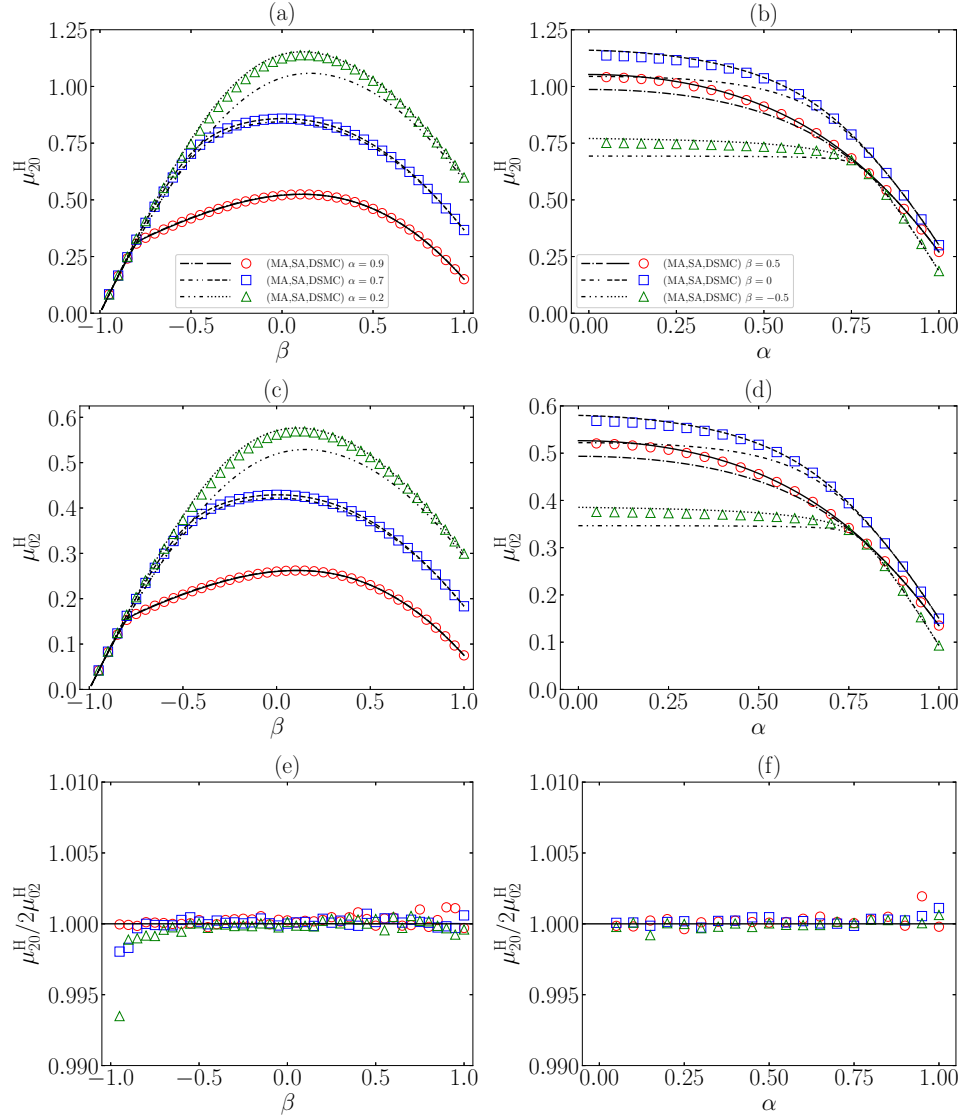


FIG. 4. Plots of (a, b) the collisional moment μ_{20}^H , (c, d) the collisional moment μ_{02}^H , and (e, f) the ratio $\mu_{20}^H/2\mu_{02}^H$ for uniform disks ($\kappa = \frac{1}{2}$). The quantities are plotted versus (a, c, e) the coefficient of tangential restitution β (at $\alpha = 0.9, 0.7$, and 0.2) and (b, d, f) the coefficient of normal restitution α (at $\beta = 0.5, 0$, and -0.5). Symbols represent DSMC values and lines in panels (a-d) correspond to the Sonine-approximation predictions. The thick black lines in panels (e, f) represent the HCS condition $\mu_{20}^H/2\mu_{02}^H = 1$.

VI. SOME TECHNICAL DETAILS ABOUT THE HIGH-VELOCITY FITTING

A. Fitting of the exponents γ_c , γ_w , and γ_{cw}

To get the high-velocity tail exponents γ_c , γ_w , and γ_{cw} from simulations (see Fig. 9 of the main text), we fitted the data according to some conditions. First of all, we defined threshold values for the velocity variables $x = c, w, c^2w^2$,

beyond which the velocities were considered high enough as to observe the asymptotic behavior. Those thresholds are defined as $x_{\text{thres}} = \max\{\tilde{x}, x_*^{\text{M}}\}$, where the values of \tilde{x} are

$$\tilde{c} = \frac{5/2}{\sqrt{\frac{\bar{\alpha}^2}{2\alpha^2} + \frac{\bar{\beta}^2}{2\beta^2}}}, \quad \tilde{w} = \frac{5}{2} \frac{\kappa|\beta|}{\beta}, \quad \widetilde{c^2 w^2} = \tilde{c}^2 \tilde{w}^2. \quad (6.1)$$

This ensures that $c_2'' \gg 1$ and $w_2'' \gg 1$ in Eqs. (B2) and (B4) of the main text. In what concerns to the values of x_*^{M} , they were determined under the condition of fulfilling a continuous and differentiable match between the Maxwellian approximation VDF and the high-velocity tail behavior, as derived in Section VI B.

For each histogram, we firstly chose the range of points comprised between x_{thres} and x_{max} , where x_{max} represents the maximum value of x in our dataset for a given system. If $x_{\text{max}} < x_{\text{thres}}$, we concluded that there were not enough data to get a trusted fitting. On the other hand, if $x_{\text{max}} > x_{\text{thres}}$, we proceeded to choose the proper subrange of data to be fitted from a minimization of $|\chi^2/\text{d.o.f} - 1|$, [5] where χ^2 is the *chi-square* statistic (computed assuming diagonal covariance) and d.o.f is the number of degrees of freedom of the fit. If the number of points in the subrange were larger than 5, we fitted them to the desirable form, getting the slope, as well as the standard deviation of the chosen points in the dataset with respect to the fitting parameters. Finally, we computed Pearson's coefficient of determination, R^2 , concluding that the fit was trustable if $R^2 \geq 0.9$, discarding the results otherwise.

B. Matching points x_*^{M}

In previous works for the smooth case [6], a merged HCS VDF was built from a match of the thermal part (as described by the Sonine approximation) and the asymptotic tail, the matching point c_* being determined by imposing continuity of the VDF and of its first derivative. In our work, we used this same method to compute the matching points x_* for the marginal distributions ϕ_c^{H} , ϕ_w^{H} , and ϕ_{cw}^{H} .

Although we present below the derivation of x_* from the Sonine approximation, we actually considered in the fitting the matching points x_*^{M} provided by the MA. This is due to the appearance of bimodal thermal regions of the VDF (especially for ϕ_w^{H}) in the Sonine approximation, not observed in simulations, and even unphysical negative values in a small range of values, as previously reported for HS. [1] We exclusively show below the results for hard disks ($d_t = 2$, $d_r = 1$).

1. Matching of $\phi_c^{\text{H}}(\mathbf{c})$: c_*^{M}

We construct a merged distribution $\phi_c^{\text{H}}(\mathbf{c})$, such that it coincides with that of the Sonine approximation for $c < c_*$ and with its asymptotic high-velocity tail for $c > c_*$, i.e.,

$$\phi_c^{\text{H}}(\mathbf{c}) = \mathcal{A}_c^{\text{th}} e^{-c^2} [1 + a_{20}^{\text{H}} S_2(c^2)] \Theta(c_* - c) + \mathcal{A}_c e^{-\gamma c} \Theta(c - c_*). \quad (6.2)$$

Imposing the continuity of $\phi_c^{\text{H}}(\mathbf{c})$ and its first derivative at the matching point c_* yields the following 5th-degree polynomial equation:

$$c_* = \frac{\gamma c}{2} - \frac{a_{20}^{\text{H}} c_* (c_* - 2)}{1 + a_{20}^{\text{H}} S_2(c_*^2)}. \quad (6.3)$$

As said above, however, we take the Maxwellian approximation for the thermal part ($c < c_*$), i.e., $c_*^{\text{M}} = \gamma c/2$.

2. Matching of $\phi_w^{\text{H}}(\mathbf{w})$: w_*^{M}

In this case, we have

$$\phi_w^{\text{H}}(\mathbf{w}) = \mathcal{A}_w^{\text{th}} e^{-w^2} [1 + a_{02}^{\text{H}} S_2(w^2)] \Theta(w_* - w) + \mathcal{A}_w w^{-\gamma w} \Theta(w - w_*). \quad (6.4)$$

Again, we assume continuity of the function and its first derivative at w_* , which gives a cubic equation for w_*^2 ,

$$w_*^2 = \frac{\gamma w}{2} - \frac{a_{02}^{\text{H}} w_*^2 (3 - 2w_*^2)}{1 + a_{02}^{\text{H}} S_2(w_*^2)}. \quad (6.5)$$

Thus, $w_*^{\text{M}} = \sqrt{\gamma w/2}$.

3. Matching of $\phi_{c^2w^2}^H(x): x_*^M$

The merged function is now

$$\begin{aligned} \phi_{cw}^H(x) = & \mathcal{A}_{cw}^{\text{th}} x^{-\frac{1}{2}} e^{-2\sqrt{x}} \left(1 + \frac{16a_{20}^H + 4a_{11}^H + 6a_{02}^H}{8} - \sqrt{x} \frac{5a_{20}^H + 6a_{11}^H + 5a_{02}^H}{4} + x \frac{a_{20}^H + 2a_{11}^H + a_{02}^H}{2} \right) \Theta(x_* - x) \\ & + \mathcal{A}_{cw} x^{-\gamma_{cw}} \Theta(x - x_*), \end{aligned} \quad (6.6)$$

where we have used $K_{\frac{1}{2}}(2\sqrt{x}) = \sqrt{\pi} e^{-2\sqrt{x}} / 2x^{1/4}$. From the continuity conditions one gets the cubic equation

$$\begin{aligned} & x_*^{3/2} (a_{20}^H + 2a_{11}^H + a_{02}^H) - x_* [(a_{20}^H + a_{02}^H)(3 + \gamma_{cw}) + a_{11}^H(2 + \gamma_{cw})] \\ & + x_*^{1/2} \left[2 + a_{20}^H \left(4 + \frac{5\gamma_{cw}}{2} \right) + a_{11}^H(1 + 3\gamma_{cw}) + \frac{a_{02}^H}{2}(3 + 5\gamma_{cw}) \right] \\ & - (2\gamma_{cw} - 1) \left[1 + 2a_{20}^H + \frac{1}{2}a_{11}^H + \frac{3}{4}a_{02}^H \right] = 0. \end{aligned} \quad (6.7)$$

$$\begin{aligned} (2\gamma_{cw} - 1) \left(1 + 2a_{20}^H + \frac{1}{2}a_{11}^H + \frac{3}{4}a_{02}^H \right) = & x_*^{3/2} (a_{20}^H + 2a_{11}^H + a_{02}^H) - x_* [(a_{20}^H + a_{02}^H)(3 + \gamma_{cw}) + a_{11}^H(2 + \gamma_{cw})] \\ & + x_*^{1/2} \left[2 + a_{20}^H \left(4 + \frac{5\gamma_{cw}}{2} \right) + a_{11}^H(1 + 3\gamma_{cw}) + \frac{a_{02}^H}{2}(3 + 5\gamma_{cw}) \right]. \end{aligned} \quad (6.8)$$

In the Maxwellian approximation, we simply get $x_*^M = (\gamma_{cw} - \frac{1}{2})^2$.

-
- [1] F. Vega Reyes, A. Santos, and G. M. Kremer, Role of roughness on the hydrodynamic homogeneous base state of inelastic spheres, *Phys. Rev. E* **89**, 020202(R) (2014).
 [2] V. Garzó, *Granular Gaseous Flows. A Kinetic Theory Approach to Granular Gaseous Flows* (Springer Nature, Switzerland, 2019).
 [3] N. V. Brilliantov and T. Pöschel, *Kinetic Theory of Granular Gases* (Oxford University Press, Oxford, 2004).
 [4] A. Megias and A. Santos, Kullback–Leibler divergence of a freely cooling granular gas, *Entropy* **22**, 1308 (2020).
 [5] P. Young, *Everything You Wanted to Know About Data Analysis and Fitting but Were Afraid to Ask*, SpringerBriefs in Physics (Springer, Cham, 2015).
 [6] T. Pöschel, N. V. Brilliantov, and A. Formella, Impact of high-energy tails on granular gas properties, *Phys. Rev. E* **74**, 041302 (2006).

Mpemba-like effect in the IRHS model

9

9.1 Summary

In this chapter, the emergence of the **ME** in a homogeneous and dilute granular gas of inelastic and rough **HD** driven by the **ST** is studied. The granular gas is assumed to be made of identical disks of diameter σ , mass m , and reduced moment of inertia κ . The binary collisions between granular particles are described by the **IRHS** model, where the inelasticity is accounted for by a coefficient of normal restitution, α , and the surface roughness by a coefficient of tangential restitution, β , both assumed to be constant. The **ST** models an injection of energy into the granular gaseous flow via its translational and rotational degrees of freedom, by means of a stochastic force and a stochastic torque, both with the properties of a white noise, and with noise intensities χ_t^2 and χ_r^2 , respectively. A particular case of the thermostat can be determined by a noise temperature, T^{wn} , and a rotational-to-total relative noise intensity, ε , which is equivalent to give the values of the noise intensities, as introduced in **Subsection 2.4.2**. This system is studied in the context of the homogeneous version of the **BFPE** appearing in Eq. (2.54) [see Eq. (11) of Article 6 (**Section 9.2**)].

The main aim of this chapter is to design, in this system, a preparation protocol to generate the proper initial states of the samples involved in a Mpemba-like effect experiment. In fact, from previous works of the same collisional model, but with the external energy injection supplying just to the translational degrees of freedom ($\varepsilon = 0$), we know that **ME** appears [**Tor+19**]. However, it does not seem obvious how to initially prepare the system. In Article 6 (**Section 9.2**), after the introduction of the model, we characterize the homogeneous states of the system. Here, a noise-induced time and temperature scales of the problem appear, these being $1/\nu^{\text{wn}}$ and T^{wn} , respectively. In order to do that, the evolution equation of the mean granular temperature, T/T^{wn} , and the rotational-to-translational temperature ratio, θ , are derived from the **BFPE** [see

Eqs. (23) of Article 6 (Section 9.2)]. However, the system of differential equations formed by \dot{T}/T^{wn} and $\dot{\theta}$ is not closed, since the energy production rates or, equivalently, the collisional moments μ_{20} and μ_{02} , depend on the whole VDF. Thus, we need to introduce some approximations to give quantitative predictions of the system. From previous studies of the homogeneous states of a granular gas under the IRHS model, but restricted to $\varepsilon = 0$, the steady-state values of the cumulants are not too large [VS15] as compared with the freely evolving case [VSK14b; MS23]. Then, if the initial conditions are not too far from a Maxwellian distribution, a MA for the time-dependent and steady VDF seems to be plausible, at least a first approach to the problem. This is found to be a good approach in accordance with DSMC and EDMD—with the AGF algorithm applied to the ST—computer simulation results from hand-made programs [Meg23]. We reproduce sets of uniform hard disks, that is, with $\kappa = 1/2$, and for different values of the coefficients of restitution, α and β , and of the parameter ε . From them, the MA is tested both for steady-state values, $(T^{\text{st}}/T^{\text{wn}}, \theta^{\text{st}})$, and for transient stages, $(T(t)/T^{\text{st}}, \theta^{\text{st}})$, as can be observed in Figures 5 and 6 of Article 6 (Section 9.2). From the steady states of the system, it is important to highlight that θ^{st} is an increasing function of ε . In addition, it is found from the theoretical prediction of the slope of $\dot{T}/T^{\text{st}} \equiv \Phi$, and confirmed by the latter simulation results, that for every pair of initial conditions $(T^0/T^{\text{st}}, \theta^0)$, there exists a critical value of the rotational-to-total noise intensity ratio, $\varepsilon_{\text{cr}}(T^0/T^{\text{st}}, \theta^0)$, such that, for every $\varepsilon > \varepsilon_{\text{cr}}$, the mean granular temperature overshoots, at a certain time, its future steady-state value. Then, we numerically compute the value of ε_{cr} with respect to different initial conditions, and different values of the coefficients of restitution, for uniform HD, as showed in Figure 7 of Article 6 (Section 9.2).

Once the homogeneous states have been theoretically described, and the approximated scheme is validated by means of computer simulation results, we study the conditions under which the standard DME shows up in this system. Let us first imagine that, given a reference ST, $(T_{\text{ref}}^{\text{wn}}, \varepsilon_{\text{ref}})$, the value of the noise intensity ratio, ε_{ref} , is below the critical value for every initial condition. That is, we impose that there is no overshoot of any thermal curve. Then, for two different systems, A and B, the former, assumed to be initially hotter than the latter, will evolve up to the same steady state. The appearance of the DME is detected if there exists a crossover between the two temperature curves at a certain crossing time. Therefore, we study the necessary conditions for the DME to appear in terms of the mean temperature slopes. That is, we impose $\Phi(T_A^0/T_{\text{ref}}^{\text{st}}, \theta_A^0) < \Phi(T_B^0/T_{\text{ref}}^{\text{st}}, \theta_B^0)$. From the MA, it is deduced that $\theta_A^0 < \theta_B^0$ is needed, which was already known from Ref. [Tor+19] in the particular case of $\varepsilon = 0$. Then, to enhance (and ensure) the effect, the condition should be exaggerated to $\theta_A^0 \ll \theta_B^0$.

On the other hand, we also analyze the DME via the OME. Then, we impose that, at least, the initially colder system must suffer an overshoot with respect to its steady value, i.e., $\varepsilon_{\text{ref}} > \varepsilon_{\text{cr}}(T_B^0/T_{\text{ref}}^{\text{st}}, \theta_B^0)$. Following the results in Article 1 (Section 5.2), we

study the **OME** by means of a functional, \mathfrak{D} , which is a convex and positive function of $T(t)/T^{\text{st}}$, recalling the expression of the local-equilibrium functional introduced in Article 1 (**Section 5.2**). Then, to detect the direct **OME**, we need a crossover between \mathfrak{D}_A and \mathfrak{D}_B at a certain crossing time, with system B overshooting the steady state, and without any intersection (or an odd number of them) between the mean granular temperatures of A and B. The necessary condition for the initial slopes is the opposite to that of the standard version of the **DME**, that is, $\Phi(T_A^0/T_{\text{ref}}^{\text{st}}, \theta_A^0) > \Phi(T_B^0/T_{\text{ref}}^{\text{st}}, \theta_B^0)$, which translates into $\theta_A^0 > \theta_B^0$. However, according to the theoretical description of the thermal slope Φ , we prefer for θ_A^0 not to be excessively large, in order to avoid an extremely slow relaxation of system A that could preclude the emergence of the effect.

After the latter analysis, we derive preparation protocols for the initial states in a Mpemba-like cooling experiment, which allows us to observe the standard **DME** and the **OME** in the described system. These initial states are based on the steady states of the system. Those protocols are described in Section 3.3 of Article 6 (**Section 9.2**), and sketched in Figures 8 and 9 of Article (**Section 9.2**). Finally, **DSMC** and **EDMD** computer simulation results validate the theoretical protocols, as can be observed in Figures 11 and 12 of Article 6 (**Section 9.2**).

9.2 Article 6

Title: Mpemba-like effect protocol for granular gases of inelastic and rough hard disks

Authors: Alberto Megías¹ and Andrés Santos^{1,2}

Affiliations:

¹ Departamento de Física, Universidad de Extremadura, E-06006 Badajoz, Spain

² Instituto de Computación Científica Avanzada (ICCAEx), Universidad de Extremadura, E-06006 Badajoz, Spain

Journal: Frontiers in Physics

Volume: 10

Pages: 971671

Year: 2022

DOI: [10.1051/epjconf/202124904006](https://doi.org/10.1051/epjconf/202124904006)



Copy of the preprint of the work: “Alberto Megías, and Andrés Santos, ‘Mpemba-like effect protocol for granular gases of inelastic and rough hard disks’, *Frontiers in Physics* 10, 971671 (2022) <https://doi.org/10.3389/fphy.2022.971671>.”



Mpemba-like effect protocol for granular gases of inelastic and rough hard disks

Alberto Megías^{1,*} and Andrés Santos^{1,2}

¹Departamento de Física, Universidad de Extremadura, E-06006 Badajoz, Spain

²Instituto de Computación Científica Avanzada (ICCAEx), Universidad de Extremadura, E-06006 Badajoz, Spain

Correspondence*:
A. Megías
albertom@unex.es

ABSTRACT

We study the conditions under which a Mpemba-like effect emerges in granular gases of inelastic and rough hard disks driven by a class of thermostats characterized by the splitting of the noise intensity into translational and rotational counterparts. Thus, granular particles are affected by a stochastic force and a stochastic torque, which inject translational and rotational energy, respectively. We realize that a certain choice of a thermostat of this class can be characterized just by the total intensity and the fraction of noise transferred to the rotational degree of freedom with respect to the translational ones. Firstly, Mpemba effect is characterized by the appearance of a crossing between the temperature curves of the considered samples. Later, an overshoot of the temperature evolution with respect to the steady-state value is observed and the mechanism of Mpemba effect generation is changed. The election of parameters allows to design plausible protocols based on these thermostats for generating the initial states to observe the Mpemba-like effect in experiments. In order to obtain explicit results, we use a well-founded Maxwellian approximation for the evolution dynamics and the steady-state quantities. Finally, theoretical results are compared with direct simulation Monte Carlo and molecular dynamics results, and a very good agreement is found.

Keywords: granular gases, kinetic theory, Mpemba effect, direct simulation Monte Carlo, molecular dynamics

1 INTRODUCTION

Since the Antiquity, the fact that water could start freezing earlier for initially hotter samples was observed and commented by very influential people of different epochs like Aristotle [1], Francis Bacon [2], or René Descartes [3]. This counterintuitive phenomenon contradicts Isaac Newton's formulation of its well-known cooling's law [4, 5], but otherwise it is part of the popular belief in cold countries. The scientific community started to pay attention to this effect since the late 60s of the last century thanks to its accidental rediscovery by a Tanzanian high-school student, Erasto B. Mpemba. Later, he and Dr. Denis Osborne reported their findings [6, 7] and since then the effect is usually known as Mpemba effect (ME).

Whereas the original tested system for ME has been water [6–37], it is still under discussion and no consensus about its occurrence has been agreed [38–40]. In fact, the statistical physics community is currently paying attention to Mpemba-like effects that have been described in a huge variety of complex systems in the last decades, such as ideal gases [41], molecular gases [42–44], gas mixtures [45], granular

gases [46–52], inertial suspensions [53, 54], spin glasses [55], Ising models [56–58], non-Markovian mean-field systems [59, 60], carbon nanotube resonators [61], clathrate hydrates [62], active systems [63], or quantum systems [64]. The theoretical approach to the fundamentals of the problem has been done via different routes like Markovian statistics [65–69] or Landau’s theory of phase transitions [70]. Recently, in the context of a molecular gas under a nonlinear drag force, new interpretations and definitions of ME from thermal and entropic point of views, as well as a classification of the whole possible phenomenology, have been carried out [44]. In addition, ME has been experimentally observed in colloids [71, 72], proving that it is a real effect present in nature.

The very first time that ME was observed theoretically in granular gaseous rapid flows was in Ref. [46]. The considered system was a set of inelastic and smooth hard spheres (with constant coefficient of normal restitution) heated by a stochastic thermostat, the effect arising by initially preparing the system in far from Maxwellian states. The same type of initial preparation was applied to the case of molecular gases with nonlinear drag [42, 44]. Essentially, the temperature evolution depends on the whole moment hierarchy of the velocity distribution function (particularly on the excess kurtosis, or fourth cumulant, and, more weakly, on the sixth cumulant), this dependence giving rise to the possible appearance of ME.

On the other hand, there is no need to consider an initial velocity distribution function (VDF) far from the Maxwell–Boltzmann one if the temperature is coupled to other basic variables that can be fine-tuned in the initial preparation of the system. This occurs in the case of a monocomponent granular gas made by inelastic and rough hard spheres thermostatted by a stochastic force [47], as well as in driven binary mixtures of either molecular or inelastic gases [45, 48]. In those systems, one does not need to invoke strong nonGaussianities, since the temperature relaxation essentially depends on the rotational-to-translational temperature ratio (in the case of rough particles) or on the partial component temperatures (in the case of mixtures). A similar situation applies in the presence of anisotropy in either the injection of energy [51] or in the velocity flow [53]. However, there is still a lack of protocol defining a possible nearly realistic preparation of the initial states for a granular or molecular gas in homogeneous and isotropic states. Unlike other memory effects, such as Kovac’s effect [73, 74], ME has not a predefined way to elaborate a protocol.

In this work, we have addressed the latter preparation problem for a specific model of granular gases. We consider a monodisperse granular gas of inelastic and rough hard disks, where inelasticity is parameterized via a constant coefficient of normal restitution, α , and the roughness is accounted for by a coefficient of tangential restitution, β , assumed to be constant as well. Disks are “heated” by a stochastic thermostat which injects energy to both translational and rotational degrees of freedom through a combination of a stochastic force and a stochastic torque, both with properties of a white noise. The relative amount of energy injected to the rotational degree of freedom, relative to that injected to the translational degrees of freedom, can be freely chosen. Therefore, we will denote this thermostat as *splitting thermostat* (ST). The quantity coupled to the temperature that will monitor the possible occurrence of ME will be the rotational-to-translational temperature ratio, as in Ref. [47], where, however, a stochastic torque was absent. This double energy-injection based on ST allows us to fix the initial conditions of the variables that play a role in the evolution process, namely the temperature and its coupling. A side effect of providing energy to the rotational degree of freedom is that it favors the possibility of an overshoot of the temperature with respect to its steady-state value. This might cause ME, even in the absence of a crossing between the temperatures of the two samples [44]. Therefore, the protocol must be adapted to this specific phenomenon.

It is worth saying that our theoretical approach is based on a Maxwellian approximation (MA), that is, we assume that both transient and steady-state VDFs are close to a two-temperature Maxwellian. This

approach is founded on previous works for the case of zero stochastic torque [75] and on preliminary results for the system at hand [76]. Moreover, the two-dimensional characterization of the physical system is thought to be plausible for hopefully being reproduced in some experimental setup. As will be seen, the reliability of our theoretical approach is confirmed by computer simulations via the direct simulation Monte Carlo (DSMC) method and event-driven molecular dynamics (EDMD).

The paper is structured as follows. In section 2, the model system for a granular gas of inelastic and rough hard disks thermostatted by stochastic force and torque is introduced. Also, explicit evolution equations and expressions for the steady-state dynamic variables are shown under the MA, and the theoretical results are compared with DSMC and EDMD. Section 3 collects the definition and necessary conditions for ME to occur taking into account the emergence or not of overshoot during evolution. Subsequently, and based on the analysis of this section, two different protocols are presented for observing ME in cases without and with overshoot, respectively. This discussion is accompanied by its proper comparison with simulation results. Finally, concluding remarks are presented in section 4.

2 THE MODEL

We consider a set of mechanically identical inelastic and rough hard disks of mass m , diameter σ , and reduced moment of inertia $\kappa \equiv 4I/m\sigma^2$ (I being the moment of inertia). The translational velocities lie on the xy plane, i.e., $\mathbf{v} = v_x\hat{\mathbf{x}} + v_y\hat{\mathbf{y}}$, while the angular velocities point along the orthogonal z axis, $\boldsymbol{\omega} = \omega\hat{\mathbf{z}}$. Inelasticity and roughness are characterized by the coefficients of normal and tangential restitution, α and β , respectively, which are assumed to be constant and defined as [77]

$$\hat{\boldsymbol{\sigma}} \cdot \mathbf{v}'_{12} = -\alpha\hat{\boldsymbol{\sigma}} \cdot \mathbf{v}_{12}, \quad \hat{\boldsymbol{\sigma}}_{\perp} \cdot \mathbf{v}'_{12} = -\beta\hat{\boldsymbol{\sigma}}_{\perp} \cdot \mathbf{v}_{12}, \quad (1)$$

where $\hat{\boldsymbol{\sigma}} \equiv (\mathbf{r}_2 - \mathbf{r}_1)/|\mathbf{r}_2 - \mathbf{r}_1|$ is the unit intercenter vector along the line of centers from particle 1 to particle 2, $\hat{\boldsymbol{\sigma}}_{\perp} \equiv \hat{\boldsymbol{\sigma}} \times \hat{\mathbf{z}}$ is orthogonal to $\hat{\boldsymbol{\sigma}}$, $\mathbf{v}_{12} \equiv \mathbf{v}_1 - \mathbf{v}_2$ is the relative velocity between particles 1 and 2, and primed quantities account for their postcollisional values. Because of their definitions, the ranges of the coefficients of restitution are $0 \leq \alpha \leq 1$ and $-1 \leq \beta \leq 1$, $\alpha = 1$ corresponding to elastic collisions, $\beta = -1$ describing a perfectly smooth disks, and $\beta = 1$ standing for completely rough disks. In fact, total kinetic energy is only conserved if $\alpha = |\beta| = 1$ [77–80].

In the case $\alpha \neq 1$ or $|\beta| \neq 1$, that is, when kinetic energy is dissipated upon collisions, the undriven system will evolve up to a completely frozen state. In order to avoid that quench, we will force the particles to externally receive energy via a homogeneous stochastic force \mathbf{F}^{wn} and a homogeneous stochastic torque τ^{wn} that inject translational and rotational kinetic energy, respectively, with the properties of a white noise. That is,

$$\langle \mathbf{F}_i^{\text{wn}}(t) \rangle = 0, \quad \langle \mathbf{F}_i^{\text{wn}}(t) \mathbf{F}_j^{\text{wn}}(t') \rangle = l m^2 \chi_{\text{tr}}^2 \delta_{ij} \delta(t - t'), \quad (2a)$$

$$\langle \tau_i^{\text{wn}}(t) \rangle = 0, \quad \langle \tau_i^{\text{wn}}(t) \tau_j^{\text{wn}}(t') \rangle = m I \chi_{\text{rot}}^2 \delta_{ij} \delta(t - t'), \quad (2b)$$

where l is the 2×2 identity matrix, i and j are particle indices, and χ_{tr}^2 and χ_{rot}^2 are the intensities of the noises applied to the translational and rotational degrees of freedom, respectively. The combination of the stochastic force and torque is characterized by the pair of parameters $(\chi_{\text{tr}}^2, \chi_{\text{rot}}^2)$ and defines the ST, as described in section 1. In section 2.1 we will introduce a more manageable pair of equivalent parameters. An illustration of the system is represented in Figure 1.

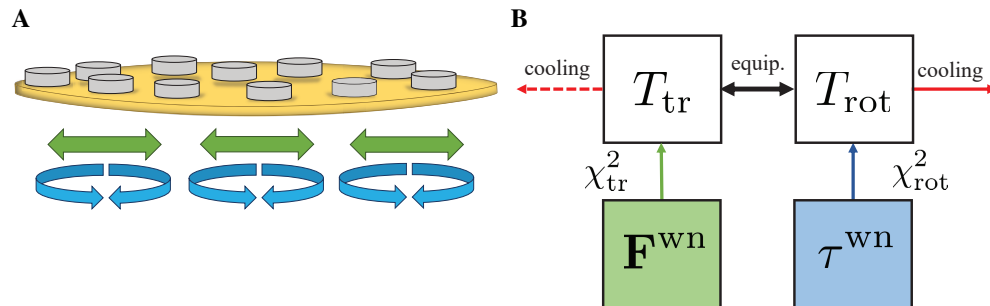


Figure 1. (A) Illustration of the system, where the green horizontal straight arrows and the blue curved ones represent the stochastic force \mathbf{F}^{wn} and the stochastic torque τ^{wn} in Equations (2), respectively. (B) Mechanism of injection-dissipation of energy in the introduced model. Dissipative collisions produce a cooling effect on the translational and rotational temperatures (T_{tr} and T_{rot}), together with a transfer between the translational and rotational energies (equipartition effect). Additionally, the external white-noise force and torque inject energy (heating effect).

To dynamically describe the system, we will work under the assumptions of the homogeneous Boltzmann–Fokker–Planck equation (BFPE). That is, we consider a homogeneous and isotropic gas in a dilute regime, such that the evolution due to the collisional process is determined by just binary collisions, assuming *Stosszahlansatz* (or molecular chaos). The BFPE for this collisional model together, with the ST, is written as follows

$$\frac{\partial}{\partial t} f(\mathbf{v}, \omega; t) - \frac{\chi_{\text{tr}}^2}{2} \left(\frac{\partial}{\partial \mathbf{v}} \right)^2 f(\mathbf{v}, \omega; t) - \frac{\chi_{\text{rot}}^2}{2} \left(\frac{\partial}{\partial \omega} \right)^2 f(\mathbf{v}, \omega; t) = J[\mathbf{v}, \omega | f], \quad (3)$$

where f is the one-particle VDF, $J[\mathbf{v}, \omega | f]$ is the usual Boltzmann collision operator for hard disks defined as [78–80]

$$J[\mathbf{v}_1, \omega_1 | f] = n\sigma \int d\mathbf{v}_2 \int_{-\infty}^{\infty} d\omega_2 \int_+ d\hat{\boldsymbol{\sigma}} |\mathbf{v}_{12} \cdot \hat{\boldsymbol{\sigma}}| \left[\frac{f(\mathbf{v}_1'', \omega_1''; t) f(\mathbf{v}_2'', \omega_2''; t)}{\alpha|\beta|} - f(\mathbf{v}_1, \omega_1; t) f(\mathbf{v}_2, \omega_2; t) \right], \quad (4)$$

where n is the number density, the subscript $+$ in the integral over $\hat{\boldsymbol{\sigma}}$ means the constraint $\mathbf{v}_{12} \cdot \hat{\boldsymbol{\sigma}} > 0$, and double primed quantities are precollisional velocities, which are given by [78–80]

$$\mathbf{v}_{1/2}'' = \mathbf{v}_{1/2} \mp \left\{ \frac{1 + \alpha^{-1}}{2} (\mathbf{v}_{12} \cdot \hat{\boldsymbol{\sigma}}) \hat{\boldsymbol{\sigma}} + \frac{\kappa}{1 + \kappa} \frac{1 + \beta^{-1}}{2} \left[\mathbf{v}_{12} \cdot \hat{\boldsymbol{\sigma}}_{\perp} - \frac{\sigma}{2} (\omega_1 + \omega_2) \right] \hat{\boldsymbol{\sigma}}_{\perp} \right\}. \quad (5)$$

2.1 Dynamics

The time evolution of the system is fully described by the BFPE, Equation (3), which allows one to determine the dynamics of macroscopic quantities. The most important and basic quantities to study the dynamics of the system will be the translational and rotational *granular* temperatures defined at a certain time t as

$$T_{\text{tr}}(t) = \frac{1}{2} m \langle v^2 \rangle, \quad T_{\text{rot}}(t) = I \langle \omega^2 \rangle, \quad (6)$$

where the notation $\langle \cdot \rangle$ means the average over the instantaneous VDF,

$$\langle X(\mathbf{v}, \omega; t) \rangle = n^{-1} \int d\mathbf{v} \int_{-\infty}^{\infty} d\omega X(\mathbf{v}, \omega; t) f(\mathbf{v}, \omega; t). \quad (7)$$

One should notice that the *partial* noise intensities χ_{tr}^2 and χ_{rot}^2 affect directly the evolution equations of $T_{\text{tr}}(t)$ and $T_{\text{rot}}(t)$, respectively. On the other hand, those quantities are coupled due to the transfer of energy during collisions (see Figure 1B). The description of the dynamics from $T_{\text{tr}}(t)$ and $T_{\text{rot}}(t)$ is equivalent to consider the mean granular temperature, $T(t)$, and the rotational-to-translational temperature, $\theta(t)$, defined as follows

$$T(t) = \frac{2}{3}T_{\text{tr}}(t) + \frac{1}{3}T_{\text{rot}}(t), \quad \theta(t) = \frac{T_{\text{rot}}(t)}{T_{\text{tr}}(t)}. \quad (8)$$

In the definition of $T(t)$ we have taken into account that there are two translational and one rotational degrees of freedom. This new pair of variables will be useful to study ME, which will be related to the evolution of the mean granular temperature $T(t)$. In addition, this change of dynamical quantities in Equation (8) induces a change of parameters describing the ST. Thus, we introduce the *total* noise intensity, χ^2 , and the *rotational-to-total* noise intensity ratio, ε , as

$$\chi^2 = \chi_{\text{tr}}^2 + \frac{I}{2m}\chi_{\text{rot}}^2, \quad \varepsilon = \frac{I}{2m} \frac{\chi_{\text{rot}}^2}{\chi^2}. \quad (9)$$

Notice that $\chi_{\text{tr}}^2 = (1 - \varepsilon)\chi^2$. Therefore, $0 \leq \varepsilon \leq 1$, $\varepsilon = 0$ and $\varepsilon = 1$ corresponding to the purely translational and the purely rotational thermostat, respectively. The total noise intensity χ^2 is unbounded from above and, by dimensional analysis, can be equivalently characterized by a *noise temperature*

$$T^{\text{wn}} \equiv m \left(\frac{\chi^2}{\sqrt{\pi}n\sigma} \right)^{2/3}. \quad (10)$$

Therefore, from now on the ST will be characterized by the pair $(T^{\text{wn}}, \varepsilon)$. In terms of the new parameters, the BFPE, Equation (3), reads

$$\frac{\partial}{\partial t} f(\mathbf{v}, \omega; t) - \frac{\nu^{\text{wn}} T^{\text{wn}}}{4m} \left[(1 - \varepsilon) \left(\frac{\partial}{\partial \mathbf{v}} \right)^2 + \varepsilon \frac{2m}{I} \left(\frac{\partial}{\partial \omega} \right)^2 \right] f(\mathbf{v}, \omega; t) = J[\mathbf{v}, \omega | f], \quad (11)$$

$$\nu^{\text{wn}} = 2n\sigma \sqrt{\frac{\pi T^{\text{wn}}}{m}} \quad (12)$$

being a reference *noise-induced* collisional frequency.

Inserting the definitions of partial granular temperatures, Equation (6), into Equation (11), one obtains

$$\partial_t T_{\text{tr}} = -\xi_{\text{tr}} T_{\text{tr}} + \frac{1 - \varepsilon}{2} \nu^{\text{wn}} T^{\text{wn}}, \quad \partial_t T_{\text{rot}} = -\xi_{\text{rot}} T_{\text{rot}} + \varepsilon \nu^{\text{wn}} T^{\text{wn}}, \quad (13)$$

where

$$\xi_{\text{tr}} = -\frac{m}{2nT_{\text{tr}}} \int d\mathbf{v} \int_{-\infty}^{\infty} d\omega v^2 J[\mathbf{v}, \omega | f], \quad \xi_{\text{rot}} = -\frac{I}{nT_{\text{rot}}} \int d\mathbf{v} \int_{-\infty}^{\infty} d\omega \omega^2 J[\mathbf{v}, \omega | f] \quad (14)$$

are the translational and rotational energy production rates [78, 80].

In terms of the quantities defined in Equation (8), Equations (13) become

$$\partial_t \tilde{T} = -\zeta \tilde{T} + \frac{1}{3} \nu^{\text{wn}}, \quad \partial_t \theta = \theta (\xi_{\text{tr}} - \xi_{\text{rot}}) - \nu^{\text{wn}} \frac{2 + \theta}{6\tilde{T}} [\theta - \varepsilon(2 + \theta)], \quad (15)$$

where $\tilde{T} \equiv T/T^{\text{wn}}$ and

$$\zeta \equiv \frac{2}{3} \frac{\xi_{\text{tr}} T_{\text{tr}}}{T} + \frac{1}{3} \frac{\xi_{\text{rot}} T_{\text{rot}}}{T} = \frac{2\xi_{\text{tr}} + \xi_{\text{rot}} \theta}{2 + \theta} \quad (16)$$

is the *cooling rate*.

According to Equation (15), the steady-state quantities $\tilde{T}^{\text{st}} = T^{\text{st}}/T^{\text{wn}}$ and $\theta^{\text{st}} = T_{\text{rot}}^{\text{st}}/T_{\text{tr}}^{\text{st}}$ satisfy the conditions

$$\zeta^{\text{st}} \tilde{T}^{\text{st}} = \frac{1}{3} \nu^{\text{wn}}, \quad \varepsilon \xi_{\text{tr}}^{\text{st}} = \frac{1 - \varepsilon}{2} \xi_{\text{rot}}^{\text{st}} \theta^{\text{st}}, \quad (17)$$

which imply a balance between collisional cooling and external heating. The steady-state temperature can be used to define a reduced temperature $T^* \equiv \tilde{T}/\tilde{T}^{\text{st}} = T/T^{\text{st}}$ and a reduced time $t^* = \frac{1}{2} \nu^{\text{st}} t$, where

$$\nu^{\text{st}} = 2n\sigma \sqrt{\frac{\pi T_{\text{tr}}^{\text{st}}}{m}} = \nu^{\text{wn}} \sqrt{\frac{3\tilde{T}^{\text{st}}}{2 + \theta^{\text{st}}}} \quad (18)$$

is the steady-state collision frequency. More in general, the time-dependent collision frequency is

$$\nu(t) = 2n\sigma \sqrt{\frac{\pi T_{\text{tr}}(t)}{m}} = \nu^{\text{wn}} \sqrt{\frac{3\tilde{T}(t)}{2 + \theta(t)}} = \nu^{\text{st}} G(T^*(t), \theta(t)), \quad G(T^*, \theta) \equiv \sqrt{T^* \frac{2 + \theta^{\text{st}}}{2 + \theta}}. \quad (19)$$

The above collision frequency can be used to nondimensionalize the energy production rates as

$$\mu_{20} \equiv \frac{\xi_{\text{tr}}}{\nu}, \quad \mu_{02} \equiv \frac{\xi_{\text{rot}}}{2\nu}, \quad (20)$$

where

$$\mu_{k\ell} = - \int d\mathbf{c} \int_{-\infty}^{\infty} dw c^k w^\ell \mathcal{J}[\mathbf{c}, w|f] \quad (21)$$

are the reduced collisional moments. In Equation (21), $\mathbf{c} = \mathbf{v}/\sqrt{2T_{\text{tr}}/m}$ and $w = \omega/\sqrt{2T_{\text{rot}}/I}$ are the reduced translational and angular velocities, respectively, and $\mathcal{J} \equiv (2T_{\text{tr}}/m)\sqrt{2T_{\text{rot}}/I}/(n\nu)J$ is the reduced collision operator. Thus, the steady-state conditions (17) become

$$2(\mu_{20}^{\text{st}} + \mu_{02}^{\text{st}} \theta^{\text{st}}) = \left(\frac{2 + \theta^{\text{st}}}{3\tilde{T}^{\text{st}}} \right)^{3/2} \equiv \gamma^{\text{st}}, \quad \varepsilon \mu_{20}^{\text{st}} = (1 - \varepsilon) \mu_{02}^{\text{st}} \theta^{\text{st}}. \quad (22)$$

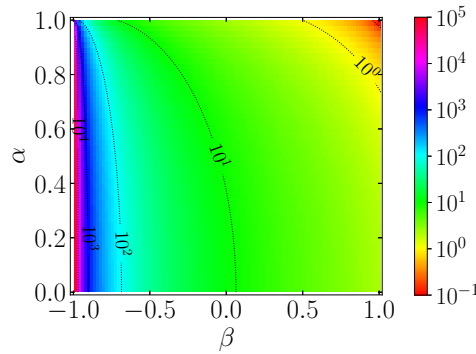


Figure 2. Difference $\theta^{\text{st}}(\varepsilon = 1) - \theta^{\text{st}}(\varepsilon = 0)$ [see Equations (28)] in the plane (α, β) .

Using these dimensionless definitions, Equations (15) yield

$$\frac{1}{2} \partial_{t^*} \ln T^* = -2G(T^*, \theta) \frac{\mu_{20} + \mu_{02}\theta}{2 + \theta} + \frac{2}{T^*} \frac{\mu_{20}^{\text{st}} + \mu_{02}^{\text{st}}\theta^{\text{st}}}{2 + \theta^{\text{st}}}, \tag{23a}$$

$$\frac{1}{2} \partial_{t^*} \ln \theta = G(T^*, \theta) (\mu_{20} - 2\mu_{02}) - \frac{1}{T^*} \frac{2 + \theta}{2 + \theta^{\text{st}}} \frac{\theta^{\text{st}}}{\theta} \frac{\theta - \varepsilon(2 + \theta)}{\theta^{\text{st}} - \varepsilon(2 + \theta^{\text{st}})} (\mu_{20}^{\text{st}} - 2\mu_{02}^{\text{st}}), \tag{23b}$$

where use has been made of Equations (17) and (22).

According to the definition of collisional moments, Equation (21), they depend on the whole VDF. This implies that Equations (23) do not make a closed set of equations. The same applies to the steady-state solution, Equation (22). This shortcoming, however, can be circumvented if an *approximate* closure is applied. This is the subject of section 2.2.

2.2 Maxwellian approximation

In order to get explicit results from Equations (22) and (23) by using the simplest possible closure, we resort to the two-temperature MA

$$f(\mathbf{v}, \omega) \rightarrow n \frac{m}{2\pi T_{\text{tr}}} \sqrt{\frac{I}{2\pi T_{\text{rot}}}} \exp\left(-\frac{mv^2}{2T_{\text{tr}}} - \frac{I\omega^2}{2T_{\text{rot}}}\right). \tag{24}$$

This approximation does a very good job in the three-dimensional case with $\varepsilon = 0$ [75] and it is reasonably expected to perform also well in the case of disks with $\varepsilon \neq 0$.

Within this approximation, the relevant collisional moments can be evaluated with the result [78–80]

$$\mu_{20} = \frac{1 - \alpha^2}{2} + \frac{\mathcal{K}}{2} \left[\frac{\kappa(1 - \beta)}{2} \left(1 + \frac{\theta}{\kappa}\right) + 1 - \theta \right], \tag{25a}$$

$$\mu_{02} = \frac{\mathcal{K}}{2} \left[\frac{1 - \beta}{2\kappa} \left(1 + \frac{\kappa}{\theta}\right) + 1 - \theta^{-1} \right], \quad \mathcal{K} \equiv \kappa \frac{1 + \beta}{(1 + \kappa)^2}. \tag{25b}$$

Solving Equations (22), we get the steady-state expressions

$$\theta^{\text{st}} = \kappa \left[\frac{2}{\mathcal{K}} \frac{(1 - \alpha^2)\varepsilon + \mathcal{K}(1 + \kappa)}{(1 - \beta)[1 - \varepsilon(1 + \kappa)] + 2\kappa} - 1 \right], \quad \tilde{T}^{\text{st}} = \frac{2 + \theta^{\text{st}}}{3(\gamma^{\text{st}})^{2/3}}, \quad (26)$$

with

$$\gamma^{\text{st}} = 1 - \alpha^2 + \mathcal{K} \frac{1 + \kappa}{2\kappa} (1 - \beta) (\kappa + \theta^{\text{st}}). \quad (27)$$

In particular,

$$\varepsilon = 0 \Rightarrow \theta^{\text{st}} = \frac{1 + \beta}{2 + \kappa^{-1}(1 - \beta)}, \quad (28a)$$

$$\varepsilon = 1 \Rightarrow \theta^{\text{st}} = 2 \frac{1 + \mathcal{K}^{-1}(1 - \alpha^2) + \frac{\kappa}{2}(1 - \beta)}{1 + \beta}. \quad (28b)$$

Equation (28a) agrees with a previous result [78]. Notice that, for the special value $\varepsilon = 0$, θ^{st} is independent of the coefficient of normal restitution α both for disks and spheres [47, 75, 78–80]. However, this property is broken down when energy is injected into the rotational degree of freedom ($\varepsilon \neq 0$).

From Equation (26) one can observe that θ^{st} is independent of T^{wn} and, at given α and β , it is a monotonically increasing function of ε . This is physically expected since, by growing ε , we are increasing the relative amount of rotational energy injected with respect to the total energy; therefore, it is presumed that the stationary value of T_{rot} rises with respect to T_{tr} at fixed T^{wn} . Thus, the most disparate values of θ^{st} correspond to $\varepsilon = 1$ and 0, their difference being plotted in Figure 2 as a function of α and β .

It is interesting to note that, in the MA, Equation (24), one simply has

$$2(\mu_{20} + \mu_{02}\theta) = \gamma^{\text{st}} + \mathcal{K}(1 - \beta) \frac{1 + \kappa}{2\kappa} (\theta - \theta^{\text{st}}), \quad (29a)$$

$$\mu_{20} - 2\mu_{02} = \left(1 - \varepsilon \frac{2 + \theta^{\text{st}}}{\theta^{\text{st}}}\right) \frac{\gamma^{\text{st}}}{2} - \mathcal{K} \frac{1 + \beta}{4} \left(1 + \frac{2}{\theta\theta^{\text{st}}}\right) (\theta - \theta^{\text{st}}). \quad (29b)$$

As a consequence, Equations (23) can be recast as,

$$\frac{1}{2} \partial_{t^*} \ln T^* = \Phi(T^*, \theta) \equiv -\gamma^{\text{st}} \left[\frac{G(T^*, \theta)}{2 + \theta} - \frac{1/T^*}{2 + \theta^{\text{st}}} \right] - G(T^*, \theta) \mathcal{K}(1 - \beta) \frac{1 + \kappa}{2\kappa} \frac{\theta - \theta^{\text{st}}}{2 + \theta}, \quad (30a)$$

$$\begin{aligned} \frac{1}{2} \partial_{t^*} \ln \theta = & \left(1 - \varepsilon \frac{2 + \theta^{\text{st}}}{\theta^{\text{st}}}\right) \frac{\gamma^{\text{st}}}{2} \left[G(T^*, \theta) - \frac{1}{T^*} \frac{2 + \theta}{2 + \theta^{\text{st}}} \frac{\theta - \varepsilon(2 + \theta)}{\theta\theta^{\text{st}} - \varepsilon(2 + \theta^{\text{st}})} \right] \\ & - G(T^*, \theta) \mathcal{K} \frac{1 + \beta}{4} \left(1 + \frac{2}{\theta\theta^{\text{st}}}\right) (\theta - \theta^{\text{st}}). \end{aligned} \quad (30b)$$

Equations (30) make a closed set of two ordinary differential equations that can be (numerically) solved with arbitrary initial conditions $T^*(0) \equiv T_0^*$ and $\theta(0) \equiv \theta_0$. Although the theoretical results have been derived for arbitrary values of the reduced moment of inertia κ , henceforth all the graphs are obtained for the conventional case of a uniform mass distribution of the disks, i.e., $\kappa = \frac{1}{2}$.

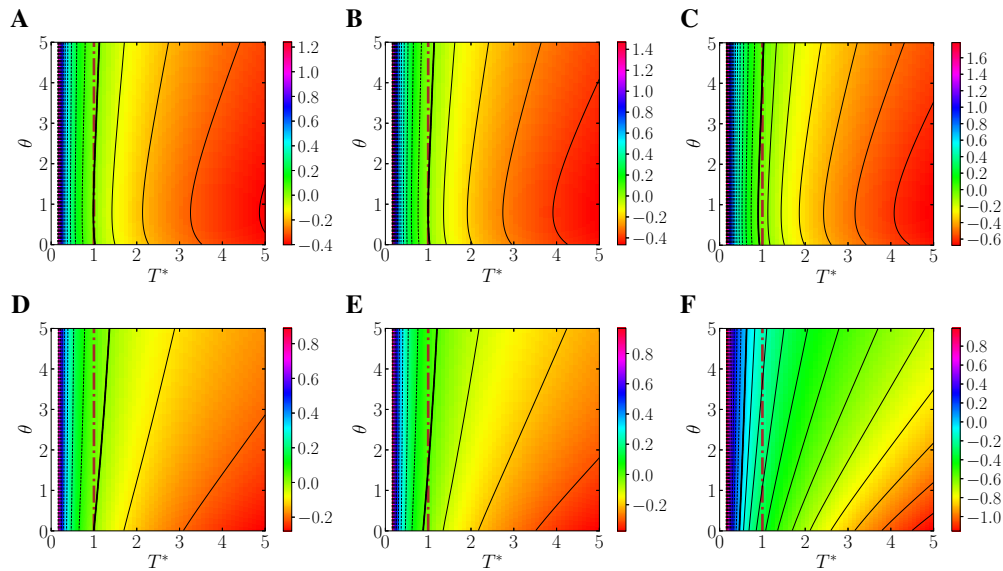


Figure 3. Density plots of $\Phi(T^*, \theta)$ for $\alpha = 0.9$ and (A) $\beta = 0, \varepsilon = 0$; (B) $\beta = 0, \varepsilon = 0.5$; (C) $\beta = 0, \varepsilon = 1$; (D) $\beta = -0.7, \varepsilon = 0$; (E) $\beta = -0.7, \varepsilon = 0.5$; and (F) $\beta = -0.7, \varepsilon = 1$. The contour lines (solid for $\Phi < 0$, dashed for $\Phi > 0$) are separated by an amount $\Delta\Phi = 0.1$. The thick solid line is the locus $\Phi(T^*, \theta) = 0$. It intercepts the (brown dash-dotted) vertical line $T^* = 1$ at $\theta = \theta^{\text{st}}$.

Figures 3 and 4 show density plots of $\Phi(T^*, \theta)$ for $\alpha = 0.9$ and 0.7 , respectively. In each case, two values of β (0 and -0.7) and three values of ε (0, 0.5, and 1) are considered. We observe that, typically, $\Phi(T^*, \theta)$ increases with increasing θ at fixed T^* , while it decreases with increasing T^* at fixed θ .

2.3 Comparison with simulation results

In order to check the validity of the MA, we have compared our theoretical predictions against DSMC and EDMD simulation results both for transient and steady-state values.

The DSMC algorithm used is based on the one presented in, e.g., Refs. [81, 82], and adapted for the model presented in this work. For our DSMC simulations we have dealt with $N = 10^4$ particles and chosen a time step $\Delta t = 4 \times 10^{-5}/\nu^{\text{wn}}$. In addition, the way of implementing the stochastic force and torque in the EDMD code is based on the *approximate Green function* algorithm [83], as applied to the ST. We have chosen $N = 3.6 \times 10^3$ particles, a density $n\sigma^2 = 5 \times 10^{-4}$ (implying a box length of $L/\sigma \approx 1897.37$), and a time step $\Delta t \approx 4 \times 10^{-4}/\nu^{\text{wn}}$. No instabilities were observed.

In Figure 5, results for the steady-state values \tilde{T}^{st} and θ^{st} as functions of ε and different values of α and β are presented. Simulation results for DSMC and EDMD come from averages over 100 replicas and over 50 data points, once the steady state is ensured to be reached. A very good agreement between DSMC and EDMD with expressions in Equation (26) is observed. Whereas θ^{st} is an increasing function of ε , this is not the case, in general, with \tilde{T}^{st} , as can be observed in Figure 5E.

As a test of the transient stage, we present in Figure 6 the evolution of T^* and θ (starting from a Gaussian-generated VDF with $T_0^* = 1.5$ and $\theta_0 = 1$) for the same choices of α and β as in Figure 5 and for the representative values $\varepsilon = 0$ (translational noise only), 0.8 (both translational and rotational noise), and

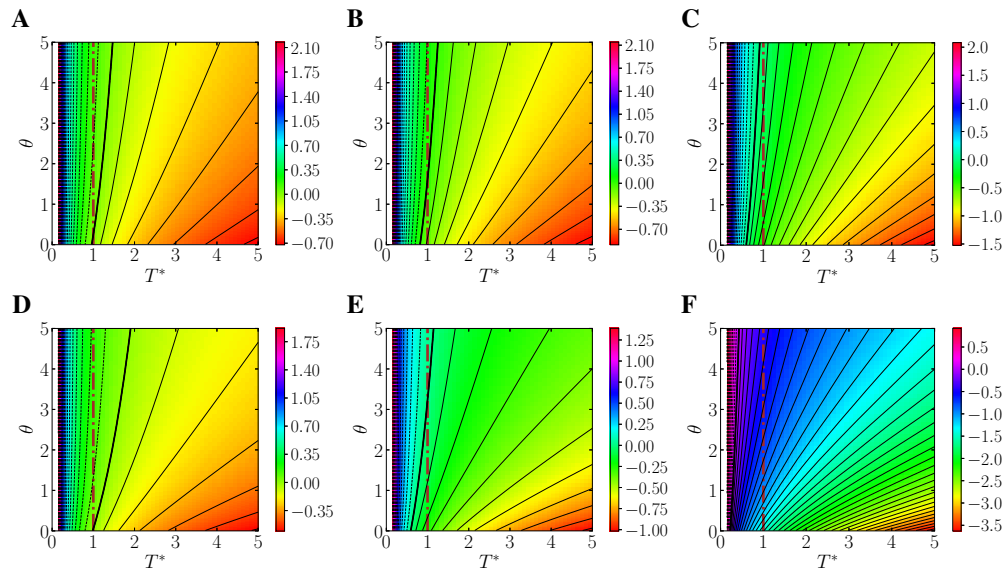


Figure 4. Same as Figure 3 but for $\alpha = 0.7$.

$\varepsilon = 1$ (rotational noise only). We observe again an excellent agreement of the MA, Equations (30), with simulation results.

2.4 Temperature overshoot

As illustrated in Figure 6, the evolution of $T^*(t^*)$ for certain initial states might experiment an overshoot $T^*(t_O^*) = 1$ at a finite time t_O^* , followed by a minimum, and then relax to the steady state from below. This overshoot effect becomes more pronounced as $\Phi(T_0^*, \theta_0)$ takes more negative values, i.e., as ε increases and/or θ_0 decreases.

In general, at a given initial condition (T_0^*, θ_0) , there exists a critical value $\varepsilon_{cr}(T_0^*, \theta_0)$, such that the $T^*(t^*)$ exhibits overshoot if $\varepsilon > \varepsilon_{cr}(T_0^*, \theta_0)$. The determination of $\varepsilon_{cr}(T_0^*, \theta_0)$ within the MA requires the numerical solution of Equations (30). We have analyzed those numerical solutions up to $t^* = 15$ since the overshoot typically takes place in the first stage of the evolution. Thus, the numerical value $\varepsilon = \varepsilon_{cr}$ corresponds to $t_O^* = 15$.

Figure 7 shows $\varepsilon_{cr}(T_0^*, \theta_0)$ as a function of T_0^* at a specific value of θ_0 , namely the one given by Equation (28a), and for the same four pairs of coefficients of restitution as in Figures 3–6. In each case, the curve $\varepsilon_{cr}(T_0^*, \theta_0)$ splits the plane ε vs T_0^* into two regions: the region above the curve, where the overshoot effect is present, and the one below the curve, where temperature relaxes to the steady-state value from above. Note that the shape of the curve ε_{cr} in Figure 7 associated with the pair $(\alpha, \beta) = (0.7, -0.7)$ differs in curvature from the curves associated with the other three pairs.

3 MPEMBA EFFECT

As already said in section 1, ME refers to the counterintuitive phenomenon according to which an initially hotter sample of a given fluid relaxes earlier to the steady state than an initially colder one. In a recent

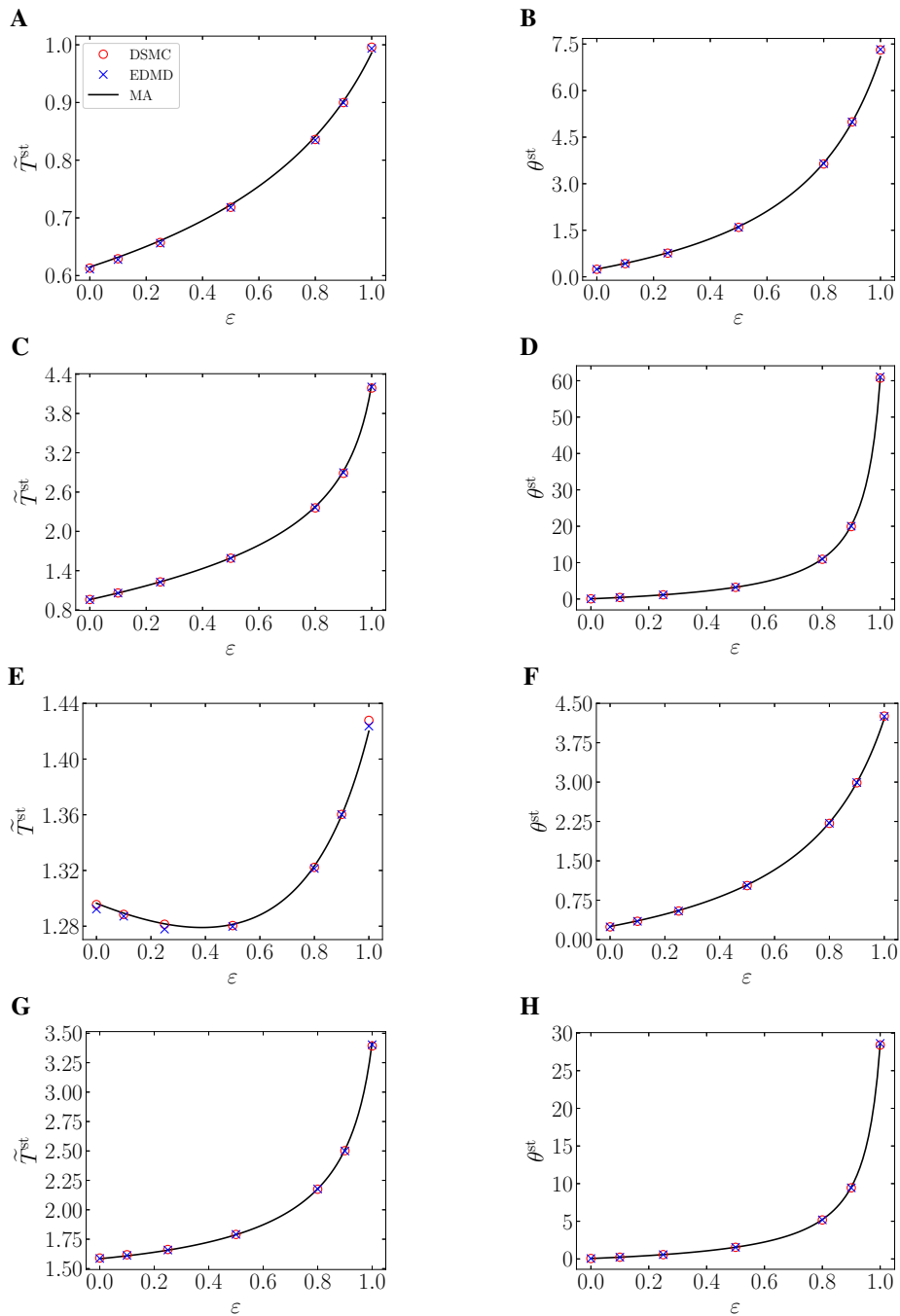


Figure 5. Steady-state values \tilde{T}^{st} and θ^{st} as a function of ε . The values of the coefficients of restitution are (A) and (B): $(\alpha, \beta) = (0.7, 0)$; (C) and (D): $(\alpha, \beta) = (0.7, -0.7)$; (E) and (F): $(\alpha, \beta) = (0.9, 0)$; and (G) and (H): $(\alpha, \beta) = (0.9, -0.7)$. Thick black lines correspond to the theoretical prediction in Equation (26), and symbols refer to DSMC (\circ) and EDMD (\times) simulation results for $\varepsilon = 0, 0.1, 0.25, 0.5, 0.8, 0.9$, and 1.

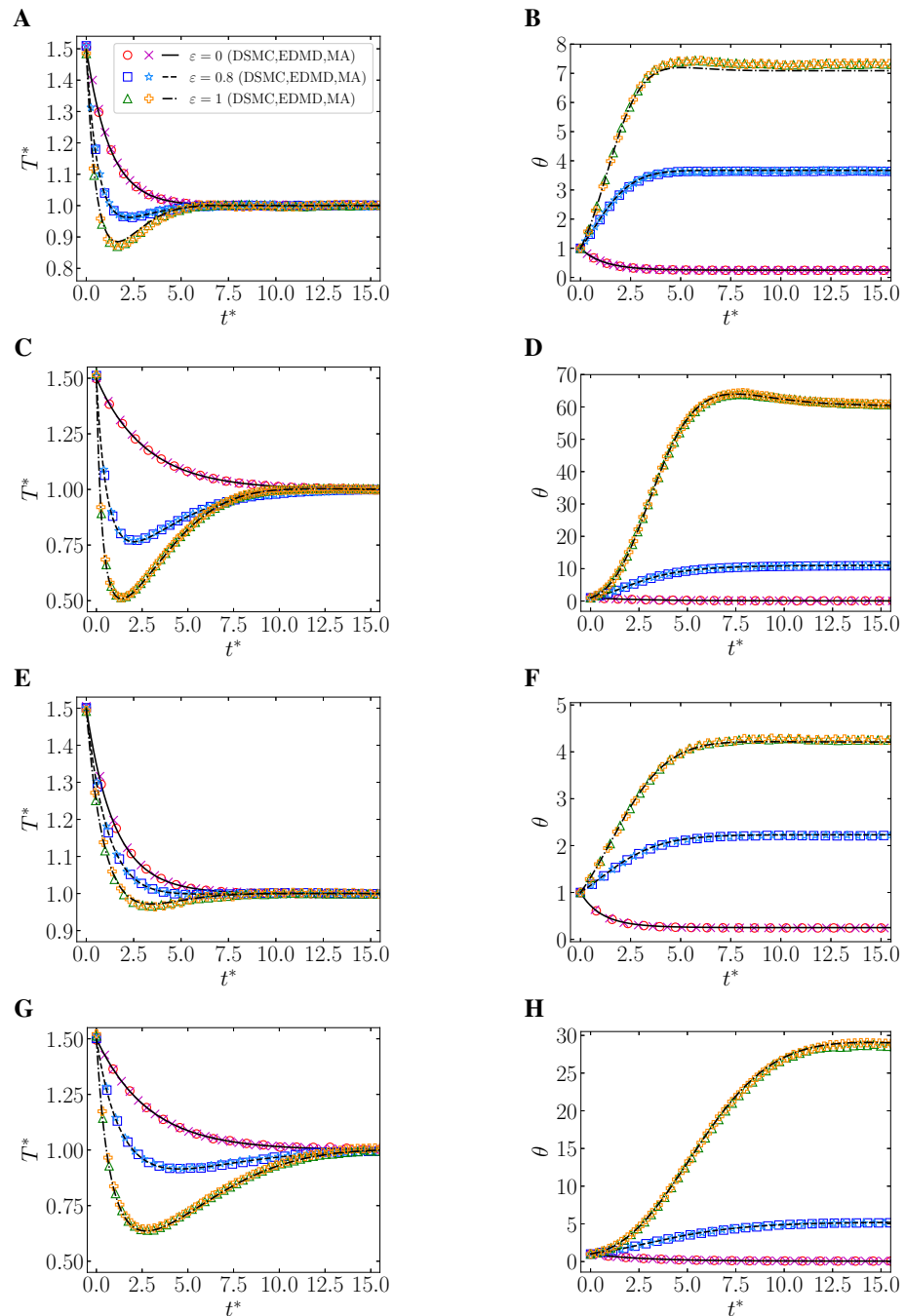


Figure 6. Time evolution of T^* and θ for $\varepsilon = 0, 0.8$, and 1 . The initial conditions are $T_0^* = 1.5$ and $\theta_0 = 1$ in all the cases. The values of the coefficients of restitution are **(A)** and **(B)**: $(\alpha, \beta) = (0.7, 0)$; **(C)** and **(D)**: $(\alpha, \beta) = (0.7, -0.7)$; **(E)** and **(F)**: $(\alpha, \beta) = (0.9, 0)$; and **(G)** and **(H)**: $(\alpha, \beta) = (0.9, -0.7)$. Lines correspond to the theoretical prediction from Equations (30), and symbols refer to DSMC and EDMD simulation results.

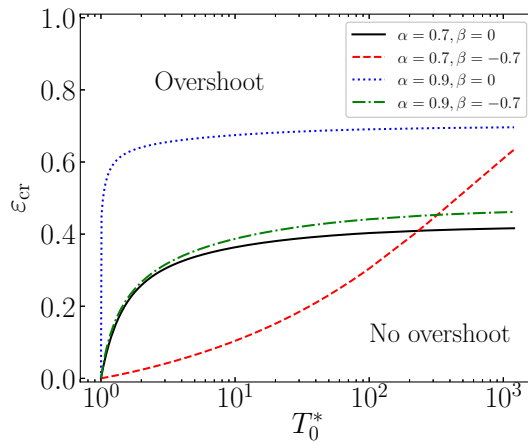


Figure 7. Phase diagram for the emergence of overshoot. The numerical critical value $\varepsilon_{cr}(T_0^*, \theta_0)$ is presented as a function of T_0^* for θ_0 given by Equation (28a) and four different pairs of the coefficients of restitution: $(\alpha, \beta) = (0.7, 0), (0.7, -0.7), (0.9, 0),$ and $(0.9, -0.7)$.

paper [44], we distinguished between the thermal ME—where the relaxation process is described by the temperature of the system (second moment of the VDF)— and the entropic ME—where the deviation from the final steady state is monitored by the Kullback–Leibler divergence (thus involving the full VDF). Whereas this distinction is interesting and the relationship between the thermal ME and the entropic ME is not always biunivocal [44], we focus this paper on the thermal version due to its simpler characterization and its relationship with the original results [6]. Moreover, only cooling processes will be considered throughout this work.

Let us assume two samples—denoted by A and B—of the same gas, subject to the same noise temperature T_{ref}^{wn} and the same splitting parameter ε_{ref} , so that the final steady-state values \tilde{T}_{ref}^{st} and θ_{ref}^{st} will also be the same. Both samples differ in the initial conditions (T_{0A}^*, θ_{0A}) and (T_{0B}^*, θ_{0B}) , respectively, where $T_{0A}^* > T_{0B}^* > 1$, that is, A refers to the initially hotter sample and we are considering a cooling experiment.

3.1 Standard Mpemba effect

Let us first consider the standard form of thermal ME [42, 44–47], where both $T_A^*(t^*)$ and $T_B^*(t^*)$ cross over at a certain crossing time t_c^* and then relax from above, i.e., $T_A^*(t_c^*) = T_B^*(t_c^*)$ and $T_B^*(t^*) > T_A^*(t^*) > 1$ for $t^* > t_c^*$. The emergence of ME can be subdued to the appearance of a crossing time (or an odd number of them) in the absence of any overshoot effect in the thermal evolution [44]. We will refer to this situation as the standard ME (SME). According to the discussion in section 2.4, the SME implies that $\varepsilon_{ref} < \min\{\varepsilon_{cr}(T_{0A}^*, \theta_{0A}), \varepsilon_{cr}(T_{0B}^*, \theta_{0B})\}$. The case when a temperature overshoot takes place will be discussed in section 3.2.

It can be reasonably expected that a necessary condition for the occurrence of the SME is that the initial slope is smaller in sample A than in sample B, i.e.,

$$\Phi(T_{0A}^*, \theta_{0A}) < \Phi(T_{0B}^*, \theta_{0B}). \tag{31}$$

Note here that the usual situation is that both slopes are negative, in which case $|\Phi(T_{0A}^*, \theta_{0A})| > |\Phi(T_{0B}^*, \theta_{0B})|$. Of course, Equation (31) is not sufficient for the SME since the latter also depends on how close T_{0A}^* and T_{0B}^* are and how far both initial temperatures are from unity. From Figures 3 and 4 we can conclude that, in general, the inequality (31) is best satisfied if $\theta_{0A} \ll \theta_{0B}$.

3.2 Overshoot Mpemba effect

The emergence of the temperature overshoot described in section 2.4 makes the crossover criterion employed in the SME become meaningless. Imagine that such a crossover takes place with $T_A^*(t_c^*) = T_B^*(t_c^*) > 1$, but then $T_B(t^*)$ relaxes from above while $T_A^*(t^*)$ overshoots the steady-state value, $T_A^*(t_o^*) = 1$. It is then possible that $T_A^*(t^*)$ relaxes (from below) later than $T_B^*(t^*)$. In that case, the initially hotter sample (A) would reach the steady state later than the initially colder sample (B), thus contradicting the existence of a ME, despite the crossover.

Reciprocally, imagine that $T_A^*(t^*)$ and $T_B^*(t^*)$ never cross each other but $T_B^*(t^*)$ overshoots the steady-state value and then relaxes from below. It is now possible that the initially hotter sample (A) reaches the steady state earlier than the initially colder sample (B), thus qualifying as a ME, despite the absence of any crossover. We will refer to this phenomenon as overshoot ME (OME) [44]. From the discussion in section 2.4 we conclude that the OME requires $\varepsilon_{\text{ref}} > \varepsilon_{\text{cr}}(T_{0B}^*, \theta_{0B})$.

To characterize the existence of OME without a thermal crossover, we adopt the quantity [44]

$$\mathfrak{D}(T^*(t)) \equiv T^*(t) - 1 - \ln T^*(t). \quad (32)$$

This quantity is (except for a factor) the Kullback–Leibler divergence of the Maxwellian VDF given by Equation (24) (with $T_{\text{rot}}/T_{\text{tr}} \rightarrow \theta^{\text{st}}$) with respect to the steady-state Maxwellian. Note that $\mathfrak{D}(T^*)$ is a positive-definite convex function of T^* . Therefore, we can define the OME by the crossover of $\mathfrak{D}(T_A^*)$ and $\mathfrak{D}(T_B^*)$ with, however, $T_A^* < 1$ and $T_A^* < T_B^*$.

In order to look for OME, the necessary condition for SME [given by Equation (31)] must be reversed. That is,

$$\Phi(T_{0A}^*, \theta_{0A}) > \Phi(T_{0B}^*, \theta_{0B}). \quad (33)$$

Establishing the most favorable conditions for OME is not as simple as just declaring the opposite of the SME condition. Firstly, we want for the colder sample to overshoot as much as possible the steady state, so that the relaxation from below is retarded maximally. This reasoning is translated into the condition of highly negative initial slope $\Phi(T_{0B}^*, \theta_{0B})$, which implies small θ_{0B} (see Figures 3 and 4). On the other hand, two competing phenomena exist for the hotter sample: we want to either avoid any overshoot or force it to be as weak as possible, but we also want the relaxation to be faster than in the colder sample. Therefore, one needs $\theta_{0A} > \theta_{0B}$ but, for very large values of θ_{0A} , one might not find OME due to a slower relaxation of the hotter sample.

3.3 Initial preparation protocols

In order to study the absence or existence of ME, one needs to specify the initial conditions (T_{0A}^*, θ_{0A}) and (T_{0B}^*, θ_{0B}) of both samples. In previous studies [42, 44, 47] the values of θ_{0A} and θ_{0B} were freely chosen, without a specific reference to a previous protocol to initially prepare the samples.

Most of the interest of the present work resides in the proposal of protocols to generate the initial states of the samples involved in a ME experiment. The protocols are based on the proposed ST, and the

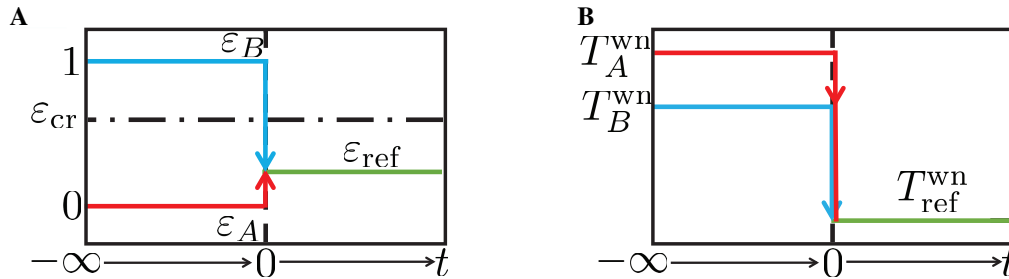


Figure 8. Scheme of the protocol for SME. (A) Choice of the splitting parameters ε . (B) Choice of the noise temperatures T^{wn} .

initial states will be generated by assuming *prior* thermostat values $(T_i^{wn}, \varepsilon_i)$, $i = A, B$, and allowing both samples to reach their respective steady states $(T_i^{st}, \theta_i^{st})$ before switching to the common *posterior* thermostat $(T_{ref}^{wn}, \varepsilon_{ref})$ at $t = 0$. The values of the prior thermostats will be chosen to optimize the necessary conditions (31) and (33) for SME and OME, respectively.

According to Equations (26) and (27), the ratios between the prior and posterior noise temperatures for desired values of $T_{0i}^* = T_i^{st}/T_{ref}^{st}$, $i = A, B$, where $T_i^{st} = T_i^{wn}\tilde{T}^{st}(\varepsilon_i)$ and $T_{ref}^{st} = T_{ref}^{wn}\tilde{T}^{st}(\varepsilon_{ref})$, are

$$\frac{T_i^{wn}}{T_{ref}^{wn}} = T_{0i}^* \frac{2 + \theta_{ref}^{st}}{2 + \theta_i^{st}} \left(\frac{\gamma_i^{st}}{\gamma_{ref}^{st}} \right)^{2/3}, \quad i = A, B. \quad (34)$$

3.3.1 Protocol for the standard Mpemba effect

In this case, we want to have $\theta_{0A} \ll \theta_{0B}$. According to Equation (26), and as observed in Figure 5, θ^{st} is an increasing function of ε and independent of T^{wn} . Therefore, the most disparate values of θ_{0A} and θ_{0B} are obtained if the prior thermostats of samples A and B have $\varepsilon_A = 0$ and $\varepsilon_B = 1$, respectively. According to Figure 2, SME would be stronger and/or easier to find for lower values of β at fixed α and for lower values of α at fixed β . In addition, in order to define a cooling process, we need to choose proper values of T_A^{wn}/T_{ref}^{wn} and T_B^{wn}/T_{ref}^{wn} [see Equation (34)], such that $T_{0A}^* = T_A^{st}/T_{ref}^{st} > T_{0B}^* = T_B^{st}/T_{ref}^{st} > 1$. Finally, one must fix $\varepsilon_{ref} < \min\{\varepsilon_{cr}(T_{0A}^*, \theta_{0A}), \varepsilon_{cr}(T_{0B}^*, \theta_{0B})\}$ to prevent any possible overshoot. This minimum of the critical rotational-to-total noise intensity parameter is expected to be $\varepsilon_{cr}(T_{0A}^*, \theta_{0A})$ because it corresponds to a more negative initial slope.

Thus, the designed protocol for SME reads as follows (see Figure 8 for an illustrative scheme):

1. Start by fixing $\varepsilon_A = 0$ and $\varepsilon_B = 1$, in order to ensure $\theta_{0A} < \theta_{0B}$.
2. Choose T_A^{wn}/T_{ref}^{wn} and T_B^{wn}/T_{ref}^{wn} , such that $T_{0A} > T_{0B} > T_{ref}^{st}$.
3. Let both samples evolve and reach the steady states corresponding to their respective prior thermostats. These steady states will play the role of the initial conditions for our ME experiment.
4. Switch the values of the thermostats of both samples to a common reference pair of values $(T_{ref}^{wn}, \varepsilon_{ref})$, such that no overshoot is expected, that is, $\varepsilon_{ref} < \min\{\varepsilon_{cr}(T_{0A}^*, \theta_{0A}), \varepsilon_{cr}(T_{0B}^*, \theta_{0B})\}$. This thermostat switch fixes the origin of time, $t = 0$.
5. Finally, let both samples evolve and reach a common steady state.

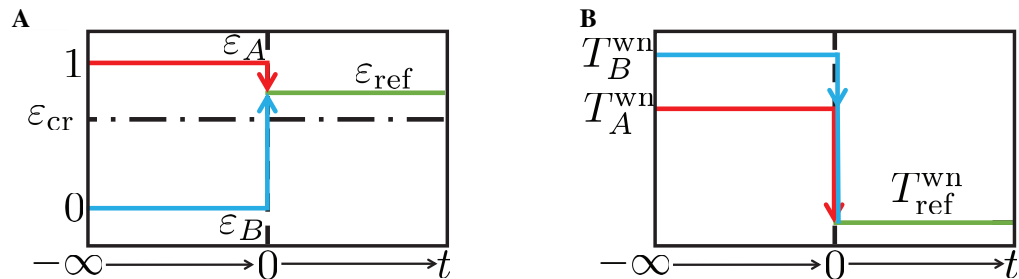


Figure 9. Same as in Figure 8, but for OME.

For given (α, β) , the numerical solutions of Equations 30 for different values of T_{0A}^* and T_{0B}^* —and with θ_{0A} and θ_{0B} given by Equations (28a) and (28b), respectively— can be analyzed to determine whether SME is present or not. This provides the phase diagram presented in Figure 10A for $\varepsilon_{\text{ref}} = 0.1$ and some pairs of coefficients of restitution.

3.3.2 Protocol for the overshoot Mpemba effect

In the OME case, it is convenient to have $\theta_{0A} \gg \theta_{0B}$, so that the adopted choices of ε for the prior thermostats are the reverse of those of SME, i.e., $\varepsilon_A = 1$ and $\varepsilon_B = 0$. Whereas in section 3.2 we commented that the best situation for the OME is not always the opposite to that of the SME, the above choice helps us avoid or weaken a possible overshoot for the hotter sample. Again, in order to define a cooling process, we need to choose proper values of $T_A^{\text{wn}}/T_{\text{ref}}^{\text{wn}}$ and $T_B^{\text{wn}}/T_{\text{ref}}^{\text{wn}}$ [see Equation (34)], and such that $T_{0A} > T_{0B} > T_{\text{ref}}^{\text{st}}$. Finally, $\varepsilon_{\text{ref}} > \varepsilon_{\text{cr}}(T_{0B}^*, \theta_{0B})$ to ensure overshoot of $T_B^*(t^*)$.

In analogy with the SME case, a protocol for observing OME is designed as follows (see Figure 9):

1. Start by fixing $\varepsilon_A = 1$ and $\varepsilon_B = 0$, in order to ensure $\theta_{0A} > \theta_{0B}$.
2. Choose $T_A^{\text{wn}}/T_{\text{ref}}^{\text{wn}}$ and $T_B^{\text{wn}}/T_{\text{ref}}^{\text{wn}}$, such that $T_{0A} > T_{0B} > T_{\text{ref}}^{\text{st}}$.
3. Let both samples evolve and reach the steady states corresponding to their respective prior thermostats. These steady states will play the role of the initial conditions for our ME experiment.
4. Switch the values of the thermostats of both samples to a common reference pair of values $(T_{\text{ref}}^{\text{wn}}, \varepsilon_{\text{ref}})$, such that overshoot is ensured, that is, $\varepsilon_{\text{ref}} > \varepsilon_{\text{cr}}(T_{0B}^*, \theta_{0B})$. This thermostat switch fixes the origin of time, $t = 0$.
5. Finally, let both samples evolve and reach a common steady state.

Figure 10B shows a phase diagram for the occurrence of OME (with $\varepsilon_{\text{ref}} = 0.9$) for the same pairs of coefficients of restitution as before.

3.4 Comparison with simulation results

In order to check the initialization protocols for detecting SME and OME, we have run DSMC and EDMD simulations. The simulation details are the same as introduced in section 2.3. Simulation points correspond to the average over ensembles of 100 replicas. Again, no instabilities were observed.

3.4.1 Standard Mpemba effect

Figure 11 presents results for the SME protocol introduced in section 3.3.1. As we can observe, the theoretical predictions agree very well with DSMC and EDMD simulation data.

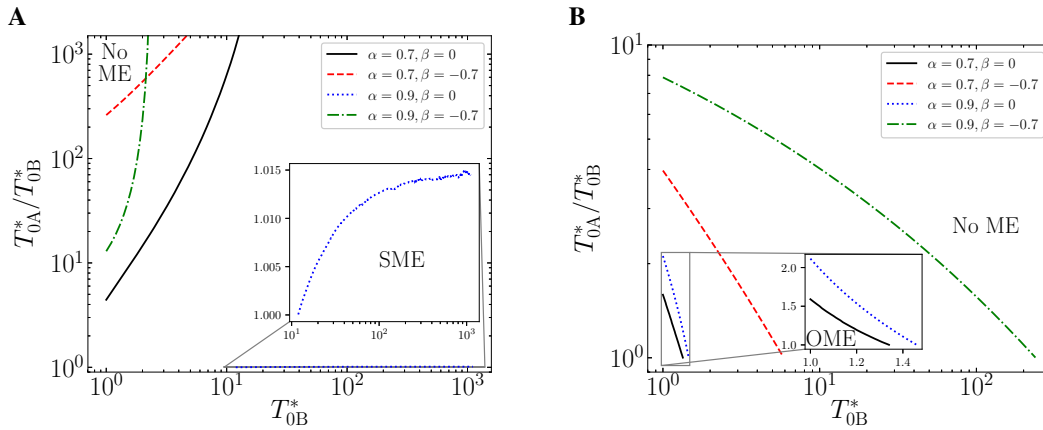


Figure 10. Phase diagrams in the plane T_{0A}^*/T_{0B}^* vs T_{0B}^* for the emergence of (A) SME (with $\varepsilon_{\text{ref}} = 0.1$) and (B) OME (with $\varepsilon_{\text{ref}} = 0.9$). Four different pairs of the coefficients of restitution are considered: $(\alpha, \beta) = (0.7, -0.7)$, $(0.7, 0)$, $(0.9, -0.7)$, and $(0.9, 0)$. The insets show magnified views of the indicated regions.

The chosen initial temperature conditions are $(T_{0A}^*, T_{0B}^*) = (3, 2)$ for Figure 11A, $(T_{0A}^*, T_{0B}^*) = (4, 2)$ for Figures 11C and 11G, and $(T_{0A}^*, T_{0B}^*) = (3, 2.92)$ for Figure 11E. Moreover, $\varepsilon_{\text{ref}} = 0.1$ for all cases, except for the case of Figures 11E and 11F, that is chosen to be $\varepsilon_{\text{ref}} = 0.6$. The values of $T_A^{\text{wn}}/T_{\text{ref}}^{\text{wn}}$ and $T_B^{\text{wn}}/T_{\text{ref}}^{\text{wn}}$ are given in each case by Equation (34) to ensure the desired initial temperatures. All these cases avoid overshoot, in agreement with the case $\theta_0 = \theta^{\text{st}}(\varepsilon = 0)$ shown in Figure 7. Moreover, the cases with $\varepsilon_{\text{ref}} = 0.1$ are inside the region where SME is predicted to be present in Figure 10A.

The value $\varepsilon_{\text{ref}} = 0.6$ for the system $(\alpha = 0.9, \beta = 0)$ was chosen instead of $\varepsilon_{\text{ref}} = 0.1$ to avoid the need of taking very high initial temperatures (see Figure 10A) and also to prevent overshoot (see Figure 7). The price paid for this choice of coefficients of restitution is that the difference $\theta_{0A} - \theta_{0B}$ is not too high, see Figures 2 and 11F. Then, initial temperature values are restricted to be very similar and the crossing characterizing the SME is much less pronounced than in the other cases. However, the inset in Figure 11E shows a well defined change of sign of the the difference $T_A^* - T_B^*$.

3.4.2 Overshoot Mpemba effect

The theoretical results stemming from the OME protocol introduced in section 3.3.2 are compared with simulations in Figure 12, again with an excellent agreement.

The initial temperatures are $(T_{0A}^*, T_{0B}^*) = (1.22, 1.1)$ for Figure 12A, $(T_{0A}^*, T_{0B}^*) = (2, 1.5)$ for Figures 12D and 12J, and $(T_{0A}^*, T_{0B}^*) = (1.2, 1.1)$ for Figure 12G. Moreover, a common value $\varepsilon_{\text{ref}} = 0.9$ is chosen to ensure that overshoot appears for the colder samples, as depicted in Figure 7, and that OME is expected from the phase diagram shown in Figure 10B.

Whereas no crossing between T_A^* and T_B^* is observed in Figure 12, such a crossing is present between the entropy-like quantities \mathcal{D}_A and \mathcal{D}_B [see Equation (32)]. As explained in section 3.2, this characterizes the OME, where the initially colder system relaxes later to the steady state.

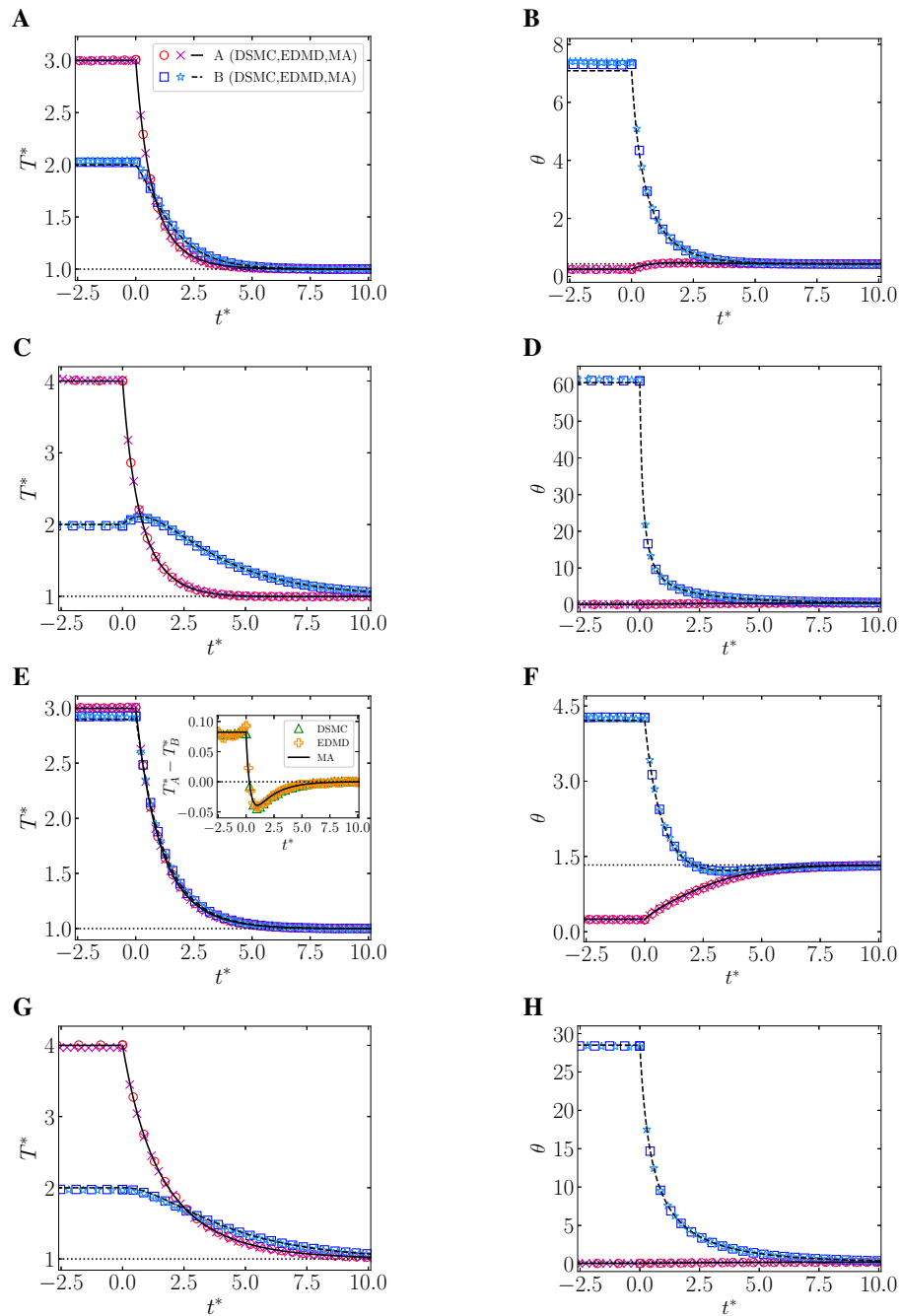


Figure 11. Time evolution of T^* and θ for SME initialization protocol, as described in section 3.3.1. **(A)** and **(B)**: $(\alpha, \beta) = (0.7, 0)$ and $\varepsilon_{\text{ref}} = 0.1$; **(C)** and **(D)**: $(\alpha, \beta) = (0.7, -0.7)$ and $\varepsilon_{\text{ref}} = 0.1$; **(E)** and **(F)**: $(\alpha, \beta) = (0.9, 0)$ and $\varepsilon_{\text{ref}} = 0.6$; and **(G)** and **(H)**: $(\alpha, \beta) = (0.9, -0.7)$ and $\varepsilon_{\text{ref}} = 0.1$. Thick and dashed lines correspond to the theoretical prediction from Equations (30), dotted lines represented the steady state value, and symbols refer to DSMC and EDMD simulation results. The inset in panel **(E)** shows the evolution of the temperature difference $T_A^* - T_B^*$.

A. Megías and A. Santos

Mpemba effect for inelastic and rough hard disks

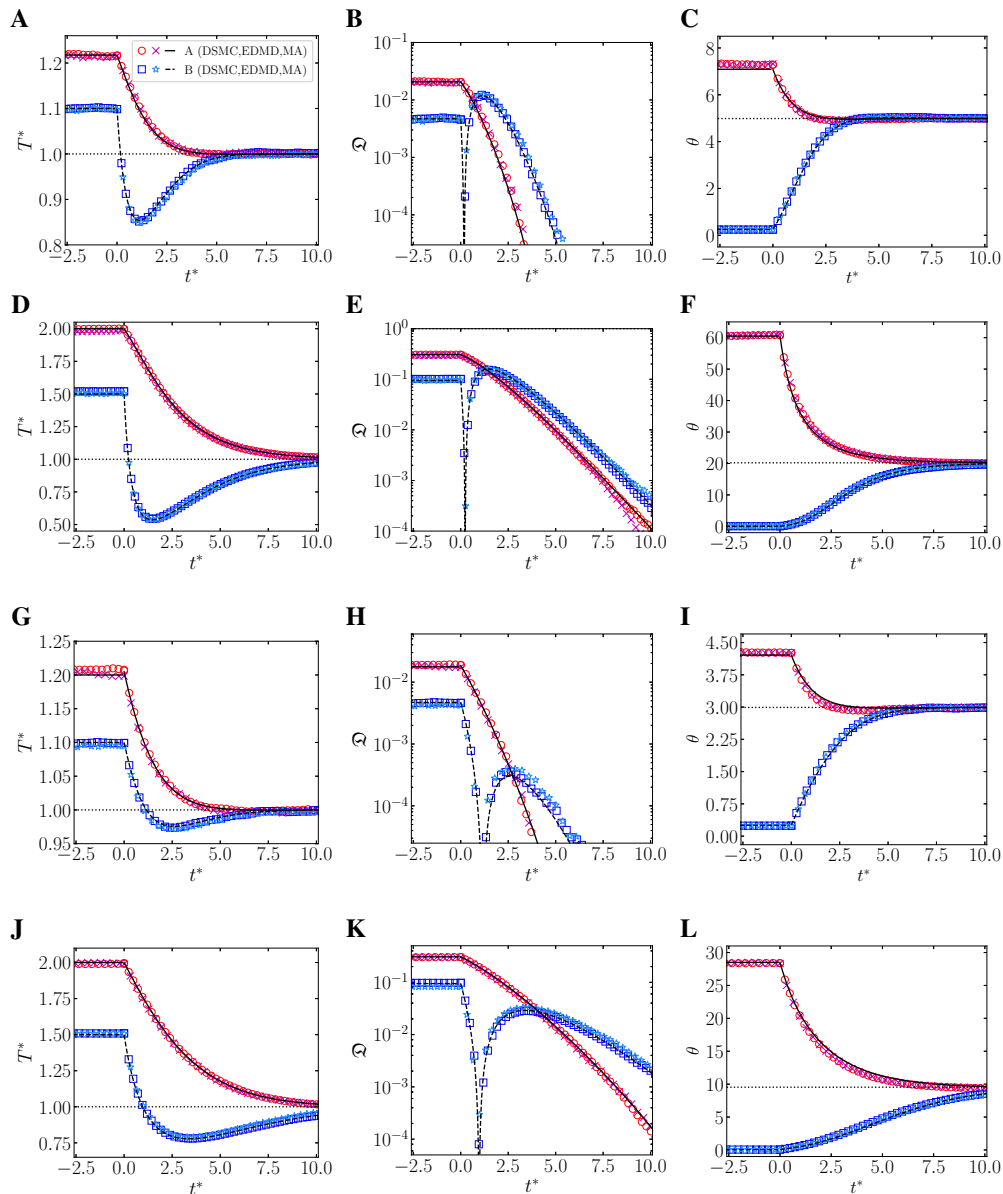


Figure 12. Time evolution of T^* , \mathcal{Q} , and θ for OME initialization protocol described in section. 3.3.2 with $\varepsilon_{\text{ref}} = 0.9$. (A)–(C): $(\alpha, \beta) = (0.7, 0)$; (D)–(F): $(\alpha, \beta) = (0.7, -0.7)$; (G)–(I): $(\alpha, \beta) = (0.9, 0)$; and (J)–(L): $(\alpha, \beta) = (0.9, -0.7)$. Thick and dashed lines correspond to the theoretical prediction from Equations (30), dotted lines represented the steady state value, and symbols refer to DSMC and EDMD simulation results.

4 CONCLUDING REMARKS

In this work, we have studied the homogeneous states of a dilute granular gas made of inelastic and rough hard disks lying on a two-dimensional plane. The inelasticity and roughness are mathematically described

by constant coefficients of normal (α) and tangential (β) restitution, respectively. In order to avoid frozen long-time limiting states, the disks are assumed to be heated by the stochastic force- and torque-based ST. This novel stochastic thermostat injects energy to both translational and rotational degrees of freedom. Each specific thermostat of this type is univocally determined by its associated noise temperature, $T^{\text{wn}} \geq 0$ [see Equation (10)], and the rotational-to-total noise intensity, $0 \leq \varepsilon \leq 1$ [see Equation (9)].

The system is assumed to be fully described by the instantaneous one-particle VDF, its dynamics being then given by the BFPE, Equation 11. It is known that the steady-state VDF is not a Maxwellian, as occurs for $\varepsilon = 0$ [75], and this is even more the case with the instantaneous transient VDF. However, these nonGaussianities are expected to be small enough as to approximate the VDF by a Maxwellian, as previously done for $\varepsilon = 0$ [47]. Therefore, we have worked under the two-temperature MA introduced in section 2.2, which allows us to account for the dynamics of the systems just in terms of the reduced total granular temperature, T^* , and the rotational-to-translational temperature ratio, θ , according to Equations (30). The steady-state values can be explicitly expressed in terms of the mechanical properties of the disks, see Equation (26). Steady and transient states predicted by the MA are tested via DSMC and EDMD, with very good agreement, as observed in Figures 5 and 6. This reinforces the validity of our approach. As expected, θ^{st} is an increasing function of ε and independent of T^{wn} , whereas $\tilde{T}^{\text{st}} \equiv T^{\text{st}}/T^{\text{wn}}$ can be a nonmonotonic function of ε (see Figure 5).

The main core of this work has been the description of ME in cooling processes in this system, with special emphasis on the elaboration of preparation protocols for the generation of the initial states. We noted that, if $T^* - 1$ does not change its sign during the evolution, the usual form of ME, SME, can emerge if $\theta_{0A} \ll \theta_{0B}$, A being the initially hotter sample. This SME is characterized by a single crossing (or, in general, an odd number of them) between the temperature curves, thus inducing that the initially colder system, B, relaxes more slowly toward the final steady state. However, we have realized that an overshoot (or change of sign of $T^* - 1$) might appear if the rotational-to-total noise intensity is larger than a certain critical value $\varepsilon_{\text{cr}}(T_0^*, \theta_0)$, as shown for some cases in Figure 7. Therefore, the SME is no longer ensured and, following a recent work [44], ME might appear without a crossing between T_A^* and T_B^* but with a crossing between the entropy-like quantities \mathcal{D}_A and \mathcal{D}_B [see Equation (32)]. This peculiar type of ME is termed OME and is described in section 3.2. According to the MA, the most favorable condition for the OME changes from the SME one to $\theta_{0A} \gg \theta_{0B}$.

Protocols for generating initial conditions to observe both SME and OME have been presented in sections 3.3.1 and 3.3.2, respectively. While reminiscent of the protocols previously considered in the case of sheared inertial suspensions [53], the protocols proposed here represent novel instructions to elaborate a ME experiment in homogeneous states of granular gaseous systems. We have based those protocols on the steady states of the ST, taking advantage of the increase of θ^{st} as ε increases. Thus, to guarantee the biggest possible difference $|\theta_{0B} - \theta_{0A}|$ we have fixed prior thermalization processes with $(\varepsilon_A, \varepsilon_B) = (0, 1)$ for SME and $(\varepsilon_A, \varepsilon_B) = (1, 0)$ for OME. Moreover, in this prior thermalization stage, $T_A^{\text{wn}}/T_{\text{ref}}^{\text{wn}}$ and $T_B^{\text{wn}}/T_{\text{ref}}^{\text{wn}}$, where $(T_{\text{ref}}^{\text{wn}}, \varepsilon_{\text{ref}})$ characterizes the posterior thermostat, are chosen to fine-tune both T_{0A}^* and T_{0B}^* . It is crucial to choose $\varepsilon_{\text{ref}} < \min\{\varepsilon_{\text{cr}}(T_{0A}^*, \theta_{0A}), \varepsilon_{\text{cr}}(T_{0B}^*, \theta_{0B})\}$ for SME to avoid overshoot, and $\varepsilon_{\text{ref}} > \varepsilon_{\text{cr}}(T_{0B}^*, \theta_{0B})$ for OME to ensure the overshoot of the initially colder sample. These protocols, together with the MA predictions, allowed us to elaborate phase diagrams for SME and OME emergences, as depicted in Figure 10.

The theoretical descriptions of the SME and OME initialization protocols have been tested by DSMC and EDMD simulations, finding a very good agreement between theory and simulations, as observed in Figures 11 and 12, respectively.

One can then conclude that, despite its simplicity, the MA captures very well the dynamics for this system. In turn, this implies that the SME and OME protocols for the initial-state preparation described in this paper are trustworthy.

Finally, we expect that this work will be useful to the ME community in the search for practical protocols able to generate the adequate initial states. In addition, given the simplicity of the hard-disk system studied in this paper, we hope it can be experimentally realizable, thus opening up the possibility of reproducing the ME by an adequate control of the external forcing mechanisms.

CONFLICT OF INTEREST STATEMENT

The authors declare that the research was conducted in the absence of any commercial or financial relationships that could be construed as a potential conflict of interest.

AUTHOR CONTRIBUTIONS

AM and AS contributed to the conception and design of the study. AM performed the computer simulations and wrote the first draft of the manuscript. Both authors contributed to manuscript revision, read, and approved the submitted version.

FUNDING

The authors acknowledge financial support from Grant No. PID2020-112936GB-I00 funded by MCIN/AEI/10.13039/501100011033, and from Grants No. IB20079 and No. GR21014 funded by Junta de Extremadura (Spain) and by ERDF “A way of making Europe.” AM is grateful to the Spanish Ministerio de Ciencia, Innovación y Universidades for a predoctoral fellowship FPU2018-3503.

ACKNOWLEDGMENTS

The authors are grateful to the computing facilities of the Instituto de Computación Científica Avanzada of the University of Extremadura (ICCAEx), where the simulations were run.

DATA AVAILABILITY STATEMENT

The datasets presented in this study can be found in online repositories. The names of the repository/repositories and accession number(s) can be found below: [<https://github.com/amegiasf/MpembaSp>]

REFERENCES

- [1] Ross WD, editor. *The Works of Aristotle (Translated into English under the editorship of W.D. Ross)*, vol. III. London: (Oxford Clarendon Press) (1931).
- [2] Bacon F. *Novum Organum Scientiarum (in Latin). Translated into English in: The New Organon. Under the editorship of L. Jardine, M. Silverthorne (2000)*. Cambridge: (Cambridge Univ Press) (1620).
- [3] Descartes R. *Discours de la méthode pour bien conduire sa raison, et chercher la vérité dans les sciences (in French). Translated into English in: Discourse on Method, Optics, Geometry, and Meteorology. Under the editorship of P. J. Olscamp (2001)* (Hackett Publishing Company) (1637).

- [4] Newton I. VII. Scala graduum caloris. *Phil. Trans. R. Soc.* **22** (1701) 824–829. doi:10.1098/rstl.1700.0082.
- [5] Newton I. *Isaaci Newtoni Opera quae exstant omnia*, vol. 4 (Londini : excudebat Joannes Nichols) (1782), 403–407 .
- [6] Mpemba EB, Osborne DG. Cool? *Phys. Educ.* **4** (1969) 172–175. doi:10.1088/0031-9120/4/3/312.
- [7] Osborne DG. Mind on ice. *Phys. Educ.* **14** (1979) 414–417. doi:10.1088/0031-9120/14/7/313.
- [8] Elkin S, editor. *The 100 greatest unsolved mysteries*. New York: Cavendish Square (2018): 14.
- [9] Kell GS. The freezing of hot and cold water. *Am. J. Phys.* **37** (1969) 564–565. doi:10.1119/1.1975687.
- [10] Firth I. Cooler? *Phys. Educ.* **6** (1971) 32–41. doi:10.1088/0031-9120/6/1/310.
- [11] Deeson E. Cooler-lower down. *Phys. Educ.* **6** (1971) 42–44. doi:10.1088/0031-9120/6/1/311.
- [12] Frank FC. The Descartes–Mpemba phenomenon. *Phys. Educ.* **9** (1974) 284–284. doi:10.1088/0031-9120/9/4/121.
- [13] Gallear R. The Bacon–Descartes–Mpemba phenomenon. *Phys. Educ.* **9** (1974) 490–490. doi:10.1088/0031-9120/9/7/114.
- [14] Walker J. Hot water freezes faster than cold water. Why does it do so? *Sci. Am.* **237** (1977) 246–257. doi:10.1038/scientificamerican0977-246.
- [15] Freeman M. Cooler still—an answer? *Phys. Educ.* **14** (1979) 417–421. doi:10.1088/0031-9120/14/7/314.
- [16] Kumar K. Mpemba effect and 18th century ice-cream. *Phys. Educ.* **15** (1980) 268–268. doi:10.1088/0031-9120/15/5/101.
- [17] Hanneken JW. Mpemba effect and cooling by radiation to the sky. *Phys. Educ.* **16** (1981) 7–7. doi:10.1088/0031-9120/16/1/102.
- [18] Wojciechowski B, Owczarek I, Bednarz G. Freezing of aqueous solutions containing gases. *Cryst. Res. Technol.* **23** (1988) 843–848. doi:10.1002/crat.2170230702.
- [19] Auerbach D. Supercooling and the Mpemba effect: When hot water freezes quicker than cold. *Am. J. Phys.* **63** (1995) 882–885. doi:doi.org/10.1119/1.18059.
- [20] Knight CA. The Mpemba effect: The freezing times of cold and hot water. *Am. J. Phys.* **64** (1996) 524–524. doi:10.1119/1.18275.
- [21] Maciejewski PK. Evidence of a convective instability allowing warm water to freeze in less time than cold water. *J. Heat Transf.* **118** (1996) 65–72. doi:10.1115/1.2824069.
- [22] Jeng M. The Mpemba effect: When can hot water freeze faster than cold? *Am. J. Phys.* **74** (2006) 514–522. doi:10.1119/1.2186331.
- [23] Esposito S, De Risi R, Somma L. Mpemba effect and phase transitions in the adiabatic cooling of water before freezing. *Physica A* **387** (2008) 757–763. doi:10.1016/j.physa.2007.10.029.
- [24] Katz JI. When hot water freezes before cold. *Am. J. Phys.* **77** (2009) 27–29. doi:10.1119/1.2996187.
- [25] Vynnycky M, Mitchell SL. Evaporative cooling and the Mpemba effect. *Heat Mass Transf.* **46** (2010) 881–890. doi:10.1007/s00231-010-0637-z.
- [26] Brownridge JD. When does hot water freeze faster than cold water? A search for the Mpemba effect. *Am. J. Phys.* **79** (2011) 78–84. doi:10.1119/1.3490015.
- [27] Vynnycky M, Maeno N. Axisymmetric natural convection-driven evaporation of hot water and the Mpemba effect. *Int. J. Heat Mass Transf.* **55** (2012) 7297–7311. doi:10.1016/j.ijheatmasstransfer.2012.07.060.
- [28] Balážovič M, Tomášik B. The Mpemba effect, Shechtman’s quasicrystals and student exploration activities. *Phys. Educ.* **47** (2012) 568–573. doi:10.1088/0031-9120/47/5/568.

- [29] Zhang X, Huang Y, Ma Z, Zhou Y, Zhou J, Zheng W, et al. Hydrogen-bond memory and water-skin supersolidity resolving the Mpemba paradox. *Phys. Chem. Chem. Phys.* **16** (2014) 22995–23002. doi:10.1039/C4CP03669G.
- [30] Vynnycky M, Kimura S. Can natural convection alone explain the Mpemba effect? *Int. J. Heat Mass Transf.* **80** (2015) 243–255. doi:10.1016/j.ijheatmasstransfer.2014.09.015.
- [31] Sun CQ. Behind the Mpemba paradox. *Temperature* **2** (2015) 38–39. doi:10.4161/23328940.2014.974441.
- [32] Balážovič M, Tomášik B. Paradox of temperature decreasing without unique explanation. *Temperature* **2** (2015) 61–62. doi:10.4161/23328940.2014.975576.
- [33] Romanovsky AA. Which is the correct answer to the Mpemba puzzle? *Temperature* **2** (2015) 63–64. doi:10.1080/23328940.2015.1009800.
- [34] Jin J, Goddard WA. Mechanisms underlying the Mpemba effect in water from molecular dynamics simulations. *J. Phys. Chem. C* **119** (2015) 2622–2629. doi:10.1021/jp511752n.
- [35] Ibekwe RT, Cullerne JP. Investigating the Mpemba effect: when hot water freezes faster than cold water. *Phys. Educ.* **51** (2016) 025011. doi:10.1088/0031-9120/51/2/025011.
- [36] Gijón A, Lasanta A, Hernández ER. Paths towards equilibrium in molecular systems: The case of water. *Phys. Rev. E* **100** (2019) 032103. doi:10.1103/PhysRevE.100.032103.
- [37] Bechhoefer J, Kumar A, Chétrite R. A fresh understanding of the Mpemba effect. *Nat. Rev. Phys.* **3** (2021) 534–535. doi:10.1038/s42254-021-00349-8.
- [38] Burridge HC, Linden PF. Questioning the Mpemba effect: hot water does not cool more quickly than cold. *Sci. Rep.* **6** (2016) 37665. doi:10.1038/srep37665.
- [39] Burridge HC, Hallstadius O. Observing the Mpemba effect with minimal bias and the value of the Mpemba effect to scientific outreach and engagement. *Proc. R. Soc. A* **476** (2020) 20190829. doi:10.1098/rspa.2019.0829.
- [40] Elton DC, Spencer PD. Pathological Water Science — Four Examples and What They Have in Common. Gadoski A, editor, *Biomechanical and Related Systems* (Cham.: Springer) (2021), *Biologically-Inspired Systems*, vol. 17, 155–169.
- [41] Žuk PJ, Makuch K, Hlyst R, Maciołek A. Transient dynamics in the outflow of energy from a system in a nonequilibrium stationary state. *Phys. Rev. E* **105** (2022) 054133. doi:10.1103/PhysRevE.105.054133.
- [42] Santos A, Prados A. Mpemba effect in molecular gases under nonlinear drag. *Phys. Fluids* **32** (2020) 072010. doi:10.1063/5.0016243.
- [43] Patrón A, Sánchez-Rey B, Prados A. Strong nonexponential relaxation and memory effects in a fluid with nonlinear drag. *Phys. Rev. E* **104** (2021) 064127. doi:10.1103/PhysRevE.104.064127.
- [44] Megías A, Santos A, Prados A. Thermal versus entropic Mpemba effect in molecular gases with nonlinear drag. *Phys. Rev. E* **105** (2022) 054140. doi:10.1103/PhysRevE.105.054140.
- [45] Gómez González R, Khalil N, Garzó V. Mpemba-like effect in driven binary mixtures. *Phys. Fluids* **33** (2021) 053301. doi:10.1063/5.0050530.
- [46] Lasanta A, Vega Reyes F, Prados A, Santos A. When the hotter cools more quickly: Mpemba effect in granular fluids. *Phys. Rev. Lett.* **119** (2017) 148001. doi:10.1103/PhysRevE.99.060901.
- [47] Torrente A, López-Castaño MA, Lasanta A, Vega Reyes F, Prados A, Santos A. Large Mpemba-like effect in a gas of inelastic rough hard spheres. *Phys. Rev. E* **99** (2019) 060901(R). doi:10.1103/PhysRevE.99.060901.
- [48] Biswas A, Prasad VV, Raz O, Rajesh R. Mpemba effect in driven granular Maxwell gases. *Phys. Rev. E* **102** (2020) 012906. doi:10.1103/PhysRevE.102.012906.

- [49] Mompó E, López Castaño MA, Torrente A, Vega Reyes F, Lasanta A. Memory effects in a gas of viscoelastic particles. *Phys. Fluids* **33** (2021) 062005. doi:10.1063/5.0050804.
- [50] Gómez González R, Garzó V. Time-dependent homogeneous states of binary granular suspensions. *Phys. Fluids* **33** (2021) 093315. doi:10.1063/5.0062425.
- [51] Biswas A, Prasad VV, Rajesh R. Mpemba effect in an anisotropically driven granular gas. *EPL* **136** (2021) 46001. doi:10.1209/0295-5075/ac2d54.
- [52] Biswas A, Prasad VV, Rajesh R. Mpemba effect in anisotropically driven inelastic Maxwell gases. *J. Stat. Phys.* **186** (2022) 45. doi:10.1007/s10955-022-02891-w.
- [53] Takada S, Hayakawa H, Santos A. Mpemba effect in inertial suspensions. *Phys. Rev. E* **103** (2021) 032901. doi:10.1103/PhysRevE.103.032901.
- [54] Takada S. Homogeneous cooling and heating states of dilute soft-core gases under nonlinear drag. *EPJ Web Conf.* **249** (2021) 04001. doi:10.1051/epjconf/202124904001.
- [55] Baity-Jesi M, Calore E, Cruz A, Fernandez LA, Gil-Narvió JM, Gordillo-Guerrero A, et al. The Mpemba effect in spin glasses is a persistent memory effect. *Proc. Natl. Acad. Sci. U.S.A.* **116** (2019) 15350–15355. doi:10.1073/pnas.1819803116.
- [56] González-Adalid Pemartín I, Mompó E, Lasanta A, Martín-Mayor V, Salas J. Slow growth of magnetic domains helps fast evolution routes for out-of-equilibrium dynamics. *Phys. Rev. E* **104** (2021) 044114. doi:10.1103/PhysRevE.104.044114.
- [57] Teza G, Yaacoby R, Raz O. Relaxation shortcuts through boundary coupling. *arXiv:2112.10187* (2021). doi:10.48550/arXiv.2112.10187.
- [58] Vadakkayila N, Das SK. Should a hotter paramagnet transform quicker to a ferromagnet? Monte Carlo simulation results for Ising model. *Phys. Chem. Chem. Phys.* **23** (2021) 11186–11190. doi:10.1039/d1cp00879j.
- [59] Yang ZY, Hou JX. Non-Markovian Mpemba effect in mean-field systems. *Phys. Rev. E* **101** (2020) 052106. doi:10.1103/PhysRevE.101.052106.
- [60] Yang ZY, Hou JX. Mpemba effect of a mean-field system: The phase transition time. *Phys. Rev. E* **105** (2022) 014119. doi:10.1103/PhysRevE.105.014119.
- [61] Greaney PA, Lani G, Cicero G, Grossman JC. Mpemba-like behavior in carbon nanotube resonators. *Metall. Mater. Trans. A* **42** (2011) 3907–3912. doi:10.1007/s11661-011-0843-4.
- [62] Ahn YH, Kang H, Koh DY, Lee H. Experimental verifications of Mpemba-like behaviors of clathrate hydrates. *Korean J. Chem. Eng.* **33** (2016) 1903–1907. doi:10.1007/s11814-016-0029-2.
- [63] Schwarzendahl FJ, Löwen H. Anomalous cooling and overcooling of active colloids. *Phys. Rev. Lett.* **129** (2022) 138002. doi:10.1103/PhysRevLett.129.138002.
- [64] Carollo F, Lasanta A, Lesanovsky I. Exponentially accelerated approach to stationarity in Markovian open quantum systems through the Mpemba effect. *Phys. Rev. Lett.* **127** (2021) 060401. doi:10.1103/PhysRevLett.127.060401.
- [65] Lu Z, Raz O. Nonequilibrium thermodynamics of the Markovian Mpemba effect and its inverse. *Proc. Natl. Acad. Sci. U.S.A.* **114** (2017) 5083–5088. doi:10.1073/pnas.1701264114.
- [66] Klich I, Raz O, Hirschberg O, Vucelja M. Mpemba index and anomalous relaxation. *Phys. Rev. X* **9** (2019) 021060. doi:10.1103/PhysRevX.9.021060.
- [67] Chérite R, Kumar A, Bechhoefer J. The metastable Mpemba effect corresponds to a non-monotonic temperature dependence of extractable work. *Front. Phys.* **9** (2021) 654271. doi:10.3389/fphy.2021.654271.
- [68] Busiello DM, Gupta D, Maritan A. Inducing and optimizing Markovian Mpemba effect with stochastic reset. *New J. Phys.* **23** (2021) 103012. doi:10.1088/1367-2630/ac2922.

- [69] Lin J, Li K, He J, Ren J, Wang J. Power statistics of Otto heat engines with the Mpemba effect. *Phys. Rev. E* **105** (2022) 014104. doi:10.1103/PhysRevE.105.014104.
- [70] Holtzman R, Raz O. Landau theory for the Mpemba effect through phase transitions. *arXiv:2204.03995* (2022). doi:10.48550/arXiv.2204.03995.
- [71] Kumar A, Bechhoefer J. Exponentially faster cooling in a colloidal system. *Nature (Lond.)* **584** (2020) 64–68. doi:10.1038/s41586-020-2560-x.
- [72] Kumar A, Chétrite R, Bechhoefer J. Anomalous heating in a colloidal system. *Proc. Natl. Acad. Sci. U.S.A.* **119** (2022) e2118484119. doi:10.1073/pnas.2118484119.
- [73] Kovacs AJ. Transition vitreuse dans les polymères amorphes. Etude phénoménologique. *Fortschr. Hochpolym.-Forsch.* **3** (1963) 394–507. doi:10.1007/BFb0050366.
- [74] Kovacs AJ, Aklonis JJ, Hutchinson JM, Ramos AR. Isobaric volume and enthalpy recovery of glasses. II. A transparent multiparameter theory. *J. Polym. Sci. Polym. Phys. Ed.* **17** (1979) 1097–1162. doi:10.1002/pol.1979.180170701.
- [75] Vega Reyes F, Santos A. Steady state in a gas of inelastic rough spheres heated by a uniform stochastic force. *Phys. Fluids* **27** (2015) 113301. doi:10.1063/1.4934727.
- [76] Megías A, Santos A. Translational and angular velocity cumulants in granular gases of inelastic and rough hard disks or spheres. *In preparation* (2022).
- [77] Garzó V. *Granular Gaseous Flows. A Kinetic Theory Approach to Granular Gaseous Flows* (Switzerland: Springer Nature) (2019).
- [78] Megías A, Santos A. Driven and undriven states of multicomponent granular gases of inelastic and rough hard disks or spheres. *Granul. Matter* **21** (2019) 49. doi:10.1007/s10035-019-0901-y.
- [79] Megías A, Santos A. Energy production rates of multicomponent granular gases of rough particles. A unified view of hard-disk and hard-sphere systems. *AIP Conf. Proc.* **2132** (2019) 080003. doi:10.1063/1.5119584.
- [80] Santos A. Interplay between polydispersity, inelasticity, and roughness in the freely cooling regime of hard-disk granular gases. *Phys. Rev. E* **98** (2018) 012904. doi:10.1103/PhysRevE.98.012904.
- [81] Bird GA. *The DSMC Method* (Scotts Valley, CA: CreateSpace Independent Publishing Platform) (2013).
- [82] Montanero JM, Santos A. Computer simulation of uniformly heated granular fluids. *Granul. Matter* **2** (2000) 53–64. doi:10.1007/s100350050035.
- [83] Scala A. Event-driven Langevin simulations of hard spheres. *Phys. Rev. E* **86** (2012) 026709. doi:10.1103/PhysRevE.86.026709.

Nonhomogeneous states in the IRHS model

10

10.1 Summary

The transport properties of a dilute granular gas of freely evolving inelastic and rough identical [HD](#) or [HS](#), under a common mathematical framework, in terms of the translational and rotational degrees of freedom, d_t and d_r , respectively, is studied. The granular particles are set to be identical with diameter σ , mass m , and reduced moment of inertia κ . Their collisional rules are characterized by the [IRHS](#) model, where the inelasticity of the particles is accounted for by a coefficient of normal restitution, α , and a coefficient of tangential restitution, β . Both of them are assumed to be velocity independent, as described by the [IRHS](#) model.

In this chapter, the main objective consists in solving the inhomogeneous [BE](#) for this freely evolving dilute granular gaseous system from a [CE](#) expansion up to the [NSF](#) level. This leads to the computation of the [NSF](#) transport coefficient, which is detailed in [Article 7 \(Section 10.2\)](#). Furthermore, this solution allows one to determine the stability of the homogeneous solution under linear inhomogeneous perturbations, such an analysis being carried out in [Article 8 \(Section 10.3\)](#). First, the macroscopic hydrodynamic description of the system is given by the set of hydrodynamic fields $\{n, \mathbf{u}, T\}$, as already discussed in [Subsection 2.7.2](#), with T being the mean granular temperature. Then, we first derive the hydrodynamic balance equations associated with those fields. More details about their derivation can be found in [Appendix D](#).

Before entering into more details about the inhomogeneous description of the system, the homogeneous [BE](#) must be first characterized. The homogeneous state for this system has been already studied, first introduced in [Subsection 2.5.2](#) and, then, its non-Gaussianities being studied in detail in [Article 5 \(Section 8.2\)](#). A granular gas in free evolution and in the absence of spatial gradients is known to reach a scaling solution for its [VDF](#) at the so-called [HCS](#), where all the time dependence of the system is driven

through the mean granular temperature continuous decay. As a first approach to the problem, despite the non-Gaussianities of the **HCS VDF**, it seems to be reasonable to work under the **MA** proposed in Eq. (2.103), as a first approach, which has been already used in Ref. [KSG14]. That is, the **HCS VDF** is assumed to decompose into a product of its translational and rotational marginal **VDF**, the former being approximated by a Maxwellian **VDF** at the instantaneous translational granular temperature, whereas the latter does not need to be specified.

After the description of the **HCS**, we look for a normal solution to the **BE** described by the **IRHS** collisional model and in the absence of external forces, by means of the **CE** expansion around the local version of the **HCS** solution, which coincides with the zeroth order contribution to the **VDF**, $f^{(0)}$. As introduced in Subsection 2.7.2, the **VDF** is proposed to have a functional dependence on the set of the hydrodynamic fields, see Eq. (2.130). Therefore, to characterize the **VDF**, it suffices to know the instantaneous values of those fields, as well as their spatial gradients. In addition, all quantities different from the hydrodynamic fields would be characterized similarly, and expanded in terms of gradients of the hydrodynamic fields. This occurs with the cooling rate ζ and the fluxes appearing in the balance equations: the heat flux \mathbf{q} and the pressure tensor \mathbf{P} . The first-order contribution to the **VDF**, $f^{(1)}$, is a function of gradients of the hydrodynamic fields [see Eq. (29) of Article 7 (Section 10.2)], whose coefficients \mathcal{A} , \mathcal{B} , \mathcal{C}_{ij} , and \mathcal{E} are the solutions to certain linear integral equations [see Eqs. (30) of Article 7 (Section 10.2)]. To complete the description, we need to introduce the first-order contributions of the cooling rate, due to a dependence on the velocity divergence [see Eq. (32) of Article 7 (Section 10.2)], and the fluxes via their phenomenological constitutive equations [see Eq. (34) of Article 7 (Section 10.2)]. From the constitutive relation of the pressure tensor, the shear and bulk viscosities appear, η and η_b , respectively. Moreover, the proposed form for the heat flux assumes a dependence on the gradients of the mean granular temperature and the number density. The former is accompanied by the thermal conductivity λ , whereas the latter arises from a nonzero Dufour-like coefficient μ , which is observed to be present in granular gaseous flows [BC01; BP03; Gar+12; KSG14; GSK18; Gar19]. These two latter coefficients have a translational and a rotational contribution to their complete expression. Then, our main interest resides in the computation of those coefficients, which is straightforward from the knowledge of the coefficients of $f^{(1)}$. They are derived from the simplest Sonine-like approximation, permitting to solve the corresponding linear integral equations [see Eqs. (40) of Article 7 (Section 10.2)]. Thus, we obtain explicit expressions in terms of d_t and d_r —only valid for **HD** ($d_t = 2d_r = 1$) and **HS** ($d_t = d_r = 3$)—which are summarized in Table I of Article 7 (Section 10.2). Even more, we obtain the expressions of such coefficients for different limiting situations, the smooth limit ($\beta = -1$), the quasismooth limit ($\beta \rightarrow -1$), and Pidduck's gas limit ($\alpha = \beta = 1$), which are summed up in Table II of Article 7 (Section 10.2).

Once the transport coefficients are computed, in Article 8 (Section 10.3), we generalize the linear stability analysis of Ref. [GSK18] to the introduced unified scheme for HD and HS in terms of the translational and rotational degrees of freedom, allowing us to obtain novel results for the HD case. From previous studies, the HCS is unstable by means of the emergence of either clusters or vortices, both predicted in the smooth [GZ93; BRM98; BRC99; LH99; Gar05; Mit+11; Mit+12; Mit+14; FH17; Gar19] case and for rough HS [Mit+13; GSK18]. We deduce the presence of these two types of instabilities by means of critical wave numbers, k_{\perp} and k_{\parallel} , associated with the divergence of the transverse and longitudinal modes, respectively. Then, in the regions where $k_{\parallel} > k_{\perp}$, the onset of the instability is due to the longitudinal modes, which give rise to the appearance of clusters (clustering instability). On the other hand, if $k_{\perp} > k_{\parallel}$, the instability is due to the transverse modes and it is then dominated by the emergence of vortices (vortex instability). Then, although our analysis of the BE assumes an infinite system, in the real (and MD-computational) world, the granular gaseous systems are formed by a finite number of particles and confined within a certain finite volume. From those critical wave numbers, we compute the critical length of the system, L_c , such that if the characteristic length of the system is larger than L_c , then the HCS becomes unstable. The theoretical computations show a divergence of k_{\parallel} in a certain region of the parameter space, always present for HD, and only in some cases for HS. Hence, according to this description, one would expect that cluster instability is always present and hydrodynamics would break down within that region of the parameter space [see Figures 3 and 5 of Article 8 (Section 10.3)]. This result seems to be too devastating. In order to check whether the prediction is reliable or not, we performed EDMD computer simulations from a hand-made program [Meg23].

The objective of these computer simulations is to check whether this highly unstable region (HUR) is present or not for freely cooling HD systems. We elaborate a protocol to detect the clustering instability by means of the KLD of the particle spatial distribution compared with a Poisson distribution, as a reference for a homogeneous distribution. According to this protocol, a spontaneous and noticeable—compared with the statistical error—increment of the KLD is associated with the formation of a granular cluster. Moreover, we compare time-dependent simulation values of the rotational-to-translational temperature ratio θ and first nontrivial cumulants of the VDF, a_{20} , a_{02} , a_{11} , with their HCS values derived from the SA. Large deviations from these values indicate the possible presence of an instability. We compare first two different systems in a point inside the predicted HUR ($\alpha = 0.2$, $\beta = 0.25$, $\kappa = 1/2$), and we add a third one in a point outside this region ($\alpha = 0.7$, $\beta = 0.25$, $\kappa = 1/2$). Whereas in the former point, the two compared systems are expected to be unstable, we do observe instabilities just in one of them. On the other hand, in the point of the parameter space outside the HUR, we obtain an agreement with the theoretical prediction [see

Figures 8–11 of Article 8 (Section 10.3)].

10.2 Article 7

Title: Hydrodynamics of granular gases of inelastic and rough hard disks or spheres. I. Transport coefficients

Authors: Alberto Megías¹ and Andrés Santos^{1,2}

Affiliations:

¹ Departamento de Física, Universidad de Extremadura, E-06006 Badajoz, Spain

² Instituto de Computación Científica Avanzada (ICCAEx), Universidad de Extremadura, E-06006 Badajoz, Spain

Journal: Physical Review E

Volume: 104

Pages: 034901

Year: 2021

DOI: [10.1103/PhysRevE.104.034901](https://doi.org/10.1103/PhysRevE.104.034901)



Copy of the preprint of the work: “Alberto Megías, and Andrés Santos, ‘Hydrodynamics of granular gases of inelastic and rough hard disks or spheres. I. Transport coefficients’, *Physical Review E* **104**, 034901 (2021) <https://doi.org/10.1103/PhysRevE.104.034901>.”

Hydrodynamics of granular gases of inelastic and rough hard disks or spheres. I. Transport coefficients

Alberto Megías^{1,*} and Andrés Santos^{1,2,†}

¹*Departamento de Física, Universidad de Extremadura, E-06006 Badajoz, Spain*

²*Instituto de Computación Científica Avanzada (ICCAE),
Universidad de Extremadura, E-06006 Badajoz, Spain*

(Dated: September 14, 2021)

The transport coefficients for dilute granular gases of inelastic and rough hard disks or spheres with constant coefficients of normal (α) and tangential (β) restitution are obtained in a unified framework as functions of the number of translational (d_t) and rotational (d_r) degrees of freedom. The derivation is carried out by means of the Chapman–Enskog method with a Sonine-like approximation in which, in contrast to previous approaches, the reference distribution function for angular velocities does not need to be specified. The well-known case of purely smooth d -dimensional particles is recovered by setting $d_t = d$ and formally taking the limit $d_r \rightarrow 0$. In addition, previous results [G. M. Kremer, A. Santos, and V. Garzó, *Phys. Rev. E* **90**, 022205 (2014)] for hard spheres are reobtained by taking $d_t = d_r = 3$, while novel results for hard-disk gases are derived with the choice $d_t = 2$, $d_r = 1$. The singular quasismooth limit ($\beta \rightarrow -1$) and the conservative Pidduck’s gas ($\alpha = \beta = 1$) are also obtained and discussed.

I. INTRODUCTION

A granular gas is essentially a system of particles that move erratically and collide inelastically. The simplest model to describe its kinetic behavior consists in a collection of inelastic hard disks (HD) or spheres (HS) with a constant coefficient of normal restitution α (with $0 \leq \alpha \leq 1$) [1–5]. A plausible improvement of the model is the addition of collisional friction due to surface roughness (as demanded by recent experiments [6]), which can be quantified via a constant coefficient of tangential restitution β (with $-1 \leq \beta \leq 1$) [7].

Certainly, this simple two-parameter model does not account for sliding effects that can be relevant in grazing collisions [8]. Models with a Coulomb friction constant [9, 10] are more realistic but less theoretically tractable outside of the quasielastic and/or quasismooth limits [11–13]. Therefore, the (α, β) model for granular fluids, which captures satisfactorily well the basics of collision processes, represents an excellent compromise between simplicity and physical content [14–16].

In analogy with a conventional fluid, a hydrodynamic description is also applicable and useful in the case of granular gases [5, 13, 17–32]. If the gas is made of perfectly elastic ($\alpha = 1$) and either perfectly smooth ($\beta = -1$) or perfectly rough ($\beta = 1$) hard particles [33], then kinetic energy is conserved upon collisions. Therefore, a complete set of hydrodynamic variables is defined from the densities of the conserved quantities, that is, particle density n (reflecting mass conservation), flow velocity \mathbf{u} (due to momentum conservation), and temperature T (associated with energy conservation). However, for inelastic ($\alpha \neq 1$) and/or imperfectly rough ($|\beta| \neq 1$)

hard particles, energy is no longer preserved at the collisional level. Despite that, temperature is usually included as a hydrodynamic variable [5], except that a sink term (the so-called cooling rate) needs to be included in the energy balance equation. Therefore, as done in Refs. [34, 35] for (three-dimensional) HS, in this paper we will choose $\{n, \mathbf{u}, T\}$ as hydrodynamic variables. In contrast, the mean angular velocity $\mathbf{\Omega}$ is not a collisional invariant, even if $\alpha = \beta = 1$, and thus it is not included as a hydrodynamic field in our description.

To the best of our knowledge, the derivation by means of the Chapman–Enskog method of the Navier–Stokes–Fourier (NSF) hydrodynamic description (for generic constant coefficients of restitution α and β) of a two-dimensional granular gas of inelastic and rough HD has not been carried out yet. The aim of this work is to fill this gap in an inclusive way by generalizing the study to a hard-particle system with d_t and d_r translational and rotational degrees of freedom, respectively, in analogy with our previous study on the energy production rates in granular mixtures [36, 37]. In this way, apart from obtaining the sought results for HD gases with the choice $(d_t, d_r) = (2, 1)$, the results for rough HS [34] are recovered by setting $(d_t, d_r) = (3, 3)$. Additionally, the expressions for d -dimensional smooth particles ($\beta = -1$) [38] are also reobtained by formally taking $d_r \rightarrow 0$.

Whereas the three-dimensional is perhaps the most general, verisimilar, and intuitive geometry, a two-dimensional constrained system is also found in ordinary life, like a set of marbles moving and spinning on a plane or the pucks and strikers in the air hockey game. But the most important asset of the two-dimensional geometry resides in its ordinary use in experiments setups [39–47]. Thus, this work aims at providing testable results for the hydrodynamic transport coefficients within a general framework that encompasses the three- and two-dimensional geometries of spinning particles.

The intricacy of the (d_t, d_r) -generalization resides in

* albertom@unex.es

† andres@unex.es

the difficulties associated with a uniform characterization of the HS and HD vector spaces. The HS case is described by a three-dimensional Euclidean space common to both translational and angular velocities. However, to preserve the two-dimensional confinement of the HD system, angular velocities are orthogonal to the translational ones. To unify both descriptions in a common framework, we will consider the three-dimensional Euclidean space as an embedding space for the translational and angular velocity subspaces. Those subspaces coincide with the embedding space for HS systems, whereas they form an orthogonal decomposition of the vector space in the HD case. Within such a description, all vector operations and relations can be written as in the HS system [36, 37]. Although this mathematical description seems to be straightforward, it is rather tricky in some aspects, as will be seen.

The present paper is structured as follows. In Sec. II, the Boltzmann equation framework is established and the balance equations of the $d_t + 2$ hydrodynamic fields, $\{n, \mathbf{u}, T\}$, are derived in terms of d_t and d_r . This mathematical description allows us to introduce in Sec. III the Chapman–Enskog method around the homogeneous cooling state (HCS), from which we obtain the velocity distribution function (VDF) to first order in the hydrodynamic gradients, $f^{(1)}$, under the form of four linear integral equations. To solve those equations, two successive approximations are worked out in Sec. IV. First, a Sonine-like approximation is assumed without prejudicing the form of the zeroth-order HCS VDF $f^{(0)}$; this allows us to express the NSF transport coefficients in terms of velocity cumulants and collision integrals of $f^{(0)}$. As a second step, the unknown function $f^{(0)}$ is approximated by a Maxwellian distribution for the translational velocities times a generic marginal distribution for the angular velocities, what allows us to derive explicit expressions for the transport coefficients (see Table I below). The results are illustrated in Sec. V for both spheres and disks, including some interesting limiting situations. Finally, concluding remarks and main results are summed up in Sec. VI.

II. GRANULAR GAS OF INELASTIC AND ROUGH HARD PARTICLES

A. Boltzmann equation

We consider a HD or HS granular gas made of identical particles of diameter σ , mass m , and moment of inertia $I = \kappa m \sigma^2 / 4$. The reduced moment of inertia takes the values $\kappa = \frac{1}{2}$ for uniform disks and $\kappa = \frac{2}{5}$ for uniform spheres; its maximum value is $\kappa_{\max} = 1$ (HD) and $\kappa_{\max} = \frac{2}{3}$ (HS). The translational and angular velocities of a particle will be denoted by \mathbf{v} and $\boldsymbol{\omega}$, respectively. Whenever convenient, we will use the short-hand notations $\boldsymbol{\Gamma} \equiv \{\mathbf{v}, \boldsymbol{\omega}\}$ and $\int d\boldsymbol{\Gamma} \equiv \int d\mathbf{v} \int d\boldsymbol{\omega}$ for simplicity.

Particle-particle collisions are characterized by con-

stant coefficients of normal (α) and tangential (β) restitution (see Appendix A for a summary of the collision rules). As said in Sec. I, vector relations within our generalized description belongs to an embedding space, namely the three-dimensional Euclidean space \mathcal{E} . Therefore, the collision rules in Appendix A are presented in the three-dimensional framework.

We will carry out a kinetic-theory description of a dilute granular gas, in the sense that the one-body VDF will be enough to characterize the system. This approach is complemented with the assumption of molecular chaos or *Stosszahlansatz*. The analytical treatment is then based on the Boltzmann equation in the absence of external forces, which reads

$$\partial_t f + \mathbf{v} \cdot \nabla f = J_{\boldsymbol{\Gamma}}[f, f], \quad (1)$$

where $f = f(\mathbf{r}, \boldsymbol{\Gamma}; t)$ is the VDF at time t and $J_{\boldsymbol{\Gamma}}$ is the Boltzmann bilinear collision operator:

$$J_{\boldsymbol{\Gamma}_i}[f, f] = \sigma^{d_t-1} \int d\boldsymbol{\Gamma}_2 \int_+ d\hat{\boldsymbol{\sigma}} (\mathbf{v}_{12} \cdot \hat{\boldsymbol{\sigma}}) \times \left[\frac{f_1'' f_2''}{\alpha^2 |\beta|^{2d_r/d_t}} - f_1 f_2 \right]. \quad (2)$$

Here, $\mathbf{v}_{12} \equiv \mathbf{v}_1 - \mathbf{v}_2$ is the relative translational velocity, $\hat{\boldsymbol{\sigma}} = (\mathbf{r}_2 - \mathbf{r}_1)/|\mathbf{r}_2 - \mathbf{r}_1|$ is the intercenter unit vector at contact, the subscript $+$ in the integral over $\hat{\boldsymbol{\sigma}}$ designates the constraint $\hat{\boldsymbol{\sigma}} \cdot \mathbf{v}_{12} > 0$, and $f_{1,2} = f(\boldsymbol{\Gamma}_{1,2})$ and $f_{1,2}'' = f(\boldsymbol{\Gamma}_{1,2}'')$, the double primes denoting precollisional quantities giving rise to unprimed quantities as postcollisional values. Moreover, use has been made of the Jacobian given by (A7).

B. Hydrodynamic balance equations

From a macroscopic point of view, the flow of a low-density granular gas can be fully described by the knowledge of the following hydrodynamic fields: particle number density $n(\mathbf{r}, t)$, hydrodynamic flow velocity $\mathbf{u}(\mathbf{r}, t)$, and total granular temperature $T(\mathbf{r}, t)$. They are given by

$$n(\mathbf{r}, t) = \int d\boldsymbol{\Gamma} f(\mathbf{r}, \boldsymbol{\Gamma}; t), \quad (3a)$$

$$\mathbf{u}(\mathbf{r}, t) = \langle \mathbf{v} \rangle, \quad (3b)$$

$$T(\mathbf{r}, t) = \frac{d_t T_t(\mathbf{r}, t) + d_r T_r(\mathbf{r}, t)}{d_t + d_r}, \quad (3c)$$

where

$$T_t(\mathbf{r}, t) = \frac{m}{d_t} \langle V^2 \rangle, \quad T_r(\mathbf{r}, t) = \frac{I}{d_r} \langle \boldsymbol{\omega}^2 \rangle, \quad (4)$$

$\mathbf{V} = \mathbf{v} - \mathbf{u}$ being the peculiar velocity. The angular brackets denote averages defined generically as

$$\langle \psi \rangle = \frac{1}{n(\mathbf{r}, t)} \int d\boldsymbol{\Gamma} \psi(\mathbf{r}, \boldsymbol{\Gamma}; t) f(\mathbf{r}, \boldsymbol{\Gamma}; t). \quad (5)$$

Note that the rotational temperature T_r is not defined with respect to the mean angular velocity $\boldsymbol{\Omega} = \langle \boldsymbol{\omega} \rangle$ because the latter is not a conserved quantity [34].

Given a quantity $\psi(\mathbf{r}, \boldsymbol{\Gamma}; t)$, its associated transfer equation can be obtained by multiplying both sides of the Boltzmann equation, Eq. (1), by ψ and integrating over translational and angular velocities. The result is

$$\partial_t(n\langle\psi\rangle) + \nabla \cdot (n\langle\mathbf{v}\psi\rangle) - n\langle(\partial_t + \mathbf{v} \cdot \nabla)\psi\rangle = \mathcal{J}[\psi|f, f], \quad (6)$$

where $\mathcal{J}[\psi|f, f]$ is the collisional production term of the quantity ψ , given by

$$\begin{aligned} \mathcal{J}[\psi|f, f] &= \int d\boldsymbol{\Gamma}_1 \psi(\mathbf{r}_1, \boldsymbol{\Gamma}_1; t) J_{\boldsymbol{\Gamma}_1}[f, f] \\ &= \frac{\sigma^{d_t-1}}{2} \int d\boldsymbol{\Gamma}_1 \int d\boldsymbol{\Gamma}_2 \int_+ d\hat{\boldsymbol{\sigma}} (\hat{\boldsymbol{\sigma}} \cdot \mathbf{v}_{12}) \\ &\quad \times \Delta(\psi_1 + \psi_2) f_1 f_2. \end{aligned} \quad (7)$$

Here, the operator Δ acting on a generic quantity ψ yields the difference between the postcollisional and precollisional values of ψ , i.e., $\Delta\psi(\boldsymbol{\Gamma}) \equiv \psi(\boldsymbol{\Gamma}') - \psi(\boldsymbol{\Gamma})$.

The balance equations for mass, momentum, and energy are obtained from Eq. (6) by choosing $\psi = 1$, $\psi = m\mathbf{v}$, $\psi = \frac{1}{2}mV^2$, $\psi = \frac{1}{2}I\boldsymbol{\omega}^2$, and $\psi = \frac{1}{2}mV^2 + \frac{1}{2}I\boldsymbol{\omega}^2$. This yields, respectively,

$$\mathcal{D}_t n + n\nabla \cdot \mathbf{u} = 0, \quad (8a)$$

$$\mathcal{D}_t \mathbf{u} + \rho^{-1} \nabla \cdot \mathbf{P} = 0, \quad (8b)$$

$$\mathcal{D}_t T_t + \frac{2}{nd_t} (\nabla \cdot \mathbf{q}_t + \mathbf{P} : \nabla \mathbf{u}) + T_t \zeta_t = 0, \quad (8c)$$

$$\mathcal{D}_t T_r + \frac{2}{nd_r} \nabla \cdot \mathbf{q}_r + T_r \zeta_r = 0, \quad (8d)$$

$$\mathcal{D}_t T + \frac{2}{n(d_t + d_r)} (\nabla \cdot \mathbf{q} + \mathbf{P} : \nabla \mathbf{u}) + T\zeta = 0. \quad (8e)$$

In these equations, $\mathcal{D}_t \equiv \partial_t + \mathbf{u} \cdot \nabla$ is the material time derivative and $\rho \equiv mn$ is the mass density. Moreover, \mathbf{P} is the pressure tensor, \mathbf{q}_t (\mathbf{q}_r) is the translational (rotational) contribution to the total heat flux \mathbf{q} , ζ_t (ζ_r) is the translational (rotational) energy production rate, and ζ is the cooling rate. These quantities are defined as

$$P_{ij} = \rho \langle V_i V_j \rangle, \quad p = \frac{1}{d_t} \text{Tr} \mathbf{P} = nT_t, \quad (9a)$$

$$\mathbf{q}_t = \frac{\rho}{2} \langle V^2 \mathbf{V} \rangle, \quad \mathbf{q}_r = \frac{I n}{2} \langle \boldsymbol{\omega}^2 \mathbf{V} \rangle, \quad \mathbf{q} = \mathbf{q}_t + \mathbf{q}_r, \quad (9b)$$

$$\zeta_t = -\frac{m}{d_t n T_t} \mathcal{J}[v^2|f, f], \quad \zeta_r = -\frac{I}{d_r n T_r} \mathcal{J}[\boldsymbol{\omega}^2|f, f], \quad (9c)$$

$$\zeta = \frac{d_t \zeta_t T_t + d_r \zeta_r T_r}{(d_t + d_r) T}. \quad (9d)$$

In Eq. (9c), the collisional rates of change $\mathcal{J}[v^2|f, f]$ and $\mathcal{J}[\boldsymbol{\omega}^2|f, f]$ are obtained from Eq. (7) by setting $\psi = v^2$ and $\psi = \boldsymbol{\omega}^2$, respectively.

C. Homogeneous cooling state

Before analyzing inhomogeneous states in terms of the transport coefficients at the NSF order in Secs. III–V, let us consider the HCS, henceforth represented by the superscript (0). In that case ($\nabla \rightarrow 0$), Eqs. (8a) and (8b) yield $n = \text{const}$ and $\mathbf{u} = \text{const}$, while Eqs. (8c)–(8e) become

$$\dot{T}_t^{(0)} + T_t^{(0)} \zeta_t^{(0)} = 0, \quad (10a)$$

$$\dot{T}_r^{(0)} + T_r^{(0)} \zeta_r^{(0)} = 0, \quad (10b)$$

$$\dot{T} + T\zeta^{(0)} = 0. \quad (10c)$$

Note that we have not attached a superscript (0) to the global temperature T because of its status as a hydrodynamic variable. The Boltzmann equation, Eq. (1), reduces in the HCS to

$$\partial_t f^{(0)}(\boldsymbol{\Gamma}; t) = J_{\boldsymbol{\Gamma}}[f^{(0)}, f^{(0)}]. \quad (11)$$

Since in the HCS all the time-dependence of $f^{(0)}$ occurs through a dependence on T , we can write [5, 34]

$$\partial_t f^{(0)} = \dot{T} \frac{\partial f^{(0)}}{\partial T} = \frac{\zeta^{(0)}}{2} \left(\frac{\partial}{\partial \mathbf{V}} \cdot \mathbf{V} + \frac{\partial}{\partial \boldsymbol{\omega}} \cdot \boldsymbol{\omega} \right) f^{(0)}. \quad (12)$$

The rotational-to-translational, translational-to-total, and rotational-to-total temperature ratios are defined as

$$\theta \equiv \frac{T_r^{(0)}}{T_t^{(0)}}, \quad (13a)$$

$$\tau_t \equiv \frac{T_t^{(0)}}{T} = \frac{d_t + d_r}{d_t + d_r \theta}, \quad \tau_r \equiv \frac{T_r^{(0)}}{T} = \frac{d_t + d_r}{d_t/\theta + d_r}. \quad (13b)$$

Those temperature ratios are stationary in the HCS, so that Eqs. (10) imply that $\zeta_t^{(0)} = \zeta_r^{(0)} = \zeta^{(0)}$.

The exact solution to Eq. (11) is not known, but good estimates for the production rates $\zeta_t^{(0)}$, $\zeta_r^{(0)}$, and $\zeta^{(0)}$ can be obtained by assuming the simple trial function

$$f^{(0)}(\boldsymbol{\Gamma}) \rightarrow n v_{\text{th}}^{-d_t} \omega_{\text{th}}^{-d_r} \pi^{-d_t/2} e^{-c^2} \varphi_r(\mathbf{w}), \quad (14)$$

where

$$v_{\text{th}} = \sqrt{\frac{2T_t^{(0)}}{m}}, \quad \omega_{\text{th}} = \sqrt{\frac{2T_r^{(0)}}{I}} \quad (15)$$

are the translational and rotational thermal velocities, and

$$\mathbf{c} = \frac{\mathbf{V}}{v_{\text{th}}}, \quad \mathbf{w} = \frac{\boldsymbol{\omega}}{\omega_{\text{th}}} \quad (16)$$

are the scaled translational and angular velocities. Note that, while a Maxwellian translational distribution has

been assumed, the (isotropic) marginal rotational distribution $\varphi_r(\mathbf{w})$ does not need to be specified. Within this approximation, the results are [36, 37]

$$\zeta_t^{(0)} = \frac{\nu}{d_t} \left\{ 1 - \alpha^2 + \frac{2d_r\kappa(1+\beta)}{d_t(1+\kappa)^2} \left[1 - \theta + \frac{\kappa(1-\beta)}{2} \left(1 + \frac{\theta}{\kappa} \right) \right] \right\}, \quad (17a)$$

$$\zeta_r^{(0)} = \frac{2\nu\kappa(1+\beta)}{d_t(1+\kappa)^2} \left[1 - \frac{1}{\theta} + \frac{1-\beta}{2} \left(\frac{1}{\theta} + \frac{1}{\kappa} \right) \right], \quad (17b)$$

$$\zeta^{(0)} = \frac{\nu}{d_t + d_r\theta} \left[1 - \alpha^2 + \frac{d_r}{d_t} \frac{1-\beta^2}{1+\kappa} (\kappa + \theta) \right], \quad (17c)$$

where ν is the collision frequency defined as

$$\nu = Kn\sigma^{d_t-1}v_{\text{th}}, \quad K \equiv \frac{\sqrt{2\pi}^{d_t-1}}{\Gamma(d_t/2)}. \quad (18)$$

Note that $\nu = \frac{d_t+2}{4}\nu_0$, where ν_0 is the collision frequency associated with the shear viscosity of a molecular gas [48]. Insertion of Eqs. (17) into the condition $\zeta_t^{(0)} = \zeta_r^{(0)}$ yields the quadratic equation $\theta - 1 - (d_t/d_r)(1/\theta - 1) = 2h$, where

$$h \equiv \frac{d_t(1+\kappa)^2}{2d_r\kappa(1+\beta)^2} \left[1 - \alpha^2 - \frac{1 - \frac{d_r}{d_t}\kappa}{1+\kappa} (1-\beta^2) \right], \quad (19)$$

whose physical solution is

$$\theta = \sqrt{\left[h - \frac{1}{2} \left(\frac{d_t}{d_r} - 1 \right) \right]^2 + \frac{d_t}{d_r}} + h - \frac{1}{2} \left(\frac{d_t}{d_r} - 1 \right). \quad (20)$$

III. CHAPMAN-ENSKOG METHOD

The main goal of this paper is to obtain the NSF constitutive equations with explicit expressions for the associated transport coefficients. As usual, this will be done by assuming that the VDF depends on space and time only through the *slow* hydrodynamic fields introduced before (n , \mathbf{u} , and T) and applying the Chapman-Enskog expansion method [4, 5].

A. General scheme

The Chapman-Enskog method consists essentially in introducing multi-scale space-time derivatives and a perturbation expansion of the VDF in powers of the gradients of the hydrodynamic fields, namely

$$\nabla \rightarrow \epsilon \nabla, \quad f = f^{(0)} + \epsilon f^{(1)} + \epsilon^2 f^{(2)} + \dots, \quad (21a)$$

$$\mathcal{D}_t = \mathcal{D}_t^{(0)} + \epsilon \mathcal{D}_t^{(1)} + \epsilon^2 \mathcal{D}_t^{(2)} + \dots, \quad (21b)$$

where ϵ is a bookkeeping parameter. Thus, the Boltzmann equation, Eq. (1), decouples into a hierarchy of equations of orders $k = 0, 1, 2, \dots$. The zeroth- and first-order equations are

$$\mathcal{D}_t^{(0)} f^{(0)} = J_{\mathbf{r}}[f^{(0)}, f^{(0)}], \quad (22a)$$

$$\left(\mathcal{D}_t^{(0)} + \mathcal{L} \right) f^{(1)} = - \left(\mathcal{D}_t^{(1)} + \mathbf{V} \cdot \nabla \right) f^{(0)}. \quad (22b)$$

In Eq. (22b), the linear collision operator \mathcal{L} is defined as

$$\mathcal{L}\Phi(\mathbf{\Gamma}_1) = -J_{\mathbf{r}_1}[\Phi, f^{(0)}] - J_{\mathbf{r}_1}[f^{(0)}, \Phi]. \quad (23)$$

Comparison between Eqs. (11) and (22a) shows that the zeroth-order VDF $f^{(0)}$ is the local version of the HCS VDF. This will be further confirmed below.

Substituting Eq. (21a) into Eqs. (9), one obtains

$$P_{ij} = p^{(0)}\delta_{ij} + \epsilon P_{ij}^{(1)} + \epsilon^2 P_{ij}^{(2)} + \dots, \quad (24a)$$

$$\mathbf{q} = \epsilon \mathbf{q}^{(1)} + \epsilon^2 \mathbf{q}^{(2)} + \dots, \quad (24b)$$

$$\zeta = \zeta^{(0)} + \epsilon \zeta^{(1)} + \epsilon^2 \zeta^{(2)} + \dots. \quad (24c)$$

Here, $p^{(0)} = n\tau_t T$, τ_t being defined by Eq. (13b) and

$$\zeta^{(1)} = \frac{d_t\tau_t\zeta_t^{(1)} + d_r\tau_r\zeta_r^{(1)}}{d_t + d_r}, \quad (25a)$$

$$\zeta_t^{(1)} = -\frac{m}{d_t n \tau_t T} \Lambda[V^2|f^{(1)}], \quad \zeta_r^{(1)} = -\frac{I}{d_r n \tau_r T} \Lambda[\omega^2|f^{(1)}], \quad (25b)$$

where, in general,

$$\begin{aligned} \Lambda[\psi|\Phi] &\equiv \int d\mathbf{\Gamma}_1 \psi(\mathbf{\Gamma}_1) \mathcal{L}\Phi(\mathbf{\Gamma}_1) \\ &= -\frac{\sigma^{d_t-1}}{2} \int d\mathbf{\Gamma}_1 \int d\mathbf{\Gamma}_2 \int_+ d\hat{\boldsymbol{\sigma}} (\hat{\boldsymbol{\sigma}} \cdot \mathbf{v}_{12}) \\ &\quad \times \Delta(\psi_1 + \psi_2) \left(f_1^{(0)} \Phi_2 + \Phi_1 f_2^{(0)} \right). \end{aligned} \quad (26)$$

Note that, within the approximation described by Eq. (14), θ and $\zeta^{(0)}$ are given by Eqs. (20) and (17c), respectively.

Furthermore, the action of the operator $\mathcal{D}_t^{(k)}$ on a generic function $\psi(n, \mathbf{u}, T)$ of the hydrodynamic fields is

$$\mathcal{D}_t^{(k)} \psi = \frac{\partial \psi}{\partial n} \mathcal{D}_t^{(k)} n + \frac{\partial \psi}{\partial \mathbf{u}} \cdot \mathcal{D}_t^{(k)} \mathbf{u} + \frac{\partial \psi}{\partial T} \mathcal{D}_t^{(k)} T, \quad (27)$$

where $\mathcal{D}_t^{(k)} n$, $\mathcal{D}_t^{(k)} \mathbf{u}$, and $\mathcal{D}_t^{(k)} T$ are obtained from the balance equations, Eqs. (8a), (8b), and (8e). In particular,

$$\mathcal{D}_t^{(0)} n = 0, \quad \mathcal{D}_t^{(0)} \mathbf{u} = 0, \quad \mathcal{D}_t^{(0)} T = -T\zeta^{(0)}, \quad (28a)$$

$$\mathcal{D}_t^{(1)}n = -n\nabla \cdot \mathbf{u}, \quad \mathcal{D}_t^{(1)}\mathbf{u} = -\frac{\tau_t}{\rho}\nabla(nT), \quad (28b)$$

$$\mathcal{D}_t^{(1)}T = -\frac{2\tau_t}{d_t + d_r}T\nabla \cdot \mathbf{u} - T\zeta^{(1)}. \quad (28c)$$

Equation (28a) implies that $\mathcal{D}_t^{(0)}f^{(0)} = -\zeta^{(0)}T\partial_T f^{(0)}$, in agreement with Eq. (12). This confirms that $f^{(0)}$ is the local version of the HCS VDF.

B. First-order distribution

By following the same steps as in Sec. IVB of Ref. [34], it is possible to express the solution to Eq. (22b) as

$$f^{(1)} = \mathcal{A} \cdot \nabla \ln T + \mathcal{B} \cdot \nabla \ln n + C_{ij} \nabla_j u_i + \mathcal{E} \nabla \cdot \mathbf{u}, \quad (29)$$

where the functions \mathcal{A} , \mathcal{B} , C_{ij} , and \mathcal{E} obey the following set of linear integral equations:

$$\left(-\frac{\zeta^{(0)}}{2} - \zeta^{(0)}T\partial_T + \mathcal{L}\right)\mathcal{A} = \mathbf{A}, \quad (30a)$$

$$\left(-\zeta^{(0)}T\partial_T + \mathcal{L}\right)\mathcal{B} - \zeta^{(0)}\mathcal{A} = \mathbf{B}, \quad (30b)$$

$$\left(-\zeta^{(0)}T\partial_T + \mathcal{L}\right)C_{ij} = C_{ij}, \quad (30c)$$

$$\left(-\zeta^{(0)}T\partial_T + \mathcal{L}\right)\mathcal{E} + \xi T\partial_T f^{(0)} = E. \quad (30d)$$

Here, the functions in the inhomogeneous terms are defined by the relation $-(\mathcal{D}_t^{(1)} + \mathbf{V} \cdot \nabla)f^{(0)} = \mathbf{A} \cdot \nabla \ln T + \mathbf{B} \cdot \nabla \ln n + C_{ij} \nabla_j u_i + E \nabla \cdot \mathbf{u} + \zeta^{(1)}T\partial_T f^{(0)}$. They are given by

$$\mathbf{A} = -\frac{v_{\text{th}}}{2}(\partial_{\mathbf{c}} - \mathbf{c}\partial_{\mathbf{c}} \cdot \mathbf{c} - \mathbf{c}\partial_{\mathbf{w}} \cdot \mathbf{w})f^{(0)}, \quad (31a)$$

$$\mathbf{B} = -\frac{v_{\text{th}}}{2}(2\mathbf{c} + \partial_{\mathbf{c}})f^{(0)}, \quad (31b)$$

$$C_{ij} = -\left(\frac{1}{d_t}\delta_{ij}\mathbf{c} \cdot \partial_{\mathbf{c}} - c_j\partial_{c_i}\right)f^{(0)}, \quad (31c)$$

$$E = -\frac{d_r\tau_t\tau_r}{d_t + d_r}\left(\frac{\partial_{\mathbf{w}} \cdot \mathbf{w}}{d_r\tau_r} - \frac{d_t + \mathbf{c} \cdot \partial_{\mathbf{c}}}{d_t\tau_t}\right)f^{(0)}, \quad (31d)$$

where δ_{ij} is the identity tensor in the translational velocity Euclidean subspace, the scaled velocities \mathbf{c} and \mathbf{w} are defined by Eq. (16), and use has been made of the general property $T\partial_T f^{(0)} = -\frac{1}{2}(\partial_{\mathbf{v}} \cdot \mathbf{V} + \partial_{\mathbf{w}} \cdot \mathbf{w})f^{(0)}$ [see the second equality in Eq. (12)]. In Eq. (30d), ξ is the

velocity-divergence transport coefficient in the constitutive equation

$$\zeta^{(1)} = -\xi\nabla \cdot \mathbf{u}, \quad (32)$$

which is given by

$$\xi = \frac{d_t\tau_t\xi_t + d_r\tau_r\xi_r}{d_t + d_r}, \quad (33a)$$

$$\xi_t = -\frac{m}{d_t n \tau_t T} \Lambda[V^2|\mathcal{E}], \quad \xi_r = -\frac{I}{d_r n \tau_r T} \Lambda[\omega^2|\mathcal{E}], \quad (33b)$$

Note that C_{ij} is a traceless tensor. However, in general, it is not symmetric. In the HS case, due to isotropy, the local version of the HCS function $f^{(0)}$ is a function of V^2 , ω^2 , and $\vartheta \equiv (\mathbf{V} \cdot \boldsymbol{\omega})^2$ [49–51]. This implies [34] $C_{ij} - C_{ji} = 2(\partial f^{(0)}/\partial \vartheta)(\mathbf{V} \cdot \boldsymbol{\omega})(V_j \omega_i - V_i \omega_j)$. However, the vectors \mathbf{V} and $\boldsymbol{\omega}$ are mutually orthogonal in the HD case and hence the tensor C_{ij} is symmetric in the two-dimensional geometry.

C. Navier–Stokes–Fourier transport coefficients

The formal derivation from Eq. (29) of the constitutive equations for the pressure tensor and the heat flux follows the same steps as in Sec. V of Ref. [34], except that special care must be exerted to redo those steps keeping d_t and d_r generic. For the sake of conciseness, we skip some of the technical details.

The first-order pressure tensor and heat flux can be expressed as

$$P_{ij}^{(1)} = -\eta\left(\nabla_i u_j + \nabla_j u_i - \frac{2}{d_t}\delta_{ij}\nabla \cdot \mathbf{u}\right) - \eta_b\delta_{ij}\nabla \cdot \mathbf{u}, \quad (34a)$$

$$\mathbf{q}^{(1)} = -\lambda\nabla T - \mu\nabla n, \quad (34b)$$

where η is the shear viscosity, η_b is the bulk viscosity, λ is the thermal conductivity, and μ is a Dufour-like coefficient [5, 24, 34, 35, 38, 52]. Since $\mathbf{q}^{(1)}$ has a translational and a rotational contribution [see Eq. (9b)] so do λ and μ :

$$\lambda = \tau_t\lambda_t + \tau_r\lambda_r, \quad \mu = \mu_t + \mu_r. \quad (35)$$

The transport coefficients can be expressed in terms of the solutions to Eqs. (30) as

$$\eta = -\frac{m}{(d_t + 2)(d_t - 1)} \int d\Gamma \left(V_i V_j - \frac{1}{d_t}\delta_{ij}V^2\right) C_{ij} = \frac{n\tau_t T}{\nu_\eta - \frac{1}{2}\zeta^{(0)}}, \quad (36a)$$

$$\eta_b = -\frac{m}{d_t} \int d\Gamma V^2 \mathcal{E} = \frac{\tau_t\tau_r n T}{\zeta^{(0)}} \frac{2d_r}{d_t + d_r} \left(\xi_t - \xi_r - \frac{2}{d_t}\right), \quad (36b)$$

$$\lambda_t = -\frac{m}{2d_t\tau_t T} \int d\Gamma V^2 \mathbf{V} \cdot \mathcal{A} = \frac{d_t + 2}{2} \frac{n\tau_t T}{m} \frac{1 + 2a_{20}^{(0)}}{\nu_{\lambda_t} - 2\zeta^{(0)}}, \quad (36c)$$

$$\lambda_r = -\frac{I}{2d_t\tau_r T} \int d\Gamma \omega^2 \mathbf{V} \cdot \mathcal{A} = \frac{d_r}{2} \frac{n\tau_r T}{m} \frac{1 + 2a_{11}^{(0)}}{\nu_{\lambda_r} - 2\zeta^{(0)}}, \quad (36d)$$

$$\mu_t = -\frac{m}{2d_t n} \int d\Gamma V^2 \mathbf{V} \cdot \mathcal{B} = \frac{\tau_t T}{n} \frac{\lambda_t \zeta^{(0)} + \frac{d_t + 2}{2} \frac{n\tau_t T}{m} a_{20}^{(0)}}{\nu_{\mu_t} - \frac{3}{2}\zeta^{(0)}}, \quad (36e)$$

$$\mu_r = -\frac{I}{2d_t n} \int d\Gamma \omega^2 \mathbf{V} \cdot \mathcal{B} = \frac{\tau_r T}{n} \frac{\lambda_r \zeta^{(0)} + \frac{d_r}{2} \frac{n\tau_r T}{m} a_{11}^{(0)}}{\nu_{\mu_r} - \frac{3}{2}\zeta^{(0)}}, \quad (36f)$$

where we have introduced the HCS cumulants

$$a_{20}^{(0)} = \frac{m^2}{d_t(d_t + 2)\tau_t^2 T^2} \langle V^4 \rangle^{(0)} - 1, \quad (37a)$$

$$a_{11}^{(0)} = \frac{mI}{d_r d_t \tau_t \tau_r T^2} \langle V^2 \omega^2 \rangle^{(0)} - 1, \quad (37b)$$

and the collision frequencies

$$\nu_\eta = \frac{\Lambda[V_i V_j - \frac{1}{d_t} V^2 \delta_{ij}] \mathcal{C}_{ij}}{\int d\Gamma \left(V_i V_j - \frac{1}{d_t} V^2 \delta_{ij} \right) \mathcal{C}_{ij}}, \quad (38a)$$

$$\nu_{\lambda_t} = \frac{\Lambda[V^2 V_i] \mathcal{A}_i}{\int d\Gamma V^2 \mathbf{V} \cdot \mathcal{A}}, \quad \nu_{\lambda_r} = \frac{\Lambda[\omega^2 V_i] \mathcal{A}_i}{\int d\Gamma \omega^2 \mathbf{V} \cdot \mathcal{A}}, \quad (38b)$$

$$\nu_{\mu_t} = \frac{\Lambda[V^2 V_i] \mathcal{B}_i}{\int d\Gamma V^2 \mathbf{V} \cdot \mathcal{B}}, \quad \nu_{\mu_r} = \frac{\Lambda[\omega^2 V_i] \mathcal{B}_i}{\int d\Gamma \omega^2 \mathbf{V} \cdot \mathcal{B}}. \quad (38c)$$

It is interesting to remark that the rotational-to-translational temperature ratio is affected by the presence of $\nabla \cdot \mathbf{u}$. Taking the trace in both sides of Eq. (34a), we get, to first order, $T_t = \tau_t T - (\eta_b/n) \nabla \cdot \mathbf{u}$. Since Eq. (3c) must hold to any order, this implies $T_r = \tau_r T + (d_t/d_r)(\eta_b/n) \nabla \cdot \mathbf{u}$. As a consequence,

$$\frac{T_r}{T_t} = \theta + \frac{\tau_r}{\tau_t} \frac{2}{\zeta^{(0)}} \left(\xi_t - \xi_r - \frac{2}{d_t} \right) \nabla \cdot \mathbf{u}. \quad (39)$$

IV. EXPLICIT EXPRESSIONS FOR THE TRANSPORT COEFFICIENTS

All the expressions in Sec. III are formally exact within the Chapman–Enskog scheme but they are not explicit since neither the zeroth-order VDF $f^{(0)}$ nor the solutions to the linear integral equations (30) are known exactly.

By symmetry arguments, \mathcal{A} and \mathcal{B} can be expressed, in the HS case, as linear combinations of the vectors \mathbf{V} , $(\mathbf{V} \cdot \boldsymbol{\omega})\boldsymbol{\omega}$, and $\mathbf{V} \times \boldsymbol{\omega}$, while \mathcal{C}_{ij} is a linear combination

of the dyadic products of those three vectors. However, $\mathbf{V} \perp \boldsymbol{\omega}$ in a HD system, and thus \mathcal{A} and \mathcal{B} are vector functions residing in the two-dimensional subspace \mathfrak{V} of translational velocities, so that they can be expressed as linear combinations of the mutually orthogonal vectors \mathbf{V} and $\mathbf{V} \times \boldsymbol{\omega}$ (which form an orthogonal basis of \mathfrak{V}), where the latter vector product is done in the embedding space $\mathfrak{E} = \mathfrak{V} \oplus \mathfrak{W}$, \mathfrak{W} being the one-dimensional subspace where angular velocities live. Then, in the case of disks, \mathcal{C}_{ij} is a linear combination of the dyadic products of the two vectors \mathbf{V} and $\mathbf{V} \times \boldsymbol{\omega}$ only.

A. Sonine-like approximation for \mathcal{A}_i , \mathcal{B}_i , \mathcal{C}_{ij} , and \mathcal{E}

To get explicit expressions for the NSF transport coefficients we need to resort to approximations. We will proceed in two steps. First, the structure of Eqs. (31) suggests to propose the following approximate forms for the solutions of Eqs. (30):

$$\mathcal{A} \rightarrow -\frac{v_{\text{th}}}{2\nu} [\gamma_{A_t} (\partial_{\mathbf{c}} - \mathbf{c} \partial_{\mathbf{c}} \cdot \mathbf{c}) - \gamma_{A_r} \mathbf{c} \partial_{\mathbf{w}} \cdot \mathbf{w}] f^{(0)}, \quad (40a)$$

$$\mathcal{B} \rightarrow -\frac{v_{\text{th}}}{2\nu} [\gamma_{B_t} (\partial_{\mathbf{c}} - \mathbf{c} \partial_{\mathbf{c}} \cdot \mathbf{c}) - \gamma_{B_r} \mathbf{c} \partial_{\mathbf{w}} \cdot \mathbf{w}] f^{(0)}, \quad (40b)$$

$$\mathcal{C}_{ij} \rightarrow -\frac{\gamma_C}{2\nu} \left(\frac{1}{d_t} \delta_{ij} \mathbf{c} \cdot \partial_{\mathbf{c}} - c_j \partial_{c_i} \right) f^{(0)}, \quad (40c)$$

$$\mathcal{E} \rightarrow -\frac{\gamma_E d_r \tau_t \tau_r}{2\nu} \left(\frac{\partial_{\mathbf{w}} \cdot \mathbf{w}}{d_r \tau_r} - \frac{d_t + \mathbf{c} \cdot \partial_{\mathbf{c}}}{d_t \tau_t} \right) f^{(0)}, \quad (40d)$$

where ν is defined by Eq. (18) and the γ coefficients remain to be determined. In the case of conservative collisions ($\alpha = |\beta| = 1$), $f^{(0)}$ is the Maxwellian equilibrium distribution and then Eqs. (40) define the simplest Sonine approximation [53, 54]. Therefore, Eqs. (40) will be referred to as Sonine-like approximation.

Inserting Eqs. (40) into the first equalities in Eqs. (36), one can relate the transport coefficients to the γ coefficients as follows:

$$\eta^* \equiv \frac{\eta}{\eta_0} = \frac{2\gamma_C}{d_t + 2}, \quad \eta_b^* \equiv \frac{\eta_b}{\eta_0} = \frac{4d_r \tau_r \gamma_E}{d_t(d_t + 2)}, \quad (41a)$$

$$\lambda_t^* \equiv \frac{\lambda_t}{\lambda_0} = \frac{4(d_t - 1)}{d_t(d_t + 2)} [1 + 2a_{20}^{(0)}] \gamma_{A_t}, \quad (41b)$$

$$\lambda_r^* \equiv \frac{\lambda_r}{\lambda_0} = \frac{4(d_t - 1)d_r}{d_t(d_t + 2)^2} [\gamma_{A_r} + (\gamma_{A_r} + \gamma_{A_t}) a_{11}^{(0)}], \quad (41c)$$

$$\mu_t^* \equiv \frac{n\mu_t}{\lambda_0 T} = \frac{4(d_t - 1)\tau_t}{d_t(d_t + 2)} [1 + 2a_{20}^{(0)}] \gamma_{B_t}, \quad (41d)$$

$$\mu_r^* \equiv \frac{n\mu_r}{\lambda_0 T} = \frac{4(d_t - 1)d_r\tau_r}{d_t(d_t + 2)^2} \left[\gamma_{B_r} + (\gamma_{B_r} + \gamma_{B_t}) a_{11}^{(0)} \right], \quad (41e)$$

where

$$\eta_0 = \frac{d_t + 2}{4} \frac{n\tau_t T}{\nu}, \quad \lambda_0 = \frac{d_t(d_t + 2)}{2(d_t - 1)} \frac{\eta_0}{m}, \quad (42)$$

are the shear viscosity and thermal conductivity, respectively, in the elastic ($\alpha = 1$) and smooth ($\beta = -1$) case. Appendix B shows that the γ coefficients can be expressed in terms of collision integrals involving the HCS VDF $f^{(0)}$.

B. Approximate form for $f^{(0)}$

Thus far, we did not need in this section to specify the VDF $f^{(0)}$. Furthermore, the dependence on the number of degrees of freedom d_t and d_r in the equations above obeys to purely geometric considerations from the point of view that the explicit form of the collision rules has not been used yet. Now, as a second step in the quest for explicit expressions for the transport coefficients, we adopt the semi-Maxwellian approximation given by Eq. (14), which implies that the cumulants $a_{20}^{(0)}$ and $a_{11}^{(0)}$ [see Eqs. (37)] vanish. As a matter of fact, it has been previously observed [49–51] that those cumulants are indeed generally small, at least in the HS case. Preliminary results [55] show that the cumulants are also relatively small in the HD case, except for high inelasticity.

Equation (14) allows us to carry out the collision integrals in Eqs. (B1) and (B2) by applying the collision rules, which include vector products (see Appendix A). This gives rise to a much subtler and complex dependence on the number of degrees of freedom d_t and d_r [36], which we simplify under the constraints that the results remain being valid for three-dimensional rough HS ($d_t = d_r = 3$), two-dimensional rough HD ($d_t = 2$, $d_r = 1$), and d -dimensional smooth particles ($d_t = d$, $d_r \rightarrow 0$). The algebra involved in the computation of the collision integrals is rather tedious, so here we only provide the final results. A summary of the main explicit expressions obtained by the combination of Eqs. (14) and (40) is presented in Table I. Those expressions are equivalent, in the HS case ($d_t = d_r = 3$), to those shown in Table I of Ref. [34].

V. RESULTS

A. Limiting cases

While Table I gives the transport coefficients in terms of the coefficients of restitution (α , β), the reduced moment of inertia (κ), and the number of degrees of freedom (d_t , d_r), it is interesting to consider some important limiting cases.

TABLE I. Summary of the main explicit expressions in the approximations (14) and (40).

$\tilde{\alpha} = \frac{1 + \alpha}{2}$, $\tilde{\beta} = \frac{1 + \beta}{2} \frac{\kappa}{1 + \kappa}$
$\frac{T_t^{(0)}}{T} = \tau_t = \frac{d_t + d_r}{d_t + d_r\theta}$, $\frac{T_r^{(0)}}{T} = \tau_r = \frac{d_t + d_r}{d_t/\theta + d_r}$
$\theta = \sqrt{\left[h - \frac{1}{2} \left(\frac{d_t}{d_r} - 1 \right) \right]^2 + \frac{d_t}{d_r} + h - \frac{1}{2} \left(\frac{d_t}{d_r} - 1 \right)}$
$h \equiv \frac{d_t(1 + \kappa)^2}{2d_r\kappa(1 + \beta)^2} \left[1 - \alpha^2 - \frac{1 - \frac{d_r}{d_t}\kappa}{1 + \kappa} (1 - \beta^2) \right]$
$\nu = K n \sigma^{d_t-1} \sqrt{2\tau_t T/m}$, $K \equiv \frac{\sqrt{2\pi} \frac{d_t-1}{2}}{\Gamma(d_t/2)}$
$\frac{\zeta^{(0)}}{\nu} = \zeta^* = \frac{1}{d_t + d_r\theta} \left[1 - \alpha^2 + \frac{d_r}{d_t} \frac{1 - \beta^2}{1 + \kappa} (\kappa + \theta) \right]$
$\eta = \frac{n\tau_t T}{\nu} \frac{1}{\nu_r^* - \frac{1}{2}\zeta^*}$, $\eta_b = \frac{d_r n\tau_t \tau_r T}{d_t \nu} \gamma_E$
$\lambda = \tau_t \lambda_t + \tau_r \lambda_r$, $\lambda_t = \frac{d_t + 2}{2} \frac{n\tau_t T}{m\nu} \gamma_{A_t}$, $\lambda_r = \frac{d_r}{2} \frac{n\tau_r T}{m\nu} \gamma_{A_r}$
$\mu = \mu_t + \mu_r$, $\mu_t = \frac{d_t + 2}{2} \frac{\tau_t^2 T^2}{m\nu} \gamma_{B_t}$, $\mu_r = \frac{d_r}{2} \frac{\tau_r T^2}{m\nu} \gamma_{B_r}$
$\xi = \frac{d_t \tau_t \xi_t + d_r \tau_r \xi_r}{d_t + d_r} = \gamma_E \Xi$, $\xi_t = \gamma_E \Xi_t$, $\xi_r = \gamma_E \Xi_r$
$\nu_r^* = \frac{4}{d_t(d_t + 2)} \left[(d_t + 3) \left(\tilde{\alpha} + \frac{d_r}{d_t} \tilde{\beta} \right) - 3\tilde{\alpha}^2 - \frac{d_r^2}{d_t} \tilde{\beta}^2 - \frac{4d_r \tilde{\beta}}{d_t - 1} \left(\tilde{\alpha} - \frac{\tilde{\beta}\theta}{4d_t} \right) \right]$
$\gamma_E = \frac{2}{d_t} \left(\Xi_t - \Xi_r - \frac{d_t + d_r}{2d_t} \zeta^* \right)^{-1}$
$\Xi_t = \frac{3d_r \tau_r}{2d_t^2} \left\{ 1 - \alpha^2 + \frac{d_r}{d_t} \frac{\kappa}{1 + \kappa} (1 - \beta^2) - \left(\frac{1 + \beta}{1 + \kappa} \right)^2 \frac{\kappa}{3} \left[\frac{d_r}{d_t} (\theta - 3) - 2 \right] \right\}$
$\Xi_r = \frac{\tau_t}{2d_t} \frac{1 + \beta}{1 + \kappa} \left\{ (1 - \beta) \left(\frac{d_r}{d_t} \theta - 2 \right) + \frac{1 + \beta}{1 + \kappa} \kappa \left[\frac{d_r}{d_t} (\theta - 3) - 2 \right] \right\}$
$\Xi = \frac{3d_r \tau_t \tau_r}{2d_t(d_t + d_r)} \left\{ 1 - \alpha^2 + \frac{1 - \beta^2}{3(1 + \kappa)} \left[\frac{d_r}{d_t} (3\kappa + \theta) - 2 \right] \right\}$
$\gamma_{A_t} = \frac{Z_r - Z_t - 2\zeta^*}{(Y_t - 2\zeta^*)(Z_r - 2\zeta^*) - Y_r Z_t}$
$\gamma_{A_r} = \frac{Y_t - Y_r - 2\zeta^*}{(Y_t - 2\zeta^*)(Z_r - 2\zeta^*) - Y_r Z_t}$
$\gamma_{B_t} = \zeta^* \frac{\gamma_{A_t} (Z_r - \frac{3}{2}\zeta^*) - \gamma_{A_r} Z_t}{(Y_t - \frac{3}{2}\zeta^*)(Z_r - \frac{3}{2}\zeta^*) - Y_r Z_t}$
$\gamma_{B_r} = \zeta^* \frac{\gamma_{A_r} (Y_t - \frac{3}{2}\zeta^*) - \gamma_{A_t} Y_r}{(Y_t - \frac{3}{2}\zeta^*)(Z_r - \frac{3}{2}\zeta^*) - Y_r Z_t}$
$Y_t = \frac{1}{d_t(d_t + 2)} \left[(20 + 7d_t) \left(\tilde{\alpha} + \frac{d_r}{d_t} \tilde{\beta} \right) - 3(d_t + 8)\tilde{\alpha}^2 - \frac{(12 + 7d_t)d_r}{d_t} \tilde{\beta}^2 - \frac{16d_r}{d_t} \tilde{\alpha}\tilde{\beta} - \tilde{\beta}^2 \frac{\theta}{\kappa} \frac{d_r(d_t + 4)}{d_t} \right]$
$Y_r = \frac{d_t + 2}{d_t^2} \frac{\tilde{\beta}}{\kappa} \left(1 - \frac{3\tilde{\beta}}{\theta} - \frac{\tilde{\beta}}{\kappa} \right)$, $Z_t = -\frac{2d_r}{d_t^2} \tilde{\beta}^2 \frac{\theta}{\kappa}$
$Z_r = \frac{2}{d_t} \left[\tilde{\alpha} + \frac{d_r}{d_t} \tilde{\beta} + \frac{\tilde{\beta}}{\kappa} \left(\frac{2d_t + 1}{d_t} - \frac{\tilde{\beta}}{\kappa} - 2\tilde{\beta} - \frac{4\tilde{\alpha}}{d_t} \right) \right]$

TABLE II. Temperature ratios (θ and τ_t), reduced cooling rate (ζ^*), and reduced transport coefficients (η^* , η_b^* , λ^* , μ^* , and ξ) in certain limits.

Quantity	Purely smooth particles	Quasismooth limit	Perfectly rough and elastic particles:
	$(d_t = d, d_r \rightarrow 0)$	$(\beta \rightarrow -1)$	Pidduck's limit ($\alpha = \beta = 1$)
θ	Irrelevant	$\frac{d_t}{d_r} \frac{(1+\kappa)^2(1-\alpha^2)}{\kappa(1+\beta)^2} \rightarrow \infty$	1
τ_t	1	0	1
ζ^*	$\frac{1-\alpha^2}{d}$	$\frac{2(1+\beta)}{d_t(1+\kappa)} \rightarrow 0$	0
η^*	$\frac{8d}{(1+\alpha)[d(3+\alpha)+4(1-\alpha)]}$	$\frac{4d_t(d_t-1)}{(1+\alpha)[2(d_t^2-1)+d_t(1-3\alpha)+2\alpha]}$	$\frac{2d_t(1+\kappa)^2}{2d_t+(d_t^2+2d_t-2)\kappa}$
η_b^*	0	$\frac{8}{(d_t+2)(1-\alpha^2)}$	$\frac{2d_t d_r (1+\kappa)^2}{(d_t+2)(d_t+d_r)^2 \kappa}$
λ^*	$\frac{16(d-1)}{(1+\alpha)[d(3+5\alpha)-8\alpha]}$	$\frac{4(d_t-1)(d_t+d_r)}{(d_t+2)^2(1+\alpha)}$	$\frac{4d_r(1+\kappa)^2 P_N(\kappa)}{(d_t+2)^2 P_D(\kappa)}$
μ^*	$\frac{4(d+2)(1-\alpha)}{d(5+3\alpha)+4(1-3\alpha)} \lambda^*$	0	0
ξ	0	0	0

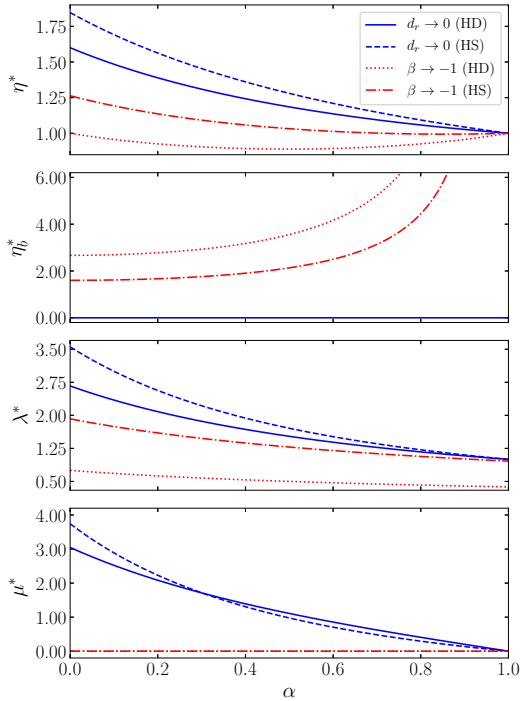


FIG. 1. Dependence of the relevant (reduced) transport coefficients for the smooth ($d_r \rightarrow 0$) and quasismooth ($\beta \rightarrow -1$) limits on the coefficient of normal restitution for HS and HD granular gases.

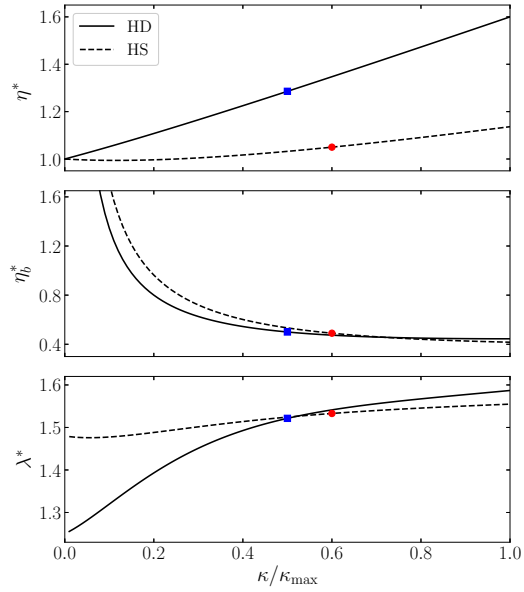


FIG. 2. Dependence of the nonzero (reduced) transport coefficients for perfectly elastic and perfectly rough particles (Pidduck's gas) on the reduced moment of inertia κ , relative to its maximum value $\kappa_{\max} = 1$ (HD) or $\kappa_{\max} = \frac{2}{3}$ (HS). The symbols correspond to uniform disks ($\kappa/\kappa_{\max} = \frac{1}{2}$) and uniform spheres ($\kappa/\kappa_{\max} = \frac{2}{3}$).

The first situation corresponds to a d -dimensional gas of *smooth* particles. In that case, $d_t \rightarrow d$ and, given that $\beta \rightarrow -1$ is a singular limit (see below), we formally take $d_r \rightarrow 0$. Since the rotational-to-translational temperature ratio lacks any physical meaning in the purely smooth case, its irrelevant precise value is not needed. In fact, on purely mathematical grounds, Eq. (20) shows that $\lim_{d_r \rightarrow 0} \theta = \text{finite}$ if $\alpha > |\beta - \kappa|/1 + \kappa$. Upon taking the limit $d_r \rightarrow 0$ in Table I, one can easily obtain the expressions shown in the second column of Table II. They agree with previous results [38, 48] particularized to the Maxwellian approximation. The same results are obtained by formally setting $\theta = 0$ and either $\beta = -1$ or $\kappa = 0$, except that a spurious factor $\tau_t = 1 + d_r/d_t$ is attached to λ and μ [34].

As said before, the quasismooth limit $\beta \rightarrow -1$ is singular and completely different from the smooth case [34, 56]. This distinction is physical and independent of the approximations carried out in this paper. The physical origin of the quasismooth singularity of the HCS can be summarized as follows. If the particles are strictly smooth ($\beta = -1$), then the rotational degrees of freedom are quenched, so that the (physically irrelevant) rotational temperature remains constant while the translational temperature monotonically decreases with time. The rotational-to-translational temperature ratio diverges but there is no mechanism transferring energy from the rotational to the translational degrees of freedom; in other words, the channel transferring energy between the rotational and translational degrees of freedom via collisions is broken if $\beta = -1$. However, if $\beta = -1 + \varepsilon$, where $0 < \varepsilon \ll 1$, then the rotational-to-translational temperature ratio becomes so huge that it is eventually able to activate and “feed” the weak energy channel connecting the rotational and translational temperatures, thus producing a nonnegligible effect on the HCS VDF [49–51, 57].

After carefully taking the limit $\beta \rightarrow -1$, the results for the quasismooth limit displayed in the third column of Table II are obtained. As already noticed in Ref. [34], $\theta \sim (1 + \beta)^{-2} \rightarrow \infty$, $\zeta \sim (1 + \beta) \rightarrow 0$, and no dependence on the reduced moment of inertia κ remains in the transport coefficients after taking the quasismooth limit.

Figure 1 shows the differences between the smooth and quasismooth (reduced) transport coefficients. In the cases of the shear viscosity η^* and the thermal conductivity λ^* , we observe that those coefficients are higher for HS than for HD; additionally, they are higher for smooth particles (monotonic behavior) than in the quasismooth limit (nonmonotonic behavior). In what respects the bulk shear viscosity η_b^* , it vanishes for smooth particles, but not in the quasismooth limit, in which case it takes higher values for HD than for HS. Finally, the Dufour-like coefficient μ^* vanishes in the quasismooth limit, but not for smooth particles, the HD value being larger than the HS one if $\alpha > 0.303$.

As a third limiting situation, we now consider a system of particles perfectly elastic ($\alpha = 1$) and perfectly

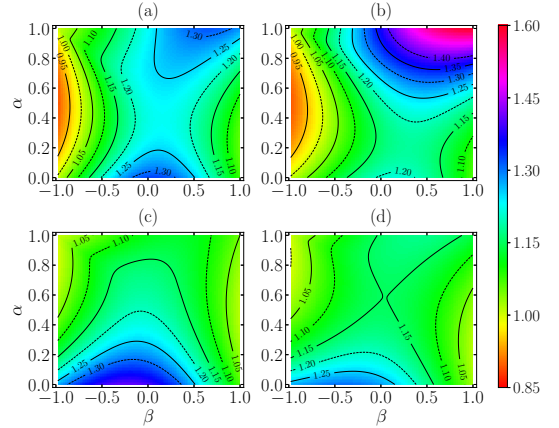


FIG. 3. Density plots of the reduced shear viscosity η^* in the plane β vs α for (a) HD with a uniform mass distribution ($\kappa = \frac{1}{2}$), (b) HD with a mass distribution concentrated on the outer surface ($\kappa = 1$), (c) HS with a uniform mass distribution ($\kappa = \frac{2}{3}$), and (d) HS with a mass distribution concentrated on the outer surface ($\kappa = \frac{2}{3}$).

rough ($\beta = 1$). Since energy is conserved by collisions [see Eq. (A6)], the equipartition principle holds. In the HS case, this system was first introduced about one hundred years ago by Pidduck [33] and is frequently used to model polyatomic molecules [53, 58, 59]. The results for HS and HD gases are given in the fourth column of Table II. In the case of λ , $P_N(\kappa) = N_0 + N_1\kappa + N_2\kappa^2$ and $P_D(\kappa) = D_0 + D_1\kappa + D_2\kappa^2 + D_3\kappa^3$ are polynomials with coefficients $(N_0, N_1, N_2, D_0, D_1, D_2, D_3) = (10, 39, 24, 2, 11, 12, 21)$ and $(37, 151, 50, 12, 75, 101, 102)$ for HD and HS, respectively. It must be noted that, when setting $\alpha = \beta = 1$ in the expressions of Table I, we took the licence of using $d_r = \frac{1}{2}d_t(d_t - 1)$ to simplify the final results for η^* and λ^* . Actually, the relation $d_r = \frac{1}{2}d_t(d_t - 1)$ is exact due to the relation of rotational mechanics on a d_t -translational geometry and the orthogonal group $O(d_t)$ [60, 61].

The dependence of η^* , η_b^* , and λ^* on the reduced moment of inertia for the HS and HD Pidduck gases is displayed in Fig. 2. Given a common value of κ/κ_{\max} , while the shear viscosity is higher for HD than for HS, the opposite happens in the case of the bulk viscosity (except if $\kappa/\kappa_{\max} > 0.718$, in which case the HD curve is slightly above the HS one). The thermal conductivity is higher for HD than for HS only if $\kappa/\kappa_{\max} > 0.522$. If the particles have a uniform mass distribution, then the HD-to-HS ratios are equal to 1.22, 1.02, and 0.99 for η^* , η_b^* , and λ^* , respectively.

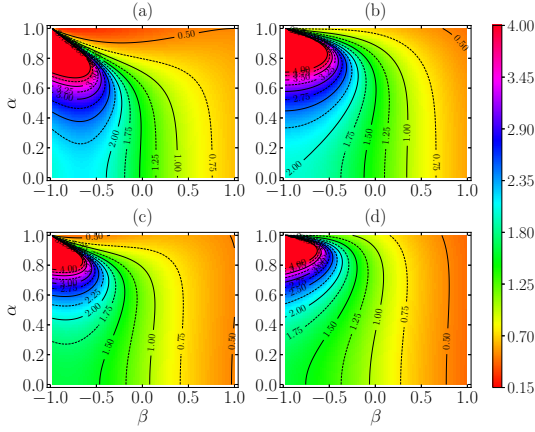


FIG. 4. Same as described in the caption of Fig. 3 but for the reduced bulk viscosity η_b^* .

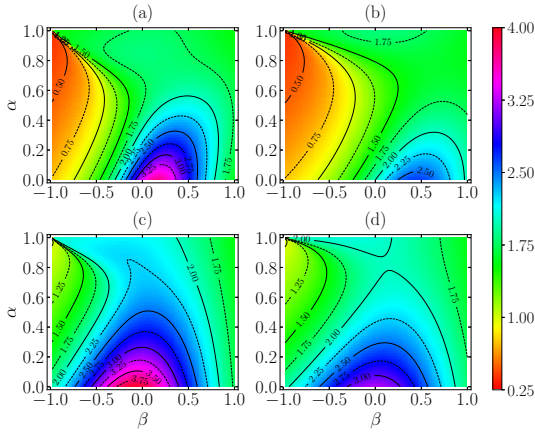


FIG. 5. Same as described in the caption of Fig. 3 but for the thermal conductivity λ^* .

B. General system

Now we go back to the general case and illustrate the dependence of the five transport coefficients η^* , η_b^* , λ^* , μ^* , and ξ on the coefficients of restitution (α , β) and the reduced moment of inertia (κ) for both HS and HD granular gases. The results are displayed as density plots in Figs. 3–7. Two characteristic cases of mass distribution are considered: uniform distribution ($\kappa = \frac{1}{2}$ and $\frac{2}{3}$ for HD and HS, respectively) and mass concentrated on the outer surface ($\kappa = \kappa_{\max} = 1$ and $\frac{2}{3}$ for HD and HS, respectively).

We observe an intricate influence of both α and β on the transport coefficients, with typically a strong non-monotonic dependence on β with, at fixed α , a single

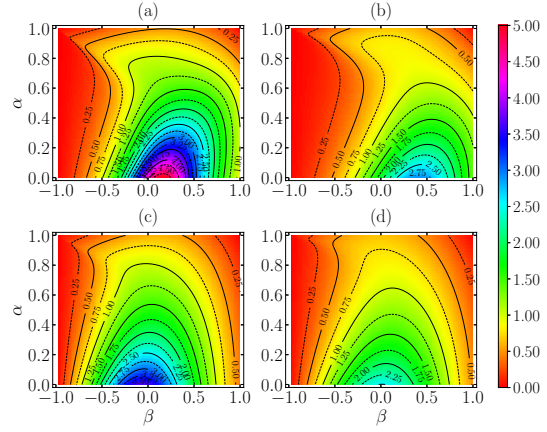


FIG. 6. Same as described in the caption of Fig. 3 but for the Dufour-like coefficient μ^* .

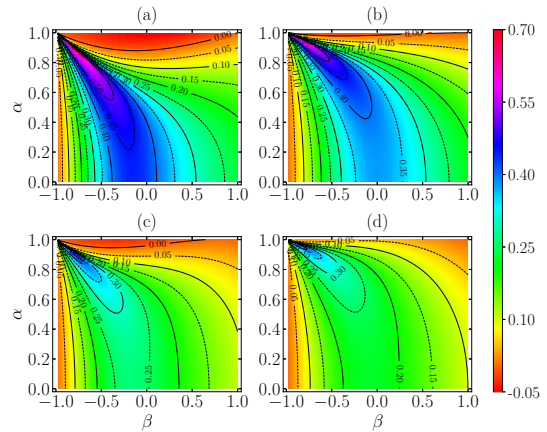


FIG. 7. Same as described in the caption of Fig. 3 but for the velocity-divergence transport coefficient ξ .

maximum around $\beta \approx 0$ for η^* , λ^* , and μ^* , a maximum near $\beta \rightarrow -1$ for η_b^* , and a more complex behavior for ξ . Note that the bulk viscosity reaches very high values in the quasielastic and quasismooth region (see Fig. 4); in fact, as shown in Fig. 1 and Table II, η_b^* diverges in the combined limit $\beta \rightarrow -1$ and $\alpha \rightarrow 1$. Moreover, η^* and λ^* are the transport coefficients more sensitive to the dimensionality and to the mass distribution. It is also worth mentioning that ξ reaches negative values in a narrow lobe region near $\alpha = 1$ (see Fig. 7). That region is wider for HD than for HS and tends to shrink as the moment of inertia grows; in fact, it disappears for HS with a surface mass distribution.

VI. CONCLUDING REMARKS

In this study, we have considered a model of a granular gas as composed by spherical particles with constant coefficients of normal (α) and tangential (β) restitution. Previous results [34] for the transport coefficients of a dilute gas of inelastic and rough HS have been complemented with novel results for the parallel case of HD. We have developed this analysis in a unified vector space framework, based on previous works [36, 37], which allows us to obtain general expressions in terms of the number of translational (d_t) and rotational (d_r) degrees of freedom. The choice of the embedding Euclidean three-dimensional space is essential to get results for both geometries within a common framework. Particular aspects, especially the orthogonality condition between rotational and translational velocities in the HD case, permit us to neglect the computation of certain quantities and reduce them to already known HS terms being parameterized by $d_t - 2$ or $(d_r - 1)/2$ prefactors, as convenience, in the spirit of Refs. [36, 37].

The analysis has been carried out in the context of the nonlinear Boltzmann equation, where the system is assumed to be fully described by the one-particle VDF $f(\mathbf{r}, \mathbf{v}, \boldsymbol{\omega}; t)$. Under the assumptions of (i) small gradients of the hydrodynamic fields [number density $n(\mathbf{r}, t)$, flow velocity $\mathbf{u}(\mathbf{r}, t)$, and granular temperature $T(\mathbf{r}, t)$] and (ii) a “normal” solution (i.e., the space and time dependence of the one-particle VDF takes place through a functional dependence on n , \mathbf{u} , and T), the Chapman-Enskog method has been used to solve the Boltzmann equation up to first order in the gradients. In that way, the NSF hydrodynamic equations are obtained by supplementing the balance equations for mass [Eq. (8a)], momentum [Eq. (8b)], and energy [Eq. (8e)] with constitutive equations for the pressure tensor $P_{ij}(\mathbf{r}, t)$ [Eq. (34a)], the heat flux $\mathbf{q}(\mathbf{r}, t)$ [Eq. (34b)], and the cooling rate $\zeta(\mathbf{r}, t)$ [Eq. (32)].

The derivation of the associated transport coefficients has been carried out along three successive stages of increasing concreteness and level of approximation. In a first stage, the transport coefficients are expressed [see Eqs. (36) and (38)] in terms of collision integrals involving the zeroth-order (HCS) VDF $f^{(0)}$ and the functions \mathcal{A} , \mathcal{B} , \mathcal{C}_{ij} , and \mathcal{E} characterizing the first-order VDF $f^{(1)}$ [see Eq. (29)]; those functions are the solutions of a set of linear integral equations [see Eqs. (30)] with inhomogeneous terms related to $f^{(0)}$ [see Eqs. (31)]. Next, in a second stage, Sonine-like forms for the functions \mathcal{A} , \mathcal{B} , \mathcal{C}_{ij} , and \mathcal{E} are assumed [see Eqs. (40)], with coefficients (γ_{A_t} , γ_{A_r} , γ_{B_t} , γ_{B_r} , γ_C , and γ_E) that can be expressed in terms of collisional integrals involving $f^{(0)}$ [see Eqs. (B2) and (B3)]. Finally, as the third and final stage, the HCS VDF $f^{(0)}$ is approximated by the product of a Maxwellian translational VDF times the marginal rotational VDF [see Eq. (14)]. The resulting explicit expressions for the transport coefficients as functions of the coefficients of restitution (α and β), the reduced moment of

inertia (κ), and the numbers of degrees of freedom (d_t and d_r) are displayed in Table I. In general, the transport coefficients exhibit a rather complex nonlinear dependence on α , β , and κ , as exposed in the density plots of Figs. 3–7.

The choice $(d_t, d_r) = (3, 3)$ allows us to recover known results for three-dimensional HS [34], except that in our approach we did not need to assume a Maxwellian form for the marginal rotational VDF. Moreover, novel results for two-dimensional HD are derived via the choice $(d_t, d_r) = (2, 1)$. Thus, the outcome quantities can be used as a unified set of formulas for theoretical and experimental researchers, as well as a source of comparison between HD and HS setups.

Some special limiting cases have been exposed in Table II: smooth, quasismooth, and Pidduck’s limits. The common description in terms of translational and rotational degrees of freedom let a direct recovery of the purely smooth case results by formally taking the limit $d_r \rightarrow 0$ at fixed β , thus circumventing the singular nature of the quasismooth limit $\beta \rightarrow -1$. In the latter limit, a universal lack of dependence on κ of the transport coefficients, already seen for HS [34], is observed. The quasismooth limit is quite distinct from the purely smooth case, as shown in Fig. 1. Furthermore, we have extended the original Pidduck’s system [33] ($\alpha = \beta = 1$) to our description, and novel results for HD are obtained; the dependencies with the reduced moment of inertia are shown in Fig. 2, where one can observe that the values of the coefficients η_b^* and λ^* with a uniform mass distribution are similar for the two considered setups. It is also interesting to remark that the transport coefficient (ξ) associated with the velocity-divergence correction of the cooling rate vanishes in all these limits, for both HD and HS, as expected.

An immediate application of this work is the use of the closed set of NSF hydrodynamic equations to analyze the stability of the HCS, again in a unified framework encompassing the special HS and HD cases. This is the subject of the companion paper [62]. Additionally, the extension of the results to stochastically driven granular gases is straightforward (since the evaluation of the collision integrals has already been done in the present paper) and will be published elsewhere. Another future goal of our research is to go back to the second stage mentioned above and assume a form for $f^{(0)}$ where excess velocity kurtoses and translational-rotational velocity correlations are not neglected. Preliminary results [55] are quite promising.

Lastly, we hope that this research will inspire future works in the field, which could provide simulation and experimental results to compare with, as well as the introduction of alternative collisional models to describe systems of inelastic and rough particles.

ACKNOWLEDGMENTS

The authors acknowledge financial support from the Grant No. PID2020-112936GB-

I00/AEI/10.13039/501100011033 and from the Junta de Extremadura (Spain) through Grants No. IB20079 and No. GR18079, all of them partially financed by Fondo Europeo de Desarrollo Regional funds. A.M. is grateful to the Spanish Ministerio de Ciencia, Innovación y Universidades for support from a predoctoral fellowship Grant No. FPU2018-3503.

Appendix A: Collision rules

The direct binary collision rules read

$$m\mathbf{v}'_{1,2} = m\mathbf{v}_{1,2} \mp \mathbf{Q}, \quad I\boldsymbol{\omega}'_{1,2} = I\boldsymbol{\omega}_{1,2} - \frac{\sigma}{2}\hat{\boldsymbol{\sigma}} \times \mathbf{Q}, \quad (\text{A1})$$

where \mathbf{Q} is the impulse that particle 1 exerts on particle 2. Our collision model is based on the existence of two constant coefficients of restitution, normal ($0 < \alpha \leq 1$) and tangential ($-1 \leq \beta \leq 1$), which are defined by the following relations:

$$\hat{\boldsymbol{\sigma}} \cdot \mathbf{g}' = -\alpha(\hat{\boldsymbol{\sigma}} \cdot \mathbf{g}), \quad \hat{\boldsymbol{\sigma}} \times \mathbf{g}' = -\beta(\hat{\boldsymbol{\sigma}} \times \mathbf{g}). \quad (\text{A2})$$

Here,

$$\mathbf{g} = \mathbf{v}_{12} - \hat{\boldsymbol{\sigma}} \times \mathbf{S}_{12} \quad (\text{A3})$$

is the relative velocity of the contact points at the moment of collision, $\mathbf{v}_{12} \equiv \mathbf{v}_1 - \mathbf{v}_2$ being the center-of-mass relative velocity and $\mathbf{S}_{12} = \sigma(\boldsymbol{\omega}_1 + \boldsymbol{\omega}_2)/2$ being directly related to the center-of-mass angular velocity. Then, from the conservation of angular and linear momenta in each collision, the impulse can be expressed as [34]

$$\mathbf{Q} = m\tilde{\alpha}(\hat{\boldsymbol{\sigma}} \cdot \mathbf{v}_{12})\hat{\boldsymbol{\sigma}} - m\tilde{\beta}\hat{\boldsymbol{\sigma}} \times (\hat{\boldsymbol{\sigma}} \times \mathbf{v}_{12} + \mathbf{S}_{12}), \quad (\text{A4})$$

where

$$\tilde{\alpha} \equiv \frac{1+\alpha}{2}, \quad \tilde{\beta} \equiv \frac{\kappa}{1+\kappa} \frac{1+\beta}{2}. \quad (\text{A5})$$

The loss of energy due to inelasticity and roughness is observed in the change of total kinetic energy, which is given by

$$\begin{aligned} \Delta E_K &\equiv \frac{m}{2}\Delta(v_1^2 + v_2^2) + \frac{I}{2}\Delta(\omega_1^2 + \omega_2^2) \\ &= -\frac{m}{4}(1-\beta^2)\frac{\kappa}{1+\kappa}[\hat{\boldsymbol{\sigma}} \times (\hat{\boldsymbol{\sigma}} \times \mathbf{v}_{12} + \mathbf{S}_{12})]^2 \\ &\quad - \frac{m}{4}(1-\alpha^2)(\hat{\boldsymbol{\sigma}} \cdot \mathbf{v}_{12})^2, \end{aligned} \quad (\text{A6})$$

where $\Delta\psi(\mathbf{v}, \boldsymbol{\omega}) \equiv \psi(\mathbf{v}', \boldsymbol{\omega}') - \psi(\mathbf{v}, \boldsymbol{\omega})$. One can observe that, except if $\alpha = 1$ and either $\beta = -1$ or $\beta = 1$, the total kinetic energy is dissipated upon collisions. This expected fact is translated into a decay of the total granular temperature in Sec. II B.

The previous equations apply to both HS and HD. In the HS case, the translational velocity $\mathbf{v} = v_x\hat{\mathbf{i}} + v_y\hat{\mathbf{j}} + v_z\hat{\mathbf{k}}$ and the angular velocity $\boldsymbol{\omega} = \omega_x\hat{\mathbf{i}} + \omega_y\hat{\mathbf{j}} + \omega_z\hat{\mathbf{k}}$ have

$d_t = 3$ and $d_r = 3$ nontrivial components, respectively. However, in the HD case, $\mathbf{v} = v_x\hat{\mathbf{i}} + v_y\hat{\mathbf{j}}$ and $\boldsymbol{\omega} = \omega_z\hat{\mathbf{k}}$ have $d_t = 2$ and $d_r = 1$ nontrivial components, respectively, what simplifies the collision rules [63]. An important consequence of the distinction between spheres and disks is that the Jacobian of the transformation between pre- and postcollisional velocities turns out to depend on d_r , namely

$$\left| \frac{\partial(\mathbf{v}'_1, \mathbf{v}'_2, \boldsymbol{\omega}'_1, \boldsymbol{\omega}'_2)}{\partial(\mathbf{v}_1, \mathbf{v}_2, \boldsymbol{\omega}_1, \boldsymbol{\omega}_2)} \right| = \alpha|\beta|^{2d_r/d_t}. \quad (\text{A7})$$

Appendix B: The γ coefficients in terms of collision integrals

When Eqs. (40) are inserted into Eqs. (38) and (33b), one obtains

$$\nu_\eta^* \equiv \frac{\nu_\eta}{\nu} = \frac{\Lambda[V_i V_j - \frac{1}{d_t} V^2 \delta_{ij}] \left(\frac{1}{d_t} \delta_{ij} \mathbf{c} \cdot \partial_{\mathbf{c}} - c_j \partial_{c_i} \right) f^{(0)}}{\frac{1}{2}(d_t - 1)(d_t + 2) n v_{\text{th}}^2}, \quad (\text{B1a})$$

$$\nu_{\lambda_t}^* \equiv \frac{\nu_{\lambda_t}}{\nu} = Y_t + \frac{\gamma_{A_r}}{\gamma_{A_t}} Z_t, \quad (\text{B1b})$$

$$\nu_{\lambda_r}^* \equiv \frac{\nu_{\lambda_r}}{\nu} = \frac{\gamma_{A_t} Y_r + \gamma_{A_r} Z_r}{\gamma_{A_r} + \gamma_{A_t} \frac{a_{11}^{(0)}}{1+a_{11}^{(0)}}}, \quad (\text{B1c})$$

$$\nu_{\mu_t}^* \equiv \frac{\nu_{\mu_t}}{\nu} = Y_t + \frac{\gamma_{B_r}}{\gamma_{B_t}} Z_t, \quad (\text{B1d})$$

$$\nu_{\mu_r}^* \equiv \frac{\nu_{\mu_r}}{\nu} = \frac{\gamma_{B_t} Y_r + \gamma_{B_r} Z_r}{\gamma_{B_r} + \gamma_{B_t} \frac{a_{11}^{(0)}}{1+a_{11}^{(0)}}}, \quad (\text{B1e})$$

$$\xi_t = \gamma_E \Xi_t, \quad \xi_r = \gamma_E \Xi_r, \quad (\text{B1f})$$

where

$$Y_t = \frac{\Lambda[V^2 V_i] (\partial_{c_i} - c_i \partial_{\mathbf{c}} \cdot \mathbf{c}) f^{(0)}}{\frac{1}{2}(d_t + 2) n n v_{\text{th}}^3 [1 + 2a_{20}^{(0)}]}, \quad (\text{B2a})$$

$$Z_t = -\frac{\Lambda[V^2 V_i] c_i \partial_{\mathbf{w}} \cdot \mathbf{w}}{\frac{1}{2}(d_t + 2) n n v_{\text{th}}^3 [1 + 2a_{20}^{(0)}]}, \quad (\text{B2b})$$

$$Y_r = \frac{\Lambda[\omega^2 V_i] (\partial_{c_i} - c_i \partial_{\mathbf{c}} \cdot \mathbf{c}) f^{(0)}}{\frac{1}{2} d_t d_r n n v_{\text{th}} \omega_{\text{th}}^2 [1 + a_{11}^{(0)}]}, \quad (\text{B2c})$$

$$Z_r = -\frac{\Lambda[\omega^2 V_i] c_i \partial_{\mathbf{w}} \cdot \mathbf{w}}{\frac{1}{2} d_t d_r n n v_{\text{th}} \omega_{\text{th}}^2 [1 + a_{11}^{(0)}]}, \quad (\text{B2d})$$

$$\Xi_t = d_r \tau_t \tau_r \frac{\Lambda[V^2] \left(\frac{\partial_{\mathbf{w}} \cdot \mathbf{w}}{d_r \tau_r} - \frac{d_t + \mathbf{c} \cdot \partial_{\mathbf{c}}}{d_t \tau_t} \right) f^{(0)}}{d_t \nu n v_{\text{th}}^2}, \quad (\text{B2e})$$

$$\Xi_r = d_r \tau_t \tau_r \frac{\Lambda[\omega^2] \left(\frac{\partial_{\mathbf{w}} \cdot \mathbf{w}}{d_r \tau_r} - \frac{d_t + \mathbf{c} \cdot \partial_{\mathbf{c}}}{d_t \tau_t} \right) f^{(0)}}{d_t \nu n \omega_{\text{th}}^2}. \quad (\text{B2f})$$

The six quantities in Eqs. (B2), together with ν_η^* in Eq. (B1a), define the fundamental collision integrals within the approximation given by Eqs. (40).

By comparing Eqs. (41) to the second equalities in Eqs. (36), one obtains, after some algebra,

$$\gamma_C = \frac{2}{\nu_\eta^* - \frac{1}{2}\zeta^*}, \quad \gamma_E = \frac{2/d_t}{\Xi_t - \Xi_r - \frac{d_t + d_r}{2d_t} \zeta^*}, \quad (\text{B3a})$$

$$\gamma_{A_t} = \frac{Z_r - Z_t(1 + \tilde{a}_{11}) - 2\zeta^*}{(Y_t - 2\zeta^*)(Z_r - 2\zeta^*) - (Y_r - 2\zeta^* \tilde{a}_{11}) Z_t}, \quad (\text{B3b})$$

$$\gamma_{A_r} = \frac{Y_t(1 + \tilde{a}_{11}) - Y_r - 2\zeta^*}{(Y_t - 2\zeta^*)(Z_r - 2\zeta^*) - (Y_r - 2\zeta^* \tilde{a}_{11}) Z_t}, \quad (\text{B3c})$$

$$\gamma_{B_t} = \frac{\zeta^* [\gamma_{A_t} (Z_r - \frac{3}{2}\zeta^* - Z_t \tilde{a}_{11}) - \gamma_{A_r} Z_t] + (Z_r - \frac{3}{2}\zeta^*) \tilde{a}_{20} - Z_t \tilde{a}_{11}}{(Y_t - \frac{3}{2}\zeta^*)(Z_r - \frac{3}{2}\zeta^*) - (Y_r - \frac{3}{2}\zeta^* \tilde{a}_{11}) Z_t}, \quad (\text{B3d})$$

$$\gamma_{B_r} = \frac{\zeta^* [\gamma_{A_r} (Y_t - \frac{3}{2}\zeta^*) - \gamma_{A_t} (Y_r - Y_t \tilde{a}_{11})] + [Y_t - \frac{3}{2}\zeta^*(1 - \tilde{a}_{20})] \tilde{a}_{11} - Y_r \tilde{a}_{20}}{(Y_t - \frac{3}{2}\zeta^*)(Z_r - \frac{3}{2}\zeta^*) - (Y_r - \frac{3}{2}\zeta^* \tilde{a}_{11}) Z_t}, \quad (\text{B3e})$$

where

$$\tilde{a}_{11} = \frac{a_{11}^{(0)}}{1 + a_{11}^{(0)}}, \quad \tilde{a}_{20} = \frac{a_{20}^{(0)}}{1 + 2a_{20}^{(0)}}. \quad (\text{B4})$$

-
- [1] C. S. Campbell, *Annu. Rev. Fluid Mech.* **22**, 57 (1990).
[2] T. Pöschel and S. Luding, eds., *Granular Gases*, Lecture Notes in Physics, Vol. 564 (Springer, Berlin, 2001).
[3] I. Goldhirsch, Rapid granular flows, *Annu. Rev. Fluid Mech.* **35**, 267 (2003).
[4] N. V. Brilliantov and T. Pöschel, *Kinetic Theory of Granular Gases* (Oxford University Press, Oxford, 2004).
[5] V. Garzó, *Granular Gaseous Flows. A Kinetic Theory Approach to Granular Gaseous Flows* (Springer Nature, Switzerland, 2019).
[6] P. Yu, M. Schröter, and M. Sperl, Velocity distribution of a homogeneously cooling granular gas, *Phys. Rev. Lett.* **124**, 208007 (2020).
[7] J. T. Jenkins and M. W. Richman, Kinetic theory for plane flows of a dense gas of identical, rough, inelastic, circular disks, *Phys. Fluids* **28**, 3485 (1985).
[8] S. F. Foerster, M. Y. Louge, H. Chang, and K. Allia, Measurements of the collision properties of small spheres, *Phys. Fluids* **6**, 1108 (1994).
[9] O. R. Walton, Numerical simulations of inelastic, frictional particle-particle interactions, in *Particle Two-Phase Flow*, edited by M. C. Roco (Butterworth, London, 1993) pp. 884–907.
[10] M. Louge, <http://grainflowresearch.mae.cornell.edu/impact/data/Impact%20Results.html>.
[11] J. T. Jenkins and C. Zhang, Kinetic theory for identical, frictional, nearly elastic spheres, *Phys. Fluids* **14**, 1228 (2002).
[12] I. Goldhirsch, S. H. Noskovicz, and O. Bar-Lev, Nearly smooth granular gases, *Phys. Rev. Lett.* **95**, 068002 (2005).
[13] I. Goldhirsch, S. H. Noskovicz, and O. Bar-Lev, Hydrodynamics of nearly smooth granular gases, *J. Phys. Chem. B* **109**, 21449 (2005).
[14] N. V. Brilliantov, T. Pöschel, W. T. Kranz, and A. Zippelius, Translations and rotations are correlated in granular gases, *Phys. Rev. Lett.* **98**, 128001 (2007).
[15] B. Gayen and M. Alam, Orientational correlation and velocity distributions in uniform shear flow of a dilute granular gas, *Phys. Rev. Lett.* **100**, 068002 (2008).
[16] P. P. Mitrano, S. R. Dahl, A. M. Hilger, C. J. Ewasko, and C. M. Hrenya, Dual role of friction in granular flows: attenuation versus enhancement of instabilities, *J. Fluid Mech.* **729**, 484 (2013).
[17] S. McNamara, Hydrodynamic modes of a uniform granular medium, *Phys. Fluids A* **5**, 3056 (1993).
[18] A. Goldshtein and M. Shapiro, Mechanics of collisional motion of granular materials. Part 1. General hydrody-

- namic equations, *J. Fluid Mech.* **282**, 75 (1995).
- [19] E. L. Grossman, T. Zhou, and E. Ben-Naim, Towards granular hydrodynamics in two dimensions, *Phys. Rev. E* **55**, 4200 (1997).
- [20] N. Sela and I. Goldhirsch, Hydrodynamic equations for rapid flows of smooth inelastic spheres, to Burnett order, *J. Fluid Mech.* **361**, 41 (1998).
- [21] J. W. Dufty, Statistical mechanics, kinetic theory, and hydrodynamics for rapid granular flow, *J. Phys.: Condens. Matter* **12**, A47 (2000).
- [22] J. W. Dufty, Kinetic theory and hydrodynamics for a low density granular gas, *Adv. Complex Syst.* **4**, 397 (2001).
- [23] V. Garzó and J. W. Dufty, Hydrodynamics for a granular mixture at low density, *Phys. Fluids* **14**, 1476 (2002).
- [24] N. Brilliantov and T. Pöschel, Hydrodynamics and transport coefficients for dilute granular gases, *Phys. Rev. E* **67**, 061304 (2003).
- [25] D. Serero, I. Goldhirsch, S. H. Noskovicz, and M.-L. Tan, Hydrodynamics of granular gases and granular gas mixtures, *J. Fluid Mech.* **554**, 237 (2006).
- [26] F. Vega Reyes and J. S. Urbach, Steady base states for Navier-Stokes granular hydrodynamics with boundary heating and shear, *J. Fluid Mech.* **636**, 279 (2009).
- [27] F. Vega Reyes, A. Santos, and V. Garzó, Non-Newtonian granular hydrodynamics. What do the inelastic simple shear flow and the elastic Fourier flow have in common?, *Phys. Rev. Lett.* **104**, 028001 (2010).
- [28] J. W. Dufty and J. J. Brey, Choosing hydrodynamic fields, *Math. Model. Nat. Phenom.* **6**, 19 (2011).
- [29] V. Garzó and A. Santos, Hydrodynamics of inelastic Maxwell models, *Math. Model. Nat. Phenom.* **6**, 37 (2011).
- [30] G. Gradenigo, A. Sarracino, D. Villamaina, and A. Puglisi, Fluctuating hydrodynamics and correlation lengths in a driven granular fluid, *J. Stat. Mech.* , P08017 (2011).
- [31] G. Gradenigo, A. Sarracino, D. Villamaina, and A. Puglisi, Non-equilibrium length in granular fluids: From experiment to fluctuating hydrodynamics, *EPL* **96**, 14004 (2011).
- [32] M. I. García de Soria, P. Maynar, and E. Trizac, Linear hydrodynamics for driven granular gases, *Phys. Rev. E* **87**, 022201 (2013).
- [33] F. B. Pidduck, The kinetic theory of a special type of rigid molecule, *Proc. R. Soc. Lond. A* **101**, 101 (1922).
- [34] G. M. Kremer, A. Santos, and V. Garzó, Transport coefficients of a granular gas of inelastic rough hard spheres, *Phys. Rev. E* **90**, 022205 (2014).
- [35] V. Garzó, A. Santos, and G. M. Kremer, Impact of roughness on the instability of a free-cooling granular gas, *Phys. Rev. E* **97**, 052901 (2018).
- [36] A. Megías and A. Santos, Energy production rates of multicomponent granular gases of rough particles. a unified view of hard-disk and hard-sphere systems, *AIP Conf. Proc.* **2132**, 080003 (2019).
- [37] A. Megías and A. Santos, Driven and undriven states of multicomponent granular gases of inelastic and rough hard disks or spheres, *Granul. Matter* **21**, 49 (2019).
- [38] J. J. Brey and D. Cubero, Hydrodynamic transport coefficients of granular gases, in *Granular Gases*, Lectures Notes in Physics, Vol. 564, edited by T. Pöschel and S. Luding (Springer, Berlin, 2001) pp. 59–78.
- [39] E. Clement and J. Rajchenbach, Fluidization of a bidimensional powder, *Europhys. Lett.* **16**, 133 (1991).
- [40] K. Feitosa and N. Menon, Breakdown of energy equipartition in a 2D binary vibrated granular gas, *Phys. Rev. Lett.* **88**, 198301 (2002).
- [41] B. Painter, M. Dutt, and R. P. Behringer, Energy dissipation and clustering for a cooling granular material on a substrate, *Physica D* **175**, 43 (2003).
- [42] C. Yanpei, P. Evesque, M. Hou, C. Lecoutre, F. Palencia, and Y. Garrabos, Long range boundary effect of 2D intermediate number density vibro-fluidized granular media in micro-gravity, *J. Phys.: Conf. Ser.* **327**, 012033 (2011).
- [43] Y. Grasselli, G. Bossis, and R. Morini, Translational and rotational temperatures of a 2D vibrated granular gas in microgravity, *Eur. Phys. J. E* **38**, 8 (2015).
- [44] C. Scholz and T. Pöschel, Velocity distribution of a homogeneously driven two-dimensional granular gas, *Phys. Rev. Lett.* **118**, 198003 (2017).
- [45] Y. Grasselli, G. Bossis, A. Meunier, and O. Volkova, Dynamics of a 2D vibrated model granular gas in micro-gravity, in *Granular Materials*, edited by M. Sakellariou (IntechOpen, Rijeka, Croatia, 2017) Chap. 4, pp. 71–96.
- [46] M. A. López-Castaño, J. F. González-Saavedra, A. Rodríguez-Rivas, E. Abad, S. B. Yuste, and F. Vega Reyes, Pseudo-two-dimensional dynamics in a system of macroscopic rolling spheres, *Phys. Rev. E* **103**, 042903 (2021).
- [47] M. A. López Castaño, A. Márquez Seco, A. Márquez Seco, A. Rodríguez-Rivas, and F. Vega Reyes, Chirality transitions in a system of active flat spinners, *arXiv:2105.02850* (2021).
- [48] V. Garzó, A. Santos, and J. M. Montanero, Modified Sonine approximation for the Navier–Stokes transport coefficients of a granular gas, *Physica A* **376**, 94 (2007).
- [49] A. Santos, G. M. Kremer, and M. dos Santos, Sonine approximation for collisional moments of granular gases of inelastic rough spheres, *Phys. Fluids* **23**, 030604 (2011).
- [50] F. Vega Reyes, A. Santos, and G. M. Kremer, Role of roughness on the hydrodynamic homogeneous base state of inelastic spheres, *Phys. Rev. E* **89**, 020202(R) (2014).
- [51] F. Vega Reyes, A. Santos, and G. M. Kremer, Properties of the homogeneous cooling state of a gas of inelastic rough particles, *AIP Conf. Proc.* **1628**, 494 (2014).
- [52] V. Garzó, S. Tenneti, S. Subramaniam, and C. M. Hrenya, *J. Fluid Mech.* **712**, 129 (2012).
- [53] S. Chapman and T. G. Cowling, *The Mathematical Theory of Non-Uniform Gases*, 3rd ed. (Cambridge University Press, Cambridge, UK, 1970).
- [54] G. M. Kremer, *An Introduction to the Boltzmann Equation and Transport Processes in Gases* (Springer, Berlin, 2010).
- [55] A. Megías and A. Santos, Translational and angular velocity cumulants in granular gases of inelastic and rough hard disks or spheres (unpublished).
- [56] A. Santos, Homogeneous free cooling state in binary granular fluids of inelastic rough hard spheres, *AIP Conf. Proc.* **1333**, 128 (2011).
- [57] A. Santos, G. M. Kremer, and V. Garzó, Energy production rates in fluid mixtures of inelastic rough hard spheres, *Prog. Theor. Phys. Suppl.* **184**, 31 (2010).
- [58] B. J. McCoy, S. I. Sandler, and J. S. Dahler, Transport properties of polyatomic fluids. IV. The kinetic theory of a dense gas of perfectly rough spheres, *J. Chem. Phys.* **45**, 3485 (1966).
- [59] A. Kudrolli, Concentration dependent diffusion of self-propelled rods, *Phys. Rev. Lett.* **104**, 088001 (2010).

- [60] B. C. Hall, *Lie Groups, Lie Algebras, and Representations. An Elementary Introduction*, 2nd ed., Graduate Texts in Mathematics, Vol. 222 (Springer, Heidelberg, 2015).
- [61] F. Guillard and B. Marks, Frictional hyperspheres in hyperspace, *Phys. Rev. E* **103**, 052901 (2021).
- [62] A. Megías and A. Santos, Hydrodynamics of granular gases of inelastic and rough hard disks or spheres. II. Stability analysis, *Phys. Rev. E* **104**, 034902 (2021).
- [63] A. Santos, Interplay between polydispersity, inelasticity, and roughness in the freely cooling regime of hard-disk granular gases, *Phys. Rev. E* **98**, 012904 (2018).

10.3 Article 8

Title: Hydrodynamics of granular gases of inelastic and rough hard disks or spheres. II. Stability analysis

Authors: Alberto Megías¹ and Andrés Santos^{1,2}

Affiliations:

¹ Departamento de Física, Universidad de Extremadura, E-06006 Badajoz, Spain

² Instituto de Computación Científica Avanzada (ICCAEx), Universidad de Extremadura, E-06006 Badajoz, Spain

Journal: Physical Review E

Volume: 104

Pages: 034902

Year: 2021

DOI: [10.1103/PhysRevE.104.034902](https://doi.org/10.1103/PhysRevE.104.034902)



Copy of the preprint of the work: “Alberto Megías, and Andrés Santos, ‘Hydrodynamics of granular gases of inelastic and rough hard disks or spheres. II. Stability analysis’, *Physical Review E* **104**, 034902 (2021) <https://doi.org/10.1103/PhysRevE.104.034902>.”

Hydrodynamics of granular gases of inelastic and rough hard disks or spheres. II. Stability analysis

Alberto Megías^{1,*} and Andrés Santos^{1,2,†}

¹*Departamento de Física, Universidad de Extremadura, E-06006 Badajoz, Spain*

²*Instituto de Computación Científica Avanzada (ICCAE),
Universidad de Extremadura, E-06006 Badajoz, Spain*

(Dated: September 16, 2021)

Conditions for the stability under linear perturbations around the homogeneous cooling state are studied for dilute granular gases of inelastic and rough hard disks or spheres with constant coefficients of normal (α) and tangential (β) restitution. After a formally exact linear stability analysis of the Navier–Stokes–Fourier hydrodynamic equations in terms of the translational (d_t) and rotational (d_r) degrees of freedom, the transport coefficients derived in the companion paper [A. Megías and A. Santos, “Hydrodynamics of granular gases of inelastic and rough hard disks or spheres. I. Transport coefficients,” *Phys. Rev. E* **104**, 034901 (2021)] are employed. Known results for hard spheres [V. Garzó, A. Santos, and G. M. Kremer, *Phys. Rev. E* **97**, 052901 (2018)] are recovered by setting $d_t = d_r = 3$, while novel results for hard disks ($d_t = 2$, $d_r = 1$) are obtained. In the latter case, a high-inelasticity peculiar region in the (α, β) parameter space is found, inside which the critical wave number associated with the longitudinal modes diverges. Comparison with event-driven molecular dynamics simulations for dilute systems of hard disks at $\alpha = 0.2$ shows that this theoretical region of absolute instability may be an artifact of the extrapolation to high inelasticity of the approximations made in the derivation of the transport coefficients, although it signals a shrinking of the conditions for stability. In the case of moderate inelasticity ($\alpha = 0.7$), however, a good agreement between the theoretical predictions and the simulation results is found.

I. INTRODUCTION

Hard disks and spheres are very common models for describing fluids. In the molecular case, energy is conserved upon collisions, which are set to be elastic. As a consequence, the equilibrium state is obviously stable. In contrast, a distinctive feature of a granular gas, as compared to a common fluid, is the possible instability of spatially uniform states and the associated appearance of structure formations (clusters and vortices). Characterization of the spontaneous formation of these instabilities has been widely studied for granular gases modeled as inelastic but smooth particles [1–8]. In these systems, it is always possible to find a range of parameters and perturbation wave numbers where a hydrodynamic description holds and instabilities are suppressed. In recent years, this study has been expanded to the case of rough spheres [9, 10], where a dual role of roughness on instability has been observed.

Structure phenomena are important and appealing from a physical point of view. At a cosmological level, whereas the universe is considered to be generally isotropic and homogeneous, clustering is essential to forge galaxies and is present in planetary systems, dust agglomerations, planet rings, etc. Moreover, vortex formation can remind the rotational motion of disk or spiral galaxies like our Milky Way. From that point of view, granular gases, apart from their intrinsic interest,

can serve as useful examples for the formation of clusters and vortices. However, whereas attractive gravitational forces are the key of the clustering in the universe, in a granular gas the inelastic nature of the interacting particles is enough to produce it. Even more, the instabilities in self-gravitating granular gas systems has also been recently studied [11]. A similarity aspect between both classes of systems is that in cosmology one needs primordial perturbations in the early universe for the formation of agglomerations, while in a granular gas one can observe cluster formation spontaneously due to the growth of a given long enough perturbation. Furthermore, granular friction effects are known to have an influence on some astronomical problems [12, 13].

In this paper, we consider a dilute granular gas modeled as a collection of hard spheres (HS) or hard disks (HD) which collide with constant coefficients of normal (α) and tangential (β) restitution; while $0 < \alpha \leq 1$ controls the degree of inelasticity, $-1 \leq \beta \leq 1$ measures the degree of surface roughness. In general, each particle is animated with d_t components of the translational velocity \mathbf{v} and d_r components of the angular velocity $\boldsymbol{\omega}$, where $(d_t, d_r) = (3, 3)$ and $(2, 1)$ for HS and HD, respectively. Our main aim is to perform a linear stability analysis of the homogeneous cooling state (HCS) of the granular gas by means of a Navier–Stokes–Fourier (NSF) hydrodynamic description in terms of the number of translational (d_t) and rotational (d_r) degrees of freedom, thus encompassing the HS and HD systems within a unified treatment, as done in previous works [14–16]. To that end, we make explicit use of the approximate expressions for the NSF transport coefficients derived in the companion paper I [16]. The HS results [10] are recov-

* albertom@unex.es

† andres@unex.es

ered by setting $(d_t, d_r) = (3, 3)$, while novel results, to the best of our knowledge, are presented for HD by the choice $(d_t, d_r) = (2, 1)$. In the latter case, we additionally present event-driven molecular dynamics (MD) simulations, where the possible emergence of instability is monitored via a coarse-grained Kullback–Leibler divergence (KLD) [17, 18], which measures the degree of spatial heterogeneities, as well as by the evolution of other relevant quantities (temperature ratio and velocity cumulants). As we will see, our results do not confirm previous studies [19], where different cooling laws for rotational and translational temperatures were reported.

The paper is structured as follows. In Sec. II, the NSF hydrodynamic equations are presented for a granular gas in terms of the translational (d_t) and rotational (d_r) degrees of freedom. Afterwards, the linear stability analysis of the $d_t + 2$ hydrodynamic equations around the HCS is completed in Sec. III in a formally exact way, that is, without assuming any particular form for the NSF transport coefficients. Next, in Sec. IV, use is made of the approximate transport coefficients computed in Ref. [16] and the results of the stability analysis are discussed. To clarify some unexpected outcomes in the HD case, our MD simulation results are exposed in Sec. V. Finally, concluding remarks of the work are presented in Sec. VI.

II. NAVIER–STOKES–FOURIER HYDRODYNAMIC EQUATIONS

Let us consider a dilute granular gas made of identical HD ($d_t = 2, d_r = 1$) or HS ($d_t = d_r = 3$) of diameter σ , mass m , and moment of inertia $I = \kappa m \sigma^2 / 4$, where κ is the reduced moment of inertia. As said before, the collision dynamics will be assumed to be governed by two constant coefficients of restitution: normal (α) and tangential (β). In a kinetic-theory description of the gas, the mesoscopic relevant quantity is the one-body velocity distribution function $f(\mathbf{r}, \mathbf{v}, \boldsymbol{\omega}; t)$, which obeys the Boltzmann equation.

At a macroscopic level, the adopted hydrodynamic fields are the number density $n(\mathbf{r}, t)$, the flow velocity $\mathbf{u}(\mathbf{r}, t)$, and the temperature $T(\mathbf{r}, t)$, which are defined as

$$n(\mathbf{r}, t) = \int d\mathbf{v} \int d\boldsymbol{\omega} f(\mathbf{r}, \mathbf{v}, \boldsymbol{\omega}; t), \quad (1a)$$

$$\mathbf{u}(\mathbf{r}, t) = \frac{\int d\mathbf{v} \int d\boldsymbol{\omega} \mathbf{v} f(\mathbf{r}, \mathbf{v}, \boldsymbol{\omega}; t)}{n(\mathbf{r}, t)}, \quad (1b)$$

$$T(\mathbf{r}, t) = \frac{\int d\mathbf{v} \int d\boldsymbol{\omega} \left\{ m [\mathbf{v} - \mathbf{u}(\mathbf{r}, t)]^2 + I\boldsymbol{\omega}^2 \right\} f(\mathbf{r}, \mathbf{v}, \boldsymbol{\omega}; t)}{(d_t + d_r)n(\mathbf{r}, t)}. \quad (1c)$$

By assuming a Chapman–Enskog expansion around the HCS, the hydrodynamic equations to first order in the hydrodynamic gradients (NSF order) become

$$\mathcal{D}_t n = -n \nabla \cdot \mathbf{u}, \quad (2a)$$

$$mn \mathcal{D}_t u_i = -\tau_t \nabla_i (nT) + \nabla_j \left[\eta (\nabla_i u_j + \nabla_j u_i) - \left(\frac{2}{d_t} \eta - \eta_b \right) \delta_{ij} \nabla \cdot \mathbf{u} \right], \quad (2b)$$

$$\begin{aligned} (\mathcal{D}_t + \zeta^{(0)})T &= \left(\xi - \frac{2\tau_t}{d_t + d_r} \right) T \nabla \cdot \mathbf{u} \\ &+ \frac{2}{(d_t + d_r)n} \nabla \cdot (\lambda \nabla T + \mu \nabla n) \\ &+ \frac{2}{(d_t + d_r)n} \left[\eta (\nabla_i u_j + \nabla_j u_i) - \left(\frac{2}{d_t} \eta - \eta_b \right) \delta_{ij} \nabla \cdot \mathbf{u} \right] \nabla_i u_j. \end{aligned} \quad (2c)$$

In these equations, $\mathcal{D}_t = \partial_t + \mathbf{u} \cdot \nabla$ is the material time derivative, τ_t is the HCS translational-to total temperature ratio, $\zeta^{(0)}$ is the Euler-order cooling rate, η is the shear viscosity, η_b is the bulk viscosity, λ is the thermal conductivity, μ is a Dufour-like transport coefficient, and ξ is a dimensionless transport coefficient associated with the velocity-divergence contribution to the cooling rate [16].

Dimensional analysis dictates that $\zeta^{(0)} = \zeta^* \nu$, $\eta = \eta^* \eta_0$, $\eta_b = \eta_b^* \eta_0$, $\lambda = \lambda^* \lambda_0$, and $\mu = \mu^* \lambda_0 T / n$, where

$$\nu = K n \sigma^{d_t-1} \sqrt{\frac{2\tau_t T}{m}}, \quad K \equiv \frac{\sqrt{2\pi} \frac{d_t-1}{2}}{\Gamma(d_t/2)}, \quad (3)$$

is a collision frequency, and

$$\eta_0 = K_\ell \frac{n\tau_t T}{\nu}, \quad \lambda_0 = \frac{2d_t K_\ell^2 n\tau_t T}{d_t - 1 m\nu}, \quad K_\ell \equiv \frac{d_t + 2}{4}, \quad (4)$$

are the shear viscosity and thermal conductivity, respectively, of a gas of elastic ($\alpha = 1$) and smooth ($\beta = -1$) particles. Apart from that, the explicit forms of the dimensionless coefficients τ_t , ζ^* , ξ , η^* , η_b^* , λ^* , and μ^* will not be needed for the moment.

III. LINEAR STABILITY ANALYSIS OF THE HOMOGENEOUS COOLING STATE

The set of hydrodynamic equations given by Eqs. (2) admits the HCS as a special solution, in which $\nabla \rightarrow 0$ and thus the right-hand sides vanish. In that case, $n_H = \text{const}$, $\mathbf{u}_H = \text{const}$, and $\dot{T}_H = -\zeta^* \nu_H T_H$, where the quantities in the HCS are denoted with the subscript H . Thus, $\nu \rightarrow \nu_H \propto n_H \sqrt{T_H}$, $\eta_0 \rightarrow \eta_{0H} \propto \sqrt{T_H}$, and $\lambda_0 \rightarrow \lambda_{0H} \propto \sqrt{T_H}$. Moreover, we introduce the thermal (translational) velocity in the HCS as $v_H = \sqrt{2\tau_t T_H / m}$.

In this section we study the stability of the HCS by means of a linear perturbation analysis of the NSF equations, Eqs. (2). This study is essential to characterize the well-known structure formation that appears in granular gases.

The perturbations of the hydrodynamic fields around the HCS are written as

$$n(\mathbf{r}, t) = n_H + \delta n(\mathbf{r}, t), \quad \mathbf{u}(\mathbf{r}, t) = \delta \mathbf{u}(\mathbf{r}, t), \quad (5a)$$

$$T(\mathbf{r}, t) = T_H + \delta T(\mathbf{r}, t), \quad (5b)$$

where, without loss of generality, we have chosen a reference frame with $\mathbf{u}_H = 0$. By inserting Eqs. (5) into Eqs. (2), and neglecting terms nonlinear in the perturbations, we find

$$\partial_t \frac{\delta n}{n_H} = -v_H \nabla \cdot \frac{\delta \mathbf{u}}{v_H}, \quad (6a)$$

$$\begin{aligned} \partial_t \frac{\delta u_i}{v_H} = & \frac{\zeta^* \nu_H}{2} \frac{\delta u_i}{v_H} - \frac{v_H}{2} \nabla_i \left(\frac{\delta n}{n_H} + \frac{\delta T}{T_H} \right) + \frac{\eta_{0H}}{mn_H} \\ & \times \left[\left(\frac{d_t - 2}{d_t} \eta^* + \eta_b^* \right) \nabla_i \nabla \cdot \frac{\delta \mathbf{u}}{v_H} + \eta^* \nabla^2 \frac{\delta u_i}{v_H} \right], \end{aligned} \quad (6b)$$

$$\begin{aligned} \partial_t \frac{\delta T}{T_H} = & -\zeta^* \nu_H \left(\frac{\delta n}{n_H} + \frac{\delta T}{2T_H} \right) + \left(\xi - \frac{2\tau_t}{d_t + d_r} \right) v_H \\ & \times \nabla \cdot \frac{\delta \mathbf{u}}{v_H} + \frac{2\lambda_{0H}}{(d_t + d_r)n_H} \nabla^2 \left(\lambda^* \frac{\delta T}{T_H} + \mu^* \frac{\delta n}{n_H} \right). \end{aligned} \quad (6c)$$

Equations (6) form a closed set of $d_t + 2$ linear partial differential equations.

It is now convenient to introduce the following scaled time and space variables,

$$s(t) = \frac{1}{2} \int_0^t dt' \nu_H(t'), \quad \ell = \frac{\nu_H}{\sqrt{2}K_\ell v_H} \mathbf{r}. \quad (7)$$

The variable s measures the average number of collisions per particle, while ℓ represents distance in units of a nominal mean free path (note that ν_H/v_H is independent of time). Given a perturbation field $\delta y(\mathbf{r}, t)$, we define its Fourier transform as

$$\delta \tilde{y}_{\mathbf{k}}(s) = \int d\ell e^{-i\mathbf{k}\cdot\ell} \delta y(\mathbf{r}, t), \quad (8)$$

where i is the imaginary unit and \mathbf{k} is the reduced wave vector. Thus, by defining the dimensionless quantities

$$\rho_{\mathbf{k}}(s) = \frac{\delta \tilde{n}_{\mathbf{k}}(s)}{n_H}, \quad \mathbf{U}_{\mathbf{k}}(s) = \sqrt{2} \frac{\delta \tilde{\mathbf{u}}_{\mathbf{k}}(s)}{v_H}, \quad \Theta_{\mathbf{k}}(s) = \frac{\delta \tilde{T}_{\mathbf{k}}(s)}{T_H}, \quad (9)$$

and taking the Fourier transform of Eqs. (6), we obtain

$$K_\ell \partial_s \rho_{\mathbf{k}} = -i\mathbf{k} \cdot \mathbf{U}_{\mathbf{k}}, \quad (10a)$$

$$\begin{aligned} K_\ell \partial_s \mathbf{U}_{\mathbf{k}} = & \left(K_\ell \zeta^* - \frac{\eta^* k^2}{2} \right) \mathbf{U}_{\mathbf{k}} - \left[i(\Theta_{\mathbf{k}} + \rho_{\mathbf{k}}) \right. \\ & \left. + \frac{1}{2} \left(\frac{d_t - 2}{d_t} \eta^* + \eta_b^* \right) \mathbf{k} \cdot \mathbf{U}_{\mathbf{k}} \right] \mathbf{k}, \end{aligned} \quad (10b)$$

$$\begin{aligned} K_\ell \partial_s \Theta_{\mathbf{k}} = & -K_\ell \zeta^* (2\rho_{\mathbf{k}} + \Theta_{\mathbf{k}}) + i \left(\xi - \frac{2\tau_t}{d_t + d_r} \right) \mathbf{k} \cdot \mathbf{U}_{\mathbf{k}} \\ & - \frac{2d_t K_\ell}{(d_t - 1)(d_t + d_r)} k^2 (\lambda^* \Theta_{\mathbf{k}} + \mu^* \rho_{\mathbf{k}}). \end{aligned} \quad (10c)$$

Taking the inner product with \mathbf{k} in both sides of Eq. (10b), one gets

$$\begin{aligned} K_\ell \partial_s U_{\mathbf{k},\parallel} = & \left(K_\ell \zeta^* - \frac{\eta^* k^2}{2} \right) U_{\mathbf{k},\parallel} - \left[i(\Theta_{\mathbf{k}} + \rho_{\mathbf{k}}) \right. \\ & \left. + \frac{1}{2} \left(\frac{d_t - 2}{d_t} \eta^* + \eta_b^* \right) k U_{\mathbf{k},\parallel} \right] k, \end{aligned} \quad (11)$$

where $U_{\mathbf{k},\parallel} = k^{-1} \mathbf{k} \cdot \mathbf{U}_{\mathbf{k}}$ is the longitudinal component of the vector $\mathbf{U}_{\mathbf{k}}$. Next, combination of Eqs. (10b) and (11) yields the following equation for the $d_t - 1$ transverse components $\mathbf{U}_{\mathbf{k},\perp} = \mathbf{U}_{\mathbf{k}} - U_{\mathbf{k},\parallel} \mathbf{k}/k$,

$$\left(\partial_s - \zeta^* + \frac{\eta^* k^2}{2K_\ell} \right) \mathbf{U}_{\mathbf{k},\perp} = 0. \quad (12)$$

Thus, the transverse vector $\mathbf{U}_{\mathbf{k},\perp}$ decouples from the other three hydrodynamic fields. The solution to Eq. (12) is simply

$$\mathbf{U}_{\mathbf{k},\perp}(s) = \mathbf{U}_{\mathbf{k},\perp}(0) e^{\varpi_\perp(k)s}, \quad \varpi_\perp(k) = \zeta^* - \frac{\eta^* k^2}{2K_\ell}. \quad (13)$$

This characterizes the behavior of the $d_t - 1$ shear modes. They decay in time if $\varpi_\perp(k) < 0$, i.e., if the (reduced) wave number k is larger than a critical value

$$k_\perp = \sqrt{\frac{2K_\ell \zeta^*}{\eta^*}}. \quad (14)$$

However, if $k < k_\perp$, then the shear modes grow in time and the HCS is unstable under those transverse perturbations.

We consider now the three longitudinal modes $\rho_{\mathbf{k}}$, $\Theta_{\mathbf{k}}$, and $U_{\mathbf{k},\parallel}$. Equations (10a), (10c), and (11) can be rewritten in matrix form as

$$\partial_s \begin{pmatrix} \rho_{\mathbf{k}} \\ \Theta_{\mathbf{k}} \\ U_{\mathbf{k},\parallel} \end{pmatrix} = \mathbf{M} \cdot \begin{pmatrix} \rho_{\mathbf{k}} \\ \Theta_{\mathbf{k}} \\ U_{\mathbf{k},\parallel} \end{pmatrix}, \quad (15)$$

where

$$\mathbf{M}(k) = - \begin{pmatrix} 0 & 0 & ik/K_\ell \\ 2\zeta^* + C_\mu k^2 & \zeta^* + C_\lambda k^2 & -C_\xi ik/K_\ell \\ ik/K_\ell & ik/K_\ell & -\zeta^* + C_\eta k^2 \end{pmatrix}. \quad (16)$$

Here,

$$C_\lambda \equiv \frac{2d_t \lambda^*}{(d_t - 1)(d_t + d_r)}, \quad C_\mu \equiv \frac{2d_t \mu^*}{(d_t - 1)(d_t + d_r)}, \quad (17a)$$

$$C_\xi \equiv \xi - \frac{2\tau_t}{d_t + d_r}, \quad C_\eta \equiv \frac{1}{K_\ell} \left(\frac{d_t - 1}{d_t} \eta^* + \frac{\eta_b^*}{2} \right). \quad (17b)$$

Let us denote as $\varpi_{\parallel,1}(k)$, $\varpi_{\parallel,2}(k)$, and $\varpi_{\parallel,3}(k)$ the three eigenvalues of the matrix \mathbf{M} . They are given by the roots of the characteristic polynomial

$$\varpi_{\parallel}^3 + F_2(k)\varpi_{\parallel}^2 + F_1(k)\varpi_{\parallel} + F_0(k), \quad (18)$$

with

$$F_0(k) = [-\zeta^* + (C_\lambda - C_\mu)k^2] \frac{k^2}{K_\ell^2}, \quad (19a)$$

$$F_1(k) = -\zeta^{*2} + \left[\frac{1 - C_\xi}{K_\ell^2} + (C_\eta - C_\lambda)\zeta^* \right] k^2 + C_\eta C_\lambda k^4, \quad (19b)$$

$$F_2(k) = (C_\eta + C_\lambda)k^2. \quad (19c)$$

In the long-wavelength limit ($k \ll 1$), the roots of Eq. (18) reduce to

$$\varpi_{\parallel,1}(k) = -\zeta^* + \left(\frac{1 - C_\xi/2}{K_\ell^2 \zeta^*} - C_\lambda \right) k^2 + \dots, \quad (20a)$$

$$\varpi_{\parallel,2}(k) = -\frac{k^2}{K_\ell^2 \zeta^*} + \dots, \quad (20b)$$

$$\varpi_{\parallel,3}(k) = \zeta^* - \left(C_\eta - \frac{C_\xi}{2K_\ell^2 \zeta^*} \right) k^2 + \dots. \quad (20c)$$

The two eigenvalues $\varpi_{\parallel,1}$ and $\varpi_{\parallel,2}$ define a pair of *sound* modes, while $\varpi_{\parallel,3}$ corresponds to the *heat* mode. The heat mode is unstable for wave numbers ($k < k_{\parallel}$) such that $\varpi_{\parallel,3}(k)$ becomes positive. To determine the associated critical value k_{\parallel} , we set $\varpi_{\parallel} = 0$ in Eq. (18), i.e., $F_0(k_{\parallel}) = 0$. Therefore,

$$k_{\parallel} = \sqrt{\frac{(d_t - 1)(d_t + d_r)}{2d_t}} \sqrt{\frac{\zeta^*}{\lambda^* - \mu^*}}. \quad (21)$$

IV. ANALYSIS

All the results in Secs. II and III are general in the sense that the explicit expressions for the dimensionless coefficients τ_t , ζ^* , ξ , η^* , η_b^* , λ^* , and μ^* have not been used. Those coefficients are functions of the coefficients of restitution (α , β) and the reduced moment of inertia (κ), and they also depend on the number of degrees of freedom (d_t and d_r). As shown in paper I [16], the exact determination of τ_t and ζ^* would require to solve the nonlinear Boltzmann equation for the zeroth-order HCS velocity distribution function $f^{(0)}$. The situation is even more involved in the case of the transport coefficients ξ , η^* , η_b^* , λ^* , and μ^* , whose determination, assuming $f^{(0)}$ were already known, would require to solve four linear

TABLE I. Summary of the explicit expressions of the transport coefficients for a granular gas of inelastic and rough HD in a Sonine-like approximation [16].

$\tilde{\alpha} = \frac{1 + \alpha}{2}$, $\tilde{\beta} = \frac{1 + \beta}{2} \frac{\kappa}{1 + \kappa}$
$\frac{T_t^{(0)}}{T} = \tau_t = \frac{3}{2 + \theta}$, $\frac{T_r^{(0)}}{T} = \tau_r = \frac{3\theta}{2 + \theta}$
$\theta = \sqrt{\left(h - \frac{1}{2}\right)^2 + 2 + h - \frac{1}{2}}$
$h \equiv \frac{(1 + \kappa)^2}{\kappa(1 + \beta)^2} \left[1 - \alpha^2 - \frac{1 - \frac{1}{2}\kappa}{1 + \kappa} (1 - \beta^2) \right]$
$\nu = 2n\sigma\sqrt{\pi\tau_t T/m}$
$\frac{\zeta^{(0)}}{\nu} = \zeta^* = \frac{1}{2 + \theta} \left[1 - \alpha^2 + \frac{1}{2} \frac{1 - \beta^2}{1 + \kappa} (\kappa + \theta) \right]$
$\eta = \frac{n\tau_t T}{\nu} \frac{1}{\nu_\eta^* - \frac{1}{2}\zeta^*}$, $\eta_b = \frac{n\tau_t \tau_r T}{2\nu} \gamma_E$
$\lambda = \tau_t \lambda_t + \tau_r \lambda_r$, $\lambda_t = \frac{2n\tau_t T}{m\nu} \gamma_{A_t}$, $\lambda_r = \frac{n\tau_r T}{2m\nu} \gamma_{A_r}$
$\mu = \mu_t + \mu_r$, $\mu_t = \frac{2\tau_t^2 T^2}{m\nu} \gamma_{B_t}$, $\mu_r = \frac{\tau_t \tau_r T^2}{2m\nu} \gamma_{B_r}$
$\xi = \frac{1}{3} (2\tau_t \xi_t + \tau_r \xi_r) = \gamma_E \Xi$, $\xi_t = \gamma_E \Xi_t$, $\xi_r = \gamma_E \Xi_r$
$\nu_\eta^* = \frac{5\tilde{\alpha}}{2} + \frac{5\tilde{\beta}}{4} - \frac{3\tilde{\alpha}^2}{2} - \frac{\beta^2}{-4} - 2\tilde{\alpha}\tilde{\beta} + \frac{\beta^2\theta}{4}$
$\gamma_E = \left(\Xi_t - \Xi_r - \frac{3}{4}\zeta^* \right)$
$\Xi_t = \frac{3\tau_r}{8} \left[1 - \alpha^2 + \frac{1}{2} \frac{\kappa}{1 + \kappa} (1 - \beta^2) - \left(\frac{1 + \beta}{1 + \kappa} \right)^2 \kappa \frac{\theta - 7}{6} \right]$
$\Xi_r = \frac{\tau_t}{4} \frac{1 + \beta}{1 + \kappa} \left[(1 - \beta) \frac{\theta - 4}{2} + \frac{1 + \beta}{1 + \kappa} \kappa \frac{\theta - 7}{2} \right]$
$\Xi = \frac{\tau_t \tau_r}{4} \left(1 - \alpha^2 + \frac{1 - \beta^2}{1 + \kappa} \frac{3\kappa + \theta - 4}{6} \right)$
$\gamma_{A_t} = \frac{Z_r - Z_t - 2\zeta^*}{(Y_t - 2\zeta^*)(Z_r - 2\zeta^*) - Y_r Z_t}$
$\gamma_{A_r} = \frac{Y_t - 2\zeta^*}{(Y_t - 2\zeta^*)(Z_r - 2\zeta^*) - Y_r Z_t}$
$\gamma_{B_t} = \zeta^* \frac{\gamma_{A_t} (Z_r - \frac{3}{2}\zeta^*) - \gamma_{A_r} Z_t}{(Y_t - \frac{3}{2}\zeta^*)(Z_r - \frac{3}{2}\zeta^*) - Y_r Z_t}$
$\gamma_{B_r} = \zeta^* \frac{\gamma_{A_r} (Y_t - \frac{3}{2}\zeta^*) - \gamma_{A_t} Y_r}{(Y_t - \frac{3}{2}\zeta^*)(Z_r - \frac{3}{2}\zeta^*) - Y_r Z_t}$
$Y_t = \frac{17\tilde{\alpha}}{4} + \frac{17\tilde{\beta}}{8} - \frac{15\tilde{\alpha}^2}{8} - \frac{13\tilde{\beta}^2}{8} - \tilde{\alpha}\tilde{\beta} - \frac{3\tilde{\beta}^2\theta}{8\kappa}$
$Y_r = \frac{\tilde{\beta}}{\kappa} \left(1 - \frac{3\tilde{\beta}}{\theta} - \frac{\tilde{\beta}}{\kappa} \right)$, $Z_t = -\frac{\tilde{\beta}^2\theta}{2\kappa}$
$Z_r = \tilde{\alpha} + \frac{\tilde{\beta}}{2} + \frac{\tilde{\beta}}{\kappa} \left(\frac{5}{2} - 2\tilde{\alpha} - 2\tilde{\beta} - \frac{\tilde{\beta}}{\kappa} \right)$

integral equations for the first-order distribution function $f^{(1)}$.

To overcome the above difficulties, in paper I we adopted a Sonine-like approximation for $f^{(1)}$ supplemented by a quasi-Maxwellian approximation for $f^{(0)}$ (see Ref. [16] for details) that allowed us to obtain (ap-

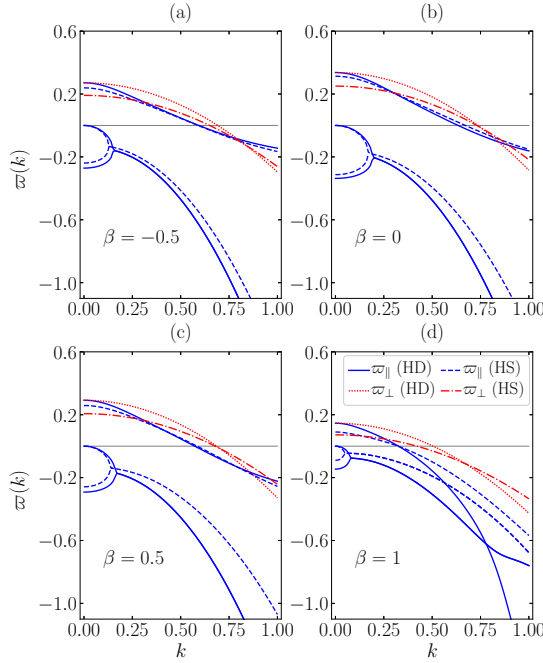


FIG. 1. Dispersion relations $\varpi(k)$ for the hydrodynamic modes vs the reduced wave number k . The curves correspond to the degenerate shear mode ϖ_{\perp} (red lines), the heat mode $\varpi_{\parallel,3}$, and the sound modes $\varpi_{\parallel,1}$ and $\varpi_{\parallel,2}$ (blue lines). Note that when $\varpi_{\parallel,1}$ and $\varpi_{\parallel,2}$ become a complex conjugate pair, only the (common) real part is plotted. The solid and dotted lines represent the HD system, while the dashed and dash-dotted lines refer to HS systems. The coefficient of normal restitution is $\alpha = 0.7$, the reduced moment of inertia is $\kappa = \frac{1}{2}$ (HD) or $\kappa = \frac{2}{5}$ (HS), and the coefficients of tangential restitution are (a) $\beta = -0.5$, (b) $\beta = 0$, (c) $\beta = 0.5$, and (d) $\beta = 1$.

proximate) explicit expressions for τ_t , ζ^* , ξ , η^* , η_b^* , λ^* , and μ^* as functions of α , β , κ , d_t , and d_r . The results are summarized in Table I of paper I and agree with those previously derived [20] for HS ($d_t = d_r = 3$). For completeness, we present in Table I the results for HD ($d_t = 2$, $d_r = 1$), which, to the best of our knowledge, have not been shown before.

In the case of purely smooth particles ($\beta = -1$ or, in our approach, $d_r \rightarrow 0$), it is known that the HCS becomes unstable under perturbations with a sufficiently small wave number ($k < \max\{k_{\perp}, k_{\parallel}\}$) [5, 8]. Interestingly, the quasismooth limit $\beta \rightarrow -1$ is singular and yields $\zeta^* \rightarrow 0$ and $\mu^* \rightarrow 0$. Consequently, according to Eqs. (14) and (21), $k_{\perp}, k_{\parallel} \rightarrow 0$. In the general case, however, the HCS of a granular gas of rough HD or HS can be unstable.

Figure 1 shows the dispersion relations $\varpi(k)$, as obtained from Eqs. (13) and (18), at $\alpha = 0.7$ and for sev-

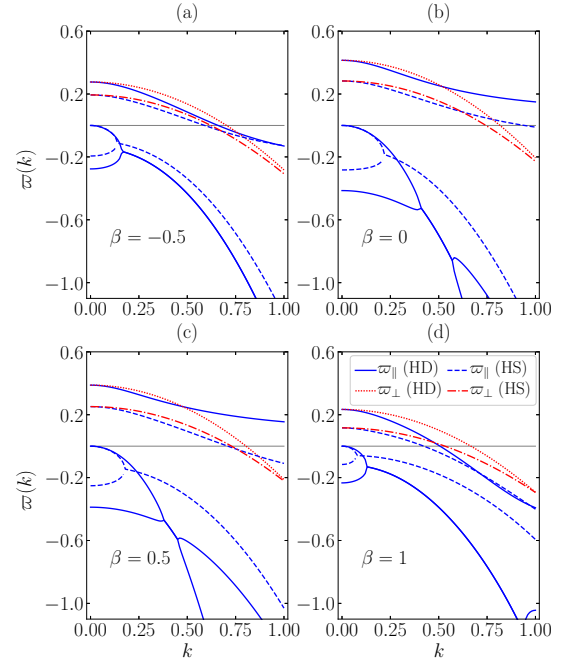


FIG. 2. Same as described in the caption of Fig. 1, except that $\alpha = 0.2$.

eral representative values of β . In each case, uniform HD ($\kappa = \frac{1}{2}$) and uniform HS ($\kappa = \frac{2}{5}$) are considered. The curves for HD and HS are qualitatively similar. In both systems, the real part of the sound modes ($\varpi_{\parallel,1}$ and $\varpi_{\parallel,2}$) remain negative for all k , thus indicating that those perturbative modes decay in time. However, the shear (ϖ_{\perp}) and heat ($\varpi_{\parallel,3}$) modes grow in time if the wavenumber is smaller than k_{\perp} and k_{\parallel} , respectively. Note that both frequencies (ϖ_{\perp} and $\varpi_{\parallel,3}$) tend to ζ^* in the small wave number limit $k \rightarrow 0$ [see Eqs. (13) and (20c)].

The scenario becomes much more complex for highly inelastic particles, as illustrated in Fig. 2 at $\alpha = 0.2$. In the cases $\beta = -0.5$ [Fig. 2(a)] and $\beta = 1$ [Fig. 2(d)], the HD and HS curves are still qualitatively similar. However, if $\beta = 0$ [Fig. 2(b)] or $\beta = 0.5$ [Fig. 2(c)], then $\varpi_{\parallel,3} > 0$ for all k (i.e., $k_{\parallel} \rightarrow \infty$) in the HD case. From Eq. (21) we see that the locus in the plane α versus β separating the region where $k_{\parallel} = \text{finite}$ from the region where $k_{\parallel} \rightarrow \infty$ is defined by the condition $\lambda^* = \mu^*$.

The locus $\lambda^* = \mu^*$ for HD is shown in Fig. 3(a) for several values of κ . For each κ , $k_{\parallel} \rightarrow \infty$ in the region enclosed by the locus. The latter curve presents an apex at a point $(\alpha, \beta) = (\alpha_{\text{apex}}, \beta_{\text{apex}})$, so that $k_{\parallel} = \text{finite}$ if $\alpha > \alpha_{\text{apex}}$, regardless of the value of β . A similar behavior occurs in the HS case [10], except that the regions where $k_{\parallel} \rightarrow \infty$ are much smaller and disappear if $\kappa > 0.277$. The dependence of α_{apex} and β_{apex} on κ for

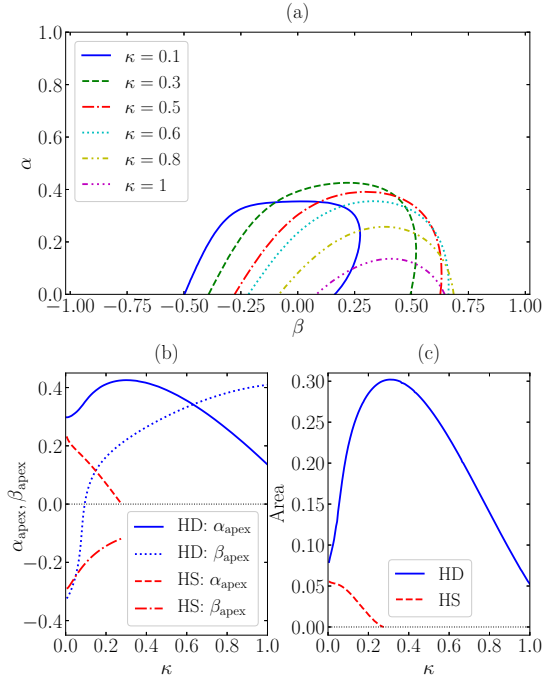


FIG. 3. (a) Plane α vs β showing the locus $\lambda^* = \mu^*$ for HD with a reduced moment of inertia $\kappa = 0.1, 0.3, 0.5, 0.8$, and 1 . In each case, $k_{\parallel} \rightarrow \infty$ in the region below the locus, which has an apex located at $(\alpha, \beta) = (\alpha_{\text{apex}}, \beta_{\text{apex}})$. (b) Dependence of α_{apex} and β_{apex} on κ for HD and HS. (c) Variation with κ of the area of the region where $k_{\parallel} \rightarrow \infty$ for HD and HS.

both HD and HS is shown in Fig. 3(b). While α_{apex} for HS decays monotonically as κ increases (and eventually vanishes at $\kappa = 0.277$), it exhibits a nonmonotonic behavior for HD, with a maximum value $\alpha_{\text{apex}} = 0.426$ at $\kappa = 0.302$. However, β_{apex} grows monotonically with κ both for HD and HS. The contrast between the HD and HS behaviors is clearly highlighted in Fig. 3(c), which shows the κ -dependence of the area of the region where $k_{\parallel} \rightarrow \infty$.

Let us now visualize the dependence of the two critical wave numbers k_{\perp} and k_{\parallel} on α , β , and κ for both HD and HS systems. The results are shown as density plots in the plane α versus β in Figs. 4 and 5, where two representative mass distributions of the particles are considered: a uniform distribution ($\kappa = \frac{1}{2}$ and $\frac{2}{3}$ for HD and HS, respectively) and a distribution concentrated on the surface ($\kappa = 1$ and $\frac{2}{3}$ for HD and HS, respectively). In the case of the transverse shear-mode critical wave number k_{\perp} , the dependence on α , β , and κ is qualitatively similar for HD and HS granular gases. However, this similarity disappears in what respects the longitudinal heat-mode critical wave number k_{\parallel} as one approaches the HD locus

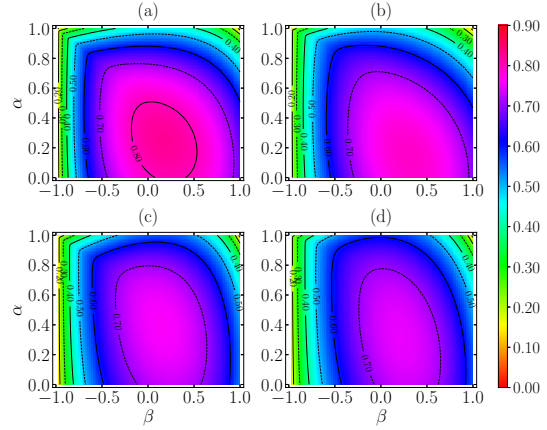


FIG. 4. Density plots of the reduced critical wave number k_{\perp} in the plane α vs β for (a) HD with a uniform mass distribution ($\kappa = \frac{1}{2}$), (b) HD with a mass distribution concentrated on the outer surface ($\kappa = 1$), (c) HS with a uniform mass distribution ($\kappa = \frac{2}{3}$), and (d) HS with a mass distribution concentrated on the outer surface ($\kappa = \frac{2}{3}$).

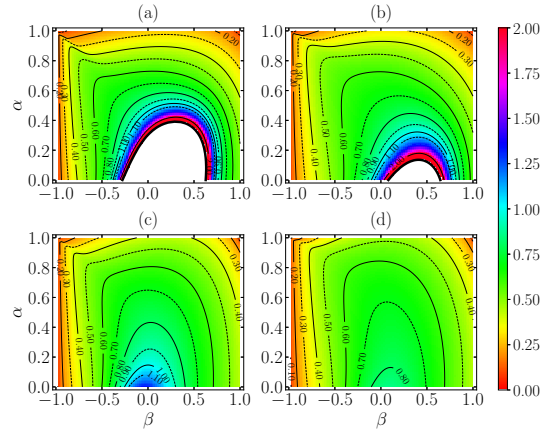


FIG. 5. Same as described in the caption of Fig. 4, but for the reduced critical wave number k_{\parallel} .

$\lambda^* = \mu^*$, in agreement with the previous discussion of Fig. 3.

Depending on the values of α and β , the most unstable mode could be either the transverse shear mode (if $k_{\perp} > k_{\parallel}$) or the longitudinal heat one (if $k_{\parallel} > k_{\perp}$). Figure 6 depicts the locus $k_{\perp} = k_{\parallel}$ for HD and HS gases and the same values of κ as in Figs. 4 and 5. In each case, $k_{\perp} > k_{\parallel}$ or $k_{\parallel} > k_{\perp}$ above or below the locus, respectively. We observe that the region where the heat mode dominates ($k_{\parallel} > k_{\perp}$) is generally wider for HD than for HS; moreover, its area decreases as κ increases for HS,

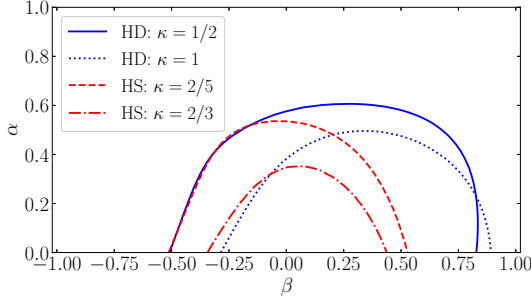


FIG. 6. Plane α vs β showing the locus $k_{\perp} = k_{\parallel}$ for HD ($\kappa = \frac{1}{2}$ and 1) and HS ($\kappa = \frac{2}{5}$ and $\frac{2}{3}$). In each case, the longitudinal heat mode is the most unstable one ($k_{\parallel} > k_{\perp}$) in the region below the locus.

while for HD it has a nonmonotonic κ -dependence with a maximum at about $\kappa = 0.348$ (not shown).

The critical wave numbers k_{\perp} and k_{\parallel} imply that the HCS becomes unstable if the (reduced) length of the system is larger than the critical value $\ell_c = 2\pi/k_c$, where $k_c = \max\{k_{\perp}, k_{\parallel}\}$. In real units, the critical length is $L_c = (\sqrt{2}K_{\ell}v_H/\nu_H)\ell_c$, i.e.,

$$\frac{L_c}{\sigma} = \frac{(d_t + 2)\pi^{3/2}}{d_t 2^{d_t} \phi} k_c^{-1}, \quad (22)$$

where

$$\phi = \frac{\pi^{d_t/2}}{2^{d_t-1} d_t \Gamma(d_t/2)} n \sigma^{d_t} \quad (23)$$

is the solid fraction of the system. At a given value of the reduced moment of inertia κ , L_c is associated with either vortex or clustering instability in the region above or below, respectively, the corresponding locus in Fig. 6. Moreover, $L_c \rightarrow 0$ in the region below the locus on Fig. 3(a) for HD gases. In other words, in that region (henceforth referred to as the region of absolute instability), the HCS would always be unstable for any system size. This is a very strong statement that needs some discussion.

Note that the condition $\lambda^* \leq \mu^*$ takes place for very inelastic disks and never holds if $\alpha > 0.426$. Since the explicit expressions for the transport coefficients derived in paper I [16] made use of a Sonine-like approximation for the first-order distribution $f^{(1)}$ and a quasi-Maxwellian approximation for the zeroth-order distribution $f^{(0)}$, it cannot be discarded that the combination of those two approximations is responsible for the existence of the region of absolute instability. If that were the case, then a more sophisticated approximation, for instance, by consistently including the cumulants of $f^{(0)}$ in the description, would erase such a region and λ^* would be larger than μ^* for any α , β , and κ .

To put that possibility in context, let us recall the case of purely smooth particles ($d_r \rightarrow 0$). It is then easy to

TABLE II. Values of the main parameters of the systems analyzed by event-driven MD simulations.

System	N	$n\sigma^2$	L/σ	k	M	L_{cell}/σ	$\langle N_{\text{cell}} \rangle$
A	1 600	0.005	565.7	1.253	625	22.63	2.56
B	1 600	0.010	400.0	0.886	625	16.00	2.56
C	6 400	0.005	1 131.4	0.627	2 500	22.63	2.56

find that $\lambda^* \leq \mu^*$ if $\alpha \leq (4 - d_t)/(7d_t - 4)$ (i.e., $\alpha < \frac{1}{5} = 0.2$ and $\alpha < \frac{1}{17} \simeq 0.06$ for HD and HS, respectively) when the fourth-degree cumulant a_2 of $f^{(0)}$ is neglected. Paradoxically, if the role of a_2 is introduced in a standard way [5, 21], the interval of absolute instability grows to $\alpha \leq 0.333$ (HD) and $\alpha \leq 0.175$ (HS). However, if the cumulant a_2 is taken into account in a more consistent manner [22], then $\lambda^* > \mu^*$ for all α , both for HD and HS. To make things even more complicated, it is known that the cumulant expansion of $f^{(0)}$ for smooth particles breaks down if α is small [23].

The situation is much more delicate in the case of rough particles. First, instead of a single fourth-degree cumulant of $f^{(0)}$, there are three (HD) or four (HS) independent fourth-degree cumulants [24]. Second, those cumulants have been reported for HS [25–29], but not for HD. And third, the known cumulants for HS can take rather large values [27, 28], except for small inelasticity, and this effect is expected to become even more dramatic for HD [24].

Considering all of this, the prediction of a region of absolute instability in the HD case must be taken with much caution. In any case, one can conclude that the HD gas typically develops clustering instabilities with much larger reduced wave numbers than the HS gas if the values of α and β belong to the regions signaled in Figs. 3 and 5.

V. MOLECULAR DYNAMICS SIMULATIONS FOR INELASTIC AND ROUGH HARD DISKS

Although the main aim of this paper is theoretical, we present in this section event-driven MD results for freely cooling HD gases to check the stability of the HCS.

We have considered systems characterized by a certain number N of uniform disks ($\kappa = \frac{1}{2}$) and a certain reduced number density $n\sigma^2$. The particles were enclosed in a square box of side length $L/\sigma = \sqrt{N/n\sigma^2}$ and periodic boundary conditions were applied. Since the largest wavelength of a perturbation is L , the smallest (reduced) wave number is $k = 2\sqrt{\pi}/n\sigma L = 2\sqrt{\pi}/Nn\sigma^2$. For each choice of α and β , the system was allowed to evolve for $s = 1\,000$ average number of collisions per particle and data were extracted every 0.5 collisions per particle. To avoid dealing with extremely low temperatures and velocities after a large number of collisions per particle, thus compromising the accuracy of the simulation data, a velocity rescaling [30] was performed every 0.5 collisions

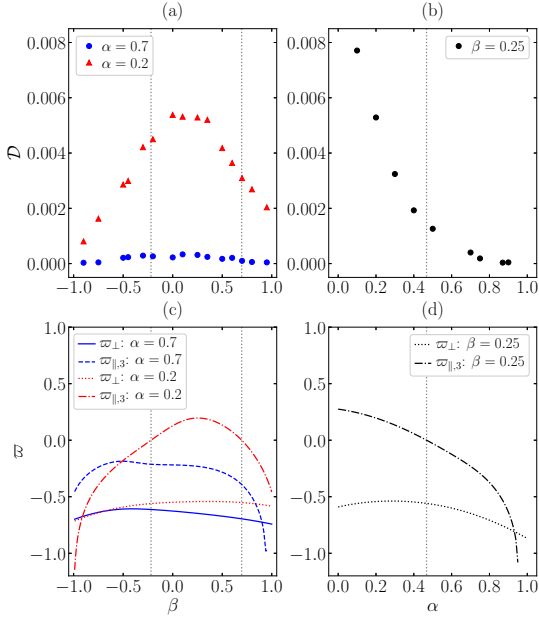


FIG. 7. (a) Plot of the MD simulation values of the KLD \mathcal{D} vs β at $\alpha = 0.2$ and $\alpha = 0.7$ for system A (see Table II). (b) Plot of the MD simulation values of the KLD \mathcal{D} vs α at $\beta = 0.25$ for the same system. (c) Theoretical eigenvalues ϖ_{\perp} (transverse shear mode) and $\varpi_{\parallel,3}$ (longitudinal heat mode) vs β at $\alpha = 0.2$ and $\alpha = 0.7$ for a reduced wave number $k = 1.253$. (d) Theoretical eigenvalues ϖ_{\perp} (transverse shear mode) and $\varpi_{\parallel,3}$ (longitudinal heat mode) vs α at $\beta = 0.25$ for a reduced wave number $k = 1.253$. The vertical dotted lines denote the borders of the regions where, according to theory, the HCS of the system is unstable ($\varpi_{\parallel,3} > 0$) at (a, c) $\alpha = 0.2$ and (b, d) $\beta = 0.25$.

per particle. Moreover, inelastic collapse was prevented by switching to elastic collisions whenever two successive collisions involved the same pair in a very short period of time [31].

The appearance of clustering instabilities in simulations is usually identified by means of visual snapshots [9]. However, this might be difficult if N is not large enough, as happens in a dilute gas. It is then very convenient to monitor the degree of spatial homogeneity of the gas by means of a single quantity that oversees the whole system. To this end, we propose here the (discrete and coarse-grained) KLD [17, 18] of the spatial distribution of particles in the box with respect to a reference homogeneous distribution as a control parameter to detect clustering inhomogeneities. Although the KLD is not actually a metric function, it somehow measures the *distance* (divergence) of a distribution with respect to a reference one as the amount of information lost when the reference model distribution is used to approximate the true distribution. The KLD has been used to mea-

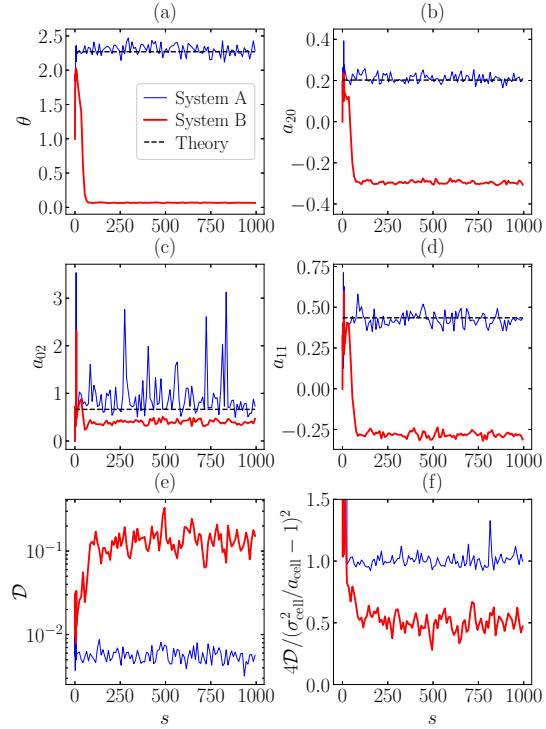


FIG. 8. MD temporal evolution of (a) the rotational-translational temperature ratio θ , (b) the excess translational velocity kurtosis a_{20} , (c) the excess angular velocity kurtosis a_{02} , (d) the translational-angular correlation cumulant a_{11} , (e) the KLD \mathcal{D} , and (f) the ratio $4\mathcal{D}/(\sigma_{\text{cell}}^2/a_{\text{cell}} - 1)^2$ [see Eq. (27)]. The (blue) thin and (red) thick lines correspond to systems A and B, respectively (see Table II), in both cases with $\alpha = 0.2$ and $\beta = 0.25$. The horizontal dashed lines in panels (a–d) are theoretical values [24].

sure inhomogeneities in other physical contexts [32, 33]. More recently, Shannon's entropy [34] (which is related to the KLD but with a constant reference distribution) has been used to study clustering in granular dynamics experiments [35].

To construct the coarse-grained KLD, the HD simulation box is split into $M \gg 1$ square cells of side length L_{cell} and area L_{cell}^2 . Let us denote by $N_{\text{cell}} = 0, 1, \dots, N$ the number of disks inside a given cell. The fraction of cells having exactly N_{cell} particles will be denoted as $p(N_{\text{cell}})$; equivalently, this is the probability that a cell chosen at random has N_{cell} particles. Obviously, the average number of particles per cell is $a_{\text{cell}} \equiv \langle N_{\text{cell}} \rangle = N/M = nL_{\text{cell}}^2$. A relevant quantity is the variance $\sigma_{\text{cell}}^2 = \langle N_{\text{cell}}^2 \rangle - a_{\text{cell}}^2$, measuring fluctuations around the

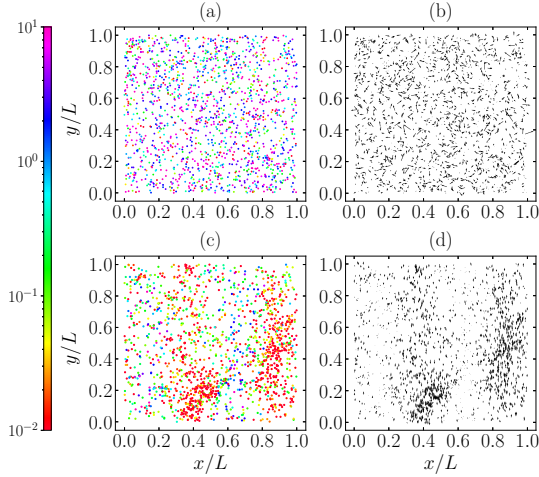


FIG. 9. MD snapshots at $s = 100$ collisions per particle showing the positions [left panels (a, c)] and translational velocities [right panels (b, d)] in the cases of systems A [top panels (a, b)] and B [bottom panels (c, d)] (see Table II), in both cases with $\alpha = 0.2$ and $\beta = 0.25$. In the left panels, the color code refers to the ratio between the rotational and the translational kinetic energies of each particle.

average number. Now, we define the KLD as

$$\mathcal{D} = \sum_{N_{\text{cell}}=0}^N p(N_{\text{cell}}) \ln \frac{p(N_{\text{cell}})}{p_{\text{ref}}(N_{\text{cell}})}, \quad (24)$$

where $p_{\text{ref}}(N_{\text{cell}})$ is a *reference* distribution modeling a spatially uniform system. Here we choose such a distribution as that of a system of totally uncorrelated point particles. If we randomly “shoot” a particle to the simulation box, then the probability that it hits a given cell is M^{-1} . Thus, in the reference model, the probability that N_{cell} particles have hit the cell after N shootings is given by the binomial distribution

$$p_{\text{ref}}(N_{\text{cell}}) = M^{-N} \binom{N}{N_{\text{cell}}} (M-1)^{N-N_{\text{cell}}}. \quad (25)$$

In this reference model, $\sigma_{\text{cell,ref}}^2 = a_{\text{cell}}(1-M^{-1})$. Taking into account that $M \gg 1$ (so that $a_{\text{cell}} \ll N$), it is possible to approximate the binomial distribution by the Poisson one, $p_{\text{ref}}(N_{\text{cell}}) \simeq e^{-a_{\text{cell}}} a_{\text{cell}}^{N_{\text{cell}}} / N_{\text{cell}}!$. In that case, $\langle N_{\text{cell}}^2 \rangle_{\text{ref}} \simeq a_{\text{cell}}(1+a_{\text{cell}})$, $\langle N_{\text{cell}}^3 \rangle_{\text{ref}} \simeq a_{\text{cell}}(1+3a_{\text{cell}}+a_{\text{cell}}^2)$, and $\langle N_{\text{cell}}^4 \rangle_{\text{ref}} \simeq a_{\text{cell}}(1+7a_{\text{cell}}+6a_{\text{cell}}^2+a_{\text{cell}}^3)$.

While the KLD defined by Eq. (24) compares the distributions $p(N_{\text{cell}})$ and $p_{\text{ref}}(N_{\text{cell}})$ for all values of N_{cell} , a simple relationship between \mathcal{D} and the variance difference $\delta\sigma_{\text{cell}}^2 \equiv \sigma_{\text{cell}}^2 - \sigma_{\text{cell,ref}}^2$ can be established if $p(N_{\text{cell}}) \approx p_{\text{ref}}(N_{\text{cell}})$, so we can write

$$p(N_{\text{cell}}) \simeq p_{\text{ref}}(N_{\text{cell}}) \left[1 + \frac{\delta\sigma_{\text{cell}}^2}{2} S_2(N_{\text{cell}}) \right], \quad (26a)$$

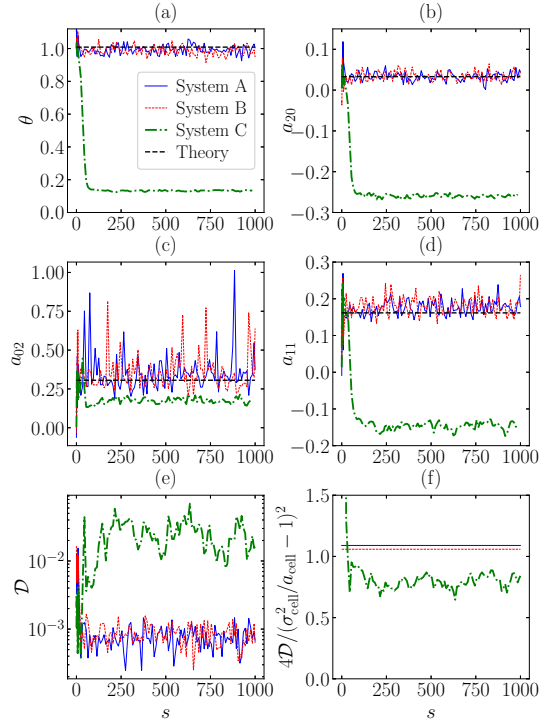


FIG. 10. MD temporal evolution of (a) the rotational-to-translational temperature ratio θ , (b) the excess translational velocity kurtosis a_{20} , (c) the excess angular velocity kurtosis a_{02} , (d) the translational-angular correlation cumulant a_{11} , (e) the KLD \mathcal{D} , and (f) the ratio $4\mathcal{D}/(\sigma_{\text{cell}}^2/a_{\text{cell}} - 1)^2$ [see Eq. (27)]. The (blue) thin solid, the (red) thin dashed, and the (green) thick dash-dotted lines correspond to systems A, B, and C, respectively (see Table II), in the three cases with $\alpha = 0.7$ and $\beta = 0.25$. The horizontal dashed lines in panels (a-d) are theoretical values [24].

$$S_2(N_{\text{cell}}) = 1 - \frac{1+2a_{\text{cell}}}{a_{\text{cell}}^2} N_{\text{cell}} + \frac{N_{\text{cell}}^2}{a_{\text{cell}}^2}. \quad (26b)$$

Note that $\langle S_2(N_{\text{cell}}) \rangle_{\text{ref}} = \langle N_{\text{cell}} S_2(N_{\text{cell}}) \rangle_{\text{ref}} = 0$ and $\langle N_{\text{cell}}^2 S_2(N_{\text{cell}}) \rangle_{\text{ref}} = 2$ within the Poisson approximation. By inserting Eq. (26a) into Eq. (24) and expanding up to second order in $\delta\sigma_{\text{cell}}^2$, one gets

$$\mathcal{D} \simeq \frac{(\delta\sigma_{\text{cell}}^2)^2}{8} \langle [S_2(N_{\text{cell}})]^2 \rangle_{\text{ref}} = \frac{1}{4} \left(\frac{\sigma_{\text{cell}}^2}{a_{\text{cell}}} - 1 \right)^2. \quad (27)$$

It is important to bear in mind that the reference model neglects excluded-volume effects and nonequilibrium spatial correlations. Therefore, it is possible to have $\mathcal{D} \neq 0$ and $\sigma_{\text{cell}}^2 \neq a_{\text{cell}}(1-M^{-1}) \simeq a_{\text{cell}}$, even if the system remains homogeneous. However, significant nonzero values of \mathcal{D} and/or $\sigma_{\text{cell}}^2/a_{\text{cell}} - 1$ are expected to be indicators

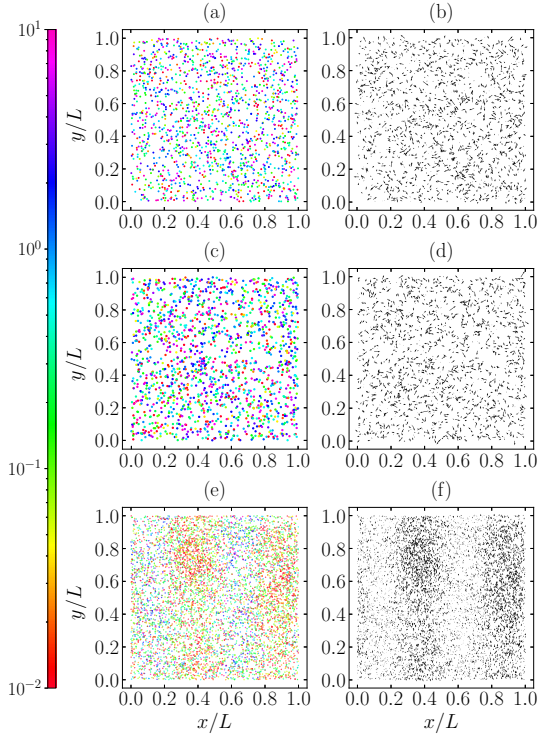


FIG. 11. MD snapshots at $s = 100$ collisions per particle showing the positions [left panels (a, c, e)] and translational velocities [right panels (b, d, f)] in the cases of systems A [top panels (a, b)], B [middle panels (c, d)], and C [bottom panels (e, f)] (see Table II), in the three cases with $\alpha = 0.7$ and $\beta = 0.25$. In the left panels, the color code refers to the ratio between the rotational and the translational kinetic energies of each particle.

of spontaneous heterogeneities in the spatial particle distributions.

In most of our simulations, we have chosen the system identified with the label A in Table II. After an aging stage of $s = 500$ collisions per particle, the coarse-grained spatial distribution $p(N_{\text{cell}})$ was obtained by averaging the histograms corresponding to the population of the M cells from $s = 500$ to $s = 1000$. The KLD was then evaluated from Eqs. (24) and (25). Figures 7(a) and 7(b) show the dependence of the computed KLD versus β (at fixed $\alpha = 0.2$ and $\alpha = 0.7$) and versus α (at fixed $\beta = 0.25$), respectively. The behavior of the theoretical eigenvalues ϖ_{\perp} and $\varpi_{\parallel,3}$ for the value of the wave number corresponding to system A ($k = 1.253$) are shown in Figs. 7(c) and 7(d), respectively. We observe that the MD values of the KLD and the theoretical values of the eigenvalue $\varpi_{\parallel,3}$ are rather correlated: in general, the larger $\varpi_{\parallel,3}$ the larger \mathcal{D} . The relevant point here is that theory predicts that the system becomes unstable

if $\alpha = 0.2$ in the interval $-0.217 < \beta < 0.695$ and if $\beta = 0.25$ for $\alpha < 0.466$. However, the MD data for \mathcal{D} do not seem to experience a big increase in those cases, thus casting doubts about the true instability of perturbations with $k = 1.253$ if $\alpha = 0.2$.

To clarify the situation, we have selected the coefficients of restitution $\alpha = 0.2$ and $\beta = 0.25$, and performed additional simulations for system B (see Table II), in which the associated wave number is $k = 0.886$. Figure 8 shows the temporal evolution of some relevant quantities for both systems (A and B). The considered quantities are (a) the rotational-to translational temperature ratio $\theta = 3/\tau_t - 2$, (b) the excess translational velocity kurtosis $a_{20} \equiv \langle V^4 \rangle / 2 \langle V^2 \rangle^2 - 1$, (c) the excess angular velocity kurtosis $a_{02} \equiv \langle \omega^4 \rangle / 3 \langle \omega^2 \rangle^2 - 1$, (d) the translational-angular correlation cumulant $a_{11} \equiv \langle V^2 \omega^2 \rangle / \langle V^2 \rangle \langle \omega^2 \rangle - 1$, (e) the KLD \mathcal{D} , and (f) the ratio $4\mathcal{D} / (\sigma_{\text{cell}}^2 / a_{\text{cell}} - 1)^2$. In a first stage (lasting about 10 collisions per particle) we have observed that both systems evolve in an analogous way. However, as clearly seen from Fig. 8, their evolutions depart from each other in later stages. System B evolves to a state where (a) almost all the kinetic energy is concentrated on the translational degrees of freedom ($\theta \ll 1$), (b) the distribution of translational velocities is strongly platykurtic ($a_{20} < 0$), (c) the distribution of angular velocities is much less leptokurtic ($a_{02} > 0$) than in system A, (d) the translational velocities are negatively correlated with the angular ones ($a_{11} < 0$), (e) the KLD takes values more than an order of magnitude higher ($\mathcal{D} \sim 10^{-1}$) than in system A, and (f) the estimate given by (27) is much less accurate than in system A. Moreover, the simulation data in the case of system A agree very well with HCS theoretical estimates for θ , a_{20} , a_{02} , and a_{11} [24], in sharp contrast to system B.

Figure 8 is supplemented by Fig. 9, which presents snapshots (at $s = 100$) of systems A and B with $\alpha = 0.2$ and $\beta = 0.25$ [36]. While system A does not present any visible signature of instability, system B exhibits clusters and vortices. Furthermore, the color code in Figs. 9(a) and 9(c) shows that disks in system B have typically less rotational energy than translational energy, in contrast to what happens in system A. The loss of rotational energy (relative to the translational one) in system B is stronger in the particles belonging to the clusters, which are also those participating in the vortices and moving with a higher translational velocity.

Therefore, from Figs. 8 and 9 we can conclude that a dilute HD gas with coefficients of restitution $\alpha = 0.2$ and $\beta = 0.25$ is stable against perturbations of (reduced) wave number $k = 1.253$ (system A), while it is unstable against perturbations of (reduced) wave number k_c for $\alpha = 0.2$ and $\beta = 0.25$ must be $0.89 < k_c < 1.25$. In contrast, in our approximation we obtain $k_{\perp} = 0.822$ but $k_{\parallel} \rightarrow \infty$. As a consequence, a more accurate theoretical treatment of very inelastic particles ($\alpha = 0.2$) demands for the inclusion of velocity cumulants in the description.

Let us consider now the case of less inelastic particles, namely $\alpha = 0.7$, but still with $\beta = 0.25$. In such a case, the theoretical wave numbers are $k_{\perp} = 0.721$ and $k_{\parallel} = 0.626$, so that the clustering instability is preempted by the vortex one and the theoretical critical wave number is $k_c = 0.721$. Systems A ($k = 1.253$) and B ($k = 0.886$) are expected to be stable if $(\alpha, \beta) = (0.7, 0.25)$, despite the fact that Figs. 8 and 9 showed the instability of system B at $(\alpha, \beta) = (0.2, 0.25)$. To complement the picture, we have also considered the point $(\alpha, \beta) = (0.7, 0.25)$ for a third system C (see Table II) for which $k = 0.627$; since $k < k_c$, system C is expected to be unstable. The simulation results are displayed in Figs. 10 and 11, which confirm that systems A and B are stable, while system C is unstable [36]. Note that in Fig. 10(f), due to the low signal-to-noise ratio of the evolution curves of both \mathcal{D} and $(\sigma_{\text{cell}}^2/a_{\text{cell}} - 1)^2/4$ in systems A and B, only the steady-state ratio $4\mathcal{D}/(\sigma_{\text{cell}}^2/a_{\text{cell}} - 1)^2$ is shown in the case of those systems.

Thus, according to our MD simulations, the true critical wave number for $(\alpha, \beta) = (0.7, 0.25)$ lies in the interval $0.63 < k_c < 0.89$, in close agreement with the theoretical prediction $k_c = 0.721$. Moreover, $k < k_{\perp}$ and, as can be observed from Figs. 10 and 11, clustering is indeed present, which means that the theoretical prediction is pretty reliable for this moderately inelastic case.

VI. CONCLUDING REMARKS

In this work, we have carried out a detailed linear stability analysis of the HCS of a dilute gas of inelastic and rough HD or HS within a common framework, thus extending previous HS results [10] to the case of HD gases. First, the NSF equations have been linearized around the HCS solution by a formally exact analysis. Next, the final results have been obtained by the introduction of the approximate expressions of the transport coefficients derived in the companion paper I [16], which are nonlinear functions of the coefficients of normal (α) and tangential (β) restitution, the reduced moment of inertia (κ), and the numbers of degrees of freedom (d_t and d_r).

As happens with rough HS [10] and the case of d_t -dimensional smooth particles [5, 21, 22], there are two longitudinal (sound) modes that are always stable, whereas the third longitudinal (heat) mode and the $(d_t - 1)$ -fold transverse (shear) modes become unstable for long enough wavelengths. The heat mode is associated with cluster instabilities, while the shear modes are related to vortex formation. This analysis has allowed us to determine the critical length L_c , such that systems with a size $L > L_c$ are unstable under linear perturbations. The outcome highlights that, in general, two-dimensional HD systems become unstable for smaller reduced wavelengths than their three-dimensional HS counterparts. Additionally, the dual role of roughness, according to which small and large levels of roughness make the system less unstable than the frictionless system, previously observed in

the HS geometry [9, 10], still holds in the HD case. Moreover, we have established that the region in the parameter space where cluster instabilities dominate against vortices (i.e., $k_{\parallel} > k_{\perp}$) is generally larger for HD than for HS.

The most surprising consequence of our analysis is the appearance of a region of absolute instability, where the critical longitudinal wave number diverges ($k_{\parallel} \rightarrow \infty$ or, equivalently, $L_c \rightarrow 0$). The boundary of this region is defined by the condition $\lambda^* = \mu^*$, which, while residually present in HS systems, is especially relevant in the HD case (see Fig. 3). In fact, the HS region of absolute instability vanishes if $\kappa > 0.277$ (what includes the case of a uniform mass distribution, $\kappa = \frac{2}{5}$) but it always emerges in the HD case, regardless of the value of κ .

The absolute instability zone for HD is a very peculiar prediction, and one must be wary of it. First of all, we have established that this region materializes for very inelastic systems (at least $\alpha < 0.426$ if $\kappa = 0.302$ and $\alpha < 0.392$ if $\kappa = \frac{1}{2}$). Even for the smooth case, one can face a similar issue in standard approximations [5, 21], which disappears if a more consistent approach is employed [22]. In addition, it is known for HS that velocity cumulants in the HCS may play an important role [26–28], its effect being even more noticeable for HD [24]. Therefore, to study whether the absolute instability phenomenon actually exists or is an artifact of the performed approximations, we have carried out event-driven MD simulations which address this question.

To deal with the problem, small system sizes must be tested in the simulations, which implies a small number of particles in the dilute case. Because of that, we have chosen not to rely only on a visual determination of clustering or vortices via snapshots. This fact was the clincher to use a coarse-grained KLD (with a binomial distribution as the reference probability distribution) to monitor the presence of spatial heterogeneities. Moreover, instead of analyzing deviations from Haff's cooling law as indicators of instability [19, 37], we have focused on the temporal evolution of quantities (such as the rotational-to-translational temperature ratio θ and velocity cumulants) that are unaffected by the velocity scaling performed in our simulations.

Two-dimensional MD simulations of HD with a uniform mass distribution ($\kappa = \frac{1}{2}$) were established under three different setups (A, B, and C), as summarized in Table II. The solid fraction $\phi = \frac{4}{3}n\sigma^2$ of each system is low enough as to expect the Boltzmann description for dilute gases to be applicable. For instance, the Enskog factor is 1.006 (systems A and C) and 1.012 (system B). The reliability of the Boltzmann equation is also supported by the good agreement between theory and simulations observed for the temperature ratio θ and the cumulants a_{20} , a_{02} , and a_{11} in Fig. 8 for system A and in Fig. 10 for systems A and B.

The high-inelasticity point $(\alpha, \beta) = (0.2, 0.25)$ lies inside the theoretical region of absolute instability. However, according to Figs. 8 and 9, although system B

($k \simeq 0.89$) is indeed unstable, system A ($k \simeq 1.25$) is not. Thus, the (reduced) critical wave number at $(\alpha, \beta) = (0.2, 0.25)$ does not diverge but is bounded as $0.89 < k_c < 1.25$; this critical value is anyway relatively high, as compared with HS values or with values in other regions of the HD parameter space (see Figs. 4 and 5). The picture is complemented with the moderate-inelasticity point $(\alpha, \beta) = (0.7, 0.25)$, in which case systems A and B are stable, while system C ($k \simeq 0.63$) is not (see Figs. 10 and 11). The determined range $0.63 < k_c < 0.89$ is now consistent with the theoretical prediction $k_c = 0.721$.

It is worth noting that in the cases where our MD simulations indicated instability (system B in Fig. 8, system C in Fig. 10), the temperature ratio θ reached small but nonzero stationary values after a certain number of collisions per particle. This implies a dramatic loss of rotational energy relative to the translational one, which is stronger in the particles involved in cluster and vortex formation. The fact that $\lim_{t \rightarrow \infty} \theta(t) \neq 0$ in the unstable regime contrasts with results for moderately dense HD systems reported in Ref. [19], according to which $\theta(t) \sim t^{-0.6} \rightarrow 0$. A possible explanation is that the different cooling power laws observed in Ref. [19] may be present in a transient evolution stage, but for a sufficiently large number of collisions per particle both average energies reach a common decay and thus an asymptotic stationary value $\theta \neq 0$ is obtained.

While signaling a region of strong instability, the predicted high-inelasticity region of absolute instability

seems to be a consequence of the neglect of HCS velocity cumulants in the derivation of the NSF transport coefficients carried out in paper I [16]. This calls for a more complex and consistent treatment which we plan to undertake in the near future [24]. We will also carry out a similar work for stochastically driven granular gases, in which case the ansatz of a semi-Maxwellian form for the velocity distribution function of the base reference state is more accurate than in the free cooling situation.

To conclude, we hope this work may encourage further investigation on this topic, such as better approximations, more computer simulations by both MD and the direct simulation Monte Carlo (DSMC) method, and even experimental tests about the impact of roughness on the hydrodynamic properties and stability of HD and HS granular gases.

ACKNOWLEDGMENTS

The authors acknowledge financial support from the Grant No. PID2020-112936GB-I00/AEI/10.13039/501100011033 and from the Junta de Extremadura (Spain) through Grants No. IB20079 and No. GR18079, all of them partially financed by Fondo Europeo de Desarrollo Regional funds. A.M. is grateful to the Spanish Ministerio de Ciencia, Innovación y Universidades for support from a predoctoral fellowship Grant No. FPU2018-3503.

-
- [1] I. Goldhirsch and G. Zanetti, Clustering instability in dissipative gases, *Phys. Rev. Lett.* **70**, 1619 (1993).
 - [2] S. McNamara, Hydrodynamic modes of a uniform granular medium, *Phys. Fluids A* **5**, 3056 (1993).
 - [3] S. McNamara and W. R. Young, Inelastic collapse in two dimensions, *Phys. Rev. E* **50**, R28 (1994).
 - [4] S. McNamara and W. R. Young, Dynamics of a freely evolving, two-dimensional granular medium, *Phys. Rev. E* **53**, 5089 (1996).
 - [5] J. J. Brey, J. W. Dufty, C. S. Kim, and A. Santos, Hydrodynamics for granular flow at low density, *Phys. Rev. E* **58**, 4638 (1998).
 - [6] S. Luding and H. J. Herrmann, Cluster-growth in freely cooling granular media, *Chaos* **9**, 673 (1999).
 - [7] W. D. Fullmer and C. M. Hrenya, The clustering instability in rapid granular and gas-solid flows, *Annu. Rev. Fluid Mech.* **49**, 485 (2017).
 - [8] V. Garzó, *Granular Gaseous Flows. A Kinetic Theory Approach to Granular Gaseous Flows* (Springer Nature, Switzerland, 2019).
 - [9] P. P. Mitrano, S. R. Dahl, A. M. Hilger, C. J. Ewasko, and C. M. Hrenya, Dual role of friction in granular flows: attenuation versus enhancement of instabilities, *J. Fluid Mech.* **729**, 484 (2013).
 - [10] V. Garzó, A. Santos, and G. M. Kremer, Impact of roughness on the instability of a free-cooling granular gas, *Phys. Rev. E* **97**, 052901 (2018).
 - [11] G. M. Kremer, Instabilities in a self-gravitating granular gas, *Physica A* **545**, 123667 (2020).
 - [12] N. Brilliantov, P. L. Krapivsky, A. Bodrova, F. Spahn, H. Hayakawa, V. Stadnichuk, and J. Schmidt, Size distribution of particles in Saturn's rings from aggregation and fragmentation, *Proc. Natl. Acad. Sci. U. S. A.* **112**, 9536 (2015).
 - [13] R.-L. Ballouz, D. C. Richardson, and R. Morishima, Numerical simulations of Saturn's B ring: Granular friction as a mediator between self-gravity wakes and viscous overstability, *Astron. J.* **153**, 146 (2017).
 - [14] A. Megías and A. Santos, Driven and undriven states of multicomponent granular gases of inelastic and rough hard disks or spheres, *Granul. Matter* **21**, 49 (2019).
 - [15] A. Megías and A. Santos, Energy production rates of multicomponent granular gases of rough particles. a unified view of hard-disk and hard-sphere systems, *AIP Conf. Proc.* **2132**, 080003 (2019).
 - [16] A. Megías and A. Santos, Hydrodynamics of granular gases of inelastic and rough hard disks or spheres. I. Transport coefficients, *Phys. Rev. E* **104**, 034901 (2021).
 - [17] S. Kullback and R. A. Leibler, On information and sufficiency, *Ann. Math. Statist.* **22**, 79 (1951).
 - [18] S. Kullback, *Information Theory and Statistics* (Dover, New York, 1978).

- [19] S. N. Pathak, D. Das, and R. Rajesh, Inhomogeneous cooling of the rough granular gas in two dimensions, *EPL* **107**, 44001 (2014).
- [20] G. M. Kremer, A. Santos, and V. Garzó, Transport coefficients of a granular gas of inelastic rough hard spheres, *Phys. Rev. E* **90**, 022205 (2014).
- [21] J. J. Brey and D. Cubero, Hydrodynamic transport coefficients of granular gases, in *Granular Gases*, Lectures Notes in Physics, Vol. 564, edited by T. Pöschel and S. Luding (Springer, Berlin, 2001) pp. 59–78.
- [22] V. Garzó, A. Santos, and J. M. Montanero, Modified Sonine approximation for the Navier–Stokes transport coefficients of a granular gas, *Physica A* **376**, 94 (2007).
- [23] N. Brilliantov and T. Pöschel, Breakdown of the Sonine expansion for the velocity distribution of granular gases, *Europhys. Lett.* **74**, 424 (2006); Erratum: Breakdown of the Sonine expansion for the velocity distribution of granular gases, *Europhys. Lett.* **75**, 188 (2006).
- [24] A. Megías and A. Santos, Translational and angular velocity cumulants in granular gases of inelastic and rough hard disks or spheres (unpublished).
- [25] N. V. Brilliantov, T. Pöschel, W. T. Kranz, and A. Zippelius, Translations and rotations are correlated in granular gases, *Phys. Rev. Lett.* **98**, 128001 (2007).
- [26] A. Santos, G. M. Kremer, and M. dos Santos, Sonine approximation for collisional moments of granular gases of inelastic rough spheres, *Phys. Fluids* **23**, 030604 (2011).
- [27] F. Vega Reyes, A. Santos, and G. M. Kremer, Role of roughness on the hydrodynamic homogeneous base state of inelastic spheres, *Phys. Rev. E* **89**, 020202(R) (2014).
- [28] F. Vega Reyes, A. Santos, and G. M. Kremer, Properties of the homogeneous cooling state of a gas of inelastic rough particles, *AIP Conf. Proc.* **1628**, 494 (2014).
- [29] F. Vega Reyes and A. Santos, Steady state in a gas of inelastic rough spheres heated by a uniform stochastic force, *Phys. Fluids* **27**, 113301 (2015).
- [30] J. F. Lutsko, Model for the atomic-scale structure of the homogeneous cooling state of granular fluids, *Phys. Rev. E* **63**, 061211 (2001).
- [31] S. Luding and S. McNamara, How to handle the inelastic collapse of a dissipative hard-sphere gas with the TC model, *Granul. Matter* **1**, 113 (1998).
- [32] A. Hosoya, T. Buchert, and M. Morita, Information entropy in cosmology, *Phys. Rev. Lett.* **92**, 141302 (2004).
- [33] N. Akerblom and G. Cornelissen, Relative entropy as a measure of inhomogeneity in general relativity, *J. Math. Phys.* **53**, 012502 (2012).
- [34] C. E. Shannon, A mathematical theory of communication, *Bell Syst. Tech. J.* **27**, 379 (1948).
- [35] N. Schneider, G. Musiolik, J. E. Kollmer, T. Steinpilz, M. Kruss, F. Jungmann, T. Demirci, J. Teiser, and G. Wurm, Experimental study of clusters in dense granular gas and implications for the particle stopping time in protoplanetary disks, *Icarus* **360**, 114307 (2021).
- [36] See Supplemental Material at <http://link.aps.org/supplemental/10.1103/PhysRevE.104.034901> for videos with snapshots from $s = 0$ to $s = 1000$.
- [37] P. P. Mitrano, S. R. Dahl, D. J. Cromer, M. S. Pacella, and C. M. Hrenya, Instabilities in the homogeneous cooling of a granular gas: A quantitative assessment of kinetic-theory predictions, *Phys. Fluids* **23**, 093303 (2011).

RESULTS AND CONCLUSIONS

The aim of this chapter is to explain and highlight the different results derived from this thesis, as well as comment on their implications in the considered system and introduce possible improvements of the analyses carried out. This discussion is classified into the different systems considered throughout this thesis.

11.1 Molecular gases

We have studied the homogeneous states of a dilute molecular gas of identical elastic hard d_t -spheres in contact with a background fluid at temperature T_b , which is acting on the molecular gas as a thermal bath. The nonequilibrium states of this system have been studied by means of the corresponding **BFPE**. The evolution of the one-particle **VDF** is due to two main events. On the one hand, the **VDF** evolves due to binary collisions between the gas particles, which is accounted for by the Boltzmann collisional operator, in this case, described by the **EHS** model. On the other hand, the **VDF** changes due to the interaction between the gas and the surrounding fluid. This latter evolution is modeled by two force terms: a viscous drag force, whose associated drag coefficient is assumed to be velocity dependent, together with a stochastic force with nonlinear variance. The drag coefficient and the noise intensity are related via the **FDT**.

The goal of this thesis, with respect to this system, resides in the analysis of the **ME**, which is already known to emerge in this kinetic description [**SP20**; **PSP21**]. In fact, we have distinguished between a thermal description, **TME**, and an entropic one, **EME**. The former is guided by the kinetic nonequilibrium temperature of the system, whereas the latter has been described by the nonequilibrium entropy by means of the **KLD** of the one-body **VDF** with respect to the equilibrium one, the Maxwellian **VDF** at T_b .

Regarding thermal description, we firstly derived the evolution equation of the temperature, coming from the **BFPE**, and we already knew that it must be directly

coupled to the excess kurtosis of the **VDF** from the results of Ref. [SP20]. This is an indicator of the presence of memory effects due to the dependence of the nonequilibrium states of a macroscopic variable, the temperature, on an inner variable of the system, the excess kurtosis. Then, to complete the description, we have derived the infinite hierarchy of moment or, equivalently, cumulant equations. It was observed that the evolution equation of the k^{th} cumulant, a_k , is related to the equation of a_{k-1} and a_{k+1} , for $k \geq 2$, implying that all the equations of the hierarchy are coupled. Then, in order to manage the system of differential equations, we introduced some approximations, based on a Sonine expansion of the **VDF**, to truncate the infinite system of coupled differential equations. The first approach is referred as the **BSA** in Article 1 (Section 5.2) and it consisted in the truncation of the description up to a_2 , considering a_k with $k \geq 3$ to be negligible, and properly linearizing the differential equations with respect to the excess kurtosis, a_2 . Moreover, we improved this approach by a more *sophisticated* one, called the **ESA** in Article 1 (Section 5.2), where the Sonine coefficient that determines the truncation limit is a_3 , plus a proper linearization of the equations with respect to a_2 and a_3 . Moreover, in Ref. [SP20], it was observed that the **TME** occurs at the first stages of the evolution—if there is no an exaggerated quenching or heating [PSP21]—implying that a solution of the **BSA** in terms of a linearization of the evolution equations around the initial conditions applies. The latter approach was referred to as **LBSA** in Article 1 (Section 5.2) and it allowed for an analytical solution of the system. Furthermore, with respect to the evolution of $\mathcal{D}_{\text{KL}}(f(t)|f_{\text{M}}^{\text{eq}})$, we demonstrated that it could be divided into kinetic and local-equilibrium counterparts (see Figure 5.1). The former absorbs the evolution of the **VDF** with respect to the local-equilibrium **VDF**, which was approximated by a **SA**, obtaining that $\mathcal{D}_{\text{kin}} \propto a_2^2$. On the other hand, the latter describes the distance of the local-equilibrium distribution from the equilibrium **VDF**, which was found to be a function only of $T(t)/T_b$. Due to the rapid relaxation of the system—from initial conditions not excessively far from the equilibrium temperature—we concluded that the kinetic part of the **KLD** evolution determines the appearance or not of the **EME**.

In order to study the **ME**, we have defined two arbitrary samples of our molecular fluid, A and B, the latter with a temperature further from T_b . The **TME** was said to occur if T_A relaxes toward T_b earlier than T_B . On the other hand, the **EME** was established to emerge if a system with an initially greater **KLD**¹ arrives earlier to equilibrium. To gain some insight, we firstly restricted the **TME** to cases in the absence of any overshoot of the equilibrium temperature, T_b . Thus, from heuristic arguments, we have identified different events related to the **TME** and **EME**, as Table I of Article 1 (Section 5.2) summarizes. Under these considerations, the **TME** (**EME**) was characterized by the emergence of a crossover—or an odd number of them—between the thermal (entropic) curves at a certain crossing time, t_θ ($t_{\mathcal{D}}$). From the **LBSA**, we have predicted

¹Whereas for systems close to the equilibrium **VDF**, $\mathcal{D}_{\text{KL}A}^0 > \mathcal{D}_{\text{KL}B}^0$, this might not be the case if system B is initialized to a **VDF** much further from the Maxwellian one than A.

the regions of the initial-temperature conditions, where these different phenomena arise, for representative choices of the initial values of the excess kurtosis, as pictured in Figure 4 of Article 1 (Section 5.2). Afterwards, we have observed that a type of TME may arise without a crossover (or with an even number of crossovers) between $T_A(t)$ and $T_B(t)$. This may occur due to an overshoot of (at least) system B through the equilibrium temperature, T_b . If the overshoot lasts enough, system A could take advantage and relax to equilibrium sooner than B. This phenomenon has been termed as the OME, which is meaningless in the EME description, due to the monotonic decay of the KLD. However, as an important result, the local-equilibrium counterpart of the KLD—which is indeed only a function of $T(t)/T_b$ —absorbs both the standard version of the TME and the OME via the single (or odd number of) crossover of the \mathcal{D}^{LE} curves, acting as the thermal distance introduced in Section 3.3.

In order to check the validity of our heuristic argumentation and the approximations, we have compared the theoretical results with DSMC and EDMD computer simulation outcomes. The excellent agreement between the simulation results and the theoretical predictions have confirmed the great phenomenological variety observed in this system. These results open the way to different manners to look for the emergence of ME in complex systems.

11.2 Granular gases of inelastic particles

The very first and simplest description of the interaction of particles in a granular gas is the IHS model [BP04; Gar19]. In addition, granular matter, under rapid-flow conditions, can be described by the Boltzmann kinetic equation, whose collisional operator must be adapted to the choice of the collisional model. In the inelastic and smooth case for hard d_t -spheres, the properties of the granular gaseous flows have been widely studied in the last three decades, some examples being Refs. [Cam90; Meh93; GS95; GZB97; NE98; SG98; Duf00; Duf01; GD02; Go103; BP03; BP04; GNB05; Ser+06; VSG10; DB11; GS11; GMT13; Gar19]. In this thesis, we have got immersed more in some properties of this model for the monodisperse case. First, to the freely evolving system and, then, to the case of a granular gas interacting with an interstitial fluid.

11.2.1 Freely evolving granular gases of inelastic particles

Whereas new and interesting phenomena arise in an inelastic granular gas, as compared with the widely studied case of molecular gaseous flows, most of the tools derived from the latter have been applied to the former. The simplest studied states of the system are the homogeneous ones, as in molecular gases. It is widely known and studied that

the homogeneous and inelastic BE is compatible with a limiting scaling solution, called the HCS (see Subsection 2.5.2). This state has been observed experimentally [YSS20] and turns out to be unstable under certain conditions, as derived from linear stability analyses [GZ93; Meh93; MY96; Bre+98; BRM98; LH99; SMM00; Gar05; Gar19]. However, the H -theorem, which is one of the most important results of the Boltzmann kinetic theory applied to molecular fluids, proving the continuous evolution of the system toward equilibrium via its nonequilibrium entropy, has not been extended rigorously to the inelastic case, mathematically speaking. References [BPV13; Gar+15] address this problem and conjecture, from different arguments, that, given a granular gas described by the IHS model, the quantity $\mathcal{D}_{\text{KL}}(f | \lim_{t \rightarrow \infty} f(t))$ may act as the nonequilibrium entropy of the system. In a driven granular gaseous system, $\lim_{t \rightarrow \infty} f(t)$ coincides clearly with the steady-state VDF, whereas, in the freely evolving case, this limit is more subtle and admitted to be the HCS VDF. However, whereas, in Ref. [BPV13] the conjecture is presented and some arguments are given in its favor, for the freely evolving case, Ref. [Gar+15] gave positive arguments for the conjecture in the context of Kac's master equation [Kac56]. Moreover, in both works some computer simulations, for systems of inelastic HD ($d_t = 2$) and HS ($d_t = 3$), also supported the hypothesis.

In this thesis, we have studied this problem in Article 2 (Section 6.2) and Article 3 (Section 6.3). To gain some insight into the issues making this H -theorem problem to be hard to be formally solved, we have firstly studied the homogeneous states of the BE under standard Sonine-like approximations in Article 2 (Section 6.2). We have derived the evolution equations for the second and third Sonine coefficients, a_2 and a_3 , under a truncation and proper linearization of the moment evolution equations. The way of linearizing the rates of change of those two cumulants was compatible with the asymptotic HCS values discussed in Ref. [SM09]. The approximate forms of the evolution equations were supported by comparison with EDMD computer simulation results for transient and steady states, thus extending and improving the analysis and results of Ref. [HOB00].

Once the homogeneous evolution and the HCS VDF have been approximately characterized, the KLD is introduced as a proper functional to describe the nonequilibrium entropy of the system. It solves certain issues that Shannon's H functional presents, associated with problems of measure [MT11]. Then, we have focused the problem on the choice of the proper reference VDF. We have compared the choices $\mathcal{D}_{\text{KL}}(f | f_M)$ and $\mathcal{D}_{\text{KL}}(f | f_H)$ from numerical approximate schemes and computer simulations, for a wide variety of initial conditions, observing monotonic evolutions for the latter and not for the former. These results support the original conjecture and discard the choice of $\mathcal{D}_{\text{KL}}(f | f_M)$. Moreover, to elucidate why the monotonic parts of the evolution appear in the HCS choice and not in the Maxwellian one, we have derived a toy model for the KLD, which is based on a SA. Introducing the evolution equations derived under our

initial approach into this toy model, $\mathcal{D}_{\text{KL}}(f|f_{\text{H}})$ resulted to be a Lyapunov functional, proved only under this approach. On the other hand, in Article 3 (Section 6.3), this has been further analyzed and the toy model also explains why, for certain initial conditions, the nonmonotonic behaviors of the $\mathcal{D}_{\text{KL}}(f|f_{\text{M}})$ appear.

Furthermore, in Article 2 (Section 6.2), we have used the mathematical meaning of the KLD in the context of information theory to study how far the HCS VDF is from the Maxwellian one. This relation has been found to be nonmonotonic with respect to the coefficient of normal restitution, α , for the least inelastic values. More specifically, within approximately the interval $0.7 \lesssim \alpha \lesssim 1$, we cannot obtain univocally the coefficient of restitution from $\mathcal{D}_{\text{KL}}(f_{\text{H}}|f_{\text{M}})$. This has been inferred from numerical schemes and EDMD results, as showed in Figure 10 of Article 2 (Section 6.2). For the sake of completeness, we have carried out EDMD simulations for the inelastic generalization of the original velocity-inversion computer experiments of Orban and Bellemans [OB67; OB69] by a sort of a Maxwell-demon-based mechanism. The evolution of the VDF is guided by $\mathcal{D}_{\text{KL}}(f(t)|f_{\text{H}})$, such that in the elastic case ($\alpha = 1$) it was set to be $\mathcal{D}_{\text{KL}}(f(t)|f_{\text{M}})$. We have recovered, for the elastic case, an anti-kinetic stage in the evolution, symmetric to the previous kinetic evolution up to the waiting time, t_w , when this velocity inversion was carried out. However, in granular gases of inelastic particles, $\alpha < 1$, this anti-kinetic stage is found to be almost fully suppressed as a result of the breakdown of the *time* symmetry of the binary collisional rules. This suppression was found to be present even in the quasi-elastic limit.

We expect that these results could encourage a formal proof for the conjecture of the nonequilibrium entropy of the granular gas of inelastic hard d_t -spheres. Moreover, we hope the analysis derived could be useful to other nonequilibrium systems in statistical physics contexts.

11.2.2 Granular gases of inelastic particles under nonlinear drag

After the analysis of the freely evolving case, we took a step further in the study of granular gases under the IHS model. Whereas, in the outer universe, grains, like dust, evolve freely, on planet Earth, they are not in pure vacuum, except if we force them to be isolated in a laboratory setup. Thus, a granular gas can be found surrounded by other fluids, this system being usually called a *granular suspension*. It is assumed that the background fluid acts as a thermal bath at a certain temperature, T_b . The interaction between the granular phase and the surrounding fluid has been usually modeled in the literature by a coarse-grained description. This consists in the assumption of the action of a linear drag force, plus a stochastic force with the properties of a white noise. The noise intensity and the drag coefficient values are usually constrained to obey a fluctuation-dissipation relation. Then, in the dilute regime, this system can be studied

in terms of a [BFPE](#), where the Fokker–Planck part of the equation is related to the associated [LE](#) for the velocities. This kind of description can be found in, for example, Refs. [[CVG12](#); [CVG13](#); [GKG20](#); [THS21](#)]. In this thesis, we have studied the monodisperse case and have improved the latter Langevin-like model from the inelastic extension of the molecular system introduced in Article 1 ([Section 5.2](#)). That is, we have assumed that the drag force is nonlinear, i.e., the drag coefficient is, in general, a function of the velocity modulus. The simplest nonlinear term has a quadratic dependence on v , which can be derived from a [QR](#) approximation, as detailed in [Appendix B](#). The effect of the nonlinear term is assumed to be small and is controlled by a constant coefficient, γ , which is defined through the ratio between the mass of the grains and the mass of the background fluid particles from the [QR](#) approach [see Eq. ([B.11](#))].

In Article 4 ([Section 7.2](#)), our analysis of the latter system has focused on its homogeneous states. After the identification of the corresponding [BFPE](#), we have derived formally the evolution equation of the granular temperature and a full hierarchy of moment equations. Attending to the structure of the differential equation of the granular temperature, a two-source dependence from the cumulants of the instantaneous [VDF](#) has been identified. The first dependence is explicit on a_2 due to the coupling of the quadratic nonlinear term of the drag coefficient, as already observed in the molecular model of Article 1 ([Section 5.2](#)). On the other hand, the granular inelastic interactions made the energy to be not conserved upon collisions, this energy dissipation being accounted for by the cooling rate. This quantity is a function of all the moments of the [VDF](#), thus acting as a the second coupling source. All this complex dependence has been studied in the context of a Sonine expansion of the [VDF](#) and, in order to get a closed and finite system of differential equations for a manageable mathematical description, we have truncated the expansion in two manners. First, the simplest approach consisted in the assumption of the time-dependent and steady-state [VDF](#) to be a Maxwellian distribution. However, from this approach, the couplings to the cumulants of the [VDF](#) are completely lost. Then, we introduced a [FSA](#) to study the transient and steady states of the system in terms of the granular temperature, T , and the excess kurtosis, a_2 . This approach consists in the truncation of the Sonine expansion up to its second coefficient plus a proper linearization of the dynamical set of equation with respect to a_2 . For the sake of completeness, we have checked that the stationary values of those quantities coincide, under certain limits, with already known expressions of different granular systems. Once the theoretical bases have been established, the predictions have been compared with [DSMC](#) and [EDMD](#), obtaining quite a good agreement with the [FSA](#).

From the [FSA](#), we have observed a nontrivial relaxation toward the steady state. As already studied in Article 1 ([Section 5.2](#)) in the molecular case, this is due to the explicit dependence of the rate of change of the granular temperature on the instantaneous value of a_2 . However, in the granular case, this gets more involved due to the presence

of the cooling rate. The dependence of the granular temperature evolution on the inner variables of the system, during nonequilibrium stages, is proper of systems that exhibit memory effects (see [Chapter 3](#)). Then, using the knowledge of Refs. [[SP20](#); [PSP21](#); [MSP22](#)], and as an application of the theoretical scheme, we have predicted the presence of the [ME](#) and the [KE](#). It must be highlighted that the coupling of a_2 with the evolution of the temperature dominates the description of the memory effects. Moreover, from the difference $a_2(t) - a_2^{\text{st}}$, the sign of the humps appearing in a Kovacs-like protocol can be deduced [see Eq. (29) of Article 4 ([Section 7.2](#))]. In fact, the theoretical predictions of the latter two effects agree with [DSMC](#) and [EDMD](#) computer simulation results. These results open the path to study more complex granular gaseous suspensions flows from a more realistic description.

11.3 Granular gases of inelastic and rough particles

Although the [IHS](#) model is very simple, it has an important predictive power, at least, qualitatively or semi-quantitatively. Recent experiments [[YSS20](#)], in fact, favor this model against velocity-dependent coefficients of normal restitution, such as in the viscoelastic model. However, the numerical discrepancies between experimental results and kinetic theory predictions are expected to be solved by the introduction of rotational degrees of freedom into the system dynamics, as the authors of Ref. [[YSS20](#)] claim. The simplest introduction of this effect is done by means of the [IRHS](#) model, where energy is lost upon collision not only by the inelasticity of the particles, but also due to their surface roughness, which is characterized by a coefficient of tangential restitution, β , assumed to be constant. This model has also been studied before in the literature, see, for example, Refs. [[BP04](#); [Bri+07](#); [Kra+09](#); [VSK14b](#); [San18](#); [Gar19](#); [MS19a](#); [MS19b](#)]. In this thesis, we have studied deeply the homogeneous and inhomogeneous states of its free-evolution version, as well as its homogeneous states and the presence of memory effects in driven setups.

11.3.1 Freely evolving granular gases of inelastic and rough particles

A homogeneous granular gas in free evolution, described by the [IRHS](#), admits a scaling limiting form for its [VDF](#), as occurs in the [IHS](#) model. When this happens, the system is said to be at the [HCS](#), and all the time evolution of the system is absorbed by the temperature evolution. In general, the homogeneous transient and [HCS](#) states of a freely evolving granular gases have been previously studied. First, in terms of a [MA](#) (see, for example, Refs. [[AHZ01](#); [Zip06](#); [San18](#); [MS19a](#); [MS19b](#)]), where rotations and translations are assumed to be uncorrelated at the level of the one-particle [VDF](#). However, this was found to be false, as observed in, for example, Refs. [[Bri+07](#); [Kra+09](#)]. Hence, the [HCS](#)

has been observed to be non-Maxwellian, similarly as occurs in the inelastic and smooth case. Approaches to their deviations from the Maxwellian **VDF** had been studied only in the context of **HS**, and only attending to the first nontrivial cumulants by means a Sonine expansion of the **HCS VDF** [SKS11; SK12; VSK14b; VSK14a]. Moreover, the transport properties and the instability of the **HCS** had only been studied in systems of **HS** [KSG14; GSK18].

In this thesis, the goals related to this topic have been mainly four, and they have been restricted to the monodisperse case. First, we have generalized the whole description related to this system in terms of the translational and rotational degrees of freedom of the problem, d_t and d_r , respectively, with the aim of being descriptive for both **HD** ($d_t = 2$, $d_r = 1$) and **HS** ($d_t = 3$, $d_r = 3$) systems. For that, steps similar to those carried out in Refs. [MS19a; MS19b] have been introduced. The second goal consisted in analyzing the non-Gaussianities of the **HCS VDF**, within this generalized context, embedding the results for **HD** and **HS** in a single description. The studied non-Gaussian properties have not been just the first nontrivial Sonine coefficients, but also the **HVT** of the most important marginal **VDF** at the **HCS**. This is summarized in Article 5 (Section 8.2). On the other hand, the transport properties of a granular gas of inelastic and rough **HD** or **HS** have been investigated by means of the **NSF** transport coefficients. These quantities have been derived from the **CE** method applied to this context, as described in Article 7 (Section 10.2). Finally, the last aim corresponds to the study of the instabilities of the **HCS** from inhomogeneous and linear perturbations, as an application of the knowledge of the transport coefficients [see Article 8 (Section 10.3)].

With respect to the description of the **HCS**, we have studied a monodisperse dilute granular gas of inelastic and rough **HD** or **HS**, in the context of the homogeneous **BE**, for the **IRHS** model. To study, in general, the homogeneous transient and **HCS** states of the system, we have firstly introduced a Sonine expansion of the **VDF**. Then, we have truncated the expansion up to the first nontrivial Sonine coefficients. In the **HD**, these are a_{20} , a_{02} , and a_{11} . However, in the **HS**, we had one extra coefficient, $a_{00}^{(1)}$. Thus, the transient states of the system under this approach, see Article 5 (Section 8.2), were guided by the evolution of the latter Sonine coefficients plus the rotational-to-translational temperature ratio, θ . Afterwards, we have derived the collisional moments involved in this scheme in terms of two-body averages. These expressions are exact in the context of the **BE**. Then, by introducing the mentioned truncation of the **VDF**, we have obtained certain approximate values of the two-body averages and, thus, of the collisional moments. All these quantities have been then expressed in terms of the dynamic quantities θ , a_{20} , a_{02} , a_{11} [and $a_{00}^{(1)}$ for **HS**], and as functions of the coefficients of restitution, α and β , the degrees of freedom, d_t and d_r , and the mechanical properties of the system, i.e., the diameter, σ , the mass, m , and the reduced moment of inertia, κ . In other words, the evolution of the system toward the **HCS** has been described by a

closed set of differential equations in terms of the parameters of the problem. It is worth highlighting that the implemented SA scheme has been validated by a homogeneous linear stability analysis, as explained in Appendix A of Article 5 (Section 8.2).

From the development of the Sonine description, we have obtained the HCS values of the dynamic quantities. The results for HS reported in Ref. [VSK14b] were again obtained, as well as novel results for the HD case. Furthermore, we have observed very large values of a_{02} , indicating a possible breakdown of the SA. In order to localize the regions of the parameter space where this approach is expected to worsen, we have developed a scheme in terms of an entropy-like functional derived from a toy-model-like approach of $\mathcal{D}_{\text{KL}}(\phi_{\text{H}}|\phi_{\text{M}})$. These regions have been identified to appear as lobes emerging, paradoxically, from the elastic and smooth case ($\alpha = -\beta = 1$), as can be observed in Figure 4 of Article 5 (Section 8.2). These regions are dominated by the values of a_{02} , as expected. As a matter of fact, generally speaking, HD systems present slightly higher deviations from the Maxwellian than HS ones. Furthermore, we have determined the HVT of the marginal VDF, ϕ_c , ϕ_w , and ϕ_{cw} , at the HCS. The asymptotic treatment of this problem has been founded from the prevalence of the loss term of the Boltzmann collisional operator over the gain one (those terms have been introduced in Section 2.2). This is a standard approach already used in the IHS model [EP97; NE98]. In the case of ϕ_c , the IHS exponential form of the tail has been recovered, i.e., $\phi_c^{\text{H}} \sim e^{-\gamma_c^{\text{IRHS}} c}$. In fact, $\gamma_c^{\text{IHS}} \rightarrow \gamma_c^{\text{IRHS}}$ if $\mu_2^{\text{H}} \rightarrow \mu_{20}^{\text{H}}$. Moreover, for the rotational marginal VDF, an algebraic decay has been predicted after certain approximations, i.e., $\phi_w^{\text{H}} \sim w^{-\gamma_w}$. Finally, for the joint distribution of the product $c^2 w^2$, an algebraic decay has also been obtained, $\phi_{cw}^{\text{H}} \sim (c^2 w^2)^{-\gamma_{cw}}$. The latter two resulting HVT imply the divergence of cumulants of the forms a_{0k} if $2k \geq \gamma_w - 1$ and a_{kk} if $k \geq \gamma_{cw} - 1$. These consequences are another indicator of a possible breakdown of the SA.

Finally, we have performed DSMC and EDMD computer simulations for HD systems in the absence of instabilities. We have firstly compared the simulation and theoretical outcomes for the quantities θ^{H} , a_{20}^{H} , a_{02}^{H} , and a_{11}^{H} , concluding that the predictions from the HCS reproduce qualitatively well the outcomes from the SA, even in the regions of larger values, as observed in Figures 5 and 6 of Article 5 (Section 8.2). Furthermore, the averaged histograms for the marginal VDF at the HCS seem to fulfill the predicted HVT, as shown in Figures 7 and 8 of Article 5 (Section 8.2). In fact, the derived form of the rotational exponent, γ_w , has been very well reproduced by the simulation results. However, in the case of γ_c and γ_{cw} , their values agree with simulation in a more qualitative way [see Figure 9 of Article 5 (Section 8.2)].

Once the reference homogeneous state, the HCS, has been characterized, we have analyzed the influence of roughness in the transport properties of monodisperse granular gases. We have worked under the assumptions underlying the CE method, as described in detail in Subsection 2.7.2. The fields considered for the hydrodynamic description, in

this case, are the number density n , the flow field \mathbf{u} , and the mean granular temperature T . The main difference with the smooth case is the influence of the rotational degrees of freedom, which translates, for example, translated in two contributions of T by means of the translational partial temperature, T_t , and the rotational one, T_r . Then, we have applied a CE expansion and retained terms up to the NSF order. This unified analysis is applicable to both HD ($d_t = 2, d_r = 1$) and HS ($d_t = 3, d_r = 3$) systems. With respect to the proper application of the CE method, the zeroth order VDF, $f^{(0)}$, is compatible with a local version of the HCS VDF. Although we knew that the HCS is non-Maxwellian, we have followed the steps in Ref. [KSG14], in which, as a first reasonable insight to the problem, a MA is used. In the final computations of the NSF transport coefficients, which were described by the integration of certain quantities with respect to the zeroth-order VDF, the thermal part of the distribution, which was expected to be well described by a Maxwellian VDF, was expected to dominate. The same occurs with the inelastic and smooth case, but it is worth mentioning that corrections by means of the introduction of the Sonine coefficients improve the results [BC01; GSM07; Gar19]. Nonetheless, we have worked within the MA for $f^{(0)}$.

The derivation of the NSF transport coefficients has been divided into two parts. First, the attainment of the balance equations directly from the BE, represented in Eqs. (8) of Article 7 (Section 10.2) and detailed in Appendix D. The main difference with respect to the molecular case has been the contribution of the cooling rate, whereas, with respect to the smooth case, it has been the appearance of a contribution of the rotational degrees of freedom to the heat flux, \mathbf{q}_r , as well as to the cooling rate via the energy production rates [see Eqs. (9) of Article 7 (Section 10.2)]. Therefore, comparing the first-order VDF of the CE expansion, $f^{(1)}$, with the balance equations and the phenomenological form of the fluxes [see Eqs. (34) of Article 7 (Section 10.2)], we have obtained explicit forms for the transport coefficients as functions of the parameters of the system. These computations were performed under a sort of SA for the coefficients of $f^{(1)}$, as detailed in Eqs. (40) of Article 7 (Section 10.2). The NSF transport coefficients are, using the notation of Article 7 (Section 10.2), $\{\eta, \eta_b, \lambda, \mu, \xi\}$, namely, the shear viscosity, η , the bulk viscosity, η_b , the thermal conductivity, λ , the Dufour-like coefficient, μ , and the velocity-divergence transport coefficient, ξ , which is associated with the first-order correction to the cooling rate.²

We have explicitly reproduced the theoretical values of the transport coefficients, in Figures 3-6 of Article 7 (Section 10.2), for uniform ($\kappa = 1/2$) HD systems and with a mass distribution concentrated on the outer surface ($\kappa = 1$). Moreover, we have done the same for HS granular gases, again with a uniform mass distribution ($\kappa = 2/5$) and with a mass distribution concentrated on the outer surface ($\kappa = 2/3$). The results

²Do not confuse this ξ , which corresponds to the contribution of the cooling rate to the velocity divergence, i.e., $\zeta^{(1)} = -\xi \nabla \cdot \mathbf{u}$, with the notation of the friction coefficient for the LE in other contexts.

for **HS** are in agreement with the ones previously reported on Ref. [KSG14]. All the relevant theoretical expressions for the transport coefficients have been summarized in Table I of Article 7 (Section 10.2). For the sake of completeness, we have checked that results for smooth particles are recovered, and they have also been computed in the quasismooth limit ($\beta \rightarrow -1$) and in the case of a Pidduck's gas ($\alpha = \beta = 1$). Apart from the new dependences of β and κ , as compared with the smooth case, we can extract some important remarks. For example, the Dufour-like coefficient, μ , characteristic of granular gases, becomes more relevant in the rough case than in the perfectly smooth one. Moreover, the effect of the rotational degrees of freedom make the bulk viscosity, η_b , to be nonzero, contrarily to the dilute smooth case. In fact, in arbitrarily small presence of roughness, η_b is still nonzero, as showed by the quasismooth limit. This recalls some arguments about the origin of the bulk viscosity in molecular fluids due to the rotational (and vibrational) molecular motions [Tem81; DG02]. Finally, in the quasielastic ($1 - \alpha \ll 1$) smooth case, the velocity-divergence transport coefficient, ξ , admits small negative values, which is identically null in the dilute regime in the smooth limit.

As a first application of the transport properties of a granular gas of inelastic and rough **HD** or **HS**, we have studied the stability of the **HCS** under linear inhomogeneous perturbations, within the generalized degrees-of-freedom scheme, as reported on Article 8 (Section 10.3). We have first slightly perturbed the hydrodynamic fields for small gradients around the **HCS**. After the proper linearization of the **NSF** equations with respect to the perturbations, and transforming the time-evolving equations from spatial gradients to wave vectors via Fourier analysis, we have obtained the hydrodynamic modes as functions of the parameters of the system. These modes can decompose into a $(d_t - 1)$ -degenerated shear mode [see Eq. (13) of Article 8 (Section 10.3)], ω_\perp , and three other transverse modes, $\omega_{\parallel,i}$ with $i = 1, 2, 3$, which are the solutions to the cubic equation written in Eq. (18) of Article 8 (Section 10.3). Their dispersion relations show the existence of critical value of the wave number, from which some of the modes become positive [see Figures 1 and 2 of Article 8 (Section 10.3)]. This implies that the system becomes unstable under perturbations related to values of the wave number k greater than this critical one, which has been already observed to occur in the smooth case [GZ93; BRM98; BRC99; LH99; Gar05; Mit+11; Mit+12; Mit+14; FH17; Gar19]. In fact, the instabilities occur due to the positiveness of the shear and one of the longitudinal modes, but the critical value of k , below which the mode becomes negative, is different for both type of modes. In fact, we have computed the explicit forms of these two critical wave numbers, k_\perp and k_\parallel [see Eqs. (14) and (21) of Article 8 (Section 10.3)], as a generalization of the **HS** results reported in Refs. [Mit+13; GSK18]. From them, we can deduce a critical length, L_c , of a real (or **MD**-computational) system, such that the **HCS** is stable only for characteristic lengths $L < L_c$.

The most outstanding result of this analysis is the observation of the **HUR**, in which our approximate theory predicts that hydrodynamics breaks down for certain values of the coefficients of restitution due to the spontaneous emergence of granular clusters. This occurs due to a divergence and complex-valued regime of k_{\parallel} , as a consequence of a negative-valued difference between the (reduced) thermal conductivity and the (reduced) Dufour-like coefficients in the equation of this critical wave number [see Eq. (21) of Article 8 ([Section 10.3](#))]. The origin lies on the large values that the Dufour-like transport coefficient admits, as compared with the smooth case [see Figure 6 of Article 7 ([Section 10.2](#))]. Whereas this region is slightly observed in **HS**—just for a small region of values of the reduced moment of inertia—it is always present in **HD** systems [see Figure 3 of Article 8 ([Section 10.3](#))]. Due to the importance of this result, we have performed **EDMD** simulations to check it. In order to detect the possible appearance of clustering, we have developed a decision scheme based on the **KLD** of the position distribution inside the simulation box, with respect to a reference binomial homogeneous distribution, as well as a comparison of the long-time values of the quantities θ , a_{20} , a_{02} , and a_{11} with respect to the **HCS** predicted values within the methods of Article 5 ([Section 8.2](#)). The **EDMD** outcomes have shown that, outside the **HUR**, theoretical predictions about the stability are apparently valid. However, inside the **HUR**, we have observed a stable system in a computer realization up to 1000 of collisions per particle. The simulation results indicate that this region might be *very* unstable, instead of totally unstable. Thus, the theoretical prediction might be an artifact of the approximations in the evaluation of the transport coefficients. In addition, we have observed an interesting qualitative connection between the spatially defined **KLD** in systems at **HCS** and the values of the hydrodynamic modes, as reported in Figure 7 of Article 8 ([Section 10.3](#)).

We expect this work could motivate further research in this topic, especially in the nature of the **HUR**, from theory and computer simulations. In addition, the determination of the transport coefficients by means of computer simulations would establish the goodness of the approximations. Moreover, we hope that the simplicity of the **HD** systems could encourage the comparison of these results with real experiments. Finally, it would be interesting to investigate how the non-Gaussianities of the **HCS** of this freely evolving gas of rough particles, studied in [Chapter 8](#), affect to the final results of the transport properties.

11.3.2 Driven granular gases of inelastic and rough particles

A very interesting problem in the study of granular fluids is the consideration of driven states, both in theory [[WM96](#); [Wil96](#); [NE98](#); [CCG00](#); [MS00](#); [BT02](#); [GM02](#); [EB02](#); [Her+05](#); [MR06](#); [GMT12](#); [CVG12](#); [MGT12](#); [CVG13](#); [KG13](#); [Gar19](#); [KG20](#)] and experiments [[Gra+11a](#); [Gra+11b](#); [Mic+22](#); [CZ22](#)]. Moreover, driven granular gases of inelastic and rough hard

particles have been also considered in the context of kinetic theory [CLH02; VS15; MS19a; Tor+19; GG20]. In this thesis, we have focused on the homogeneous states of a monodisperse and dilute granular gas driven by the ST. That is, we have assumed that the energy injection is performed via a stochastic force and a stochastic torque to the translational and rotational degrees of freedom, respectively. The ST can be characterized by two quantities, a reference temperature (T^{wn}) associated with the noise intensity and the rotational-to-total noise intensity ratio (ε), the latter accounting for the part of the energy injected directly to the rotational degrees of freedom. This thermostat includes as particular cases the system already proposed in Ref. [CLH02] for purely rotationally driven states ($\varepsilon = 1$), the one in Refs. [VS15; MS19a; Tor+19] for purely translational driven systems ($\varepsilon = 0$), as well as all their intermediate cases ($0 < \varepsilon < 1$). In fact, our goal has been the extension of the study of the TME in homogeneous and driven granular gases of rough HD, which began in Ref. [Tor+19], with the aim of proposing a preparation protocol for the observation of the effect. Recall that in Chapter 3 we already mentioned that, whereas the KE is associated with a given protocol, this is not the case, in general, with the ME. Therefore, the absence of a predetermined preparation protocol makes more difficult its experimental reproducibility.

In Article 6 (Section 9.2), we have described this system by means of its corresponding homogeneous BFPE [see Eq. (3) of Article 6 (Section 9.2)]. From it, we have derived the thermal evolution of the system for the mean granular temperature, T , and the rotational-to-translational temperature ratio, θ [see Eqs. (23) of Article 6 (Section 9.2)]. As usual, to manage analytically the equations, we have introduced approximations. From a previous work in the $\varepsilon = 0$ case [VS15], we already know that the homogeneous steady states are also not too far from the two-temperature Maxwellian VDF. Therefore, if the initial conditions are not too far from it, a MA seems to apply at all stages of the evolution. Under this approach, Eqs. (23) of Article 6 (Section 9.2) for $\dot{T} \equiv \Phi(T/T^{\text{st}}, \theta)$ and $\dot{\theta}$, which are exact in the context of the BFPE, can be written as Eqs. (30) of Article 6 (Section 9.2), the latter consisting in a closed set of two coupled differential equations. From them, we have numerically inferred the evolution of the system and also we have derived explicit expressions for the steady-state values of $T^{\text{st}}/T^{\text{wn}}$ and θ^{st} [see Eqs. (26) of Article 6 (Section 9.2)]. In fact, we have tested these approximate transient and steady states by means of DSMC and EDMD simulations, obtaining an excellent agreement, as can be observed in Figures 5 and 6 of Article 6 (Section 9.2). It is worth stressing that θ^{st} is always an increasing function of ε .

Once the theoretical scheme for transient and steady states was developed and checked by computer simulations, we focused on the description of the TME in cooling experiments, i.e., the DME. First, we have studied the effect from the mean granular temperature as the guiding variable. That is, assuming two systems, A and B, such that the former is initially hotter than the latter, and both of them hotter than the

steady state, the **DME** occurs if A relaxes toward the steady state earlier than B. In the first instance, we have described the **DME** in its standard form, that is, assuming that there is no overshoot of the temperature through the stationary value during its evolution. We realized that, for each initial condition, and fixed values of the coefficients of restitution and the reduced moment of inertia, there exists a critical value of the rotational-to-total noise ratio, $\varepsilon_{\text{cr}}(T_0/T^{\text{st}}, \theta_0)$, then such that if $\varepsilon > \varepsilon_{\text{cr}}(T_0/T^{\text{st}}, \theta_0)$, the temperature will surpass its steady-state value at finite time. For a fixed value of θ_0 , this ε_{cr} is an increasing function of T_0/T^{st} [see Figure 7 of Article 6 ([Section 9.2](#))]. Therefore, we have inferred that the necessary condition is that the initial slopes of the evolution must fulfill $\Phi_{0,A} < \Phi_{0,B}$, which is equivalent to the condition $\theta_{0,A} < \theta_{0,B}$ for the initial values of θ . However, this is, of course, not sufficient, and we need to study numerically which initial conditions ensure the **DME** emergence. Moreover, this is expected to be better satisfied for $\theta_{0,A} \ll \theta_{0,B}$.

Furthermore, we have also considered the presence of the **OME** version of the **DME**, assuming that T overshoots its steady-state value. Then, the necessary condition for this effect is the opposite to the previous one. We have imposed that $\Phi_{0,A} > \Phi_{0,B}$ because we need for system B to exhibit a sufficiently strong overshoot effect, which is equivalent to $\theta_{0,A} > \theta_{0,B}$. However, the extreme condition $\theta_{0,A} \gg \theta_{0,B}$ might not be valid because, even if we want for system B to surpass enough system A, very high initial values of the temperature slope $\Phi_{0,A}$ could prevent system A from arriving earlier because of a very slow relaxation. Whereas the standard version of the **DME** is described by a crossing (or an odd number of them) of the corresponding thermal curves, the **OME** has no crossing (or an even number of them) in the standard thermal picture. Therefore, we have proposed a function of T/T^{st} , similar to the local-equilibrium **KLD** functional derived in Article 1 ([Section 5.2](#)), and denoted as \mathfrak{D} [see Eq. (32) for Article 6 ([Section 9.2](#))], which plays the role of the thermal distance introduced in [Section 3.3](#). That is, the properties of \mathfrak{D} implies that both the standard **TME** and the **OME** are described by a crossover (or an odd number of them) of the evolution curves $\mathfrak{D}_A(t)$ and $\mathfrak{D}_B(t)$.

From the identification of the necessary conditions for the initial values of the variables of the system, we have elaborated a preparation protocol for observing the **DME** in this type of setup. This preparation protocol is based on the steady states of the described system, in which we have properly used the property of θ^{st} to be an increasing value of ε , as well as the characterization of the absence or presence of overshoot via ε_{cr} . Owing to these results, for the observation of the standard **DME**, we have proposed the initial values $\theta_{0,A} = \theta^{\text{st}}(\varepsilon = 0)$ and $\theta_{0,B} = \theta^{\text{st}}(\varepsilon = 1)$, in order to ensure the necessary condition $\theta_{0,A} < \theta_{0,B}$. Afterwards, we must choose the proper values of T_A^{wn} and T_B^{wn} , such that the associated steady states ($T_{0,A}$ and $T_{0,B}$) verify the conditions $T_{0,A}/T_{\text{ref}}^{\text{wn}} > T_{0,B}/T_{\text{ref}}^{\text{wn}} > T_{\text{ref}}^{\text{st}}/T_{\text{ref}}^{\text{wn}}$, with $T_{\text{ref}}^{\text{wn}}$ and $T_{\text{ref}}^{\text{st}}$ being the noise and stationary temperature at the reference or final thermostat. In addition, we must choose

$\varepsilon_{\text{ref}} < \min\{\varepsilon_{\text{cr}}(T_{0,A}/T_{\text{ref}}^{\text{st}}, \theta_{0,A}), \varepsilon_{\text{cr}}(T_{0,B}/T_{\text{ref}}^{\text{st}}, \theta_{0,B})\}$ to prevent overshoots. Finally, we let both samples evolve.

The proposed protocol to observe the **OME** has been practically identical, except for two main points. Firstly, the choice of the initial conditions of θ is exchanged, i.e., $\theta_{0,A} = \theta^{\text{st}}(\varepsilon = 1)$ and $\theta_{0,B} = \theta^{\text{st}}(\varepsilon = 0)$. This has been imposed to ensure the necessary condition for the **OME**, $\theta_{0,A} > \theta_{0,B}$. Secondly, the reference value of the noise ratio has set to be $\varepsilon_{\text{ref}} > \varepsilon_{\text{ref}}(T_{0,B}/T_{\text{ref}}^{\text{st}}, \theta_{0,B})$ to force the overshoot in system B.

These two protocols have been summarized in Figures 8 and 9 of Article 6 ([Section 9.2](#)). Moreover, in Figure 10 of Article 6 ([Section 9.2](#)), we have computed numerically a phase diagram in which the presence or absence of the standard **DME** and the **OME** is settled.

Finally, we have prepared **DSMC** and **EDMD** computer simulations following the protocols proposed, and for initial conditions inside the standard **DME** and **OME** regions of the mentioned phase diagrams. As shown in Figures 11 and 12 of Article 6 ([Section 9.2](#)), there is quite an excellence agreement between simulation results and theoretical predictions.

We hope this work could encourage the experimental reproducibility of this system, motivated by an apparent simplicity of the two-dimensional setup, as well as further investigation in **ME** protocols. In fact, it would be interesting to compute the non-Gaussianities of these homogeneous states to reinforce the **MA** used in this work, which has been concluded to be in good accordance with the computer simulations.

The aim of this chapter is to expose the main concluding remarks that must be highlighted from the results and procedures developed in this thesis, as well as planned or possible future work continuing this research line.

12.1 Conclusions

The core of the thesis has been structured in three main blocks: one dedicated to molecular gases and the other two centered on granular gases, first the **IHS** model and then the **IRHS** one. In the three blocks, dynamical properties of homogeneous states of freely evolving and driven setups have been studied, as well as the emergence of memory effects. Remarkably, in the last block, the influence of roughness on the transport properties and the stability of the **HCS** have been detailed. All these analyses were performed in the context of the **BE**, which includes Fokker–Planck-like terms in the cases of thermostatted systems. In what follows, the main conclusions for each block of thesis will be specified.

12.1.1 Molecular gases

We have described the relaxation of the homogeneous states of a dilute molecular gas of identical **HS** immersed in an interstitial fluid acting as a thermal bath at constant temperature T_b and interacting with it via a random force and a nonlinear drag force. This has been developed in the context of the corresponding **BFPE**.

Article 1

- ▶ The phenomenology of the **ME** emergence in the latter system has been described in much detail. In addition, a conceptual and mathematical differentiation between the thermal and entropic descriptions has been developed.
- ▶ We have observed a novel **TME** scenario based on an overshoot through the equilibrium temperature of one of the samples in a **ME** experiment, referred to as the **OME**. In a description based on the nonequilibrium (time-dependent) temperature, T , there is no crossing between the thermal curves. To solve this issue, we have proposed the study of the **TME** through a thermal distance—coinciding with the local-equilibrium **KLD**—which detects either the usual forms of **TME** and the **OME** by means of the crossing-point-based arguments.
- ▶ Finally, **DSMC** simulations agree with the approximations of the theory, reinforcing the hypotheses of the developed mathematical approach. Moreover, **EDMD** simulation outcomes show quite a good accordance with **DSMC** results and the theory, indicating a validation of the description with respect to realistic (computer) experiments.

12.1.2 Inelastic granular gases

We have addressed two problems in granular gases described by the **IHS** model. The first one, in Article 2 (Section 6.2) and Article 3 (Section 6.3), has been the absence of a formal proof for a granular version of the H -theorem in freely evolving granular gases. On the other hand, in Article 4 (Section 7.2), we have developed the Boltzmann kinetic theory and an analysis of some memory effects, which are present in a dilute and homogeneous granular gas of inelastic and hard d_t -spheres immersed in an interstitial fluid, whose interaction with the granular fluid is characterized via the same model as in the molecular gaseous system studied in Article 1 (Section 5.2).

Articles 2 and 3

- ▶ In Article 2 (Section 6.2), we have proposed an approximate theoretical scheme based on a **SA**, in which we have recovered previous values for the cumulants at the **HCS**, and the evolution of T , a_2 and a_3 from arbitrary initial conditions toward the **HCS**.
- ▶ Moreover, in Article 2 (Section 6.2), the problems of the Boltzmann's H quantity that prevent it from being a proper nonequilibrium entropy functional have been identified. Fundamentally, they are based on the noninvariance of H under nonunitary transformations and they are solved by the introduction of the **KLD**. Then, the problem has been reduced to find the proper reference **VDF** (if it exists)

that could allow this quantity to behave as a nonequilibrium entropy.

- ▶ In Articles 2 (Section 6.2) and 3 (Section 6.3), a numerical scheme and a toy model to study the evolution toward the HCS of the KLD with an arbitrary reference VDF has been derived. In fact, it has been proved under the SA theoretical scheme that the HCS VDF could solve the problem, as it has been conjectured by other authors [BPV13; Gar+15; PP17]. Moreover, this theoretical approach indicates that the Maxwellian VDF is not a proper reference, in which case nonmonotonic behaviors are predicted.
- ▶ The before theoretical analysis is supported, in Articles 2 (Section 6.2) and 3 (Section 6.3), by DSMC and EDMD simulations from a wide range of values of the coefficient of normal restitution, α , and different initial VDF.
- ▶ Furthermore, the proper meaning of the KLD functional has indicated the deviations of the HCS VDF from a Maxwellian one, in Article 2 (Section 6.2), revealing a nonmonotonic dependence with α .
- ▶ A velocity-inversion experiment is developed in Article 3 (Section 6.3) for granular gases described by the IHS model. It has revealed a strong suppression of the antikinetic stages observed in the elastic case due to the role of inelasticity at the collisional level, which is present even in the quasi-elastic case.

Article 4

- ▶ The nonequilibrium time-dependent and steady states of a granular gas of inelastic hard d_t -spheres under nonlinear drag have been described in Article 4 (Section 7.2). The theoretical analysis, under a SA, reveals that this system is, at its steady state, further from equilibrium as compared with the linear drag case. This is deduced from the steady-state values of the quantities $T/T_b - 1$ and a_2 , which are, in general, further from the equilibrium values as the nonlinear control quantity, γ , increases. In fact, a critical value of the nonlinear quantity has found beyond which the steady-state VDF is leptokurtic for every value of the coefficient of normal restitution. Those results have been confirmed by DSMC and EDMD simulation results.
- ▶ This system has shown the emergence of the Mpemba and Kovacs-like memory effects. The characterization of the evolution of the system toward the steady state from the SA has allowed us to describe them. In the case of the KE, we have identified the conditions related to the direction of the Kovacs humps which depends on the sign of the difference $a_2^{\text{st}} - a_2(t_K^*)$. Concretely, upward humps correspond with the fulfillment of the condition $a_2(t_K^*) < a_2^{\text{st}}$ and a downward hump with $a_2(t_K^*) > a_2^{\text{st}}$. Outcomes from DSMC and EDMD simulations are in quite a good agreement with the theoretical predictions, supporting the findings.

12.1.3 Inelastic and rough granular gases

We have studied how the implementation of surface roughness via the **IRHS** model affects the granular gaseous dynamics. We have developed the description of the homogeneous states for the case of free evolution in Article 5 (Section 8.2) and for the driven case with the **ST** in Article 6 (Section 9.2). Moreover, the transport properties of the freely evolving granular gas and the stability of the **HCS** have been analyzed in Articles 7 (Section 10.2) and Article 8 (Section 10.3), respectively.

Article 5

- ▶ We have characterized the non-Gaussianities of the **HCS** of a dilute granular gas described by the **IRHS** model via the first-order nontrivial cumulants and the **HVT** of the main marginal **VDF** for **HD** and **HS**.
- ▶ The analysis of the cumulants has been carried out by a **SA**. The theoretical results have shown values for **HD** further from equilibrium than those for **HS**, in general, and some values $a_{02}^H, a_{11}^H \sim \mathcal{O}(1)$. This could indicate a possible breakdown of the **SA**.
- ▶ The theoretical predictions of the cumulants for **HD** are accurate as compared with **DSMC** and **EDMD** results for small values of these quantities and agree, in a more qualitative way, with the cases of larger predicted values, where the **SA** is expected to worsen.
- ▶ We have extended the well-known overpopulated **HVT** of the **HCS VDF** to the rough case. The **HVT** form of the translational marginal **VDF** coincides with the **IHS** case, as expected, which fulfills an exponential decay, i.e., $\phi_c^H \sim e^{-\gamma_c c}$, but with the exponent modified by the implementation of the surface roughness of the particles. Moreover, we have made predictions, under certain approximations, of the **HVT** for ϕ_w^H and ϕ_{cw}^H , in which scale-free forms have been derived, i.e., $\phi_w^H \sim w^{-\gamma_w}$ and $\phi_{cw}^H \sim (cw)^{-\gamma_{cw}}$. The latter results indicate the existence of divergences for an infinite set of higher-order cumulants related essentially to the rotational degrees of freedom.
- ▶ The latter scaling forms have been observed in **DSMC** and **EDMD** simulations for **HD**. A quite good accurate prediction for the theoretical value of γ_w has been observed as compared with simulations, whereas for γ_c and γ_{cw} the agreement is more qualitative.

Article 6

- ▶ The homogeneous states of a dilute granular gas of inelastic and rough **HD** under the action of the **ST** have been described from a kinetic-theory perspective and under a **MA** for the time-dependent and the nonequilibrium steady-state **VDF**.

- ▶ The steady-state value of the granular mean temperature, T^{st} , is proportional to the noise temperature, T^{wn} , and depends, in a nonmonotonic way, on the rotational-to-total noise ratio, ε . On the other hand, the steady-state value of the rotational-to-translational temperature ratio, θ^{st} , follows a monotonic dependence on ε .
- ▶ The **DME** condition has been extended for the **TME** (without overshoot) of Ref. [Tor+19] (which was based on $\varepsilon = 0$) to all possible values of ε . The condition of the standard form of the **DME** reveals that a system with initially more translational energy than rotational could relax earlier to the steady state. On the contrary, a system with much more initial rotational energy than translational could evolve more slowly to the steady state as compared with the latter case. The main reason is that translational energy favors collisions which produce the cooling toward the steady-state temperature.
- ▶ We have detailed the emergence of the **OME** and derived its necessary condition for the initial slopes of a pair of samples in a **ME** experiment. In addition, the overshoot phenomenon of a thermal curve has been demonstrated to emerge for values of ε greater than a critical value, ε_{cr} , for each initial condition. The detection of the **OME** has been guided by a thermal distance recalling the one derived in Article 1 (Section 5.2).
- ▶ From the knowledge of the dependence of nonequilibrium steady states of the system on the parameters of the **ST**, $(T^{\text{wn}}, \varepsilon)$, as well as the developed necessary conditions, we have elaborated a protocol to detect the **DME** in the standard and **OME** forms. In those protocols, using that the necessary conditions for the initial slopes depend on very disparate values of θ^0 , the initial conditions are elaborated from previous thermalizations of the involved samples to steady-states of the **ST** with either $\varepsilon = 0$ or $\varepsilon = 1$. This is to fulfill that one sample must possess much more translational than rotational energy, and the other way around for the other sample.
- ▶ Finally, **DSMC** and **EDMD** simulation results confirm the theoretical approaches in the transient and steady states of the system, as well as the protocol designed to observe the **ME** in this setup.

Articles 7 and 8

- ▶ In Article 7 (Section 10.2), the transport properties of a freely evolving monodisperse and dilute granular gas of inelastic and rough **HD** and **HS** have been computed in a common mathematical framework, by means of the **NSF** transport coefficients from the **CE** method and using a **MA** for $f^{(0)}$ (the local version of the **HCS VDF**) and a Sonine-like approximation for $f^{(1)}$.
- ▶ Explicit expressions of the (reduced) transport coefficients for this model of

granular gas have been obtained: the (reduced) shear viscosity η^* , the (reduced) bulk viscosity η_b^* , the (reduced) thermal conductivity λ^* , the (reduced) Dufour-like coefficient μ^* , and the velocity-divergence transport coefficient ξ , all of them as functions of the coefficients of restitution, (α, β) , the reduced moment of inertia, κ , and the translational and rotational degrees of freedom, (d_t, d_r) .

- ▶ From the expressions of the transport coefficients, we have recovered, in Article 7 (Section 10.2), already known results for purely smooth particles ($\beta = -1, d_r \rightarrow 0$), as well as novel ones in terms of the degrees of freedom for the quasismooth ($\beta \rightarrow -1$) and Pidduck's ($\alpha = \beta = 1$) limits.
- ▶ From the knowledge of the transport coefficients, in Article 8 (Section 10.3), we have analyzed the stability of the HCS under linear nonhomogeneous perturbations, in which we have recovered known results for HS, and obtained novel results for HD. We have computed the critical wave numbers associated with cluster and vortex instabilities, as well as the critical length of the system for instabilities, L_c .
- ▶ The theoretical linear stability analysis predicts a region of the parameter space where the HCS is always unstable due to clustering, referred to as HUR in this thesis, which would imply a breakdown of the hydrodynamics of the granular gaseous system. However, EDMD has revealed that there exist stable conditions in contradiction with this strong prediction, although a good agreement is observed outside the HUR. This could be signaling that, whereas this region seems to be highly unstable, it might not be absolutely unstable. The theoretical strong prediction could fail due to the breakdown of the approximations. This is probably linked to the strong non-Gaussianities of the HCS VDF studied in Article 5 (Section 8.2).
- ▶ Finally, the clustering detection in the EDMD simulations has been addressed via the application of the KLD of the spatial particle distribution with respect to a homogeneous Poisson distribution as reference. This has been complemented by the control of some non-Gaussianities of the HCS VDF computed in Article 5 (Section 8.2).

12.2 Outlooks

In this thesis, different theoretical tools have been developed, accompanied by the implementation of the corresponding simulation methods to check whether the approximations and predictions were reasonable or not. We hope that the knowledge created in the works appearing in this thesis could encourage future works, not only from the most personal point of view, but also, in general, in the granular gas community.

One of the objectives of the thesis has been the study of driven states in granular gases of inelastic and rough particles under the ST. However, the non-Gaussian properties

of the *steady* VDF have been restricted to the freely evolving case. We are planning to study in deep those properties for the ST, which absorbs the limiting cases of purely translational ($\varepsilon = 0$) or rotational ($\varepsilon = 1$) drivings. It would be interesting to determine whether the MA used in Article 6 (Section 9.2) is a good approach at the steady state for every pair of values of the coefficients of restitution (α, β), as well as for different values of the reduced moment of inertia κ , as computer simulations in Article 6 (Section 9.2) indicate. The first nontrivial cumulants and the HVT of the marginals VDF at the steady state would be again a good measure for that. Moreover, once the homogeneous steady state is described, it would be important the determination of the transport properties by means of the NSF transport coefficients, as well as checking whether the action of the driving associated with the ST erases, or not, any sort of instability, as occurs with stochastic thermostats acting on granular gases of inelastic particles [KG18; KG19; Gar19].

Furthermore, a connection between the nonlinear drag analysis and the driving by means of the ST would be the consideration of nonlinear driving to the translational and rotational degrees of freedom. An extension of Refs. [CLH00; Her+05] with the tools developed in this thesis would be quite an interesting research topic.

Moreover, the results from Section 10.3 for the HUR in a freely cooling granular gas of inelastic and rough HD, indicates that the approach to the transport properties of this system should be improved. Some methodologies could be, firstly, a modification due to the effect of the Sonine coefficients of the HCS VDF, as done in Ref. [GSM07] for the IHS model, or the introduction of the predicted HVT into the computations in a proper way. The investigation of this issue could be complemented by the determination of the NSF transport coefficients by means of computer simulations. In addition, the application of this knowledge to the rheological properties of a granular gas of rough particles could lead to interesting results, as already studied in the case of inertial suspensions in Ref. [GG20].

Whereas the models studied in this thesis seem to describe properly the granular gas dynamics, being the main predicted (translational) properties of the freely evolving and driven systems observed in experiments [Maa+08; Tat+09; Har+18; YSS20; GF23], the hard d_t -sphere and the constant coefficient of normal restitution are, at the end, approaches and simplifications. In fact, in Ref. [YSS20] is observed an excess of cooling as compared with the IHS, that could be explained by introducing the role of the rotational degrees of freedom, which has been already commented throughout his memoir. Nevertheless, this latter implementation, might not explain all the discrepancies as commented in Ref. [Yu+21] for a model for rough particles [HHZ00] different from the IRHS one studied in this thesis. Even more, the consideration for β to be constant is also an approximation. The effective coefficient of tangential restitution could depend on the impact angle because of friction [MBF76; LTL97]. Moreover, the theory usually

characterizes systems of infinitely many particles without any boundary interaction. But, particle-wall collisions could explain the observed excess of cooling too. All these issues, as well as past and future experimental observation should guide our future theoretical modeling of these systems toward more realistic theories, with the attempt of explaining, in more detail, the real behavior of granular gases.

Another compelling topic, which would extend the present studies, is the application of all these techniques to polydisperse systems. Moreover, in a polydisperse system, its properties would depend on the set of coefficients of restitution, generally different, $\{\alpha_{ij}, \beta_{ij}\}$, the concentrations of the different species $\{x_i \equiv n_i / \sum_k n_k\}$, and the mechanical parameters of the mixture, that is, the masses, $\{m_i\}$, diameters, $\{\sigma_i\}$, and reduced moments of inertia, $\{\kappa_i\}$. Therefore, from this huge number of parameters, we could look for very interesting phenomena. The expressions of the energy production rates have been computed via [MA](#) in previous works within our degrees-of-freedom context [[MS19a](#); [MS19b](#)] as a generalization of the results of Ref. [[SKG10](#)]. Moreover, during my visiting period at the [PMMH of the ESPCI](#) in Paris (France), with Prof. Hans J. Herrmann, we started an analysis of diffusion phenomena in granular gases of inelastic and rough particles, in which we have already computed the diffusion coefficients associated with a binary system described by a [IRHS](#) model, and we are studying their influence into the segregation mechanisms. We expect to publish soon the results, which would generalize previous works in the inelastic but smooth case [[JY02](#); [BRM05](#); [Gar06](#); [GV10](#); [Gar11](#); [BKD11](#); [BKD12](#); [GMV13](#); [VGK14](#); [Gar19](#)] and would reveal novel phenomena due to the role of roughness into the collision dynamics. Another interesting effect appearing in polydisperse granular systems is a situation in which intruders, added to a host gas, mimic the thermal behavior of the latter. In fact, during the predoctoral period, some computations about the so-called *mimicry effect* [[San18](#); [Las+19](#)] in this type of systems, initiated at Ref. [[MS19a](#)], have been carried out and it would be desirable to continue those in the future.

In addition, we have worked in this thesis under the assumptions of instantaneous collisions in granular interactions. However, this could lead to problems, such as the inelastic collapse, as explained, for example, in Ref. [[LM98](#)]. Therefore, the consideration of a finite-time duration of a collision, due to the particle softness, could solve this issue, implying corrections to the transport properties of the granular gases [[ST20](#); [Tak21](#); [THH22](#)]. In fact, during my stay at [Skolkovo Institute of Science and Technology](#) in Moscow (Russia), with Prof. Nikolai V. Brilliantov, we started to study how this consideration affects the self-diffusion properties of a granular gas of inelastic [HS](#). We expect to publish soon the results of this work and extend the analysis to the rest of transport properties.

Finally, it would be interesting to study the homogeneous and transport properties of active matter within the tools described in this thesis. In fact, an interesting topic would

be the study of memory effects from a kinetic-theory point of view, such as the [ME](#) or [KE](#), which have already been of interest in the statistical physics community [[KSI17](#); [SL22](#)], but from other approaches. Furthermore, an analysis of the transport properties could lead to interesting collective phenomena in active systems.

APPENDICES

Fokker–Planck equation associated with a Langevin-like equation



Paul Langevin derived his famous equation in 1908 [Lan08; LG97], with the aim to understand the Brownian motion. The LE was derived after the pioneering Einstein's [Ein05] and Smoluchowski's [Smo06] works, in 1905 and 1906, respectively, which had already put into manifest the relevance of the action of atomic motion in fluids. On the other hand, the FPE is named after Adriaan Fokker and Max Planck, who independently derived this equation in 1914 [Fok14] and 1917 [Pla17], respectively. After its derivation in different contexts, the first application of this equation was, again, to describe statistically the Brownian motion [QG13]. These two equations, the LE and the FPE, became fundamental in the study of diffusion processes.

The aim of this appendix is to summarize the relationship between a Langevin-like equation and a FPE and finally specify this for the thermostatted states used in this thesis (see Subsection 2.4.1 and Subsection 2.4.2). Whereas the former is a SDE, usually written in terms of the velocity, \mathbf{v} , of a particle, the latter is a partial differential equation on the probability density, i.e., the one-body VDF in velocity terms. In general, there is not always a relationship between an arbitrary SDE and a FPE, but we will work under the proper circumstances where this is guaranteed.

A.1 General relations

Let us work in a d_t -dimensional velocity space and let us consider a general nonlinear Langevin-like equation, which in differential form reads

$$d\mathbf{v} = \mathbf{a}(\mathbf{v})dt + \mathbf{b}(\mathbf{v}) \cdot d\mathbf{W}_t, \quad (\text{A.1})$$

where \mathbf{W}_t is a Wiener process [Ris12; Tab19], \mathbf{a} is a vector function, and \mathbf{b} is a matrix function. Then, the latter SDE can be written as [Ris12; Tab19]

$$\dot{\mathbf{v}} = \mathbf{a}(\mathbf{v}) + \mathbf{b}(\mathbf{v}) \cdot \bar{\eta}(t), \quad (\text{A.2})$$

with the random vector $\bar{\eta}(t)$ following the properties of a white noise with unit variance,

$$\langle \bar{\eta}(t) \rangle = \mathbf{0}, \quad \langle \bar{\eta}(t) \bar{\eta}(t') \rangle = \mathbb{1}_{d_t} \delta(t - t'). \quad (\text{A.3})$$

On the other hand, a FPE is a second order partial differential equation on the VDF, which reads

$$\frac{\partial f(\mathbf{v}, t)}{\partial t} + \frac{\partial}{\partial \mathbf{v}} \cdot \left[\mathbf{D}^{(1)}(\mathbf{v}, t) f(\mathbf{v}, t) \right] - \left(\frac{\partial}{\partial \mathbf{v}} \frac{\partial}{\partial \mathbf{v}} \right) : \left[\mathbf{D}^{(2)}(\mathbf{v}, t) f(\mathbf{v}, t) \right] = 0, \quad (\text{A.4})$$

where $\mathbf{D}^{(1)}$ and $\mathbf{D}^{(2)}$ are usually called the *drift vector* and the *diffusion matrix*, respectively.

In other words, the FPE is the truncation of the Kramers–Moyal [Kam07; Ris12; Tab19] expansion of the VDF up to second order terms (higher order truncations are forbidden by Pawula theorem [Paw67; Tab19]). Then, the link between both equations become from the identification of the drift vector and the diffusion matrix with the two first coefficients of such expansion. The result depends on the interpretation in which Eq. (A.2) is solved. The drift and diffusion coefficients associated with Eq. (A.2) read [Kam07; Vol+10; MM12; Ris12; Tab19]

$$D_i^{(1)} \equiv \lim_{h \rightarrow 0} \left. \frac{\langle v_i(t+h) - v_i(t) \rangle}{h} \right|_{\mathbf{v}(t)=\mathbf{v}} = a_i(\mathbf{v}) + \epsilon \sum_{j=1}^{d_t} \sum_{k=1}^{d_t} b_{kj}(\mathbf{v}) \frac{\partial}{\partial v_k} b_{ij}(\mathbf{v}), \quad i = 1, \dots, d_t \quad (\text{A.5a})$$

$$D_{ij}^{(2)} \equiv \lim_{h \rightarrow 0} \left. \frac{\langle [v_i(t+h) - v_i(t)][v_j(t+h) - v_j(t)] \rangle}{2h} \right|_{\mathbf{v}(t)=\mathbf{v}} = \frac{1}{2} \sum_{k=1}^{d_t} b_{ik}(\mathbf{v}) b_{jk}(\mathbf{v}), \quad i, j = 1, \dots, d_t, \quad (\text{A.5b})$$

for the Itô ($\epsilon = 0$) [Kam07], Stratonovich ($\epsilon = 1/2$) [Kam07], and Klimontovich ($\epsilon = 1$) [Kli94] interpretations. Moreover, from Itô's lemma [Tab19], $D_{i_1, \dots, i_n}^{(n)} = 0, \forall i_1, \dots, i_n$ and $\forall n \geq 3$. Then, the relationship between the nonlinear LE defined by Eq. (A.2) and the FPE is guaranteed, and higher-order terms for the Kramers–Moyal expansion do not apply.

In particular, the original LE coincides with the case in which $\mathbf{a}(\mathbf{v}) \equiv -\xi_0 \mathbf{v}$, and $\mathbf{b}(\mathbf{v}) \equiv \sqrt{2\xi_0 T_b / m} \mathbb{1}_{d_t}$, in which the FDT has been already assumed [see Eq. (2.39)]. Then,

the latter three interpretations give the same **FPE**, reading

$$\frac{\partial f(\mathbf{v}, t)}{\partial t} - \frac{\partial}{\partial \mathbf{v}} \cdot \left(\xi_0 \mathbf{v} + \frac{\xi_0 T_b}{m} \frac{\partial}{\partial \mathbf{v}} \right) f(\mathbf{v}, t) = 0. \quad (\text{A.6})$$

Let us particularize for the two thermostats considered in this thesis.

A.2 Langevin dynamics with a nonlinear drag

Let us work under the conditions of **Subsection 2.4.1**. Here, in the free streaming, the (Brownian) particles of the dilute gas are considered to follow a nonlinear **LE** with a velocity-dependent quadratic drag coefficient,

$$\dot{\mathbf{v}} = -\xi(v)\mathbf{v} + \chi(v)\bar{\boldsymbol{\eta}}(t), \quad \xi(v) = \xi_0 \left(1 + \gamma \frac{mv^2}{T_b} \right), \quad (\text{A.7})$$

such that $\bar{\boldsymbol{\eta}}(t)$ corresponds to a random variable, describing a white noise with unit variance following Eq. (A.3). Comparing Eq. (A.7) with Eq. (A.2), one can identify that $\mathbf{a}(\mathbf{v}) = -\xi(v)\mathbf{v}$, and $\mathbf{b}(\mathbf{v}) = \chi(v)\mathbb{1}_{d_t}$. Then, the drift vector and diffusion matrix read

$$\mathbf{D}^{(1)} = - \left[\xi(v) - \frac{\epsilon}{v} \chi(v) \chi'(v) \right] \mathbf{v}, \quad \mathbf{D}^{(2)} = \frac{\chi^2(v)}{2} \mathbb{1}_{d_t}. \quad (\text{A.8})$$

From this, we infer that the **FPE** depends on the interpretation of the Brownian process, and it reads

$$\frac{\partial f}{\partial t} - \frac{\partial}{\partial \mathbf{v}} \cdot \left[\xi(v)\mathbf{v} + \frac{\chi^{2\epsilon}(v)}{2} \frac{\partial}{\partial \mathbf{v}} \chi^{2(\epsilon-1)}(v) \right] f = 0. \quad (\text{A.9})$$

Thus, the (differential) fluctuation-dissipation relation that can be deduced from the latter **FPE** turns out to be

$$\xi(v) + \frac{1-\epsilon}{2v} \frac{\partial \chi^2(v)}{\partial v} = \frac{m\chi^2(v)}{2T_b}. \quad (\text{A.10})$$

Hence, only for $\epsilon = 1$, i.e., the Klimontovich interpretation, one recovers the original fluctuation-dissipation relation. Therefore, if we impose that relation to be held, the resulting **FPE** is

$$\frac{\partial f}{\partial t} - \frac{\partial}{\partial \mathbf{v}} \cdot \left[\xi(v)\mathbf{v} + \frac{\chi^2(v)}{2} \frac{\partial}{\partial \mathbf{v}} \right] f = 0. \quad (\text{A.11})$$

It can be proved from Eqs. (A.8) and (A.10) that the latter **FPE** is recovered from the following nonlinear **LE** in the Itô interpretation,

$$\dot{\mathbf{v}} = -\xi_{\text{eff}}(v)\mathbf{v} + \chi^2(v)\bar{\boldsymbol{\eta}}(t), \quad \xi_{\text{eff}}(v) \equiv \xi(v) - 2\xi_0\gamma = \xi_0 \left(1 - 2\gamma + \gamma \frac{mv^2}{T_b} \right), \quad (\text{A.12})$$

where we have used the explicit form of the nonlinear drag coefficient written in Eq. (A.7). The latter nonlinear LE, Eq. (A.12), will be helpful in the numerical resolution of this dynamics in the Itô interpretation (see Appendix C).

A.3 Splitting thermostat

In the case of the thermostat introduced in Subsection 2.4.2 and, according to the stochastic force and torque acting on the system [see Eqs. (2.49) and (2.50), respectively], we obtain the following two Langevin-like equations

$$\dot{\mathbf{v}} = \chi_t \bar{\boldsymbol{\eta}}_{d_t}(t), \quad \dot{\boldsymbol{\omega}} = \chi_r \bar{\boldsymbol{\eta}}_{d_r}(t), \quad (\text{A.13})$$

with $\bar{\boldsymbol{\eta}}_{d_t}$ and $\bar{\boldsymbol{\eta}}_{d_r}$ being d_t - and d_r -dimensional random vectors describing a white noise with unit variance such that, from Eq. (A.3), it can be interpreted that

$$\langle \bar{\boldsymbol{\eta}}_{d_t}(t) \rangle = \mathbf{0}, \quad \langle \bar{\boldsymbol{\eta}}_{d_t}(t) \bar{\boldsymbol{\eta}}_{d_t}(t') \rangle = \mathbb{1}_{d_t} \delta(t - t'), \quad (\text{A.14a})$$

$$\langle \bar{\boldsymbol{\eta}}_{d_r}(t) \rangle = \mathbf{0}, \quad \langle \bar{\boldsymbol{\eta}}_{d_r}(t) \bar{\boldsymbol{\eta}}_{d_r}(t') \rangle = \mathbb{1}_{d_r} \delta(t - t'). \quad (\text{A.14b})$$

In a more compact way, working with the variable $\boldsymbol{\Gamma} \in \mathbb{R}^{d_t} \times \mathbb{R}^{d_r}$, Eq. (A.13) can be expressed as

$$\dot{\boldsymbol{\Gamma}} = \mathbf{X} \cdot \bar{\boldsymbol{\eta}}(t), \quad \mathbf{X} \equiv \begin{pmatrix} \chi_t \mathbb{1}_{d_t} & \mathbf{0} \\ \mathbf{0} & \chi_r \mathbb{1}_{d_r} \end{pmatrix}, \quad \bar{\boldsymbol{\eta}} \equiv \begin{pmatrix} \bar{\boldsymbol{\eta}}_{d_t} \\ \bar{\boldsymbol{\eta}}_{d_r} \end{pmatrix}. \quad (\text{A.15})$$

Therefore, as it occurs with the original LE, the associated FPE coincides for Itô, Stratonovich, and Klimontovich interpretations. The drift vector and diffusion matrix, for this case, are

$$\mathbf{D}^{(1)} = \mathbf{0}, \quad \mathbf{D}^{(2)} = \frac{1}{2} \mathbf{X} \mathbf{X}^\top = \frac{1}{2} \begin{pmatrix} \chi_t^2 \mathbb{1}_{d_t} & \mathbf{0} \\ \mathbf{0} & \chi_r^2 \mathbb{1}_{d_r} \end{pmatrix}. \quad (\text{A.16})$$

Then, the FPE is straightforwardly derived, reading

$$\frac{\partial f}{\partial t} - \frac{\chi_t^2}{2} \left(\frac{\partial}{\partial \mathbf{v}} \right)^2 f - \frac{\chi_r^2}{2} \left(\frac{\partial}{\partial \boldsymbol{\omega}} \right)^2 f = 0. \quad (\text{A.17})$$

Note that this coincides with the Fokker–Planck-related part of the BFPE in Eq. (2.51), acting on the free-streaming contribution.

Derivation of the nonlinear drag coefficient for a quasi-Rayleigh gas

B

Let us work under the conditions introduced in [Subsection 2.4.1](#). That is, we consider a [QR](#) gas of Brownian heavy particles with masses m , number density n , and velocities \mathbf{v} , in contact with a dilute gas of lighter particles with masses m_b , number density n_b , and velocities \mathbf{v}_b in equilibrium at temperature T_b . The ensemble corresponding to the dilute gas of light particles is assumed to be acting as a thermal bath on the heavy ones. The aim of this section is to obtain formally an expression for the drag coefficient appearing in [Eq. \(2.44\)](#) from a power expansion in terms of m_b/m . For that, we will follow the derivations developed already in Refs. [[Fer00](#); [Fer07](#); [Fer14](#)] for [HS](#), but generalized to hard d_t -spheres.

We know that the average change of momentum of a Brownian particle due to a collision with a bath particle¹ is $m(\mathbf{v}' - \mathbf{v})/\tau$, such that τ is the mean free time, i.e., $\tau = (n_b \bar{Q}(g)g)^{-1}$, where $\mathbf{g} = \mathbf{v}_b - \mathbf{v}$ is the relative velocity and $\bar{Q}(g) = \int_{\Omega_{d_t}} d\bar{\Omega}_{d_t} B(g, \bar{\vartheta}_1)$ is the total cross section, $B(g, \bar{\vartheta}_1)$ being the differential cross section and $\bar{\vartheta}_1$ being the angle between \mathbf{g}' and \mathbf{g} . We will use that the d_t -differential solid angle is [[Blu60](#)]

$$d\Omega_{d_t} = \prod_{j=1}^{d_t-1} \sin^{d_t-j-1} \vartheta_j d\vartheta_j, \quad (\text{B.1})$$

where $0 \leq \vartheta_j \leq \pi$ for $j = 1, \dots, d_t - 2$ and $0 \leq \vartheta_{d_t-1} \leq 2\pi$. Its integration gives the total solid angle,

$$\Omega_{d_t} = \frac{2\pi^{\frac{d_t}{2}}}{\Gamma\left(\frac{d_t}{2}\right)}. \quad (\text{B.2})$$

Therefore, the average change of momentum of a Brownian particle due to a collision

¹Note that primed quantities refer to postcollisional values.

with a background fluid particle per unit time is given by

$$m \left(\frac{d\mathbf{v}}{dt} \right)_{\text{Brown}} = \Omega_{d_t-1}^2 \pi^{-d_t/2} n_b \mathbf{v} \frac{m m_b}{m + m_b} v_{\text{th},b}^{-d_t} \int_0^\infty dv_b v_b^{d_t-1} e^{-\frac{v_b^2}{v_{\text{th},b}^2}} \int_0^\pi d\vartheta_1 \sin^{d_t-2} \vartheta_1 \\ \times g \left(\frac{v_b}{v} \cos \vartheta_1 - 1 \right) \int_0^\pi d\bar{\vartheta}_1 \sin^{d_t-2} \bar{\vartheta}_1 (1 - \cos \bar{\vartheta}_1) B(g, \bar{\vartheta}_1), \quad (\text{B.3})$$

where we have used the collisional rule from the [EHS](#) model for two particles of different masses, m and m_b , for the gas and bath particles, respectively,

$$\mathbf{v}' - \mathbf{v} = -\frac{m_b}{m + m_b} (\mathbf{g}' - \mathbf{g}), \quad (\text{B.4})$$

that the background fluid particles are at equilibrium,

$$f_b(\mathbf{v}_b) \rightarrow f_M(\mathbf{v}_b) = \pi^{-d_t/2} v_{\text{th},b}^{-d_t} e^{-\frac{v_b^2}{v_{\text{th},b}^2}}, \quad (\text{B.5})$$

and $g' = g$ due to the elastic collision between gas and background fluid particles, i.e., no relative velocity magnitude is lost in the collision. Moreover, from the definition of the relative velocity, its modulus is given by the expression

$$g = v_b \sqrt{1 - 2 \frac{v}{v_b} \cos \vartheta_1 + \left(\frac{v}{v_b} \right)^2}, \quad (\text{B.6})$$

so that $\vartheta_1 = \arccos(|\mathbf{v}_b \cdot \mathbf{v}|/v_b v)$. From the [QR](#) gas assumption, one can expand the product $gB(g, \bar{\vartheta}_1)$ as a MacLaurin series for v/v_b or, equivalently $\sqrt{m_b/m}$, which up to the term of order $(m_b/m)^{3/2}$ is

$$gB(g, \bar{\vartheta}_1) = v_b \left\{ B(c_b, \bar{\vartheta}_1) - \left(\frac{m_b}{m} \right)^{1/2} \frac{c}{c_b} \cos \vartheta_1 \frac{\partial}{\partial c_b} \left[c_b B(c_b, \bar{\vartheta}_1) \right] + \frac{1}{2} \frac{m_b}{m} \left(\frac{c}{c_b} \right)^2 \right. \\ \times \left[\sin^2 \vartheta_1 B(c_b, \bar{\vartheta}_1) + c_b (1 + \cos^2 \vartheta_1) \frac{\partial B(c_b, \bar{\vartheta}_1)}{\partial c_b} + c_b^2 \cos^2 \vartheta_1 \frac{\partial^2 B(c_b, \bar{\vartheta}_1)}{\partial c_b^2} \right] \\ + \frac{1}{2} \left(\frac{m_b}{m} \right)^{3/2} \left(\frac{c}{c_b} \right)^3 \left[\sin^2 \vartheta_1 \cos \vartheta_1 \left(B(c_b, \bar{\vartheta}_1) - c_b \frac{\partial B(c_b, \bar{\vartheta}_1)}{\partial c_b} \right) - c_b^2 \cos \vartheta_1 \right. \\ \left. \times \frac{\partial^2 B(c_b, \bar{\vartheta}_1)}{\partial c_b^2} - \frac{1}{3} c_b^3 \cos^2 \vartheta_1 \frac{\partial^3 B(c_b, \bar{\vartheta}_1)}{\partial c_b^3} \right] \left. \right\} + \mathcal{O} \left[\left(\frac{m_b}{m} \right)^2 \right]. \quad (\text{B.7})$$

Inserting Eq. (B.7) into Eq. (B.3), and comparing with Eq. (2.44), we obtain for hard d_t -hyperspheres, whose differential cross-section is independent of the velocity and the

angle, $B(c, \bar{\vartheta}_1) = [(\sigma + \sigma_b)/4]^{d_t-1}$, that

$$\xi(v) \approx \xi_0 \left[1 - \frac{mv^2}{T_b} \frac{m_b}{2m} \left(1 - \frac{\xi_1}{\xi_0} \right) \right], \quad (\text{B.8})$$

with

$$\xi_0 = \frac{\Omega_{d_t}^2}{2^{d_t-1} \pi^{d_t/2} d_t} \Gamma\left(\frac{d_t+3}{2}\right) n_b \left(\frac{\sigma + \sigma_b}{2}\right)^{d_t-1} v_{\text{th},b} \frac{m_b}{m + m_b}, \quad \xi_1 = \xi_0 \frac{d_t+3}{d_t+2}. \quad (\text{B.9})$$

Thus, Eq. (B.8) can be expressed as

$$\xi(v) = \xi_0 \left(1 + \gamma \frac{mv^2}{T_b} \right), \quad (\text{B.10})$$

with

$$\gamma = \frac{m_b}{2(d_t+2)m}, \quad (\text{B.11})$$

which is expected to be small. The quadratic expression in Eq. (B.10) for the nonlinear drag coefficient, $\xi(v)$, has been used throughout this thesis, specifically in the development of Article 1 (Section 5.2) and Article 4 (Section 7.2).

Tests and numerical schemes for the thermostatted states

C

In [Subsection 4.3.6](#) we introduced the numerical scheme associated with the [AGF](#) algorithm proposed in Refs. [[SVM07](#); [Sca12](#)] for the usual [LE](#). That is, given the [LE](#) for the velocities, positions follow a [SDE](#) coming from a second integration of the [LE](#). The solutions to these equations are fundamental to reproduce the free-streaming evolution of particles in the absence of collisions. In the case of homogeneous [DSMC](#) simulations, only a first integration of the [LE](#) is enough. However, for the [AGF](#) scheme in [EDMD](#) simulations, the equation for the particle positions becomes fundamental.

The aim of this chapter is two-fold. First, results of the implementation of the [AGF](#) algorithm in the [EDMD](#) computer simulations for some test systems are shown. Then, the numerical schemes used for N -particle ensembles of the thermostatted systems introduced in this thesis (see [Section 2.4](#)) are exposed.

C.1 Test results

In order to test the implementation of the [AGF](#) algorithm in an [EDMD](#) custom-made program [[Meg23](#)], two homogeneous granular gaseous systems made of a monodisperse set of inelastic [HD](#) are proposed, whose results have been previously studied in the literature. The first one consists in a model of a granular suspension in a three-dimensional setup, where the [IHS](#) are in contact with an interstitial fluid, acting as a thermal bath at T_b . The interaction between the granular gas and the bath particles is described by the [LE](#). In the second system, the granular gas is driven by a stochastic thermostat.

C.1.1 Granular gas of inelastic HD with Langevin dynamics

Here, the numerical scheme for the solutions of the LE are the same as the ones derived in Subsection 4.3.6. The collisional part of the EDMD algorithm is described by the IHS model (see Subsection 2.3.2) in two dimensions. Previous works in Refs. [CVG12; CVG13] studied this homogeneous granular gaseous system with a linear drag force, $\mathbf{F}_{\text{drag}} = -m\xi_0\mathbf{v}$, plus a stochastic force with variance $2m\xi_0T_b$ (assuming the fulfillment of the FDT). Note that this is a particular case of the system analyzed in Article 4 (Section 7.2), concretely, in the linear drag limit ($\gamma \rightarrow 0$).

We have computed 14 runs of a system of 10^4 HD with $\xi_0/\nu_b \approx 0.89$ and $n\sigma^2 = 10^{-3}$, for different values of the coefficient of normal restitution, and for a time step $\Delta t \approx 0.02/\nu_b$. The initial velocities follow a Maxwellian distribution, 6 of the runs at temperature $T(0) = T_b/2$, and the other 6 at $T(0) = 2T_b$, for each value of the coefficient of normal restitution. In Figure C.1, the steady-state values T^{st}/T_b and a_2^{st} are compared with the theoretical results approximated by a SA, consisting in a truncation of the VDF up to the first nontrivial Sonine coefficient. Then, the theoretical values under this approach are given by the numerical solution of the following system of equations [see [CVG12] and the linear drag limit in Article 4 (Section 7.2)]

$$\frac{T_b}{T^{\text{st}}} - 1 = \frac{\mu_2^{(0)} + \mu_2^{(1)} a_2^{\text{st}}}{d_t \xi_0^*} \sqrt{\frac{T^{\text{st}}}{T_b}}, \quad (\text{C.1a})$$

$$a_2^{\text{st}} = \frac{\mu_4^{(0)} - (d_t + 2)\mu_2^{(0)}}{\mu_2^{(0)} - (d_t + 2) \left[\mu_2^{(0)} + \mu_2^{(1)} - d_t \xi_0^* (T^{\text{st}}/T_b)^{-3/2} \right]}, \quad (\text{C.1b})$$

with the coefficients

$$\mu_2^{(0)} = 1 - \alpha^2, \quad \mu_4^{(0)} = \left(d_t + \frac{3}{2} + \alpha^2 \right) \mu_2^{(0)}, \quad (\text{C.2a})$$

$$\mu_2^{(1)} = \frac{3}{16} \mu_2^{(0)}, \quad \mu_4^{(1)} = \frac{3}{32} (10d_t + 39 + 10\alpha^2) \mu_2^{(0)} + (d_t - 1)(1 + \alpha), \quad (\text{C.2b})$$

coming from the linearization of the collisional moments [GS95; NE98; MS00; BP04; BP06a; BP06b; SM09; Gar19; MS22a], introduced also in Section 7.2,

$$\mu_2 \approx \mu_2^{(0)} + a_2 \mu_2^{(1)}, \quad \mu_4 \approx \mu_4^{(0)} + a_2 \mu_4^{(1)}. \quad (\text{C.3})$$

Furthermore, the thermal evolution is compared, in Figure C.2, with the MA of its evolution equation, which reads [CVG12; CVG13; MS22a]

$$\frac{\partial(T/T_b)}{\partial t^*} = 2 \left(1 - \frac{T}{T_b} \right) \xi_0^* - \frac{2\mu_2^{(0)}}{d_t} \left(\frac{T}{T_b} \right)^{3/2}, \quad (\text{C.4})$$

with $\xi_0^* \equiv \xi_0/v_b$, and $t^* = tv_b$.

The simulation steady-state values in Figure C.1 come from the average over the 14 simulation runs and the last 50 points, for which the curve is ensured to be stationary. On the other hand, the evolution curves in Figure C.2 are the result of the average over the 6 different runs, according to the different initial conditions. We can conclude that the simulation results are in very good agreement with the theoretical predictions.

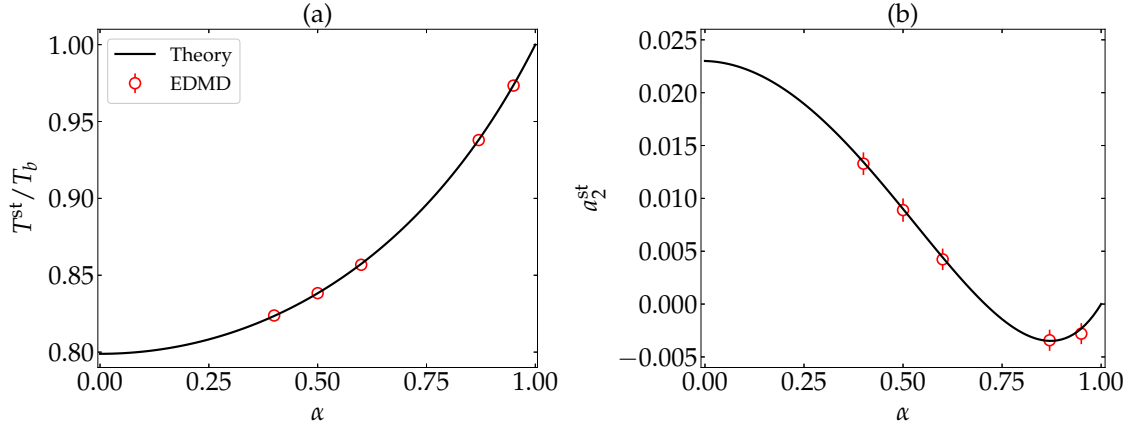


Figure C.1: Steady-state values of (a) the granular temperature, T^{st}/T_b , and (b) the excess kurtosis a_2^{st} , vs. the coefficient of normal restitution α for $\xi_0^* \approx 0.89$ and HS ($d_t = 2$). The circles (\circ) stand for EDMD simulation results, while the thick black lines (—) refer to the values corresponding to Eqs. (C.1). The values of the coefficient of normal restitution used in the simulations are $\alpha = 0.95, 0.87, 0.6, 0.5, 0.4$.

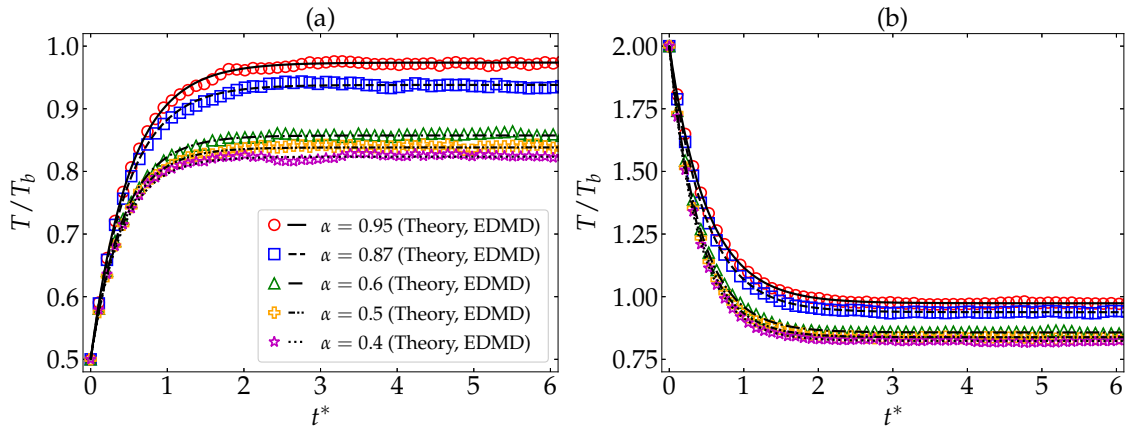


Figure C.2: Plot T/T_b vs. $t^* \equiv tv_b$ for a system of HD ($d_t = 2$), with $\xi_0^* \approx 0.89$, and for (a) $T(0) = T_b/2$ and (b) $T(0) = 2T_b$. The symbols ($\circ, \square, \triangle, +, *$) stand for EDMD simulation results, while the lines (—, - - - , · · ·) refer to the values corresponding to the differential equation, Eq. (C.4), for the different values of the coefficient of normal restitution, $\alpha = 0.95, 0.87, 0.6, 0.5, 0.4$.

C.1.2 Granular gas of inelastic HD driven by a stochastic thermostat

The system under consideration is a monodisperse and homogeneous granular gas, whose binary collisional rules are described by the IHS model, and the cooling is

counterbalanced by a constant energy injection via a stochastic force with variance $m^2\chi^2$. Its associated BFPE is

$$\frac{\partial f}{\partial t} + \chi^2 \left(\frac{\partial}{\partial \mathbf{v}} \right)^2 f = J[\mathbf{v}|f, f], \quad (\text{C.5})$$

with the Boltzmann collisional operator given by that of the IHS model [see Eq. (2.24)]. Note that this is a particular case of the ST restricted to translational degrees of freedom ($\varepsilon \rightarrow 0$) and acting on an inelastic but smooth system. Then, its associated Langevin-like equations for the free-streaming stage of the particles are

$$\dot{\mathbf{r}}(t) = \mathbf{v}(t), \quad \dot{\mathbf{v}}(t) = \chi \bar{\boldsymbol{\eta}}(t), \quad (\text{C.6})$$

with $\bar{\boldsymbol{\eta}}(t)$ being a random vector, representing a white noise of zero mean and unit variance [see Eqs. (4.7)]. Then, according to the description in Subsection 4.3.6, we obtain the following numerical scheme

$$\mathbf{v}_i(t + \Delta t) = \mathbf{v}_i(t) + \chi \mathcal{W}_i, \quad (\text{C.7a})$$

$$\mathbf{r}_i(t + \Delta t) = \mathbf{r}_i(t) + \mathbf{v}_i(t)\Delta t + \chi \bar{\mathcal{W}}_i, \quad (\text{C.7b})$$

for $i = 1, \dots, N$, with

$$\mathcal{W}_i = \int_0^{\Delta t} dt' \bar{\boldsymbol{\eta}}_i(t'), \quad \bar{\mathcal{W}}_i = \int_0^{\Delta t} dt' \int_0^{t'} dt'' \bar{\boldsymbol{\eta}}_i(t''), \quad (\text{C.8})$$

and

$$\langle \mathcal{W}^2 \rangle = \Delta t, \quad \langle \mathcal{W} \cdot \bar{\mathcal{W}} \rangle = \frac{1}{2} \Delta t^2, \quad \langle \bar{\mathcal{W}}^2 \rangle = \frac{2}{3} \Delta t^3. \quad (\text{C.9})$$

The latter values are recovered from the leading-order term in the approximation $\xi_0 \Delta t \ll 1$ in Eqs. (4.12). Therefore,

$$\mathcal{W} = \sqrt{\Delta t} \boldsymbol{\mathcal{Y}}, \quad \bar{\mathcal{W}} = \frac{\Delta t^{3/2}}{2} \left(\boldsymbol{\mathcal{Y}} + \sqrt{\frac{5}{3}} \bar{\boldsymbol{\mathcal{Y}}} \right). \quad (\text{C.10})$$

Here, $\boldsymbol{\mathcal{Y}}$ and $\bar{\boldsymbol{\mathcal{Y}}}$ are d_t -dimensional Gaussian variables [see Eq. (4.11)].

We have performed 10 runs for a system of 10^4 inelastic HD with a time step $\Delta t = 6 \times 10^4 / \nu^{\text{wn}}$. Those runs were initialized to a Maxwellian distribution for the velocities at a temperature $T(0) \approx 1.46 T^{\text{wn}}$. The simulation outcomes are compared with theoretical results of transient and steady states. For the former, a MA for the temperature evolution [MS00; SM09],

$$\frac{\partial(T/T^{\text{wn}})}{\partial t^*} = -\zeta^* \left(\frac{T}{T^{\text{wn}}} \right)^{3/2} + \frac{1}{2}, \quad (\text{C.11})$$

with $t^* = t\nu^{\text{wn}}$. For the steady values, $T^{\text{st}}/T^{\text{wn}}$ and a_2^{st} , we used a SA based on a truncation of the Sonine expansion of the VDF up to the fourth cumulant, with those theoretical values computed upon linearization on the a_2 [MS00; SM09], reading

$$\frac{T^{\text{st}}}{T^{\text{wn}}} = m \left[\frac{d_t}{2 \left(\mu_2^{(0)} + \mu_2^{(1)} a_2^{\text{st}} \right)} \right]^{2/3}, \quad a_2^{\text{st}} = \frac{4(1-\alpha)(1-2\alpha^2)}{19 + 14d - 3\alpha(9+2d) + 6(1-\alpha)\alpha^2}. \quad (\text{C.12})$$

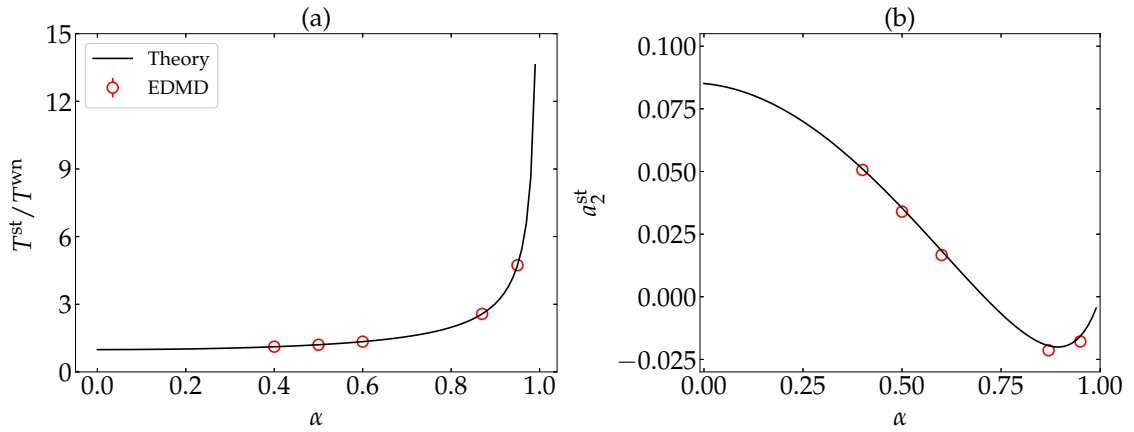


Figure C.3: Steady-state values of (a) the granular temperature, $T^{\text{st}}/T^{\text{wn}}$, and (b) the excess kurtosis, a_2^{st} vs. the coefficient of normal restitution α , for HS ($d_t = 2$). The circles (\circ) stand for EDMD simulation results, while the thick black lines (—) refer to the values corresponding to Eq. (C.12). The values of the coefficient of normal restitution used in the simulations are $\alpha = 0.95, 0.87, 0.6, 0.5, 0.4$.

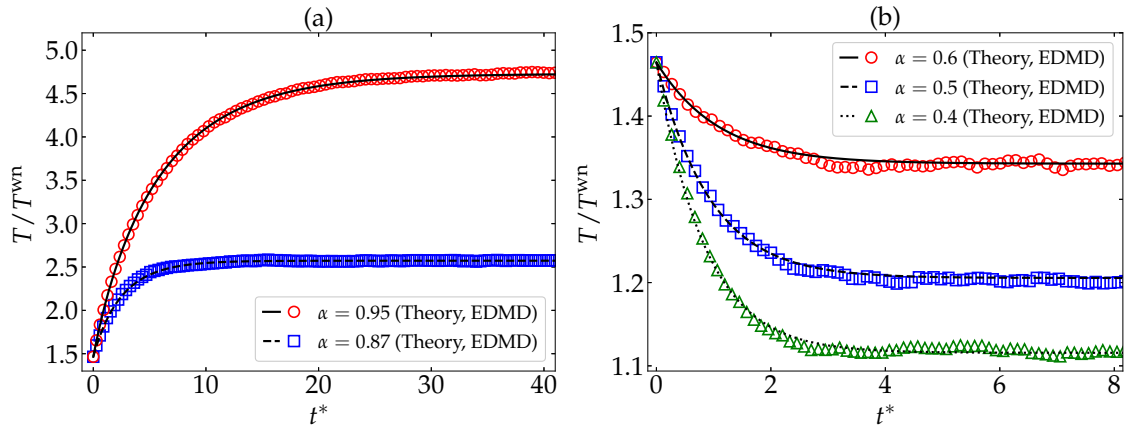


Figure C.4: Plot T/T^{wn} vs. $t^* \equiv t\nu_b$, for a system of HD ($d_t = 2$), for an initial condition $T(0) \approx 1.46T^{\text{wn}}$ and (a) $\alpha = 0.95, 0.87$ (whose steady value is greater than the initial condition), and (b) $\alpha = 0.6, 0.5, 0.4$ (whose stationary temperature is below its initial value). The symbols ($\circ, \square, \triangle$) stand for EDMD simulation results, while the lines (—, —, \cdots) refer to the values corresponding to the differential equation, Eq. (C.11).

In Figure C.3, the theoretical approximation for the steady-state values in Eq. (C.12) are compared with computer outcomes. The simulation results are computed as the average of the 10 simulation curves and 50 points of the evolution curve, where the stationary state is ensured, and for each value of the coefficient of normal restitution.

On the other hand, in [Figure C.4](#), the numerical solutions of Eq. (C.11) are plotted, together with the corresponding simulation curves resulting as the average over the 10 runs. We conclude that there is quite a good agreement between theory and simulation results. Therefore, we confirm that the implementation of the algorithm in our computer programs [[Meg23](#)] works properly.

C.2 Numerical scheme for the Langevin dynamics with nonlinear drag

In order to reproduce the simulation results of Article 1 ([Section 5.2](#)) and Article 4 ([Section 7.2](#)), it is necessary to elaborate the corresponding numerical scheme for the integration of the associated LE in Eq. (A.12). That is, from the discussion in [Section A.2](#), it is deduced that the choice of interpretation of the integration of a Wiener process is subtle and plays an important role on the integration for this case. We have chosen the Itô interpretation to work with [[Kam07](#)]. Then, the system will follow the LE derived in [Section A.2](#) [Eq. (A.12)]. The integration of the nonlinear LE, for the positions and velocities, in a small time interval Δt , reads [[Sca12](#); [MSP22](#); [MS22a](#)]

$$\mathbf{v}_i(t + \Delta t) = \mathbf{v}_i(t) [1 - \xi_{\text{eff}}(v(t))\Delta t] + \sqrt{\chi^2(v(t))\Delta t} \mathbf{y}_i + \mathcal{O}(\Delta t^{3/2}), \quad (\text{C.13a})$$

$$\begin{aligned} \mathbf{r}_i(t + \Delta t) = & \mathbf{r}_i(t) + \mathbf{v}_i(t)\Delta t \left[1 - \frac{\xi_{\text{eff}}(v(t))}{2}\Delta t \right] + \frac{1}{2}\sqrt{\chi^2(v(t))\Delta t^3} \left(\mathbf{y}_i + \sqrt{\frac{5}{3}}\bar{\mathbf{y}}_i \right) \\ & + \mathcal{O}(\Delta t^{5/2}), \end{aligned} \quad (\text{C.13b})$$

for $i = 1, \dots, N$, with \mathbf{y} and $\bar{\mathbf{y}}$ being Gaussian variables [see Eq. (4.11)], and the quantities $\xi_{\text{eff}}(v)$ and $\chi^2(v)$ being defined in [Section A.2](#). Here, we have approximated the random variables \mathcal{W} and $\bar{\mathcal{W}}$ to those of Eq. (C.9). This approximated scheme coincides with an Euler–Maruyama expansion for the system of SDE of the Langevin description [[KP92](#)].

C.3 Numerical scheme for the ST

To derive the proper numerical scheme for the integration of the LE associated with the thermostatted states of a granular gas driven by the ST, we use the results derived in [Section A.3](#). In the free streaming, the particles admit the following equations of

motion,

$$\dot{\mathbf{r}} = \mathbf{v}, \quad \dot{\mathbf{v}} = \sqrt{\frac{\nu^{\text{wn}} T^{\text{wn}}}{m} \frac{1 - \varepsilon}{2}} \bar{\boldsymbol{\eta}}_t(t), \quad \dot{\boldsymbol{\omega}} = \sqrt{\frac{\nu^{\text{wn}} T^{\text{wn}}}{I} \frac{\varepsilon d_t}{2 d_r}} \bar{\boldsymbol{\eta}}_r(t), \quad (\text{C.14})$$

with $\bar{\boldsymbol{\eta}}_{d_t}$ and $\bar{\boldsymbol{\eta}}_{d_r}$ being d_t - and d_r -dimensional random white noise vectors, which follow Eqs. (A.14). Note that, to derive Eq. (C.14), we have introduced in Eq. (A.13) the definitions of T^{wn} , ν^{wn} , and ε , appearing in Eqs. (2.53), (2.55), and (2.52), respectively. Thus, the integration of the equations of motion yields

$$\mathbf{v}_i(t + \Delta t) = \mathbf{v}_i(t) + \sqrt{\frac{\nu^{\text{wn}} T^{\text{wn}}}{m} \frac{1 - \varepsilon}{2}} \Delta t \boldsymbol{\mathcal{Y}}_{t,i}, \quad (\text{C.15a})$$

$$\boldsymbol{\omega}_i(t + \Delta t) = \boldsymbol{\omega}_i(t) + \sqrt{\frac{\nu^{\text{wn}} T^{\text{wn}}}{I} \frac{\varepsilon d_t}{2 d_r}} \Delta t \boldsymbol{\mathcal{Y}}_{r,i}, \quad (\text{C.15b})$$

$$\mathbf{r}_i(t + \Delta t) = \mathbf{r}_i(t) + \mathbf{v}_i(t) \Delta t + \frac{1}{2} \sqrt{\frac{\nu^{\text{wn}} T^{\text{wn}}}{m} \frac{1 - \varepsilon}{2}} \Delta t^3 \left(\boldsymbol{\mathcal{Y}}_{t,i} + \sqrt{\frac{5}{3}} \bar{\boldsymbol{\mathcal{Y}}}_{t,i} \right), \quad (\text{C.15c})$$

for $i = 1, \dots, N$, with $\boldsymbol{\mathcal{Y}}_t$ and $\bar{\boldsymbol{\mathcal{Y}}}_t$ being d_t -dimensional Gaussian variables, and $\boldsymbol{\mathcal{Y}}_r$ being a d_r -dimensional Gaussian random vector. Note that the translational equations of the scheme in Eqs. (C.15) coincide with those of Eqs. (C.7) by changing $\chi \rightarrow \chi_t$.

Balance equations for the IRHS model

D

One of the main goals of any fundamental or microscopic theory is to reproduce macroscopic phenomena. From the BE, one can derive the equations describing the macroscopic behavior of the hydrodynamic fields of the (monodisperse) system: n , \mathbf{u} , T . These equations are the so-called *balance equations*, and they are essential in fluid mechanics. Let us derive them for the particular case of a monodisperse granular gas described by the IRHS model described by the BE,

$$\frac{\partial f(\Gamma_1; t)}{\partial t} + \mathbf{v} \cdot \nabla f(\Gamma_1; t) = \sigma^{d_t-1} \int d\Gamma_2 \int_+ d\hat{\sigma} (\mathbf{v}_{12} \cdot \hat{\sigma}) \left[\frac{f(\Gamma_1''; t) f(\Gamma_2''; t)}{\alpha^2 |\beta|^{2d_r/d_t}} - f(\Gamma_1; t) f(\Gamma_2; t) \right]. \quad (\text{D.1})$$

Let us start by multiplying an arbitrary one-body hydrodynamic function, $\phi(\Gamma)$, at both sides of Eq. (D.1), and integrating over all values of Γ , yielding

$$\frac{\partial}{\partial t} (n \langle \psi \rangle) + \nabla \cdot (n \langle \mathbf{v} \psi \rangle) = \mathcal{J}[\psi | f, f], \quad (\text{D.2})$$

where

$$\begin{aligned} \mathcal{J}[\psi | f, f] &\equiv \int d\Gamma_1 \psi J[\Gamma | f, f] \\ &= \sigma^{d_t-1} \int d\Gamma_1 \int d\Gamma_2 \int_+ d\hat{\sigma} (\mathbf{v}_{12} \cdot \hat{\sigma}) f_1 f_2 (\mathfrak{B}_{12, \hat{\sigma}} - 1) \psi(\Gamma_1) \end{aligned} \quad (\text{D.3})$$

is the collisional production term of ψ , corresponding to the nonreduced version of Eq. (2.99). Substituting $\psi(\Gamma) = 1$, $m\mathbf{v}$, $mV^2/2 + I\omega^2/2$ into Eq. (D.2), the balance equations for the mass density, n , the flow field, \mathbf{u} , and the mean temperature, T , are directly obtained.

D.1 Particle (mass) density balance equation

Let us define $\psi(\Gamma) = 1$ and substitute into Eq. (D.2). Then, one gets

$$\frac{\partial}{\partial t}n + \nabla \cdot (n\langle \mathbf{v} \rangle) = 0, \quad (\text{D.4})$$

where the collision term vanishes because of the conservation of mass. That is, if the system is closed, the total mass of the system must be preserved.

Using the definition of the material derivative, \mathcal{D}_t [see Eq. (2.132)], Eq. (D.4) becomes

$$\mathcal{D}_t n + n \nabla \cdot \mathbf{u} = 0. \quad (\text{D.5})$$

D.2 Momentum density balance equation

If we now consider $\psi(\Gamma) = m\mathbf{v}$ and we substitute that quantity into Eq. (D.2), the balance equation associated with the linear momentum reads

$$\frac{\partial}{\partial t}(nm\langle \mathbf{v} \rangle) + \nabla \cdot (nm\langle \mathbf{v}\mathbf{v} \rangle) = 0. \quad (\text{D.6})$$

Again, \mathbf{v} is a collisional invariant and thus the collisional integral is identically null. Introducing the definition of the peculiar velocity, \mathbf{V} , and the mass density $\rho = nm$, Eq. (D.6) can be rewritten as

$$\frac{\partial}{\partial t}(\rho\mathbf{u}) + \nabla \cdot [\rho\langle (\mathbf{u} + \mathbf{V})(\mathbf{u} + \mathbf{V}) \rangle] = 0. \quad (\text{D.7})$$

To elaborate more this expression, we use again Eq. (D.5), the definition of the material time-derivative, and the pressure tensor \mathbf{P} , defined as

$$\mathbf{P} \equiv \rho\langle \mathbf{V}\mathbf{V} \rangle. \quad (\text{D.8})$$

Finally, the momentum density balance equation becomes

$$\mathcal{D}_t \mathbf{u} + \rho^{-1} \nabla \cdot \mathbf{P} = 0. \quad (\text{D.9})$$

The latter equation is a conservation equation for \mathbf{u} . This is expected due to the linear momentum conservation.

Up to now, in Eqs. (D.5) and (D.9), there is no explicit signature coming from the IRHS model. In fact, those equations are the same for both the EHS and IHS models. Of course, this is due to the already mentioned laws of conservation of mass and momentum.

D.3 Energy density balance equation

Let us now look for the inhomogeneous equation for the mean temperature in a monodisperse gas of inelastic and rough HD or HS. First of all, we derive the equations for the partial temperatures, T_t and T_r . We already know that, if $\alpha < 1$ or $|\beta| < 1$, the total kinetic energy is not a collisional invariant any more.

D.3.1 Equation for the translational temperature

Let us first consider that, $\psi = \frac{1}{2}mV^2$, and using Eq. (D.2), we get

$$\frac{\partial}{\partial t} \left(\frac{nm}{2} \langle V^2 \rangle \right) + \nabla \cdot \left(\frac{nm}{2} \langle \mathbf{v} V^2 \rangle \right) = \frac{m}{2} \mathcal{J} [V^2 | f, f]. \quad (\text{D.10})$$

Taking into account the definitions of the peculiar velocity, $\mathbf{V} = \mathbf{v} - \mathbf{u}$, of the translational temperature $T_t = \frac{d_t}{2} m \langle V^2 \rangle$ [see Eq. (2.84)], and of ξ_t [see Eq. (2.86a)], after some algebra, one obtains

$$\frac{d_t}{2} \frac{\partial}{\partial t} (nT_t) + \frac{d_t}{2} \nabla \cdot (n\mathbf{u}T_t + \mathbf{q}_t) + \mathbf{P} : \nabla \mathbf{u} - n\xi_t T_t = 0, \quad (\text{D.11})$$

where,

$$\mathbf{q}_t \equiv \frac{\rho}{2} \langle \mathbf{V} V^2 \rangle \quad (\text{D.12})$$

is the translational contribution of the heat flux.

If we use the mass balance equation, Eq. (D.5), and the definition of material derivative, then, Eq. (D.10) becomes

$$\mathcal{D}_t T_t + \frac{2}{d_t n} (\nabla \cdot \mathbf{q}_t + \mathbf{P} : \nabla \mathbf{u}) + \xi_t T_t = 0. \quad (\text{D.13})$$

D.3.2 Equation for the rotational temperature

We consider now $\psi = \frac{1}{2}I\omega^2$ in Eq. (D.2). Then, we get

$$\frac{\partial}{\partial t} \left(\frac{nI}{2} \langle \omega^2 \rangle \right) + \nabla \cdot \left(\frac{nI}{2} \langle \omega^2 \mathbf{v} \rangle \right) = \frac{I}{2} \mathcal{J} [\omega^2 | f, f]. \quad (\text{D.14})$$

Hence, using $T_r = \frac{d_r}{2} I \langle \omega^2 \rangle$ [see Eq. (2.84)], ξ_r [see Eq. (2.86b)], and defining the rotational contribution to the heat flux, \mathbf{q}_r , as

$$\mathbf{q}_r \equiv \frac{\rho}{2} \langle \mathbf{V} \omega^2 \rangle, \quad (\text{D.15})$$

it is possible to rewrite Eq. (D.14) as

$$\mathcal{D}_t T_r + \frac{2}{d_r n} (\nabla \cdot \mathbf{q}_r) + \xi_r T_r = 0. \quad (\text{D.16})$$

D.3.3 Balance equation for the mean temperature

In order to obtain the equation for the mean temperature, we will just use its definition as a weighted sum of the translational and rotational partial temperatures, i.e., $T \equiv (d_t T_t + d_r T_r)/(d_t + d_r)$ [see Eq. (2.85)]. Then, from the latter definition, and Eqs. (D.13) and (D.16), one obtains

$$\mathcal{D}_t T + \frac{2}{(d_t + d_r)n} (\nabla \cdot \mathbf{q} + \mathbf{P} : \nabla \mathbf{u}) + T \zeta = 0, \quad (\text{D.17})$$

where we have introduced the total heat flux, defined by

$$\mathbf{q} \equiv \mathbf{q}_t + \mathbf{q}_r, \quad (\text{D.18})$$

and the cooling rate, ζ , already defined in the context of homogeneous states in Eq. (2.87).

This derivation is equivalent to the one found by directly substituting $\psi(\Gamma) = \frac{1}{2}mV^2 + \frac{1}{2}I\omega^2$ into Eq. (D.2). Finally, it can be stressed that the balance equations, Eqs. (D.5), (D.9), and (D.17), are formally exact regardless of the use of any approximation to the VDF.

Bibliography

- [AD06] A. R. Abate and D. J. Durian. ‘Approach to jamming in an air-fluidized granular bed’. In: *Phys. Rev. E* 74 (2006), p. 031308. doi: [10.1103/PhysRevE.74.031308](https://doi.org/10.1103/PhysRevE.74.031308) (cited on page 7).
- [AFP13] B. Andreotti, Y. Forterre, and O. Pouliquen. *Granular Media. Between Fluid and Solid*. Cambridge University Press, Cambridge, 2013 (cited on page 6).
- [AG00] J. V. Austin and D. B. Goldstein. ‘Rarefied Gas Model of Io’s Sublimation-Driven Atmosphere’. In: *Icarus* 148 (2000), pp. 370–383. doi: [10.1006/icar.2000.6466](https://doi.org/10.1006/icar.2000.6466) (cited on page 68).
- [Aha71] A. Aharony. ‘Time reversal symmetry violation and the H -theorem’. In: *Phys. Lett. A* 37 (1971), pp. 45–46. doi: [10.1016/0375-9601\(71\)90324-0](https://doi.org/10.1016/0375-9601(71)90324-0) (cited on page 121).
- [Ahn+16] Y.-H. Ahn, H. Kang, D.-Y. Koh, and H. Lee. ‘Experimental verifications of Mpemba-like behaviors of clathrate hydrates’. In: *Korean J. Chem. Eng.* 33 (2016), pp. 1903–1907. doi: [10.1007/s11814-016-0029-2](https://doi.org/10.1007/s11814-016-0029-2) (cited on page 62).
- [AHZ01] T. Aspelmeier, M. Huthmann, and A. Zippelius. ‘Free cooling of particles with rotational degrees of freedom’. In: *Granular Gases*. Ed. by T. Pöschel and S. Luding. Vol. 564. Lectures Notes in Physics. Berlin: Springer, 2001, pp. 31–58. doi: [10.1007/3-540-44506-4_2](https://doi.org/10.1007/3-540-44506-4_2) (cited on pages 44, 283).
- [ALN06] G. Aquino, L. Leuzzi, and T. M. Nieuwenhuizen. ‘Kovacs effect in a model for a fragile glass’. In: *Phys. Rev. B* 73 (2006), p. 094205. doi: [10.1103/PhysRevB.73.094205](https://doi.org/10.1103/PhysRevB.73.094205) (cited on page 60).
- [AS04] J. J. Arenzon and M. Sellitto. ‘Kovacs effect in facilitated spin models of strong and fragile glasses’. In: *Eur. Phys. J. B* 42 (2004), pp. 543–548. doi: [10.1140/epjb/e2005-00012-0](https://doi.org/10.1140/epjb/e2005-00012-0) (cited on page 60).
- [AS72] M. Abramowitz and I. A. Stegun, eds. *Handbook of Mathematical Functions*. New York: Dover, 1972 (cited on page 44).
- [AT17] M. P. Allen and D. J. Tildesley. *Computer Simulation of Liquids*. Oxford University Press, June 2017 (cited on page 79).
- [Aue95] D. Auerbach. ‘Supercooling and the Mpemba effect: When hot water freezes quicker than cold’. In: *Am. J. Phys.* 63 (1995), pp. 882–885. doi: [10.1119/1.18059](https://doi.org/10.1119/1.18059) (cited on pages 62, 65).
- [AW57] B. J. Alder and T. E. Wainwright. ‘Phase Transition for a Hard Sphere System’. In: *J. Chem. Phys.* 27 (1957), pp. 1208–1209. doi: [10.1063/1.1743957](https://doi.org/10.1063/1.1743957) (cited on page 71).

- [AW59] B. J. Alder and T. E. Wainwright. ‘Studies in Molecular Dynamics. I. General Method’. In: *J. Chem. Phys.* 31 (1959), pp. 459–466. DOI: [10.1063/1.1730376](https://doi.org/10.1063/1.1730376) (cited on page 71).
- [Bac20] F. Bacon. *Novum Organum Scientiarum (in Latin). Translated into English in: The New Organon. Under the editorship of L. Jardine, M. Silverthorne (2000).* Cambridge Univ Press, 1620 (cited on page 61).
- [Bai+19] M. Baity-Jesi, E. Calore, A. Cruz, L. A. Fernandez, J. M. Gil-Narvi3n, A. Gordillo-Guerrero, D. Iñiguez, A. Lasanta, A. Maiorano, E. Marinari, V. Martin-Mayor, J. Moreno-Gordo, A. Muñoz-Sudupe, D. Navarro, G. Parisi, S. Perez-Gaviro, F. Ricci-Tersenghi, J. J. Ruiz-Lorenzo, S. F. Schifano, B. Seoane, A. Taranc3n, R. Tripiccione, and D. Yllanes. ‘The Mpemba effect in spin glasses is a persistent memory effect’. In: *Proc. Natl. Acad. Sci. U.S.A.* 116 (2019), pp. 15350–15355. DOI: [10.1073/pnas.1819803116](https://doi.org/10.1073/pnas.1819803116) (cited on page 62).
- [Bal06] P. Ball. ‘Does hot water freeze first?’ In: *Phys. World* (2006) (cited on page 62).
- [Ban+14] M. N. Bannerman, S. Strobl, A. Formella, and T. P3schel. ‘Stable algorithm for event detection in event-driven particle dynamics’. In: *Comput. Part. Mech.* 1 (2014), pp. 191–198. DOI: [10.1007/s40571-014-0021-8](https://doi.org/10.1007/s40571-014-0021-8) (cited on pages 74, 77).
- [Bar+02] A. Barrat, T. Biben, Z. R3acz, E. Trizac, and F. van Wijland. ‘On the velocity distributions of the one-dimensional inelastic gas’. In: *J. Phys. A* 35 (2002), p. 463. DOI: [10.1088/0305-4470/35/3/302](https://doi.org/10.1088/0305-4470/35/3/302) (cited on page 37).
- [Bat06] L. Bates. ‘Bulk Solids Characterisation-The Need for industrial Education in Bulk Technology’. In: *Bulk Solids Handl.* 26 (2006), pp. 464–475 (cited on page 6).
- [BB02] L. Berthier and J.-P. Bouchaud. ‘Geometrical aspects of aging and rejuvenation in the Ising spin glass: A numerical study’. In: *Phys. Rev. B* 66 (2002), p. 054404. DOI: [10.1103/PhysRevB.66.054404](https://doi.org/10.1103/PhysRevB.66.054404) (cited on page 60).
- [BC01] J. J. Brey and D. Cubero. ‘Hydrodynamic transport coefficients of granular gases’. In: *Granular Gases*. Ed. by T. P3schel and S. Luding. Vol. 564. Lectures Notes in Physics. Berlin: Springer, 2001, pp. 59–78. DOI: [10.1007/3-540-44506-4_3](https://doi.org/10.1007/3-540-44506-4_3) (cited on pages 54, 242, 286).
- [BC19] R. P. Behringer and B. Chakraborty. ‘The physics of jamming for granular materials: a review’. In: *Rep. Prog. Phys.* 82 (2019), 012601. DOI: [10.1088/1361-6633/aadc3c](https://doi.org/10.1088/1361-6633/aadc3c) (cited on page 7).
- [BCR99] J. J. Brey, D. Cubero, and M. J. Ruiz-Montero. ‘High energy tail in the velocity distribution of a granular gas’. In: *Phys. Rev. E* 59 (1999), pp. 1256–1258. DOI: [10.1103/PhysRevE.59.1256](https://doi.org/10.1103/PhysRevE.59.1256) (cited on page 37).

- [BD05] J. J. Brey and J. W. Dufty. ‘Hydrodynamic modes for a granular gas from kinetic theory’. In: *Phys. Rev. E* 72 (2005), p. 011303. DOI: [10.1103/PhysRevE.72.011303](https://doi.org/10.1103/PhysRevE.72.011303) (cited on page 54).
- [Ber+16] L. Berthier, D. Coslovich, A. Ninarello, and M. Ozawa. ‘Equilibrium Sampling of Hard Spheres up to the Jamming Density and Beyond’. In: *Phys. Rev. Lett.* 116 (2016), p. 238002. DOI: [10.1103/PhysRevLett.116.238002](https://doi.org/10.1103/PhysRevLett.116.238002) (cited on page 7).
- [Ber98] G. Bertotti. *Hysteresis in Magnetism For Physicists, Materials Scientists, and Engineers*. Academic Press Ltd., 1998 (cited on page 58).
- [BFP18] Nikolai V. Brilliantov, Arno Formella, and Thorsten Pöschel. ‘Increasing temperature of cooling granular gases’. In: *Nature Comm.* 9 (2018), p. 797. DOI: [10.1038/s41467-017-02803-7](https://doi.org/10.1038/s41467-017-02803-7) (cited on page 7).
- [BG46] M. Born and H. S. Green. ‘A general kinetic theory of liquids I. The molecular distribution functions’. In: *Proc. R. Soc. Lond. A* 188 (1946), pp. 10–18. DOI: [10.1098/rspa.1946.0093](https://doi.org/10.1098/rspa.1946.0093) (cited on page 16).
- [BGM21] D. M. Busiello, D. Gupta, and A. Maritan. ‘Inducing and optimizing Markovian Mpemba effect with stochastic reset’. In: *New J. Phys.* 23 (2021), p. 103012. DOI: [10.1088/1367-2630/ac2922](https://doi.org/10.1088/1367-2630/ac2922) (cited on pages 63, 85).
- [BH20] H. C. Burridge and O. Hallstadius. ‘Observing the Mpemba effect with minimal bias and the value of the Mpemba effect to scientific outreach and engagement’. In: *Proc. R. Soc. A* 476 (2020), p. 20190829. DOI: [10.1098/rspa.2019.0829](https://doi.org/10.1098/rspa.2019.0829) (cited on page 62).
- [Bir13] G. A. Bird. *The DSMC Method*. Scotts Valley, CA: CreateSpace Independent Publishing Platform, 2013 (cited on pages 68, 69).
- [Bir63] G. A. Bird. ‘Approach to Translational Equilibrium in a Rigid Sphere Gas’. In: *Phys. Fluids* 6 (1963), pp. 1518–1519. DOI: [10.1063/1.1710976](https://doi.org/10.1063/1.1710976) (cited on page 68).
- [Bir94] G. A. Bird. *Molecular Gas Dynamics and the Direct Simulation of Gas Flows*. Oxford, UK: Clarendon, 1994 (cited on pages 68, 69).
- [Bis+20] A. Biswas, V. V. Prasad, O. Raz, and R. Rajesh. ‘Mpemba effect in driven granular Maxwell gases’. In: *Phys. Rev. E* 102 (2020), p. 012906. DOI: [10.1103/PhysRevE.102.012906](https://doi.org/10.1103/PhysRevE.102.012906) (cited on pages 63, 64, 85).
- [BKC21] J. Bechhoefer, A. Kumar, and R. Chétrite. ‘A fresh understanding of the Mpemba effect’. In: *Nat. Rev. Phys.* 3 (2021), pp. 534–535. DOI: [10.1038/s42254-021-00349-8](https://doi.org/10.1038/s42254-021-00349-8) (cited on page 62).

- [BKD11] J. J. Brey, N. Khalil, and J. W. Dufty. ‘Thermal segregation beyond Navier–Stokes’. In: *New J. Phys.* 13 (2011), p. 055019. doi: [10.1088/1367-2630/13/5/055019](https://doi.org/10.1088/1367-2630/13/5/055019) (cited on page 300).
- [BKD12] J. J. Brey, N. Khalil, and J. W. Dufty. ‘Thermal segregation of intruders in the Fourier state of a granular gas’. In: *Phys. Rev. E* 85 (2012), p. 021307. doi: [10.1103/PhysRevE.85.021307](https://doi.org/10.1103/PhysRevE.85.021307) (cited on page 300).
- [BL16] H. C. Burridge and P. F. Linden. ‘Questioning the Mpemba effect: hot water does not cool more quickly than cold’. In: *Sci. Rep.* 6 (2016), p. 37665. doi: [10.1038/srep37665](https://doi.org/10.1038/srep37665) (cited on page 62).
- [Blu60] L. E. Blumenson. ‘A Derivation of n -Dimensional Spherical Coordinates’. In: *Am. Math. Mon.* 67 (1960), pp. 63–66. doi: [10.2307/2308932](https://doi.org/10.2307/2308932) (cited on page 309).
- [BMB21] F. Bregoli, V. Medina, and A. Bateman. ‘The energy transfer from granular landslides to water bodies explained by a data-driven, physics-based numerical model’. In: *Landslides* 18 (2021), pp. 1337–1348. doi: [10.1007/s10346-020-01568-3](https://doi.org/10.1007/s10346-020-01568-3) (cited on page 6).
- [BO07] G. W. Baxter and J. S. Olafsen. ‘Experimental Evidence for Molecular Chaos in Granular Gases’. In: *Phys. Rev. Lett.* 99 (2007), p. 028001. doi: [10.1103/PhysRevLett.99.028001](https://doi.org/10.1103/PhysRevLett.99.028001) (cited on page 16).
- [Bog46] N. N. Bogoliubov. ‘Kinetic Equations’. In: *JETP (in Russian)* 16 (8 1946), pp. 691–702 (cited on page 16).
- [Bol03] L. Boltzmann. ‘Further Studies on the Thermal Equilibrium of Gas Molecules’. In: *The Kinetic Theory of Gases*. 2003, pp. 262–349. doi: [10.1142/9781848161337_0015](https://doi.org/10.1142/9781848161337_0015) (cited on pages 47, 48).
- [Bol72] L. Boltzmann. ‘Weitere Studien über das Wärmegleichgewicht unter Gas-molekülen’. In: *Sitzungsberichte Akad. Wiss.* 66 (1872), pp. 275–370 (cited on pages 47, 48).
- [Bol95] L. Boltzmann. *Lectures on Gas Theory*. New York: Dover, 1995 (cited on pages 47, 48).
- [BP03] N. Brilliantov and T. Pöschel. ‘Hydrodynamics and transport coefficients for dilute granular gases’. In: *Phys. Rev. E* 67 (2003), p. 061304. doi: [10.1103/PhysRevE.67.061304](https://doi.org/10.1103/PhysRevE.67.061304) (cited on pages 36, 242, 279).
- [BP04] N. V. Brilliantov and T. Pöschel. *Kinetic Theory of Granular Gases*. Oxford: Oxford University Press, 2004 (cited on pages 7, 8, 16, 22, 279, 283, 314).

- [BP06a] N. Brilliantov and T. Pöschel. ‘Breakdown of the Sonine expansion for the velocity distribution of granular gases’. In: *Europhys. Lett.* 74 (2006), pp. 424–430. DOI: [10.1209/ep1/i2005-10555-6](https://doi.org/10.1209/ep1/i2005-10555-6) (cited on pages 36, 37, 314).
- [BP06b] N. Brilliantov and T. Pöschel. ‘Erratum: Breakdown of the Sonine expansion for the velocity distribution of granular gases’. In: *Europhys. Lett.* 75 (2006), pp. 188–188. DOI: [10.1209/ep1/i2006-10099-3](https://doi.org/10.1209/ep1/i2006-10099-3) (cited on pages 36, 37, 314).
- [BPR21] A. Biswas, V. V. Prasad, and R. Rajesh. ‘Mpemba effect in an anisotropically driven granular gas’. In: *EPL* 136 (2021), p. 46001. DOI: [10.1209/0295-5075/ac2d54](https://doi.org/10.1209/0295-5075/ac2d54) (cited on pages 63, 64, 85).
- [BPR22] A. Biswas, V. V. Prasad, and R. Rajesh. ‘Mpemba effect in anisotropically driven inelastic Maxwell gases’. In: *J. Stat. Phys.* 186 (2022), p. 45. DOI: [10.1007/s10955-022-02891-w](https://doi.org/10.1007/s10955-022-02891-w) (cited on pages 63, 64, 85).
- [BPV13] U. M. Bettolo Marconi, A. Puglisi, and A. Vulpiani. ‘About an H-theorem for systems with non-conservative interactions’. In: *J. Stat. Mech.* (2013), P08003. DOI: [10.1088/1742-5468/2013/08/P08003](https://doi.org/10.1088/1742-5468/2013/08/P08003) (cited on pages 12, 119, 280, 295).
- [BRC96] J. J. Brey, M. J. Ruiz-Montero, and D. Cubero. ‘Homogeneous cooling state of a low-density granular flow’. In: *Phys. Rev. E* 54 (1996), p. 3664. DOI: [10.1103/PhysRevE.54.3664](https://doi.org/10.1103/PhysRevE.54.3664) (cited on pages 36, 37).
- [BRC99] J. J. Brey, M. J. Ruiz-Montero, and D. Cubero. ‘On the validity of linear hydrodynamics for low-density granular flows described by the Boltzmann equation’. In: *Europhys. Lett.* 48 (1999), pp. 359–364. DOI: [10.1209/ep1/i1999-00490-0](https://doi.org/10.1209/ep1/i1999-00490-0) (cited on pages 45, 243, 287).
- [Bre+98] J. J. Brey, J. W. Dufty, C. S. Kim, and A. Santos. ‘Hydrodynamics for granular flow at low density’. In: *Phys. Rev. E* 58 (1998), pp. 4638–4653. DOI: [10.1103/PhysRevE.58.4638](https://doi.org/10.1103/PhysRevE.58.4638) (cited on pages 37, 54, 280).
- [Bri+07] N. V. Brilliantov, T. Pöschel, W. T. Kranz, and A. Zippelius. ‘Translations and Rotations Are Correlated in Granular Gases’. In: *Phys. Rev. Lett.* 98 (2007), p. 128001. DOI: [10.1103/PhysRevLett.98.128001](https://doi.org/10.1103/PhysRevLett.98.128001) (cited on pages 44, 283).
- [Bri+15] N. Brilliantov, P. L. Krapivsky, A. Bodrova, F. Spahn, H. Hayakawa, V. Stadnichuk, and J. Schmidt. ‘Size distribution of particles in Saturn’s rings from aggregation and fragmentation’. In: *Proc. Natl. Acad. Sci. U. S. A.* 112 (2015), pp. 9536–9541. DOI: [10.1073/pnas.1503957112](https://doi.org/10.1073/pnas.1503957112) (cited on pages 6, 7).
- [Bri+96] N. V. Brilliantov, F. Spahn, J.-M. Hertzsch, and T. Pöschel. ‘Model for collisions in granular gases’. In: *Phys. Rev. E* 53 (1996), pp. 5382–5392. DOI: [10.1103/PhysRevE.53.5382](https://doi.org/10.1103/PhysRevE.53.5382) (cited on page 22).

- [BRM05] J. J. Brey, M. J. Ruiz-Montero, and F. Moreno. ‘Energy partition and segregation for an intruder in a vibrated granular system under gravity’. In: *Phys. Rev. Lett.* 95 (2005), p. 098001. DOI: [10.1103/PhysRevLett.95.098001](https://doi.org/10.1103/PhysRevLett.95.098001) (cited on pages 27, 300).
- [BRM98] J. J. Brey, M. J. Ruiz-Montero, and F. Moreno. ‘Instability and spatial correlations in a dilute granular gas’. In: *Phys. Fluids* 10 (1998), pp. 2976–2982. DOI: [10.1063/1.869817](https://doi.org/10.1063/1.869817) (cited on pages 45, 243, 280, 287).
- [Bro11] J. D. Brownridge. ‘When does hot water freeze faster than cold water? A search for the Mpemba effect’. In: *Am. J. Phys.* 79 (2011), pp. 78–84. DOI: [10.1119/1.3490015](https://doi.org/10.1119/1.3490015) (cited on page 62).
- [Bru66] S. G. Brush. *Kinetic theory. Irreversible Processes*. Vol. 2. Pergamon, Oxford, 1966 (cited on page 50).
- [Bru86a] S. G. Brush. *The Kind of Motion We Call Heat: A History of the Kinetic Theory of Gases in the 19th Century. 1. Physics and the Atomists*. Vol. 1. North Holland Personal Library, 1986 (cited on pages 15, 48).
- [Bru86b] S. G. Brush. *The Kind of Motion We Call Heat: A History of the Kinetic Theory of Gases in the 19th Century. 2. Statistical Physics and Irreversible Processes*. Vol. 2. North Holland Personal Library, 1986 (cited on pages 15, 48).
- [BS92] J. J. Brey and A. Santos. ‘Nonequilibrium entropy of a gas’. In: *Phys. Rev. A* 45 (1992), pp. 8566–8572. DOI: [10.1103/PhysRevA.45.8566](https://doi.org/10.1103/PhysRevA.45.8566) (cited on page 47).
- [BSL11] M. N. Bannerman, R. Sargant, and L. Lue. ‘DynamO: A Free $\mathcal{O}(N)$ General Event-Driven Molecular Dynamics Simulator’. In: *J. Comput. Chem.* 32 (2011), pp. 3329–3338. DOI: [10.1002/jcc.21915](https://doi.org/10.1002/jcc.21915) (cited on pages 71, 75, 120).
- [BT02] A. Barrat and E. Trizac. ‘Lack of energy equipartition in homogeneous heated binary granular mixtures’. In: *Granul. Matter* 4 (2002), pp. 57–63. DOI: [10.1007/s10035-002-0108-4](https://doi.org/10.1007/s10035-002-0108-4) (cited on page 288).
- [BT12] M. Balážovič and B. Tomášik. ‘The Mpemba effect, Shechtman’s quasicrystals and student exploration activities’. In: *Phys. Educ.* 47 (2012), pp. 568–573. DOI: [10.1088/0031-9120/47/5/568](https://doi.org/10.1088/0031-9120/47/5/568) (cited on page 62).
- [Cam90] C. S. Campbell. ‘Rapid Granular Flows’. In: *Annu. Rev. Fluid Mech.* 22 (1990), pp. 57–92. DOI: [10.1146/annurev.fl.22.010190.000421](https://doi.org/10.1146/annurev.fl.22.010190.000421) (cited on pages 7, 8, 279).
- [CC70] S. Chapman and T. G. Cowling. *The Mathematical Theory of Non-Uniform Gases*. 3rd ed. Cambridge, UK: Cambridge University Press, 1970 (cited on pages 36, 53).

- [CCG00] J. A. Carrillo, C. Cercignani, and I. M. Gamba. ‘Steady states of a Boltzmann equation for driven granular media’. In: *Phys. Rev. E* 62 (2000), pp. 7700–7707. DOI: [10.1103/PhysRevE.62.7700](https://doi.org/10.1103/PhysRevE.62.7700) (cited on page 288).
- [Cer88] C. Cercignani. *The Boltzmann Equation and Its Applications*. New York: Springer-Verlag, 1988 (cited on pages 52, 53).
- [Cer98] C. Cercignani. *The Man Who Trusted Atoms*. Oxford: Oxford University Press, 1998 (cited on pages 16, 17, 48–50).
- [Che+18] M.-L. Chen, G.-J. Wu, B.-R. Gan, W.-H. Jiang, and J.-W. Zhou. ‘Physical and Compaction Properties of Granular Materials with Artificial Grading behind the Particle Size Distributions’. In: *Adv. Mater. Sci. Eng.* 2018 (2018), p. 8093571. DOI: [10.1155/2018/8093571](https://doi.org/10.1155/2018/8093571) (cited on page 6).
- [CKB21] R. Chétrite, A. Kumar, and J. Bechhoefer. ‘The Metastable Mpemba Effect Corresponds to a Non-monotonic Temperature Dependence of Extractable Work’. In: *Front. Phys.* 9 (2021), p. 654271. DOI: [10.3389/fphy.2021.654271](https://doi.org/10.3389/fphy.2021.654271) (cited on pages 63, 85).
- [Cla50] R. Clausius. ‘Über die bewegende Kraft der Wärme’. In: *Ann. Phys. Chem.* 79 (1850), pp. 368–397, 500–524. DOI: [10.1002/andp.18501550306](https://doi.org/10.1002/andp.18501550306) (cited on page 47).
- [CLH00] R. Cafiero, S. Luding, and H. J. Herrmann. ‘Two-Dimensional Granular Gas of Inelastic Spheres with Multiplicative Driving’. In: *Phys. Rev. Lett.* 84 (2000), pp. 6014–6017. DOI: [10.1103/PhysRevLett.84.6014](https://doi.org/10.1103/PhysRevLett.84.6014) (cited on page 299).
- [CLH02] R. Cafiero, S. Luding, and H. J. Herrmann. ‘Rotationally driven gas of inelastic rough spheres’. In: *Europhys. Lett.* 60 (2002), pp. 854–860. DOI: [10.1209/epl/i2002-00295-7](https://doi.org/10.1209/epl/i2002-00295-7) (cited on pages 30, 289).
- [CLL04] L. F. Cugliandolo, G. Lozano, and H. Lozza. ‘Memory effects in classical and quantum mean-field disordered models’. In: *Eur. Phys. J. B* 41 (2004), pp. 87–96. DOI: [10.1140/epjb/e2004-00298-2](https://doi.org/10.1140/epjb/e2004-00298-2) (cited on page 60).
- [CLL21] F. Carollo, A. Lasanta, and I. Lesanovsky. ‘Exponentially Accelerated Approach to Stationarity in Markovian Open Quantum Systems through the Mpemba Effect’. In: *Phys. Rev. Lett.* 127 (2021), p. 060401. DOI: [10.1103/PhysRevLett.127.060401](https://doi.org/10.1103/PhysRevLett.127.060401) (cited on pages 62, 85).
- [Cop+03] F. Coppex, M. Droz, J. Piasecki, and E. Trizac. ‘On the first Sonine correction for granular gases’. In: *Physica A* 329 (2003), pp. 114–126. DOI: [10.1016/S0378-4371\(03\)00593-4](https://doi.org/10.1016/S0378-4371(03)00593-4) (cited on pages 36, 37).

- [CTH23] A. M. Chatterjee, S. Takada, and H. Hayakawa. ‘Quantum Mpemba effect in a quantum dot with reservoirs’. In: *arXiv:2304.02411* (2023). DOI: [10.48550/arXiv.2304.02411](https://doi.org/10.48550/arXiv.2304.02411) (cited on page 62).
- [CVG12] M. G. Chamorro, F. Vega Reyes, and V. Garzó. ‘Homogeneous states in granular fluids driven by thermostats’. In: *AIP Conf. Proc.* 1501 (2012), pp. 1024–1030. DOI: [10.1063/1.4769654](https://doi.org/10.1063/1.4769654) (cited on pages 46, 152, 282, 288, 314).
- [CVG13] M. G. Chamorro, F. Vega Reyes, and V. Garzó. ‘Homogeneous steady states in a granular fluid driven by a stochastic bath with friction’. In: *J. Stat. Mech.* (2013), P07013. DOI: [10.1088/1742-5468/2013/07/P07013](https://doi.org/10.1088/1742-5468/2013/07/P07013) (cited on pages 46, 152, 282, 288, 314).
- [CW51] H. B. Callen and T. A. Welton. ‘Irreversibility and Generalized Noise’. In: *Phys. Rev.* 83 (1951), pp. 34–40. DOI: [10.1103/PhysRev.83.34](https://doi.org/10.1103/PhysRev.83.34) (cited on page 27).
- [CZ22] Y. Chen and J. Zhang. ‘High-energy velocity tails in uniformly heated granular materials’. In: *Phys. Rev. E* 106 (2022), p. L052903. DOI: [10.1103/PhysRevE.106.L052903](https://doi.org/10.1103/PhysRevE.106.L052903) (cited on pages 46, 288).
- [Dah+02] S. R. Dahl, C. M. Hrenya, V. Garzó, and J. W. Dufty. ‘Kinetic temperatures for a granular mixture’. In: *Phys. Rev. E* 66 (2002), p. 041301. DOI: [10.1103/PhysRevE.66.041301](https://doi.org/10.1103/PhysRevE.66.041301) (cited on page 38).
- [DB11] J. W. Dufty and J. J. Brey. ‘Choosing Hydrodynamic Fields’. In: *Math. Model. Nat. Phenom.* 6 (2011), pp. 19–36. DOI: [10.1051/mmnp/20116402](https://doi.org/10.1051/mmnp/20116402) (cited on pages 54, 279).
- [DB97] P. Deltour and J. L. Barrat. ‘Quantitative Study of a Freely Cooling Granular Medium’. In: *J. Phys. I* 7 (1997), pp. 137–151. DOI: [10.1051/jp1:1997130](https://doi.org/10.1051/jp1:1997130) (cited on page 78).
- [Dee71] E. Deeson. ‘Cooler-lower down’. In: *Phys. Educ.* 6 (1971), pp. 42–44. DOI: [10.1088/0031-9120/6/1/311](https://doi.org/10.1088/0031-9120/6/1/311) (cited on page 62).
- [Des37] R. Descartes. *Discours de la méthode pour bien conduire sa raison, et chercher la vérité dans les sciences (in French)*. Translated into English in: *Discourse on Method, Optics, Geometry, and Meteorology*. Under the editorship of P. J. Olscamp (2001). Hackett Publishing Company, 1637 (cited on page 61).
- [DG02] A. S. Dukhin and P. J. Goetz. ‘Chapter 3. Fundamentals of acoustics in liquids’. In: *Ultrasound for Characterizing Colloids*. Ed. by A. S. Dukhin and P. J. Goetz. Vol. 15. Studies in Interface Science. Elsevier, 2002, pp. 75–99. DOI: [10.1016/S1383-7303\(02\)80014-X](https://doi.org/10.1016/S1383-7303(02)80014-X) (cited on page 287).

- [Dia14] J. C. Dias. *Hysteresis: Types, Applications and Behavior Patterns in Complex Systems*. Materials Science and Technologies. NOVA, 2014 (cited on page 58).
- [DTS05] A. Donev, S. Torquato, and F. H. Stillinger. ‘Neighbor list collision-driven molecular dynamics simulation for nonspherical hard particles. I. Algorithmic details’. In: *J. Comput. Phys.* 202 (2005), pp. 737–764. doi: [10.1016/j.jcp.2004.08.014](https://doi.org/10.1016/j.jcp.2004.08.014) (cited on page 76).
- [Duf00] J. W. Dufty. ‘Statistical mechanics, kinetic theory, and hydrodynamics for rapid granular flow’. In: *J. Phys.: Condens. Matter* 12 (2000), A47–A56. doi: [10.1088/0953-8984/12/8A/306](https://doi.org/10.1088/0953-8984/12/8A/306) (cited on page 279).
- [Duf01] J. W. Dufty. ‘Kinetic theory and hydrodynamics for a low density granular gas’. In: *Adv. Complex Syst.* 4 (2001), pp. 397–406. doi: [10.1142/S0219525901000395](https://doi.org/10.1142/S0219525901000395) (cited on page 279).
- [Dur12] J. Duran. *Sands, Powders, and Grains: An Introduction to the Physics of Granular Materials*. Springer, New York, 2012 (cited on page 6).
- [EB02] M. H. Ernst and R. Brito. ‘Driven inelastic Maxwell models with high energy tails’. In: *Phys. Rev. E* 65 (2002), p. 040301(R). doi: [10.1103/PhysRevE.65.040301](https://doi.org/10.1103/PhysRevE.65.040301) (cited on page 288).
- [EE02] P. Ehrenfest and T. Ehrenfest. *The Conceptual Foundations of the Statistical Approach in Mechanics*. Dover Phoenix editions. Dover Publications, 2002 (cited on page 16).
- [Ein05] A. Einstein. ‘Über die von der molekularkinetischen Theorie der Wärme geforderte Bewegung von in ruhenden Flüssigkeiten suspendierten Teilchen’. In: *Ann. Phys.* 322 (1905), pp. 549–560. doi: [10.1002/andp.19053220806](https://doi.org/10.1002/andp.19053220806) (cited on page 305).
- [Elk18] S. Elkin, ed. *The 100 greatest unsolved mysteries*. New York: Cavendish Square, 2018 (cited on page 62).
- [EP97] S. E. Esipov and T. Pöschel. ‘The granular phase diagram’. In: *J. Stat. Phys.* 86 (1997), pp. 1385–1395. doi: [10.1007/BF02183630](https://doi.org/10.1007/BF02183630) (cited on pages 7, 37, 285).
- [ERS08] S. Esposito, R. De Risi, and L. Somma. ‘Mpemba effect and phase transitions in the adiabatic cooling of water before freezing’. In: *Physica A* 387 (2008), pp. 757–763. doi: [10.1016/j.physa.2007.10.029](https://doi.org/10.1016/j.physa.2007.10.029) (cited on page 62).
- [ES21] D. C. Elton and P. D. Spencer. ‘Pathological Water Science — Four Examples and What They Have in Common’. In: *Biomechanical and Related Systems*. Ed. by A. Gadomski. Vol. 17. Biologically-Inspired Systems. Cham.: Springer, 2021, pp. 155–169 (cited on page 62).

- [Fer00] L. Ferrari. 'A proper mobility formula for large, heavy particles in gases in any regime'. In: *Chem. Phys.* 257 (2000), pp. 63–77. DOI: [10.1016/S0301-0104\(00\)00120-8](https://doi.org/10.1016/S0301-0104(00)00120-8) (cited on pages 28, 29, 309).
- [Fer07] L. Ferrari. 'Particles dispersed in a dilute gas: Limits of validity of the Langevin equation'. In: *Chem. Phys.* 336 (2007), pp. 27–35. DOI: [10.1016/j.chemphys.2007.05.001](https://doi.org/10.1016/j.chemphys.2007.05.001) (cited on pages 28, 309).
- [Fer14] L. Ferrari. 'Particles dispersed in a dilute gas. II. From the Langevin equation to a more general kinetic approach'. In: *Chem. Phys.* 428 (2014), pp. 144–155. DOI: [10.1016/j.chemphys.2013.10.024](https://doi.org/10.1016/j.chemphys.2013.10.024) (cited on pages 28, 309).
- [FH17] W. D. Fullmer and C. M. Hrenya. 'The Clustering Instability in Rapid Granular and Gas-Solid Flows'. In: *Annu. Rev. Fluid Mech.* 49 (2017), pp. 485–510. DOI: [10.1146/annurev-fluid-010816-060028](https://doi.org/10.1146/annurev-fluid-010816-060028) (cited on pages 45, 243, 287).
- [Fir71] I. Firth. 'Cooler?' In: *Phys. Educ.* 6 (1971), pp. 32–41. DOI: [10.1088/0031-9120/6/1/310](https://doi.org/10.1088/0031-9120/6/1/310) (cited on page 62).
- [FK72] J. H. Ferziger and G. H. Kaper. *Mathematical Theory of Transport Processes in Gases*. Amsterdam: North-Holland, 1972 (cited on page 36).
- [Fla73] D. Flamm. 'Life and Personality of Ludwig Boltzmann'. In: *The Boltzmann Equation*. Ed. by E. G. D. Cohen and W. Thirring. Vienna: Springer Vienna, 1973, pp. 3–16. DOI: [10.1007/978-3-7091-8336-6_2](https://doi.org/10.1007/978-3-7091-8336-6_2) (cited on page 16).
- [Fok14] A. D. Fokker. 'Die mittlere Energie rotierender elektrischer Dipole im Strahlungsfeld'. In: *Ann. Phys.* 348 (1914), pp. 810–820. DOI: [10.1002/andp.19143480507](https://doi.org/10.1002/andp.19143480507) (cited on page 305).
- [FR13] F. Filbet and T. Rey. 'A rescaling velocity method for dissipative kinetic equations. Applications to granular media'. In: *J. Comput. Phys.* 248 (2013), pp. 177–199. DOI: [10.1016/j.jcp.2013.04.023](https://doi.org/10.1016/j.jcp.2013.04.023) (cited on page 77).
- [Fra74] F. C. Frank. 'The Descartes–Mpemba phenomenon'. In: *Phys. Educ.* 9 (1974), pp. 284–284. DOI: [10.1088/0031-9120/9/4/121](https://doi.org/10.1088/0031-9120/9/4/121) (cited on page 62).
- [Fre79] M. Freeman. 'Cooler still—an answer?' In: *Phys. Educ.* 14 (1979), pp. 417–421. DOI: [10.1088/0031-9120/14/7/314](https://doi.org/10.1088/0031-9120/14/7/314) (cited on page 62).
- [Gal74] R. Gallear. 'The Bacon–Descartes–Mpemba phenomenon'. In: *Phys. Educ.* 9 (1974), pp. 490–490. DOI: [10.1088/0031-9120/9/7/114](https://doi.org/10.1088/0031-9120/9/7/114) (cited on page 62).
- [Gar+12] V. Garzó, S. Tenneti, S. Subramaniam, and C. M. Hrenya. In: *J. Fluid Mech.* 712 (2012), pp. 129–168 (cited on page 242).

- [Gar+15] M. I. García de Soria, P. Maynar, S. Mischler, C. Mouhot, T. Rey, and E. Trizac. ‘Towards an H-theorem for granular gases’. In: *J. Stat. Mech.* (2015), P11009. DOI: [10.1088/1742-5468/2015/11/p11009](https://doi.org/10.1088/1742-5468/2015/11/p11009) (cited on pages 12, 50, 119, 280, 295).
- [Gar05] V. Garzó. ‘Instabilities in a free granular fluid described by the Enskog equation’. In: *Phys. Rev. E* 72 (2005), p. 021106. DOI: [10.1103/PhysRevE.72.021106](https://doi.org/10.1103/PhysRevE.72.021106) (cited on pages 45, 243, 280, 287).
- [Gar06] V. Garzó. ‘Segregation in granular binary mixtures: Thermal diffusion’. In: *Europhys. Lett.* 75 (2006), pp. 521–527. DOI: [10.1209/epl/i2006-10143-4](https://doi.org/10.1209/epl/i2006-10143-4) (cited on page 300).
- [Gar08] V. Garzó. ‘Brazil-nut effect versus reverse Brazil-nut effect in a moderately granular dense gas’. In: *Phys. Rev. E* 78 (2008), 020301(R). DOI: [10.1103/PhysRevE.78.020301](https://doi.org/10.1103/PhysRevE.78.020301) (cited on page 7).
- [Gar11] V. Garzó. ‘Thermal diffusion segregation in granular binary mixtures described by the Enskog equation’. In: *New J. Phys.* 13 (2011), p. 055020. DOI: [10.1088/1367-2630/13/5/055020](https://doi.org/10.1088/1367-2630/13/5/055020) (cited on page 300).
- [Gar19] V. Garzó. *Granular Gaseous Flows. A Kinetic Theory Approach to Granular Gaseous Flows*. Switzerland: Springer Nature, 2019 (cited on pages 7–9, 12, 16, 19, 36–38, 40, 43–45, 54, 242, 243, 279, 280, 283, 286–288, 299, 300, 314).
- [GCV13a] V. Garzó, M. G. Chamorro, and F. Vega Reyes. ‘Erratum: Transport properties for driven granular fluids in situations close to homogeneous steady states [Phys. Rev. E 87, 032201 (2013)]’. In: *Phys. Rev. E* 87 (2013), p. 059906. DOI: [10.1103/PhysRevE.87.059906](https://doi.org/10.1103/PhysRevE.87.059906) (cited on page 46).
- [GCV13b] V. Garzó, M. G. Chamorro, and F. Vega Reyes. ‘Transport properties for driven granular fluids in situations close to homogeneous steady states’. In: *Phys. Rev. E* 87 (2013), p. 032201. DOI: [10.1103/PhysRevE.87.032201](https://doi.org/10.1103/PhysRevE.87.032201) (cited on page 46).
- [GD02] V. Garzó and J. W. Dufty. ‘Hydrodynamics for a granular mixture at low density’. In: *Phys. Fluids* 14 (2002), pp. 1476–1490. DOI: [10.1063/1.1458007](https://doi.org/10.1063/1.1458007) (cited on page 279).
- [GD99] V. Garzó and J. W. Dufty. ‘Homogeneous cooling state for a granular mixture’. In: *Phys. Rev. E* 60 (1999), pp. 5706–5713. DOI: [10.1103/PhysRevE.60.5706](https://doi.org/10.1103/PhysRevE.60.5706) (cited on page 38).
- [Gen99] P. G. de Gennes. ‘Granular matter: a tentative view’. In: *Rev. Mod. Phys.* 71 (1999), S374–S382. DOI: [10.1103/RevModPhys.71.S374](https://doi.org/10.1103/RevModPhys.71.S374) (cited on page 7).

- [GF23] J.-B. Gorce and E. Falcon. ‘Statistics of a two-dimensional immersed granular gas magnetically forced in volume’. In: *Phys. Rev. E* 107 (2023), p. 034903. DOI: [10.1103/PhysRevE.107.034903](https://doi.org/10.1103/PhysRevE.107.034903) (cited on page 299).
- [GG20] R. Gómez González and V. Garzó. ‘Non-Newtonian rheology in inertial suspensions of inelastic rough hard spheres under simple shear flow’. In: *Phys. Fluids* 32 (2020), 073315. DOI: [10.1063/5.0015241](https://doi.org/10.1063/5.0015241) (cited on pages 289, 299).
- [GG21] R. Gómez González and V. Garzó. ‘Time-dependent homogeneous states of binary granular suspensions’. In: *Phys. Fluids* 33 (2021), p. 093315. DOI: [10.1063/5.0062425](https://doi.org/10.1063/5.0062425) (cited on pages 63, 64, 85).
- [GKG20] R. Gómez González, N. Khalil, and V. Garzó. ‘Enskog kinetic theory for multicomponent granular suspensions’. In: *Phys. Rev. E* 101 (2020), p. 012904. DOI: [10.1103/PhysRevE.101.012904](https://doi.org/10.1103/PhysRevE.101.012904) (cited on page 282).
- [GLH19] A. Gijón, A. Lasanta, and E. R. Hernández. ‘Paths towards equilibrium in molecular systems: The case of water’. In: *Phys. Rev. E* 100 (2019), p. 032103. DOI: [10.1103/PhysRevE.100.032103](https://doi.org/10.1103/PhysRevE.100.032103) (cited on page 62).
- [GM02] V. Garzó and J. M. Montanero. ‘Transport coefficients of a heated granular gas’. In: *Physica A* 313 (2002), pp. 336–356. DOI: [10.1016/S0378-4371\(02\)00994-9](https://doi.org/10.1016/S0378-4371(02)00994-9) (cited on page 288).
- [GMT12] M. I. García de Soria, P. Maynar, and E. Trizac. ‘Universal reference state in a driven homogeneous granular gas’. In: *Phys. Rev. E* 85 (2012), p. 051301. DOI: [10.1103/PhysRevE.85.051301](https://doi.org/10.1103/PhysRevE.85.051301) (cited on page 288).
- [GMT13] M. I. García de Soria, P. Maynar, and E. Trizac. ‘Linear hydrodynamics for driven granular gases’. In: *Phys. Rev. E* 87 (2013), p. 022201. DOI: [10.1103/PhysRevE.87.022201](https://doi.org/10.1103/PhysRevE.87.022201) (cited on page 279).
- [GMV13] V. Garzó, J. A. Murray, and F. Vega Reyes. ‘Diffusion transport coefficients for granular binary mixtures at low density: Thermal diffusion segregation’. In: *Phys. Fluids* 25 (2013), p. 043302. DOI: [10.1063/1.4800775](https://doi.org/10.1063/1.4800775) (cited on page 300).
- [GNB05] I. Goldhirsch, S. H. Noskowitz, and O. Bar-Lev. ‘Nearly Smooth Granular Gases’. In: *Phys. Rev. Lett.* 95 (2005), 068002. DOI: [10.1103/PhysRevLett.95.068002](https://doi.org/10.1103/PhysRevLett.95.068002) (cited on page 279).
- [Gol03] I. Goldhirsch. ‘Rapid granular flows’. In: *Annu. Rev. Fluid Mech.* 35 (2003), pp. 267–293. DOI: [10.1146/annurev.fluid.35.101101.161114](https://doi.org/10.1146/annurev.fluid.35.101101.161114) (cited on pages 7, 8, 279).

- [Gon+21] I. González-Adalid Pemartín, E. Mompó, A. Lasanta, V. Martín-Mayor, and J. Salas. ‘Slow growth of magnetic domains helps fast evolution routes for out-of-equilibrium dynamics’. In: *Phys. Rev. E* 104 (2021), p. 044114. DOI: [10.1103/PhysRevE.104.044114](https://doi.org/10.1103/PhysRevE.104.044114) (cited on page 62).
- [Gra+11a] G. Gradenigo, A. Sarracino, D. Villamaina, and A. Puglisi. ‘Fluctuating hydrodynamics and correlation lengths in a driven granular fluid’. In: *J. Stat. Mech.* 08 (2011), P08017. DOI: [10.1088/1742-5468/2011/08/P08017](https://doi.org/10.1088/1742-5468/2011/08/P08017) (cited on page 288).
- [Gra+11b] G. Gradenigo, A. Sarracino, D. Villamaina, and A. Puglisi. ‘Non-equilibrium length in granular fluids: From experiment to fluctuating hydrodynamics’. In: *EPL* 96 (2011), 14004. DOI: [10.1209/0295-5075/96/14004](https://doi.org/10.1209/0295-5075/96/14004) (cited on page 288).
- [Gre+11] P. A. Greaney, G. Lani, G. Cicero, and J. C. Grossman. ‘Mpemba-Like Behavior in Carbon Nanotube Resonators’. In: *Metall. Mater. Trans. A* 42 (2011), pp. 3907–3912. DOI: [10.1007/s11661-011-0843-4](https://doi.org/10.1007/s11661-011-0843-4) (cited on page 62).
- [Gro97] E. L. Grossman. ‘Effects of container geometry on granular convection’. In: *Phys. Rev. E* 56 (1997), pp. 3290–3300. DOI: [10.1103/PhysRevE.56.3290](https://doi.org/10.1103/PhysRevE.56.3290) (cited on page 78).
- [GS03] V. Garzó and A. Santos. *Kinetic Theory of Gases in Shear Flows: Nonlinear Transport*. Fundamental Theories of Physics. Dordrecht: Springer, 2003 (cited on pages 19, 48, 49).
- [GS11] V. Garzó and A. Santos. ‘Hydrodynamics of inelastic Maxwell models’. In: *Math. Model. Nat. Phenom.* 6.4 (2011), pp. 37–76. DOI: [10.1051/mmnp/20116403](https://doi.org/10.1051/mmnp/20116403) (cited on page 279).
- [GS95] A. Goldshtein and M. Shapiro. ‘Mechanics of collisional motion of granular materials. Part 1. General hydrodynamic equations’. In: *J. Fluid Mech.* 282 (1995), pp. 75–114. DOI: [10.1017/S0022112095000048](https://doi.org/10.1017/S0022112095000048) (cited on pages 44, 54, 279, 314).
- [GSK18] V. Garzó, A. Santos, and G. M. Kremer. ‘Impact of roughness on the instability of a free-cooling granular gas’. In: *Phys. Rev. E* 97 (2018), 052901. DOI: [10.1103/PhysRevE.97.052901](https://doi.org/10.1103/PhysRevE.97.052901) (cited on pages 14, 45, 242, 243, 284, 287).
- [GSM07] V. Garzó, A. Santos, and J. M. Montanero. ‘Modified Sonine approximation for the Navier–Stokes transport coefficients of a granular gas’. In: *Physica A* 376 (2007), pp. 94–107. DOI: [10.1016/j.physa.2006.10.081](https://doi.org/10.1016/j.physa.2006.10.081) (cited on pages 54, 286, 299).

- [Guj22] P. D. Gujrati. 'Nonequilibrium Entropy in Extended State Space'. In: *Frontiers in Entropy Across the Disciplines*. World Scientific, 2022. Chap. 18, pp. 627–669. DOI: [10.1142/9789811259401_0018](https://doi.org/10.1142/9789811259401_0018) (cited on page 47).
- [GV10] V. Garzó and F. Vega Reyes. 'Segregation by thermal diffusion in granular shear flows'. In: *J. Stat. Mech.* (2010), P07024. DOI: [10.1088/1742-5468/2010/07/P07024](https://doi.org/10.1088/1742-5468/2010/07/P07024) (cited on page 300).
- [GZ93] I. Goldhirsch and G. Zanetti. 'Clustering instability in dissipative gases'. In: *Phys. Rev. Lett.* 70 (1993), pp. 1619–1622. DOI: [10.1103/PhysRevLett.70.1619](https://doi.org/10.1103/PhysRevLett.70.1619) (cited on pages 45, 243, 280, 287).
- [GZB97] E. L. Grossman, T. Zhou, and E. Ben-Naim. 'Towards granular hydrodynamics in two dimensions'. In: *Phys. Rev. E* 55 (1997), p. 4200. DOI: [10.1103/PhysRevE.55.4200](https://doi.org/10.1103/PhysRevE.55.4200) (cited on page 279).
- [Haf83] P. K. Haff. 'Grain flow as a fluid-mechanical phenomenon'. In: *J. Fluid Mech.* 134 (1983), pp. 401–430. DOI: [10.1017/S0022112083003419](https://doi.org/10.1017/S0022112083003419) (cited on page 34).
- [Hah50] E. L. Hahn. 'Spin Echoes'. In: *Phys. Rev.* 80 (1950), pp. 580–594. DOI: [10.1103/PhysRev.80.580](https://doi.org/10.1103/PhysRev.80.580) (cited on page 58).
- [Han81] J. W. Hanneken. 'Mpemba effect and cooling by radiation to the sky'. In: *Phys. Educ.* 16 (1981), pp. 7–7. DOI: [10.1088/0031-9120/16/1/102](https://doi.org/10.1088/0031-9120/16/1/102) (cited on page 62).
- [Har+18] K. Harth, T. Trittel, S. Wegner, and R. Stannarius. 'Free Cooling of a Granular Gas of Rodlike Particles in Microgravity'. In: *Phys. Rev. Lett.* 120 (2018), 214301. DOI: [10.1103/PhysRevLett.120.214301](https://doi.org/10.1103/PhysRevLett.120.214301) (cited on page 299).
- [Her+05] O. Herbst, R. Cafiero, A. Zippelius, H. J. Herrmann, and S. Luding. 'A driven two-dimensional granular gas with Coulomb friction'. In: *Phys. Fluids* 17 (2005), p. 107102. DOI: [10.1063/1.2049277](https://doi.org/10.1063/1.2049277) (cited on pages 288, 299).
- [Her06] H. J. Herrmann. 'Aeolian Transport and Dune Formation'. In: *Modelling Critical and Catastrophic Phenomena in Geoscience: A Statistical Physics Approach*. Ed. by P. Bhattacharyya and B. K. Chakrabarti. Berlin, Heidelberg: Springer Berlin Heidelberg, 2006, pp. 363–386. DOI: [10.1007/3-540-35375-5_13](https://doi.org/10.1007/3-540-35375-5_13) (cited on page 6).
- [Her07] H. J. Herrmann. 'Dune Formation'. In: *Traffic and Granular Flow'05*. Ed. by A. Schadschneider, T. Pöschel, R. Kühne, M. Schreckenberg, and D. E. Wolf. Springer Berlin Heidelberg, 2007, pp. 63–77. DOI: [10.1007/978-3-540-47641-2_5](https://doi.org/10.1007/978-3-540-47641-2_5) (cited on page 6).
- [Her95] H. J. Herrmann. 'Physics of granular media'. In: *Chaos Solit. Fractals* 6 (1995), pp. 203–212. DOI: [10.1016/0960-0779\(95\)80026-D](https://doi.org/10.1016/0960-0779(95)80026-D) (cited on pages 6, 7).

- [Her99] H.J. Herrmann. 'The importance of computer simulations of granular flow'. In: *Comput. Sci. Eng.* 1 (1999), pp. 72–73. doi: [10.1109/5992.743626](https://doi.org/10.1109/5992.743626) (cited on page 7).
- [HHP87] B. L. Holian, W. G. Hoover, and H. A. Posch. 'Resolution of Loschmidt's Paradox: The Origin of Irreversible Behavior in Reversible Atomistic Dynamics'. In: *Phys. Rev. Lett.* 59 (1987), pp. 10–13. doi: [10.1103/PhysRevLett.59.10](https://doi.org/10.1103/PhysRevLett.59.10) (cited on page 50).
- [HHZ00] O. Herbst, M. Huthmann, and A. Zippelius. 'Dynamics of inelastically colliding spheres with Coulomb friction: relaxation of translational and rotational energy'. In: *Granul. Matter* 2 (2000), pp. 211–219. doi: [10.1007/PL00010915](https://doi.org/10.1007/PL00010915) (cited on page 299).
- [HM16] J. Horabik and M. Molenda. 'Parameters and contact models for DEM simulations of agricultural granular materials: A review'. In: *Biosyst. Eng.* 147 (2016), pp. 206–225. doi: [10.1016/j.biosystemseng.2016.02.017](https://doi.org/10.1016/j.biosystemseng.2016.02.017) (cited on page 6).
- [HOB00] M. Huthmann, J. A. G. Orza, and R. Brito. 'Dynamics of deviations from the Gaussian state in a freely cooling homogeneous system of smooth inelastic particles'. In: *Granul. Matter* 2 (2000), pp. 189–199. doi: [10.1007/s100350000047](https://doi.org/10.1007/s100350000047) (cited on pages 36, 37, 280).
- [Hod94] I.M. Hodge. 'Enthalpy relaxation and recovery in amorphous materials'. In: *J. Non-Cryst. Solids* 169.3 (1994), pp. 211–266. doi: [10.1016/0022-3093\(94\)90321-2](https://doi.org/10.1016/0022-3093(94)90321-2) (cited on page 60).
- [Hop82] J. J. Hopfield. 'Neural networks and physical systems with emergent collective computational abilities.' In: *Proc. Natl. Acad. Sci. U.S.A.* 79 (1982), pp. 2554–2558. doi: [10.1073/pnas.79.8.2554](https://doi.org/10.1073/pnas.79.8.2554) (cited on page 58).
- [HQL01] D. C. Hong, P. V. Quinn, and S. Luding. 'Reverse Brazil nut problem: Competition between percolation and condensation'. In: *Phys. Rev. Lett.* 86 (2001), pp. 3423–3426. doi: [10.1103/PhysRevLett.86.3423](https://doi.org/10.1103/PhysRevLett.86.3423) (cited on page 7).
- [HR22] R. Holtzman and O. Raz. 'Landau theory for the Mpemba effect Through Phase Transitions'. In: *Commun. Phys.* 5 (2022), p. 280. doi: [10.1038/s42005-022-01063-2](https://doi.org/10.1038/s42005-022-01063-2) (cited on page 63).
- [IC16] R. T. Ibekwe and J. P. Cullerne. 'Investigating the Mpemba Effect: when hot water freezes faster than cold water'. In: *Phys. Educ.* 51 (2016), p. 025011. doi: [10.1088/0031-9120/51/2/025011](https://doi.org/10.1088/0031-9120/51/2/025011) (cited on page 62).

- [IK15] M. Isobe and W. Krauth. ‘Hard-sphere melting and crystallization with event-chain Monte Carlo’. In: *J. Chem. Phys.* 143 (2015), p. 084509. DOI: [10.1063/1.4929529](https://doi.org/10.1063/1.4929529) (cited on page 72).
- [Iso16] M. Isobe. ‘Hard sphere simulation in statistical physics — methodologies and applications’. In: *Mol. Simul.* 42 (2016), pp. 1317–1329. DOI: [10.1080/08927022.2016.1139106](https://doi.org/10.1080/08927022.2016.1139106) (cited on page 72).
- [Iso17] M. Isobe. ‘Hard Sphere Simulation by Event-Driven Molecular Dynamics: Breakthrough, Numerical Difficulty, and Overcoming the issues’. In: *Advances in the Computational Sciences*. 2017. Chap. Chapter 6, pp. 83–107. DOI: [10.1142/9789813209428_0006](https://doi.org/10.1142/9789813209428_0006) (cited on page 72).
- [Iso99] M. Isobe. ‘Simple and efficient algorithm for large scale molecular dynamics simulation in hard disk system’. In: *Int. J. Mod. Phys. C* 10 (1999), pp. 1281–1293. DOI: [10.1142/S0129183199001042](https://doi.org/10.1142/S0129183199001042) (cited on page 72).
- [Jan22] C. Jana. ‘A study of non-linear Langevin dynamics under non-Gaussian noise with quartic cumulant’. In: *J. Stat. Mech.* (2022), p. 023205. DOI: [10.1088/1742-5468/ac4aef](https://doi.org/10.1088/1742-5468/ac4aef) (cited on page 29).
- [JCL93] D. Jou, J. Casas-Vázquez, and G. Lebon. ‘Nonequilibrium entropy and the second law of thermodynamics: A simple illustration’. In: *Int. J. Thermophys.* 14 (1993), pp. 671–683. DOI: [10.1007/BF00502101](https://doi.org/10.1007/BF00502101) (cited on page 47).
- [Jen06] M. Jeng. ‘The Mpemba effect: When can hot water freeze faster than cold?’ In: *Am. J. Phys.* 74 (2006), pp. 514–522. DOI: [10.1119/1.2186331](https://doi.org/10.1119/1.2186331) (cited on page 62).
- [Jen98] J. T. Jenkins. ‘Kinetic Theory for Nearly Elastic Spheres’. In: *Physics of Dry Granular Media*. Ed. by H. J. Herrmann, J.-P. Hovi, and S. Luding. Dordrecht: Springer Netherlands, 1998, pp. 353–370. DOI: [10.1007/978-94-017-2653-5_26](https://doi.org/10.1007/978-94-017-2653-5_26) (cited on page 54).
- [JG15] J. Jin and W. A. Goddard. ‘Mechanisms Underlying the Mpemba Effect in Water from Molecular Dynamics Simulations’. In: *J. Phys. Chem. C* 119 (2015), pp. 2622–2629. DOI: [10.1021/jp511752n](https://doi.org/10.1021/jp511752n) (cited on page 62).
- [JM89] J. T. Jenkins and F. Mancini. ‘Kinetic theory for binary mixtures of smooth, nearly elastic spheres’. In: *Phys. Fluids A* 1 (1989), pp. 2050–2057. DOI: [10.1063/1.857479](https://doi.org/10.1063/1.857479) (cited on page 54).
- [JNB96] H. M. Jaeger, S. R. Nagel, and R. Behringer. ‘The Physics of Granular Materials’. In: *Phys. Today* 49 (1996), pp. 32–38. DOI: [10.1063/1.881494](https://doi.org/10.1063/1.881494) (cited on page 7).

- [JR85] J. T. Jenkins and M. W. Richman. 'Kinetic theory for plane flows of a dense gas of identical, rough, inelastic, circular disks'. In: *Phys. Fluids* 28 (1985), pp. 3485–3494. DOI: [10.1063/1.865302](https://doi.org/10.1063/1.865302) (cited on page 54).
- [JY02] J. T. Jenkins and D. K. Yoon. 'Segregation in Binary Mixtures Under gravity'. In: *Phys. Rev. Lett.* 88 (2002), p. 194301. DOI: [10.1103/PhysRevLett.88.194301](https://doi.org/10.1103/PhysRevLett.88.194301) (cited on pages 27, 300).
- [Kac56] M. Kac. 'Foundations of Kinetic Theory'. In: *Proceedings of the Third Berkeley Symposium on Mathematical Statistics and Probability, Volume 3: Contributions to Astronomy and Physics*. Ed. by J. Neyman. Berkeley and Los Angeles: University of California Press, 1956, pp. 171–19 (cited on page 280).
- [Kam07] N. G. Van Kampen. *Stochastic Processes in Physics and Chemistry*. Amsterdam: North-Holland, 2007 (cited on pages 27, 306, 318).
- [Kan17] Kiyoshi Kanazawa. 'Analytical Solution to Nonlinear Non-Gaussian Langevin Equation'. In: *Statistical Mechanics for Athermal Fluctuation: Non-Gaussian Noise in Physics*. Singapore: Springer Singapore, 2017, pp. 103–132. DOI: [10.1007/978-981-10-6332-9_8](https://doi.org/10.1007/978-981-10-6332-9_8) (cited on page 29).
- [Kat09] J. I. Katz. 'When hot water freezes before cold'. In: *Am. J. Phys.* 77 (2009), pp. 27–29. DOI: [10.1119/1.2996187](https://doi.org/10.1119/1.2996187) (cited on page 62).
- [KB20] A. Kumar and J. Bechhoefer. 'Exponentially faster cooling in a colloidal system'. In: *Nature* 584 (2020), pp. 64–68. DOI: [10.1038/s41586-020-2560-x](https://doi.org/10.1038/s41586-020-2560-x) (cited on pages 63, 85).
- [KCB22] A. Kumar, R. Chétrite, and J. Bechhoefer. 'Anomalous heating in a colloidal system'. In: *Proc. Natl. Acad. Sci. U.S.A.* 119 (2022), e2118484119. DOI: [10.1073/pnas.2118484119](https://doi.org/10.1073/pnas.2118484119) (cited on page 63).
- [KCD22] L. Kool, P. Charbonneau, and K. E. Daniels. 'Gardner-like crossover from variable to persistent force contacts in granular crystals'. In: *Phys. Rev. E* 106 (2022), p. 054901. DOI: [10.1103/PhysRevE.106.054901](https://doi.org/10.1103/PhysRevE.106.054901) (cited on page 7).
- [KE19] M. Klement and M. Engel. 'Efficient equilibration of hard spheres with Newtonian event chains'. In: *J. Chem. Phys.* 150 (2019), p. 174108. DOI: [10.1063/1.5090882](https://doi.org/10.1063/1.5090882) (cited on page 72).
- [Kei+19] N. C. Keim, J. D. Paulsen, Z. Zeravcic, S. Sastry, and S. R. Nagel. 'Memory formation in matter'. In: *Rev. Mod. Phys.* 91 (2019), p. 035002. DOI: [10.1103/RevModPhys.91.035002](https://doi.org/10.1103/RevModPhys.91.035002) (cited on page 58).
- [Kel69] G. S. Kell. 'The freezing of hot and cold water'. In: *Am. J. Phys.* 37 (1969), pp. 564–565. DOI: [10.1119/1.1975687](https://doi.org/10.1119/1.1975687) (cited on page 62).

- [KG13] N. Khalil and V. Garzó. ‘Transport coefficients for driven granular mixtures at low density’. In: *Phys. Rev. E* 88 (2013), p. 052201. DOI: [10.1103/PhysRevE.88.052201](https://doi.org/10.1103/PhysRevE.88.052201) (cited on page 288).
- [KG18] N. Khalil and V. Garzó. ‘Heat flux of driven granular mixtures at low density: Stability analysis of the homogeneous steady state’. In: *Phys. Rev. E* 97 (2018), p. 022902. DOI: [10.1103/PhysRevE.97.022902](https://doi.org/10.1103/PhysRevE.97.022902) (cited on page 299).
- [KG19] N. Khalil and V. Garzó. ‘Erratum: Transport coefficients for driven granular mixtures at low density [Phys. Rev. E 88, 052201 (2013)] and Heat flux of driven granular mixtures at low density: Stability analysis of the homogeneous steady state [Phys. Rev. E 97, 022902 (2018)]’. In: *Phys. Rev. E* 99 (2019), p. 059901. DOI: [10.1103/PhysRevE.99.059901](https://doi.org/10.1103/PhysRevE.99.059901) (cited on page 299).
- [KG20] N. Khalil and V. Garzó. ‘Unified hydrodynamic description for driven and undriven inelastic Maxwell mixtures at low density’. In: *J. Phys. A: Math. Theor.* 53 (2020), 355002. DOI: [10.1088/1751-8121/ab9f72](https://doi.org/10.1088/1751-8121/ab9f72) (cited on page 288).
- [Kir46] J. G. Kirkwood. ‘The Statistical Mechanical Theory of Transport Processes I. General Theory’. In: *J. Chem. Phys.* 14 (1946), pp. 180–201. DOI: [10.1063/1.1724117](https://doi.org/10.1063/1.1724117) (cited on page 16).
- [Kir47] J. G. Kirkwood. ‘The Statistical Mechanical Theory of Transport Processes II. Transport in Gases’. In: *J. Chem. Phys.* 15 (1947), pp. 72–76. DOI: [10.1063/1.1746292](https://doi.org/10.1063/1.1746292) (cited on page 16).
- [KL51] S. Kullback and R. A. Leibler. ‘On Information and Sufficiency’. In: *Ann. Math. Statist.* 22 (1951), pp. 79–86. DOI: [10.1214/aoms/1177729694](https://doi.org/10.1214/aoms/1177729694) (cited on pages 12, 86).
- [Kli+19] I. Klich, O. Raz, O. Hirschberg, and M. Vucelja. ‘Mpemba Index and Anomalous Relaxation’. In: *Phys. Rev. X* 9 (2019), p. 021060. DOI: [10.1103/PhysRevX.9.021060](https://doi.org/10.1103/PhysRevX.9.021060) (cited on pages 63, 85).
- [Kli94] Y. L. Klimontovich. ‘Nonlinear Brownian motion’. In: *Physics-Uspokhi* 37 (1994), pp. 737–767. DOI: [10.1070/PU1994v037n08ABEH000038](https://doi.org/10.1070/PU1994v037n08ABEH000038) (cited on page 306).
- [Kni96] C. A. Knight. ‘The Mpemba effect: The freezing times of cold and hot water’. In: *Am. J. Phys.* 64 (1996), pp. 524–524. DOI: [10.1119/1.18275](https://doi.org/10.1119/1.18275) (cited on page 62).
- [Kov+79] A. J. Kovacs, J. J. Aklonis, J. M. Hutchinson, and A. R. Ramos. ‘Isobaric volume and enthalpy recovery of glasses. II. A transparent multiparameter theory’. In: *J. Polym. Sci. Polym. Phys. Ed.* 17 (1979), pp. 1097–1162. DOI: [10.1002/pol.1979.180170701](https://doi.org/10.1002/pol.1979.180170701) (cited on page 59).

- [Kov63] A. J. Kovacs. 'Transition vitreuse dans les polymères amorphes. Etude phénoménologique'. In: *Fortschr. Hochpolym.-Forsch.* 3 (1963), pp. 394–507. doi: [10.1007/BFb0050366](https://doi.org/10.1007/BFb0050366) (cited on page 59).
- [KP92] P. E. Kloeden and E. Platen. *Numerical Solution of Stochastic Differential Equations*. Springer Berlin, Heidelberg, 1992 (cited on pages 81, 318).
- [Kra+09] W. T. Kranz, N. V. Brilliantov, T. Pöschel, and A. Zippelius. 'Correlation of spin and velocity in the homogeneous cooling state of a granular gas of rough particles'. In: *Eur. Phys. J. Spec. Top.* 179 (2009), pp. 91–111. doi: [10.1140/epjst/e2010-01196-0](https://doi.org/10.1140/epjst/e2010-01196-0) (cited on page 283).
- [KSF63] A. J. Kovacs, R. A. Stratton, and J. D. Ferry. 'Dynamic Mechanical Properties of Polyvinyl Acetate in Shear in the Glass Transition Temperature Range'. In: *J. Phys. Chem.* 67 (1963), pp. 152–161. doi: [10.1021/j100795a037](https://doi.org/10.1021/j100795a037) (cited on page 59).
- [KSG14] G. M. Kremer, A. Santos, and V. Garzó. 'Transport coefficients of a granular gas of inelastic rough hard spheres'. In: *Phys. Rev. E* 90 (2014), p. 022205. doi: [10.1103/PhysRevE.90.022205](https://doi.org/10.1103/PhysRevE.90.022205) (cited on pages 13, 242, 284, 286, 287).
- [KSI17] R. Kürsten, V. Sushkov, and T. Ihle. 'Giant Kovacs-Like Memory Effect for Active Particles'. In: *Phys. Rev. Lett.* 119 (2017), p. 188001. doi: [10.1103/PhysRevLett.119.188001](https://doi.org/10.1103/PhysRevLett.119.188001) (cited on pages 60, 301).
- [Kub66] R. Kubo. 'The fluctuation-dissipation theorem'. In: *Rep. Prog. Phys.* 29 (1966), p. 255. doi: [10.1088/0034-4885/29/1/306](https://doi.org/10.1088/0034-4885/29/1/306) (cited on page 27).
- [Kum80] K. Kumar. 'Mpemba effect and 18th century ice-cream'. In: *Phys. Educ.* 15 (1980), pp. 268–268. doi: [10.1088/0031-9120/15/5/101](https://doi.org/10.1088/0031-9120/15/5/101) (cited on page 62).
- [Lan08] P. Langevin. 'Sur la théorie du mouvement brownien'. In: *C. R. Acad. Sci. Paris* 146 (1908), pp. 530–533 (cited on pages 11, 27, 305).
- [Las+17] A. Lasanta, F. Vega Reyes, A. Prados, and A. Santos. 'When the Hotter Cools More Quickly: Mpemba Effect in Granular Fluids'. In: *Phys. Rev. Lett.* 119 (2017), p. 148001. doi: [10.1103/PhysRevE.99.060901](https://doi.org/10.1103/PhysRevE.99.060901) (cited on pages 11, 63, 64, 85).
- [Las+19] A. Lasanta, F. Vega Reyes, V. Garzó, and A. Santos. 'Intruders in disguise: Mimicry effect in granular gases'. In: *Phys. Fluids* 31 (2019), p. 063306. doi: [10.1063/1.5097398](https://doi.org/10.1063/1.5097398) (cited on page 300).
- [Lee+19] L. M. Lee, J. P. Ryan, Y. Lahini, M. Holmes-Cerfon, and S. M. Rubinstein. 'Geometric frustration induces the transition between rotation and counter-rotation in swirled granular media'. In: *Phys. Rev. E* 100 (2019), p. 012903. doi: [10.1103/PhysRevE.100.012903](https://doi.org/10.1103/PhysRevE.100.012903) (cited on page 7).

- [LG97] D. S. Lemons and A. Gythiel. ‘Paul Langevin’s 1908 paper “On the Theory of Brownian Motion” [“Sur la théorie du mouvement brownien,” C. R. Acad. Sci. (Paris) 146, 530–533 (1908)]’. In: *Am. J. Phys.* 65 (1997), pp. 1079–1081. DOI: [10.1119/1.18725](https://doi.org/10.1119/1.18725) (cited on pages 11, 27, 305).
- [LH99] S. Luding and H. J. Herrmann. ‘Cluster-growth in freely cooling granular media’. In: *Chaos* 9 (1999), pp. 673–681. DOI: [10.1063/1.166441](https://doi.org/10.1063/1.166441) (cited on pages 9, 45, 243, 280, 287).
- [Lin+22] J. Lin, K. Li, J. He, J. Ren, and J. Wang. ‘Power statistics of Otto heat engines with the Mpemba effect’. In: *Phys. Rev. E* 105 (2022), p. 014104. DOI: [10.1103/PhysRevE.105.014104](https://doi.org/10.1103/PhysRevE.105.014104) (cited on page 85).
- [LM98] S. Luding and S. McNamara. ‘How to handle the inelastic collapse of a dissipative hard-sphere gas with the TC model’. In: *Granul. Matter* 1 (1998), pp. 113–128. DOI: [10.1007/s100350050017](https://doi.org/10.1007/s100350050017) (cited on pages 78, 300).
- [Lob+08] A. E. Lobkovsky, A. V. Orpe, R. Molloy, A. Kudrolli, and D. H. Rothman. ‘Erosion of a granular bed driven by laminar fluid flow’. In: *J. Fluid Mech.* 605 (2008), pp. 47–58. DOI: [10.1017/S0022112008001389](https://doi.org/10.1017/S0022112008001389) (cited on page 6).
- [LR17] Z. Lu and O. Raz. ‘Nonequilibrium thermodynamics of the Markovian Mpemba effect and its inverse’. In: *Proc. Natl. Acad. Sci. U.S.A.* 114 (2017), pp. 5083–5088. DOI: [10.1073/pnas.1701264114](https://doi.org/10.1073/pnas.1701264114) (cited on pages 63, 85).
- [LTL97] A. Lorenz, C. Tuozzolo, and M. Y. Louge. ‘Measurements of impact properties of small, nearly spherical particles’. In: *Exp. Mech.* 37 (1997), pp. 292–298. DOI: [10.1007/BF02317421](https://doi.org/10.1007/BF02317421) (cited on page 299).
- [Lul+21] M. Lulli, L.-H. Zhang, C.-S. Lee, H.-Y. Deng, and C.-H. Lam. ‘Kovacs effect in glass with material memory revealed in non-equilibrium particle interactions’. In: *J. Stat. Mech.* (2021), p. 093303. DOI: [10.1088/1742-5468/ac1f26](https://doi.org/10.1088/1742-5468/ac1f26) (cited on page 60).
- [Lun+84] C. K. K. Lun, S. B. Savage, D. J. Jeffrey, and N. Chepurniy. ‘Kinetic theories for granular flow: inelastic particles in Couette flow and slightly inelastic particles in a general flowfield’. In: *J. Fluid Mech.* 140 (1984), pp. 223–256. DOI: [10.1017/S0022112084000586](https://doi.org/10.1017/S0022112084000586) (cited on page 54).
- [Lut01] J. F. Lutsko. ‘Model for the atomic-scale structure of the homogeneous cooling state of granular fluids’. In: *Phys. Rev. E* 63 (2001), p. 061211. DOI: [10.1103/PhysRevE.63.061211](https://doi.org/10.1103/PhysRevE.63.061211) (cited on page 77).
- [Maa+08] C. C. Maaß, N. Isert, G. Maret, and C. M. Aegerter. ‘Experimental Investigation of the Freely Cooling Granular Gas’. In: *Phys. Rev. Lett.* 100 (2008), 248001. DOI: [10.1103/PhysRevLett.100.248001](https://doi.org/10.1103/PhysRevLett.100.248001) (cited on page 299).

- [Mac96] P. K. Maciejewski. 'Evidence of a Convective Instability Allowing Warm Water to Freeze in Less Time Than Cold Water'. In: *J. Heat Transf.* 118 (1996), pp. 65–72. doi: [10.1115/1.2824069](https://doi.org/10.1115/1.2824069) (cited on page 62).
- [Max67] J. C. Maxwell. 'IV. On the Dynamical Theory of Gases'. In: *Phil. Trans. Roy. Soc. (London)* 157 (1867), pp. 49–88. doi: [10.1098/rstl.1867.0004](https://doi.org/10.1098/rstl.1867.0004) (cited on page 16).
- [MBF76] N. Maw, J. R. Barber, and J. N. Fawcett. 'The oblique impact of elastic spheres'. In: *Wear* 38 (1976), pp. 101–114. doi: [https://doi.org/10.1016/0043-1648\(76\)90201-5](https://doi.org/10.1016/0043-1648(76)90201-5) (cited on page 299).
- [MC95] M. Marín and P. Cordero. 'An empirical assessment of priority queues in event-driven molecular dynamics simulation'. In: *Comput. Phys. Commun.* 92 (1995), pp. 214–224. doi: [10.1016/0010-4655\(95\)00120-2](https://doi.org/10.1016/0010-4655(95)00120-2) (cited on page 76).
- [Meg23] A. Megías. *Computer programs of the PhD thesis "Influence of roughness on the dynamical properties of granular gases"*. 2023. URL: https://github.com/amegiasf/IRDPGG_PhD_thesis_23 (visited on 05/15/2023) (cited on pages 71, 89, 153, 176, 214, 243, 313, 318).
- [Meh93] A. Mehta, ed. *Granular Matter: An Interdisciplinary Approach*. Springer-Verlag, Berlin, 1993 (cited on pages 279, 280).
- [Met+53] N. Metropolis, A. W. Rosenbluth, M. N. Rosenbluth, A. H. Teller, and E. Teller. 'Equation of State Calculations by Fast Computing Machines'. In: *J. Chem. Phys.* 21 (1953), pp. 1087–1092. doi: [10.1063/1.1699114](https://doi.org/10.1063/1.1699114) (cited on page 68).
- [MG02] J. M. Montanero and V. Garzó. 'Rheological properties in a low-density granular mixture'. In: *Physica A* 310 (2002), pp. 17–38. doi: [10.1016/S0378-4371\(02\)00786-0](https://doi.org/10.1016/S0378-4371(02)00786-0) (cited on page 38).
- [MGT12] P. Maynar, M. I. García de Soria, and E. Trizac. 'Which reference state for a granular gas heated by the stochastic thermostat?' In: *AIP Conf. Proc.* 1501 (2012), pp. 1009–1016. doi: [10.1063/1.4769652](https://doi.org/10.1063/1.4769652) (cited on page 288).
- [Mic+22] B. Michael, M. Simon, C. Gustavo, and F. Eric. 'Wave spectroscopy in a driven granular material'. In: *Proc. R. Soc. A* 476 (2022), p. 20220014. doi: [10.1098/rspa.2022.0014](https://doi.org/10.1098/rspa.2022.0014) (cited on page 288).
- [Mic10] C. De Michele. 'Simulating hard rigid bodies'. In: *J. Comput. Phys.* 229 (2010), pp. 3276–3294. doi: [10.1016/j.jcp.2010.01.002](https://doi.org/10.1016/j.jcp.2010.01.002) (cited on page 76).

- [Mit+11] P. P. Mitrano, S. R. Dahl, D. J. Cromer, M. S. Pacella, and C. M. Hrenya. ‘Instabilities in the homogeneous cooling of a granular gas: A quantitative assessment of kinetic-theory predictions’. In: *Phys. Fluids* 23 (2011), p. 093303. doi: [10.1063/1.3633012](https://doi.org/10.1063/1.3633012) (cited on pages 45, 243, 287).
- [Mit+12] P. P. Mitrano, V. Garz3, A. M. Hilger, C. J. Ewasko, and C. M. Hrenya. ‘Assessing a modified-Sonine kinetic theory for instabilities in highly dissipative, cooling granular gases’. In: *Phys. Rev. E* 85 (2012), p. 041303. doi: [10.1103/PhysRevE.85.041303](https://doi.org/10.1103/PhysRevE.85.041303) (cited on pages 45, 243, 287).
- [Mit+13] P. P. Mitrano, S. R. Dahl, A. M. Hilger, C. J. Ewasko, and C. M. Hrenya. ‘Dual role of friction in granular flows: attenuation versus enhancement of instabilities’. In: *J. Fluid Mech.* 729 (2013), pp. 484–495. doi: [10.1017/jfm.2013.328](https://doi.org/10.1017/jfm.2013.328) (cited on pages 45, 243, 287).
- [Mit+14] P. P. Mitrano, J. R. Zenk, S. Benyahia, J. E. Galvin, S. R. Dahl, and C. M. Hrenya. ‘Kinetic-theory predictions of clustering instabilities in granular flows: beyond the small-Knudsen-number regime’. In: *J. Fluid Mech.* 738 (2014), p. 041303. doi: [10.1017/jfm.2013.602](https://doi.org/10.1017/jfm.2013.602) (cited on pages 45, 243, 287).
- [ML04] S. Miller and S. Luding. ‘Event-driven molecular dynamics in parallel’. In: *J. Comput. Phys.* 193 (2004), pp. 306–316. doi: [10.1016/j.jcp.2003.08.009](https://doi.org/10.1016/j.jcp.2003.08.009) (cited on pages 72, 75, 76).
- [MM12] R. Mannella and P. V. E. McClintock. ‘It3 versus Stratonovich: 30 years later’. In: *Fluct. Noise Lett.* 11 (2012), p. 1240010. doi: [10.1142/S021947751240010X](https://doi.org/10.1142/S021947751240010X) (cited on page 306).
- [MO69] E. B. Mpemba and D. G. Osborne. ‘Cool?’ In: *Phys. Educ.* 4 (1969), pp. 172–175. doi: [10.1088/0031-9120/4/3/312](https://doi.org/10.1088/0031-9120/4/3/312) (cited on page 61).
- [Mom+21] E. Momp3, M. A. M. A. L3pez-Casta3o, A. Lasanta, F. Vega Reyes, and A. Torrente. ‘Memory effects in a gas of viscoelastic particles’. In: *Phys. Fluids* 33 (2021), p. 062005. doi: [10.1063/5.0050804](https://doi.org/10.1063/5.0050804) (cited on pages 60, 63, 64, 85).
- [Mor+20] I. L. Morgan, R. Avinery, G. Rahamim, R. Beck, and O. A. Saleh. ‘Glassy Dynamics and Memory Effects in an Intrinsically Disordered Protein Construct’. In: *Phys. Rev. Lett.* 125 (2020), p. 058001. doi: [10.1103/PhysRevLett.125.058001](https://doi.org/10.1103/PhysRevLett.125.058001) (cited on page 60).
- [MR06] D. van der Meer and P. Reimann. ‘Temperature anisotropy in a driven granular gas’. In: *Europhys. Lett.* 74 (2006), pp. 384–390. doi: [10.1209/epl/i2005-10552-9](https://doi.org/10.1209/epl/i2005-10552-9) (cited on page 288).

- [MS00] J. M. Montanero and A. Santos. ‘Computer simulation of uniformly heated granular fluids’. In: *Granul. Matter* 2 (2000), pp. 53–64. doi: [10.1007/s100350050035](https://doi.org/10.1007/s100350050035) (cited on pages 36, 37, 46, 69, 288, 314, 316, 317).
- [MS04] S. Mossa and F. Sciortino. ‘Crossover (or Kovacs) Effect in an Aging Molecular Liquid’. In: *Phys. Rev. Lett.* 92 (2004), p. 045504. doi: [10.1103/PhysRevLett.92.045504](https://doi.org/10.1103/PhysRevLett.92.045504) (cited on page 60).
- [MS19a] A. Megías and A. Santos. ‘Driven and undriven states of multicomponent granular gases of inelastic and rough hard disks or spheres’. In: *Granul. Matter* 21 (2019), p. 49. doi: [10.1007/s10035-019-0901-y](https://doi.org/10.1007/s10035-019-0901-y) (cited on pages 13, 38, 42, 43, 47, 283, 284, 289, 300).
- [MS19b] A. Megías and A. Santos. ‘Energy Production Rates of Multicomponent Granular Gases of Rough Particles. A Unified View of Hard-Disk and Hard-Sphere Systems’. In: *AIP Conf. Proc.* 2132 (2019), 080003. doi: [10.1063/1.5119584](https://doi.org/10.1063/1.5119584) (cited on pages 13, 38, 42–44, 283, 284, 300).
- [MS20] A. Megías and A. Santos. ‘Kullback–Leibler divergence of a freely cooling granular gas’. In: *Entropy* 22 (2020), p. 1308. doi: [10.3390/e22040469](https://doi.org/10.3390/e22040469) (cited on page 10).
- [MS21a] A. Megías and A. Santos. ‘Hydrodynamics of granular gases of inelastic and rough hard disks or spheres. I. Transport coefficients’. In: *Phys. Rev. E* 104 (2021), p. 034901. doi: [10.1103/PhysRevE.104.034901](https://doi.org/10.1103/PhysRevE.104.034901) (cited on page 10).
- [MS21b] A. Megías and A. Santos. ‘Hydrodynamics of granular gases of inelastic and rough hard disks or spheres. II. Stability analysis’. In: *Phys. Rev. E* 104 (2021), p. 034902. doi: [10.1103/PhysRevE.104.034902](https://doi.org/10.1103/PhysRevE.104.034902) (cited on page 10).
- [MS21c] A. Megías and A. Santos. ‘Relative entropy of freely cooling granular gases. A molecular dynamics study’. In: *EPJ Web Conf.* 249 (2021), p. 04006. doi: [10.1051/epjconf/202124904006](https://doi.org/10.1051/epjconf/202124904006) (cited on pages 10, 43).
- [MS22a] A. Megías and A. Santos. ‘Kinetic Theory and Memory Effects of Homogeneous Inelastic Granular Gases under Nonlinear Drag’. In: *Entropy* 10 (2022). doi: [10.3390/e24101436](https://doi.org/10.3390/e24101436) (cited on pages 10, 314, 318).
- [MS22b] A. Megías and A. Santos. ‘Mpemba-like effect protocol for granular gases of inelastic and rough hard disks’. In: *Front. Phys.* 10 (2022), p. 971671. doi: [10.3389/fphy.2022.971671](https://doi.org/10.3389/fphy.2022.971671) (cited on page 10).
- [MS23] A. Megías and A. Santos. ‘Translational and rotational non-Gaussianities in homogeneous freely evolving granular gases’. In: *Phys. Rev. E* 108 (2023), p. 014902. doi: [10.1103/PhysRevE.108.014902](https://doi.org/10.1103/PhysRevE.108.014902) (cited on pages 10, 44, 214).

- [MS96] J. M. Montanero and A. Santos. ‘Nonequilibrium entropy of a sheared gas’. In: *Physica A* 225 (1996), pp. 7–18. DOI: [10.1016/0378-4371\(95\)00384-3](https://doi.org/10.1016/0378-4371(95)00384-3) (cited on page 47).
- [MSG05] J. M. Montanero, A. Santos, and V. Garzó. ‘DSMC evaluation of the Navier-Stokes shear viscosity of a granular fluid’. In: *AIP Conf. Proc.* 762 (2005), pp. 797–802. DOI: [10.1063/1.1941632](https://doi.org/10.1063/1.1941632) (cited on page 54).
- [MSG07] J. M. Montanero, A. Santos, and V. Garzó. ‘First-order Chapman-Enskog velocity distribution function in a granular gas’. In: *Physica A* 376 (2007), pp. 75–93. DOI: [10.1016/j.physa.2006.10.080](https://doi.org/10.1016/j.physa.2006.10.080) (cited on page 54).
- [MSP22] A. Megías, A. Santos, and A. Prados. ‘Thermal versus entropic Mpemba effect in molecular gases with nonlinear drag’. In: *Phys. Rev. E* 105 (2022), p. 054140. DOI: [10.1103/PhysRevE.105.054140](https://doi.org/10.1103/PhysRevE.105.054140) (cited on pages 10, 64, 152, 283, 318).
- [MT11] P. Maynar and E. Trizac. ‘Entropy of Continuous Mixtures and the Measure Problem’. In: *Phys. Rev. Lett.* 106 (2011), p. 160603. DOI: [10.1103/PhysRevLett.106.160603](https://doi.org/10.1103/PhysRevLett.106.160603) (cited on pages 120, 280).
- [Mul02] T. Mullin. ‘Mixing and De-mixing’. In: *Science* 295 (2002), pp. 1851–1851. DOI: [10.1126/science.1070258](https://doi.org/10.1126/science.1070258) (cited on page 7).
- [Mur21] Y. Murashita, ed. *Fluctuation Theorems under Divergent Entropy Production and their Applications for Fundamental Problems in Statistical Physics*. Springer Singapore, 2021 (cited on page 49).
- [MY94] S. McNamara and W. R. Young. ‘Inelastic collapse in two dimensions’. In: *Phys. Rev. E* 50 (1994), pp. R28–R31. DOI: [10.1103/PhysRevE.50.R28](https://doi.org/10.1103/PhysRevE.50.R28) (cited on page 78).
- [MY96] S. McNamara and W. R. Young. ‘Dynamics of a freely evolving, two-dimensional granular medium’. In: *Phys. Rev. E* 53 (1996), pp. 5089–5100. DOI: [10.1103/PhysRevE.53.5089](https://doi.org/10.1103/PhysRevE.53.5089) (cited on page 280).
- [NBE98] T. P. C. van Noije, R. Brito, and M. H. Ernst. ‘Spatial correlations in compressible granular flows’. In: *Phys. Rev. E* 57 (1998), p. R4891. DOI: [10.1103/PhysRevE.57.R4891](https://doi.org/10.1103/PhysRevE.57.R4891) (cited on page 46).
- [NE98] T. P. C. van Noije and M. H. Ernst. ‘Velocity distributions in homogeneous granular fluids: the free and the heated case’. In: *Granul. Matter* 1 (1998), pp. 57–64. DOI: [10.1007/s100350050009](https://doi.org/10.1007/s100350050009) (cited on pages 36, 37, 46, 279, 285, 288, 314).
- [New01] I. Newton. ‘VII. Scala graduum caloris’. In: *Phil. Trans. R. Soc.* 22 (1701), pp. 824–829. DOI: [10.1098/rstl.1700.0082](https://doi.org/10.1098/rstl.1700.0082) (cited on page 62).

- [Noi+97] T. P. C. van Noije, M. H. Ernst, R. Brito, and J. A. G. Orza. ‘Mesoscopic Theory of Granular Fluids’. In: *Phys. Rev. Lett.* 79 (1997), pp. 411–414. doi: [10.1103/PhysRevLett.79.411](https://doi.org/10.1103/PhysRevLett.79.411) (cited on page 46).
- [Noi+99] T. P. C. van Noije, M. H. Ernst, E. Trizac, and I. Pagonabarraga. ‘Randomly driven granular fluids: Large-scale structure’. In: *Phys. Rev. E* 59 (1999), pp. 4326–4341. doi: [10.1103/PhysRevE.59.4326](https://doi.org/10.1103/PhysRevE.59.4326) (cited on page 46).
- [OB67] J. Orban and A. Bellemans. ‘Velocity-inversion and irreversibility in a dilute gas of hard disks’. In: *Phys. Lett. A* 24 (1967), pp. 620–621. doi: [10.1016/0375-9601\(67\)90651-2](https://doi.org/10.1016/0375-9601(67)90651-2) (cited on pages 12, 121, 281).
- [OB69] J. Orban and A. Bellemans. ‘Entropy and irreversibility in a dilute gas of hard disks’. In: *J. Stat. Phys.* 1 (1969), pp. 467–474. doi: [10.1007/BF01106581](https://doi.org/10.1007/BF01106581) (cited on pages 12, 121, 281).
- [Osb79] D. G. Osborne. ‘Mind on ice’. In: *Phys. Educ.* 14 (1979), pp. 414–417. doi: [10.1088/0031-9120/14/7/313](https://doi.org/10.1088/0031-9120/14/7/313) (cited on page 61).
- [OUO80] S. Ogawa, A. Umemura, and N. Oshima. ‘On the equations of fully fluidized granular materials’. In: *Z. Angew. Math. Phys.* 31 (1980), pp. 483–493. doi: [10.1007/BF01590859](https://doi.org/10.1007/BF01590859) (cited on page 7).
- [Ova+14] C. Ovalle, E. Frossard, C. Dano, W. Hu, S. Maiolino, and P.-Y. Hicher. ‘The effect of size on the strength of coarse rock aggregates and large rockfill samples through experimental data’. In: *Acta Mech.* 225 (2014), pp. 2199–2216. doi: [10.1007/s00707-014-1127-z](https://doi.org/10.1007/s00707-014-1127-z) (cited on page 6).
- [Paw67] R. F. Pawula. ‘Approximation of the Linear Boltzmann Equation by the Fokker-Planck Equation’. In: *Phys. Rev.* 162 (1967), pp. 186–188. doi: [10.1103/PhysRev.162.186](https://doi.org/10.1103/PhysRev.162.186) (cited on page 306).
- [PB10] A. Prados and J. J. Brey. ‘The Kovacs effect: a master equation analysis’. In: *J. Stat. Mech.* (2010), P02009. doi: [10.1088/1742-5468/2010/02/P02009](https://doi.org/10.1088/1742-5468/2010/02/P02009) (cited on page 60).
- [PBF06] T. Pöschel, N. V. Brilliantov, and A. Formella. ‘Impact of high-energy tails on granular gas properties’. In: *Phys. Rev. E* 74 (2006), p. 041302. doi: [10.1103/PhysRevE.74.041302](https://doi.org/10.1103/PhysRevE.74.041302) (cited on page 37).
- [Pid22] F. B. Pidduck. ‘The Kinetic Theory of a Special Type of Rigid Molecule’. In: *Proc. R. Soc. Lond. A* 101 (1922), pp. 101–112. doi: [10.1098/rspa.1922.0028](https://doi.org/10.1098/rspa.1922.0028) (cited on page 24).
- [Pla17] M. Planck. ‘Über einen Satz der statistischen Dynamik und seine Erweiterung in der Quantentheorie’. In: *Sitzber. Preuss. Akad. Wiss.* 24 (1917), pp. 324–341 (cited on page 305).

- [Poi90] H. Poincaré. ‘Sur le problème des trois corps et les équations de la dynamique’. In: *Acta Math.* 13 (1890), pp. 1–270. DOI: [10.1007/BF02392506](https://doi.org/10.1007/BF02392506) (cited on page 50).
- [PP17] C. A. Plata and A. Prados. ‘Global stability and H theorem in lattice models with nonconservative interactions’. In: *Phys. Rev. E* 95 (2017), 052121. DOI: [10.1103/PhysRevE.95.052121](https://doi.org/10.1103/PhysRevE.95.052121) (cited on pages 119, 295).
- [PS05] T. Pöschel and T. Schwager. *Computational Granular Dynamics. Models and algorithms*. Springer Berlin, Heidelberg, 2005 (cited on pages 7, 9, 68, 69, 74, 78).
- [PSF03] J. R. Pomerening, E. D. Sontag, and J. E. Ferrell. ‘Building a cell cycle oscillator: hysteresis and bistability in the activation of Cdc2’. In: *Nat. Cell Biol.* 5 (2003), pp. 346–351. DOI: [10.1038/ncb954](https://doi.org/10.1038/ncb954) (cited on page 58).
- [PSP21] A. Patrón, B. Sánchez-Rey, and A. Prados. ‘Strong nonexponential relaxation and memory effects in a fluid with nonlinear drag’. In: *Phys. Rev. E* 104 (2021), p. 064127. DOI: [10.1103/PhysRevE.104.064127](https://doi.org/10.1103/PhysRevE.104.064127) (cited on pages 11, 60, 63, 85, 86, 152, 277, 278, 283).
- [PT14] A. Prados and E. Trizac. ‘Kovacs-Like Memory Effect in Driven Granular Gases’. In: *Phys. Rev. Lett.* 112 (2014), p. 198001. DOI: [10.1103/PhysRevLett.112.198001](https://doi.org/10.1103/PhysRevLett.112.198001) (cited on page 60).
- [Pyt23] Python Software Foundation. *HEAPQ - heap queue algorithm*. 2023. URL: <https://docs.python.org/3/library/heapq.html> (visited on 04/13/2023) (cited on page 76).
- [QG13] H. Qian and H. Ge. ‘Stochastic Processes, Fokker-Planck Equation’. In: *Encyclopedia of Systems Biology*. Ed. by W. Dubitzky, O. Wolkenhauer, K.-H. Cho, and H. Yokota. New York, NY: Springer New York, 2013, pp. 2000–2004. DOI: [10.1007/978-1-4419-9863-7_279](https://doi.org/10.1007/978-1-4419-9863-7_279) (cited on page 305).
- [Raj90] J. Rajchenbach. ‘Flow in Powders: From Discrete Avalanches to Continuous Regime’. In: *Phys. Rev. Lett.* 65 (1990), pp. 2221–2224. DOI: [10.1103/PhysRevLett.65.2221](https://doi.org/10.1103/PhysRevLett.65.2221) (cited on page 6).
- [Rap04] D. C. Rapaport. *The Art of Molecular Dynamics Simulations*. 2nd ed. Cambridge University Press, Cambridge, 2004 (cited on page 75).
- [Rap80] D.C Rapaport. ‘The event scheduling problem in molecular dynamic simulation’. In: *J. Comput. Phys.* 34.2 (1980), pp. 184–201. DOI: [10.1016/0021-9991\(80\)90104-7](https://doi.org/10.1016/0021-9991(80)90104-7) (cited on page 76).
- [RCW76] K. M. Ralls, T. H. Courtney, and J. Wulff. *Introduction to Materials Science and Engineering*. John Wiley & Sons, 1976 (cited on page 58).

- [Ris12] H. Risken. *The Fokker-Planck Equation. Methods of Solution and Applications*. Springer-Verlag, 2012 (cited on page 306).
- [Ros31] W. D. Ross, ed. *The Works of Aristotle (Translated into English under the editorship of W.D. Ross)*. Vol. III. Oxford Clarendon Press, 1931 (cited on page 61).
- [RP14] M. Ruiz-García and A. Prados. ‘Kovacs effect in the one-dimensional Ising model: A linear response analysis’. In: *Phys. Rev. E* 89 (2014), p. 012140. doi: [10.1103/PhysRevE.89.012140](https://doi.org/10.1103/PhysRevE.89.012140) (cited on page 60).
- [SA05] A. Santos and A. Astillero. ‘System of elastic hard spheres which mimics the transport properties of a granular gas’. In: *Phys. Rev. E* 72 (2005), p. 031308. doi: [10.1103/PhysRevE.72.031308](https://doi.org/10.1103/PhysRevE.72.031308) (cited on page 54).
- [Sán+17] Sánchez, P., Scheeres, D., Hirabayashi, M., and Tardivel, S. ‘Looking into the evolution of granular asteroids in the Solar System’. In: *EPJ Web Conf.* 140 (2017), p. 14004. doi: [10.1051/epjconf/201714014004](https://doi.org/10.1051/epjconf/201714014004) (cited on page 6).
- [San18] A. Santos. ‘Interplay between polydispersity, inelasticity, and roughness in the freely cooling regime of hard-disk granular gases’. In: *Phys. Rev. E* 98 (2018), p. 012904. doi: [10.1103/PhysRevE.98.012904](https://doi.org/10.1103/PhysRevE.98.012904) (cited on pages 43, 283, 300).
- [SC13] Z. Shang and S. Chen. ‘3D DSMC Simulation of Rarefied Gas Flows around a Space Crew Capsule Using OpenFOAM’. In: *Open J. Appl. Sci.* 3 (2013), pp. 35–38. doi: [10.4236/ojapps.2013.31005](https://doi.org/10.4236/ojapps.2013.31005) (cited on page 68).
- [Sca12] A. Scala. ‘Event-driven Langevin simulations of hard spheres’. In: *Phys. Rev. E* 86 (2012), p. 026709. doi: [10.1103/PhysRevE.86.026709](https://doi.org/10.1103/PhysRevE.86.026709) (cited on pages 78–80, 89, 313, 318).
- [Sch+09] L. E. Schmidt, N. C. Keim, W. W. Zhang, and S. R. Nagel. ‘Memory-encoding vibrations in a disconnecting air bubble’. In: *Nat. Phys.* 5 (2009), pp. 343–346. doi: [10.1038/nphys1233](https://doi.org/10.1038/nphys1233) (cited on page 58).
- [Sch+21] N. Schneider, G. Musiolik, J. E. Kollmer, T. Steinpilz, M. Kruss, F. Jungmann, T. Demirci, J. Teiser, and G. Wurm. ‘Experimental study of clusters in dense granular gas and implications for the particle stopping time in protoplanetary disks’. In: *Icarus* 360 (2021), p. 114307. doi: [10.1016/j.icarus.2021.114307](https://doi.org/10.1016/j.icarus.2021.114307) (cited on page 6).
- [Ser+06] D. Serero, I. Goldhirsch, S. H. Noskowitz, and M.-L. Tan. ‘Hydrodynamics of granular gases and granular gas mixtures’. In: *J. Fluid Mech.* 554 (2006), pp. 237–258. doi: [10.1017/S0022112006009281](https://doi.org/10.1017/S0022112006009281) (cited on page 279).
- [SG98] N. Sela and I. Goldhirsch. ‘Hydrodynamic equations for rapid flows of smooth inelastic spheres, to Burnett order’. In: *J. Fluid Mech.* 361 (1998), pp. 41–74. doi: [10.1017/S0022112098008660](https://doi.org/10.1017/S0022112098008660) (cited on pages 54, 279).

- [SH91] S. B. Savage and K. Hutter. ‘The dynamics of avalanches of granular materials from initiation to runout. Part I: Analysis’. In: *Acta Mech.* 86 (1991), pp. 201–223. DOI: [10.1007/BF01175958](https://doi.org/10.1007/BF01175958) (cited on page 6).
- [Sha15] S. Shanmugam. ‘Granulation techniques and technologies: recent progresses’. In: *Bioimpacts* 5 (2015), pp. 55–63. DOI: [10.15171/bi.2015.04](https://doi.org/10.15171/bi.2015.04) (cited on page 6).
- [Sha48] C. E. Shannon. ‘A mathematical theory of communication’. In: *Bell Syst. Tech. J.* 27 (1948), pp. 379–423. DOI: [10.1002/j.1538-7305.1948.tb01338.x](https://doi.org/10.1002/j.1538-7305.1948.tb01338.x) (cited on page 48).
- [SK12] A. Santos and G. M. Kremer. ‘Relative Entropy of a Freely Cooling Granular Gas’. In: *AIP Conf. Proc.* 1501 (2012), pp. 1044–1050. DOI: [10.1063/1.4769657](https://doi.org/10.1063/1.4769657) (cited on page 284).
- [SKG10] A. Santos, G. M. Kremer, and V. Garzó. ‘Energy production rates in fluid mixtures of inelastic rough hard spheres’. In: *Prog. Theor. Phys. Suppl.* 184 (2010), pp. 31–48. DOI: [10.1143/PTPS.184.31](https://doi.org/10.1143/PTPS.184.31) (cited on page 300).
- [SKS11] A. Santos, G. M. Kremer, and M. dos Santos. ‘Sonine approximation for collisional moments of granular gases of inelastic rough spheres’. In: *Phys. Fluids* 23 (2011), p. 030604. DOI: [10.1063/1.3558876](https://doi.org/10.1063/1.3558876) (cited on pages 45, 284).
- [SL22] F. J. Schwarzendahl and H. Löwen. ‘Anomalous cooling and overcooling of active systems’. In: *Phys. Rev. Lett.* 129 (2022), p. 138002. DOI: [10.1103/PhysRevLett.129.138002](https://doi.org/10.1103/PhysRevLett.129.138002) (cited on pages 62, 85, 301).
- [SM09] A. Santos and J. M. Montanero. ‘The second and third Sonine coefficients of a freely cooling granular gas revisited’. In: *Granul. Matter* 11 (2009), pp. 157–168. DOI: [10.1007/s10035-009-0132-8](https://doi.org/10.1007/s10035-009-0132-8) (cited on pages 36, 37, 69, 120, 280, 314, 316, 317).
- [SMM00] R. Soto, M. Mareschal, and M. Malek Mansour. ‘Nonlinear analysis of the shearing instability in granular gases’. In: *Phys. Rev. E* 62 (2000), pp. 3836–3842. DOI: [10.1103/PhysRevE.62.3836](https://doi.org/10.1103/PhysRevE.62.3836) (cited on page 280).
- [Smo06] M. Smoluchowski. ‘Sur le chemin moyen parcouru par les molécules d’un gaz et sur son rapport avec la théorie de la diffusion’. In: *Bull. Int. Acad. Sc. Crac.* 1 (1906), pp. 202–213 (cited on page 305).
- [SP08] T. Schwager and T. Pöschel. ‘Coefficient of restitution for viscoelastic spheres: The effect of delayed recovery’. In: *Phys. Rev. E* 78 (2008), p. 051304. DOI: [10.1103/PhysRevE.78.051304](https://doi.org/10.1103/PhysRevE.78.051304) (cited on page 22).

- [SP20] A. Santos and A. Prados. ‘Mpemba effect in molecular gases under nonlinear drag’. In: *Phys. Fluids* 32 (2020), p. 072010. DOI: [10.1063/5.0016243](https://doi.org/10.1063/5.0016243) (cited on pages [11](#), [63–65](#), [85–87](#), [152](#), [277](#), [278](#), [283](#)).
- [ST20] S. Sugimoto and S. Takada. ‘Two-Step Discontinuous Shear Thickening of Dilute Inertial Suspensions Having Soft-Core Potential’. In: *J. Phys. Soc. Jpn.* 89 (2020), p. 084803. DOI: [10.7566/JPSJ.89.084803](https://doi.org/10.7566/JPSJ.89.084803) (cited on page [300](#)).
- [Ste19] S. K. Stefanov. ‘On the basic concepts of the direct simulation Monte Carlo method’. In: *Phys. Fluids* 31 (2019), p. 067104. DOI: [10.1063/1.5099042](https://doi.org/10.1063/1.5099042) (cited on page [68](#)).
- [Sti80] S. M. Stigler. ‘Stigler’s law of eponymy’. In: *Trans. N. Y. Acad. Sci.* 39.1 Series II (1980), pp. 147–157. DOI: [10.1111/j.2164-0947.1980.tb02775.x](https://doi.org/10.1111/j.2164-0947.1980.tb02775.x) (cited on page [61](#)).
- [Sun15] C. Q. Sun. ‘Behind the Mpemba paradox’. In: *Temperature* 2 (2015), pp. 38–39. DOI: [10.4161/23328940.2014.974441](https://doi.org/10.4161/23328940.2014.974441) (cited on page [62](#)).
- [SVM07] A. Scala, T. Voigtmann, and C. De Michele. ‘Event-driven Brownian dynamics for hard spheres’. In: *J. Chem. Phys.* 126 (2007), p. 134109. DOI: [10.1063/1.2719190](https://doi.org/10.1063/1.2719190) (cited on pages [78](#), [80](#), [89](#), [313](#)).
- [SW11] R. Sedgewick and K. Wayne. *Algorithms*. 4th ed. Addison-Wesley Professional, 2011 (cited on page [76](#)).
- [Tab19] M. R. R. Tabar. *Analysis and Data-Based Reconstruction of Complex Nonlinear Dynamical Systems*. Springer Cham, 2019 (cited on page [306](#)).
- [Tak21] S. Takada. ‘Homogeneous cooling and heating states of dilute soft-core gases under nonlinear drag’. In: *EPJ Web Conf.* 249 (2021), p. 04001. DOI: [10.1051/epjconf/202124904001](https://doi.org/10.1051/epjconf/202124904001) (cited on pages [63](#), [300](#)).
- [Tan+23] Z. Tang, W. Huang, Y. Zhang, Y. Liu, and L. Zhao. ‘Direct observation of the Mpemba effect with water: Probe the mysterious heat transfer’. In: *InfoMat* 5 (2023), p. e12352. DOI: [10.1002/inf2.12352](https://doi.org/10.1002/inf2.12352) (cited on page [62](#)).
- [Tar08] L. Tartar. ‘The Hilbert Expansion’. In: *From Hyperbolic Systems to Kinetic Theory: A Personalized Quest*. Berlin, Heidelberg: Springer Berlin Heidelberg, 2008, pp. 233–237. DOI: [10.1007/978-3-540-77562-1_30](https://doi.org/10.1007/978-3-540-77562-1_30) (cited on page [52](#)).
- [Tat+09] S. Tatsumi, Y. Murayama, H. Hayakawa, and M. Sano. ‘Experimental study on the kinetics of granular gases under microgravity’. In: *J. Fluid Mech.* 641 (2009), pp. 521–539. DOI: [10.1017/S002211200999231X](https://doi.org/10.1017/S002211200999231X) (cited on page [299](#)).
- [Tem81] S. Temkin. *Elements of Acoustics*. Wiley, 1981 (cited on page [287](#)).

- [THH22] S. Takada, K. Hara, and H. Hayakawa. ‘Kinetic theory of discontinuous shear thickening of a moderately dense inertial suspension of frictionless soft particles’. In: *arXiv:2207.05752* (2022). DOI: [10.48550/arXiv.2207.05752](https://doi.org/10.48550/arXiv.2207.05752) (cited on page 300).
- [THS21] S. Takada, H. Hayakawa, and A. Santos. ‘Mpemba effect in inertial suspensions’. In: *Phys. Rev. E* 103 (2021), p. 032901. DOI: [10.1103/PhysRevE.103.032901](https://doi.org/10.1103/PhysRevE.103.032901) (cited on pages 63, 65, 85, 282).
- [Tor+19] A. Torrente, M. A. López-Castaño, A. Lasanta, F. Vega Reyes, A. Prados, and A. Santos. ‘Large Mpemba-like effect in a gas of inelastic rough hard Spheres’. In: *Phys. Rev. E* 99 (2019), p. 060901(R). DOI: [10.1103/PhysRevE.99.060901](https://doi.org/10.1103/PhysRevE.99.060901) (cited on pages 13, 63, 64, 85, 213, 214, 289, 297).
- [TP19] N. Topic and T. Pöschel. ‘Inelastic collapse of perfectly inelastic particles’. In: *Commun. Phys.* 2 (2019), p. 85. DOI: [10.1038/s42005-019-0184-y](https://doi.org/10.1038/s42005-019-0184-y) (cited on page 77).
- [TYR23] G. Teza, R. Yaacoby, and O. Raz. ‘Relaxation shortcuts through boundary coupling’. In: *Phys. Rev. Lett* 131 (2023), p. 017101. DOI: [10.1103/PhysRevLett.131.017101](https://doi.org/10.1103/PhysRevLett.131.017101) (cited on page 62).
- [VAZ11] K. Vollmayr-Lee, T. Aspelmeier, and A. Zippelius. ‘Hydrodynamic correlation functions of a driven granular fluid in steady state’. In: *Phys. Rev. E* 83 (2011), p. 011301. DOI: [10.1103/PhysRevE.83.011301](https://doi.org/10.1103/PhysRevE.83.011301) (cited on page 46).
- [VD21] N. Vadakkayila and S. K. Das. ‘Should a hotter paramagnet transform quicker to a ferromagnet? Monte Carlo simulation results for Ising model’. In: *Phys. Chem. Chem. Phys.* 23 (2021), pp. 11186–1190. DOI: [10.1039/d1cp00879j](https://doi.org/10.1039/d1cp00879j) (cited on page 62).
- [VGK14] F. Vega Reyes, V. Garzó, and N. Khalil. ‘Hydrodynamic granular segregation induced by boundary heating and shear’. In: *Phys. Rev. E* 89 (2014), p. 052206. DOI: [10.1103/PhysRevE.89.052206](https://doi.org/10.1103/PhysRevE.89.052206) (cited on page 300).
- [VK15] M. Vynnycky and S. Kimura. ‘Can natural convection alone explain the Mpemba effect?’ In: *Int. J. Heat Mass Transf.* 80 (2015), pp. 243–255. DOI: [10.1016/j.ijheatmasstransfer.2014.09.015](https://doi.org/10.1016/j.ijheatmasstransfer.2014.09.015) (cited on page 62).
- [VM10] M. Vynnycky and S. L. Mitchell. ‘Evaporative cooling and the Mpemba effect’. In: *Heat Mass Transf.* 46 (2010), pp. 881–890. DOI: [10.1007/s00231-010-0637-z](https://doi.org/10.1007/s00231-010-0637-z) (cited on page 62).
- [VM12] M. Vynnycky and N. Maeno. ‘Axisymmetric natural convection-driven evaporation of hot water and the Mpemba effect’. In: *Int. J. Heat Mass Transf.* 55 (2012), pp. 7297–7311. DOI: [10.1016/j.ijheatmasstransfer.2012.07.060](https://doi.org/10.1016/j.ijheatmasstransfer.2012.07.060) (cited on page 62).

- [Vol+10] G. Volpe, L. Helden, T. Brettschneider, J. Wehr, and C. Bechinger. ‘Influence of Noise on Force Measurements’. In: *Phys. Rev. Lett.* 104 (2010), p. 170602. doi: [10.1103/PhysRevLett.104.170602](https://doi.org/10.1103/PhysRevLett.104.170602) (cited on page 306).
- [VS15] F. Vega Reyes and A. Santos. ‘Steady state in a gas of inelastic rough spheres heated by a uniform stochastic force’. In: *Phys. Fluids* 27 (2015), p. 113301. doi: [10.1063/1.4934727](https://doi.org/10.1063/1.4934727) (cited on pages 47, 214, 289).
- [VSG10] F. Vega Reyes, A. Santos, and V. Garzó. ‘Non-Newtonian Granular Hydrodynamics. What Do the Inelastic Simple Shear Flow and the Elastic Fourier Flow Have in Common?’ In: *Phys. Rev. Lett.* 104 (2010), p. 028001. doi: [10.1103/PhysRevLett.104.028001](https://doi.org/10.1103/PhysRevLett.104.028001) (cited on page 279).
- [VSK14a] F. Vega Reyes, A. Santos, and G. M. Kremer. ‘Properties of the Homogeneous Cooling State of a Gas of Inelastic Rough Particles’. In: *AIP Conf. Proc.* 1628 (2014), pp. 494–501. doi: [10.1063/1.4902634](https://doi.org/10.1063/1.4902634) (cited on page 284).
- [VSK14b] F. Vega Reyes, A. Santos, and G. M. Kremer. ‘Role of roughness on the hydrodynamic homogeneous base state of inelastic spheres’. In: *Phys. Rev. E* 89 (2014), p. 020202(R). doi: [10.1103/PhysRevE.89.020202](https://doi.org/10.1103/PhysRevE.89.020202) (cited on pages 13, 44, 45, 176, 214, 283–285).
- [Wag92] W. Wagner. ‘A convergence proof for Bird’s direct simulation Monte Carlo method for the Boltzmann equation’. In: *J. Stat. Phys.* 66 (1992), pp. 1011–1044. doi: [10.1007/BF01055714](https://doi.org/10.1007/BF01055714) (cited on page 68).
- [Wal77] J. Walker. ‘Hot water freezes faster than cold water. Why does it do so?’ In: *Sci. Am.* 237 (1977), pp. 246–257. doi: [10.1038/scientificamerican0977-246](https://doi.org/10.1038/scientificamerican0977-246) (cited on page 62).
- [Wee08] K. van der Weele. ‘Granular gas dynamics: how Maxwell’s demon rules in a non-equilibrium system’. In: *Contemp. Phys.* 49 (2008), pp. 157–178. doi: [10.1080/00107510802141226](https://doi.org/10.1080/00107510802141226) (cited on page 7).
- [Wei14] M. D. Weinberg. ‘Direct Simulation Monte Carlo for astrophysical flows – I. Motivation and methodology’. In: *Mon. Not. Roy. Astron. Soc.* 438 (2014), pp. 2995–3006. doi: [10.1093/mnras/stt2406](https://doi.org/10.1093/mnras/stt2406) (cited on page 68).
- [Wil+20] C. Wilson, A. Grubler, N. Bento, S. Healey, S. de Stercke, and C. Zimm. ‘Granular technologies to accelerate decarbonization: Smaller, modular energy technologies have advantages’. In: *Science* 368 (2020), pp. 36–39. doi: [10.1126/science.aaz8060](https://doi.org/10.1126/science.aaz8060) (cited on page 6).
- [Wil76] J.C. Williams. ‘The segregation of particulate materials. A review’. In: *Powder Techn.* 15 (1976), pp. 245–251. doi: [10.1016/0032-5910\(76\)80053-8](https://doi.org/10.1016/0032-5910(76)80053-8) (cited on page 7).

- [Wil96] D. R. M. Williams. ‘Driven granular media and dissipative gases: correlations and liquid-gas phase transitions’. In: *Physica A* 233 (1996), pp. 718–729. DOI: [10.1557/PROC-463-325](https://doi.org/10.1557/PROC-463-325) (cited on page 288).
- [WM96] D. R. M. Williams and F. C. MacKintosh. ‘Driven granular media in one dimension: Correlations and equation of state’. In: *Phys. Rev. E* 54 (1996), R9–R12. DOI: [10.1103/PhysRevE.54.R9](https://doi.org/10.1103/PhysRevE.54.R9) (cited on page 288).
- [WOB88] B. Wojciechowski, I. Owczarek, and G. Bednarz. ‘Freezing of aqueous solutions containing gases’. In: *Cryst. Res. Technol.* 23 (1988), pp. 843–848. DOI: [10.1002/crat.2170230702](https://doi.org/10.1002/crat.2170230702) (cited on page 62).
- [YH20] Z.-Y. Yang and J.-X. Hou. ‘Non-Markovian Mpemba effect in mean-field systems’. In: *Phys. Rev. E* 101 (2020), p. 052106. DOI: [10.1103/PhysRevE.101.052106](https://doi.org/10.1103/PhysRevE.101.052106) (cited on page 62).
- [YH22] Z.-Y. Yang and J.-X. Hou. ‘Mpemba effect of a mean-field system: The phase transition time’. In: *Phys. Rev. E* 105 (2022), p. 014119. DOI: [10.1103/PhysRevE.105.014119](https://doi.org/10.1103/PhysRevE.105.014119) (cited on pages 62, 85).
- [YSS20] P. Yu, M. Schröter, and M. Sperl. ‘Velocity Distribution of a Homogeneously Cooling Granular Gas’. In: *Phys. Rev. Lett.* 124 (2020), p. 208007. DOI: [10.1103/PhysRevLett.124.208007](https://doi.org/10.1103/PhysRevLett.124.208007) (cited on pages 8, 22, 37, 38, 280, 283, 299).
- [Yu+21] P. Yu, M. Schröter, M. Adachi, and M. Sperl. ‘Magnetically heated granular gas in a low-gravity environment’. In: *EPJ Web Conf.* 249 (2021), p. 04002. DOI: [10.1051/epjconf/202124904002](https://doi.org/10.1051/epjconf/202124904002) (cited on page 299).
- [Yvo35] J. Yvon. ‘La théorie statistique des fluides et l’équation d’état’. In: *Actual. Sci. & Indust.* 203 (1935) (cited on page 16).
- [ZH21] B. Zhang and Y. Huang. ‘Seismic shaking-enhanced impact effect of granular flow challenges the barrier design strategy’. In: *Soil Dyn. Earthq. Eng.* 143 (2021), p. 106655. DOI: [10.1016/j.soildyn.2021.106655](https://doi.org/10.1016/j.soildyn.2021.106655) (cited on page 6).
- [Zha+14] X. Zhang, Y. Huang, Z. Ma, Y. Zhou, J. Zhou, W. Zheng, Q. Jiang, and C. Q. Sun. ‘Hydrogen-bond memory and water-skin supersolidity resolving the Mpemba paradox’. In: *Phys. Chem. Chem. Phys.* 16 (2014), pp. 22995–23002. DOI: [10.1039/C4CP03669G](https://doi.org/10.1039/C4CP03669G) (cited on page 62).
- [Zip06] A. Zippelius. ‘Granular gases’. In: *Physica A* 369 (2006), pp. 143–158. DOI: [10.1016/j.physa.2006.04.012](https://doi.org/10.1016/j.physa.2006.04.012) (cited on page 283).
- [Żuk+22] P. J. Żuk, K. Makuch, R. Hłyst, and A. Maciołek. ‘Transient dynamics in the outflow of energy from a system in a nonequilibrium stationary state’. In: *Phys. Rev. E* 105 (2022), p. 054133. DOI: [10.1103/PhysRevE.105.054133](https://doi.org/10.1103/PhysRevE.105.054133) (cited on page 62).

Index

B

- Balance equations 45, 55, 321
 - of the mass density 322
 - of the momentum density ... 322
 - of the temperature 324
- Boltzmann collisional operator .. 20, 26,
27, 31, 32, 51
 - for EHS 21, 277
 - for IHS 23
 - for IRHS 26, 285

C

- Chapman–Enskog method 13, 38, 45, 53,
241, 242, 284–286, 297
- Coefficient of normal restitution 8, 11, 20,
22, 119, 151–153, 175, 213, 241,
281, 295, 314, 317
- Coefficient of tangential restitution 8, 24,
175, 213, 241, 283
- Collisional moments 35
 - for IHS 35–37
 - for IRHS . 41, 42, 45, 176, 214, 284
- Cooling rate 33, 36, 55
 - for IRHS 242
 - in the IHS model ... 33–37, 120, 151,
282, 283
 - in the IRHS model 39, 40, 242, 286
- Critical length 243, 287
- Critical wave number .. 243, 287, 288

D

- Drag coefficient 27, 152
 - velocity-dependent .. 28, 29, 46, 85,
152

H

- Haff’s law 33, 34, 40, 77, 120

Hydrodynamic

- description 8, 13, 14, 54
- fields 49, 53, 54, 241, 242, 287, 321
- length scale 53
- modes 287, 288
- regime 53, 54
- stage 87, 88
- time 53

I

- Inelastic collapse 77, 78
- Instability 9, 46, 243
 - clustering ... 9, 45, 51, 77, 78, 243
 - vortex 77
 - vortices 9, 45, 243

L

- Linear stability analysis .. 44, 45, 243

M

- Material time-derivative 54, 322

N

- Nonequilibrium entropy . 47, 48, 50, 51,
63, 64, 86, 119–121, 277, 280, 281,
294, 295
- Nonequilibrium steady state 30,
295–297

P

- Peculiar velocity 54, 322, 323

T

- Temperature ... 6, 16, 27, 59–64, 69, 277,
278
 - field 49, 54
 - granular .. 8, 9, 12, 29, 33–36, 38, 45,
54, 55, 60, 61, 151–153, 282

mean granular 38–40, 54, 55,
 213–215, 241, 242, 297, 321, 323,
 324
 molecular 29, 32, 35, 60
 noise 30, 213, 297
 nonequilibrium . . . 60, 64, 66, 86–88,
 152, 277, 278, 294, 316
 of the thermal bath 11, 12, 27–29, 32,
 46, 59, 60, 78, 85, 86, 88, 89, 151,
 152, 277–279, 281, 293, 294, 306,
 307, 309, 311, 314, 315
 overshoot . . 64, 88, 89, 214, 215, 278,
 279, 290, 291, 294, 297
 picture 66
 ratios 40
 rotational 38–40, 323, 324
 rotational-to-translational ratio . 40,
 43, 47, 175, 176, 213, 214, 243,
 284, 297
 steady-state 46, 47, 64, 152, 214, 315,
 317
 translational 38–40, 242, 323, 324
 Transport coefficient . . . 9, 13, 45, 54, 55,
 241
 bulk viscosity 9, 242, 286

Dufour-like coefficient 9, 242, 286
 of the cooling rate 242, 286
 shear viscosity 9, 242, 286
 thermal conductivity 9, 286

V

VDF *see* Velocity distribution function
 Velocity distribution function
 cumulants . . . 36, 37, 44–47, 51, 86
 equilibrium 32, 86
 Gamma 87
 kinetic 87
 local-equilibrium 86, 87
 marginal 13, 43, 45
 Maxwellian 32, 33, 35–37, 46, 49, 50,
 52, 53, 86
 moments . . 32, 35–37, 40, 42, 43, 60,
 86
 of the HCS 12, 35–37, 44, 53
 one-particle . 12, 18, 33, 36, 53, 54
 reduced 34, 35, 39, 41
 reference 50
 steady-state 46
 time-dependent 12, 32, 39, 86
 two-particle 16, 18